Materials Issues and Modeling for Device Nanofabrication

Symposia held November 29–December 2, 1999, Boston, Massachusetts, U.S.A.

EDITORS:

Lhadi Merhari
CERAMEC
Limoges, France

Luc T. Wille
Florida Atlantic University
Boca Raton, Florida, U.S.A.

Kenneth E. Gonsalves
University of Connecticut
Storrs, Connecticut, U.S.A.

Mark F. Gyure
Hughes Research Laboratories
Malibu, California, U.S.A.

Shinji Matsui
Himeji Institute of Technology
Hyogo, Japan

Lloyd J. Whitman
Naval Research Laboratory
Washington, D.C., U.S.A.

MRS

2 0000082 4 103

Single article reprints from this publication are available through
University Microfilms Inc., 300 North Zeeb Road, Ann Arbor, Michigan 48106

CODEN: MRSPDH

CONTENTS

ADVANCED TECHNIQUES FOR SUB-100 nm
RESOLUTION LITHOGRAPHY AND
MOLECULAR ELECTRONICS

*Invited Paper

EPITAXIAL GROWTH AND MORPHOLOGY

NOVEL CONCEPTS OF RESISTS
FOR NANOLITHOGRAPHY

*Invited Paper

ATOMIC SCALE CHARACTERIZATION
AND MEASUREMENT

MODELING AND ATOMISTIC SIMULATIONS

*Invited Paper

NANODEVICES AND NANOSTRUCTURES

*Invited Paper

PREFACE

The exploding market of information technology requires ultra-high-speed integrated circuits, which imposes formidable challenges in terms of nanofabrication, advanced materials, atomic scale measurements and modeling. The enormous costs of next-generation lithographic machines to mass produce integrated circuits with sub-100 nm resolution justify alternative approaches where the use of advanced materials and techniques for nanofabrication including epitaxial growth, and their powerful modeling, can lead to more cost-effective strategies.

This volume contains most of the papers that were presented during Symposium J, "Advanced Materials and Techniques for Nanolithography," and Symposium N, "Atomic Scale Measurements and Atomistic Models of Epitaxial Growth and Lithography," at the 1999 MRS Fall Meeting in Boston, Massachusetts. Because of the complementary nature of the two subject matters, particularly in their applicability to device nanofabrication, it was felt that a combined proceedings volume offered the best way to present the findings in a unified and comprehensive manner. The editors trust that the reader will find here a nice overview of the state of the art, both theoretical and experimental, as well as an indication of the future trends and remaining challenges in this technologically important field.

Symposium J focused on the materials aspect of nanolithography by highlighting the advances in resist technology, which is now increasingly recognized as a bottleneck for sub-100 nm resolution. Indeed, whatever the degree of sophistication of a lithographic machine, a non-optimum resist can completely ruin the overall lithographic process. Major papers describing new concepts of resists based on various nanocomposites and particularly on ordered polymer/inorganic structures to decrease electron proximity effects are included in this volume.

Advances in lithographic techniques such as X-ray lithography and electron beam lithography are described, while a special emphasis is put on ion projection lithography. Indeed, ion projection lithography is a very promising and versatile technique which has benefitted from more research and development efforts in Europe than in the U.S.A. Generally regarded as the next revolution in electronics, molecular electronics has been covered bearing in mind that future lithographies should aim at taking up the challenge of "molecular"-scale interconnections. For the sake of completeness, contributions exemplifying the fabrication of real nanostructures and useful nanodevices such as nanotransistors are included.

The papers from Symposium N contained in this volume focus on recent advances made in both atomic scale measurements and models of epitaxial growth as well as lithography. They strike a nearly equal balance between theoretical and experimental approaches. Scanning probe microscopy is the dominant experimental theme, although other techniques are also represented. As described here, advances in plan view and cross

sectional techniques make it clear that characterization of device materials has now reached the point where feedback from such measurements can be used to improve device growth. The theory papers are divided primarily between kinetic Monte Carlo (KMC) simulations of growth and ab initio calculations of basic surface properties. A few papers discuss how to combine ab initio data for transition energies with KMC simulations, and this appears to be a promising approach for the development of robust models for growth. Validation of such models by scanning probe microscopy is now at hand and promises to be an exciting area for the future, offering rich collaboration between theorists and experimentalists, ultimately leading to a faster design cycle, reduced costs, and more efficient devices.

Lhadi Merhari
Luc T. Wille
Kenneth E. Gonsalves
Mark F. Gyure
Shinji Matsui
Lloyd J. Whitman

January 2000

ACKNOWLEDGMENTS

MATERIALS RESEARCH SOCIETY SYMPOSIUM PROCEEDINGS

MATERIALS RESEARCH SOCIETY SYMPOSIUM PROCEEDINGS

Prior Materials Research Society Symposium Proceedings available by contacting Materials Research Society

**Advanced Techniques for
Sub-100 nm Resolution Lithography
and Molecular Electronics**

ION PROJECTION LITHOGRAPHY FOR NANO PATTERNING

A. HEUBERGER and W. BRUENGER
Fraunhofer-Institute for Silicon-Technology (ISiT)
Fraunhofer Str. 1, D- 25524 Itzehoe, Germany, Phone: +49-4821-17-4211
Fax: +49-4821-17-4250, e-mail: bruenger @ isit.fhg.de

ABSTRACT

As a result of continuous improvement of the resist process, the experimental ion projector in the Fraunhofer Institute in Berlin (manufactured by Ion Microfabrication Systems, IMS, Vienna) has been able to print 75 nm lines and spaces into 180 nm thick standard DUV resist UV II HS without pattern collapse. A new wafer flow process for more reliable open stencil mask making was developed by IMS –Chips, Stuttgart (Germany), based on SOI wafers. Resistless direct surface modification by He and Xe ions has been tested on metallic and magnetic films in the Berlin projector. This method opens up a new possibility for the production of patterned media for future magnetic storage disks.

INTRODUCTION

In the European MEDEA Project for the development of ion projection lithography (IPL) for next generation lithography (NGL) the Fraunhofer Institute ISiT has taken the part of resist process development. Standard deep UV chemically amplified resists have been found very useful also for ion irradiation and the latest results are reported in the following.

However, in special cases the contact of a resist with the surface to be structured is not wanted. This situation may arise, because of chemical reactions with the resist (high temperature super-conductors) or the fear of topography change and residues after resist removal (thin magnetic films for storage media). Ions have the unique feature that they can directly modify a surface without the need for a resist. Compared to electrons of the same energy, ions deposit their energy in a shorter range near the surface because they do not penetrate as much. Since direct ion processing takes place in vacuum, it can be useful for all substrates which cannot be exposed to air for example in the case of an intermediate step in in-situ processing.

In order to demonstrate this technology of direct ion processing, tests have been performed in the Berlin ion projector to structure metallic and magnetic films. For the production of magnetic nano dots other techniques are competing like optical interference lithography [1,2], e-beam lithography [3], and nano imprint lithography [4,5]. All of these methods use some kind of resist process which is not desirable to keep the topography of a surface unchanged. This is extremely important for magnetic disks with a surface roughness of a few nanometers.

EXPERIMENTAL

Exposures have been performed with the ion projector IPLM-02 at the Fraunhofer Institute in Berlin [6]. H^+ or He^+ ions pass an open stencil mask at a beam energy of 3.5 keV and are accelerated behind the mask to 75 keV(see Fig. 1). Mask features are projected with 8.7 times demagnification via the ion optical lens system onto the wafer. The original duoplasmatron ion source has been exchanged with a multicusp ion source developed at the Lawrence Berkeley Laboratory with reduced energy spread of appr. 2 eV [7]. This reduces chromatic aberration of

3

the lens system and allows the printing of 50 nm isolated lines [8]. Nested lines and spaces of this size have been difficult to print because of pattern collapse and needed further development of the resist process.

ION PROJECTION STEPPER
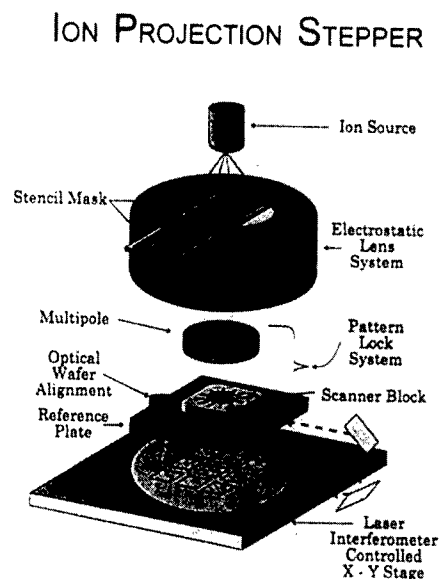
Figure 1: Principle set-up of the ion projector

SOI WAFER FLOW MASK PROCESS

Normally the production process of an open stencil mask starts with e-beam writing on the already thinned 2-3 μm thick Si mask membrane. The membrane handling is not compatible with standard wafer processing equipment. Therefore, a new process has been developed by IMS-Chips, Stuttgart and Infineon, Dresden, which employs e-beam writing of the mask features and etching on the full wafer. An SOI-wafer (Silicon On Insulator) is used with the embedded oxide layer serving as etch stop [9].The single process steps are demonstrated in Fig. 2. Trench etching of the stencil pattern is performed in a STS (Surface Technology Systems) plasma etcher. A retrograde profile of the stencils which avoids scattering of ions on the sidewalls is created by using the gas chopping etch technique, which is a controlled balance between sidewall passivation and in depth etching.

The membrane etching is also performed by a dry etch process up to a preliminary Si membrane thickness of 25 μm with final thinning in a tetramethylammoniumhydroxide (TMAH) solution. During this step the sensitive structures on the frontside of the wafer are protected by a water soluble wax.

In order to avoid ion implantation of the Si stencils during ion bombardment in the exposure process, which leads to swelling and deformation, a carbon protective layer is finally coated onto the finished mask. For this purpose a novel method of forming very low stress

4

carbon layers based on direct RF sputter coating with nitrogen added to the argon sputter gas has been developed [10].

MF-1: e-beam or laser beam lithography

MF-4: removal of all remaining layers

MF-2: trench etching of stencil pattern & resist stripping

MF-5: ion beam protective layer (Carbon) deposition

MF-3: deposition of etch protective layer and membrane etching

MF-6: Carbon etching
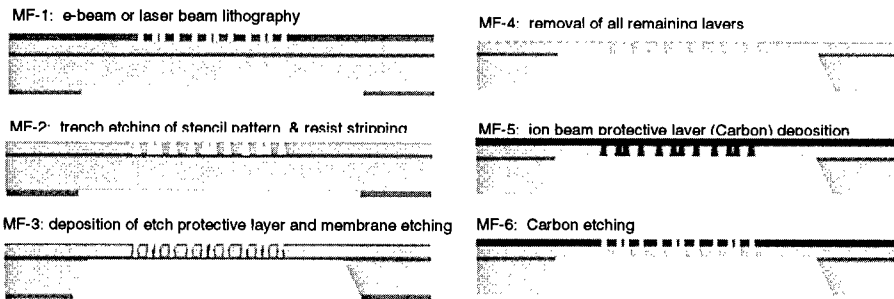
Figure 2 : SOI wafer-flow stencil mask fabrication process developed at IMS-Chips, Stuttgart.

gate forrest metal layer with
400nm support grid

350nm - 400nm isolated lines and
lines & spaces
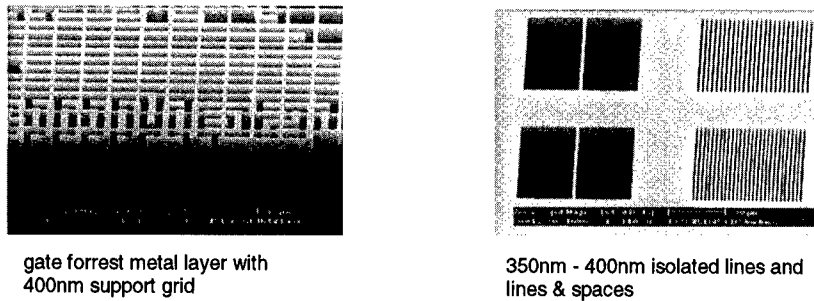
Figure 3 : Details of open stencil mask fabricated with the SOI wafer flow process

Figure 3 shows details of a finished mask with 350 – 400 nm isolated lines as well as lines and spaces, etched uniformly into a 3µm thick membrane. Even 100 nm isolated lines and 200 nm lines and spaces have been demonstrated so that after 4 times demagnification, the reduction factor planned for the production tool, sub-50 nm structures are achievable on the wafer.

RESIST PROCESS DEVELOPMENT

Resist exposures have been performed by ISiT in the Berlin IPLM-02 projector.The best results were obtained so far with the standard DUV chemically amplified resist UV II HS from Shipley. The sensitivity of this resist for 75 keV H^+ ion exposure is 1×10^{12} ions/cm², which corresponds to 0.15 µC/cm² [11].

5

The resist shows a contrast number higher than 10 and a dose gap between positive and negative development of nearly two orders of magnitude.

The standard resist treatment of UV II HS resist is optimized for optical exposure (smoothing of standing waves) of quarter micron features in 600 nm thick resist. In order to use its high resolution capability under ion exposure and avoid pattern collapse and line edge roughness, the standard resist treatment had to be modified. This optimization was accompanied by a simulation of the resist process with a model originally derived for the simulation of APEX-E resist [12].

As a result 75 nm wide lines and spaces can now be printed without pattern collapse (Fig. 4). The corresponding mask fabricated by IMS-Chips showed perfect edge quality under SEM inspection. The UV II HS resist has been diluted so that a smaller resist thickness of 180 nm could be obtained. The resist has also been made less sensitive ($0.46\ \mu C/cm^2$) by lowering the post exposure bake temperature from 140°C to 125°C. This reduces movement of the radiation generated acid and improves resolution. Because of the higher dose it also reduces edge roughness.

Stencil Mask   Wafer

650 nm L/S   →   8.7x reduction → 75 nm L/S
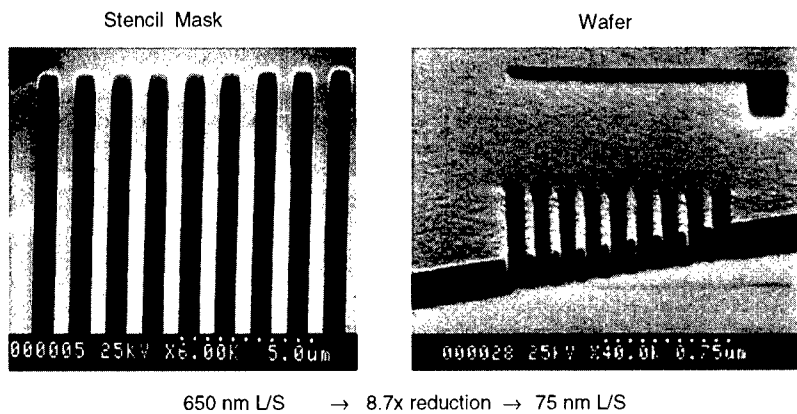
Figure 4: Ion projection exposure (Fraunhofer- ISiT) in 180 nm thick Shipley DUV resist
        UV II HS with 75 keV He$^+$ ions, dose : 0.46 μC/cm^2,
        Stencil mask fabricated by IMS-Chips, Stuttgart.

No proximity effect is visible at the line ends in figure 4 even though the resist has been removed by a second exposure of equal dose in the front part of the picture to allow SEM side view.

The high sensitivity of chemically amplified resists is a concern because statistical fluctuations in the ion beam can create line edge roughness. It is difficult to extract numerical data characterizing roughness from lines less than 100 nm wide by SEM inspection. Therefore, the printing of dot matrices has been investigated for this purpose. With decreasing dose statistical fluctuations translate into missing dots which can easily be counted. In figure 5 an evaluation of the printing probability against ion dose is plotted [13]. As expected the curve

follows a Poisson distribution . A number of 115 ions is needed to create a 50% defect probability. A number of 220 ions per 90 nm dot corresponds to a dose of 0.46 µC/cm², which is the dose used in figure 4. This confirms that in the resolution range around 90 nm this dose is sufficient for delineation. Going to smaller features the dose per pixel has to be kept constant, which means that the dose has to be increased accordingly.
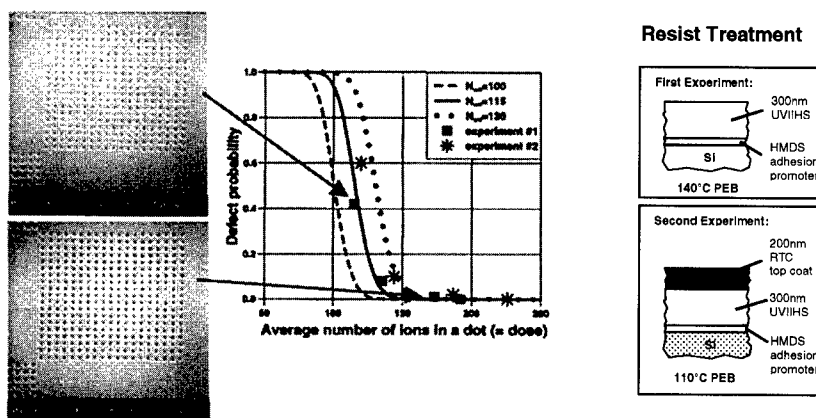
Figure 5: IPL exposure dose versus defect probability of printed dot matrices for two resist treatments.

IPL MILLING WITH Xe $^+$ IONS

Ions have the property of direct surface modification, and if the ion beam is structured like in ion projection a whole surface area can be treated in parallel. In this way a pattern can be transferred into a sample in an easy one step process without using a resist. In order to test this technique the light ions normally used in the multicusp ion source have been replaced by the heavier Xe species without any change in emission stability or uniformity.

First milling tests performed in a 35 nm thick Au film with a dose of 2×10^{15} Xe$^+$/cm² at 75 keV resulted in a milling depth of 8 nm as demonstrated by white light interferometry (Fig. 6).
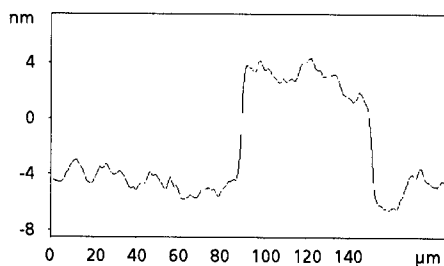
Figure 6: Surface depth profile of an Au film patterned by Xe ion milling .

7

A high resolution pattern contained narrowest lines with a line width down to 130nm (Fig.7) [14]. The apparent roughness of the gold film seems to be due to its grain structure. This encouraging result shows the promises of structured ion milling of magnetoresistive materials for sensor applications.
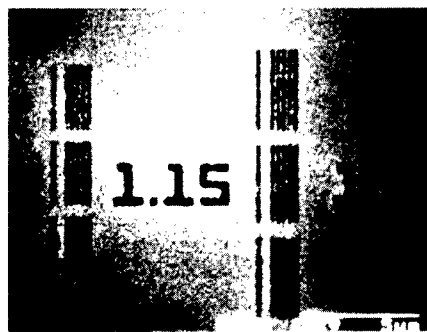
Figure 7: Xe$^+$ ion milling with IPL in polycrystalline Au film .
Smallest line width: 130 nm.

IPL PATTERNING OF MAGNETIC FILMS WITH He $^+$ IONS

The increase of storage density of magnetic disks of 100% per year is gained by a continuous shrinkage of the size of the magnetic bit cell. This process comes to an end, when the superparamagnetic limit is reached and the magnetic bits start to flip at room temperature. The superparamagnetic limit is related to the volume of a bit cell. One concept to overcome the situation is to go to prepatterned media, with bit cells separated by nonmagnetic or magnetically altered material so that the interaction of bits is prevented. We started experiments with IPL which has the ability of direct surface structuring without the need for a resist , an advantage compared to competing technologies.

Samples of chemically ordered FePt magnetic films have been supplied by Bruce Terris of the IBM, Almaden Research Center. The film preparation has been described previously in reference [15]. Under ion bombardment these layers change their magnetic properties. Experiments at Almaden with a mask in direct contact with Co/Pt multilayer magnetic films had demonstrated that a dose of 10^{16} N$^+$ ions /cm^2 was necessary to switch the magnetization direction [16]. This is a factor of 10^4 more compared to resist exposure. Therefore, in the exposure experiment in the IPLM-02 System in Berlin the He$^+$ ion intensity has been increased by a factor of 10. The discharge current in the multicusp source rose from 0.6 to 6 A. A mask with an arrangement of dots has been demagnified 8.7 times and projected onto the sample. Exposure time was 1000 s.

Irradiated samples with a dose of 10^{16} He$^+$ / cm^2 have been investigated at IBM with atomic force and magnetic force microscopy. Figure 8 shows a picture taken in magnetic force mode with 340 nm wide magnetic features[14]. With a new mask having smaller holes the ion projector should be able to print dots in the 50 nm range. This corresponds to a storage density of 64 Gbits/ in^2, assuming equal dots and spaces. The arrangement of dots in the mask, which is written by e-beam can be done with rotational symmetry. In this way the technique of rotating

disk drives can survive, which is not possible with rectangular dot arrangements created by laser interferometry.

0   5μm
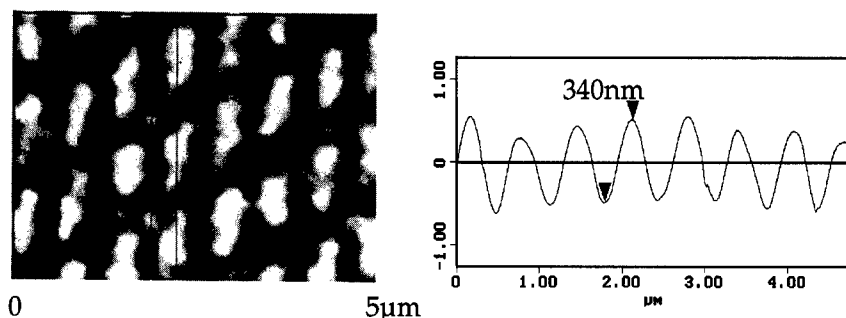
Figure 8: Magnetic force image of a FePt film showing magnetic dots structured, by resistless IPL with 10^{16} He$^+$/ cm^2 at 75 keV; The averaged intensity profile demonstrates a dot size of 340 nm.

Investigations with atomic force microscopy have shown that the topography change due to the IPL process is in the range of 2 nm. This confirms that IPL is very suitable for this application.

CONCLUSION

With the development of resistless ion nano structuring a second application field for ion projection lithography has been opened up.The method is specially suited for defect sensitive in – situ processing. This is very suitable for the fabrication of nano dots for magnetic storage devices. Improvements in ion source current density and in the sensitivity of magnetic films against ion exposure are under way to make this technique economical.

ACKNOWLEDGMENT

REFERENCES

1.   E.H. Anderson, C.M. Horwitz, H.I. Smith, Appl. Phys. Lett. **43**, 874 (1983)

2.   C.O. Bolzler, Ch.T. Harris, S. Rabe, D.D. Rathman, H.I. Smith, J. Vac. Sci. Techn. B **12**, 629 (1994)

3.   P.R. Krauss, S.Y. Chou, J. Vac .Sci. Techn. B **13**, 2850 (1995); R.M.H. New, R.F.W. Pease, R.L. White, J. Vac. Sci. Techn. B **13**,1089 (1995)

4. L. Kong, L. Zhuang, S.Y. Chou, IEEE Transactions on Magnetics **33**, 3019 (1997)

5. W. Wu, B. Cui, X. Sun, W.Zhang, L. Zhuang, L. Kong, S.Y. Chou, J. Vac. Sci. Techn.
    B **16** (6), 3825 (1998)

6. L.-M. Buchmann, U. Schnakenberg, M. Torkler, H. Löschner, G. Stengl, W.Fallmann,
    G. Stangl, E. Cekan, J. of Microelectromechanical Systems. Vol.1(3),116 (1992)

7. Y. Lee, R.A. Gough, K.N. Leung, J. Vujic, M.D. Williams, N. Zahir, W. Fallmann,
    M. Torkler, W.H. Bruenger, J. Vac. Sci. Techn. B **16** (6) , 3367 (1998)

8. W.H. Bruenger, M. Torkler, K.N. Leung, Y. Lee, M.D. Williams, H. Loeschner, G. Stengl,
    W. Fallmann, F. Paschke, G. Stangl, I.W. Rangelow, P. Hudek, Microelectronic
    Engineering **46**, 477 (1999)

9. F. Letzkus, J. Butschke, B. Höfflinger, M. Irmscher, C. Reuter, R. Springer, A. Ehrmann
    J. Manthuni, MNE-99, Microelectronic Engineering, in press

10. P. Hudek, P. Hrkut, M. Drzik, I. Kostic, M. Belov, J. Torres, J. Wasson, J.C. Wolfe,
    A. Degen, I.W. Rangelow, J. Voight, J. Butschke, F. Letzkus, R. Springer, A. Ehrmann,
    R. Kaesmaier, K. Kragler,J. Mathuni, H. Loeschner, EIPBN-99, J. Vac. Sci. Techn. Nov/
    Dec (1999) in press

11. W.H. Bruenger, H. Buschbeck, E. Cekan, S. Eder, T.H. Fedynyshyn, W.G. Hertlein,
    P. Hudek,I. Kostic,H. Loeschner, I.W. Rangelow, M. Torkler, Microelectronic
    Engineering **41/42**, 237, (1998)

12. W. Henke , M. Torkler , EIPBN-99, J. Vac. Sci. Techn., Nov/ Dec (1999) in press

13. W.H. Bruenger, M. Torkler, M. Weiss, H. Loeschner, K.N. Leung, Y. Lee, P. Hudek,
    I. W. Rangelow, G. Stangl, W. Fallmann, EIPBN-99, J. Vac. Sci. Techn., Nov/ Dec
    (1999) in press

14. W.H. Bruenger, M. Torkler, B.D. Terris, H. Rothuizen, P. Vettiger, G. Stangl,
    W. Fallmann, MNE-99, Microelectronic Engineering, in press

15. B.D. Terris, L. Folks, D. Weller, J.E.E. Baglin, J. Appl. Phys., to be published

16. B.D. Terris, L. Folks, D. Weller, J.E.E. Baglin, A.J. Kellock, H. Rothuizen,
    P. Vettiger, Appl. Phys. Lett. **75**, 403 (1999)

SOFT X-RAYS FOR DEEP SUB-100 NM LITHOGRAPHY, WITH AND WITHOUT MASKS

Henry I. Smith, D. J. D. Carter, J. Ferrera, D. Gil, J. Goodberlet, J. T. Hastings, M. H. Lim, M. Meinhold, R. Menon, E. E. Moon, C. A. Ross, T. Savas, M. Walsh, F. Zhang

Research Laboratory of Electronics
Nanostructures Laboratory
Massachusetts Institute of Technology
77 Massachusetts Avenue
Cambridge, MA 02139 USA

ABSTRACT

The development of micro- and nanofabrication, their applications, and their dependent industries has progressed to a point where a bifurcation of technology development will likely occur. On the one hand, the semiconductor industry (at least in the USA) has decided to develop EUV and SCALPEL to meet its future needs. Even if the semiconductor industry is successful in this (which is by no means certain) such tools will not be useful in most other segments of industry and research that will employ nanolithography. As examples, MEMS, integrated optics, biological research, magnetic information storage, quantum-effect research, and multiple applications not yet envisioned will not employ the lithography tools of the semiconductor industry, either because they are too expensive, insufficiently flexible, or lacking in accuracy and spatial-phase coherence. Of course, direct-write electron-beam lithography can meet many of these non-semiconductor-industry needs, but in other cases a technique of higher throughput or broader process-latitude is necessary. Our experience at MIT in applying low-cost proximity x-ray nanolithography to a wide variety of applications leads us to conclude that this technology can provide an alternative path of a bifurcation. A new projection lithography technique, zone-plate-array lithography (ZPAL), does not require a mask, can operate from UV to EUV to x-rays, and has the potential to reach the limits of the lithographic process.

INTRODUCTION

X-ray lithography was introduced in 1972 [1], and within 1 year was used to fabricate surface-acoustic-wave devices [2], and within 2 years bipolar and MOS transistors [3]. Since then, an impressive list of high-density integrated circuits (IC's) have been fabricated using x rays. Some high points are summarized in Table I [4]. In addition, a wide range of quantum-effect [5], short-channel [6], and optoelectronic devices [7, 8] have been fabricated using very low cost tools in an academic research setting [9].

Despite this demonstrated performance, the Semiconductor Industry Association decided in 1998 that development efforts for the "Next Generation Lithography" (NGL), would be directed toward 193 nm and 157 nm projection lithography, for linewidths down to 100 nm, and EUV lithography and SCALPEL for linewidths below 100 nm. This decision has redirected x-ray lithography development efforts in the USA toward monolithic microwave integrated circuits (MMIC) [10].

The primary thesis of this paper is that even if the development of EUV and SCALPEL is successful (and this is by no means certain) these technologies will not be suitable for a wide range of important sub-100 nm applications external to the semiconductor industry. X-ray lithography, on the other hand, may well provide an optimal path for certain of these applications. A new projection lithographic technology, zone-plate-array lithography (ZPAL), which does not require a mask and can operate at wavelengths from UV to x rays, may well provide the most flexible and low cost approach to meet the wide range of future lithographic needs [11-13].

Table I
Highlights, ULSI via X-Ray Lithography (from J. Silverman) [4]

Chip type	Density	Feature Size	Date	Origin	Reference
CMOS logic	6M xistors	0.2 μm	1994	IBM	[14]
DRAM	64 Mb		1995	IBM	[15]
DRAM	1Gb (test)	0.14 μm	1995	Mitsubishi	[16]
CMOS	16 ps/stage	0.10 μm	1995	IBM	[17]
DRAM	4 Gb (test)	0.12 μm	1996	Toshiba/NTT	[18]

APPLICATIONS BEYOND THE SEMICONDUCTOR INDUSTRY

It is perhaps not widely recognized that a large number of current and future industries and research applications, outside the semiconductor industry, employ 100 nm and sub-100 nm lithography. These include: monolithic microwave integrated circuits (MMIC); optical integrated circuits for optical communication; high-density magnetic-information storage; microelectromechanical (MEMS) devices; quantum-effect electronics; and biological research, to name a few. In addition, many new applications of nanometer lithography, not yet conceived, will appear in the future. For example, it is probable that via nanolithography we will make bridges to the domain of macromolecules by providing templates to guide and direct the organization of such molecules. This will open up many new fields, from chemical synthesis to displays, sensors, memory, and computation. Lithography will be the key technology, as it has been in the past, because it is lithography that enables one to imprint our conceptions onto a substrate.

It is highly unlikely that either EUV or SCALPEL will provide the lithography technology for these other applications, either because of cost, inflexibility, insufficient feature-placement accuracy, spatial coherence, or resolution. Hence, it is important to recognize the need for, and to enable, a bifurcation in the development of sub-100 nm lithography: one branch addressing the needs of the semiconductor industry, the other branch addressing the requirements of non-semiconductor industry applications (while also providing a backup if SCALPEL and EUV fail to meet expectations).

In the remainder of this paper we describe some of the work in the NanoStructures Laboratory at MIT which is aimed at developing lithographic technologies to address a broad

range of applications. In our lab, applications and lithography development go hand in hand, the one driving the other in a synergistic fashion. Hence, they are described here together.

ALTERNATIVE LITHOGRAPHIES AND APPLICATIONS

Interference lithography (IL)

Interference lithography (IL) [19] is a highly successful method, entirely outside the range of interests of the semiconductor industry, but critically important to the telecommunications industry. We believe that IL will, in the near future, provide new modes of deep-sub-100 nm metrology [20], and reference fiducials for electron beam lithography.

Spatial-Phase-Locked E-Beam Lithography (SPLEBL)

It is well known that electron-beam lithography, has a serious and fundamental problem with pattern-placement accuracy. That is, although scanning-electron-beam methods can produce patterns of arbitrary geometry, and with resolutions at the limits of the lithographic process, the accuracy with which pattern elements can be placed relative to one another is much poorer than the resolution. The fundamental reason for this is that electron-beam systems operate "open loop." That is, although the control computer keeps track of the stage position and the command signals to the deflection electronics, the actual position of the beam relative to the stage is not monitored. Beam position can drift due to charging, thermal expansion, vibrations, and a variety of other causes.

We are developing an approach to solving this problem called spatial-phase-locked e-beam lithography (SPLEBL), depicted schematically in Fig. 1 [21]. SPLEBL depends directly on the spatial coherence and accuracy of a fiducial grid, produced by interferometric lithography.
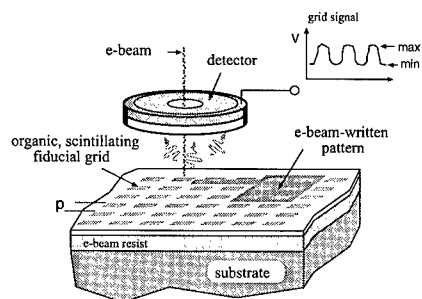
Figure 1: Schematic of the global-fiducial-grid mode of spatial-phase-locked e-beam lithography. The reference fiducial grid (made by IL) on top of the resist layer provides a scintillation signal to the control computer indicative of the beam's spatial position. This enables the feedback loop to be closed.

In addition to the global mode of SPLEBL depicted in Fig. 1 we are also developing a segmented-grid mode [22], which is readily applied to integrated-optical devices [7]. Spatial-phase-locked e-beam lithography, in both the global and the segmented-grid mode depends upon IL to provide templates having long-range spatial-phase coherence, something that is achievable only with IL.

Magnetic-Information Storage

Ross, et al. describe why interference lithography (IL) provides the optimal means of fabricating large-area arrays of nanomagnets for research on high-density magnetic-information storage [23]. Figure 2 illustrates a form of IL, called achromatic-interference lithography (AIL), which we use to fabricate magnetic elements on 100 nm pitch [24].
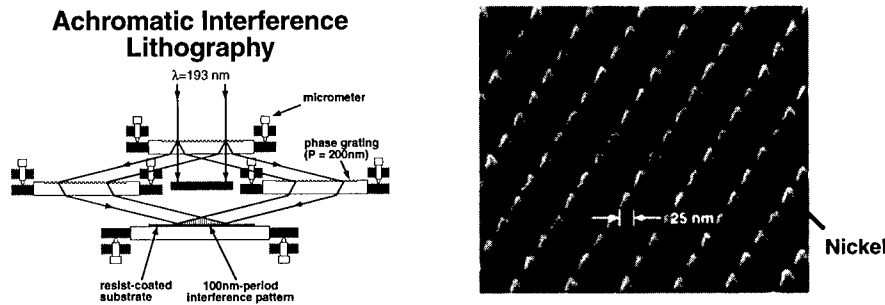
Figure 2: Schematic of achromatic-interference lithography (AIL); (b) scanning electron micrograph of 25 nm nanomagnets on 100 nm centers, fabricated using AIL and liftoff.

If the current research on high density magnetic information storage should proceed into the manufacturing stage, it is clear that neither direct-write e-beam lithography, nor EUV, nor SCALPEL will be the lithography of choice. Either some form of interference lithography or x-ray lithography are the most likely.

X-ray nanolithography and device applications

We have for many years used x-ray lithography to fabricate devices with sub-100 nm features [5-9, 25]. Figure 3 illustrates a single-electron transistor device with sub-100 nm features [26]. To achieve features well below 100 nm requires a reduction in the mask-substrate gap beyond what is assumed appropriate for semiconductor manufacturing (see Section 3.3 below). Nevertheless, we have developed methods of working at gaps of a few microns, and believe that if necessary the methods could be adapted to manufacturing [27].
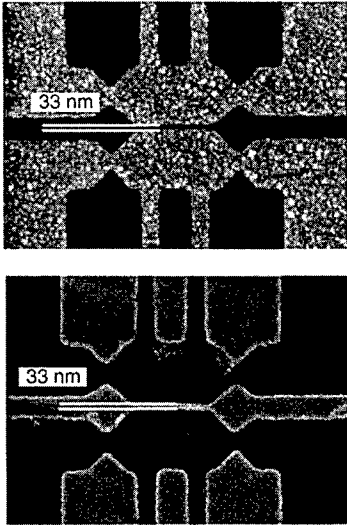
Figure 3: Scanning-electron micrographs of: (upper) an x-ray mask of a Coulomb-blockade single-electron transistor, made using e-beam lithography and electroplating; (lower) replication of the above mask onto a GaAs substrate using x-ray nanolithography and PMMA resist, followed by liftoff of Ti/Au electrodes. (The liftoff process left some residual metal particles on the substrate.)

Figure 4 depicts our plan to fabricate twin-gate MOSFETs with effective channel lengths of 25 nm. Silicon-on-insulator (SOI), in conjunction with bond and etch back, are employed. The lithography is done with small-gap x-ray nanolithography. The upper or second gate will be aligned with respect to the first using our interferometric-broad-band-imaging (IBBI) alignment system [28]. We believe that the extreme sensitivity of IBBI (0.2 nm mean, 1.4 nm sigma) will enable us to meet the required tolerance of 6 nm, 3-sigma, for the alignment of the upper gate to the lower.
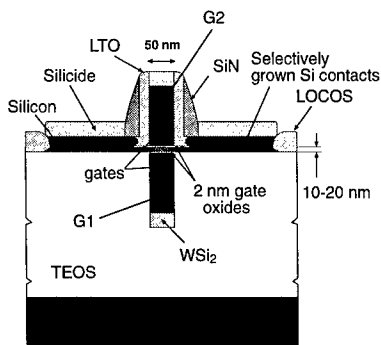
Figure 4: Schematic of the twin-gate MOSFETs we are fabricating using x-ray nanolithography. Polysilicon gate G1 is patterned first on SOI, then a bond-and-etch-back process yields a thin single-crystal Si film covered by a 2 nm gate oxide. A second x-ray exposure and etching process produces polysilicon gate G2. G2 is aligned with respect to G1 using our IBBI alignment/exposure system [28]. Such devices have been fabricated but have not yet achieved the desired 6 nm 3-sigma overlay.

Future integrated-optical circuits will utilize gratings on top of waveguides to serve as resonators and filters for communication systems. Figure 5 illustrates the extreme tolerance on the period of the gratings, required in order to separate different channels. A change in period of only 0.13 nm produces a shift of 100 GHz in the resonant frequency. Thus, to fully utilize the bandwidth capabilities of optical communication systems, one must be able to fix the spatial frequencies of such resonant structures with tolerances better than 0.1 nm. This is well beyond, and divergent from, the requirements of the semiconductor industry. The lower part of the figure indicates that we have developed means of measuring spatial period with a standard deviation of 0.03 nm [29]. Metrology is the essential first step in achieving the nanometer-level spatial control that future integrated optics will require.
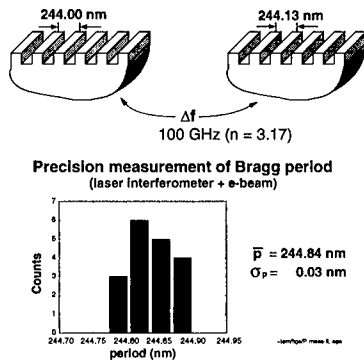
Figure 5: (upper) Schematic illustrating that for a grating in material with an index of refraction of 3.17 (e.g., Si), a difference in spatial period of 0.13 nm corresponds to a change in resonant frequency of 100GHz. (lower) Histogram illustrating that we have developed means of measuring the spatial-period of grating structures with a precision of σ = 0.03 nm.

Figure 6 is an example of the optical filters we are fabricating using x-ray nanolithography and a novel dual-mask etching process [7]. The procedure of fabricating the mask with the segmented-grid mode of spatial-phase-locked e-beam lithography [22] ensures that the k-vector of the gratings is aligned to the axes of the waveguides to much less than 10 seconds of arc.
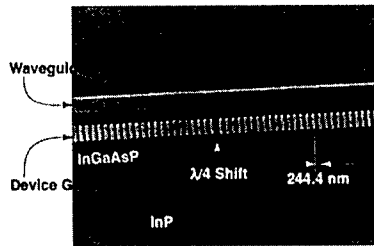
Figure 6: Scanning-electron micrograph of a portion of a channel-dropping filter in InGaAsP, consisting of two adjacent planar optical waveguides, one containing a grating resonator structure, produced by x-ray nanolithography and reactive-ion etching. The quarter-wave spatial-phase shift, essential to resonator performance, is produced on the x-ray mask using spatial-phase-locked e-beam lithography. The grating k-vector is aligned to the waveguide axis to less than 10 arc sec.

Figure 7 illustrates a configuration for a Magnetic-Random-Access Memory (MRAM), which promises high-density, permanent memory, without moving parts. The magnetic elements utilize the giant-magneto-resistance (GMR) effect. Theory indicates that GMR elements can operate effectively at 50 nm size, or even smaller. If MRAM research is successful, and demonstrates the feasibility of this

breakthrough in memory technology, how will such devices be manufactured economically? It is highly doubtful that either EUV or SCALPEL will be suitable since they are designed specifically and somewhat inflexibly for manufacturing of Si integrated circuits. We know of no currently available method other than x-ray nanolithography suitable for the MRAM task, and look forward to demonstrating this in our lab.

Giant Magneto-Resistance (GMR) Structures
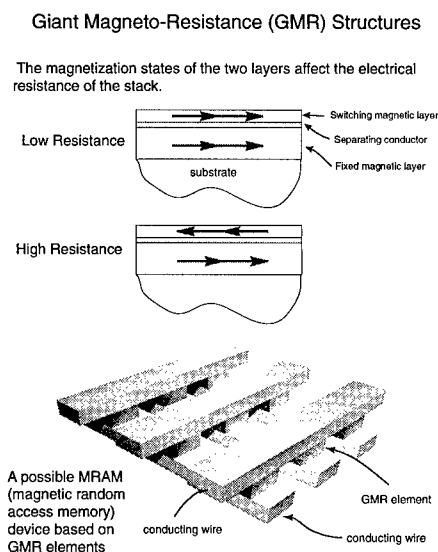
Figure 7: Schematic of a possible magnetic-random-access-memory (MRAM) device. The requirements for low cost and fine-line lithography to achieve high areal density favor the use of x-ray nanolithography to produce these devices.

The real problems with x-ray lithography

There is some confusion about the problems of x-ray lithography that led to its fall from the favor of the semiconductor industry. It is often stated that the cost of making the mask was the problem. However, there is now evidence that the alternating phase-shift mask, favored for pushing the performance of optical lithography, is a more daunting challenge, and more expensive. The same can be said for EUV masks, which require a defect-free multilayer reflector as the mask substrate. Repair of such masks seems especially daunting.

Another view is that the mask-sample gap is the Achilles heel of x-ray lithography. Figure 8 plots the minimum feature size versus mask-sample gap, for 3 different assumptions on the scaling parameter. As mentioned above, lithography at gaps of a few microns has been demonstrated in our lab. To do this in manufacturing will require some changes in longstanding practices, but cannot be ruled out as unfeasible. Nevertheless, to address the problem of gap shrinkage with feature size reduction, we are pursuing another form of lithography, applicable at UV, EUV and soft x-ray wavelengths, entitled zone-plate-array lithography (ZPAL), described below.

Proximity Gap vs. Linewidth
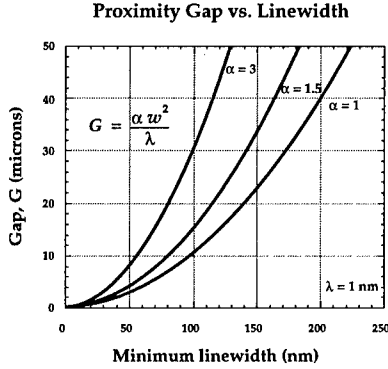
Figure 8: Plot of the mask-to-substrate gap, G, as a function of minimum feature size, for a wavelength of 1 nm and three assumptions on the scaling parameter α. At α greater than 2, significant diffraction occurs, requiring modeling of the aerial image to determine the mask structure necessary to achieve a desired image.

In our view, the real problem with x-ray lithography is the potential for pattern distortion due to stress in the absorber. It is generally assumed that the optimal approach is to eliminate stress in the absorber by means of well controlled deposition processes [30]. However, at a recent conference M. Feldman proposed an alternative view, i.e., that a membrane mask affords one the opportunity to correct distortion by controlled input of heat [31]. We are currently combining Feldman's idea with another of our in-house technologies, Holographic-Phase-Shifting Interferometry (HPSI) [32]. The latter directly measures in-plane distortion by means of a shallow fiducial grid etched into the back side of the x-ray mask membrane. The mathematical problem of determining the heat input required to cancel out a given distortion is a formidable problem, but we have reason to believe it can be solved. We are hopeful (but not certain) that distortions at or below the 1 nm level will ultimately be achieved.

ZONE-PLATE-ARRAY LITHOGRAPHY (ZPAL)

Figure 9 depicts Zone-Plate-Array Lithography (ZPAL), a new paradigm for lithography that requires no mask, and takes advantage of modern, high-speed computation and recently developed micro-electromechanical devices for multiplexing beams [11]. ZPAL has been demonstrated at 193 nm [12] and 442 nm wavelengths [13]. The latter demonstration utilized multiplexing with a Texas Instruments micromirror array. Patterns of arbitrary geometry were written in multiple unit cells, and the resolution obtained was close to theoretical predictions, as illustrated in Figure 10. This initial experiment was so successful that we believe a UV system is fully feasible There is no reason why its cost cannot be orders of magnitude less than conventional optical projection systems, in addition to the benefit of being "maskless."
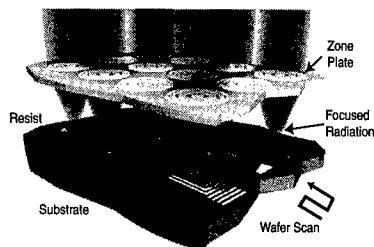
Figure 9: Schematic of zone-plate-array lithograpy (ZPAL). An Array of Fresnel zone plates focuses radiation beamlets onto a substrate. The individual beamlets are turned on and off by upstream micromechanics as the substrate is scanned under the array. In this way, patterns of arbitrary geometry can be created with a minimum linewidth equal to the minimum width of the outermost zone of the zone plates. Using 4.5 nm radiation we estimate that lines and spaces of 20 nm should be achievable, provided the zone plate can be fabricated.
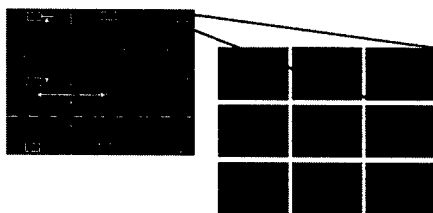
Figure 10. Pattern exposed in resist using ZPAL and a HeCd laser (442nm). An array of 9 zone plates were used to create 9 different patterns in the 9 corresponding unit cells.

One of the major virtues of zone-plates is that they work at all wavelengths. Even neutral atoms have been focused with zone plates [33]. There is a long history of x-ray microscopy with zone plates [34]. For nanolithography beyond the resolution limits of deep UV, the optimal wavelength would be 4.5 nm, i.e., at the carbon edge [11]. In 1978, D. Flanders demonstrated, using the 4.5 nm wavelength and near-zero gap, that 18 nm lines and spaces could be readily reproduced [35]. With ZPAL at 4.5 nm there will be no proximity effects induced by secondary electrons, and hence one should be able to approach the limits of the lithographic process. The resolution of ZPAL will then depend exclusively on how fine the outer zones of the zone plate can be made. This has already been pushed to 25 nm using scanning-electron-beam lithography and electroplating [36, 37].

The two main problems with soft-x-ray-based ZPAL are the radiation source and the scheme for multiplexing beams to the zone plates. Because zone plates are diffractive optical elements, they require narrow-band sources. Initially it appeared that an undulator would be required for high throughput. However, the use of filtered synchrotron radiation or hot plasma sources may also be feasible.

The problem of multiplexing the radiation to the individual zone plates is more difficult at soft x-ray wavelengths than at UV. Total external reflection from a mirror array seems attractive, as this could be 100 % efficient if the mirrors are sufficiently flat and smooth. However the problem of aligning the multiplexing mirrors to the zone-plate array appears challenging.

The diffractive nature of zone plate focusing implies that diffraction orders other than +1 will contribute to a background. To achieve the highest contrast, order-sorting apertures will likely be required, as depicted in Figure 11.
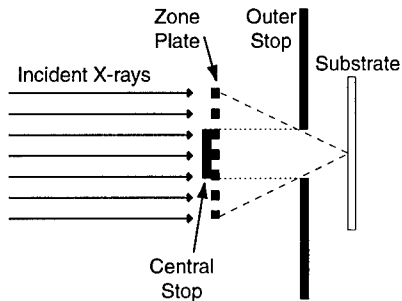
Figure 11: Schematic of a zone plate, modified by the addition of a zero-order central stop, and an outer stop about mid way between the zone plate and the substrate. This stop effectively eliminates background effects due to the diffracted orders other than + 1. The latter is focused on the substrate.

SUMMARY

In summary, there is strong evidence that "Nanostructures", in all its many meanings, interpretations, and forms, will be a key technology of the next century. We believe that nanolithography will grow in importance and find applications well beyond the semiconductor industry. For this reason it is important to view lithography from this broader perspective, and develop means of meeting specifications for a wide range of applications, including some not yet conceived. In this connection, the issue of adherence to a Cartesian grid, with sub-1 nm precision and accuracy, must be addressed. In addition, we should strive to provide low cost, flexibility, and compatibility with a wide range of substrates (i.e., not just Si wafers) and topographies.

ACKNOWLEDGEMENTS

REFERENCES

1   D. L. Spears and H. I. Smith, Electronics Lett. **8**, 102 (1972).
2   H. I. Smith, D. L. Spears, and S. E. Bernacki, J. Vac. Sci. Technol. **10**, 913 (1973).
3   S. E. Bernacki and H. I. Smith, IEEE Trans. Elec. Dev. ED**22**, 421 (1975).
4   J. P. Silverman, J. Vac. Sci. Technol. B **15**, 2177 (1997); J. P. Silverman, A White Paper for the 1998 Sematech Next Generation lithography Workshop.
5   K. Ismail, W. Chu, A. Yen, D.A. Antoniadis and H.I. Smith, Appl. Phys. Lett. **54**, 460 (1989).
6   I.Y. Yang, S. Silverman, J. Ferrera, K. Jackson, J.M. Carter, D.A. Antoniadis, and H.I. Smith, J. Vac. Sci. Technol. B **13**, 2741-2744 (1995).
7   M. H. Lim, T. E. Murphy, J. Ferrera, J. N. Damask and H. I. Smith, J. Vac. Sci. Technol. B **15** Nov/Dec. (1999).

8   J.S. Foresi, P.R. Villeneuve, J. Ferrera, E.R. Thoen, G. Steinmeyer, S. Fan, J.D. Joannopoulos, L.C. Kimerling, H.I. Smith, E.P. Ippen, Nature, **390**, 143-145, (1997).

9   H.I. Smith, M.L. Schattenburg, S.D. Hector, J. Ferrera, E.E. Moon, I.Y. Yang, and M. Burkhardt, Microelectronic Engineering **32**, 143-158 (1996).

10   R. Selzer, J. Heaton, N. Dandekar, Micro and Nano Engineering Conference, Rome, September, 1999, these proceedings.

11   H. I. Smith, J. Vac, Sci. Technol. B **14**, 4318 (1996).

12   I. Djomehri, T. Savas and H. I. Smith, J. Vac. Sci. Technol. B **16**, 3426 (1998).

13   D. J. D. Carter, D. Gil, R. Menon, M. Mondol and H. I. Smith, J. Vac. Sci. Technol. B Nov/Dec. (1999).

14   S. Subbana et al., IEDM Tech. Digest, 695 (1994).

15   R. DellaGuardia et al., Proc. SPIE 2437, 112 (1995).

16   Y. Nishioka et al., IEDM Tech. Digest, 903 (1995).

17   S. J. Wind et al., J. Vac. Sci. Technol. B **13**, 2688 (1995).

18   K. Sunouchi et al., IEDM Tech. Digest, 601 (1996).

19   J. Ferrera, M. L. Schattenburg and H. I. Smith, J. Vac. Sci. Technol. B **14** 4009 (1996)

20   M. L. Schattenburg, C. Chen, P. N. Everett, J. Ferrera, P. Konkola and H. I. Smith, J. Vac. Sci. Technol. B Nov/Dec. (1999).

21   J. Goodberlet, J. Carter and H. I. Smith, J. Vac. Sci. Technol. B **16**, 3672 (1998).

22   J. Ferrera, V. V. Wong, S. Rishton, V. Boegli, E. H. Anderson, D. P. Kern and H. I. Smith, J. Vac. Sci. Technol. B **11**, 2342 (1993).

23   C. A. Ross, M. Hwang, H. I. Smith, M. Farhoud, M. C. Abraham, R. J. Ram, T. Savas, M. Schatenburg, J. Vac. Sci. Technol. B, Nov/Dec (1999).

24   T.A. Savas, M. Farhoud, H. I. Smith, M. Hwang, and C.A. Ross, J. Appl. Physics, **85**, 6160-6162 (1999).

25   H.I. Smith, M.L. Schattenburg, , IBM J. Res. & Develop. **37** 319 (1993).

26   D. J. D. Carter, A. Pepin, M. R. Schweizer and H. I. Smith, J. Vac. Sci. Technol. B, 15, (1997) 2509; D.J.D. Carter, Ph.D. Thesis MIT (1998).

27   H. I. Smith and F. Cerrina, Microlithography World **6**, 10 (1997).

28   E. Moon, J. Lee, P. Everett and H. I. Smith, J. Vac. Sci. Technol. B 16, 3631 (1998).

29   J. Ferrera, Ph.D. Thesis, MIT (1999).

30   S. Tsuboi, S. Kotsuji, T. Yoshihara and K. Suzuki, J. Vac. Sci, Technol. B **15**(6), 2228 (1997).

31   M. Feldman and J. B. Lee, J. Vac. Sci. Technol. B Nov/Dec (1999).

32   M. H. Lim, J. Ferrera, K. P. Pipe and H. I. Smith, J. Vac. Sci. Technol. B Nov/Dec. (1999).

33   S. Rehbein, R. D. Doak, R. E. Grisenti, G. Schmahl, J. P. Toennies and Ch. Wöll, Micro and Nano Engineering Conference, Rome, September, 1999.

34   G. Schmahl, D. Rudolph, B. Niemann, P. Guttman, J. Thieme, G. Schneider, C. David, M. Diehl, and T. Wilhein, Optik 93, (1993) 95; Proceedings, Sixth International Conference on X-ray Microscopy (XRM'99), Aug. 1-6, 1999, Berkeley, CA, USA, Ed. D. Atwood..

35   H. I. Smith and D. C. Flanders, J. Vac. Sci. Technol. **17**, 533 (1980).

36   M. Peuker, Micro and Nano Engineering Conference, Rome, September, 1999.

37   E. H. Anderson, B. Harteneck, D. Olynick, Proceedings, Sixth International Conference on X-ray Microscopy (XRM'99), Aug. 1-6, 1999, Berkeley, CA, USA, Ed. D. Atwood.

Lithographic Materials Technologies: 193 nm Imaging and Beyond

ELSA REICHMANIS*, OMKARAM NALAMASU*, FRANCIS M. HOULIHAN*, ALLEN
H. GABOR**, MARK O. NEISSER**, MURRAE J. BOWDEN**
*Bell Laboratories, Lucent Technologies, 600 Mountain Ave., Murray Hill, New Jersey 07974
**Arch Chemicals, 200 Massasoit Ave., East Providence, Rhode Island 02914

ABSTRACT

Advances in microlithographic resist materials have been a key enabler of the unabated productivity gains in the electronics industry and are continuing to help push the ultimate limits of optical lithography. The challenges posed by the introduction of new optical lithography technologies that use smaller wavelengths have been successfully met by the materials community through the design of chemically amplified resist technologies and 193 nm resist materials based on aliphatic polymers and dissolution inhibitors. With continued advances in resist materials, exposure systems and resolution enhancement and mask technologies, optical lithography will be capable of patterning ≤ 0.1 μm design rule devices in future fabs.

INTRODUCTION

Advances in microlithographic resist materials have been a key enabler of the unabated productivity gains in the microelectronics industry and are continuing to help push the ultimate limits of optical lithography. [1] The business is driven by the need to build semiconductor devices that contain an increasing number of individual circuit elements. Over time, device complexity and functionality have increased while minimum feature size has dramatically decreased. [2] The ability to shrink the feature size is critically dependent upon the technologies used in the delineation of the circuit pattern. The challenges posed by the introduction of new optical lithography technologies that use smaller wavelengths have been successfully met by the materials community through the design of chemically amplified resist technologies and 193 nm resist materials based on aliphatic polymers and dissolution inhibitors. With continued advances in resist materials, exposure systems and resolution enhancement and mask technologies, optical lithography will be capable of patterning ≤ 0.10 μm design rule devices in future fabs. The focus of this article is the materials challenges that have been successfully met in the development of 193 nm lithographic materials technologies along with a perspective on future directions.

Resist Lithographic Requirements

Conventional materials used in today's semiconductor manufacturing facilities are based on traditional novolac/diazonaphthoquinone chemistry. [2] Incremental improvements in tool design and performance with concomitant refinements in materials chemistry and processing have allowed the continued use of this technology to produce devices with features as small as 0.25 μm. However, the opacity of traditional UV and DUV organic matrix resins, photoresists and photoresist components at 193 nm preclude their use at this wavelength and has necessitated a shift in resist materials design. The challenge for 193 nm resist design has been to define a chemical system largely based on aliphatic components that are functionally identical to the traditional novolac based materials.

Table 1 [1,3] identifies key resist lithographic properties and how they relate to the molecular characteristics of resist components. The issue of sensitivity can be addressed

through adoption of chemically amplified resist design principles. [4] Contrast, or the rate at which a given materials responds to incident radiation, must be high to ensure high resolution patterning and is inherent to the chemically amplified resist mechanism. Absorption, plasma etching resistance and aqueous base solubility have to be intentionally engineered into aliphatic resins for use at 193 nm. Additionally, the use of significant concentrations of aromatic or ethylenic functionalities is precluded because of absorption constraints.

TABLE 1: Key Resist Materials Properties Related to Molecular Characteristics

Resist Property	Molecular Characteristic
Absorption	No olefinic or aromatic moiety
Etching stability	High level of structural carbon and low oxygen content
Aqueous base solubility	Presence of base solubilizing groups
Substrate adhesion	Presence of polar moieties
Sensitivity (photospeed)	Catalytic chain length for acidolysis, efficiency of acid generation, acid strength, protective group chemistry
Process latitude and substrate sensitivity	Catalytic chain length for acidolysis, acid strength, protective group chemistry
Outgassing	Protective group and acid generator chemistry
Aspect ratio of images	Surface tension effects and mechanical strength of materials
Low metal ion content	Synthesis and scale-up methodology
Manufacturability and cost	Synthesis and materials scale-up methodology, lithographic process requirements

Traditionally, the ability for a material to withstand the plasma and reactive-ion-etching environments used to transfer resist images into the device substrate has been accomplished through the use of aromatic moieties. It has been proposed that the key factor affecting etching resistance is however the "effective carbon content" of a given material. [5] Thus, it was predicted, and later shown that high alicyclic content polymers should approach the performance of aromatic resins in plasma environments.

For a material to be accepted into manufacturing, aqueous base solubility is most desirable. For conventional resists, phenolic hydroxides provide the necessary aqueous solubilizing appendages. Much of the initial effort in designing 193 nm resist was focused on derivatized acrylate and methacrylate copolymers that can undergo acid catalyzed deprotection reactions to generate materials which exhibit good aqueous base solubility. [6] While the 193 nm materials challenge has greatly diversified the types of polymers used as photoresist resins, nearly all use a carboxylic acid functionality to gain solubility in aqueous base.

ALICYCLIC POLYMERS FOR 193 nm IMAGING

Cyclo-olefin maleic anhydride alternating copolymers are an attractive alternative to methacrylate-based matrix resins. [7] Compelling features of these materials include: i) facile synthesis via standard radical polymerization, ii) a large pool of cyclo-olefin feed stocks with

desired imaging and etching properties, and iii) a generic structural motif that incorporates alicyclic structures directly into the polymer backbone and provides a latent water-solubilizing group that may also be useful for further structural elaboration. A large number of cyclo-olefins, e.g. norbornene, are known to copolymerize with maleic anhydride. As a rule they yield high-T_g copolymers with a 1:1 alternating structure. Aqueous base solubility can be induced via substitution of an alicyclic ring hydrogen with a base solubilizing functionality such as COOH, or incorporation of acrylic acid units. One example of a material based on this chemistry is shown in Figure 1, namely a quaternary system composed of norbornene, maleic anhydride, acrylic acid and t-butyl acrylate units. Alternatively, substituted norbornene carboxylic acid may be copolymerized with maleic anhydride to afford two component polymeric matrix resins. [8]
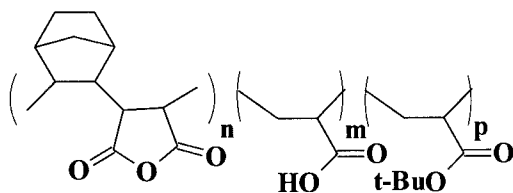
Figure 1: Example of a quaternary polymer resin for use in 193 nm resist formulations

The norbornene based polymers are readily soluble in standard organic solvents used to apply the resist to device substrates and are compatible with aqueous base media such as 0.262N tetramethyl ammonium hydroxide (TMAH), the developer of choice in semiconductor manufacturing. Thin films of these polymers also display excellent transparency at 193 nm. These resins can be used in a variety of resist approaches (Figure 2). [7] The strategies that have been examined include the use of a protected polymer in conjunction with a photoacid generator (PAG) in a "two component" chemically amplified resist process; a three-component system using the parent acidic terpolymer, a dissolution inhibitor (DI); and a PAG, and a hybrid approach that used both a DI and a partially protected polymer matrix. The latter two approaches afford added flexibility in the design of a resist.

Dissolution Inhibitor Design Issues

Multifunctional diazonaphthoquinones (DNQ's) have been shown to enhance the dissolution selectivity in conventional resist materials by inhibiting dissolution in unexposed regions while enhancing the dissolution rate in the exposed areas. [9] The multifunctional nature of the DI's allows for strong interaction between the polymer matrix resin and the DI imparting a nonlinear dissolution behavior to the resist contributing to high contrast and resolution. A similar approach with multifunctional oligomeric cholate esters as DI's also results in enhanced resist performance. [10] An additional benefit is that the cholate based inhibitors have a high level of structural carbon that results in improved etching resistance of the resist formulation. An evaluation of several monomeric and oligomeric t-butyl esters of cholic, deoxycholic and lithocholic acids as 193 nm DI's in poly(norbornene-maleic anhydride-acrylic acid-t-butyl acrylate) indicated that more polar monomeric inhibitors improve adhesion,

Two Component Resists
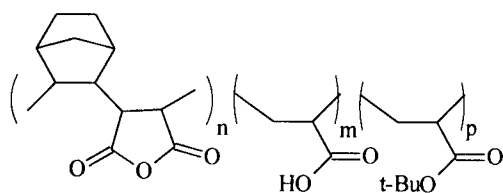
PAG's: Onium Salts

Three Component Resists
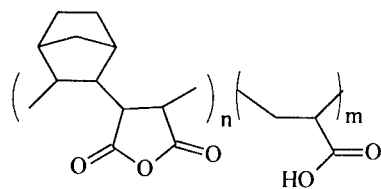
PAG's: Onium Salts

DI's
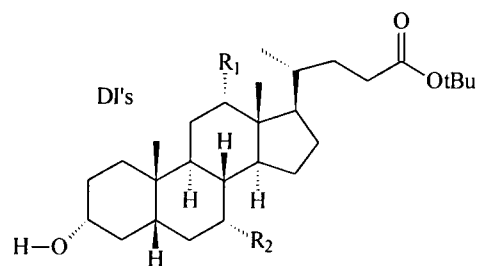
Hybrid Resists
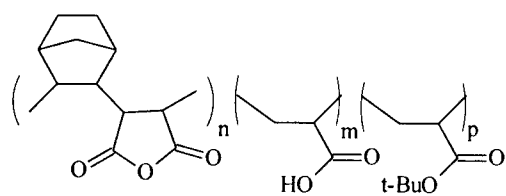
DI's, PAG's

Figure 2: Resist strategies for 193 nm applications

but display poor dissolution selectivity between the exposed and unexposed regions of the resist. As the number of OH groups is decreased from three in t-butyl cholate to one in t-butyl lithocholate, the dissolution inhibition effectiveness increased, but at the expense of adhesion. Oligomeric materials were found to behave similarly. Optimum lithographic performance has been found with resists formulated with a mixture of polar monomeric materials and oligomeric structures. Representative structures are shown in Figure 3.

Monomeric Cholate Dissolution Inhibitors
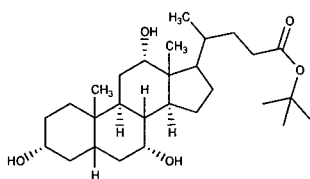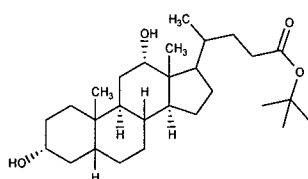
t-Butyl Cholate   t-Butyl Deoxycholate
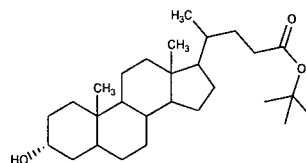
t-Butyl Lithocholate

Dimeric DI
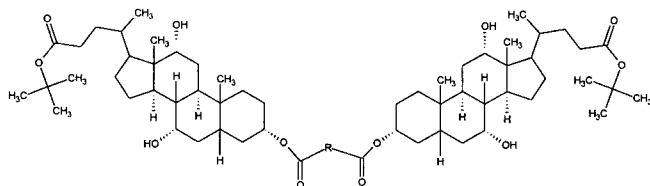
Oligomeric DI
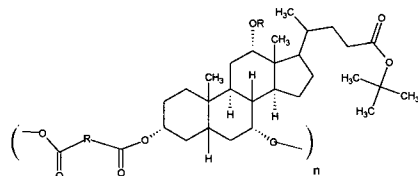
Figure 3: Examples of Cholate based dissolution inhibitors

Photoacid Generator design Issues

While aromatic PAGs are highly absorptive at 193 nm, they are only needed in small quantities (typically less than 5%) in resist formulations. Consequently, 193 nm resists could be designed using the same PAGs as those that are in use with 248 nm resists. In addition to absorption, the considerations in designing a PAG are solubility, volatility of both the PAG and its photoproducts, acid strength, cost and toxicity. For polymers with t-butyl protected carboxylic acid groups, high acid strength (often superacids are required) and high post-exposure bake (PEB) temperatures are required for complete removal of the ester appendage. Examples of applicable chemistries include photogenerators of perfluoroalkyl sulfonic acids, or aryl sulfonic acids highly activated with electron withdrawing groups. [11] One example is depicted in Figure 4.

$$CH_3$$
$$CH_3-C-CH_3$$

$$I \oplus \quad \ominus \quad O$$
$$O-S-CF_2\cdot CF_2 CF_2\cdot CF_3$$
$$O$$

$$CH_3-C-CH_3$$
$$CH_3$$
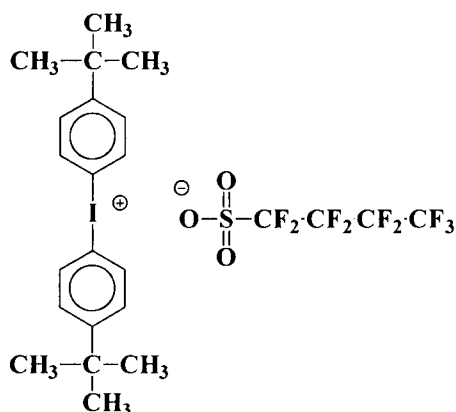
Figure 4: A representative example of an onium salt based photoacid generator

Volatility of photoproducts from resist components (resist outgassing) is an important issue for 193 nm lithography and more advanced technologies utilizing 157 nm sources, electron-beam, or EUV exposure (3). For 193 nm, researchers at MIT Lincoln Labs have demonstrated that resist photoproducts that evolve from the film condense on optical elements and degrade lens transmission and uniformity. [12] We have shown that outgassing can be dramatically alleviated using photodecomposable bases such as those depicted in Figure 5. For 193 nm lithography, the MIT study found that aromatic outgassing products from the resist more readily tended to deposit on lens materials than their aliphatic counterparts. For example, PAG's that contain diphenyliodonium chromophores evolve iodo-aromatic photoproducts that deposit on exposure tool lenses. Using PAG's that do not contain the iodonium chromophore such as tris(t-butylphenyl)sulfonium nonafluorobutanesulfonate or nitrobenzyl ester based PAGs, eliminates outgassing of iodo compounds. Notably, nitrobenzyl ester materials exhibit

no detectable aromatic outgassing products. A judicious choice of PAG and additives can effectively minimize issues related to materials outgassing during exposure.
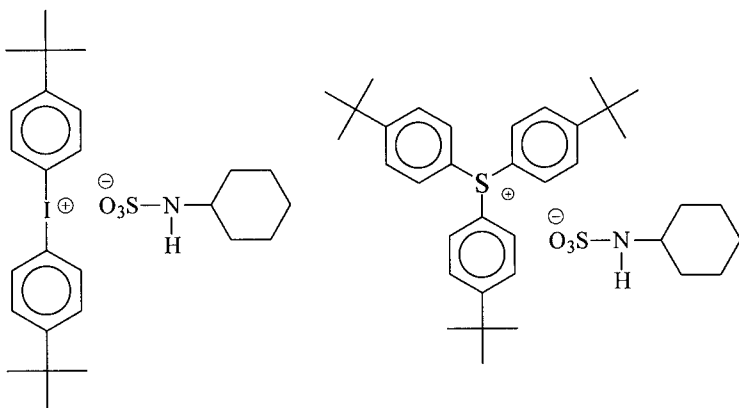
Figure 5: Representative examples of photogenerated base additives for 193 nm resist formulations

LITHOGRAPHIC PERFORMANCE

Molecular level understanding of materials issues and how those issues relate to key lithographic performance criteria allows for the design of effective, manufacturable 193 nm lithographic materials that may be implemented into next generation device fabrication environments. SEM micrographs of images that can routinely be achieved in the norbornene based systems described above are shown in Figure 6. After coating, the resist was soft-baked at a temperature of 145 °C for 90s, exposed with 23 mJ/cm^2 of 193 nm light using annular illumination (0.60NA; 0.80σ_{outer}, 0.60σ_{inner}), and then post-exposure baked at 170 °C for 90s. The substrates were then developed in 0.262 N TMAH for 20 s.

| 0.14 μm | 0.13 μm | 0.12 μm | 0.115 μm | 0.1125 μm |
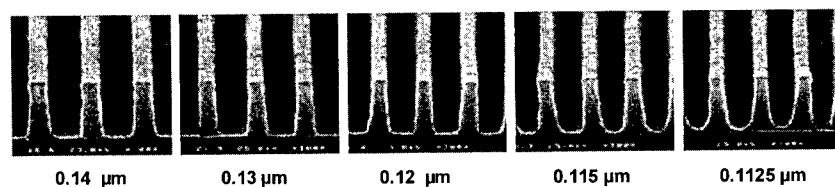
Figure 6: SEM micrographs depicting the resolution capability of a norbornene-maleic anhydride/cholate ester based dissolution inhibition resist formulations. The resolution was achieved using annular illumination and an exposure dose of 23 mJ/cm^2 .

CONCLUSION

We have established and demonstrated rational design principles for a single-layer 193 nm lithographic materials. This work reveals some of the challenges that recur frequently in designing not only photoresist materials, but any materials for a given application. For 193 nm materials, the primary challenge of incorporating requisite imaging and lithographic properties was met by the design of cyclo-olefin maleic anhydride polymers, cholate dissolution inhibitors and relevant additives. Fundamental studies into the materials properties and the interactions between resist components enabled formulation of high-performance resists that display extremely reproducible lithographic properties. The challenges faced in this arena will be exacerbated with the drive towards alternative exposure methodologies such as electron beam, 157 nm and EUV lithography.

The economic pressures dictated by Moore's Law continue to push towards lithographies capable of greater resolution which in turn dictates further design and engineering of suitable materials options. [2] All of the advanced lithography options are aimed at sub-80nm resolution and thus share in the challenges brought about by pattern collapse of high aspect ratio (>3) features. To address this issue, improved understanding of the interactions of resists with device substrates will be required. Apart from this, the alternative options differ greatly in their material related concerns.

If 157 nm lithography is to become a viable alternative, there needs to be a shift in polymer matrix chemistry because of the high absorbance of not only conventional phenolic resist but also of the resins contemplated for use at 193 nm [13]. Possible candidates include fluorinated polymers, but any candidate resin must also have good plasma etching resistance and be soluble in conventional spin casting solvents. Furthermore, the material must have good aqueous solubility once exposed to radiation. Traditional base solubilizing moieties such as CO_2H and phenolic OH are precluded because of their high absorbance at 157 nm. Consequently, one will have to resort to more exotic groups. Another complication is that this wavelength is far more energetic and will tend to be less selective, giving rise to chain scission or crosslinking phenomena which may be deleterious to the imaging mode of the resist. Outgassing of volatile organic compounds during exposure is an another issue. It might be expected that as a consequence of the higher energy radiation, greater amounts of volatiles will be formed during exposure, leading to a greater probability for those photoproducts to undergo further reaction leading to materials deposition on exposure tool lens elements degrading performance.

The advantage of projection electron-beam alternatives is that many of the presently available conventional and chemically amplified resists work quite well since absorbance is not an issue [14]. However, because of the vacuum environment associated with such exposure systems, resist materials must be designed to minimize or even eliminate outgassing. Additionally, there needs to be a better understanding of e-beam induced fragmentation of photoadditives in order to be able to maximize system performance.

The route taken in the future will depend on materials concerns such as those described above coupled with tool availability.

REFERENCES

1. E. Reichmanis, O. Nalamasu, F. M. Houlihan, *Accts. Chem. Res.* **32**, p. 659 (1999).

2. L. F. Thompson, C. G. Willson, M. J. Bowden, Introduction to Microlithography; ACS Professional Reference Book, American Chemical Society, Washington, D. C. 1994.

3. O. Nalamasu, F. M. Houlihan, R. A. Cirelli, G. P. Watson, E. Reichmanis, *Solid State Technology*, **42(5)**, p. 29 (1999).

4. a) C. G. Willson, H. Ito, J. M. J. Frechet, Technical Papers-1982 Symposium on VLSI Technology, Kanaagawa, Japan, September 1982, p. 86 b) C. G. Willson, H. Ito, J. M. J. Frechet, T. G. Tessier, F. M. Houlihan, *J. Electrochem. Soc.* **133**, p. 181 (1986), c) E. Reichmanis, F. M. Houlihan, O. Nalamasu, T. X. Neenan, *Chem. Mater.* **3**, p. 394 (1991), d) C. G. Willson, M. J. Bowden, in Electronic and Photonic Applications of Polymers, M. J. Bowden, S. R. Turner, eds, ACS Advances in Chemistry Series **218**, American Chemical Society, Washington, D. C. 1988, p. 75-108, e) T. Iwayanagi, T. Ueno, S. Nonogaki, H. Ito, C. G. Willson, *ibid*, p. 109-224.

5. a) Y. Ohnishi, M. Mizuko, H. Gokan, S. Fujiwara, *J. Vac. Sci. Technol.* **19(4)**, p. 1141 (1981), b) H. Gokan, S. Esho, Y. Ohnishi, *J. Electrochem. Soc.* **130**, p. 143 (1983), c) R. Kunz, G. M. Wallraff, R. A. DiPietro, D. C. Hofer, *Proc. SPIE*, **1925**, p. 167 (1993).

6. K. Nakano, K. Maeda, S. Iwasa, T. Ohfuji, *Proc. SPIE*, **2438**, p. 433 (1995), b) R. D. Allen, I. T. Wan, G. M. Wallraff, R. A. DiPietro, D. C. Hofer, R. R. Kunz, *J. Photopolym. Sci. Technol.* **8**, p. 623 (1995).

7. F. M. Houlihan, T. I. Wallow, O. Nalamasu, E. Reichmanis, *Macromolecules*, **30**, p. 6517 (1997).

8. I. L. Rushkin, F. M. Houlihan, J. M. Kometani, R. S. Hutton, A. G. Timko, E. Reichmanis, A. H. Gabor, A. N. Medina, S. G. Slater, M. Neisser, *Proc. SPIE*, **3678**, p. 44 (1999).

9. R. Dammel, in *Diazonaphthoquinone-based Resists*, D. Shea, Ed., SPIE Optical Engineering Press, Bellingham, WA, 1993, p. 70.

10. Wallow, T. I., F. M. Houlihan, O. Nalamasu, E. A. Chandross, T. X. Neenan, E. Reichmanis, *Proc. SPIE*, **2724**, p. 355 (1996).

11. a) F. M. Houlihan, T. I. Wallow, A. G. Timko, S. E. Neria, R. S. Hutton, R. A. Cirelli, O. Nalamasu, E. Reichmanis, *Proc. SPIE*, **3049**, p. 84 (1997), b) F. M. Houlihan, T. I. Wallow, A. G. Timko, S. E. Neria, R. S. Hutton, R. A. Cirelli, J. M. Kometani, O. Nalamasu, E. Riehcmanis, *J. Photopolym. Sci. Technol.*, **10(3)**, p511 (1997), c) R. D. Allen, J. Ortiz, C. E. Larson, T. I. Wallow, R. A. DiPietro, G. Breyta, R. Sooriyakumaran, D. C. Hofer, *J. Photopolym. Sci. Technol.*, **10(4)**, p. 503 (1997).

12. R. R. Kunz, D. K. Downs, *J. Vac. Sci. Technol.* **17(6)**, (1999), b) F. M. Houlihan, I. L. Rushkin, R. S. Hutton, A. G. Timko, O. Nalamasu, E. Reichmanis, A. H. Gabor, A. N.

Medina, S. Malik, M. Neisser, R. R. Kunz, D. K. Downs, *Proc. SPIE*, **3678**, p. 264 (1999), c) F. M. Houlihan, I. L. Rushkin, R. S. Hutton, A. G. Timko, O. Nalamasu, E. Reichmanis, A. H. Gabor, A. N. Medina, S. Malik, M. Neisser, R. R. Kunz, D. K. Downs, *J. Photopolym. Sci. Technol.*, **12**, p. 525 (1999).

13. R.R. Kunz, T.M. Bloomstein, D.E. Hardy, R.B. Goodman, D.K. Downs, and J.E. Curtin, *Proc. SPIE*, 3678, p.13 (1999).

14. A.E. Novembre, L.E. Ocola, F. Houlihan, C. Knurek, M. Blakey, *J. Photopolym. Sci. Technol.*, **11**, p. 541 (1998).

Direct-write Electron Beam Lithography: History and State of the Art

Dustin W. Carr*, Richard C. Tiberio
Cornell Nanofabrication Facility, Cornell University, Ithaca, NY 14853
*Currently at Bell Laboratories - Lucent Technologies, 700 Mountain Ave, Murray Hill, NJ 07974

Abstract

Direct-write electron beam lithography is a patterning technique that has rapidly evolved over the last 40 years. For many years it has been possible to use electrons to pattern lines with widths as narrow as 10 nm. Recent advances in resist materials, electron sources, and system integration have further enhanced the capabilities. High-sensitivity resists provide substantial increases in the throughput without sacrificing resolution. Thermal field-emission sources improve the stability and reduce the minimum attainable spot size. Modern lithography systems integrate the electron beam column with advanced control electronics, making a system capable of nanometer-scale placement accuracy. In addition to these improvements, the technology is more accessible now than ever before, thanks to the proliferation of lithography systems consisting of modified scanning electron microscopes.

Introduction and Historical Perspective

Scanning electron beam lithography uses a finely focussed beam of electrons to make changes in the surface of a material. The beam is scanned across the surface and sequentially writes a desired pattern in the surface. The term "direct-write" refers to the use of this technique for the direct patterning of devices, as opposed to mask writing. This patterning technique is capable of writing lines with widths as narrow as a few nanometers. This paper discusses some of the major historical developments of this technology, and also highlights the capabilities of modern lithography systems.

In 1959, Richard Feynman gave his famous address to the American Physical Society entitled " There's Plenty of Room at the Bottom"[1]. In this talk, he proposed a number of challenges to the scientific community in the area of miniaturization. These propositions proved to be visionary, and made remarkably accurate predictions regarding many aspects of nanofabrication. Among these was the use of scanning cathode rays for the deposition of materials

> *Why can not we write the entire 24 volumes of the Encyclopedia Britannica on the head of a pin? ... How do we write small?... We can reverse the lenses of the electron microscope in order to demagnify as well as magnify. ... We could write with that spot like we write in a TV cathode ray oscilloscope, ... and having an adjustment which determines the amount of material which is going to be deposited.*

Feynman already realized that the direct modification of metal by scanning beams would be inefficient so he proposed a yet undiscovered electron beam resist:

> *If it doesn't work for a metal surface, it must be possible to find some material with which to coat the original pin so that, where the electrons bombard, a change is made which could be recognized later.*

These ideas were prophetic, considering that they were made during the early, formative years of the scanning electron microscope. However, it would not be long before research along these lines demonstrated the capabilities of electron beams as patterning tools.

In the early 1960's, electron beams were used to deposit hydrocarbon and silicone material from the gas phase, and also to directly image metal lines by decomposing metal containing films.[2,3] In the mid-sixties, Broers, Chang, and Nixon, at Cambridge University, demonstrated high resolution metal lines using contamination writing followed by ion milling.[4,5] They did this work using a "flying spot scanner" which reverses the usual function of an electron microsocope. By scanning the electron beam synchronously with a high resolution cathode ray tube, in front of which a mask and a photodetector have been placed, it was possible to demagnify the image stored on the mask. They fabricated aluminum lines 60 to 80 nm wide by this technique. By 1966 many organic materials and dielectrics had been electron-beam deposited.

In 1966, researchers at IBM reported a lithography instrument that was prototype of today's systems. It was comprised of an electron column with submicron resolution, a motorized four inch x-y stage, a digital deflection with 12 bit digital to analog converters for pattern data stored on magnetic tape, and secondary electron imaging for pattern registration. With this system it was possible to expose photoresists and silver halides on maks plates or silicon wafers.[6]

Another group at IBM used a flying spot scanner system and an unnamed positive electron resist to fabricate a silicon bipolar transistor with 1 μm emitter widths that demonstrated 2 GHz f_t.[7] The following year, Haller and Hatzakis, reported a readily available polymer, polymethylmethacrylate (PMMA), to be a high resolution electron sensitive resist.[8] This was a significant discovery because prior attempts at using resists similar to those used for photolithography produced lackluster results. Previous to this time, most semiconductor fabrication had been performed by wet etching or ion milling, i.e. subtractive processing. By observing the tear-drop shape profile resulting from electron beam irradiation, as shown in Figure 1, the technique "lift-off" was discovered, which will be discussed below.[9]

(a)   (b)   (c)
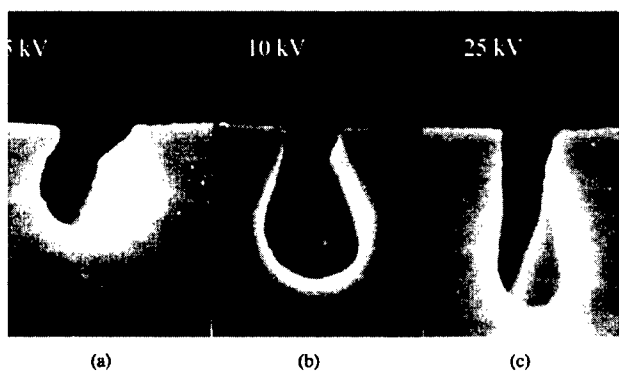
Figure 1

Cross-sections of three lines exposed in PMMA resist at varying energies.[10]

By 1970, electron beam lithography systems were in rapid development. Wolf, at Hughes Research Labs, investigated a commercially available PMMA, manufactured by DuPont under the trade name of Elvacite 2041.[11] Using a computer controlled scanning electron microscope, lines as narrow as 45 nm were fabricated. Similar work was being pursued at IBM, Westinghouse, University of California at Berkeley, and Texas instruments. System enhancements progressed rapidly. Lanthanum hexaboride (LaB$_6$) cathodes became available (see below) and provided a brighter source of electrons than the conventional tungsten filaments that had been used in SEM's up to that point. Laser interferometers began to be used to allow precise control of stage motion,[12] and high speed resists began to emerge.

By the 1980's the technology had progressed from the research laboratories, and commercial systems were available for direct-write and mask-making. These instuments were significantly different from the modified SEM type systems that had been used for research. SEMs were optimized to give high resolution over a very small field size, typically 5 nm resolution for a field size of 5 μm. The lithography systems, on the other hand, needed to have very good uniformity across large writing fields. This uniformity was difficult to attain while still achieving a small spot size. Wolf showed that aberrations significantly degraded the resolution when the beam was deflected off axis. These early lithography systems sacrificed the ultra-high resolution in order to maintain uniformity over millimeter-sized fields.[11]

Researchers also continued to investigate nanometer scale fabrication. As with earlier resolution tests, these experiments used modified SEMs, or scanning transmission electron microscopes (STEMs), which were combined with an external digital pattern generator. The highest resolution was demonstrated at the National Research and Resource Facility for Submicron Structures (NRRFSS), now the Cornell Nanofabrication Facility (CNF). Muray, Kratschmer, and Isaacson used an intense electron beam to directly dissociate metal fluoride. This process is not sensitive to secondary electrons, and therefore nearly reproduces the resolution of the primary beam. Similar resolution was demonstrated in organic resists, as researchers investigated the ultimate resolution of PMMA by fabricating 10 nm metal lines after liftoff.

These experiments demonstrated the ultimate line-width resolution of electron beam lithography. Many issues with these exposure tests made it difficult to apply the results across large areas with a high degree of uniformity, which would be necessary for practical device or circuit fabrication. As mentioned above, the maximum deflection of SEM based systems was minimal. Also, the systems were not automatic and usually required a great deal of tweaking by the user in order to achieve the stated resolution. Adjustments such as focussing and stigmation were performed manually by the operator. Any fluctuations of the height of the sample could not be corrected automatically, leading to focus errors.

In 1985 JEOL integrated the functions of the microlithography systems: pattern generation, stage motion, and registration; with the high performance of the nanolithography research instruments. The JBX5DIIU combined the fully autmotated features of a 15-bit digital pattern generator, 2.5 nm digital deflection, a λ/120 interferometer stage, and 20-nm overlay accuracy with the high resolution of LaB$_6$ emitter. The 50 keV, low aberration, short working-distance electron demonstrated the ability to write ~25 nm structures across an 80 μm field, and to have the fields stitched together with good accuracy to make large patterns.[13]

Recent Advances

Electron Sources

Electron sources have evolved steadily since the introduction of SEM systems. The oldest systems use hot filaments, typically made of tungsten due to its resistance of high temperatures. The filament is heated and hot electrons escape from the surface of the material. These filaments typically have a short lifetime, on the order of a month of operation. The current is not completely stable, and the electrons emerge with a considerable spread in the energy. Such a spread can lead to increased distortion and can limit the minimum attainable spot size. Newer filaments are made of lanthanum hexaboride (LaB_6), which has a lower work function than tungsten, allowing these filaments to be operated at lower temperatures. The energy spread is less, and the brightness (current/solid angle) is better. LaB_6 filaments can be found in most modern lithography systems.

Thermionic emitters such as these are slowly being replaced in direct-write applications by thermal field emitters made of tungsten coated with a zirconium oxide. The filament is heated to around 1800 K, and high extraction voltage (3-5 kV) pull the electrons from the tip. This produces a very small, bright source with a minimal spread in the electron energy. The stability of these systems is also remarkable, with current stability of less than 1% over several months of operation. The high brightness also increases throughput for nanoscale patterns. For example, in order to write 50 nm patterns using a LaB_6 filament, it would be common to use a current close to 100-300 pA. The same pattern on a thermal field emission system would be written with 5 nA.

Resists and Liftoff Processing

Since the discovery of PMMA, many types of organic electron beam resists have been introduced. Although PMMA is far from being the most ideal resist, it has remained popular due to its ease of use and high resolution. Other resists, which have superior speed and etch resistance, are beginning to approach the resolution of PMMA and are better suited to most applications.

The exposure mechanisms of PMMA are well understood. When exposed to e-beam radiation, the large molecules (10,000 – 1,100,000 molecular weight) are broken into smaller pieces. When these pieces become sufficiently small, they can be selectively washed away in a solvent developer. A typical developer for high resolution work would be a mixture of isopropanol and methyl isobutyl ketone (MIBK) in a 3:1 ratio. The dose required to clear large areas of resist using 100 keV electrons is about 800 $\mu C/cm^2$. The resolution limit of PMMA is going to be somewhat limited by the size of the molecule, although there is still some arguments about how much of an effect this really is. The sub-10 nm lines demonstrated by Chen and Ahmed certainly indicate that the molecular size may not be the limiting issue.

Other than its high resolution capabilities, PMMA does not have any properties which make it ideal for use as an electron beam resist. The clearing dose is very high, which causes exposure to be painstakingly slow. The etch resistance in a reactive ion etch (RIE), or in most chemicals is not good, either. For high resolution work, a much more ideal resist is ZEP-7000 from Zeon Chemical Corp. This resist has a large area clearing dose close to 50 $\mu C/cm^2$, making more than 10 times faster to expose than PMMA. The etch resistance to a typical RIE is about twice that of PMMA. In addition, the resolution is comparable to that of PMMA.

Negative tone, chemically amplified resists are becoming more commonly used for high-resolution applications. These resists contain an acid generator that is activated by electron-beam exposure followed by a hotplate bake. The acid diffusion causes the resist to crosslink. A

36

base developer will then remove the resist in the unexposed regions. The sensitivity of this resist is going to increase with the thickness. A popular negative tone resist (NEB-22) has a critical dose of 7 $\mu C/cm^2$ for 400 nm thick resist. For 150 nm thick resist, this critical does will increase to around 30 $\mu C/cm^2$. The resolution of these resists will never be as good as non-chemically amplified resists because of the acid diffusion range. However, 30 nm structures are readily achieved, as shown in Figure 2.
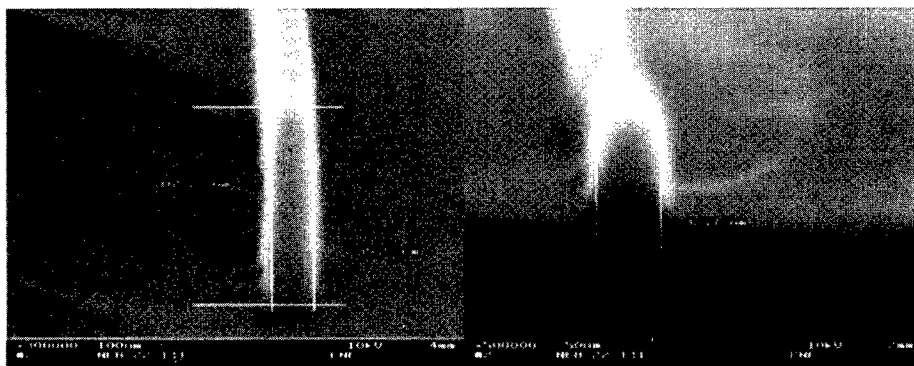
Figure 2

Cross-sections of lines patterned in NEB-22 resist.

Liftoff is a process that enables the fabrication of very narrow metal features. These metal features can be used for device gates or interconnects, or they can be used as hard masks for further etching. The liftoff process is made possible by the undercut profile produced during electron beam exposures. Metal can be evaporated onto the surface, and the undercut resist can be attacked with a solvent. Metal will adhere to the exposed regions. A few issues become immediately apparent. First of all, in evaporation, metal will accumulate at the edge of the patterned features and will ultimately close off small features. This limits the maximum aspect ratio to be about 1:1 for features patterned with liftoff. Higher aspect ratios may be possible, but the closing of the features causes structures to be narrowed towards the top.

Another issue with liftoff is that the profile is not always ideally undercut. At energies above 20 kV, the resist profile will be close to vertical in a thin layer (<100 nm) of resist. In order to improve this profile, multi-layer resists can be used which will increase the amount of undercut. A typical two layer resist would have a high molecular weight PMMA on top of a lower molecular weight PMMA or PMMA/MAA co-polymer. The bottom layer will have a higher sensitivity to electrons, and the features will be wider in this bottom layer.

Resist profiles can be further enhanced for the fabrication of special types of structures. An example of this is shown in Figure 3. Such a process is used to fabricate t-shaped transistor gates (T-Gates) for high speed mosfets. The top and bottom layers consist of PMMA. And the middle layer is a PMMA/MAA co-polymer.[14]

Liftoff is usually performed using hot-acetone or a mixture of acetone and methylene chloride. Both of these present significant health hazards. Hot acetone is highly inflammable and gives off suffocating fumes. Methylene chloride is not flammable, but it is a contact hazard that has been identified as a possible carcinogen. Obviously, extreme care must be exercised regardless of the chemical used during liftoff.

Figure 3
Resist profile used for the liftoff of metal t-gates.

Modern Lithography Systems – Recent Results

Modern lithography systems offer new capabilities which go beyond the simple ability to make nanometer scale structures. These systems are designed to be automatic and user independent. Historically, high resolution work required fine tuning by expert users. Even then, exposure parameters would need to be bracketed in order to easily achieve the ultimate resolution. It is much more desirable to be able to simply load a wafer, push a few buttons, and then unload a wafer some time later which has 20 nm structures on it. It would also be ideal for the structures to be uniform in size across the wafer, and for them to be placed with nanometer precision. Only in recent history have such systems existed. Included below are recent results which demonstrate some of the capabilities of modern lithography systems.

Fiber Bragg Grating Chirped Phase Mask

Electron beam lithography is useful for the fabrication of diffractive optics. An example of this is a chirped grating phase mask used for the patterning of optical fibers. Modern fiberoptic networks use passive subsystems for compensation of dispersion. An optical pulse will tend to widen as it travels down the fiber. This can be corrected for using a Bragg mirror that is patterned within the fiber. If the period of the grating changes as a function of length, then different wavelengths of the light will be reflected back at different times. This allows the reflected pulse to be re-focussed. Placing such a system every few kilometers in a fiber could improve the throughput of fiber-optic networks.

In order to accomplish this, the period has to change by very small amounts over a wide range. The gratings are made by burning the pattern into a fiber using UV light that is passed through a phase mask. The grating mask described by Tiberio et al.[15] was made on a quartz wafer. The grating is 10 cm long and has a change in the period over its length of about 0.5 nm. This remarkable control over the period is made possible by the high resolution digital to analog converters (DACs) available on the Leica VB6 lithography system at the Cornell Nanofabrication Facility.

The normal field of exposure of the pattern generator is accessed using 2 16 bit deflection DACs, one for x and one for y, which give 5 nm resolution over a 300 µm field. In addition to

these deflection DACs, there are scaling DACs that are used to make small corrections to the field size to correct for height changes, pattern alignment, etc. These DACs give an additional 12 bits and can scale the field by +/- 10 μm. These DACs can be directly accessed through the software used to control the system. This allows the field size to be changed by about 0.5 nm. Since the period of the grating is 1070 nm, this means that the grating period can be altered by approximately 0.001 nm. The field can be scaled each time the stage moves so that it appears that the grating pitch is almost continuously varying. Figure 4 shows the performance of such a grating after it has been transferred into a fiber. The line would ideally be somewhat more smooth, but this does demonstrate that the period did, in fact, change almost linearly by an amount of 5 angstroms over 4 cm of travel.
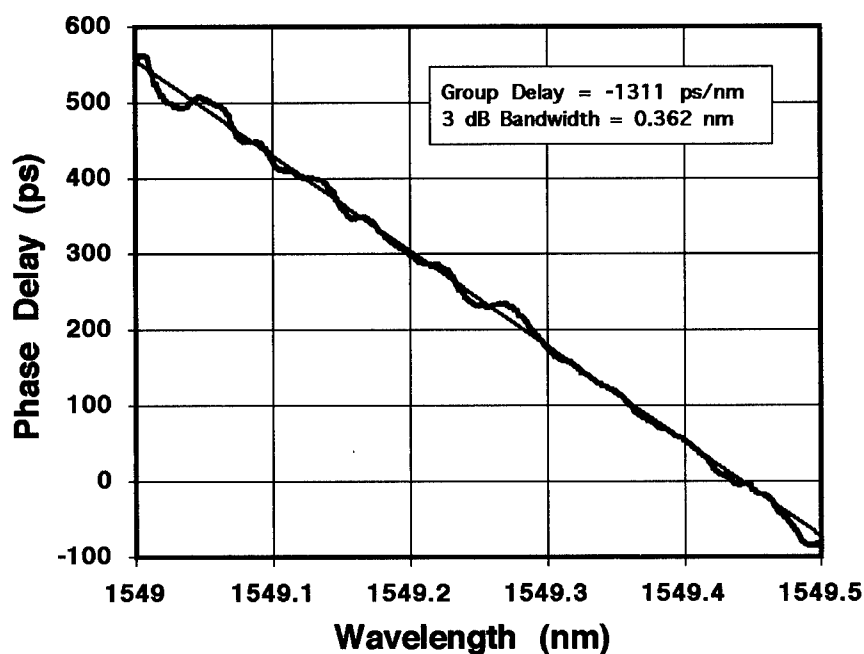
Figure 4

Phase delay as a function of the wavelength for light reflected from the chirped fiber Bragg grating.

Bi-Metal Gap Contacts

Another interesting result achieved with the Leica tool is the fabrication of metal contacts placed with nanometer precision. The structures being used in the study of molecular electronics at Oak Ridge National Laboratories by Guillorn et al. These studies require electrodes that are very closely spaced, < 30 nm, but have an open gap between them. Molecules can be deposited across this gap, and the transport properties studied. This particular project has the additional requirement in that the electrodes must be fabricated of two different metals.[16]

In order to accomplish this, the precise overlay capabilities of the lithography system were utilized. The process flow is shown in Figure 5. A single field pattern consisting of two sets of 4 alignment marks is first patterned using the ebeam. These marks are metallized using liftoff. The wafer is then reloaded and one set of marks is referenced, and the first pattern is written. The first metal is then put down using liftoff. The wafer is then put back into the system and the second set of marks are used to overlay the second pattern to the first.

Results from this process are shown in Figure 6. In Figure 6a, the top and bottom electrodes consist of two different metals. It should be noted that this narrow gap is actually 300 μm long and contains no shorts. Results such as this are reproducible with sub-5 nm precision control of the gap spacing. Figure 6b shows a 4 terminal type structure, demonstrating the placement precision that can be achieved in two axes.
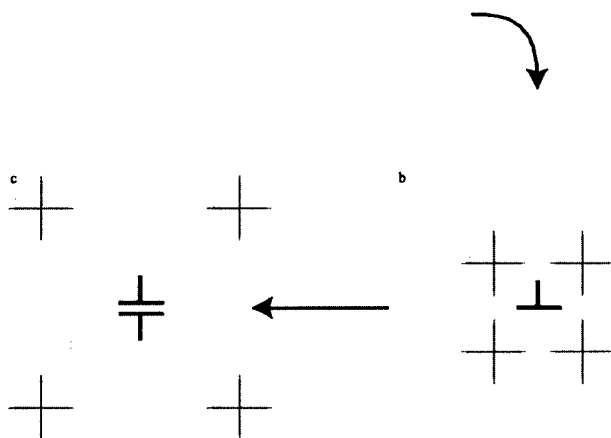
Figure 5

Process for the fabrication of bi-metal gap contacts. a) Alignment marks (octagons) are patterned with the electron beam and gold liftoff. b) The first set of marks is used for alignment of the initial pattern. c) The second set of marks is used for alignment for the patterning of the second metal.
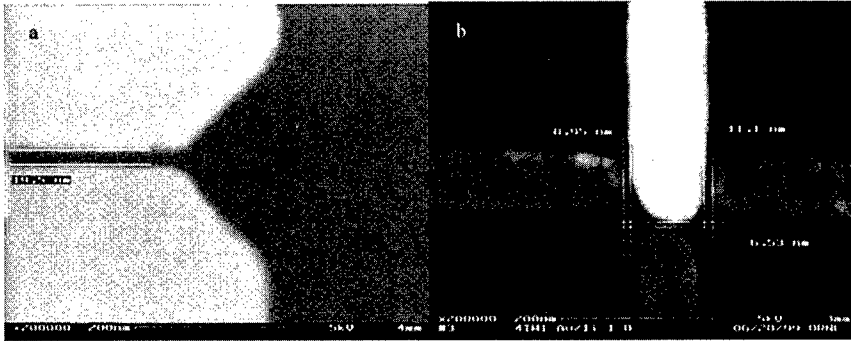
Figure 6

a) Two electrodes consisting of two different metals. The 20 nm gap continues for 300 μm without any shorts across the gap. b) 4 Electrodes, with the top electrode patterned in a different metal.

SEM-based systems

The last decade has seen a sharp increase in the accessibility of electron beam lithography. This is due primarily to the large number of SEM's that have been modified for use as lithography instruments. Commercial packages have recently become available which can turn almost any SEM into an electron beam lithography tool. Currently, there are two primary suppliers of such systems: JC Nabity Lithography Systems of the U. S. A. and Raith GmbH in Germany. The systems primarily involve a software package which can be run on a PC, in combination with digital to analog PC boards that are used for pattern generation.

These SEM systems suffer from the same problems of the early research instruments, as discussed above. The advantage of the systems is the low cost. An SEM plus the pattern generator will cost a small fraction of the amount needed for a dedicated lithography instrument. If an SEM is already available, the cost of adding a pattern generator is almost negligible. Because of this fact, these systems can be found in numerous facilities around the world. Examples of structures fabricated on such systems are shown in Figure 7.
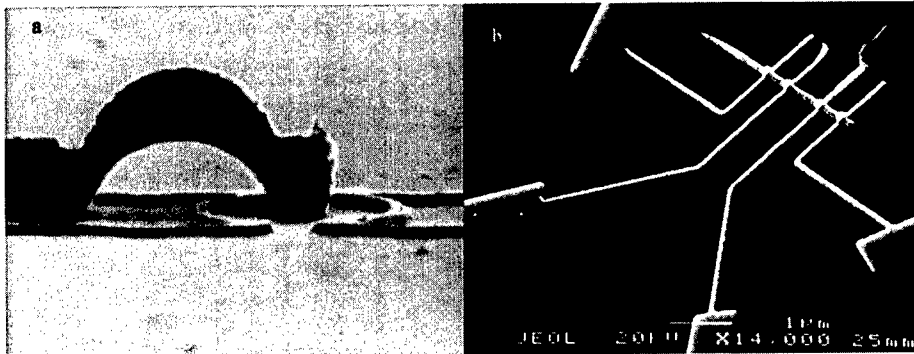
Figure 7

Photos of structures fabricated using SEMs with the Nanometer pattern Generation System from J. C. Nabity Lithography Systems. (Photos courtesy of J. C. Nabity)

a) This image shows a surface gated quantum dot device with submicron airbridge on GaAs/AlGaAs. The fabrication is done by e-beam lithography of PMMA, PMGI (a different kind of e-beam sensitive polymer) and metallization. This work was done by Dr. Yan Feng at the Institute for Microstructural Sciences, National Research Council of Canada. b) This image shows four Ag leads connecting to a Cu/Co multilayer wire. This image shows four Ag leads connecting to a Cu/Co multilayer wire.

Conclusion

Electron beam lithography has been a useful technique for nano-scale patterning since its discovery in the latter half of this century. While speed limitations will prevent its widespread use for commercial applications, it remains a useful tool for the rapid prototyping of future generations of electronics. The results above are the accumulation of 40 years of advancements. It has long been known that an electron beam can write extremely small linewidths. The latest generations make this easy to achieve over large areas, and with nanometer-scale placement accuracy.

It is still probably not possible to pattern the entire Encyclopedia Britannica on the head of a pin, but this is not far off. Now that the technology has matured, it becomes something to be used as a tool for research, and not merely the object of it. Advanced lithography systems are available in many labs around the world. SEM-based systems can be found in literally hundreds of university laboratories. The materials scientist, the physical scientist, and the biologist can all benefit from new research directions focussed on the nano-scale world. Indeed there is still plenty of room at the bottom.

Acknowledgements

42

References

1. R. P. Feynman, reprinted in J. Micromech. Sys. **1**, 60 (1992)
2. R. W. Christy, J. Appl. Phys. **31**, 1680 (1960)
3. I. Haller and P. White, J. Phys. Chem. **67**, 1784 (1963)
4. A. N. Broers, Ph. D. Thesis, Cambridge University, (1965).
5. T. H. P. Chang and W. C. Nixon, Record of the 9th Symposium on Electron, Ion and Laser Beam Technology, 123 (1967)
6. D. Zeheb, N. H. Kreitzer, and D. G. Cullum, Proc. Of the 2nd Intenational Conference on Electron and Ion Beam Science and Technology, 869 (1966).
7. R. F. M. Thornley and M. Hatzakis, Record of the 9th Symposium on Electron, Ion and Laser Beam Technology, 94, (1967)
8. I. Haller, M. Hatzakis, R. Srinivasan, IBM Journal, **12**, 251 (1968)
9. Hatzakis, M. J. Electrochem. Soc. **116**, 1033 (1969)
10. M. Hatzakis and A. N. Broers, Record of the 11th symposium on Electron, Ion, and Laser Beam Technology (1971)
11. E. D. Wolf, F. S. Ozdemir, W. E. Perkins, and P. J. Coane, Record of the 11th Symposium on Electron, Ion, and Laser Beam Technology, 331 (1971).
12. J. Pasiecznik, and J. W. Reeds, J. Vac. Sci. Technol. **15**, 909 (1978)
13. Portions of this section reproduced from R. C. Tiberio, Ph.D. Thesis, Cornell University (1994), pp. 2-6, with permission of the author.
14. R. C. Tiberio, Ph. D. Thesis, (1994) pp. 32-36.
15. R. C. Tiberio, D. W. Carr, M. J. Rooks, S. J. Mihailov, F. Bilodeau, J. Albert, D. Stryckman, D. C. Johnson, K. O. Hill, A. W. McClelland, and B. J. Hughes, J. Vac. Sci. Technol. B, **16**, 3237 (1998).
16. M. A. Guillorn, D. W. Carr, R. C. Tiberio, M. L. Simpson, and E. Greenbaum, *not yet published*

MOLECULAR SCALE ELECTRONICS. CRITICAL NANOLITHOGRAPHY ISSUES OF SYNTHESIS AND ADDRESSING

S. HUANG, E. T. MICKELSON, A. M. RAWLETT, C. L. ASPLUND, A.M. CASSELL, M. KOZAKI, T. P. BURGIN, L. JONES II, AND J. M. TOUR[*]
Department of Chemistry and Center for Nanoscale Science and Technology, MS 222, Rice University, Houston, TX 77005, USA
E-mail: tour@rice.edu

M. L. MYRICK AND P. G. VAN PATTEN
Department of Chemistry and Biochemistry, University of South Carolina, Columbia, SC 29208, USA

J. CHEN, C.-W. ZHOU, C. J. MULLER, M. R. DESHPANDE, AND M. A. REED[*]
Department of Electrical Engineering, Yale University, New Haven, CT 06520, USA
E-mail: mark.reed@yale.edu

L. A. BUMM, M. T. CYGAN, T. D. DUNBAR, P. S. WEISS[*], AND D. L. ALLARA[*]
Department of Chemistry, Pennsylvania State University, University Park, PA 16802, USA
E-mail: stm@psu.edu (Weiss), dla3@psu.edu (Allara)

ABSTRACT

As we rapidly approach the point at which solid-state electronic devices cease to be made any smaller, molecular scale electronics offers, perhaps, the best chance for a continued miniaturization of computational devices. We must, however, completely re-think our approach to lithography. Presented in this paper are our solution-phase and solid-support based syntheses of molecular wires of precise length and dimensions, and our methods of addressing these wires via molecular "alligator clips" to gold and platinum electrodes of macroscale dimensions.

INTRODUCTION

As we near the end of the road on which silicon-based electronic devices can be continually downsized [1], molecular electronics have been increasingly recognized as a promising new technology that will allow for the continued miniaturization of computational devices [2-9]. Not only do these molecules offer the possibility of fabricating extremely small computational devices, but they also offer the possibility of much lower fabrication costs, a high defect tolerance, and faster computational speeds [10,11].

To make nanoscale molecular electronic devices suitable for inclusion in a computer, we need to be able to fabricate conductive nanowires of precise length and constitution. It has been demonstrated that highly conjugated oligomers are conducting [12], whereas non-conjugated alkane chains are considerably less conductive [13]. Thus, conjugated oligomers offer promise as molecular wiring in molecular electronic devices and there has consequently been considerable recent effort to prepare large conjugated molecules of precise length and constitution [14]. The question arises, how can we make molecular wires of precise length and constitution? Conventional solid-state lithographic techniques do not apply here. Furthermore, how can we connect these wires to metal electrodes so that they may be addressed electronically? We have devised novel solution-phase and solid-supported syntheses for the generation of conjuated oligomers of precise length and constitution [15,16]. These syntheses

offer a new nanolithographic approach to the fabrication of molecular wires. We have also developed molecular alligator clips, based on chalconide and isonitrile groups, which tether the molecular wires to gold or platinum electrodes. These alligator clips serve as a linker between macroscale and nanoscale environments and afford us the ability to address the molecules via conventional electronic techniques. We have tested these wires and have demonstrated that they can be addressed from macroscale metallic electrodes using the molecular alligator clip connects.

RESULTS AND DISCUSSION

Solution-Phase Syntheses of Molecular Wires

The initial approach we took to the synthesis of these compounds maintained several key features that made it well suited for the requisite large molecular architectures for molecular scale electronics studies [17]. Specifically, the route involved (1) a rapid construction method that permits doubling the molecular length at each coupling stage to afford unbranched 100+ Å oligomers, the approximate size of present nanopatterned probe gaps, (2) an iterative approach so that the same high yielding reactions can be used throughout the sequence, (3) the syntheses of conjugated compounds that are semiconducting in the bulk, (4) products that are stable to air and light so that subsequent engineering manipulations will not be impeded, (5) products that could easily permit independent functionalization of the ends to serve as molecular alligator clips that are required for surface contacts to metal probes, (6) products that are rigid in their frameworks so as to minimize conformational flexibility yet containing substituents for maintaining solubility and processability, (7) alkynyl units (cylindrically symmetric) separating the aryl units so that ground state contiguous π-overlap will be minimally affected by rotational variations, and (8) molecular systems that do not have degenerate ground state resonance forms and are thus not subject to Peierls distortions [17,18].

The iterative divergent/convergent approach is outlined in Scheme I [17]. A batch of monomer material M, possessing inactive end groups X and Y, is divided into two portions. In one portion, the end group X is activated by conversion to X'. In the second portion, Y is activated by conversion to Y'. The two portions are then reunited to form the dimer XMMY with loss of X'Y'. Since the same end groups that were present in the monomer are now present in the dimer, the procedure can be repeated with a doubling of molecular length at each iteration. The advantages of this approach are that the molecular length grows rapidly, at a rate of 2^n were n = the number of iterations, and incomplete reactions yield unreacted material that is half the size of the desired compound. Thus, purification at each step is far simpler since separation involves, for example, an octamer from a 16-mer. This iterative divergent/convergent approach is therefore particularly attractive.

Scheme I

46
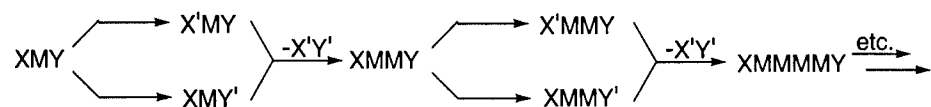
The specific iterative divergent/convergent synthetic approach is outlined in Figure 1 [17]. The sequence involves partitioning the starting monomer into two portions; iodinating the 5-position in one of the portions and desilylating the alkynyl end of the second portion. Bringing the two portions back together in the presence of a soluble Pd/Cu catalyst mixture couples the aryl iodide to the terminal alkyne, thus generating the dimer. Iteration of this reaction sequence
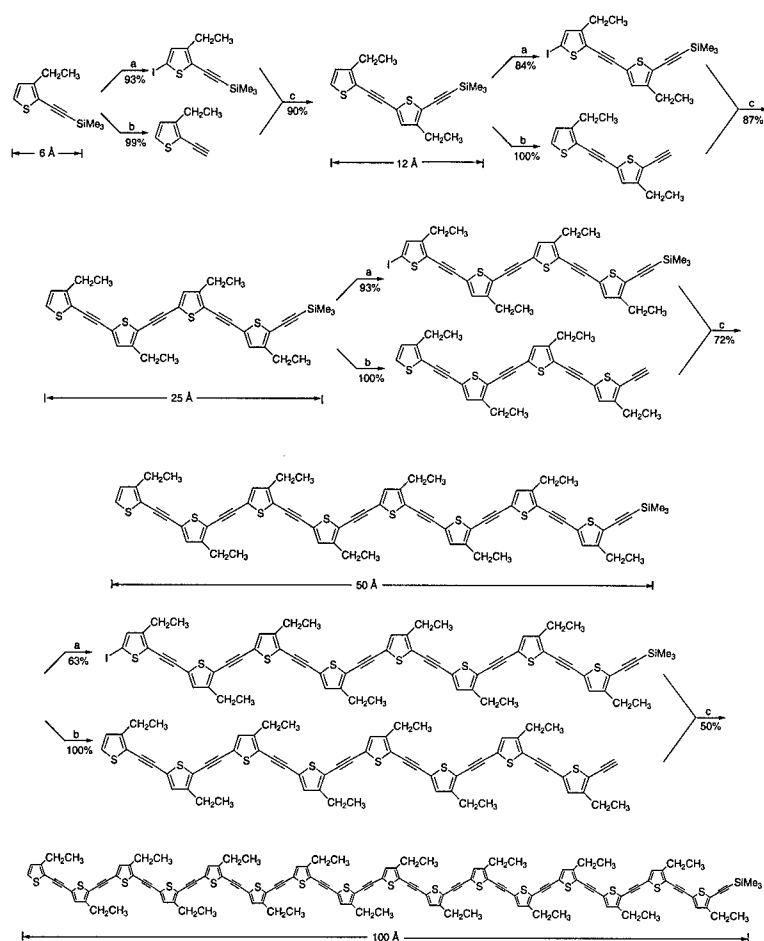
Reagents: (a) LDA, Et$_2$O, -78° to 0°C then I$_2$, -78°. (b) K$_2$CO$_3$, MeOH, 23°C. (c) Cl$_2$Pd(PPh$_3$)$_2$ (2 mol %), CuI (1.5 mol %), THF, i-Pr$_2$NH, 23 °C.

Figure 1. Solution phase synthesis of the oligo(thiophene ethynylene)s by the divergent/convergent doubling approach.

47

doubles the length of the dimer to afford the tetramer, and so on to the octamer, and finally the 16-mer. The silylated alkynes showed good oxidative stability, however, upon desilylation, the tetramer and octamer became air sensitive and immediate work-up and further coupling was necessary to minimize oxidative decomposition of these terminal alkyne intermediates. A similar molecular doubling approach approach has been used for preparing oligo(phenylene ethynylene)s which we were able to use to achieve the syntheses of 16-mers [18].

Solid-Supported Syntheses of Molecular Wires

We have extended the aforementioned molecular doubling synthetic approaches to solid phase methods for streamlining the syntheses and making them suitable for automation. Using Merrifield's resin as the solid support, we have been able to grow the oligomers from both ends; a process that can not be carried out in solution due to polymerization of the compound. This solid-support methodology is outlined in Scheme II. This gave a route to molecular length tripling at each iteration and the homooligomers proved an easy target by this process (Figure 2)

Scheme II
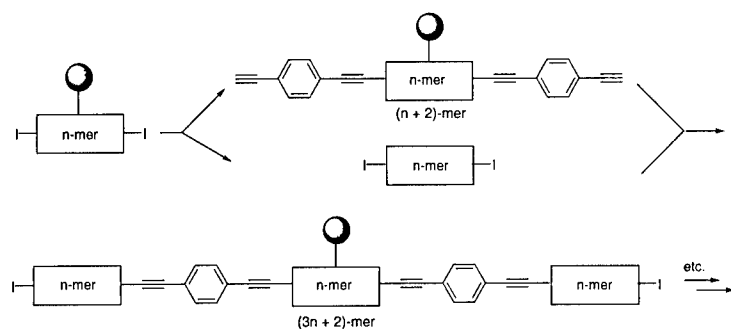
[18,19]. Additionally, the alternating block cooligomers could be rapidly prepared by this route (Figure 3) [16]. This route could be particularly attractive for preparing devices based upon linear systems since all device structures must have some element of heterogeneity for useful computational use.

Molecular Alligator Clips

Attachment of alligator clips to one or both sides of related molecules has been demonstrated [17,18]. Molecular alligator clips serve to attach or anchor the molecular wires to metal surfaces. We have utilized several types of molecular alligator clips in a quest to minimize the contact resistance with metallic probes [20]. These include sulfur, selenium, tellurium, and isonitrile end groups. We have studied these both experimentally and theoretically [21-28]. There remains, however, a need to develop molecular alligator clips that minimize the impedance mismatches between molecular structures and metal surfaces, thereby affording a better energy match between the lowest unoccupied molecular orbital of the molecule and the Fermi level of the metallic contact. For the testing described in this work thiol linkages served as

the alligator clips. Since the use of free aromatic thiols can be problematic, as they are prone to very rapid oxidative disulfide formation, we generally prefered to prepare them as thioacetates and then deprotect them later with ammonium hydroxide to give the free thiol. Shown in Scheme III is a synthetic procedure for attaching thioacetate end groups to the molecular wires.

Figure 2. Tripling iterative divergent/convergent molecular growth approach on a polymer support to prepare homooligomers.

49

Figure 3. Tripling iterative divergent/convergent molecular growth approach on a polymer support to prepare [AB] block-co-oligomers.
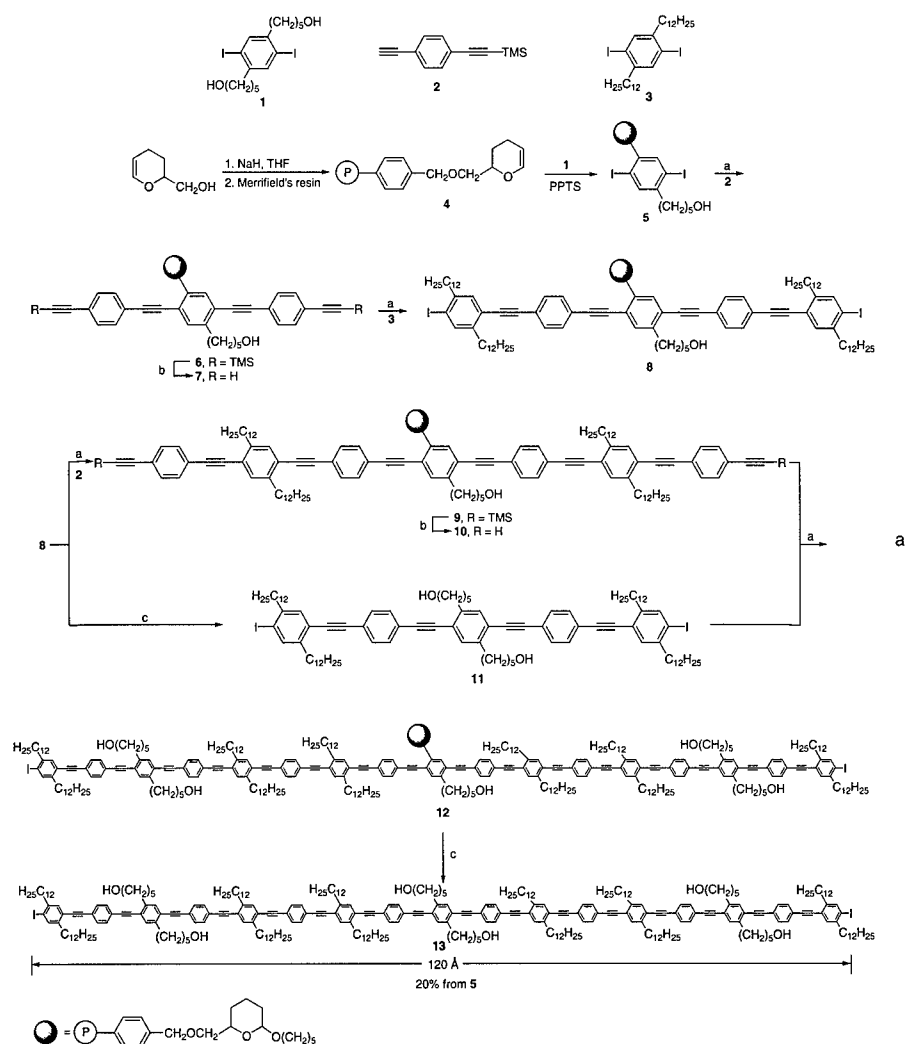
Reagents: a. Pd(dba)₂, PPh₃, and CuI (5 mol %, 10 mol %, and 5 mol %, respectively, per iodide atom), Et₂NH/THF (1:4). b. TBAF, THF. c. K₂CO₃, CH₃OH, CH₂Cl₂. d. PPTS, n-C₄H₉OH, ClCH₂CH₂Cl.

50

Scheme III

1) *t*-BuLi
2) S (powder)

3) ClCOCH₃

51%
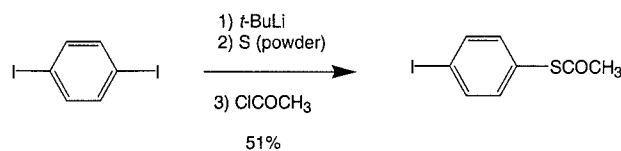
Testing of Molecular Wires

Since any potential molecular wire must be made to bridge two electrodes, the question arises as to how these rigid rod difunctional oligomers will order themselves on metallic surfaces. For example, will the oligomers bridge the gap between two gold electrodes or will they reside nearly parallel to the surface of the gold by either dithiol or aromatic adsorption to the gold surfaces [14]? By making self-assembled monolayers on gold surfaces, we have demonstrated using ellipsometry, XPS, and grazing angle IR measurements, that the rigid rod systems stand predominantly perpendicular to the surface; the thiol groups dominating the adsorption sites on the gold. Even when the oligomers were α,ω-dithiol-substituted, the rigid molecules tended to stand on end as judged by the ellipsometric thickness of the adsorbate layer [25,27,29,30]. This trend holds true for molecules that are up to approximately 50 Å; however, beyond that length, it became difficult to obtain densely packed well-ordered monolayers. Note that we utilized thioacetate end groups since these could be selectively deprotected in THF, to the free thiol, using ammonium hydroxide during the deposition process.

Our initial efforts were directed toward straddling longer molecular wires across lithographically patterned proximal gold-coated of approximately 100 Å, however, these were all unsuccessful. We then developed a technique for determining conductances of our molecular systems using a nanopore arrangement. In this embodiment, electronic measurements are performed in a nanostructure that has a metal top contact, a self-assembled monolayer (SAM) active region, and a metal bottom contact as shown in Figure 4 [31]. The essential feature of the

Figure 4. The "Nanopore."

fabrication process is the use of a nanoscale device of 30 nm in diameter that gives rise to a small number of self-assembled molecules ($\approx$ 1000) sandwiched between two metal contacts. Using this procedure, current/voltage characteristics, I(V) curves, could be recorded on a series of molecular wire systems [31]. Additionally, the contact barriers between molecule and the metallic probes, via the alligator clips, could be evaluated [31-33].

We have been able to address single molecular wires that had been inserted at grain boundaries within a self-assembled monolayer of dodecanethiolate on gold (Figure 5). Using SPM, the molecules could be individually imaged. Qualitative results of the conductance levels

Figure 5. Protocol for inserting molecular wires into dodecane thiol SAMs at grain boundaries. Relative conductance recording was done with a STM tip. The molecule at the bottom has also been used for this technique.
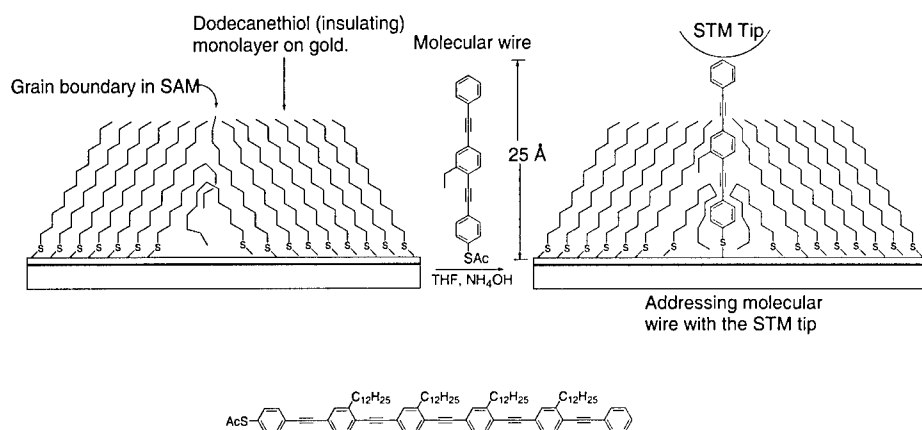
showed that the molecular wires, although topographically higher above the gold surface, were more highly conducting than the surrounding alkanethiolate structures [13,25]. Such a result is intuitive, however, it had never before been demonstrated in a single conjugated molecule, projecting on end, that was isolated from all its neighbors. We further developed methods to insert the molecular wires at controlled locations rather than at random location along grain boundaries. By applying controlled voltage pulses to an alkanethiol SAM under a solution of molecular wires (Figure 6), we could achieve precise placements of molecular wires bundles (< 10 molecules/bundle) at preprogrammed positions [34].

In order to quantify the degree of current that could be passed through a single molecule, we developed a mechanically controllable break junction (MCB) [35]. Using this device, two gold tips could be generated and moved in picometer increments with respect to each other by use of a piezo element [12]. Benzene-1,4-dithiol was permitted to self-assemble on the two tips that were, initially, widely separated. The two tips were then moved together until one molecule bridged the gap (Figure 7) [12]. Current/voltage responses were recorded for a single molecule bridging the gap. Remarkably, 0.1 microamps current could be recorded through a single molecule. Most importantly, since most computing instruments operate on microamps of current, the prospects for molecular scale electronics are quite intriguing.

Figure 6. Schematic of the lithographic pattering and replacement of conjugated molecules in an alkanethiol matrix. (a) Normal STM imaging of an alkanethiol SAM with tip bias V_b. (b) SAM removal by applying a voltage pulse V_p to the substrate. (c) Carrying out the same voltage pulse as in (b), but under a solution of molecular wires (expanded structure at bottom) causes (d) insertion of the wires into the newly vacated site.
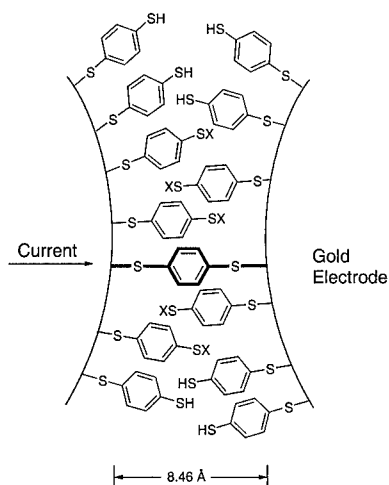
Figure 7. The desired placement of benzene-1,4-dithiolate between gold electrodes in a MCB. (X=H, Au).

SUMMARY

The age of the all silicon-based computer is drawing to a close and the dawn of silicon/molecular hybrid computers is rapidly approaching. The ability to fabricate such a molecular-based device will require the utmost in synthetic precision of molecular wires for use in the computer's circuitry. We have demonstrated nanolithography of molecular wires by utilizing novel synthetic routes that permit us to synthesize these wires with precise length and constitution. Furthermore, we have demonstrated the ability to electronically address these wires by attaching them to metal electrodes using molecular alligator clips and testing their electronic properties.

ACKNOWLEDGMENT

REFERENCES

1. P. Packan, Science **285**, 2079 (1999).

2. A. Aviram, Ed. *Molecular Electronics: Science and Technology*, Conference Proceedings No. 262 (American Institute of Physics, New York, 1992).

3. V. Mujica, M. Kemp, A. Roitberg, and M. Ratner, J. Phys. Chem. **104**, 7296 (1996).

4. A. Farazdel, M. Dupuis, E. Clementi, and A. Aviram, J. Am. Chem. Soc. **112**, 4206 (1990).

5. H. Dai, E.W. Wong, and C.M. Lieber, Science **272**, 523 (1996).

6. M.D. Ward, Chem. Ind. 568 (1996).

7. S.T. Purcell, N. Garcia, V.T. Binh, L. Jones II, and J.M. Tour, J. Am. Chem. Soc. **116**, 11985 (1994).

8. J.I. Pascual, J. Mendez, J. Gomez-Herrero, A.M. Baro, N. Garcia, U. Landman, W.D. Luedtke, E.N. Bogachek, and H.-P. Cheng, Science **267**, 1793 (1995).

9. C. Joachim, and J.F. Vinuesa, Europhys. Lett. **33**, 1100 (1996).

10. A. Aviram and M. Ratner, Eds., *Molecular Electronics: Science and Technology*, Vol. 852 (Ann. N.Y. Acad. Sci., 1998).

11. C.P. Collier, W.W. Wong, M. Belohradsky, F.M. Raymo, J.F. Stoddart, P.J. Kuekes, R.S. Williams, and J.R. Heath, Science **285**, 391 (1999).

12. M.A. Reed, C. Zhou, C.J. Muller, T.P. Burgin, and J.M. Tour, Science **278**, 252 (1997).

13. L.A. Bumm, J.J. Arnold, M.T. Cygan, T.D. Dunbar, T. P. Burgin, L. Jones II, D.L. Allara, J.M. Tour, and P.S. Weiss, Science **271**, 1705 (1996).

14. J.M. Tour, Chem. Rev. **96**, 537 (1996).

15. P. Hodge and D.C. Sherrington, Eds. *Polymer-Supported Reactions in Organic Synthesis* (J. Wiley and Sons, New York, 1980).

16. S. Huang and J.M. Tour, J. Org. Chem. (In press).

17. D.L. Pearson and J.M. Tour, J. Org. Chem. **62**, 1376 (1997).

18. L. Jones II, J.S. Schumm, and J.M. Tour, J. Org. Chem. **62**, 1388 (1997).

19. S. Huang and J.M. Tour, J. Am. Chem. Soc. **121**, 4908 (1999).

20. A.G. Zacarias, M. Castro, J.M. Tour, and J.M. Seminario, J. Phys. Chem. A. **103**, 7692 (1999).

21. J.S. Schumm, L. Jones II, D.L. Pearson, R. Hara, and J.M. Tour, Polym. Prepr. (Am. Chem. Soc., Div. Polym. Chem.) **35**(2), 687 (1994).

22. C.J. Muller, B.J. Vleeming, M.A. Reed, J.S. Lamba, R. Hara, L. Jones II, and J.M. Tour, Nanotechnology **7**, 409 (1996).

23. J.S. Schumm, D.L. Pearson, L. Jones II, R. Hara, and J.M. Tour, Nanotechnology **7**, 430 (1996).

24. W.A. Reinerth, T.P. Burgin, T.D. Dunbar, L.A. Bumm, J.J. Arnold, J. J. Jackiw, C.-w. Zhou, M.R. Deshpande, D.L. Allara, P.S. Weiss, M.A. Reed, and J.M. Tour, Polym. Mater., Sci. Engin. (Am. Chem. Soc., Div. Polym. Mater.) **78**, 178 (1998).

25. M.T. Cygan, T.D. Dunbar, J.J. Arnold, L.A. Bumm, N.F. Shedlock, T.P. Burgin, L. Jones II, D.L. Allara, J.M. Tour, and P.S. Weiss J. Am. Chem. Soc. **120**, 2721 (1998).

26. J.M. Tour, W.A. Reinerth, L. Jones II, T.P. Burgin, C.-w. Zhou, C.J. Muller, M.R. Deshpande, and M.A. Reed, *Molecular Electronics: Science and Technology* Vol. 852, edited by A. Aviram and M. Ratner (Ann. N.Y. Acad. Sci., 1998) pp. 197-204.

27. D.L. Allara, T.D. Dunbar, P.S. Weiss,L.A. Bumm, M.T. Cygan, J.M. Tour, W.A. Reinerth, Y. Yao, M. Kozaki, and L. Jones II., *Molecular Electronics: Science and Technology* Vol. 852, edited by A. Aviram and M. Ratner (Ann. N.Y. Acad. Sci., 1998) pp. 349-370.

28. J.M. Seminario, A.G. Zacarias, and J.M. Tour, J. Am. Chem. Soc. **121**, 411 (1999).

29. J.M. Tour, L. Jones II, D.L. Pearson, J.S. Lamba, T.P. Burgin, G.W. Whitesides, D.L. Allara, A.N. Parikh, and S. Atre, J. Am. Chem. Soc. **117**, 9529 (1995).

30. P.A. Weiss, L.A. Bumm, T.D. Dunbar, T.P. Burgin, J.M.Tour, and D.L. Allara, *Molecular Electronics: Science and Technology* Vol. 852, edited by A. Aviram and M. Ratner (Ann. N.Y. Acad. Sci., 1998) pp. 145-168.

31. M.A. Reed, C. Zhou, M.R. Deshpande, C.J. Muller, T.P. Burgin, L. Jones II, and J.M. Tour, *Molecular Electronics: Science and Technology* Vol. 852, edited by A. Aviram and M. Ratner (Ann. N.Y. Acad. Sci., 1998) pp. 133-144.

32. C. Zhou, C.J. Muller, M.A. Reed, T.P. Burgin, and J.M. Tour, in *Molecular Electronics*, edited by J. Jortner and M. Ratner (Blackwell Science, Oxford, 1997) pp. 191-213.

33. C. Zhou, M.R. Deshpande, M.A. Reed, L. Jones II, and J.M. Tour, Appl. Phys. Lett. **71**, 611 (1997).

34. J. Chen, M.A. Reed, C.L. Asplund, A.M. Cassell, M.L. Myrick, A.M. Rawlett, J.M. Tour, and P.G. Van Patten, Appl. Phys. Lett. **75**, 624 (1999).

35. C.J. Muller, J.M. van Ruitenbeck, and L.J. de Jough, Physica C **191**, 485 (1992).

Epitaxial Growth and Morphology

SELF-ORGANIZATION OF STEPS AND DOMAIN BOUNDARIES OF 7×7 RECONSTRUCTION ON Si(111)

H. HIBINO, Y. HOMMA, AND T. OGINO
NTT Basic Research Laboratories, Atsugi, Kanagawa 243-0198, Japan

ABSTRACT

We describe three different aspects of the self-organization of steps and domain boundaries of a 7×7 reconstruction on Si(111) surfaces. The first is the formation of a triangular-tiled pattern of '1×1' and 7×7 domains during the phase transition. '1×1' and 7×7 domains have different surface stresses. The triangular-tiled pattern is stabilized through stress relaxation. The second is the step arrangement inside a hole, which was fabricated by a standard lithographic technique. The step arrangement in the hole depends on the temperature. Below the '1×1'-to-7×7 phase transition, the hole has a three-fold symmetry consisting of step-bunched and non-bunched regions. This is because the step arrangement on the vicinal Si(111) surfaces depends on the direction of the steps. The third aspect is the formation of a pattern of steps and domain boundaries induced by Si growth. During the step-flow growth on Si(111), steps preferentially protrude along the domain boundaries on the lower terrace. The resulting changes in step shape induce a unique rearrangement of the domain boundaries, the number of which decreases during growth. However, when a periodic pattern is formed in the initial stages, it remains stable during growth.

INTRODUCTION

Much effort has been devoted to the fabrication of semiconductor nanostructures because of their great potential for semiconductor devices. While lithography and etching techniques are widely used to fabricate well-defined nanostructures, there has also been intense interest in the spontaneous formation (self-assembly) of coherently strained three-dimensional islands during strained layer growth [1,2]. Self-assembly offers an attractive route to the fabrication of nanostructures, since the islands have an unexpectedly small size distribution [3]. However, the uniformity of such structures is still insufficient for most practical applications. Furthermore, although uniformly sized but randomly distributed dots may be adequate for optical applications, a more controllable spatial arrangement is required for most electronic applications.

There have been many attempts at controlling the spatial arrangement of nanostructures. In the growth of multilayer arrays of coherent islands, the buried islands tend to influence the nucleation in the subsequent layers [4]. Tersoff *et al.* have proposed that the resulting vertical alignment of the islands in subsequent layers can lead to lateral ordering as well as to uniform island sizes [5]. We refer to such processes that cause ordering as being self-organizing processes. Multilayer steps on vicinal surfaces and slip bands on the strain relaxed substrates with misfit dislocations are preferential nucleation sites of islands, resulting in one-dimensional rows of islands [6,7]. Selective epitaxial growth mesas have been used as templates for the subsequent island growth. This approach also shows one-dimensional ordering of islands along the edges of the stripe mesas [8,9].

Heterogeneous nucleation of islands is key to controlling the spatial arrangement of islands [6-10]. The steps and domain boundaries (DB) of a 7×7 reconstruction on Si(111) surfaces serve as preferential nucleation sites of islands in epitaxial growth [11-13]. Self-organized patterns of the steps and domain boundaries lead to spatial control of the island formation. We therefore investigated self-organization of steps and DBs of the 7×7 reconstruction on Si(111). In this paper, we describe three different aspects of the self-organization. The first is the formation of a triangular-tiled pattern of '1×1' and 7×7 domains during the phase transition. The second is the

59

step arrangement inside a hole, which was fabricated by a standard lithographic technique. The third is the formation of a pattern of steps and DBs induced by Si growth.

EXPERIMENTAL

We used a complex ultrahigh vacuum (UHV) system to investigate the self-organization of steps on Si(111). The system consisted of three main chambers with different functions; a molecular-beam epitaxy (MBE) chamber for surface modification and epitaxial growth, an analysis chamber for analyzing surface electronic structures and chemical composition, and a medium-energy ion scattering chamber for analyzing surface and interface structures. The MBE chamber was equipped with two electron-beam evaporators for Si and Ge and four Knudsen cell evaporators. This chamber was also equipped with a reflection high-energy electron diffraction (RHEED) unit to observe surface structures and to control the thickness of grown layers using RHEED oscillations. The thicknesses of the grown layers were also measured using quartz crystal monitors calibrated by using RHEED oscillations. The base pressure was 3×10^{-9} Pa. The pressure during Si growth at a rate of 0.01 nm/s using the electron-gun evaporator was typically 5×10^{-8} Pa. The samples were heated by passing ac currents through them or by radiation from a W filament that was placed behind them. The step arrangement on the samples was investigated by atomic force microscopy (AFM) after they were removed from the vacuum.

UHV scanning electron microscopy (UHV-SEM) was used to observe '1×1'-to-7×7 phase transitions *in situ*. The spatial resolution of the SEM at normal incidence was about 10 nm. In SEM images, the 7×7 domains appear to be brighter than the '1×1' domains [14]. The base pressure of the chamber was 1×10^{-7} Pa, and the pressure during observations was below 2×10^{-7} Pa. Samples measuring 5×15 mm² were resistively heated with dc currents. In order to minimize the influence of heating currents on the phase transition and step arrangement [15,16], the currents were usually passed in a direction parallel to the steps.

The samples were cut from several kinds of Si(111) wafers. They were doped differently from each other, and their terrace widths and step directions were also different. We also used vicinal Si(111) surfaces misoriented 1.5° mostly toward [11$\bar{2}$] on which holes were fabricated by the standard lithographic technique. The samples were cleaned chemically, and protective oxide layers were formed in the final step. Then, the samples were introduced into UHV chambers through a load-lock. The samples were outgassed at about 550°C for several hours. The radiatively heated samples were cleaned by annealing at 900°C. In order to obtain a uniform array of steps, Si buffer layers were grown at 600°C, and the samples were annealed again at 900°C. The resistively heated samples were cleaned by flashing at 1250°C. The sample temperatures were measured with an infrared pyrometer.

TRIANGULAR-TILED ARRANGEMENT OF '1×1' and 7×7 DOMAINS [17]

We first investigated the self-organization of the '1×1' and 7×7 domains. On the Si(111) wafers that were mainly used in this study, the average terrace width was 400 nm, and the downward normal of the steps was almost [11$\bar{2}$] (hereafter referred to as [11$\bar{2}$] steps). During the '1×1'-to-7×7 phase transition, triangular 7×7 domains nucleate at the upper edges of the [11$\bar{2}$] steps [18]. '1×1' and 7×7 domains coexist in equilibrium. Figure 1 shows a SEM image of a Si(111) surface when the apex of the triangular domains reached to the lower edge of the steps. The brighter triangles correspond to 7×7 domains [14]. The 7×7 domains appeared at 860°C, and the sample temperature in Fig. 1 was 857°C. At 857°C, the areas of the 7×7 and '1×1' regions were almost the same, and their ratio did not change with time. In Fig. 1, the steps appear as lines, as indicated by the pair of arrowheads, and they run almost normal to [11$\bar{2}$]. Figure 1 clearly shows that the boundaries between '1×1' and 7×7 domains are connected straight across the steps, i.e., '1×1' and 7×7 domains form a triangular-tiled pattern.

The size of the triangular domain is mainly determined by the terrace width, because the
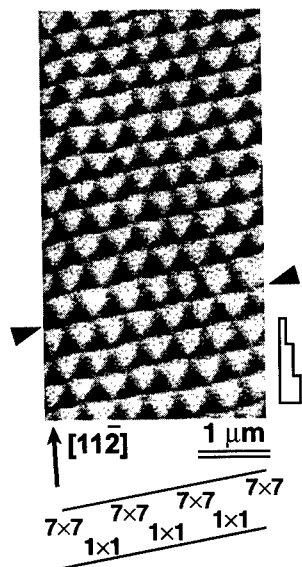
FIG. 1. SEM image of a Si(111) surface during the '1×1'-to-7×7 phase transition. The average terrace width is 400 nm, and the steps are mostly oriented to [11$\bar{2}$]. Brighter triangles correpond to the 7×7 domains. The steps run as indicated by the pair of arrowheads.
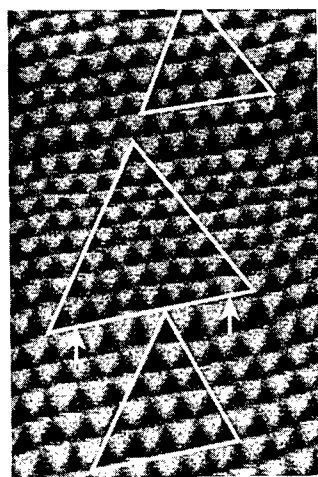
FIG. 2. SEM image of a Si(111) surface with a varying terrace width during the '1×1'-to-7×7 phase transition. The area within the triangles indicate that the surface consists of various ordered triangular-tiled regions.

triangular 7×7 domains grow until they reach the lower edge of the step. Therefore, fluctuations in the terrace width cause the domain size to fluctuate, which prevents '1×1' and 7×7 domains from forming an ordered pattern. Figure 2 shows a Si(111) sample with terrace width distribution. Here, the triangles are overlaid to highlight the ordered triangular-tiled arrangements. Comparing the sizes of the '1×1' and 7×7 domains in these triangles, one can detect a difference in their size. Between the two arrows in Fig. 2, there are six '1×1' domains in the upper region, but five 7×7 domains in the lower region. This figure clearly shows that surfaces with terrace width distributions consist of ordered triangular-tiled regions with different periods and that the boundary between the regions lies along a step. This probably indicates that the force driving the arrangement of triangular domains with the same size along a step is stronger than that driving their arrangement across the steps.

Figure 3 shows the temporal evolution of a '1×1' and 7×7 domain pattern. The sample was quenched from the temperature above the '1×1'-to-7×7 phase transition to the pattern formation temperature. Horizontal rastering produced these images, and it took about 1 min to take each one. Therefore, these SEM images themselves include information about changes that occurred over time. Just after the quench, the 7×7 domains nucleate almost randomly along the steps, and their shapes are not regular triangles. After a minute [Fig. 3(b)], the density of the 7×7 domains decreases, and their shapes become more regular. Looking at Figs. 3(c) and 3(d), one can see that the domain pattern proceeds through the shrinkage of the domains indicated by the circles in Fig. 3(c). This temporal evolution indicates that the triangular-tiled arrangement of the '1×1' and 7×7 domains is an equilibrium configuration, but that the formation of the ordered domain pattern is a relatively slow process that requires several minutes for completion.

During the '1×1'-to-7×7 phase transition on the Si(111) sample with [11$\bar{2}$] steps,
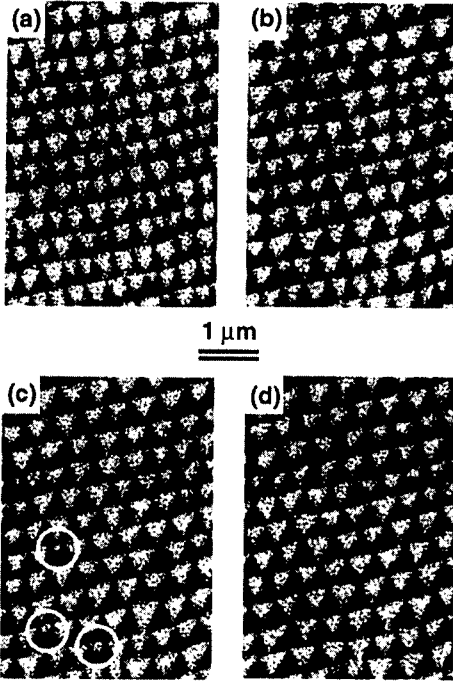
FIG. 3. Temporal evolution of '1×1' and 7×7 domain pattern after the sample was quenched from above the phase transition temperature. (a) Just after the quench; (b)-(d) 1, 2, and 3 min later. The small triangles in the circles in (c) are not seen in (d).

triangular 7×7 domains whose outside normals are directed towards [11$\bar{2}$] nucleate at the upper edges of the steps. This is because these types of domain boundaries have the lowest formation energy. The triangular shape is the consequence of the Si(111) surface having a three-fold symmetry. The 7×7 domains grow into terraces until they reach the lower edges of the steps. Therefore, the size of the triangular domains is mainly determined by the terrace width, and domains with the same size are arranged along the steps. What then induces the arrangement across the steps? We infer that the triangular-tiled arrangement is stabilized by interactions through elastic-stress relaxation. It is well-known that the 7×7 phase has a greater surface stress than the '1×1' phase [19,20]. At the 7×7 and '1×1' domain boundary, this stress difference creates a force density whose direction is normal to the boundary and whose magnitude is equal to the stress difference between '1×1' and 7×7 phases. In order to confirm that the triangular-tiled arrangement is stabilized through stress relaxation, we calculated the elastic interaction energies for a series of domain patterns. Starting from a triangular-tiled arrangement, we shifted the 7×7 domains collectively along the steps while keeping the domain size determined by the terrace width. The elastic interaction energies were calculated as a function of the relative shift. The calculations showed that the triangular-tiled arrangement has the lowest energy.

Next, we investigated the domain patterns on Si(111) surfaces whose terrace widths were much wider than that on the samples studied so far (400 nm). On these samples, 7×7 domains cannot grow to the lower edge while keeping their triangular shape; instead, additional triangular domains nucleate at the apex of the 7×7 domains. Figure 4 shows a SEM image of a Si(111) surface with a terrace width of about 750 nm. This figure clearly shows that the 7×7 domains do not have a simple triangular shape, but instead consist of 2-3 triangles. Furthermore, we can see that the position of the additional triangle (see figure) depends on the direction of the step. The steps in Fig. 4 are gradually curved, and the direction of the steps is almost [11$\bar{2}$] at the center. As one moves to the right or left side of Fig. 4, the step direction is gradually

FIG. 4. SEM image of a Si(111) surface during the '1×1'-to-7×7 phase transition. The average terrace width is 750 nm, and the steps are mostly oriented to [11$\bar{2}$]. The 7×7 domains consist of a few triangles, and their shapes depend on the direction of the step.
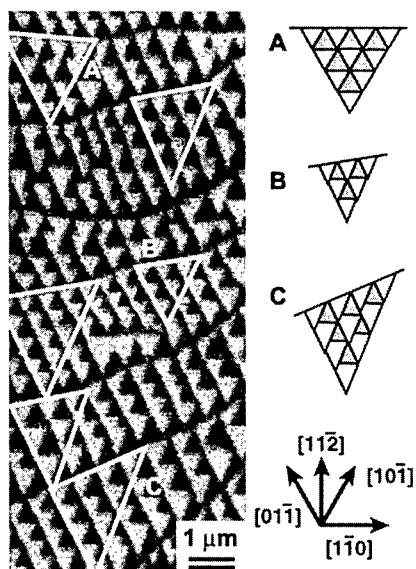
FIG. 5. SEM image of a Si(111) surface during the '1×1'-to-7×7 phase transition. The average terrace width is close to 2 μm. The 7×7 domains consist of several triangles. The '1×1' and 7×7 triangles have an orderly arranged in some areas, even on one terrace, as shown by the triangles. Three arrangements of the '1×1' and 7×7 triangles are schematically illustrated.
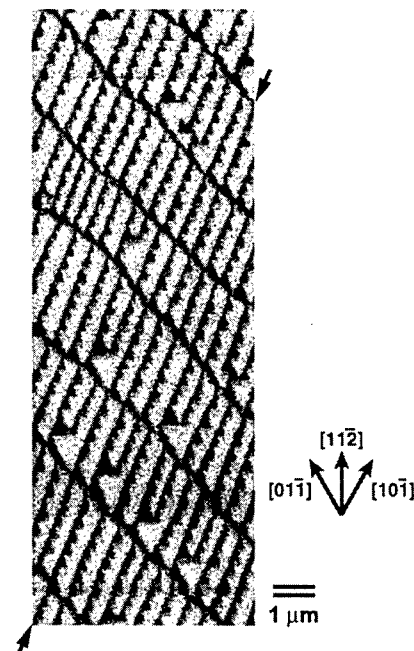
FIG. 6. SEM image of a Si(111) surface during the '1×1'-to-7×7 phase transition. The sample was the same as in Fig. 5, but was a little cooler. The 7×7 domains consist of several triangles, and look like mountain ranges.

rotated to [01 1̄] or [10 1̄]. At the [11 2̄] step, the 7×7 domains are triangular or Christmas-tree shaped. At the steps rotated from [11 2̄] to [01 1̄] or [10 1̄], the 7×7 domains consist of 2-3 triangles one of whose sides are common, and the common side is along [01 1̄] or [10 1̄], respectively.

On the sample shown in Fig. 5, the terrace width is further increased. The 7×7 domains again consist of several triangles that have common sides. Because the average step direction is rotated a little from [11 2̄] to [01 1̄], the common side is along [01 1̄]. Figure 5 also contains ordered arrangements of the '1×1' and 7×7 triangles (structures A, B, and C), even on one terrace. At the steps whose normal is close to [11 2̄], '1×1' and 7×7 domains form a triangular-tiled pattern. In the triangular-tiled pattern, all the sides of the triangles are lined up. However, at the steps whose normal direction is rotated from [11 2̄] to [01 1̄], as the schematic illustration shows, the triangles overlap each other. In this pattern, the sides of the triangles are lined up in two directions, along [01 1̄] and [10 1̄], and not in one direction along [1 1̄ 0]. The overlap between the 7×7 triangles increased after the sample was cooled down a little bit [Fig. 6]. The '1×1' and 7×7 domains line up across single steps. We believe that these phenomena, including the relation between the step direction and the shape of the 7×7 domain, are caused by the stress relaxation, but we have not confirmed this yet by calculation.

63

STEP ARRANGEMENT INSIDE HOLE [21]

It is well-known that the step arrangement on vicinal Si(111) surfaces depends on the direction of the misorientation [22-27]. On vicinal Si(111) surfaces misoriented toward the $[1\bar{1}0]$ or $[11\bar{2}]$ direction, the '1×1'-to-7×7 phase transition causes step bunching [22-24,26]. On these surfaces, the '1×1'-to-7×7 phase transition temperature T_c depends on the misorientation angle θ. Above $T_c(\theta)$, the surfaces are uniformly covered with single-layer steps. Below $T_c(\theta)$, the surfaces are separated into 7×7-reconstructed (111) facets and stepped regions, and the inclination of the stepped regions increases as the temperature decreases. On the $[11\bar{2}]$-misoriented surfaces, the step bunches are transformed into (331) facets below 600°C, which are inclined at 22° with respect to (111) [28]. On vicinal Si(111) surfaces misoriented toward $[\bar{1}\bar{1}2]$, T_c is independent of the misorientation single, and single- and triple-layer steps coexist on the surface below T_c [24,25,27].

In order to examine how the misorientation direction influences the step arrangement on vicinal Si(111) surfaces, we investigated the step arrangement inside holes. We used vicinal Si(111) samples misoriented by 1.5° mostly toward $[11\bar{2}]$ on which holes 0.6-2 µm wide and 1 µm deep were fabricated by a standard lithographic technique [29-31]. The samples were resistively heated with ac currents, because dc currents greatly influence the hole shape [32]. Cubic-shaped holes were transformed to cone-shaped holes after annealing at 1220°C. The samples were cooled to the target temperature through the 7×7 phase transition temperature at the rate of 2 K/min and then were annealed at the target temperature for 1 h. The step arrangement inside the holes was measured by AFM in air.

Figure 7(a) shows an AFM image of the hole array annealed at a temperature 25 K lower than the 7×7 phase transition temperature. This AFM image was imaged by the height difference while the tip was scanned horizontally from left to right. This figure shows highly regular patterns of the steps around each hole. The misorientation angle of the substrate was 1.5°. The steps corresponding to the misorientation were rearranged during high temperature annealing. Wide step bands were formed at the upper sides of the holes [29-31]. We can also see crossing steps between two wide step bands, which can be attributed to the misalignment between the directions of the hole array and the step. Figure 7(b) shows a magnified image of one of the holes in Fig. 7(a). The hole has threefold symmetry consisting of step-bunched and non-bunched regions. The steps in the non-bunched regions are $<1\bar{1}2>$ steps. The step arrangement inside the hole is consistent with the reported results about the step arrangement on vicinal Si(111) surfaces. However, the explanation is still qualitative. In order to get a quantitative treatment of the step arrangement inside the hole, the temperature dependence of the step arrangement should be examined.
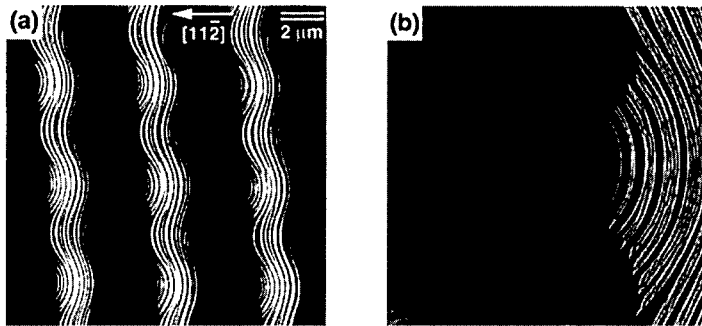
FIG. 7. AFM images of a Si(111) surface on which a hole array was fabricated by standard lithographic techniques. The sample was quenched after annealing at a temperature 25 K lower than the 7×7 phase transition temperature.

Figure 8 shows AFM images of holes annealed at various temperatures. Because the images
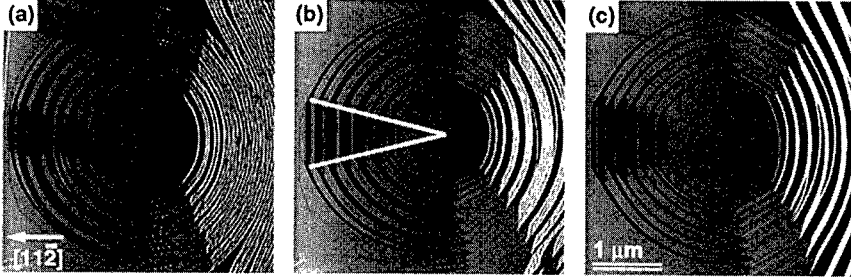
FIG. 8. AFM images of holes fabricated on Si(111). (a)-(c) were quenched after annealing at the temperature lower than the 7×7 phase transition temperature by 15, 50, and 100 K, respectively.

were taken from the different samples, the holes (inclination angle of the side, area of the base, and so on) vary in shape. However, their side inclination angles are all within 3° and 4°. The difference in shape does not affect the overall step arrangement very much. The annealing temperatures of the samples in Figs. 8(a)-8(c) were lower than the 7×7 phase transition temperature on the flat surface by 15, 50, and 100 K, respectively. Figures 7 and 8 clearly show that the width of the non-bunched region increases as the temperature decreases.

We also calculated the step arrangement inside the hole. In this calculation, we first plotted the free energies of '1×1' and 7×7 surfaces per unit area projected to a reference surface, $F_{.1\times1.}(\theta,\phi,T)$ and $F_{7\times7}(\theta,\phi,T)$, as a function of $\tan\theta$ and the azimuth angle ϕ. Then, we searched the tie bars on the plot of the surface free energies [26]. In the case of vicinal surfaces, statistical mechanical theory tells us that F can be written as

$$F(\theta,\phi,T)=f(T)+\frac{\beta(\phi,T)}{h}\tan\theta+\frac{g(\phi,T)}{h^3}\tan^3\theta,$$

where f is the surface energy of the terrace per unit area, β is the individual step free energy per unit length, h is the step height, and $g/h^3\tan^3\theta$ is the free energy per unit area due to step-step interactions [33]. Under several reasonable assumptions, the calculated results could well account for the threefold symmetry of the step arrangement inside the holes [21]. Figure 9 shows the model we used for the calculations. The original hole shape is circular. The temperature used in the calculation was 50 K lower than the 7×7 phase transition temperature. The 7×7 reconstruction is formed on the terraces in the shaded area. The sectors in the shaded region that are curved showed bunching, whereas the sectors with straight steps showed no bunching. The calculations also confirmed that the width of the non-bunched regions increases as the temperature decreases. However, the calculated temperature dependence did not agree with the experimental result perfectly. This is because the parameters used in the calculation
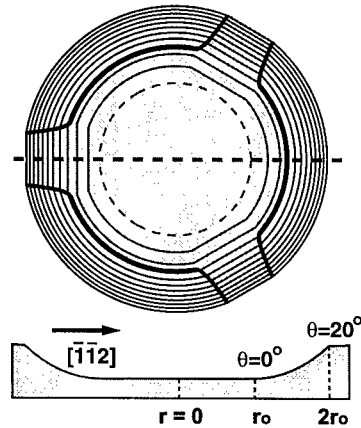
FIG. 9. An example of calculated hole shapes. The temperature used in the calculation was 50 K lower than the 7×7 phase transition temperature. The 7×7 reconstruction is formed on the terraces in the shaded area.

65

were not optimized and/or because some assumptions were too simple.

STEP REARRANGEMNET DURING Si

Clean Si(111) surface [34]

Lastly, we describe step rearrangement during Si homoepitaxy. We investigated step rearrangement on clean Si(111)7×7 surfaces. Figure 10 shows typical AFM images of Si(111) surfaces (a) before and (b)-(e) after Si MBE. The average terrace width on these samples was about 800 nm, and the outside normal of the steps before growth was mostly in the $[11\bar{2}]$ direction. The growth temperature was 750°C, and the growth rate was 0.013-0.014 nm/s. The thicknesses of the grown Si layers in (b)-(e) are 1 monolayer (ML), 1 nm, 50 nm, and 100 nm respectively. Ge layers (1-nm thick) were deposited at room temperature after the Si growth step. Then, the samples were annealed at 250-300°C. Because Ge islands were preferentially formed at steps and DBs of the 7×7 reconstruction, we could easily determine the positions of the steps and DBs using AFM [11,13]. Figure 10(a) shows that the steps are fairly straight and that the DBs cross the terraces at nearly right angles to the steps before Si MBE. The distances between DBs vary somewhat, and the average distance is 350 nm. DBs have no correlation across steps. This is because the sample was cooled through the 7×7 phase transition at the rate of 1 K/s, which is too fast for '1×1' and 7×7 domains to form a regular pattern.

After the growth of 1-ML-thick Si [Fig. 10(b)], peninsulas protrude from the upper step edges along DBs on the lower terraces. This is because the deposited Si atoms are preferentially incorporated into crystal at positions, X_1, where the steps connect with DBs on the lower terraces. After 1-nm growth [Fig. 10(c)], the steps take on a saw-tooth shape. Moreover, the neighboring steps have opposite phases. The steps and DBs form a hexagonal network. After 50-nm growth [Fig. 10(d)], the steps tend to meander, and hexagonal networks of steps and DBs are rarely observed. Additionally, there is a striking reduction in the numbers of DBs. In Fig. 10(d), the
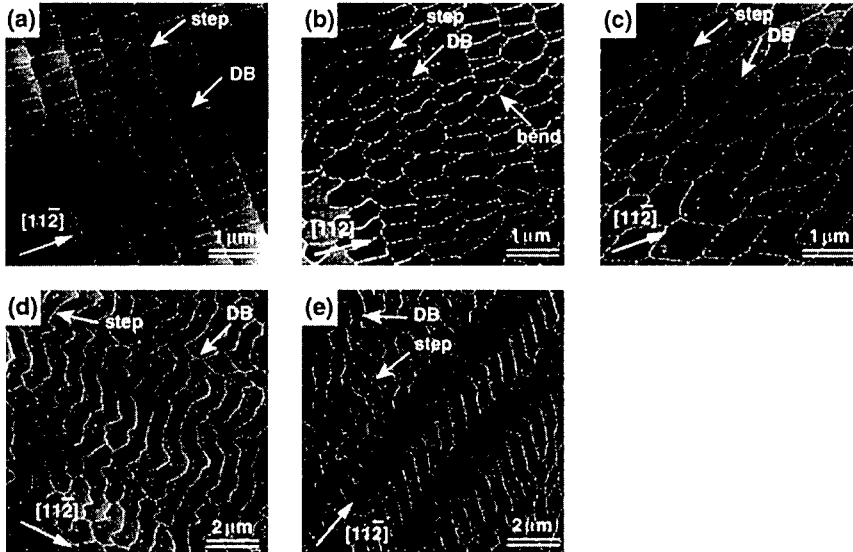
FIG. 10. AFM images of Si(111) surfaces (a) before and (b)-(e) after Si MBE. The growth temperature was 750°C, and the growth rate was 0.013-0.014 nm/s. Thicknesses of the grown Si layers in (b)-(e) are 1 ML, 1 nm, 50 nm, and 100 nm respectively.
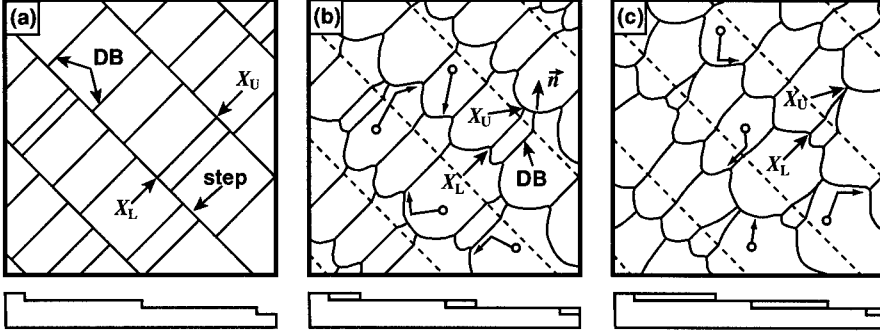
FIG. 11. Schematic illustration of step and DB rearrangement during MBE.

average distance between DBs is 2 μm. When we plotted the average DB distance as a function of the thickness of the MBE-grown Si layers, the distance increases as the thickness increases. The differences between the distances before and after MBE were well fitted to a power law [34]. When the thickness was further increased to 100 nm [Fig. 10(e)], a new feature appeared. The steps fluctuated in phase and the amplitude in the [11$\bar{2}$] direction gets much larger.

The arrangements of steps and DBs obtained before and during Si MBE are schematically shown in Fig. 11. During the '1×1'-to-7×7 phase transition, the 7×7 reconstructions nucleate at the upper edges of the steps, and the 7×7 reconstruction grows into terraces. After the phase transition, steps and DBs form a mesh pattern as shown in Fig. 11(a). This requires that there is an energy cost per unit length of DB [19]. A DB crosses the terrace normally to the steps in order to minimize the length of the DB (i.e., the energy cost). In the step-flow growth regime, deposited Si atoms migrate on this surface and eventually are incorporated into the crystal by attaching themselves to steps. During Si MBE on Si(111), peninsulas begin to protrude along the DBs on the lower terraces as shown in Fig. 11(b). This indicates that Si atoms are preferentially incorporated into the crystal at X_L. When Si atoms become attached to steps at X_L, the length of the DBs becomes shorter than when Si atoms become attached at other places. Therefore, X_L provides an energetically favorable bonding site.

Next, we consider the motion of the points, X_U, where the steps connect with DBs on the upper terraces. Before Si MBE, most of the DBs run along the average step normal. During step advancement, DBs should grow along the normal to the steps because the DBs are kept short. During MBE, however, the steps become wavy. This waviness causes the local step normal to vary with position along the step. Therefore, the DB growth direction depends on the position of X_U along the step and is not necessarily along the average step normal. When their growth direction (local step normal) is different from the average step normal, bends are formed in DBs. An example of the bend is shown by the arrow in Fig. 10(b). Thus, in a DB, the portion between the bend and X_L is a remnant of the DB on the substrate and the portion between the bend and X_U is the DB grown during MBE. This means the original steps were located at lines connecting bends in DBs, as indicated by the dashed lines in Figs. 11(b) and 11(c). Because steps protrude at X_L, X_U moves away from the neighboring X_L. Further growth causes X_Ls to move very far into the area between the peninsulas of the step. When there are two or more X_Us between two adjacent X_Ls, eventually, the DBs become combined, resulting in reduction of the number of DBs, as shown in Fig. 11(c). This is the essence of the DB reduction process during MBE, and we simulated the DB reduction process with a simple model [35]. The results of simulation were in good agreement with the dependence of the average distance between DBs on the thickness.

In Fig. 10, the steps are mostly directed along [11$\bar{2}$], and the steps favor a [$\bar{1}$ $\bar{1}$ 2] character during growth [36-38]. Therefore, the steps and DBs form a temporary hexagonal network.
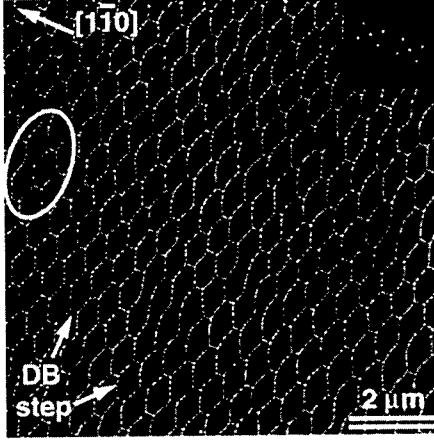
FIG. 12. Scale-shaped arrangement of steps and DBs formed after Si MBE. 50-nm-thick Si layers were grown at 750°C. The inset is the Fourier tranform of the image.

However, because DBs on the substrate have no correlation across steps, the resulting hexagonal network is incomplete. Therefore, as MBE progresses, the number of DBs is further reduced, and the hexagonal network is destroyed. However, if a pattern of steps and DBs in which there is one X_U between two adjacent X_Ls is formed, it remains stable during MBE. The scale-shaped pattern shown in Fig. 12 is an example of the self-organization of the steps and DBs. The Fourier transform of the image shown in the inset clearly shows a two-dimensional periodicity. In Fig. 12, some pairs of DBs satisfy the necessary condition of reducing DBs, that is, there are two or more domain boundaries on the upper terrace between two adjacent DBs on the lower terrace. One of these pairs is indicated by the circle. However, these pairs are not combined because the fluctuation in the steps is also self-organized and the self-organized fluctuation prevents these pairs from moving close together.

Al-adsorbed Si(111) surface

In this section, we investigate how the step rearrangement on Al-adsorbed Si(111) is different from that on clean Si(111). We deposited Al at the sample temperature of 600°C and annealed the samples at 800°C. The amount of Al was controlled by the annealing time at 800°C. We prepared two types of Al-adsorbed Si(111) substrates. The first type was fully covered with the Al-induced $\sqrt{3}\times\sqrt{3}$ reconstruction. The second type of the substrate was partially covered with the $\sqrt{3}\times\sqrt{3}$ reconstruction. The RHEED patterns showed that the $\sqrt{3}\times\sqrt{3}$ and 7×7 reconstructions coexist on the surface. On both types of the substrates, Si was grown at 750°C.
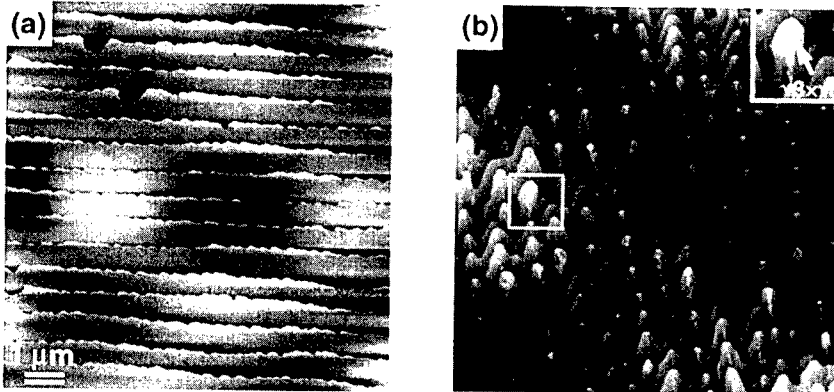
FIG. 13. AFM images of Al-adsorbed Si(111) surfaces after Si MBE. (a) was fully covered with the Al-induced $\sqrt{3}\times\sqrt{3}$ reconstruction , and $\sqrt{3}\times\sqrt{3}$ and 7×7 reconstructions coexisted on (b). The inset in (b) is a magnified image of the area indicated by the square.

Figure 13 shows AFM images of Al-adsorbed Si(111) surfaces after Si homoepitaxy. The Si thickness was 5 nm. The first and second types of the substrates were used for (a) and (b). After the Si growth on the √3×√3 surface, there was a regular array of steps. However, on the surface where the √3×√3 and 7×7 reconstructions coexist, the steps were no longer regular. The steps also fluctuated in phase. In the AFM images, the √3×√3 reconstructed area is higher than the 7×7 reconstruction area. Figure 13(b) shows that the √3×√3 reconstructed area is preferentially located at the top of the protruding steps and that the √3×√3 reconstructed area connects the two protrusions on the neighboring steps. This indicates that, on surfaces consisting of multiple phases, steps and reconstructed domains can be self-organized by step-flow growth. However, we as yet do not fully understand the mechanism of the self-organization. This is a topic for future study.

CONCLUSION

In this paper, we described three different aspects of self-organization of steps and domain boundaries of the 7×7 reconstruction on Si(111) surfaces. The first is the formation of a triangular-tiled pattern of '1×1' and 7×7 domains during the phase transition. The triangular-tiled pattern is stabilized through stress relaxation. Because this pattern is formed only during the phase transition, it is impossible to keep the pattern at different temperatures. However, it has been reported that the reaction rate with N is much higher on 7×7 than on '1×1' [39]. The preferential reaction of N with the 7×7 domains provides a possible way of stabilizing the pattern.

The second aspect is the step arrangement inside a hole fabricated by a standard lithographic technique. The step arrangement in the hole depends on the temperature. Below the '1×1'-to-7×7 phase transition, the hole has a three-fold symmetry consisting of step-bunched and non-bunched regions. Non-bunched regions consists of <1 12> steps. Therefore, the steps in the step-bunched regions have many kinks, but the kink density on the steps in the non-bunched regions is very small. It is expected that deposited Ge atoms in the hole diffuse faster on the non-bunched regions and form Ge islands preferentially on the step-bunched regions. Such a preference might cause an epitaxial pattern of GaAs islands inside a hole [40].

The third aspect is the formation of a pattern of steps and domain boundaries induced by Si growth. During the step-flow growth on Si(111), steps preferentially protrude along the domain boundaries on the lower terrace. The resulting changes in step shape induce a unique rearrangement of the domain boundaries, the number of which decreases during growth. However, when a periodic pattern is formed in the initial stages, it remains stable during growth. The periodic pattern of steps and DBs can be decorated by Ge islands. The Ge island network can be controlled through self-organization of steps and DBs during step-flow growth. Furthermore, we demonstrated that steps and reconstructed domains could be self-organized during Si MBE on a surface consisting of multiple reconstructed phases.

ACKNOWLEGEMENTS

REFERENCES
[1] D. J. Eaglesham and M. Cerullo, Phys. Rev. Lett. **64**, 1943 (1990).
[2] R. Nötzel, J. Temmyo, and T. Tamamura, Nature **369**, 132 (1994).
[3] D. Leonard, M. Krishnamurthy, C. M. Reaves, S. P. Debaars, and P. M. Petroff, Appl. Phys. Lett. **63**, 3203 (1993).
[4] Q. Xie, A. Madhukar, P. Chen, and N. P. Kobayashi, Phys. Rev. Lett. **75**, 2542 (1995).
[5] J. Tersoff, C. Teichert, and M. G. Lagally, Phys. Rev. Lett. **76**, 1675 (1996).

[6] M. Kitamura, M. Nishioka, J. Oshinowo, Y. Arakawa, Appl. Phys. Lett. **66**, 3663 (1995).

[7] S. Yu. Shiryaev, F. Jensen, J. Lundsgaard Hansen, J. Wulff Petersen, and A. Nylandsted Larsen, Phys. Rev. Lett. **78**, 503 (1997).

[8] T. I. Kamins and R. Stanley Williams, Appl. Phys. Lett. **71**, 1201 (1997).

[9] G. Jin, J. L. Liu, S. G. Thomas, Y. H. Luo, K. L. Wang, and Bich-Yen Nguyen, Appl. Phys. Lett. **75**, 2752 (1999).

[10] X. Deng and M. Krishnamurthy, Phys. Rev. Lett. **81**, 1473 (1998).

[11] U. Köhler, O. Jusko, G. Pietsh, B. Müller, and M. Henzler, Surf. Sci. **248**, 321 (1991).

[12] H. Hibino, N. Shimizu, and Y. Shinoda, J. Vac. Sci. Technol. A **11**, 2458 (1993).

[13] H. Hibino, N. Shimizu, Y. Shinoda, and T. Ogino, Mat. Res. Soc. Symp. Proc. **317**, 41 (1994).

[14] Y. Homma, M. Suzuki, and M. Tomita, Appl. Phys. Lett. **62**, 3276 (1993).

[15] H. Hibino, Y. Homma, and T. Ogino, Surf. Sci. Lett. **364**, L587 (1996).

[16] H. Yamaguchi and K. Yagi, Surf. Sci. **287/288**, 820 (1993).

[17] H. Hibino, Y. Homma, and T. Ogino, Phys. Rev. B **58**, R7503 (1998).

[18] M. Hoshino, Y. Shigeta, K. Ogawa, and Y. Homma, Surf. Sci. **365**, 29 (1996).

[19] K. Yagi, A. Yamanaka, H. Sato, M. Shima, H. Ohse, S. Ozawa, and Y. Tanishiro, Prog. Theor. Phys. Supp. **106**, 303 (1991).

[20] R. D. Twesten and J. M. Gibson, Phys. Rev. B **50**, 17628 (1993).

[21] H. Hibino, Y. Homma, N. C. Bartelt, and T. Ogino, (to be published).

[22] R. J. Phaneuf and E. D. Williams, Phys. Rev. Lett. **58**, 2563 (1987).

[23] R. J. Phaneuf, E. D. Williams, and N. C. Bartelt, Phys. Rev. B **38**, 1984 (1988).

[24] E. D. Williams and N. C. Bartelt, Science **251**, 393 (1991).

[25] J. Wei, X.-S. Wang, J. L. Goldberg, N. C. Bartelt, and E. D. Williams, Phys. Rev. Lett. **68**, 3885 (1992).

[26] E. D. Williams, R. J. Phaneuf, J. Wei, N. C. Bartelt, and T. L. Einstein, Surf. Sci. **294**, 219 (1993).

[27] H. Hibino and T. Ogino, Phys. Rev. Lett. **72**, 657 (1994).

[28] H. Hibino, T. Fukuda, M. Suzuki, Y. Homma, T. Sato, M. Iwatsuki, K. Miki, and H. Tokumoto, Phys. Rev. B 47, 13027 (1993).

[29] T. Ogino, H. Hibino, and Y. Homma, Jpn. J. Appl. Phys. **34**, L668 (1995).

[30] T. Ogino, H. Hibino, and Y. Homma, Appl. Surf. Sci. **107**, 1 (1995).

[31] T. Ogino, H. Hibino, and Y. Homma, Appl. Surf. Sci. **117/118**, 642 (1997).

[32] Y. Homma, H. Hibino, Y. Kunii, and T. Ogino, Surf. Sci. (to be published).

[33] C. Jayaprakash, C. Rottman, and W. F. Saam, Phys. Rev. B **39**, 6549 (1984).

[34] H. Hibino and T. Ogino, Appl. Phys. Lett. **67**, 915 (1995).

[35] T. Kawamura, H. Hibino, and T. Ogino, Jpn. J. Appl. Phys. **38**, 1530 (1999).

[36] R. T. Tung and F. Schrey, Phys. Rev. Lett. **63**, 1277 (1989).

[37] R. T. Tung, F. Schrey, and D. J. Eaglesham, J. Vac. Sci. Technol. B **8**, 237 (1990).

[38] T. Hasegawa, M. Kohno, S. Hosaka, and S. Hosoki, Phys. Rev. B **48**, 1943 (1993).

[39] M. Tabe, Jpn. J. Appl. Phys. **34**, L1375 (1995).

[40] P. Finnie and Y. Homma, Appl. Phys. Lett. **72**, 827 (1998).

STRUCTURAL EVOLUTION DURING THE INITIAL EPITAXIAL GROWTH OF MO ON SAPPHIRE

P.A. RYAN, F. TSUI*
Department of Physics and Astronomy, University of North Carolina, Chapel Hill, NC 27599,
*ftsui@physics.unc.edu

ABSTRACT

Structural evolution during initial epitaxial growth of Mo (111) and (110) on Al_2O_3 substrates has been studied using real-time reflection high energy electron diffraction and *in-situ* scanning tunneling microscopy. The Mo (111) growth on sapphire (0001) is initiated by the formation of small mound-like 3-dimensional (3D) islands that are correlated with unique length scales. The observed surface length scales depend on growth temperature and rate, and they coarsen as the thickness increases. The initial growth of Mo (110) on sapphire (11 $\bar{2}$ 0) begins with layer-by-layer growth for the first monolayer, and subsequently the growth is 3D with mound-like features that are larger than those corresponding (111) counterparts. In both orientations lattice relaxation occurs within the first 2 - 3 monolayers.

INTRODUCTION

The epitaxial growth of transition metals on insulating substrates has been of great interest in recent times, as these systems have many scientific and technological applications. The nature of the initial nucleation can strongly influence the symmetry and morphology of the subsequent growth, and hence influence the physical properties of the resulting films. Therefore, it is necessary to understand the initial epitaxial growth of these systems in order to control and exploit the properties of these structures. Although there have been several systematic studies of epitaxial growth of metals on metallic [1,2,3] and semiconducting [4,5] substrates, there have been few studies performed on insulating substrates, owing to various technical difficulties associated with the growth conditions. Recently, a study of initial epitaxial Mo growth [6] has shown the presence of a novel smoothening transition, where the growth front becomes the smoothest at a nominal Mo thickness of 10 Å. The 3-dimensional (3D) Mo islands appear to prefer reaching this thickness *uniformly*, before growing thicker. The observed "magic" thickness is shown to be independent of temperature and flux, indicating that it is thermal dynamically stable. In this paper, we report the structural evolution of this system during initial epitaxial growth through the smoothening transition. Results for growth along two symmetry directions are reported here, i.e. growth of Mo (111) on Al_2O_3 (0001) and Mo (110) on Al_2O_3 (11 $\bar{2}$ 0).

EXPERIMENT

This study was performed in an advanced molecular beam epitaxy (MBE) system. The base pressure was 5×10^{-11} Torr, and the pressure during deposition was $< 10^{-9}$ Torr. This system is equipped with a real-time reflection high energy electron diffraction (RHEED) imaging system, and an *in-situ* UHV Park Scientific scanning probe microscope capable of both scanning tunneling microscopy (STM) and atomic force microscopy. The sapphire substrates were ultrasonically cleaned with solvents, and subsequently they were annealed in UHV at temperatures in excess of 1000 °C for 30 min. Stable Mo rates were obtained using a 40 cc electron beam hearth at a range between 0.002 and 10 Å/s, and the substrate temperature ranged from 200 to 1100 °C. The deposition rate was measured using a quartz crystal monitor, and the

71

thickness calibrated *ex-situ* using x-ray reflectivity, Rutherford backscattering spectroscopy and profilometer measurements. The evolution of the Mo surface was characterized in real-time using RHEED and after deposition by room temperature *in-situ* STM.

RESULTS AND DISCUSSIONS

i) Growth of Mo (111) on Al_2O_3 (0001)

The initial growth of Mo on sapphire (0001) is 3D. This is indicated by a monotonic drop of RHEED intensity, including the specular reflection, at the onset of Mo deposition and through the first few Å [6], and is confirmed by the subsequent appearance of spotty and broad RHEED patterns. The 3D RHEED patterns along three different azimuths are illustrated in Figure 1, and they also confirm that the Mo film has a three-fold symmetry and is grown along the [111] direction. Specifically, the two RHEED patterns shown in Figure 1 (b) and (c) correspond to the respective azimuths that are rotated ± 30° with respective to the [112] azimuth shown Figure 1 (a). The mirror images shown by the two patterns with respect to each other indicate that there is no crystallographic twinning.
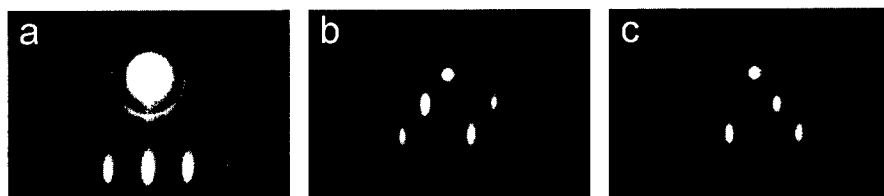
Figure 1. RHEED images of Mo (111) along the [112] (a) and <110> (b) and (c) azimuths. Images (b) and (c) are mirror images, indicating the crystal is not twinned. The bright dot with concentric circular rings near the top of each image is the direct beam and the associated artifact of the phosphorous RHEED screen.

The intensity of the RHEED patterns, and the full width at half maximum (FWHM) and the separation of the diffraction peaks together give a quantitative measure of the surface structure for the growth of Mo (111) on Al_2O_3 (0001). Their evolution as a function of film thickness is illustrated in Figure 2 for a growth at 800 °C with rate ~ 0.2 Å/s. The RHEED patterns including the specular reflection appear at ~ 3 Å coverage from the diffused background. Their intensities increase monotonically with deposition indicating a continuous enhancement of the ordering, while their FWHM show a slight sharpening reflecting a rather constant crystal coherence length. The observed FWHM corresponds to surface structures that are several nanometers wide, and the observed narrowing indicates that these surface features grow in size with increasing coverage. The RHEED intensity increases more rapidly for higher temperature growth. This is consistent with the notion that higher growth temperature promotes higher structural ordering. The observed evolution of lattice spacing indicates that lattice relaxation occurs mainly within the first 2 -3 Å before the onset of RHEED intensity, and it is fully relaxed before reaching 10 Å. The observed rapid relaxation is consistent with the presence of a large lattice mismatch and 3D growth. In the full temperature range of the study, the growth is 3D. Furthermore, surface becomes faceted for growth at temperatures greater than 1000 °C or at high coverages. This observation indicates that (111) face of Mo is not energetically favored. However, if the surface is annealed before the facets are formed, a smooth 2D (111) surface can

be obtained. Therefore, low temperature growth at a coverage slightly beyond 10 Å followed by a high temperature anneal provides a pathway to obtain a 2D (111) surface. Subsequent growth is basically homoepitaxial, and layer-by-layer growth can be obtained.
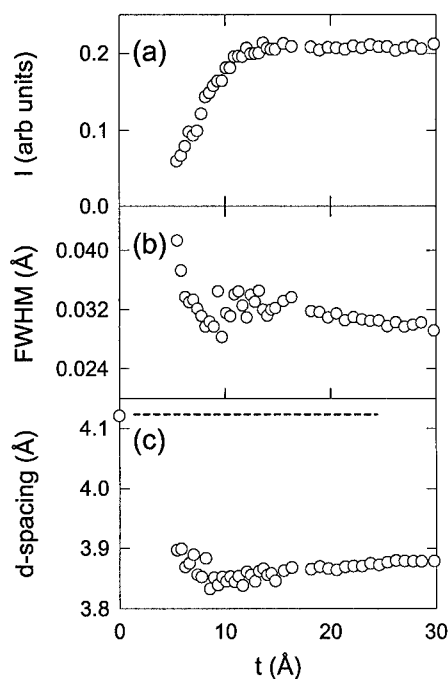
Figure 2. Evolution of diffraction features as a function of nominal film thickness for Mo (111) deposited at 800 °C and 0.2 Å/s. (a) Intensity of the 0th order diffraction, (b) FWHM of the 0th order peak, and (c) lattice spacing along [110] azimuth. The d-spacing at zero coverage corresponds to the value for sapphire (dashed line).

The Mo surfaces exhibit mound-like 3D features with unique length scales that are not self-affine. To obtain a real-space view of the surface, *in-situ* STM was performed on wedge-shaped Mo films with continuously varying thickness deposited under various conditions. Topographical images were obtained at room temperature. Figure 3 illustrates two images from samples deposited at 800 and 1000 °C and at a coverage near the "magic" thickness. As shown in Figure 3, the 3D features are about the same height, and about the same width for each image. To study this further particularly about how the observed length-scale evolves with deposition temperature and thickness, height-height correlation function analysis were performed using the STM images. The particular correlation function used is given by

$$\eta(R) = \left\langle \left[h(r_i) - \bar{h} \right] \times \left[h(r_j) - \bar{h} \right] \right\rangle_{ave},$$ (1)

where $h(r_i)$ is the height at r_i, $\bar{h}$ is the average height over the whole image, and $R = |r_i - r_j|$ is the distance between r_i and r_j. Eq. (1) gives a quantitative measure of the mean-square height product between two points a distance R apart.

73
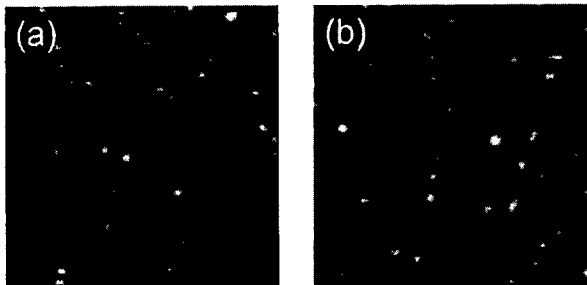
Figure 3. STM images of
10 Å Mo (111) films
deposited at (a) 800 °C
and 0.12 Å/s, and (b)
1000 °C and 0.4 Å/s.
Image size: 1000 Å ×
1000 Å.

Figure 4 illustrates the height-height correlation functions obtained from two films
deposited at different temperatures (800 and 1000 °C), and the evolution of the characteristic
length of the surface features. The oscillatory nature of the correlation function indicates the
presence of a long-range order. The value at zero coverage corresponds to the mean square
height of the surface features, and the position of the first peak (R_0) corresponds to the mean
separation of the surface features. At the same Mo coverage, R_0 is greater in the sample
deposited at higher temperature, as the diffusion length of the Mo atoms on the surface increases
with temperature.
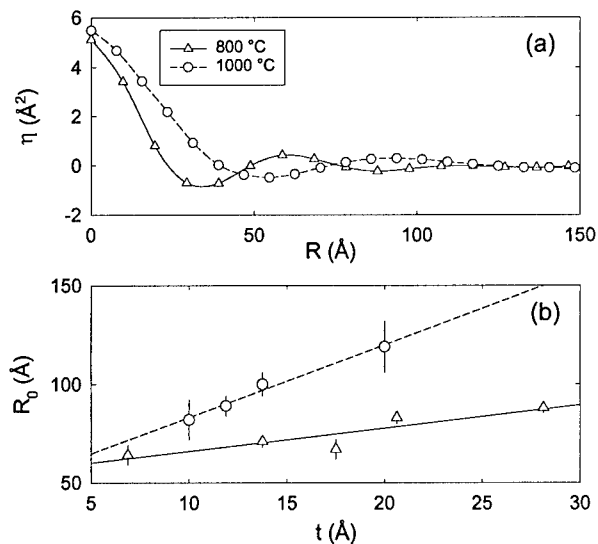
Figure 4. Correlation
and coarsening of
Mo (111) surfaces.
(a) Height-height
correlation functions
for two 13 Å films
deposited at 800 °C
(triangles) and 1000
°C (circles). (b)
Lateral length scale
as a function of film
thickness for wedge-
shaped films
deposited at 800 °C
and 1000 °C (lines
are a guide to the
eyes).

The observed surface features exhibit coarsening as a function of coverage. Both samples
shown in Figure 4 show a monotonic increase in both feature separation and height with
thickness. The observed coarsening process is consistent with the observed narrowing of the
RHEED patterns. As indicated above, the 3D islands evolve into triangular pyramids for the
sample deposited at higher growth temperature and coverage. The observed coarsening is similar

74

to those observed in homoepitaxial growth of metal, as one would expect. At larger coverages the length-scale exhibits power law dependence on Mo coverage.

ii) Growth of Mo (110) on Al_2O_3 (11$\bar{2}$0)

The growth of Mo (110) on Sapphire (11$\bar{2}$0) substrates has also been investigated. The initial growth appears to be different from that observed for the Mo (111) described above. Unlike in the Mo (111) system, a full oscillation of the RHEED specular intensity occurs during the growth of first monolayer on sapphire at low growth rates (< 0.03 Å/s), indicating an initial layer-by-layer growth. The first monolayer of (110) Mo is pseudomorphic. The subsequent growth is 3D, which is indicated by a monotonic decrease of RHEED intensity through the next few Å and by the appearance of spotty RHEED patterns at a nominal thickness of > 5 Å.
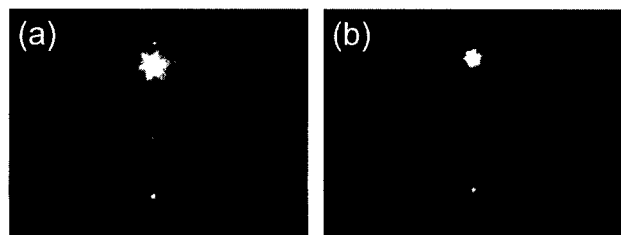
Figure 5. RHEED patterns of (a) 12 Å and (b) 30 Å Mo (110) along [110] azimuth deposited at 800 °C and 0.1 Å/s. Arrows in (a) indicate the sharp pseudomorphic features described in the text.
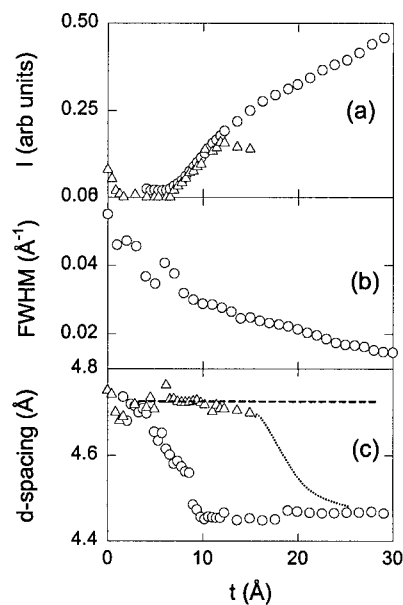
Figure 6. Evolution of diffraction features as a function of nominal film thickness for Mo (110) deposited at 800 °C and a rate of 0.1 Å/s. (a) Intensity of the broad (circles) and the sharp features (triangles). (b) FWHM of the 0th order diffraction. (c) Lattice spacing along [110] azimuth for the broad (circles) and the sharp features (triangles). The dashed curve in (c) indicates the qualitative thickness dependence of the sharp feature. The d-spacing at zero coverage corresponds to the value for sapphire substrate (horizontal dashed line in c).

The emerging 3D-like diffraction patterns after nominal thickness of 5 Å contain two distinct features, a broad 3D feature and a sharp one, as shown in Figure 5 (a) for a 12 Å thick film grown at 800 °C and a rate of 0.1 Å/s. Arrows in Figure 5 (a) indicate the sharp features. The coexistence of the two features corresponds to the presence of anisotropic (elongated) 3D islands, some of which are along the RHEED beam and others perpendicular to it. This is confirmed by our STM measurements. The intensity of the broad feature increases monotonically, while the sharp counterpart rises to a peak near 10 Å and then merges with the broad one, as illustrated in Figure 6 (a) for a growth at 800 °C and a rate of 0.1 Å/s. The evolution of lattice spacing obtained from the two features, and the FWHM of the broad feature are also illustrated in Figure 6. As the intensity increases with deposition, the FWHM exhibits a dramatic decrease, indicating an increase in crystal coherence length associated with surface smoothening. The width of the Mo (110) is substantially narrower than that of the Mo (111), which corresponds to larger surface features. Similar to Mo (111) growth, lattice relaxation for the broad feature occurs between second and third monolayer. In contrast the lattice spacing along the elongated islands, which corresponds to the sharp feature, remains pseudomorphic for close to 15 Å, and lattice relaxation in this direction occurs at a greater thickness [Figure 6 (c)]. The observed anisotropic lattice relaxation process is completed at a nominal Mo coverage greater than 25 Å. Figure 5 (b) shows a characteristic RHEED pattern in this latter regime.

SUMMARY

We have studied the structural evolution during initial MBE growth of Mo on sapphire substrates using real-time RHEED and *in-situ* STM. Growth of Mo (111) on sapphire exhibits small mound-like features from the outset, and these structures are correlated and they progressively coarsen with subsequent deposition, ultimately forming triangular pyramids. The observed correlation length is relatively short, less than 100 Å at low coverages, but it appears to be consistent with the large lattice mismatch between the Mo and substrate and 3D growth. In contrast, the initial growth of Mo (110) is layer-by layer for the first monolayer, followed by 3D-island growth. The RHEED features sharpen rapidly with Mo deposition, indicating the presence of rapid smoothening towards a 2D-growth front. The smoother (110) surface evidently arises from energetics. Both systems exhibit lattice relaxation within the first few monolayers, which is also consistent with large lattice mismatch, and the observed lattice relaxation process in (110) films is anisotropic.

ACKNOWLEDGEMENTS

REFERENCES

1. J. A. Strocio and D. T. Pierce, Phys. Rev. B **49**, 8522, (1994).
2. J. A. Strocio, D. T. Pierce, M. Stiles, A. Zangwill, and L. M. Sander, Phys. Rev. Lett. **75**, 4246 (1995).
3. F. Tsui, J. Wellman, C. Uher, and R. Clarke, Phys. Rev. Lett. **76**, 3164 (1996); Mat. Res. Soc. Symp. Proc. Vol. 399, 243 (1996).
4. L. Gavioli, K.R. Kimberlin, M.C. Tringides, J.F. Wendelken and Z. Zhang, Phys. Rev. Lett. **82**, 129 (1999).
5. Z. Zhang, Q. Niu and C.-K. Shih, Phys. Rev. Lett. **80**, 5381 (1998).
6. P. A. Ryan and F. Tsui, Appl. Phys. Lett. **75**, 3796 (1999).

STEP BUNCHING DURING SiGe GROWTH ON VICINAL Si(111) SURFACES

H. HIBINO AND T. OGINO
NTT Basic Research Laboratories, Atsugi, Kanagawa 243-0198, Japan

ABSTRACT

We investigate step bunching during SiGe growth on vicinal Si(111) surfaces. Step bunching occurs irrespective of the misorientation angle and direction of the vicinal surface, the growth temperature, and the Ge concentration. At 550°C, the average number of the steps in the bunch increases with the Ge concentration. After growth of 10-nm-thick SiGe layers, two-dimensional islands are formed on the terraces, which indicates that the terrace width has already been saturated. Therefore, the terrace width is mainly determined by the diffusion length of the adatom. The average number of steps in the bunch increases with the Ge concentration because the diffusion length increases with the Ge concentration. The diffusion length also increases with the temperature. So the higher the temperature is, the larger the step bunch becomes.

INTRODUCTION

It has been reported that step bunching occurs during strained layer growth [1,2]. Tersoff and co-workers have shown that the attractive interactions between steps on the surface of the strained layers cause the step bunching [3]. They simulated evolution of the step arrangement and showed that the average number of the steps in the bunch grows monotonically with time for no deposition flux. However, flux limits the growth of the step bunch. Stress-induced step bunching can be controlled so as to achieve uniformly sized and uniformly spaced step bunches [4].

The Tersoff's model seems to be a reasonable model for the stress-induced step bunching. However, the consistency of the model with experimental results has not been thoroughly examined. One of the reasons for this is that the stress-induced step bunching has only been studied for SiGe growth on Si(001) [1,2]. Furthermore, Si(001) is relatively complicated in the sense that it has two kinds of terraces with 2×1 and 1×2 reconstructions. Therefore, stress-induced step bunching should be examined in systems that are simpler than the SiGe/Si(001) system. In this paper, we investigate step bunching on vicinal Si(111) surfaces during SiGe growth. As mentioned below, the system is not always simpler than SiGe/Si(001), but systematic investigations of the influence of the Ge concentration, misorientation angle, misorientation direction, and growth temperature on the step bunching give deep insights into the mechanism of the stress-induced step bunching.

EXPERIMENTAL

Samples were cut from vicinal Si(111) wafers of four different orientations. Two were misoriented by 2° and 10° toward the <11$\bar{2}$> direction. The other two were misoriented by 2° and 5.6° toward <$\bar{1}$ $\bar{1}$ 2>. The samples were cleaned chemically, and protective oxide layers were formed as the final step. Then, the samples were introduced into ultrahigh vacuum chambers through a load-lock. The samples were resistively heated with ac currents. After the samples were outgassed at about 550°C for several hours, they were cleaned by flashing at 1250°C. We grew SiGe in a solid-source molecular-beam epitaxy chamber equipped with two electron-beam evaporators for Si and Ge. The pressure during SiGe growth at a rate of 0.01 nm/s was typically 2×10^{-7} Pa. After SiGe growth, the samples were immediately cooled to room temperature. The step arrangement was observed by atomic force microscopy (AFM) after the samples were taken out of vacuum.

Si GROWTH ON VICINAL Si(111)

In order to investigate the stress effect on the step arrangement on vicinal Si(111) surfaces, we first had to examine the step arrangement on stress-free vicinal Si(111) surfaces. There are a lot of studies on the step arrangement on the vicinal Si(111) surfaces under thermal equilibrium [5-9]. According to these studies, the step arrangement on the vicinal Si(111) surface depends on the temperature and the direction of the misorientation. On vicinal Si(111) surfaces misoriented toward the $<1\bar{1}0>$ or $<11\bar{2}>$ direction, the '1×1'-to-7×7 phase transition causes step bunching [5,6,8]. On these surfaces, the '1×1'-to-7×7 phase transition temperature T_c depends on the misorientation angle θ. Above $T_c(\theta)$, the surfaces are uniformly covered with single-bilayer steps, each of which is 0.31 nm in height. Below $T_c(\theta)$, the surfaces are separated into 7×7-reconstructed (111) facets and step bunches, and the inclination of the step bunch increases as the temperature decreases. On the $<11\bar{2}>$-misoriented surfaces, the step bunches are transformed into (331) facets below 600°C, which are inclined 22° from (111) [10]. On vicinal Si(111) surfaces misoriented toward $<\bar{1}\bar{1}2>$, T_c is independent of the misorientation angle. Above T_c, the surfaces are uniformly covered with single-bilayer steps, and single- and triple-bilayer steps coexist on the surface below T_c [7-9].

The step arrangement on the vicinal Si(111) surfaces under thermal equilibrium is well-known, but we do not know much about how the step arrangement changes during Si growth. Yokohama et al., have investigated the step rearrangement on vicinal Si(111) surface misoriented by 4° toward $<11\bar{2}>$, on which (111) and (331) facets coexist, during Si growth [11]. They reported that the step arrangement after the growth of 2.5–bilayer Si strongly depends on the growth temperature. However, they investigated only the initial stages of Si growth. Therefore, we investigated the step arrangement after the growth of much thicker Si layers. We also compared vicinal Si(111) surfaces misoriented toward $<11\bar{2}>$ and $<\bar{1}\bar{1}2>$.

Figure 1 shows AFM images of vicinal Si(111) surfaces misoriented by 2° toward $<11\bar{2}>$ after Si growth. Before growth, steps were bunched on the surfaces. The Si thickness was 20 nm, and the growth temperatures of (a)-(c) were 650, 700, and 750°C, respectively. In Figs. 1(b) and 1(c), we can clearly see step bunches, but it is difficult to identify step bunches in Fig. 1(a). At 750°C, adatom diffusion inside the step bunches is large enough for the step bunches to advance as one body. At 650°C, however, adatom diffusion inside the step bunches is too small to keep the steps in bunches. At 700°C, we find single-layer steps between step bunches, as shown by the arrowheads in the inset of Fig. 1(b). Such steps are called crossing steps, and they tend to limit the step bunching [12]. These results show that the step bunching is energetically stable on surfaces misoriented toward $<11\bar{2}>$ but that the growth kinetics has a tendency to
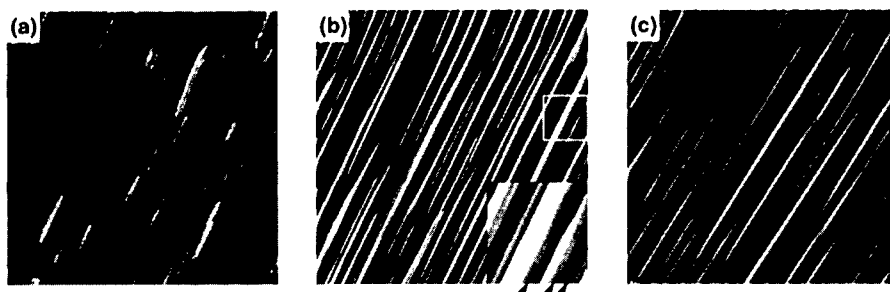
FIG. 1. AFM images of vicinal Si(111) surfaces misoriented by 2° toward $<11\bar{2}>$ after Si growth. The Si thickness was 20 nm, and the growth temperatures of (a)-(c) were 650, 700, and 750°C, respectively. The inset of (b) is a magnified image of the area in the square. The scan area of (a) was 1×1 μm², and the scan area of (b) and (c) was 2×2 μm².
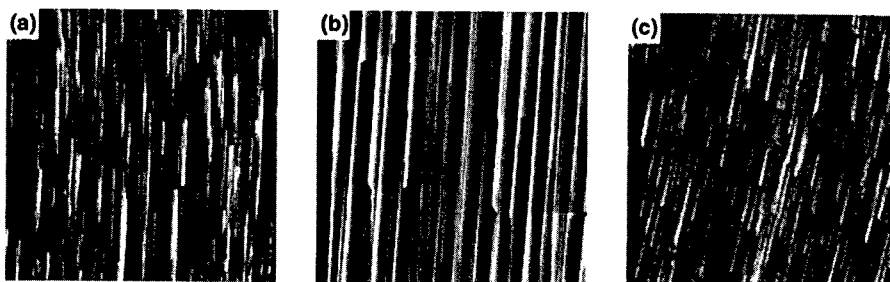
FIG. 2. AFM images of vicinal Si(111) surfaces misoriented by 2° toward $<\bar{1}\,\bar{1}\,2>$ after Si growth. The Si thickness was 20 nm, and the growth temperatures of (a)-(c) were 650, 750, and 850°C, respectively. The scan area of (a)-(c) was 2×2 μm^2, 5×5 μm^2, and 1×1 μm^2, respectively.

debunch the steps.

Next, we investigated the $<\bar{1}\,\bar{1}\,2>$-misoriented surface. Figure 2 shows AFM images of vicinal Si(111) surfaces misoriented by 2° toward $<\bar{1}\,\bar{1}\,2>$ after Si growth. The Si thickness was 20 nm, and the growth temperatures of (a)-(c) were 650, 750, and 850°C, respectively. At 650°C, the surface is mainly covered with single steps. But, at 750°C, the steps are strongly bunched. In contrast with the $<11\,\bar{2}>$-misoriented surface, the step bunching is energetically unstable on the surface misoriented toward $<\bar{1}\,\bar{1}\,2>$, but there are some kinetic effects to induce the step bunching. After Si growth at a temperature higher than the 7×7 phase transition temperature (850°C), we find only single steps. The step bunching is caused by the kinetic effects at the 7×7-reconstructed $<\bar{1}\,\bar{1}\,2>$ steps. In Fig. 3, the measured root mean square roughness of the vicinal Si(111) surfaces after Si growth is plotted as a function of the growth temperature. The roughness strongly depends on the growth temperature.
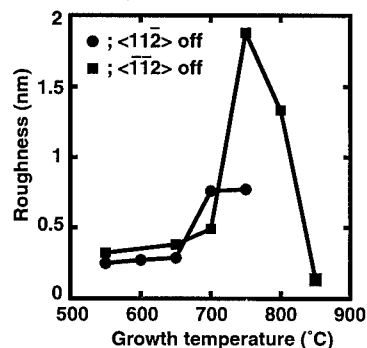
FIG. 3. Surface roughness of the vicinal Si(111) surfaces after Si growth is plotted as a function of the growth temperature. The Si thickness was 20 nm. Circles and squares indicate the data for $<11\,\bar{2}>$- and $<\bar{1}\,\bar{1}\,2>$-misoriented surfaces, respectively.

STEP BUNCHING DURING SiGe GROWTH

Based on the understanding gained above about the step arrangement of vicinal Si(111) surfaces under no stress, we were able to determine the effect of stress on the step arrangement from the results of SiGe growth. Figure 4 shows AFM images of vicinal Si(111) surfaces misoriented by 2° toward $<\bar{1}\,\bar{1}\,2>$ after 10-nm-thick SiGe growth. The sample in (a) was after growth at 550°C. During Si growth at this temperature, the steps are rarely bunched. The sample in (b) was annealed at 750°C for 10 min after SiGe growth at 550°C. Step bunching is clearly seen in both images, but the average number of the steps in the bunch of (b) is 3 times larger than that of (a). The fact that annealing enhances the step bunching indicates that the step bunching is driven by the energetics of the system. On stress-free vicinal Si(111) surfaces misoriented toward $<\bar{1}\,\bar{1}\,2>$, the step bunching is energetically unstable. Therefore, it is strongly suggested that the bunching instability is induced by stress energetically. However, we also have to check another factor, the surface reconstruction. The samples shown in Figs. 4(a) and 4(b) had a 5×5 reconstruction rather than a 7×7 reconstruction. The change in the surface reconstruction might cause the step bunching. In order to examine the influence of the surface reconstruction on

the step arrangement, we grew 2-bilayer-thick Ge layers at 550°C on a vicinal Si(111) surface misoriented at 2° toward $<\bar{1}\,\bar{1}\,2>$ and then annealed them at 750°C for 10 min. The steps were bunched on this 5×5-reconstructed surface, but the surface roughness was much lower than that of Fig. 4(b). Thus, we conclude that the misfit stress between Si and SiGe induces step bunching on the surface of SiGe layers grown on vicinal Si(111) substrates. This conclusion is also supported by the fact that step

FIG. 4. AFM images of vicinal Si(111) surfaces misoriented by 2° toward $<\bar{1}\,\bar{1}\,2>$ after 10-nm-thick SiGe growth. The sample in (a) was after growth at 550°C, and the sample in (b) was annealed at 750°C for 10 min after SiGe growth at 550°C. The Ge concentrations of (a) and (b) were 0.22 and 0.17, respectively. The scan area was 2×2 μm^2.

bunching also takes place during SiGe growth on the $<11\bar{2}>$-misoriented surface at 550°C, and the steps were bunched irrespective of the misorientation angle.

Next, we investigate how the step bunching depends on the Ge concentration. Figure 5 shows AFM images of vicinal Si(111) surfaces misoriented by 2° toward $<11\bar{2}>$ (a) before and (b)-(d) after SiGe growth. Figure 5(d) is a magnified image of the area indicated by the square in Fig. 5(c). The growth temperature was 550°C, and the SiGe thickness was 10 nm. The step bunches in Fig. 5(a) were formed during quenching of the sample from 1200°C. But the height of the bunched step is at most three bilayers. The Ge concentrations of (b) and (c) were 0.22 and 0.38, respectively. As shown in Fig. 5, SiGe growth promotes step bunching, and the average number of the steps in the bunch increases as the Ge concentration increases. In Fig. 6, the RMS roughness of the surface after SiGe growth is plotted as a function of the Ge concentration. The surface roughness is proportional to the average number of the steps in the bunch. The surface roughness increases with the Ge concentration on both the $<11\bar{2}>$- and $<\bar{1}\,\bar{1}\,2>$-misoriented surfaces. The samples in Fig. 6 were grown at the growth rate between 0.011 and 0.006 nm/s. However, the data changes systematically as a function of the Ge concentration. The growth rate does not influence the roughness very much. The curves in the figure are results of fitting the difference in the roughness before and after growth to a power law. The fitted
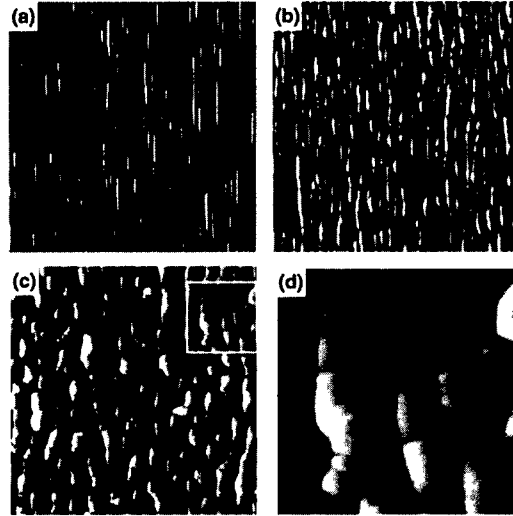
FIG. 5. AFM images of vicinal Si(111) surfaces misoriented by 2° toward $<11\bar{2}>$ (a) before and (b) and (c) after SiGe growth. (d) is a magnified image of the area indicated by the square in (c). The growth temperature was 550°C, and the SiGe thickness was 10 nm. The Ge concentrations of (b) and (c) were 0.22 and 0.38, respectively. The scan area of (a)-(c) was 2×2 μm^2.
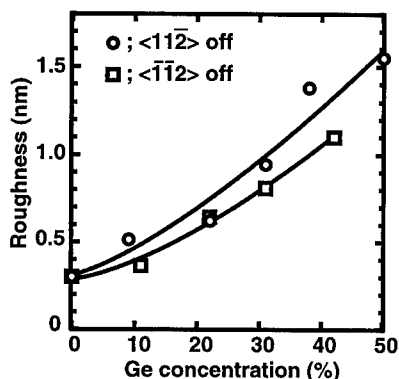
FIG. 6. Plot of the roughness of the vicinal Si(111) surfaces after SiGe growth as a function of the Ge concentration. The data measured on the <11$\bar{2}$>- and <$\bar{1}$ $\bar{1}$ 2>-misoriented surfaces are indicated by circles and squares. The samples were grown at the growth rate between 0.011 and 0.006 nm/s. The curves in the figure are results of fitting the difference in the roughness before and after growth to a power law. The fitted powers were 1.3-1.4.

powers were 1.3-1.4.

In order to understand the dependence of the roughness on the Ge concentration, we examined two factors: stress and surface diffusion. Stress is proportional to the Ge concentration, but we do not exactly know how the diffusion coefficient depends on the Ge concentration. According to the model of the stress-induced step bunching proposed by Tersoff *et al.* [3,4], there is a force monopole at the step on the surface of the strained layer. Such force monopoles lead to logarithmic interactions between steps. Successive steps have forces in the same direction, so the interaction is attractive of the form $\alpha \ln(L)$. Here, L is the distance between steps. α is proportional to the square of the stress. On the other hand, the expression for the velocity of the step includes a term that changes linearly with the diffusion coefficient. Both increases in the stress and the diffusion coefficient enhance the step bunching. We simulated how the surface roughness depends on the two parameters. Because the roughness saturates under flux, we obtained the dependence of the saturated roughness. This result indicated that the saturated roughness is almost proportional to the square of the stress and almost proportional to the diffusion coefficient. These trends probably reflect how the attractive interaction depends on the stress and how the step velocity depends on the diffusion coefficient. We therefore think these trends are essential features of stress-induced step bunching, although Tersoff's model cannot account for SiGe growth on vicinal Si(111) at 550°C, as will be shown later.

What is it that mainly determines the roughness dependence on the Ge concentration between the stress and the diffusion coefficient? If the stress is a main factor, the roughness has a square dependence on the Ge concentration because the stress is proportional to the Ge concentration. However, the measured roughness in Fig. 6 increases too slowly with the Ge concentration. Additionally, Fig. 5(d) clearly shows that two-dimensional (2D) islands were formed on the terraces during SiGe growth. Such islands are also seen in Fig. 5(b). If 2D islands are formed on the terrace during step bunching, the terrace cannot grow further [13]. Figure 7 shows the dependence of the roughness on the SiGe thickness. This figure also indicates that the roughness was saturated after the growth of 10-nm-thick SiGe layers. The 2D island nucleation on the terraces limits the step bunching during SiGe growth at 550°C. We also measured the 2D island density on the surfaces of SiGe layers grown on nominally flat Si(111) substrates. The island density decreased as the Ge concentration increased, which means

FIG. 7. Dependence of the surface roughness on the SiGe thickness. The substrates were vicinal Si(111) surfaces misoriented by 2° toward <11$\bar{2}$>. The Ge concentrations were 0.2-0.22.

that the diffusion coefficient increases with the Ge concentration. These results indicate that the surface diffusion rather than the stress determines the dependence of the roughness on the Ge concentration.

In Tersoff's model, both the stress and the surface diffusion promote the step bunching. So, when both the effects of the stress and the diffusion coefficient are included in the calculation, the surface roughness increases faster than the square of the Ge concentration and the difference between the experiment and calculation becomes larger. Why does the Tersoff's model fail to reproduce the measured dependence of the roughness on the Ge concentration? One reason is the limiting factor of the step bunching. While crossing steps limit the step bunching during Si growth, 2D islands limit the step bunching during SiGe growth. In the simulation based on the Tersoff's model, for example, in Fig. 1 of Ref. 4, crossing steps are emitted by one bunch and captured by the next. This indicates that the crossing step limits the step bunching. Thus, to account for the stress-induced step bunching during SiGe growth on vicinal Si(111) at 550°C, nucleation of 2D islands should be included in the model calculation.

As shown before, the diffusion length determines the size of the step bunch. The simplest way to increase the diffusion length is to grow the layers at higher temperatures. The temperature dependence of the surface roughness clearly showed that the average number of the steps in the bunch increases with the temperature. On the surface of 10-nm-thick SiGe layers grown at 750°C, the maximum height of the step bunch reached 20 nm. This indicates that the growth of the step bunch is limited by the thickness of the SiGe layer.

CONCLUSION

We investigated step bunching during SiGe growth on vicinal Si(111) surfaces. Step bunching occurs irrespective of the misorientation angle and direction of the vicinal surface, the growth temperature, and the Ge concentration. At 550°C, the surface roughness increases with the Ge concentration. After growth of 10-nm-thick SiGe layers, 2D islands are formed on the terraces. 2D island nucleation on the terrace rather than the crossing step emitted from the step bunch limits the growth of the step bunch. The size of the step bunch is mainly determined by the surface diffusion length. Because the diffusion length increases as the Ge concentration increases, the surface roughness increases with the Ge concentration. The diffusion length also depends on the temperature, which means that the surface roughness increases as the temperature increases.

REFERENCES
[1] Y. H. Phang, C. Teichert, M. G. Lagally, L. J. Peticolos, J. C. Bean, and E. Kasper, Phys. Rev. B **50**, 14435 (1994).
[2] C. Teichert, Y. H. Phang, L. J. Peticolos, J. C. Bean, and M. G. Lagally, in *Surface Diffusion: Atomistic and Collective Processes,* edited by M. C. Tringides, NATO-ASI Series (Plenum Press, New York, 1997), p. 297.
[3] J. Tersoff, Y. H. Phang, Z. Zhang, and M. G. Lagally, Phys. Rev. Lett. **75**, 2730 (1995).
[4] F. Liu, J. Tersoff, and M. G. Lagally, Phys. Rev. Lett. **80**, 1268 (1998).
[5] R. J. Phaneuf, E. D. Williams, and N. C. Bartelt, Phys. Rev. B**38**, 1984 (1988).
[6] E. D. Williams and N. C. Bartelt, Science **251**, 393 (1991).
[7] J. Wei, X.-S. Wang, J. L. Goldberg, N. C. Bartelt, and E. D. Williams, Phys. Rev. Lett. **68**, 3885 (1992).
[8] E. D. Williams, R. J. Phaneuf, J. Wei, N. C. Bartelt, and T. L. Einstein, Surf. Sci. **294**, 219 (1993).
[9] H. Hibino and T. Ogino, Phys. Rev. Lett. **72**, 657 (1994).
[10] H. Hibino, T. Fukuda, M. Suzuki, Y. Homma, T. Sato, M. Iwatsuki, K. Miki, and H. Tokumoto, Phys. Rev. B **47**, 13027 (1993).
[11] T. Yokohama, T. Yokotsuka, I. Sumita, and M. Nakajima, Appl. Surf. Sci. **357-358**, 855 (1996).
[12] D. Kandel and J. D. Weeks, Phys. Rev. Lett. **74**, 3632 (1995).
[13] M. Kasu and N. Kobayashi, J. Appl. Phys. **78**, 3026 (1995).

Novel Concepts of Resists
for Nanolithography

RESIST MATERIALS AND NANOLITHOGRAPHY

ELIZABETH A. DOBISZ
Electronics Science and Technology Division, Naval Research Laboratory, Washington DC
20375

ABSTRACT

The work focuses on lithographic processes and materials for sub-50 nm lithography. Lithographic results of polymethyl methacrylates of molecular weights of 50,000, 100,000, 496,000, and 950, 000 are compared. It was found that the molecular weight and developer concentration do not affect smallest linewidth, within experimental error. However, the molecular weight does affect the line-to-line resolution in dense gratings of 40-60 nm in contrast and developer induced swelling. 40 nm period gratings are shown. The work next examines the use of chemically amplified resists for nanofabrication, with a focus on SAL-601. Sub-50 nm lines are defined with latitude of an order of magnitude in dose and a factor of two in post exposure bake time. The results are modeled with a diffusion reaction kinetic model and an approach to optimize resolution and reproducibility is presented. Challenges to attaining the ultimate resolution and line-to-line resolution in polymeric resists include contrast, mechanical stability, swelling, and adhesion. Metal binding self assembled monolayers (SAMs) are presented a class of resists, that circumvent the latter three complications. Work at the Naval Research Laboratory on SAM resists is outlined.

INTRODUCTION

Nanolithography was reported as early as 1964, when Broers[1] defined 50 nm lines by e-beam writing a contamination pattern. By the late 1960's, the development of polymethyl methacrylate (PMMA) as an e-beam resist was well in progress.[2] PMMA has been the standard high resolution resist for over 30 years. Several reports have cited linewidths defined in PMMA of 10-20 nm in the laboratory.[3,4] Over this time period, the microelectronics industry has progressed at a phenomenal pace and sub-100 nm device dimensions are projected in manufacturing in the next decade.[5] Manufacturing applications present many new challenges to nanolithography including throughput and tight critical dimension control. E-beam resist sensitivities critical dimension (CD) error budgets, specified on the SIA 1997 Roadmap[5], are ~ 1-10 $\mu C/cm^2$ and 5-10%, respcetively. The error budgets of 5-10 nm or less, presents a real challenge for polymeric and the multi-component chemically amplified resists. Due to scattering processes during lithographic exposure, higher resolution lithography frequently requires increasingly thinner resists. This in turn, puts increasing demands on etch resistance of the resists.

In this work, the nanolithographic performance of resists is examined through electron beam and scanning tunneling microscope exposures. These techniques provide the very high resolution to enable study of the materials properties of the resists. The work begins with an examination of the effects of the macromolecular properties of PMMA on its ultimate resolution. Next the high sensitivity, multi-component chemically amplified resists (CARs) are addressed through an in-depth study of SAL-601. The paper ends with a description of novel resists, developed at the Naval Research Laboratory based upon metal binding self assembled monolayers (SAMs).

EXPERIMENT

PMMA

Si wafers were spin coated with 100 nm thick PMMA films of 950K, 496K, and 50K molecular weight (MW) from solutions in chlorobenzene, as received from the manufacturer.[6] Films of 40 nm and 180 nm thickness 100K resist were analyzed. The resist coated wafers were baked at 165^0C in an oven for 24 hours prior to exposure. Following exposure, the wafers were developed for 30 sec in a 25% or 50% solution of methylisobutylketone (MIBK) and isopropanol (IPA), as stated below.

SAL-601

Si substrates were cleaned in nitric acid, rinsed in DI water, placed in buffered HF, and rinsed again for 2 min in running deionized water. The wafers were baked at 115 ^{0}C for 10 min. to remove residual water. HMDS was spun onto the wafers and baked for 10 min. at 90 ^{0}C. Microposit SAL-601 was thinned with Thinner A (Shipley) 1:2 for a 140 nm thick layer and 2:5 for a 60 nm thick layer. The wafers were pre-baked in an oven at 90 ^{0}C for 10 min. Following exposure the samples were baked on a vacuum chuck hot plate. One set of samples was post exposure baked at 110 ^{0}C in an oven on a ½ inch thick Al plate, as noted below. Following the PEB the resist was developed for two minutes in Microposit MF-322 developer or acetone (if noted) and rinsed in running DI water.

Organosilane SAMs

For results shown here, STM lithography was employed. Substrates were p-Si<100>, 6-9 Ω-cm. The wafers were cleaned and passivated with 5% HF in deionized water, as described elsewhere.[7] Films of (aminoethylaminomethyl)phenyltrimethoxysilane (PEDA) and 4-chloromethylphenyltrichlorosilane (CMPTS) were deposited onto the wafers.[8] The films were lithographically exposed, which changed their ability to bind to metal. Following exposure the CMPTS required the additional step of grafting an amine onto the unexposed regions of the resist. Next the samples were treated with a Pd(II) catalyst, which bound selectively to the unexposed regions of the film. Finally Ni was electroless plated onto the Pd(II) coated regions. SAM film preparation and processing are described elsewhere.[7,8,9,10]

Lithographic Exposure

Electron beam lithography (EBL) was performed in a JEOL JBX-5DII lithography system, operated at 50 kV, under conditions to produce a Gaussian probe of standard deviation, σ, of 6-9 nm (from beam current-spot size factory specifications). Reproducibility and factory specifications of the spot size were tested by measuring linespread functions (LSFs) on samples exposed with several different spot sizes. Deconvolution of manufacturer specified spot size from measured developed resist LSfs produced the same remaining Gaussian width (resist process and electron scatter broadening function) to within ± 0.7 nm.

STM lithography was performed in a W.A. Technology UHV STM with a W tip biased negative with respect to the sample, with voltages of 10-25 eV, and tip sample currents of 10-500 pA, and a scan rate of ~ 1 µm/sec.

RESULTS AND DISCUSSION

Resist Material and Process Broadening of Linespread Function

Our understanding of e-beam lithography is based upon physical models of electron scattering in materials. The results presented here, used a Monte Carlo code, to simulate electron scattering, developed by Marrian[11]. The output of the code is energy deposited in the resist per unit volume vs. radial distance. It is the energy per unit volume deposited in the resist that causes the chemical change. The output of the code for a point source of incident electrons. is convolved with a Gaussian of the width of the incident beam. The result is the pointspread function (PSF). The PSF can be integrated along a line to form a linespread function (LSF) or into an exposed pattern.

For ease of computation, Chang et al[12]. suggested fitting the PSF to superposition of two Gaussians: The narrower Gaussian represents the incident beam broadened by low angle (forward) scattering in the resist. The longer range, 2-20 μm width, (orders of magnitude) less intense Gaussian represents the energy deposition by electrons backscattered from the substrate. The backscattered electrons give rise to proximity effects, in which the pattern dose is dependent on pattern size and density. The PSF is the basis for dose correction for proximity effects in EBL.

The Monte Carlo codes adequately model lithography and enable proximity correction in e-beam lithography at submicron dimensions. In a good resist and process, process induced broadening to the LSF, is negligible for spot sizes > 100 nm. However, when one wishes to obtain the ultimate maximum resolution, one uses a sub-10 nm probe and conditions that minimize forward scattering in the resist. A 50 kV e-beam will undergo little broadening in a 100 nm thick resist, due to small angle scattering in the resist. Under these conditions, the materials properties of even a good resist become important and broaden the primary Gaussian of the developed resist LSF. As shown below, the broader dominant Gausian manifests itself in reduced dose latitude for a critical dimension and diminished line-to-line resolution.

Shown in fig. 1 are the linespread functions of developed PMMAs of MWs of 50K, and 950K. The data consists of normalized inverse dose vs. half linewidth.[13] The Monte Carlo code output was convolved with a primary Gaussian that best fit the experimental results[14] A developer concentration change from 25% to 50% MIBK in IPA caused the width of the primary Gaussian to increase by ≤ 1 nm, which is within our experimental error.[15,16] Normalized data, from both development concentrations are shown in the fig. 1. The standard deviation, σ, of the primary Gaussian of the 50K MW PMMA was 28 nm. Deconvolution of the σ=6 nm beam gave a broadening of the primary Gaussian of 27 nm. (i.e. $27^2=28^2-6^2$.) Similarly, deconvolution of the primary beam from the other three MW resists (100K and 496K resists not shown in fig. 1) gave a process and electron scattering induced broadening of the probe of 7±0.5 nm. At the optimal doses, isolated lines of 10-20 nm were defined in all of the PMMAs. However, the variation of linewidth with dose was much greater in the 50K resist than the other resists. The effect of the developed resist LSF becomes more apparent, if one integrates the linespread functions into a grating pattern. Shown in fig. 2, is contrast function, which is the ratio of the integrated LSF intensity midway between lines to that at the center of the lines vs. grating period. Curves are shown for primary Gaussian σ's of 9, 11.7, and 28 nm.[16] One can see that for the 50K resist, σ=28 nm, we expect no contrast in the grating periods of less than 80 nm. Whereas, with the narrower LSFs, we can expect grating contrast down to 40 nm. This is shown fig. 3, in which AFM images of the best results of developed 40 nm and 60 nm period gratings in the 950K and
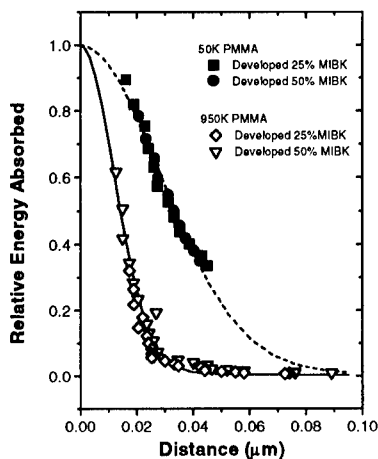
Figure 1. Linespread functions fitted to linewidth data from PMMAs of MWs of 50K, and 950K. The 950K sample was written with an incident beam with $\sigma = 9$ nm. The 50K PMMA was written with an incident beam with $\sigma = 6$ nm. [Ref. 16]
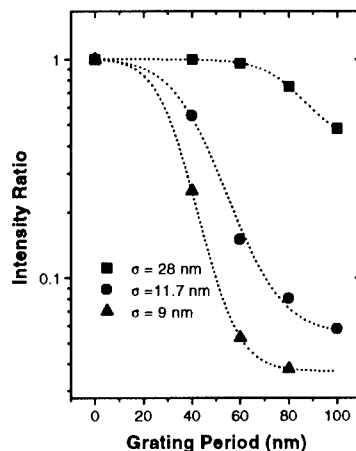
Figure 2. Grating contrast by integration of semiempirical linespread functions. Plotted is the ratio of intensity midway between lines to intensity at lines vs. grating period. Results for primary Gaussian σ's of 9, 12, and 28 nm. [Ref.16]

50K resists. The 50K resist shows no contrast in either the 40 nm or 60 nm period gratings. In the 950K resist, the 60 nm period grating shows good contrast and the 40 nm period grating shows some contrast, but exhibits problems, to be discussed below. The latent images of the
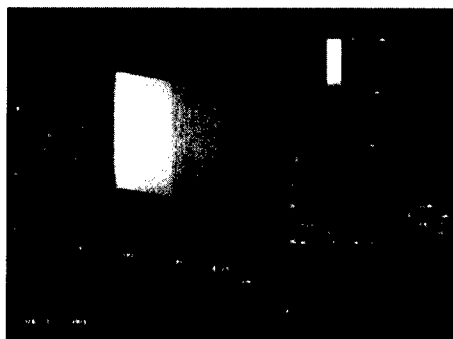
(a)   (b)

Figure 3. AFM images of 40 nm (left) and 60 nm (right) period gratings separated by a 1 μm unexposed bar in (a) 950K PMMA and (b) 50 K PMMA. [Ref.16, with permission.]

undeveloped 40 nm gratings in both resists was observed[16], consistent with fig. 2 and e-beam probe $\sigma \leq 9$ nm. Both 40 nm and 60 nm gratings were observed in the 100K and 496K resists, as shown below.

Macromolecular Effects and Resolution

From polymer science textbooks, radii of gyration for high MW polymers (500K and above) vary from ~5 nm for a tight spherical configuration to ~30-50 nm for a loose configuration in a good solvent.[17] AFM observations have shown all of the resists to have a nodular type of structure, with 25-45 nm nodules, and little difference in morphology with MW of the undeveloped resists.[18] However, following development the size of the nodules in the 950K resist in the developer front showed substantial swelling to an average particle size of ~ 80 nm.[19] The difference in developed resist morphologies is shown in fig. 4[15], in which AFM tapping mode plane view images of developed 60 nm period gratings are shown.. The developed gratings in the 100K resist exhibited similar structure to the 50K resist.[19] The 496K resist has a less apparent nodular structure and most closely resembled the 950K resist.[19] The consequences of the resist swelling in the developer are shown in fig. 5. Here are SEM images of the best results (best dose) for 40 nm period (left) and 60 nm period (right) gratings separated by a 1 μ unexposed bar in 100 K and 496K resists. Both gratings are resolved in the 100K PMMA. However, some etching (more than the 496K resist) of the resist between the lines was measured for the gratings in the 100K resist. The 40 nm period grating in the 496K resist, shows substantial swelling.
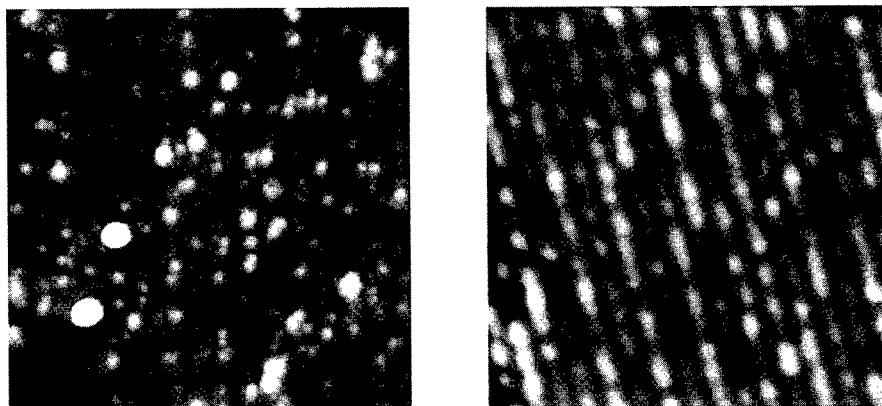
Figure 4. AFM derivative (tapping mode) plane view images of a 60 nm grating in (a) 50K PMMA and (b) 950K PMMA. Scan field size 1 μm. [Ref. 15, with permission]

The swelling was reduced, but not eliminated, by the use of a weaker developer, as shown in fig. 5(c). Similar swelling in the 40 nm grating, but worse, was observed in SEM images of the 950K resist.

Overall for PMMA, there are two competing effects limiting the line-to-line resolution: contrast at low MW and swelling of the higher MW PMMAs. The results suggest that the best resolution would be obtained by narrowing the MW distribution of a lower MW (~100K) resist. The line-to-line resolution in the higher MW polymers can be improved by reducing the solvent
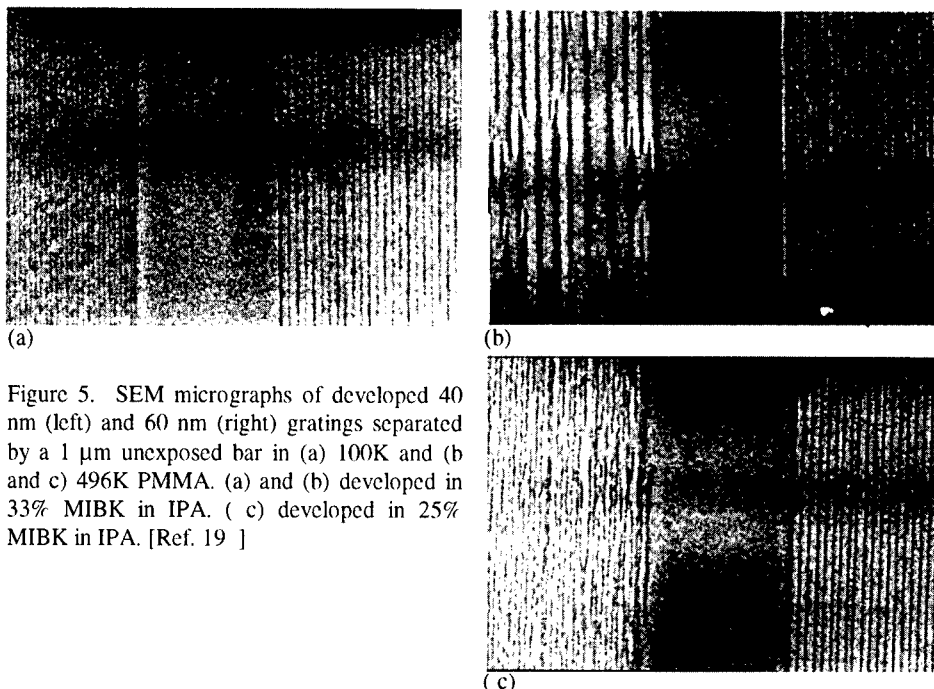
Figure 5. SEM micrographs of developed 40 nm (left) and 60 nm (right) gratings separated by a 1 μm unexposed bar in (a) 100K and (b and c) 496K PMMA. (a) and (b) developed in 33% MIBK in IPA. (c) developed in 25% MIBK in IPA. [Ref. 19]

concentration. The resists were used, as purchased from the manufacturer. It can be assumed that the vendor prepared the materials using free radical solution polymerization methods and that the MW distribution, namely the ratio of the weight average MW to the number average MW, is approximately two.[20,21] A distribution in MWs would be expected to have a larger effect on the contrast of the low MW resists than the high MW resists. The chain scission model predicts that e-beam exposure produces approximately the same average MW. This is supported by the 496K and 950K resists having similar sensitivities. Chen and Ahmed[22] claimed that the resolution limit of PMMA was the transport of the fragmented PMMA out of the higher MW matrix. They reported 5-7 nm features using ultrasonic agitation during development. H. Namatsu et al.[23] reported that surface tension between the resist and liquid during development and rinsing caused resist collapse. Only through supercritical point drying in CO_2, they produced 20 nm lines and spaces in ZEP-7000B resist.

SAL-601

Since the 1980's chemically amplified resists (CARs) have emerged to technological importance because of their high sensitivity, good resolution (in the sub-micron range), and good etch resistance. SAL-601 is a negative CAR from Shipley Corporation that has shown sub-100 nm resolution[24,25 26,27,28,29], is relatively stable, and several closely related resists are commercially available. An examples of high resolution lithography and etch resistance of SAL-601 is shown in fig. 6, with a 40 nm line etched into HgCdTe. However, under processing conditions employed in fig. 6, the standard deviations of the best Gaussian fits to linespread function data were 27-35 nm, depending on specific processing conditions.[13,14]

|—0.27 μm—|

Figure 6. 40 nm line defined in SAL-601 and etched into HgCdTe with CH_4 + H_2.[Ref. 30 with permission.]

In fig. 7(a) is plotted the calculated energy absorbed in the resist vs. distance from the center of a 100 nm gap for different LSFs in which the LSF from the Monte Carlo code was convolved with Gaussians of σ = 27 nm (measured), 10 nm (incident probe), and a point source. In fig. 7 (b-d), the measured dose range to produce a critical dimension gap of 500 nm to 100 nm with ± 10% error was plotted vs. pad width. With only a minutely small dose latitude, it was possible to fabricate dense patterns such as a 100 nm gap in a 20 μm pad.[13,14]This is consistent with the plot for σ=27 nm in fig. 7(a). It is also apparent, in fig. 7(a), that a substantial improvement in dose latitude would be obtained by reducing the effective forward Gaussian width in the developed LSF. The study of diffusion and reaction kinetics detailed below is toward this goal. An additional. goal is a procedure to optimize the resolution and process latitude with standard facilities in a processing laboratory

SAL-601 is a negative tone electron beam resist, which is composed of three components: an alkaline soluble polymeric novolak resin, an acid generator, and a melamine cross-linking agent. Exposure to electrons generates a latent image of free acid. The exposed regions of the resist undergo acid catalyzed reactions during a post exposure bake (PEB), which make the resist insoluble in an alkaline developer such as tetramethylammononium hydroxide (TMAH). (MF-322 is a TMAH aqueous solution.) The acid is not consumed in the reaction, but is freed to enable many reactions leading to dissolution inhibition. In this manner the resist is chemically amplified. For SAL-601, as for many CARs, the PEB is the most critical step in determining the performance of the resist. Because CARs are multi-component there has been a great deal of controversy as to the extent to which diffusion of the components limit the resolution of the resist. Previously diffusion coefficients have been reported in which the investigators measured the width increase of a line with PEB time.[27-29] Others have characterized the effect of the PEB on critical dimension control in terms of the change in size per degree change in PEB temperature.[31,32,33] The analyses are pattern specific and do not address both reaction kinetics and diffusion.

In novolak and phenolic CAR resists dissolution inhibition has been reported to be due to melamine protection of the OH groups at lower temperatures and crosslinking at higher temperatures.[34,35] Our first step was to identify the relative amounts of cross linking and protection reaction that occurred during the different PEB conditions. This was done by establishing resist thickness vs. dose curves for both TMAH and acetone development for each PEB condition. The resist thickness curves for PEB temperatures of 90, 100, 105, and 110 °C for PEB times of 1-11 min. were measured. . Examples, of such curves for PEB temperatures at 100 °C are shown in fig. 8. At 90 °C at PEB times of 1, 3 and 6 min. no acetone insolubility was observed.[36] Only at high overexposure doses was any acetone insolubility observed at 90 °C. In contrast, the other bake temperatures produced some amount of cross-linking. Shown in fig. 9 are linewidth vs. dose for different PEB conditions. Most significantly, sub-50 nm linewidths were produced over an order of magnitude in dose and a factor of two difference in PEB time
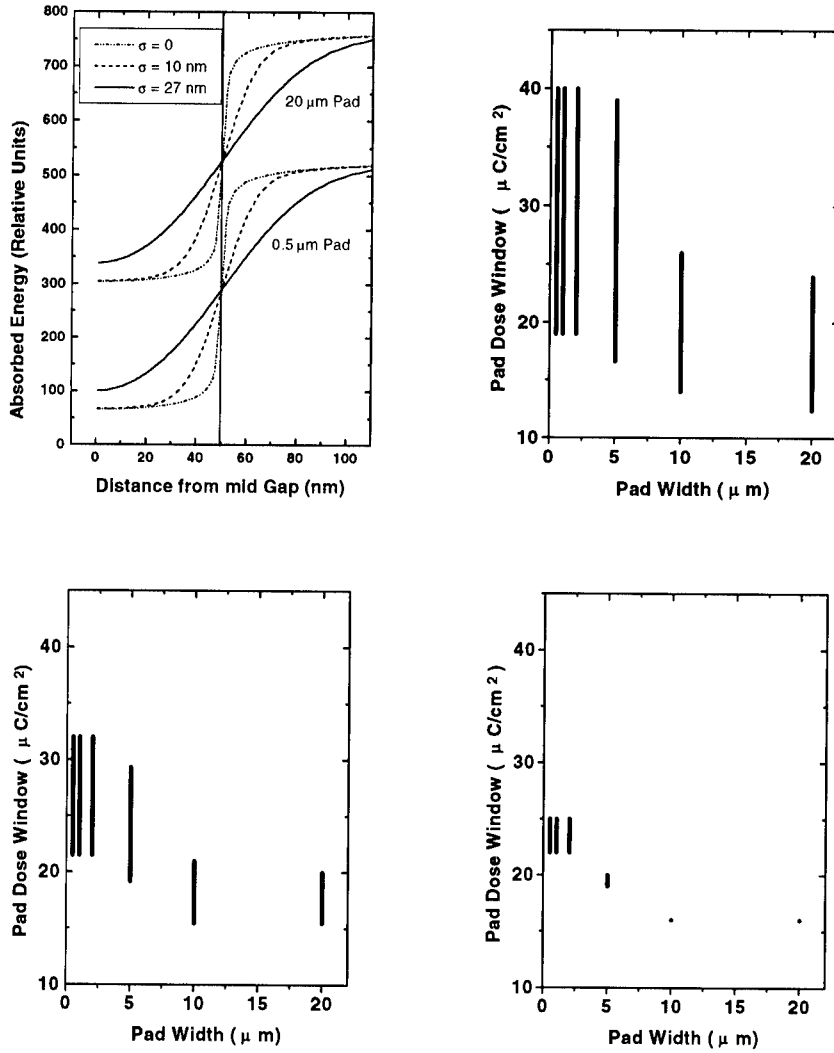
Figure 7. Dose latitude to form a critical dimension gap in a pad in SAL-601. (a) Calculated energy absorbed vs. distance from center of the gap for LSFs from the MC code convolved with σ's of 0, 9, and 27, nm. (b-d) Dose latitude to produce critical dimension (CD) gap ± 10% CD vs. pad width for gaps of (b) 500 nm, (c) 200 nm (d) 100 nm. PEB of 105 °C for 1 min. on a hot plate. [From Refs. 13,14]

in the samples PEBed at 90 °C. The resist at the other PEB temperatures showed much steeper linewidth variation with dose. One can see that at 90 °C, little has been sacrificed in sensitivity, compared to the higher PEB temperatures.
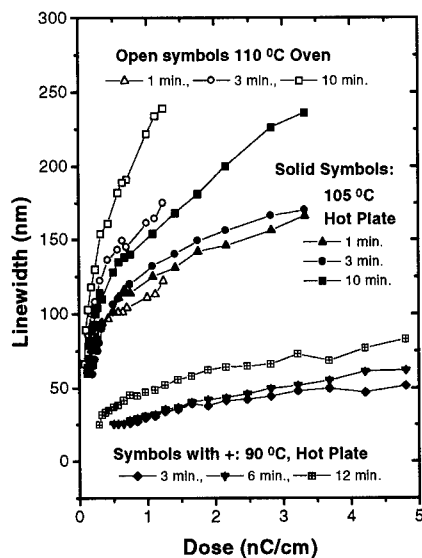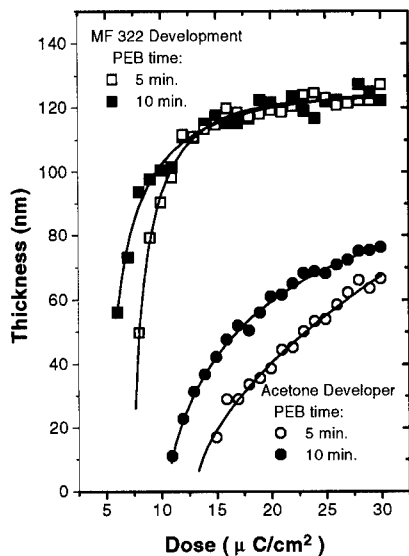
Figure 8. Negative resist thickness vs. dose for SAL-601 PEBed at 100 °C on a hot plate. Both MF-322 Development and acetone development are shown. [Ref. 36]

Figure 9. Linewidth vs. dose for SAL-601 PEBed at three temperatures and different times. Samples were developed in MF-322. [Ref. 36]

The high sensitivity retained with a 90 °C PEB temperature is due to the low acid diffusion. This is shown in fig. 10, where the linewidth data was fit to calculated link density vs. radial distance curves. The curves are calculated with a model[37] that assumes that the dose is proportional to the e-beam generated acid concentration. The model also assumes that the rate of change of links (causing insolubility) depends on the acid concentration to the mth order.

(a)

(b)
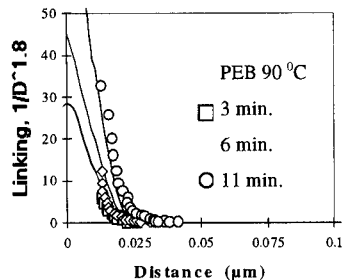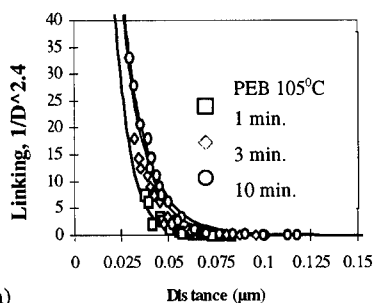
Figure 10. Normalized linewidth data (data points) fit to diffusion reaction kinetics model (solid lines). (a) PEB 105 0C: 1, 3, and 10 min. Reaction order 2.4, Diffusion coefficient 8 nm^2/s, acid loss rate 0.005%/s. (b) PEB 90 0C: 3, 6, and 11 min. Reaction order 1.8, Diffusion coefficient 0.05 nm^2/s, acid loss rate 0.0005%/s. [Ref. 36]

93

The average reaction order was determined from the resist thickness vs. dose curves.[36] For MF-322 development, the average reaction order was 2.4 for PEB temperatures of 100, 105, 110 °C.[36] At 90 °C, the average reaction order was 1.8[36]. The different average reaction order at 90 °C is believed to be due to a different average reaction stoiciometry, consistent with no indication of cross-linking at 90 °C. In the model[36], the initial acid concentration is a normalized Gaussian distribution of the same width as the incident electron beam. The model is a finite difference model, which allows the material to react with m[th] order acid reaction kinetics and Fickian acid diffusion. The model also allows acid loss to the surface. The diffusion coefficient and the acid loss rate are varied until the curves best fit the data. Shown in fig. 10 are the curves that best fit the linewidth data for PEB temperatures of 105 °C and 90 °C. At 90 °C, the acid loss rate and diffusion coefficient are one and two orders of magnitude less than those at 105 °C.

Overall, SAL-601, and related CARs are suitable for sub-100 nm lithography. Sub-50 nm lines have been defined over an order of magnitude in dose and a factor of two in PEB time. At lower temperature PEBs, the LSF width was ~ 10 nm, which shows promise for high resolution dense pattern definition. Swelling has not been addressed in SAL-601. The minimum isolated linewidth that was observed at any of the PEB temperatures was determined by resist adhesion. Some of the causes of adhesion problems include resist swelling, surface tension, and poor binding to the substrate.

Self Assembled Monolayers Resists

At the Naval Research Laboratory metal binding organosilanes have been presented as resist layers.[8,9] The resists have been developed to facilitate resist adhesion and to provide a viable thin resist system for nanolithography and applications that require thin resists. The advantage of the silane is that the monolayer will bind to any hydroxylated substrate, including Si and native oxides. The molecules are thermodynamically driven to coat the surface. The other end of the molecule is able to bind to metal. The ability of the self assembled monolayer to bind to metal is lithographically patterned. In this manner, a self assembled monolayer pattern is transferred to an etch hard mask. Shown in fig. 11, is a grating of lines patterned in PEDA with a STM. The STM exposure destroyed the ability of the SAM to bind to a metal. A Pd II catalyst was selectively deposited onto the surface and a 25 nm layer of Ni was electrolessly plated onto
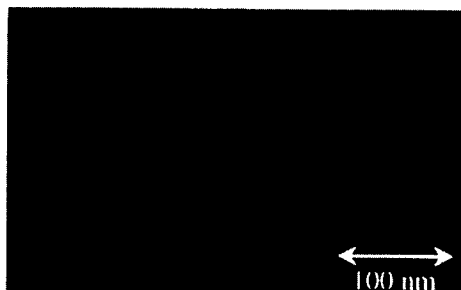
Figure 11. 15 nm lines in PEDA, metallized and etched into Si. [Ref. 7, with permission]
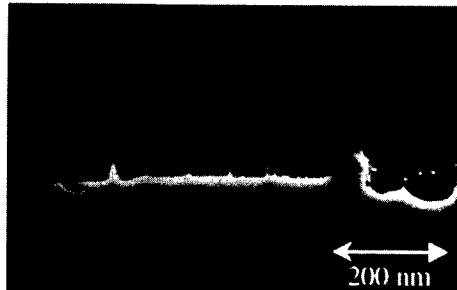
Figure 12. CMPTS pattern, metallized with 25 nm Ni and etched 5 μm into Si with SF6 [Ref. 7, with permission]

the pattern. The pattern was etched into the Si. Shown in fig. 12 is a pattern that was etched 5 μm into the underlying Si with SF_6 and a 25 nm Ni mask. One can see that although the fine lines have been undercut by the etch, the thin Ni layer provides an excellent mask.

Our metal binding organosilane SAMs have been exposed with ultraviolet, extreme ultraviolet, STM, and electron beam lithographies.[8-9] The metal binding has been achieved by binding to amines and pyrroles[38], and grafting amines to benzyl methyl halides. Most recently processes have been developed in which a molecule containing an amine or a pyrrole can be physisorbed into voids in a SAM or polymer surface.[38] SAMs represent a newly emerging field with a wide range of possible revolutionary applications.[8-38]

CONCLUSIONS

The use of resist materials for very high resolution, sub-50 nm lithography has been discussed. The importance of process broadening and a measured LSF in a developed resist is demonstrated. The developed resist LSF is a key parameter to minimize in width to obtain critical dimension control, dose latitude, and the ability to define very dense patterns. In PMMA, the effects of its macromolecular properties on line-to-line resolution has been addressed. Swelling has presented a problem in the higher molecular weight resists. The best results were obtained with the 100K PMMA. A 40 nm period grating was demonstrated. The resolution of chemically amplified resists has been examined through focusing on SAL-601. A low temperature PEB gives the least acid diffusion and best resolution without a significant loss in sensitivity. Sub-50 nm lines were defined over an order of magnitude dose and factor of two difference in PEB time. Lastly, metal binding self assembled monolayer resists are presented as potentially viable thin resists. The resists present a revolutionary approach to resists with a range of applications and possibilities.

ACKNOWLEDGEMENTS

REFERENCES

[1] A.N. Broers, Proc. First International Conference on Electron and Ion Beam Technology, ed. R. Bakish, p. 181, New York: John Wiley & Sons, Inc. (1964).

[2] I. Haller, N. Hatzakis, and R. Srinivasan, IBM J. Res. Dev. 12, 251 (1968).

[3] A.N. Broers, J.M.E. Harper, and W.W. Molzen, Appl. Phys. Lett., 33, 392 (1978).

[4] H.G. Craighead, R.E. Howard, L.D. Jackel, and P.M. Mankiewich, Appl. Phys. Lett. 42, 38 (1983). H.G. Craighead, J. Appl. Phys., 55, 4430 (1984).

[5] SIA Roadmap, 1997.

[6] Nano, private communication.

[7] F.K. Perkins, E.A. Dobisz, S.L. Brandow, J.M. Calvert, J.E. Kosakowski, C.R.K. Marrian, Appl. Phys. Lett., 68, 550 (1996).

[8] J.M. Calvert, J. Vac. Sci. Technol. B 11, 2155 (1993) and references therein.

[9] F.K. Perkins, E.A. Dobisz, S.L. Brandow, T.S. Koloski, J.M. Calvert, K.W. Rhee, J.E. Kosakowski, C.R.K. Marrian, J. Vac. Sci. Technol. B12, 3725 (1994).

[10] C.R.K. Marrian, F.K. Perkins, , S.L. Brandow, T.S. Koloski, E.A. Dobisz, and J.M. Calvert, Appl. Phys. Lett., **64**, 390 (1994).

[11] C.R.K. Marrian, F.K. Perkins, D. Park, E.A. Dobisz, M.C. Peckerar, K.W. Rhee, and R. Bass, J. Vac. Sci. Technol. **B14**, 3864 (1996).

[12] T.H.P. Chang, J. Vac. Sci. Technol., **12**, 1271 (1975).

[13] E.A. Dobisz and C.R.K. Marrian, SPIE Proc. (1997).

[14] E.A. Dobisz and C.R.K. Marrian, J. Vac. Sci. Technol., B **15**, 2327 (1997).

[15] E.A. Dobisz, S.L. Brandow, R. Bass, L.M. Shirey, J. Vac. Sci. Technol., B **16**, (1998).

[16] E.A. Dobisz, S.L. Brandow, R. Bass, L.M. Shirey, Appl. Phys. Lett., (1999).

[17] C. Tanford, *Physical Chemistry of Macromolecules*, pp. 151-168, 307-310 (New York, John Wiley & Sons, 1961).

[18] E.A. Dobisz, S.L. Brandow, E.S. Snow, and R. Bass, J. Vac. Sci. Technol., **B15**, 2318 (1997).

[19] E.A. Dobisz, S.L. Brandow, R. Bass, and J. Mitterender, J. Vac. Sci. Technol., B **18** (to be published Jan/Feb, 2000).

[20] C. Tanford, Op. Cit., pp.603-606.

[21] J.H. Baxendale, S. Bywater, and M.G. Evans, Trans. Faraday Soc., **42**, 675 (1946).

[22] W. Chen and H. Ahmed, . J. Vac. Sci. Technol., B **11**, (1993).

[23] H.Namatsu, , J. Vac. Sci. Technol., B **17**, (1999).

[24] E.A. Dobisz & C.R.K. Marrian, J. Vac. Sci. Technol., **B9**, 3024 (1991).

[25] E.A. Dobisz, C.R.K. Marrian, L.M. Shirey, M. Ancona, J. Vac. Sci. Technol., **B10**, 3067 (1992).

[26] E.A. Dobisz, C.R.K. Marrian, R.E. Salvino, M.A. Ancona, F.K. Perkins, and N.H. Turner, J. Vac. Sci. Technol., **B11**, 2733 (1993).

[27] T. Yoshimura, Y. Nakayama, and S. Okazaki, J. Vac. Sci. Technol., **B10**, 2615 (1992).

[28] E.A. Dobisz and C.R.K. Marrian, Appl. Phys. Lett., **58**, 2526 (1991).

[29] F.K. Perkins, E.A. Dobisz, and C.R.K. Marrian, J. Vac. Sci. Technol., **B11**, 2597 (1993).

[30] C.R. Eddy,Jr., E.A. Dobisz, J.R. Meyer, C. Hoffman, J. Vac. Sci. Technol., **A11**, 1763 (1994).

[31] S.D. Hector, W. Chu, M. Thompson, V. Pol, B. Dauksher, K. Cummings, D. Resnick, S. Pendharkar, J. Maldonaldo, M. McCord, A. Krasnopernova, L. Liebmann, J. Silverman, J. Guo, M. Khan, S. Bollepalli, L. Capodieci, and F. Cerrina, J. Vac. Sci. Technol., **B14**, 4288 (1996).

[32] M.A. Zuniga and A.R. Neureuther, J. Vac. Sci. Technol., **B14**, 4221 (1996).

[33] C.J. Gamsky, P.M. Dentinger, G.R. Howes, & J.W. Taylor, SPIE Proc., 2438, 143 (1995).

[34] A. Yamaguchi, S. Kishimura, K. Tsujita, H. Morimoto, K. Tsukamota, H. Nagata, J. Vac. Sci. Technol. **B11**, 2867 (1993).

[35] James W. Thackeray, George W. Orsula, Mark Denison, SPIE Proc., **2195**, 152 (1994).

[36] E.A. Dobisz, T.N. Fedynyshyn, R. Bass, D. Ma, and L.M. Shirey, J. Vac. Sci. Technol., B **16**, (1998).

[37] T.N. Fedynyshyn, C.F. Szmanda, R.F. Blacksmith, W.E. Houck, and J.C. Root, J. Vac. Sci. Technol. B **11**, 2798 (1993).

[38] S.L. Brandow, J.M. Calvert, W.J. Dressick, and C.S. Dulcey, Navy Case 78,658; 8 September 1999.

ANISOTROPIC ORGANIC/INORGANIC RESISTS: A NOVEL CONCEPT FOR ELECTRON PROXIMITY EFFECT REDUCTION

Lhadi MERHARI *, Henry H. LI **, and Kenneth E. GONSALVES **
*CERAMEC R&D, F-87000, Limoges, France, ceramec@wanadoo.fr
**Polymer Program at the Institute of Materials Science, U-136, & Department of Chemistry, U-60, University of Connecticut, Storrs, CT 06269-3136, gonsalve@uconnvm.uconn.edu

ABSTRACT

Electron projection lithography is considered to be one of the best candidates for sub-100 nm production circuits. One of the major problems that hinders its development is not related to machine fabrication issues but to electron proximity effects which stem from fundamental electron-polymer interactions. During the past two decades, efforts to reduce the electron proximity effects have essentially focused on the optimization of the resist exposure by means of dose modulation correction programs. We propose a novel approach where the structure of the resist can be tailored so that controlled anisotropy is introduced to laterally constrain the electron scattering. This novel approach does not require the use of high-voltage electron beams nor the processing of a large amount of data, which is a significant economic advantage. Some concepts for the synthesis of these anisotropic resists are discussed and the preliminary example of iron oxide nanorods aligned in poly(methylmethacrylate) (PMMA) is studied.

INTRODUCTION

To respond to the exploding market of information technology for civilian and military applications, within the next decade the microelectronic industry needs a lithographic process capable of mass-producing integrated circuits with sub-70 nm critical dimensions (CD). It is unlikely that this formidable challenge can be taken up through evolutionary steps [1]. Moreover, it is not at all sure that photolithography which is the workhorse tool in the microelectronic industry will prevail as it is now widely accepted that the shorter the radiation wavelength the finer the theoretical resolution, thus making Extreme UV, X-ray, electron beam and ion beam lithographies more promising candidates. Electron beam lithography is probably the less risky, the most accepted and the most versatile technique benefiting from the major R&D knowledge accumulated over the past 50 years. Companies such as IBM, Hitachi and Siemens [2-3] have already demonstrated that the industrial concept of electron projection lithography (EPL) is technically feasible and viable in terms of throughput since it is a parallel process. With the advent of a new EPL technique called SCALPEL (SCattering with Angular Limitation Projection Electron Lithography) developed by Bell Labs-Lucent Technologies, there is now a real platform for sub-70 nm lithography providing that one of the major problems, namely the electron proximity effect [4], is eliminated. Indeed, this effect translates into severe degradation of the pattern definition as the uniform exposure by the incident beam gives rise to a nonuniform distribution of actually received exposure in the pattern area. Moreover, it has been mathematically proven that no rigorous solution of the proximity equation [5] exists for isotropic resists like PMMA, thus showing that the fundamental problem essentially lies in the electron-polymer microscopic interactions [4] and not in the technological advances of the already sophisticated EPL system itself. During the past two decades, experimental attempts [6,7] to limit the electron proximity effects in isotropic resists have not led to any breakthrough, thus proving that the current resists used by the industry are not ideal for the promising sub-100 nm EPL.

NOVEL CONCEPT FOR ELECTRON PROXIMITY EFFECTS REDUCTION

Current methods for reduction of electron proximity effects

The electron proximity effect due to scattering of incident and secondary electrons leading to a pear-like structure [4] in standard organic resists, which degrades the overall resolution of the lithographic process, is too often macroscopically modelled by the following simplistic proximity function (effective exposure) [6,7]:

$$f(r) = k \left[\exp(-r^2/\beta_f^2) + \eta_E \beta_f^2/\beta_b^2 \exp(-r^2/\beta_b^2)\right] \qquad (1)$$

where r is the radial distance from the point of incidence of the electron beam, k is a normalizing constant, η_E is the ratio of integrated contributions of backscattered to forward-scattered electrons, and β_f, β_b are the characteristic widths respectively related to forward and backward scattered electrons.

Two methods to reduce the proximity effect have been developed, neither being fully satisfactory. The first and obvious one is to use ultrathin layers (<50 nm instead of 500-1000 nm) of resists [8] and high energy (100 keV) electron beams so that the penetration depth (or range) of the electrons is orders of magnitude higher than the resist thickness, thus reducing the lateral scattering of the electrons. The drawbacks are the high pinhole density in the ultrathin resist, the inadequate etch resistance, the inability to cover topographic steps and the significant ownership/maintenance costs of high-voltage lithographic systems. The second method is based on the modulation of the incident dose so that its convolution with the energy intensity distribution leads to the ideal exposure of the resist [9]. Unfortunately, the accuracy of the correction programs developed so far significantly decreases with decreasing feature sizes while concomitantly computing time prohibitively increases, thus making this strategy questionable for sub-100 nm lithography.

Novel concept of anisotropic resist

The above correction methods focus on the radiation aspect of the electron-polymer interactions, considering the resist structure as a fixed parameter. A more fundamental description of the proximity effect via Monte Carlo simulations takes the complex electron-polymer interactions into account and shows that a pear-like structure is inevitably generated in any isotropic organic resist by the isotropic scattering of the incident electrons and generated secondary electrons [4,7].

The original solution that we propose is to focus on the material aspect of electron-polymer interactions and to strongly reduce the lateral scattering of the primary and secondary electrons by forcing them to follow vertical paths imposed by the tailored microstructure of an anisotropic resist. The closely packed and vertically aligned nanostructures will 'guide' the electrons through the nanocomposite resist (analogue to electron chanelling). As a result, no pear-like structure can develop laterally as the electrons paths are constrained by the microstructure of the resist. The term 'anisotropic' has been chosen because the z-direction of the electron trajectories is favoured. This anisotropic resist may consist of self assembled or aligned inorganic/metallic nanorods (separated by a few nm) bound together by radiation sensitive ligands. Upon spincasting or spraying of the liquid nanocomposite resist on the wafer, the nanorods are randomly distributed. A magnetic field applied during the drying of the resist makes it possible to vertically align all the nanorods so that a regular and dense columnated structure is obtained (cf. Fig. 1). Aligned stacked nanoparticles are also suitable (cf. Fig. 2).

Ideal electron trajectories between nanorods in PMMA

electron beam
⌀ < 100 nm

0 μm

PMMA film
cross-section

-1 μm

-1 μm   0 μm   1 μm
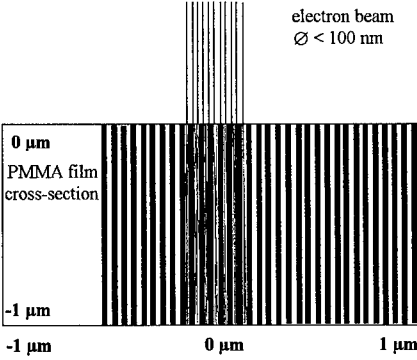
Ideal electron trajectories between stacked nanoparticles in PMMA

electron beam
⌀ < 100 nm

0 μm

PMMA film
cross-section

-1 μm

-1 μm   0 μm   1 μm
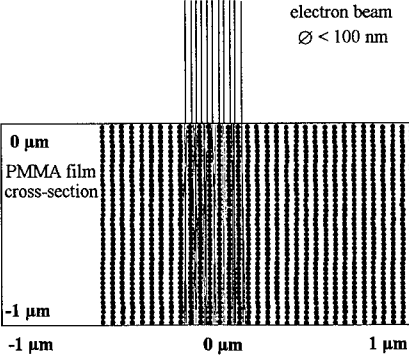
Fig. 1: nanorods aligned in PMMA.   Fig. 2: stacked nanoparticles aligned in PMMA.

During EPL, the beam will irradiate the resist through the mask openings along the z-axis. The exposed anisotropic resist areas composed of polymer ligands and vertically aligned nanorods will not undergo isotropic damage. Indeed, the nanorods will act as 'walls' stopping off-z-axis electron trajectories because the electron range in the nanorods is considerably shorter than in the polymer ligands due to material differences (different electronic stopping powers). As a consequence the electrons are forced to travel in the resist between the nanorods. In other words the electrons are forced to follow vertical paths along the nanorods and are allowed to laterally scatter only in the very limited space between the packed nanorods, hence no pear-like structure degrading the resolution can develop in this anisotropic resist. The closer and thinner the nanorods, the denser the resist and the higher the lithographic resolution. Upon wet or dry development, the exposed positive resist is removed along with the nanorods as these are no longer bound together. A similar analysis holds for stacked nanoparticles.

Obviously, the 'degree of anisotropy' of the resist and off-z-axis electron 'blocking efficiency' depend on the difference in the inorganic and organic phase characteristics. To substantiate this statement, consider the following modified Bethe continuous energy loss equation [10]:

$$(-\frac{dE}{dx})_E = \frac{785Z\rho}{AE} Ln[1.166\frac{(E+kJ)}{J}] \qquad (2)$$

where for a given medium, the quantities $(-dE/dx)_E$ denoted $S_e(E)$, Z, ρ, J, and A are, respectively, the inherent stopping power or energy loss per unit length, the average atomic number, the density, the mean ionization energy, and the average atomic weight, while the quantity E is the average electron energy across the electron trajectory. The quantity k is a parameter whose value depends on the material under consideration and is used to correct the calculated stopping powers at lower incident beam energies obtained from the original Bethe stopping power equation. Applying this equation to two different media, PMMA and Fe_3O_4, for the same average beam energy E, we can calculate the ratio of the stopping powers $(S_e)_{Fe3O4}(E)/(S_e)_{PMMA}(E)$. For our approximate calculations, the following values were assigned: $k \approx 0.77$ (for carbon), $Z_{PMMA} = 3.6$ (average atomic number for $C_5H_8O_2$), $A_{PMMA} = 6.67$ (average atomic weight for $C_5H_8O_2$), $\rho_{PMMA} = 1.19$ g/cm^3, $J_{PMMA} = 41.4$ eV, $Z_{Fe3O4} = 15.7$ (average atomic number for Fe_3O_4), $A_{Fe3O4} = 33$

99

(average atomic weight for Fe_3O_4), ρ_{Fe3O4} = 5.17 g/cm^3, J_{Fe3O4} = 180.6 eV (J has been calculated from J = 11.5 for Z < 13, which is approximate for Fe_3O_4). The following table summarizes the results obtained for several incident energies. Similar values are obtained when replacing Fe_3O_4 with Fe_2O_3.

E (keV)	2	5	10	15	25	50	100
Ratio: $(S_c)_{Fe3O4}/$ $(S_c)_{PMMA}$	2.48	2.71	2.84	2.90	2.97	3.05	3.12

This shows that $S_c(E)$ for Fe_3O_4 is greater than $S_c(E)$ for PMMA, meaning that the range of electrons in PMMA is much larger than that in Fe_3O_4, thus conferring an 'electron blocking efficiency' to the vertical iron oxide nanorods and hence a 'degree of anisotropy' to the nanocomposite resist. Moreover, it appears that a saturation of the ratio occurs above 15 keV.

Assessment of the resolution

From the above considerations it appears that the Gaussian function describing the electron backscattering vanishes in the proximity equation. As for the electron forward-scattering which is considered as the most difficult adverse effect to minimize, it is the resultant of two contributions: that of the intrinsic Gaussian electron beam emitted by the source and that of the intrinsic electron-polymer interactions. This latter is the most serious effect in terms of degradation of the lithographic resolution and is dramatically reduced by the columnated resist according to the analysis in the previous section. It appears that the Gaussian function describing the effect of the intrinsic electron beam emitted by the source will be always present in the proximity equation but it has already been proven that its contribution is negligible (below 2-5 nm) [4] when using low-energy spread electron sources (LaB_6 and field effect sources) and adopting the Kohler illumination design for the electron optics. It clearly appears that the ultimate spatial resolution leading to the final CD is given by the section of one nanorod. The smaller the nanorod diameter the higher the lithographic resolution. On practical grounds, CDs of the order of 20-50 nm can be envisaged. Moreover, it is worth noting that such a resolution should be obtained at electron accelerating voltages as low as 15 kV thus strongly decreasing the cost and maintenance of the lithographic machine (to be compared with the current costly strategies of proximity effect reduction by using 100 keV electron beams).

APPROACHES FOR THE SYNTHESIS OF ANISOTROPIC RESISTS

A critical evaluation of the above concept shows that two major points condition the success of the anisotropic resist. The first problem to overcome is the synthesis of a nanocomposite resist compatible with the constraints of microelectronic processes. The second trickier problem is the vertical and periodic alignment of the nanorods during the resist drying.

Self-assembly of stacked layers with ordered organic and inorganic phases

A priori, an elegant way to synthesize layers with ordered 3D structures would be to use the method of self-assembly of monolayers [10]. However, achievement by this synthesis method of the stacking of numerous monolayers to obtain a 300-500 nm resist layer while building a columnar structure by keeping a vertical alignment of the inorganic nanoparticles remains questionable.

<u>Dispersion and alignment of magnetic nanoparticles or nanorods in radiation sensitive polymers</u>

A more classic method is to disperse magnetic nanoparticles or nanorods in a polymer while the vertical alignment of these magnetic structures is performed with a magnetic field applied during the drying of the resist on the wafer. Once frozen in their final position and the aligning magnetic field removed, the packed columns arranged like a checkerboard must lose their magnetization. Indeed, any remaining magnetization may deflect the electron beam and induce unacceptable image distortion. This narrows the choice of the inorganic material to superparamagnetic high density nanomaterials.

The above detailed concept along with the associated constraints were given to the group at the University of Connecticut with the mission to find a suitable chemical synthesis and to make prototype resists. The successful synthesis method must lead to superparamagnetic nanoparticles or nanorods having diameters less than 20 nm (to reduce line edge roughness) while the dispersion of these structures in PMMA must be perfectly homogeneous. Upon magnetic vertical alignment, the column separation must be of the order of the column radius to maximize the 'anisotropy'. Moreover, the coating of the wafer with the resist prototype must be easily done. Figures 3 and 4 describe the chemical syntheses of Fe_3O_4 nanoparticles and Fe_2O_3 nanorods where a 5nm-thick SiO_2 coating is applied to preserve the β-FeOOH rod-shape.
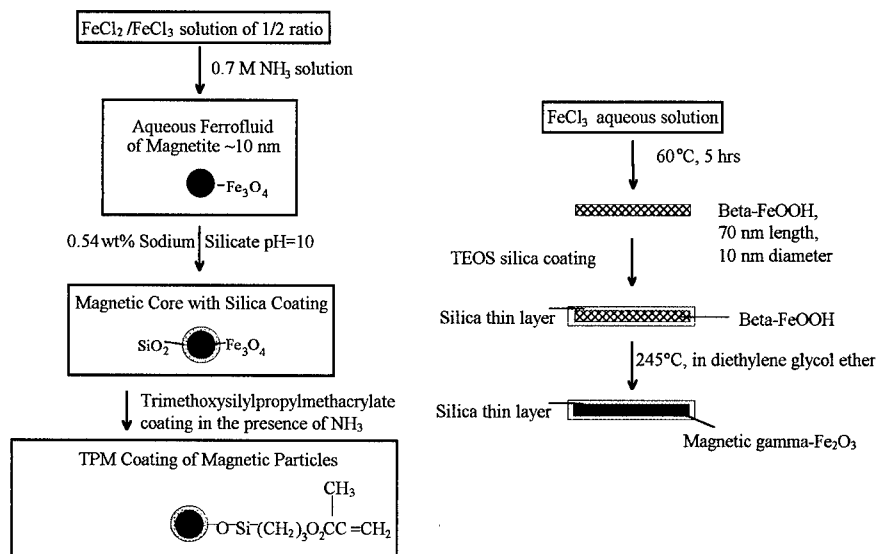
Fig. 3: synthesis flow chart of Fe_3O_4 n-particles.   Fig. 4: synthesis flow chart of Fe_2O_3 nanorods.

PRELIMINARY ANISOTROPIC RESIST PROTOTYPES

The first part of the demonstration of the concept of anisotropic resists for electron proximity effect reduction is obviously a successful synthesis of the nanocomposite. Figure 5 shows the picture of a nanocomposite film prepared by UV polymerization of a dispersion of 9-10 nm Fe_3O_4 particles in MMA monomer on C-substrate. Coating these nanoparticles with 3-(trimethoxysilyl) propyl methacrylate helps in dispersing them in MMA and organic solvents. The preliminary films

show a homogeneous and agglomeration-free nanoparticles distribution. Figure 6 shows the effect of a 12-kOe magnetic field, parallel to the glass substrate, on a dilute (1 wt%) Fe_2O_3 nanorods dispersion in a 8 wt% PMMA/MEK-MIBK polymer solution. A good alignment of the nanorods is obtained as indicated by the guiding parallel lines.

200nm-thick film of Fe_3O_4 nanoparticles/PMMA

Magnetic Field (12 KOe)
~150 nm Thick Films
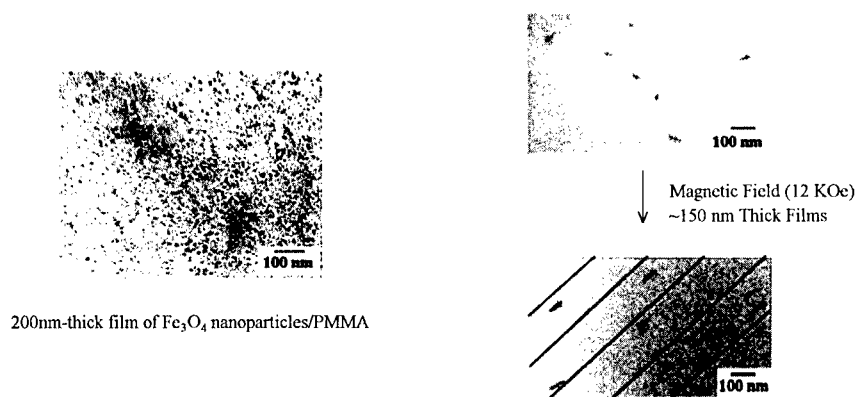
Fig. 5: SEM picture of a nanocomposite film.   Fig. 6: alignment of Fe_2O_3 nanorods in PMMA.

OUTLOOK

The synthesis part of the new concept of anisotropic resists for electron proximity effect reduction allowing mass-production of ICs with sub-70 nm CD has been demonstrated. The second part dealing with detailed lithographic characterization is under way. This new resist concept offers major advantages as it capitalizes on the versatile electron beam lithography and on the recent advances in nanostructured materials.

ACKNOWLEDGMENTS

REFERENCES

1. L.R. Harriott, Materials Today 2, 9 (1999).
2. T. Asai, S-I. Ito, T. Eto, and M. Migitaka, Japanese J. Appl. Phys. 19, 47 (1980).
3. J. Frosien, B. Lischke, and K. Anger, J. Vac. Sci. Technol. 16, 1827 (1979).
4. A.N. Broers, IBM J. Res. Develop. 32, 502 (1988).
5. P.D. Gerber, J. Vac. Sci. Technol. B 6, 432 (1988).
6. M. Parikh, IBM J. Res. Develop. 24, 438 (1980).
7. E.A. Dobisz, C.R.K. Marrian, R.E. Salvino, M.A. Ancona, F.K. Perkins, and N.H. Turner, J. Vac. Sci. Technol. B 11, 2733 (1993).
8. S.W.J. Kuan, C.W. Frank, C.C. Fu, D.R. Allee, P. Maccagno, and R.F.W. Pease, J. Vac. Sci. Technol. B 6, 2274 (1988).
9. S.J. Wind, P.D. Gerber, and H. Rothuizen, J. Vac. Sci. Technol. B 16, 3262 (1998).
10. K. Seshadri, K. Froyd, A.N. Parikh, D.L. Allara, M.J. Lercel, and H.G. Craighead, J. Phys. Chem. 100, 15900 (1996).

FULLERENE-INCORPORATED NANOCOMPOSITE RESIST SYSTEM FOR NANOLITHOGRAPY

T. Ishii*, H. Nozawa** , E. Kuramochi, * and T. Tamamura*
*NTT Basic Research Laboratories, Atsugi, Kanagawa, Japan, tishii@will.brl.ntt.co.jp
**NTT Photonics Laboratories, Atsugi, Kanagawa, Japan

ABSTRACT

A nanocomposite resist system that incorporates sub-nm fullerene molecules (C_{60} and/or C_{70}) into a conventional resist material is proposed for nanolithograpy. Fullerene has physically and chemically resistant characteristics, and its incorporation reinforces the original resist film, leading to substantial improvements in resist performance: etching resistance, pattern contrast, mechanical strength and thermal resistance. We have prepared a system composed of a positive-type electron beam resist, ZEP520, and C_{60} or a C_{60}/C_{70} mixture and through the fabrication of high electron mobility transistors (HEMTs), X-ray masks, and groove-grating mirrors for lasers with nanometer dimensions confirmed improved resist performance, particularly resolution improvements due to enhanced etching resistance. By making use of a characteristic unique to the nanocomposite, which is that sensitivity readily changes with the fullerene content due to a dissolution inhibiting effect of fullerene, we have constructed a fullerene-incorporated bilayer resist system for a lift-off process and have successfully fabricated a highly-ordered array of self-organized boxlike nanostructures and a mold for nanoprinting. Further, solubility enhancement by fullerene derivatives has been examined for a higher degree of fullerene incorporation and better sensitivity characteristics in future nanocomposite resist systems.

INTRODUCTION

Electron beam lithography (EBL) is widely employed for nanometer device fabrication. For higher resolution in EBL, the general trend has been to use a higher acceleration voltage to increase beam resolution as well as to minimize scattering effects. Several exposure tools with an acceleration voltage of 100 kV are already used on a practical basis. However, it has become increasingly difficult to fabricate ultrasmall patterns due to the poor resistant qualities of conventional resist materials. Resolution generally increases with decreasing resist film thickness, so an extremely thin film is used for ultrasmall pattern fabrication [1]. The poor etching resistance of such thin film often results in contrast

Figure 1. Problems in conventional resist processes.

degradation or rounding of the upper corners of the patterns during development and in the formation of defects during etching [Fig. 1(a)]. Another problem is pattern collapse [Fig. 1(b)]. When a thicker resist film is used for deep substrate etching, the aspect ratio of the resultant patterns, defined as the ratio of pattern height and pattern width, becomes larger. Such thin and high patterns often collapse due to their poor mechanical strength.

As a way of overcoming these problems, we have recently proposed creating a nanocomposite resist system by incorporating highly etching resistant sub-nm particles into a conventional resist material [2], [3]. Carbon clusters are promising for this purpose. The resistant quality of carbon has been investigated by several researchers. Broers et al. showed that contamination produced at the point of electron-beam impact is highly dry-etching resistant and used it as a resist for nanofabrication [4], [5]. The contamination resist is assumed to be

polymerized carbon-rich hydrocarbons and is sometimes called "carbon resist". Gokan et al. investigated the effect of the carbon content of various resist materials on dry-etching resistance and found that resistance increased with increasing carbon content [6]. Direct and explicit proof of the higher etching resistance and also the better mechanical and thermal stability of carbon was reported by Kakuchi et al. They successfully fabricated nanometer Si patterns by reactive ion etching (RIE) using an amorphous carbon film as a mask for a Si substrate in a bilayer resist system [7]. More recently, Tada et al. used fullerene C_{60} as a negative-type electron beam resist and found that it has higher dry-etching durability than novolac resist through the fabrication of Si nanopillers [8]. The fact that fullerene is a pure carbon material and its proven high etching resistance led us to examine it as possible material for the nanocomposite resist system. We found it to be an excellent material for our purposes for the following reasons: First, it is ultrasmall, having a diameter of only $\sim$ 0.7 nm (Fig. 2). Second, it is soluble in some organic solvents. Third, it can be removed completely by oxygen plasma as CO_2 gas, which is a prerequisite for resist materials in actual device fabrication.

We have constructed a nanocomposite resist system composed of fullerene (C_{60} or C_{60}/C_{70} mixture) and the relatively high-sensitivity positive-type electron beam resist ZEP520 (ZEP for simplicity) [9], and confirmed substantial improvements in resist performance through various device fabrications [10], [11]. One useful application of the nanocomposite ZEP for nanofabrication is a bilayer system for lift-off. The sensitivity of the nanocomposite resist readily changes with fullerene content due to the dissolution-inhibiting effect of fullerene. This unique characteristic makes it possible to make a difference in the sensitivity of the top and bottom layers in a bilayer resist in the same manner that the molecular weight in the PMMA bilayer system does [12]. Since ZEP has a sensitivity of $\sim$ 50 μ C/cm², which is five or six times higher than a high-resolution PMMA resist, the nanocomposite ZEP bilayer can provide better throughput for negative-type pattern fabrication represented by dot patterns. We have verified the applicability of the nanocomposite bilayer system through the fabrication of arrays of dot patterns with nanometer dimensions for a quantum box structure and a nanoprinting mold.

Presently, applications of ZEP nanocomposites and composites made of systems other than ZEP as well are limited by the poor solubility of fullerene. However, the solubility of fullerene can be greatly enhanced by introducing some solubility-promoting functional groups to a fullerene molecule. We have examined solubility enhancement by using a fullerene derivative for a higher degree of fullerene incorporation and better sensitivity characteristics in future nanocomposite resist systems.

CONCEPT

The basic idea of the nanocomposite system is shown in the Figure 2. A film of conventional resist materials spin-coated on a substrate appears to be closely packed film, but from a microscopic viewpoint, such a thin organic polymer film has spaces not occupied by polymer
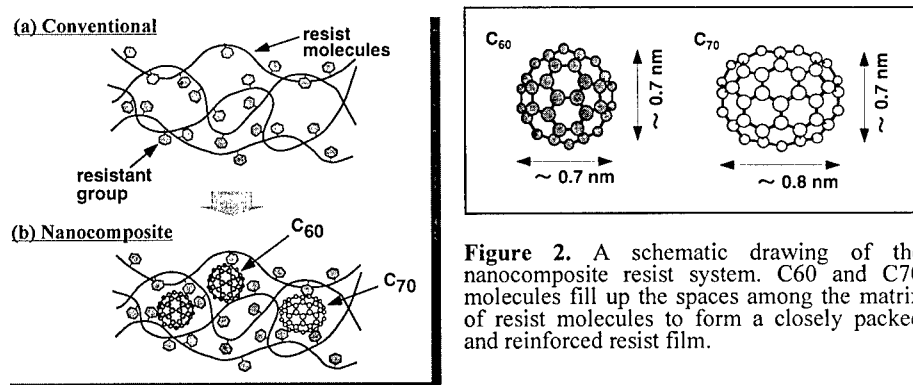
Figure 2. A schematic drawing of the nanocomposite resist system. C60 and C70 molecules fill up the spaces among the matrix of resist molecules to form a closely packed and reinforced resist film.

104

molecules and is porous in nature compared to a film of metals or other inorganic materials [Fig. 2(a)]. Developer or etching species easily pass through the pores in the resist film and bring about the degradation of pattern contrast or etching defects. In addition, such porous organic film generally has poor mechanical strength and tends to collapse during the development process due to an inability to bear surface tension caused by the rinsing solvent. By filling those spaces with ultrasmall particles having high etching resistance, the intrusion of both the developer and etching species is blocked and pattern contrast and etching resistance are thereby enhanced [Fig. 2(b)]. It is also expected that close packing with such ultrasmall particles could increase the rigidness or strength of the film by increasing its density.

EXPERIMENTAL

Commercially available fullerene C_{60}, C_{70}, and also a mixture of C_{60}/C_{70} (ratio: ~4/1), which is available at a much lower price than C_{60} or C_{70} alone, were incorporated into ZEP resist (denoted C_{60}@ZEP, C_{70}@ZEP, $C_{60/70}$@ZEP, respectively). ZEP, whose chemical structure is shown in Fig. 3, is a copolymer of methyl α-chloroacrylate and α-methylstyrene (Mw : ~ 55000) [13], and commercially supplied from Nippon Zeon Co. Fullerene powder was first dissolved in ortho-dichlorobenzene (o-DCB) and then mixed with a ZEP resist solution, whose

Figure 3. Chemical structure of ZEP520.

solvent was also o-DCB. Although o-DCB is a good solvent for fullerene compared to xylene or benzene, there is still a small quantity of fullerene dissolvable in o-DCB and this makes it difficult to prepare the nanocomposite resist. For resist preparation, the solubility of fullerene in o-DCB should be known in advance, otherwise fullerene cannot be dissolved properly. The reported solubility of C_{60} in o-DCB is ~ 25 mg/ml [14], [15], but the solubility of fullerene mixture C_{60}/C_{70} has not been reported. We investigated the solubility of a ~ 4 : 1 mixture of $C_{60/70}$ by using ulra-violet (UV) absorption measurement.

Figure 4 shows UV spectra of the saturated solutions of C_{60}, C_{70}, and a ~ 4:1 mixture of C_{60}/C_{70} in o-DCB. (All solutions were diluted thousand times due to strong absorption of fullerene.) By comparing absorption peak heights at wavelengths of 333.2 (C_{60}) and 466 nm (C_{70}) with the absorption intensity of each calibration curve of C_{60} and C_{70}, which was obtained in advance by changing the concentration of fullerene, we estimated the solubility of C_{60}, C_{70}, and a ~ 4 : 1 mixture of C_{60}/C_{70} as 25.0, 26.6 and 73.4 mg/ml , respectively. Our measured solubility for C_{60} of 25.0 mg/ml agrees well with the reported values of 24.6 and 27.0 [14], [15]

Figure 4. UV spectra of o-DCB solutions of C_{60}, C_{70}, and a ~ 4:1 mixture of C_{60}/C_{70}.

Table 1. Solubility of fullerene in o-DCB.

fullerene	solubility (mg/ml)	ref.
C_{60}	25.0	24.6 [14]
		27.0 [15]
C_{70}	26.6	—
C_{60}/C_{70}	73.4	—

105

and seems to verify our estimated value of C_{60}/C_{70} solubility. Our finding that the solubility of the fullerene mixture is three times higher might be due to a general tendency that C_{60} and C_{70} molecules hinder aggregation with each other to become thermodynamically stable. The solubility measurement suggested that a fullerene mixture would facilitate the preparation of the nanocomposite ZEP.

In resist-characterization experiments, nanocomposite ZEP resists were spin-coated on a substrate and baked at 165 ℃ for 30 min in the same way as conventional (or pure) ZEP resist. Exposure experiments were done with an electron beam machine (JBX-5FE) with an acceleration voltage of 25 kV and exposed samples were developed in ZEP developer ZED-N50 (n-amyl acetate). Pattern contrast and the mechanical and thermal strength of fabricated patterns were observed with a scanning electron microscope (SEM).

Dry-etching resistance was evaluated using electron cyclotron resonance (ECR) dry-etching under the Si etching conditions (gas: Cl_2, flow rate: 40 sccm, pressure: 0.05 Pa, microwave power: 200 W) and also RIE under the SiN etching conditions (gas: C_2F_6, flow rate: 40 sccm, pressure: 2.0 Pa, rf power:1200 W).

We also examined the resistance of the nanocomposite to wet-etching with citric acid/hydrogen peroxide ($C_6H_8O_7/H_2O_2$). This etching solution is well known to provide selective and uniform etching of various III-V semiconductor materials like GaAs and InP [16]. We evaluated wet-etching resistance by taking a rather direct approach of measuring the density of etched pits formed on a GaAs substrate through the resist film after dipping resist-coated substrate in the etching solution. GaAs substrates were first spin-coated with a 40-nm-thick film of pure ZEP and 5 wt% $C_{60/70}$@ZEP and pre-baked as described above. Then, the resist-coated substrates were dipped in a 20:1 wt% $C_6H_8O_7/H_2O_2$ solution at 23 ℃ for 2 min. After the resist films were removed in a resist remover (N-methyl-2-pyrrolidone), the substrates were dried with a spin-dryer and scanned with a conventional He-Ne laser surface-scan tool to measure etch-pit density.

We have done some pattern fabrication experiments using a nanocomposite bilayer system. Figure 5 shows a schematic drawing of the lift-off process of the bilayer resist system, which consists of a $C_{60/70}$@ZEP top layer and a ZEP bottom layer. We prepared 10, 20, and 30 wt% nanocomposites for the top layer. To minimize intermixing between the layers, we dissolved $C_{60/70}$@ZEP in a 3:10 binary solvent of o-DCB and xylene because xylene is a poor solvent for ZEP but dissolves fullerenes to some degree. For sensitivity comparison experiments, we made a bilayer system with a 250-nm-thick film to reveal the difference in sensitivity between the single layer and bilayer systems. ZEP resist was spin-coated on a Si wafer to a thickness of 200 nm and prebaked at 180 ℃ for 30 min, and then $C_{60/70}$@ZEP resist was spin-coated on the ZEP film to a thickness of 50 nm and baked at 165 ℃ for 30 min. Single layers of 0, 10, 20, 30 wt% $C_{60/70}$@ZEP with the same total thickness of 250 nm were prepared in the same manner as the top layer of the bilayer system. The exposed samples were developed in the ZEP developer for 1 min. In lift-off experiments, we used an 80-nm-thick film (30 nm for the top and 50 nm for the bottom layer) to improve resolution. Titanium (Ti) was deposited over the patterned resists to a thickness of 20 nm by electron beam deposition and lifted-off with the resist remover by ultrasonic agitation.
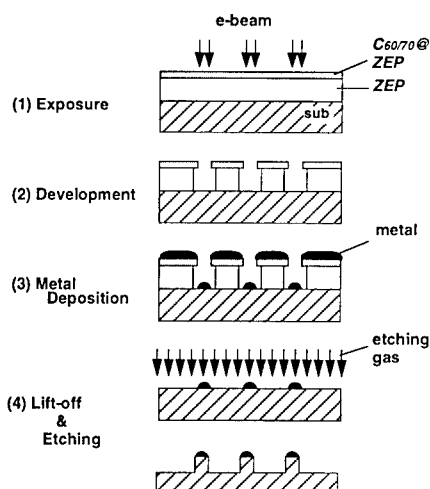
Figure 5. Bilayer resist system composed of a fullerene-incorporated ZEP top layer and a pure ZEP bottom layer. By changing the fullerene content, the sensitivity of the top layer is optimized so as to create an ideal overhang pattern for lift-off.

RESULTS AND DISCUSSION

Resist Characteristics

Figure 6 shows sensitivity curves of C_{60}@ZEP measured in a 50-nm film. Because fullerene is insoluble in ZEP developer, sensitivity decreases due to the inhibiting effect of fullerene. However, it was possible to obtain the same sensitivity as pure ZEP by increasing development time as shown in the figure. By lengthening the time from 1 min for the pure ZEP (0 wt%) to 3 min for the 5 wt% C_{60}@ZEP sensitivity became around 50 μ C/cm^2 for both. We also examined the sensitivity characteristics of $C_{60/70}$@ZEP and found that sensitivity tended to decrease with fullerene content, similar to C_{60}@ZEP. Figure 7 shows the sensitivity curves of a 250-nm-thick $C_{60/70}$@ZEP film. Sensitivity decreased with increasing fullerene content and the values were $\sim$ 50 μ C/cm^2 at 0 wt%, $\sim$ 60 μ C/cm^2 at 10 wt%, and $\sim$ 90 μ C/cm^2 at 30 wt%. Under the present development conditions, we could not obtain good-quality patterns at higher contents due to heavy residue caused by the strong dissolution inhibiting effect of the fullerenes. The best-quality patterns were obtained at around 10 wt%. While the strong dissolution inhibiting effect degrades pattern quality, a moderate inhibiting effect improves pattern contrast. We observed a contrast enhancement effect of fullerene at a content of 5 wt% as shown in Fig. 8. The profile of (b) the 5 wt% C_{60}@ZEP patterns is steeper or higher in contrast than that of (a) the pure ZEP. As mentioned, fullerene is insoluble in the ZEP developer, and this limits the dissolution of the nanocomposite resist at the upper corner of a pattern, which is weakly exposed by electron beam and is removed in the pure ZEP.
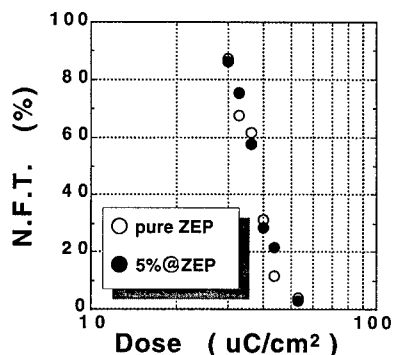
Figure 6. Sensitivity curves of pure ZEP (○) and 5 wt% C_{60}@ZEP (●) developed in ZED-N50, the former for 1 min and the latter for 3 min. The initial film thickness was 50 nm. NFT stands for normalize film thickness.
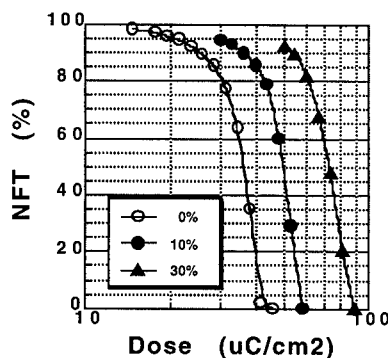
Figure 7. Sensitivity curves of 0 wt% (○), 10 wt% (●), 30 wt% (▲) $C_{60/70}$@ZEP. Developed for 1 min. Film thickness is 250 nm.
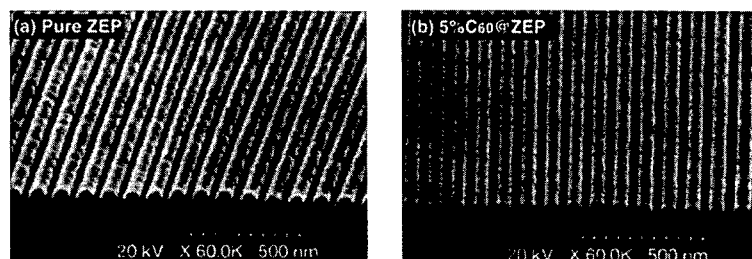
Figure 8. An example of the contrast enhancement of patterns. The pure ZEP patterns show rounded upper corners, while the 5 wt% patterns show steep profiles.

107
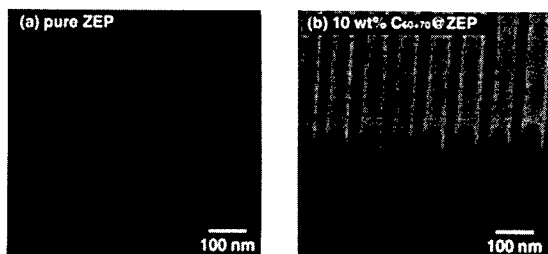
Figure 9. Enhancement in mechanical strength was evaluated by forming high aspect-ratio patterns: 90 nm pitch and 250 nm height. Patterns collapsed in (a) pure ZEP, but no collapse was observed in (b) 10 wt% C60/70@ZEP.
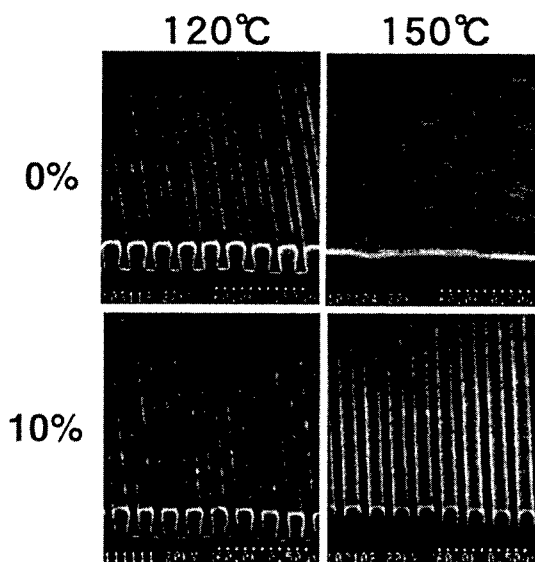
Figure 10. Enhancement of thermal resistance of C60@ZEP. The SEM photographs show 150-nm pitch 0 wt% and 10 wt% patterns after baking at 120 and 150 $^{\circ}$C.

Mechanical resistance or strength was also enhanced by fullerene incorporation. Figure 9 shows 90-nm-pitch and resist patterns of (a) pure ZEP and (b) 10 wt% C60@ZEP formed in a 250-nm-thick film, which is relatively thick for nanometer pattern fabrication. The pure ZEP patterns collapsed during development due to their poor mechanical strength On the other hand, the 10 wt% C60@ZEP patterns exhibit an extremely high aspect ratio of about 5.5 with no pattern collapse.

We also observed an enhancement of thermal resistance in the nanocomposite systems (Fig. 10). Although ZEP has a relatively high glass transition temperature of 145 $^{\circ}$C, it showed pattern swelling at around 120 $^{\circ}$C and completely flowed at 150 $^{\circ}$C. On the other hand, the 10 wt% nanocomposite showed practically no adverse swelling after heat treatment at 120 $^{\circ}$C and only slight deformation even at 150 $^{\circ}$C. This enhancement of thermal resistance facilitated the metal deposition in a bilayer lift-off process in which the resist film was exposed to high temperature.
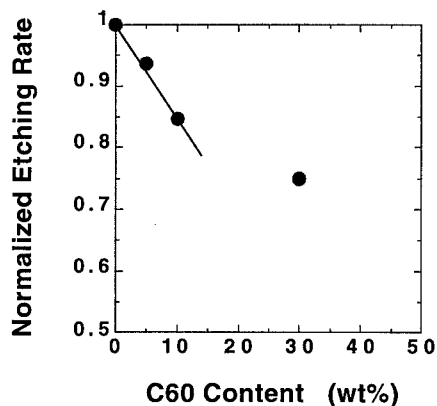
Figure 11. Enhancement of dry-etching resistance of C60@ZEP as a function of C60 content evaluated for ECR dry etching conditions (gas: Cl_2, flow rate: 40 sccm, pressure: 0.05 Pa, microwave power: 200 W).
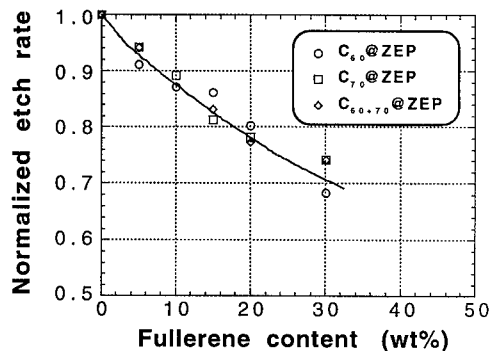
Figure 12. Enhancement of dry-etching resistance in C_{60}@ZEP, C_{70}@ZEP, and $C_{60/70}$@ZEP. The samples were etched by C_2F_6-RIE. Flow rate: 40 sccm, pressure: 2.0 Pa, rf power:1200 W.

The resistance of C_{60}@ZEP to Cl_2 ECR dry etching is shown in Fig.11. The etching rate decreased linearly with C_{60} content up to around 15 wt% and then tended to decrease gradually. This proves that C_{60} incorporation enhances etching resistance. Figure 12 shows the normalized etching rate dependence on the fullerene content for C_{60}@ZEP, C_{70}@ZEP, and $C_{60/70}$@ZEP samples etched in C_2F_6. The etching rate decreased with the fullerene content as it did for Cl_2 ECR dry etching and there was no noteworthy difference among the fullerene species. This means that the enhancement of dry-etching resistance is independent of the fullerene species.

Figure 13 shows laser scanned outputs of GaAs substrates etched in a 20:1 wt% $C_6H_8O_7/H_2O_2$ solution for 2 min. The etch-pit density of (a) ZEP was 540 /cm², while that of (b) 5 wt% $C_{60/70}$@ZEP was 50 /cm². This remarkable difference is probably due to close packing of the films by C_{60} and C_{70} incorporation. This preliminary study suggested that the nanocomposite had the potential for nanometer device fabrication in the area where a dry-etching technique cannot be employed due to the damage it causes. This was subsequently demonstrated through the fabrication of an electron wave interference transistor by Murata et al. [17].

ZEP (40nm)   5 wt% $C_{60/70}$@ZEP (40nm)
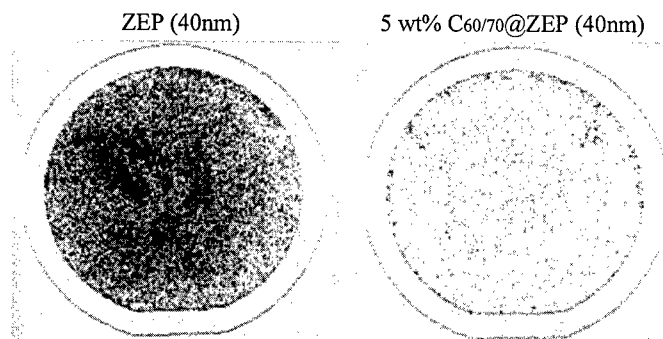
Figure 13. Example of wet-etching resistance by fullerene incorporation. ZEP and 5 wt% $C_{60/70}$@ZEP samples spin-coated on GaAs substrates wer dipped in a 20 : 1 wt% $C_6H_8O_7/H_2O_2$ solution for 2 min and scanned with a He-Ne laser surface scan tool to measure etch-pit density.

Device Fabrication

We have applied the nanocomposite resist system to various device fabrications and obtained good results. We have proved the effectiveness of resist thinning to improve resolution through the fabrication of HEMTs. Figure 14 shows SEM photographs of 30-nm gate resist patterns. The conventional ZEP is 250-nm thick and the 10 wt% nanocomposite ZEP (C60/70@ZEP) is 200-nm thick, which are the minimum thicknesses for covering the whole wafer surface after the RIE gate opening. Both resist films were exposed with the identical dose of 120 μ C/cm^2 , but the conventional ZEP was developed for 1 min and the nanocomposite ZEP for 2 min. As shown in the figure, the 30-nm dimension was clearly resolved in the nanocomposite ZEP, whereas it was not resolvable in the conventional ZEP. In addition, the profile of the nanocomposite ZEP pattern is sharper, that is, higher in contrast than that of the conventional ZEP, even though it was kept in developer longer. Figure 15 is a SEM cross-sectional photograph of the 30-nm T-shaped gate. The bottom of the gate is 30-nm long as designed. The estimated cutoff frequency fT is 350 GHz, which is one of the highest ever reported for any kind of transistor. The detailed process and device characteristics have been reported by Suemitsu et al. [18], [19].

(a) nanocomposite   (b) conventional
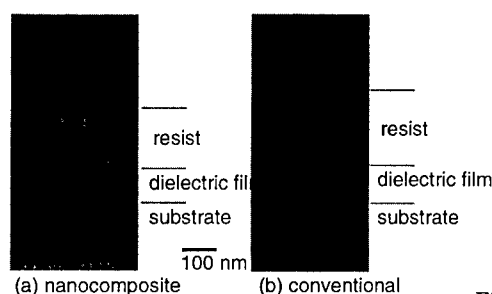
Figure 14. SEM photographs of the gate resist patterns for nanocomposite and conventional ZEP.
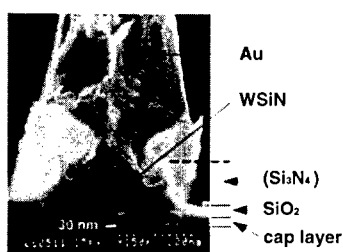
Figure 15. SEM photograph of the cleaved cross section of a 30-nm gate HEMT.

We have also fabricated an X-ray mask using the nanocomposite resist. Figure 16 shows a cross-sectional view of 50-nm Ta absorber patterns of a fabricated mask. The Ta thickness is 400 nm, so the aspect ratio is as high as 8. The mask was patterned in a film of 10 wt% C60/70@ZEP 100-nm thick. The SiO2 layer deposited over the Ta layer was first etched through the resist patterns by C2F6 RIE, and then the Ta layer was etched with the SiO2 mask by Cl2 ECR. The mask composition and fabrication process are described in detail elsewhere [20]. This successful result can be also applied to the fabrication of a Fresnel zone plate for x-ray microscopy.
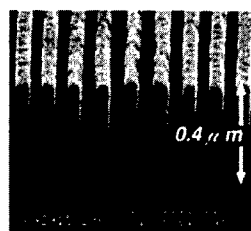
Figure 16. A fabricated Ta absorber X-ray mask with 50-nm features.

Deep substrate etching using the nanocomposite resist has been demonstrated through the fabrication of distributed Bragg reflector (DBR) lasers and Distributed Feedback (DFB) Lasers. Figure 17 shows schematic diagrams of (a) grooved-grating DBR and (b) DFB lasers. The grating etched in the upper-cladding AlGaAs layer acts as a mirror for laser oscillation. Because the grating is etched from the top surface into the upper-cladding layer after the epitaxial growth of the active layer, the DBR and DFB lasers can be fabricated without a high-temperature regrowth process, which simplifies the process and stabilizes the wavelength of the lasers. Cross-sectional SEM photographs of extremely deep groove gratings [(a) 700-nm and (b) 800 - nm] etched into the AlGaAs layer are shown in Fig. 18. The period of each grating is 150 nm. The AlGaAs layer was etched with a 150-nm-thick SiO2 mask. The SiO2 mask was fabricated
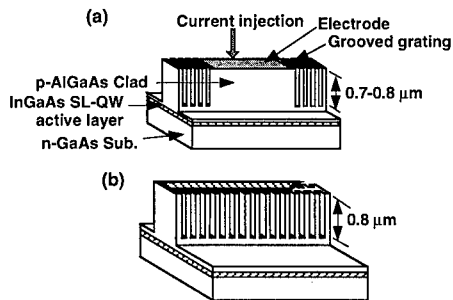
Figure 17. Schematic diagram of grooved-grating DBR and DFB lasers.
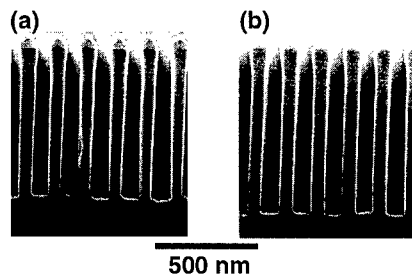
Figure 18. Cross-sectional SEM photographs of etched grooves for first-order diffracting grating.

with a 150-nm thick film of 10 wt% $C_{60/70}$@ZEP. We observed pattern collapse or pattern deformation with conventional ZEP $\sim$ 200-nm thick, which is necessary for proper SiO_2 etching. The detailed process and lasing characteristic have been reported by Oku et al. [21].

Bilayer Resist System for Lift-off

The sensitivity characteristics of the $C_{60/70}$@ZEP single-layer and bilayer systems with 10, 20, 30 wt% are plotted in Figs. 19(a), (b), (c), respectively, in comparison with the 0 wt% single-layer system. The sensitivity curves for all the bilayers change in the same manner as the curves for the nanocomposite single layers in the lower dose range, and deviate from the single layer and approach the curve for the 0 wt% single layer in the higher dose range. This is explained as follows: Each bilayer dissolves at the same rate as the corresponding nanocomposite single layer until the interface because both the bilayer and single layer contain the same amount of fullerene, and then starts to dissolve rapidly because of the absence of fullerene in the bottom layer. Since there is a large difference in the sensitivity between the single layer and the bilayer in both the 20 and 30 wt% systems compared with the 10 wt% system, we expected that the 20 and 30 wt% bilayers would produce much more favorable overhang patterns for lift-off than the 10 wt% bilayer. In addition, the bilayer systems show a sensitivity of around 60 μ C/cm^2 , which is $\sim$ 10 % lower than that of the pure ZEP but is still roughly five or ten times higher than that of PMMA resist. This proves that the nanocomposite bilayer system can provide nanometer dot patterns in a much shorter time.
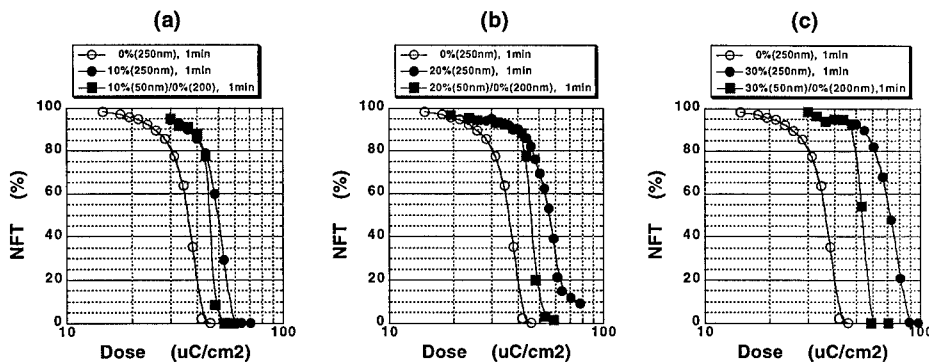
Figure 19. Sensitivity curves of nanocomposite ZEP bilayers in comparison with those of single layers. (a) $C_{60/70}$ mixture content of 10 wt%. (b) 20 wt%. (c) 30 wt%. Film thickness is 250 nm in both the bilayer and single layer.

Figure 20 shows a cross-sectional view of 150-nm-pitch patterns formed in the 20 wt% bilayer. The patterns were exposed with a dose of 0.4 nC/cm. The resist thickness is 50 nm at the top and 200 nm at the bottom, and the opening slit of the top surface is approximately 20 nm wide. Overhang patterns were successfully created as expected from the sensitivity curve measurements. We fabricated Ti dot patterns by lift-off using the 20 wt% bilayer with an 80-nm-thick film. Figure 21 shows an array of ~35-nm-diameter and 75-nm-period Ti dots obtained after lift-off on a GaAs substrate. The patterns are formed with no detachment in the exposed area and show a good uniformity. We did not observe any thermal deformation of the patterns during Ti evaporation. The dimensions of dots can be further decreased by decreasing the total film thickness of the bilayer and also by applying a beam with a higher acceleration voltage.

We have fabricated quantum box arrays using the Ti dots formed by the bilayer lift-off as an etching mask. This fabrication represents an example of lithographically-initiated self-organization. Briefly, the fabrication process is as follows: First, SiN dots formed on a GaAs substrate [(311)B] with Ti dot masks induce hollows on the AlGaAs epilayer covering the SiN dots. Next, InGaAs dots grow selectively in the hollows. Then, InGaAs/AlGaAs boxlike structures are formed over the InGaAs dots in a self-organized way due to the strain caused by the underlying InGaAs dots. The detailed fabrication process and mechanism are discussed in the literature [22]. Figure 22 shows an atomic force microscope (AFM) image of an array of fabricated InGaAs/AlGaAs boxlike nanostructures. The diameter of the boxes is about 50 nm. The boxes are well-ordered and the 310-nm pitch of the initial SiN dots is reflected in the boxlike structure array. Since the pitch of the self-organized boxes is strongly dependent on that of the initial SiN dots, the lithographic technique can initiate and define the ordering of the self-organized dot array. Another example of the bilayer application is SiC mold fabrication for nanoprinting. Since SiC is a hard material with less likelihood of breakage or pattern distortion during pressing and inert to most chemicals used for cleaning, it is an ideal mold material for nanoprinting. The mold was fabricated by C2F6 reactive ion etching using Ni dots as an etching mask. The detailed fabrication process is described in a previous report [23]. Figure 23 shows a fabricated mold. The diameter of the dots at the top is ~ 95 nm, the pitch is 150 nm and the height is 25 nm. These dot patterns can be inversely transferred into metal or polymer substrates by simply pressing the mold onto the substrates to produce high-density nanometer hole arrays with high throughput.

Figure 20. Cross-sectional view of overhang patterns formed in 20 wt% C60/70@ZEP/ZEP bilayer resist.
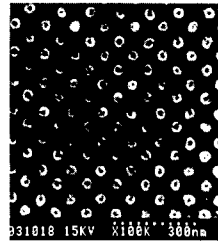
Figure 21. Array of ~ 35-nm-diameter and 75-nm-period Ti dots.
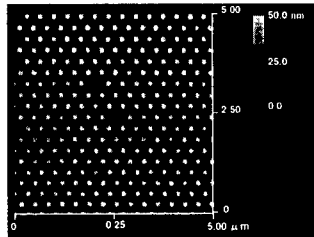
Figure 22. AFM image of ~ 50 nm self-organized InGaAs/GaAs boxlike nanostructure array.
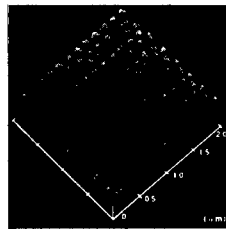
Figure 23. AFM image of the SiC mold for nanoprinting.

C60-derivative nanocomposite

The poor solubility of fullerene limits extensive applications of ZEP nanocomposites and composites made of systems other than ZEP as well. However, the solubilitiy of fullerene can be greatly enhanced by introducing some solubility-promoting functional group to a fullerene molecule [24]. We have examined a higher degree of fullerene incorporation and the exposure characteristics of a nanocomposite system using a fullerene derivative. Figure 24 shows the molecular structure of the fullerene derivative (denoted as C_{60}-drv for simplicity), which was originally synthesized for Langmiur-Blodgett film formation by Shigehara et al. [25]. Because the tail part of the C_{60}-drv is hydrophilic, it is soluble in most polar solvents. We could easily dissolve C_{60}-drv in o-DCB without being concerned about a solubility limit, whereas in the case of C_{60} or $C_{60/70}$ mixture, it is always necessary to consider the solubility limit in the preparation of the nanocomposite ZEP. We prepared 10, 30, 50 wt % nanocomposites with ZEP@ZEP. Sensitivity curves of 10, 30, 30 wt % C_{60}-drv@ZEP are shown in Fig. 25 in comparison with pure ZEP (0 wt%). Very small sensitivity changes were observed between the pure ZEP and the nanocomposites. Even the 50 wt% showed a sensitivity of ~ 60 μ C/cm^2, which approximately corresponds to that of 20 wt% $C_{60/70}$@ZEP. This small diference in sensitivity can definitely be attributed to the solubility enhancement by the fullerene derivative. Figure 26 shows 50-nm line-and-space patterns delineated in a 150 nm film of C_{60}-drv@ZEP. The patterns were exposed with a line dose of 0.39 nC/cm and developed in ZED-N50 for 30 sec. The patterns were properly fabricated in all the nanocomposite films without residues. This is also due to the solubility increase provided by C_{60}-drv to the ZEP developer. Although C_{60}-drv showed good exposure results, it was not so effective in terms of dry-etching as expected. The C_{60}-drv molecules tended to aggregate during etching presumably due to a propensity for self-ordering, which was somewhat expected from their relatively rigid and long molecular structure. This resulted in less effective enhancement of dry-etchig resistance. However, if more appropriate derivatives were used , we would be able to enhance dry-etching resistance while maintaining the same exposure characteristics as the C_{60}-drv.

Further, the solubility enhancement shown here has the potential to increase the sensitivity of nanocomposite resist when it is used with a chemical-amplification resist, in which sensitivity is greatly enhanced by the catalytic chain reaction of acids produced upon electron beam irradiation.
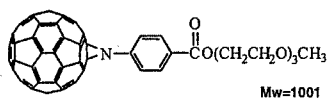
Figure 24. Molecular structure of C60 derivative (C60-drv).
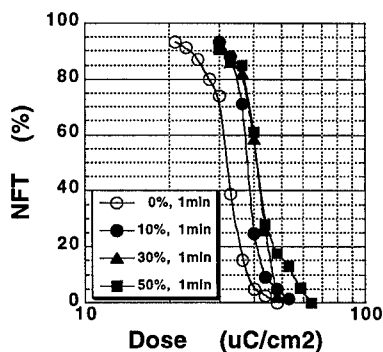
Figure 25. Sensitivity curves of C60-drv@ZEP
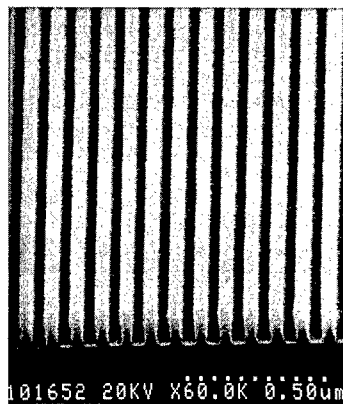
Figure 26. 50-nm line-and-space patterns delineated in the 150 nm film of 50 wt% C60-drv@ZEP. The patterns were exposed with a line dose of 0.39 nC/cm and developed in ZED-N50 for 30 sec.

113

CONCLUSIONS

We have proposed a nanocomposite resist system that incorporates sub-nm fullerene molecules (C_{60} and/or C_{70}) into a conventional resist material for nanolithograpy. A system composed of a positive-type electron beam resist, ZEP520, and a C_{60}/C_{70} mixture, or C_{60} have shown substantial improvements in resist performance: etching resistance, pattern contrast, mechanical strength and thermal resistance. Through the fabrication of high electron mobility transistors (HEMTs), X-ray masks, and groove-grating mirrors for lasers with nanometer dimensions, we have confirmed that resolution improvements by resist thinning enabled by enhanced etching resistance are particularly advantageous in nanofabrication. We have also demonstrated the uniqueness of the nanocomposite resist system, which is that sensitivity is readily changes with the fullerene content due to the dissolution inhibiting effect of fullerene, by successfully fabricating nanometer dot patterns in the bilayer lift-off process. Further, solubility enhancement by a fullerene derivative has shown a higher degree of fullerene incorporation and better sensitivity characteristics.

ACKNOWLEDGEMENTS

REFERENCES

1. W. Chen and H. Ahmed, Appl. Phys. Lett. **62** (13), 1499 (1993).
2. T. Ishii, H. Nozawa, and T. Tamamura, in Abstracts of Int. Conf. on Micro- and Nano-Engineering (Glasgow, UK 1996), p. 21.
3. T. Ishii, H. Nozawa, and T. Tamamura, Appl. Phys. Lett. **70** (9), 1110 (1997).
4. A. N. Broers, in Proc. of 1st Internat'l Conf. on Electron and Ion Beam Science and Technology, edited by R. Bakish (Wiley, New York, 1964), p. 191.
5. A. N. Broers, W. W. Molzen, J. J. Cuomo, and N. D. Wittels, Appl. Phys. Lett. **29** (9), 596 (1997).
6. H. Gokan, S. Esho, and Y. Onishi, J. Electrochem. Soc. **130** (1), 143 (1983).
7. M. Kakuchi, M. Hikita, and T. Tamamura, Appl. Phys. Lett. **48** (13), 835 (1986).
8. T. Tada and T. Kanayama, Jpn. J. Appl. Phys. **35** (1A), L63 (1996).
9. T. Nishida, M. Notomi, R. Iga, and T. Tamamura, Jpn. J. Appl. Phys. **31** (12B), 4508 (1996).
10. T. Ishii, H. Nozawa, T. Tamamura, and A. Ozawa, J. Vac. Sci. Technol. B15 (6), 2570 (1997).
11. T. Shibata, T. Ishii, H. Nozawa, and T. Tamamura, Jpn. J. Appl. Phys. 36 (12B), 7642 (1997).
12. T. Ishii, H. Tanaka, E. Kuramochi, and T. Tamamura, Jpn. J. Appl. Phys. 37 (12B), 7202 (1998).
13. Y. Nakamura, S. Takechi, Y. Tsurunaga, K. Fujino, and Y. Ban, Polymer Reprints, Jpn. **36** (7), 2078 (1987).
14. R. S. Ruoff, D. S. Tse, R. Malhotra, and D. C. Lorents, J. Phys. Chem. **97**, 3379 (1993).
15. W. A. Scrivens and J. M. Tour, J. Chem. Soc., Chem. Commun. **15**, 1207 (1993).
16. G. C. DeSalvo, W. F. Tseng, and J. Comas, J. Electrochem. Soc. **139** (3), 143 (1992).
17. T. Murata, S. Kishimoto, K. Maezawa, T. Mizutani, T. Ishii, and T. Tamamura, in Extended Abstracts of Int. Symp. on Compound Semiconductors (Berlin, 1999), p. Mo B1-1.
18. T. Suemitsu, T. Ishii, H. Yokoyama, Y. Umeda, T. Enoki, Y. Ishii, and T. Tamamur in Proc. of Int. Electron Device Meeting (IEDM 98), edited by P. Woerlee (San Francisco, 1998), pp. 223-226.
19. T. Suemitsu, T. Ishii, H. Yokoyama, T. Enoki, Y. Ishii, and T. Tamamura, Jpn. J. Appl. Phys. **38** (2B), L154 (1999).
20. A. Ozawa, S. Ohoki, M. Oda, and H. Yoshihara, IEICE Trans. Electron. ED77-C, 255 (1994).
21. S. Oku, T. Ishii, R. Iga, and T. Hirono, IEEE J. of Selected Topics in Quantum Electron. **5** (3), 682 (1999).
22. E. Kuramochi, J. Temmyo, and T. Tamamura, Appl. Phys. Lett. **71** (12), 1655 (1997).
23. S. Pang, T. Tamamura, M. Nakao, A. Ozawa, and H. Masuda, J. Vac. Sci. Technol. **B16** (3), 1145 (1997).
24. A. P. G. Robinson, R.E. Palmer, T. Tada, T. Kanayama, and J. A. Preece, Appl. Phys. Lett. **72** (11), 1302 (1998).
25. K. Shigehara, M. Matsumoto, T. Yagi, T. Watanabe, and S. Miyata, in Proc. of 4th Int. Conf. on Organic Nonlinear Optics (ICONO'4, Chitose, Japan 1998), in print.

SYSTEMATIC STUDIES OF FULLERENE DERIVATIVE ELECTRON BEAM RESISTS

A.P.G. Robinson[*], R.E. Palmer[*], T. Tada[†], T. Kanayama[†], E.J. Shelley[‡], D. Philp[‡] and J.A. Preece[‡]
[*]Nanoscale Physics Research Laboratory, School of Physics and Astronomy, The University of Birmingham, Birmingham, UK, a.p.g.robinson@bham.ac.u.
[†]Joint Research Center for Atom Technology, NAIR, 1-1-4 Higashi, Tsukuba, Ibaraki 305-8562, Japan.
[‡]School of Chemistry, The University of Birmingham, Birmingham, UK.

ABSTRACT

We report systematic studies of the response of C_{60} derivatives to electron beam irradiation. Films of fourteen different mono, tris and tetra adduct methanofullerene C_{60} derivatives were produced by spin coating on hydrogen terminated silicon substrates. Exposure of the films to a 20 keV electron beam substantially altered the dissolution rate of the derivative films in organic solvents such as monochlorobenzene. All of the derivatives exhibited negative tone resist behaviour with sensitivities between $\sim 8.5 \times 10^{-4}$ and $\sim 4 \times 10^{-3}$ C/cm^2, much higher than that of C_{60}. Features with widths of ~ 20 nm were produced using these compounds, and the etch ratios of the compounds were found to be more than twice those of a standard novolac based resist (SAL601).

INTRODUCTION

The manufacture of the current generation of microelectronic devices requires lithographic resolutions of 0.18 μm. There is great pressure to achieve further miniaturization of devices, not only to increase component packing density, but also to allow the exploitation of quantum effect devices, for instance quantum dot lasers and light emitting diodes [1,2] and single electron transistors [3,4]. The physical limits of the resolution of photolithography seem to lie at ~ 0.1 μm [5,6], and thus other methods are required to extend the miniaturization of devices into the sub-100 nm regime.

One technique that can be used to define features with sub-100 nm resolution is electron beam (e-beam) lithography, in which an e-beam is used to irradiate and thereby pattern an electron sensitive resist. The properties of the resist material used in the lithographic process represent an important factor in determining the minimum feature size. Most commercial resists are polymers, and during e-beam irradiation they are either cross-linked (negative tone), forming insoluble material, or degraded (positive tone), giving smaller soluble molecular fragments. The soluble areas are then removed. For a negative tone resist this limits the smallest definable pattern to be at least as large as the molecular area of the polymer molecule on the substrate (tens of square nanometres [7] for an average polymeric resist). Higher resolution is possible with positive tone resists, but the large molecular size of the resist polymer can lead to substantial linewidth fluctuations [7]. Patterns smaller than the polymer size have not been demonstrated in positive or negative tone polymer based resists. It is therefore desirable that the area of the resist molecules on the surface be as small as possible.

Several different materials have been investigated in order to surmount this problem, including low molecular weight organic molecules [7,8] inorganic materials such as metal fluorides [9] and fullerenes [10] which have a diameter of ~ 1 nm. We have reported previously that one class of derivatives of C_{60} [11,12], the methanofullerenes, are considerably more sensitive to electron beam irradiation than C_{60} itself, whilst retaining the high dry etch durabilities and resolution of C_{60}. We have also shown that a Diels-Alder cycloadduct of C_{60} does not exhibit the improved sensitivity of the methanofullerenes [13]. Furthermore, whilst C_{60} and the Diels-Alder cycloadduct films must be prepared *via* vacuum sublimation, methanofullerene films can be prepared using spin coating. This is due at least in part to the increased solubility of methanofullerenes in volatile solvents such as chloroform. In this paper, we summarise the results of a systematic experimental study of the methanofullerenes, with the purpose of exploring the mechanism of exposure of the resist and the origin of the observed variation of resist sensitivity for various derivatives.

EXPERIMENTS AND RESULTS

The fourteen fullerene derivatives [14] studied are shown in fig. 1. Films of the derivatives were deposited by spin coating from chloroform, at room temperature, onto hydrogen terminated Si substrates HF. The film thickness, measured using a surface profiler (Detak, Sloan), could be controlled by varying the angular frequency of the spin coater, or the solution concentration as shown previously [11,15].

To measure the response of the derivatives to electron irradiation, derivative films of ~ 100 nm thickness were prepared and exposed to 20 keV electrons using a Hitachi S4500 scanning electron microscope (SEM). There was no measurable change in the thickness of the film immediately after irradiation. Upon immersion in the organic solvent monochlorobenzene (MCB) for 60 s it was observed that the films all demonstrated negative tone resist behaviour (i.e. the irradiated areas had become insoluble). This variation of

Fig. 1 The fourteen methanofullerenes studied. See [14] for abbreviations.

the residual film thickness with electron dosage was measured using the surface profiler. The response curves of three of the derivatives are shown by way of illustration in fig. 2. (In order to make comparison of the properties of the film easier the curves have been offset along the y-axis and normalized.) The sensitivity of a derivative to electrons is defined as the dose at which the linear portion of the rising section of the response curve (fig. 2) reaches 50% of the original film thickness

[16]. The measured sensitivities are plotted in fig. 3, together with the sensitivity of the previously studied C_{60} resist, as a function of derivative mass. It can be seen from fig. 3 that with one exception (MAF3) there is a linear relationship between a derivative's sensitivity and its mass. The sensitivity of the 'fastest' derivative, THP5, is ~ 8.5 × 10^{-4} C/cm^2. In comparison the sensitivity of C_{60} is ~ 1 × 10^{-2} C/cm^2 [10] and the negative tone sensitivity of PMMA is ~ 5 × 10^{-3} C/cm^2 [17].

To investigate the reasons for the change in the derivatives solubilities after irradiation several derivatives were examined before and after irradiation with Raman spectroscopy. The Raman spectrum of C_{60} [18] shows a pentagonal pinch mode at 1469 cm^{-1}. The same peak, albeit shifted to 1455 cm^{-1}, is also seen in the spectrum of the derivative

Fig. 2 The response of three derivatives to e-beam irradiation with 20 keV electrons. Shown is the film thickness remaining after exposure and development with monochlorobenzene

116

TrAF [11,12]. Here unirradiated and irradiated films of the THP2, THP3 and THP4 (see fig. 1) were examined with Raman spectroscopy. The pentagonal pinch modes of THP2, THP3 and THP4 were identified at 1467, 1466 and 1463 cm^{-1} respectively (see fig 4(a)). After exposure to an electron dose of ~ 3×10^{-3} C/cm^2 the intensity of the pentagonal pinch mode was drastically reduced in all three cases (see fig. 4(b)). Further irradiation to a dose of ~ 3.5×10^{-2} C/cm^2 leads to spectra characteristic of glassy carbon [19], together with a background – possibly caused by photoluminescence (i.e. of material irradiated by the electron beam) (see fig. 4(c)). The absence of the pentagonal pinch mode after exposure implies, as previously proposed [11,12], that the e-beam irradiation of the derivatives leads to extensive cage fragmentation and the formation of a disordered network of graphite-like particles and/or glassy carbon particles.

In trying to understand the mechanism of exposure it is necessary to explain both the Raman spectra together with the linear relationship between derivative sensitivity and mass. We have considered two possible factors from which this variation in sensitivity may arise; (i) from the variation in the molecular mass, and therefore the electron excitation cross-section, of the derivatives and (ii) from the variation in the highest occupied molecular orbital - lowest unoccupied molecular orbital gap, and therefore the ionization potentials, of the derivatives. Possibility (ii) is ruled out because we have found no clear correlation between the sensitivity and semi-empirical self-consistent field theory PM3 calculations [20-22] of the ionization potentials of various derivatives. By contrast, mechanism (i) appears to account for the data well. However, mechanism (i) probably does not account, in itself, for the order of magnitude increase increase in sensitivity seen over C_{60} for even the smallest for the smallest of the derivatives with polyether/alkyl addends (MAF4), which is less than 40 % heavier than C_{60}. It has previously been reported [23] that C_{60} is highly reactive towards free radical species. It is also known [24] that aliphatic ethers and polyethers, such as those which make up the addends of all but one (MAF2) of the methanofullerenes studied here, are ionised to produce the corresponding oxygen-centred radical cations (i.e. positively charged fragments of the addend based around an oxygen and with at least one unpaired electron) upon exposure to electrons beams of energies in the range 20 - 100 eV. (This is the approximately same range as the secondary electrons thought to be responsible for the
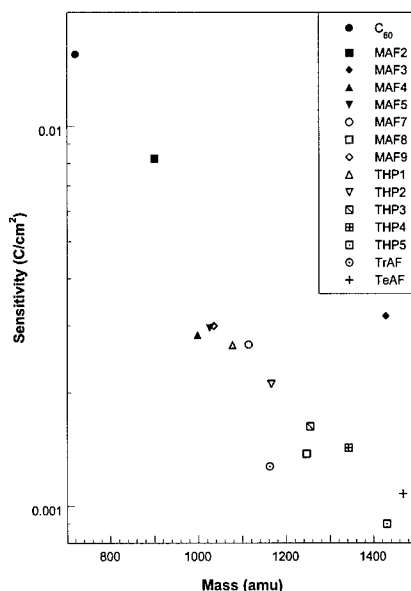
Fig. 3 Derivative sensitivity as a function of mass. The sensitivity of C_{60} is shown for comparison.
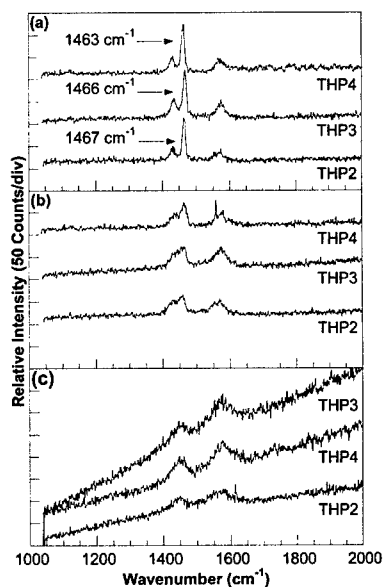
Fig. 4 Raman spectra of THP2,3 and 4 films (a) before irradiation (b) after an electron dose of 3×10^{-3} C/cm^2 and (c) after ~ 3.5×10^{-2} C/cm^2.

117

majority of resist exposure events in e-beam lithography [25].) For instance, electron impact mass spectrometry of the addend precursor for THP3, measured during the synthesis of our methanofullerene compounds, shows a large peak for the ion arising from the cleavage of the tetrahydropyran protective group, and various smaller fragments, but very little of the actual precursor. The radical cation formed by the removal of the tetrahydropyran group may initiate polyether chain scission to generate several radical species, which may then react with the C_{60}. This 'unzipping' of the adduct chain can be initiated by a single electron impact [24]. These radicals may then react with neighbouring C_{60} cages leading directly to fragmentation, or destabilizing the cages against further electron impacts. Alternatively the radicals may also react with particles that have already been fragmented, which may aid the formation of an insoluble network. Note that whilst MAF8 does not have polyether chain addends, simple alkyl chains can also fragment by chain scission. It should be noted that the one compound that does not conform to the linear relationship between sensitivity and mass, MAF3, has a crown ether joining the addend chains, which may act to stabilise them.

For nanolithography it is necessary that the resist can be patterned with a high resolution. In order to examine the

Fig. 5 (a) SEM micrography of a grid of lines defined in MAF9. The linewidth is ~ 20 nm. Inset is a magnification of a n intersection between two lines showing minimal resolution loss at double the dose. (b) SEM micrograph of a grid etched into silicon with an aspect ratio of 8:1. The wall width is ~ 20 nm and the hole depth is ~ 160 nm.

resolution of these compounds various patterns have been defined in the films. Previously dots and lines with resolutions of ~ 40 nm and ~ 20 nm respectively have been defined in a TrAF [11]. A grid of ~ 20 nm lines defined in a 20 nm thick film of MAF9 is shown in fig. 5(a) after development in MCB for 60 s. The exposure dose was 3 μC/m and the electron energy was 30 keV. The inset shows an intersection magnified four times. Although the intersections receive twice the dose of the lines there is minimal loss of resolution due to proximity effects under these conditions. This may indicate that the actual resolution of this resist is somewhat higher than seen (the 20 nm linewidth seen is limited by the apparatus). The resistance of the defined pattern to etching was evaluated using electron cyclotron resonance microwave plasma etching. The etch was performed at ~ 25°C with the etchant SF_6. The rf power was 0.5 W/cm^2, with an incident microwave power of 250 W. The SF_6 flow rate was 5 sccm at a pressure of ~ 0.4 mtorr. The etch rates of the derivatives were between 1/6 and 1/8 that of the silicon substrate (ie high etch durability). By contrast SAL601, a well known high etch durability novolac based resist, has an etch rate of ~ 1/3 that of the silicon under the same conditions, and the etch durabilities of both positive and negative tone PMMA are substantially lower than that of SAL601. The fullerene derivatives will therefore allow the etching of structures with more than twice the aspect ratio for a given resist film thickness. These etching conditions were used to produce the

grid in fig. 5(b). A 20 nm thick film of MAF9 was patterned and developed. After etching the sample the walls of the grid were 20 nm thick and the hole depth was 160 nm.

In conclusion we have explored the mechanism of the exposure of various methanofullerene derivatives of C_{60} which act as electron beam resists of substantially higher sensitivity than C_{60} itself. Systematic experiments show that the sensitivity of the derivatives is approximately linearly proportional to the derivative mass. The sensitivity the derivatives, in comparison to C_{60}, appear too high to conclude that the variation of electron cross-section with derivative mass is entirely responsible for the increased sensitivity. It is therefore proposed that free radicals generated during electron stimulated decomposition of the addends attack surrounding molecules either fragmenting them directly, or weakening them against further electron impacts. This implies that the sensitivity of the methanofullerene electron beam resists can possibly be increased both by increasing the derivative mass, and by carefully selecting the addend composition. Patterns of 20 nm lines have been defined in the resist films and the extremely good etch durability of the derivatives has allowed high aspect ratio structures to be transferred to the silicon via etching. The sensitivities of all the derivatives studied here are higher than that of negative tone PMMA, and the etch resistances of the derivatives are double that of SAL601 suggesting that these compounds may be useful for practical nanofabrication.

ACKNOWLEDGEMENTS

REFERENCES

[1] H. Shoji, Y. Nakata, K. Mukai, Y. Sugiyama, M. Sugawara, N. Yokoyama and H. Ishikawa, Appl. Phys. Lett., **71**, 193 (1997).
[2] Y. Tang, W.-X. Ni, C.M. Sotomayor Torres and G.V. Hansson, Electronics Letters, **31**, 1385 (1995).
[3] R.A. Smith and H. Ahmed, Appl. Phys. Lett., **71**, 3838 (1997).
[4] H. Ishikuro and T. Hiramoto, Appl. Phys. Lett, **71**, 3691 (1997).
[5] M.C. Peckerar, F.K. Perkins, E.A. Dobisz and O.J. Glembocki, *Handbook of Microlithography, Micromachining and Microfabrication Vol. I*, P. Rai-Choudhury ed., (IEE, London, 1997), p. 686.
[6] J.A. Rogers, K.E. Paul, R.J. Jackman and G.M. Whitesides, Appl. Phys. Lett., **70**, 2658 (1997).
[7] M. Yoshiiwa, H. Kageyama, Y. Shirota, F. Wakaya, K. Gamo and M. Takai, Appl. Phys. Lett., **69**, 2605 (1996).
[8] J. Fuijita, Y. Ohnishi, Y. Ochiai and S. Matsui, Appl. Phys. Lett., **68**, 1297 (1996).
[9] J. Fujita, H. Watanabe, Y. Ochiai, S. Manako, J.S. Tsai and S. Matsui, Appl. Phys. Lett., **66**, 3064 (1995).
[10] T. Tada and T. Kanayama, Jpn. J. Appl. Phys., **35**, L63 (1996).
[11] A.P.G. Robinson, R.E. Palmer, T. Tada, T. Kanayama and J.A. Preece, Appl. Phys. Lett., **72**, 1302 (1998).
[12] A.P.G. Robinson, R.E. Palmer, T. Tada, T. Kanayama, J.A. Preece, D. Philp, U. Jonas and F. Deiderich, Chem. Phys. Lett., **289**, 586 (1998).
[13] T. Tada, T. Kanayama, A.P.G. Robinson, R.E. Palmer and J.A. Preece, J. Photopolymer Sci. Technol., **11**, 581 (1997).
[14] (*MAF1 and MAF6 were renamed THP3 and THP2 respectively, subsequent to [11] and [12]*)
      MAF2 spiro[3'*H*-Cyclopropa[1,9][5,6]fullerene-C_{60}-*I$_h$*)-3',5"-[1",3"-diethyl-2",4",6"(1"*H*,3"*H*,5"*H*) barbiturate
      MAF3 Spiro{(3'*H*-Cyclopropa[1,9][5,6]fullerene-C_{60}-*I$_h$*)-3',30"-2",5",8",11",14",19",22",25",28",32", 35",38",41"-tridecaoxa-tricyclo{40.2.2.2,15",18"]octatetraconta-1"(45"),15"(48"),16",18"(47"), 42"(46"),43"-hexaen-29",31"-dicarbonyl
      MAF4 3'*H*-Cyclopropa[1,9][5,6]fullerene-C_{60}-*I$_h$*-3',3'-carboxylic[2-(2-hydroxyethoxy)ethyl]ester
      MAF5 3'H-cyclopropa[1,9][5,6]fullerene-C_{60}-*I$_h$*-3',3'-carboxylic{2-(2-methoxyethoxy)ethyl}ester
      MAF7 3'H-cyclopropa[1,9][5,6]fullerene-C_{60}-*I$_h$*-3',3'-carboxylic{2-(2-(2-methoxyethoxy)ethoxy)ethyl} ester
      MAF8 3'H-cyclopropa[1,9][5,6]fullerene-C_{60}-*I$_h$*-3',3'-carboxylic{8-(tetrahydropyran-2-yloxy)octyl}ester
      MAF9 3'H-cyclopropa[1,9][5,6]fullerene-C_{60}-*I$_h$*-3',3'-carboxylic{2-(2-chloroethoxy)ethyl}ester
      THP1 3'H-cyclopropa[1,9][5,6]fullerene-C_{60}-*I$_h$*-3',3'-carboxylic{2(tetrahydropyran-2-yloxy)ethyl}ester

THP2 3'H-cyclopropa[1,9][5,6]fullerene-C_{60}-I_h-3',3'-carboxylic{2-(2-(tetrahydropyran-2-yloxy)ethoxy)
ethyl}ester

THP3 3'H-cyclopropa[1,9][5,6]fullerene-C_{60}-I_h-3',3'-carboxylic{2-(2-(2-(tetrahydropyran-2-yloxy)
ethoxy)ethoxy)ethyl}ester

THP4 3'H-cyclopropa[1,9][5,6]fullerene-C_{60}-I_h-3',3'-carboxylic{2-(2-(2-(2-(tetrahydropyran-2-yloxy)
ethoxy)ethoxy)ethoxy)ethyl}ester

THP5 3'H-cyclopropa[1,9][5,6]fullerene-C_{60}-I_h-3',3'-carboxylic{2-(2-(2-(2-(2(tetrahydropyran-2-yloxy)
ethoxy)ethoxy)ethoxy)ethoxy)ethyl}ester

TrAF 3',3'',6',6''-Tetrahydro-5',3''':5'',3'''-bis(ethanol[1,4]benzenomethanoxymethano)-3'''H-dibenzo[1,
9:52,60]cyclopropa[16,17][5,6]fullerene-C_{60}-I_h-17',17''dicarbonyl

TeAF 17',17''-Dioxo-3',3'',6',6''-tetrahydro-5',3''':5'',3'''bis(ethano[1,4]benzenomethanoxy methano)-3'''
H,3''''H-dibenzo[1,9:52,60]dicyclopropa[16,17:21,40][5,6]fullerene-C_{60}-I_h-3'''',3''''-carboxylic[2-
(2-methoxyethoxy)ethyl]ester

[15] A.P.G. Robinson, PhD Thesis, The University of Birmingham, 2000.
[16] S. Manako, J-I. Fujita, Y. Ochiai, E. Nomura and S. Matsui, Jpn. J. Appl. Phys, **36**, 7773 (1997).
[17] T. Tada and T. Kanayama, J. Vac. Sci. Technol. B, **13**, 2801 (1995).
[18] D.S. Bethune, G. Meijer, W.C. Tang and H.J. Rosen, Chem. Phys. Lett., **174**, 219 (1990).
[19] M.S. Dresselhaus, G. Dresselhaus and P.C. Eklund, *Science of Fullerenes and Carbon Nanotubes*,
(Academic Press, London, 1996) p. 851.
[20] M.J.S. Dewar and W. Thiel, J. Am. Chem. Soc., **99**, 4899 (1977).
[21] J.J.P. Stewart, J. Comp. Chem., **10**, 209 (1989).
[22] J.J.P. Stewart, J. Comp. Chem., **10**, 221 (1989).
[23] P.J. Krusic, E. Wasserman, P.N. Keizer, J.R Morton and K.F. Preston, Science, **254**, 1183 (1991).
[24] H. Budzikiewicz and C. Djerassi, *Mass Spectrometry of Organic Compounds*, (Holden Day, San
Francisco, 1967).
[25] M.A. McCord and M.J. Rooks, *Handbook of Microlithography, Micromachining and Microfabrication
Vol. I*, P. Rai-Choudhury, ed., (IEE, London, 1997), p. 159.

Polymer-Inorganic High Contrast and High Sensitivity Resists for Nanolithography

Hengpeng Wu, Jianzhao Wang and Kenneth E. Gonsalves
Polymer Program at the Institute of Materials Science, U-3136
& Department of Chemistry
University of Connecticut, Storrs, CT 06269-3136

Abstract

Polyhedral oligosilsesquioxane methacrylate (POSSMA)/methyl methacrylate(MMA)/tert-butyl methacrylate(TBMA)/tert-butyl acrylate(TBA) copolymers were synthesized by solution polymerization. Their preliminary lithography-related properties were studied. It is shown that the mass ratio of MMA/POSSMA=85.8/14.2 leads to an X-ray resist with a high contrast of 23.5 without sacrificing the sensitivity(1350 mJ/cm^2) which remains comparable to that of standard PMMA. By careful manipulation of components and compositions, this generic type of polymer could potentially be utilized as a DUV or e-beam resist as well.

Introduction

For the past few decades, tremendous efforts have been expended for developing new resist materials for DUV, X-ray and electron beam lithography.[1,2,3] Ultra large Scale Integration should lead to 100 nm production circuits by 2006 as predicted by the Semiconductor Industry Association. This challenge imposes a formidable pressure on lithographic processes in terms of dimension tolerances (10 nm or less) and positioning accuracy (1 nm or less), to quote only a few specifications. For sub-100 nm lithography it is crucial to synthesize higher performance and especially higher contrast resists[4]. It has already been shown that inorganic resists are capable of exhibiting higher contrast than organic resists[5], but their intrinsically lower sensitivity and complex deposition methods make them suitable primarily for ion lithography. A combination of high contrast necessary for sub-100 nm resolution and high sensitivity necessary for industrial throughput could be reached by carefully engineering organic/inorganic nanocomposites, acting as optimum resists for a given lithographic technology. The scope of our investigation is to develop and broaden this concept into a "general resist" for next generation lithographies (NGL).

Polyhedral oligosilsesquioxane methacrylate (POSSMA, **1**) are structurally well-defined macromers that have an inorganic silica-like core as shown in Figure 1. The core is surrounded by seven inert organic groups for solubility and one polymerizable vinyl group. These POSSMA macromers have similar reactivity as common methacrylate monomers and can easily copolymerize with the latter.[6] We therefore anticipated that incorporation of POSSMA into polymeric resist materials might generate higher-

resolution and higher-contrast resists. This paper reports the synthesis and characterization of POSSMA-containing polymethacrylate copolymers. It is anticipated that these polymers may have potential applications as thin layer resists in 157 nm and EUV lithography. Also we anticipate that these copolymers are potential resists for nanolithography at 193 nm DUV wavelength, X-ray and electron beam exposure tools.
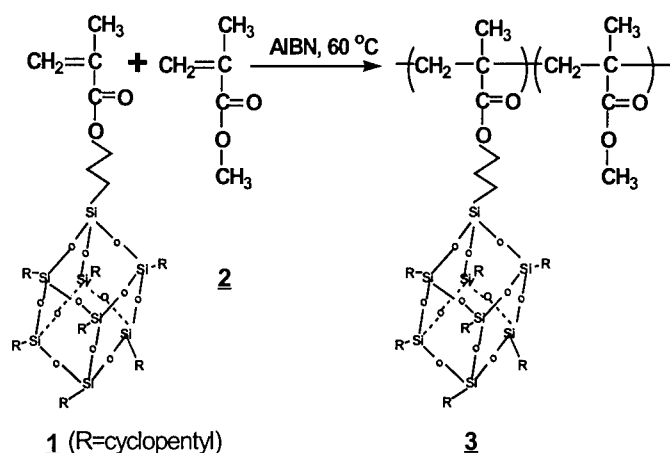
Figure 1. Scheme for the synthesis of POSSMA/MMA copolymers

Results and Discussion

Synthesis and reactivity. All polymer samples were synthesized by AIBN-initiated free radical polymerization as reported previously[7]. The monomers used were polyhedral oligosilsesquioxane methacrylate(POSSMA, **1**), methyl methacrylate(MMA, **2**), tert-butyl acrylate(TBA), and tert-butyl methacrylate(TBMA). A scheme for the synthesis of POSSMA/MMA copolymers **3** is shown in Figure 1. POSSMA and MMA were dissolved in 6 ml dry toluene. 2,2' - Azobisisobutyronitrile (AIBN, typically 1% by wt) was added to initiate the polymerization at a temperature of 60 °C. To achieve a high conversion of monomers, the reaction was maintained for 3 days. Subsequently, the reaction mixture was added dropwise into sufficient hexane or methanol to isolate the polymers. The polymers were filtered and washed by hexane or methanol. The polymer samples were then dried in vacuum at 80 °C for 1 - 2 days. Compositions and characterization data are outlined in Table 1.

According to Lichtenhan et al.,[6,8,9] the POSSMA monomer has a reactivity almost identical to MMA. Our result confirmed this, as evidenced by comparing compositions in polymers and their initial feed for samples 1 and 2. However, POSSMA showed a higher reactivity than TBMA monomer. The higher POSSMA content in polymer 7 than

in its feed was a direct consequence of its higher reactivity over TBMA monomer. TBA seemed to have a similar reactivity as TMBA. In the case of terpolymers, the situation was more complicated and no generalizations have been reached.

Glass transition temperatures. As expected, the incorporation of POSSMA units in polyacrylate copolymers did increase the glass transition temperatures of the corresponding polymers (as shown in Table 1) due to the bulkiness and inorganic character of the pendant cage groups. But the effect was limited, even if the weight percentage of POSSMA was as high as 47.6 % (polymer **7**, Tg = 124 °C). This can be explained by the low mole fraction of POSSMA in polymers. Lichtenhan et al.[6,8,9] attributed the effect of a POSSMA group on the Tg's of vinyl copolymers to the possible POSSMA-POSSMA interchain/intrachain interactions when the mole % loadings of POSSMA in polymers are greater than 10 %. Presumably, the POSSMA groups are associating to form a cage network within the polymer matrix. It is this network of physical crosslinking that causes the increases in glass transition. However, in our case, such interactions were small, if at all. For example, a weight percentage of 47.6 % of POSSMA in polymer **7** corresponds to only 9.6 mole % due to the large molecular weight (1208 g / mole) of the POSSMA monomer. Such a low mole fraction of POSSMA was insufficient to bring about a profound Tg change. For a polymeric resist to have a better performance, usually a higher Tg is desirable. In our case, increasing POSSMA loadings would be impractical, since a higher POSSMA content would make the polymers more brittle. Moreover, the sensitivity of the resists to various radiation sources would be expected to decrease as POSSMA contents increase, due to inorganic character of Si-containing ester cage in POSSMA. Considering the fact that the majority of the POSSMA 's molecular weight is contributed by its seven inert R groups, new POSSMA macromonomers with smaller R groups are being looked at in order to overcome this dilemma.

Solubility. In the process of finding effective precipitants to isolate polymers from toluene solutions, we noticed some interesting phenomena regarding the solubility properties of the polymers. While samples **1, 2, 5, 6, 9** and **10** were readily precipitated by hexane from toluene solutions, polymers **3, 4** and **7** could only be isolated from toluene by methanol. A careful analysis of the polymer compositions leads us to a conclusion that tert-butyl ester groups in the polymers, in conjunction with POSSMA units, were probably the determining factor. When the TBMA content exceeded a certain value (in our case, 47.6 % by weight), the polymers had a high solubility in hexane. Even in methanol, polymers **3, 4** and **7** showed different behavior. For the same amount of loading size (1g), 40 ml methanol was sufficient to quantitatively recover polymer **7** from methanol solution, while much more (300 ml) methanol was used to isolate polymers **3** and **4** with a low yield. For sample **8** that would be expected to have a higher TBMA content than **7**, we were not able to isolate it from toluene by either hexane or methanol. The use of other solvents such as ethanol, acetone, THF was unsuccessful. These results show that much care should be taken in choosing a proper developer when POSSMA-containing polyacrylate polymers are to be used as resists for lithography. A small variation in polymer compositions, despite the same components, might change the solubility behavior to a large extent.

Table 1 Compositions, Molecular Weights and Glass Transition Temperatures of Polymers

polymer	feed composition(wt%) POSSMA MMA TBMA			polymer composition(wt%)[a] POSSMA MMA TBMA			precipitant	Mn[b] × 10⁻⁴	Mw[b] × 10⁻⁴	PDI	Tg[c] °C
1	14.3	85.7	0	14.2	85.8	0	hexane	3.29	6.71	2.04	126
2	11.8	88.2	0	11.7	88.3	0	hexane	6.82	12.0	1.76	122
3	15.5	28.2	56.3	32.4	16.5	51.5	methanol	3.28	5.54	1.69	110
4	25.9	25.4	48.7	38.5	13.9	47.6	methanol	1.69	3.07	1.82	109
5	15.4	56.4	28.2	13.2	49.9	36.9	hexane	1.68	4.46	2.65	123
6	25.3	49.8	24.9	20.5	44.0	35.5	hexane	2.03	4.56	2.25	113
7	31.7	0	68.3	47.6	0	52.4	methanol	2.82	4.37	1.55	124
8	20.7	0	79.3	-	-	-	-	-	-	-	-
9	9.1	60.6	30.3[d]	8.8	52.3	38.9[d]	hexane	4.41	8.59	1.95	97
10	14.3	57.1	28.6[d]	13.1	50.8	32.1[d]	hexane	4.24	7.90	1.86	89

[a] wt % POSSMA determined from wt % residue left over after burning the polymers in O_2. wt % MMA, TBA and TBMA determined from area ratios of the peaks at 1.42 ~ 1.49 ppm (9 tert-butyl protons in TBMA or TBA) and 3.60 ppm (3 methyl ester protons in MMA) measured by ^{1}H NMR. [b] molecular weights measured by GPC using THF as an eluent and polystyrene as calibration standards. [c] Tg determined by DSC. [d]TBA%

Adhesion and Thin film formation.

A 3 wt% solution of each polymer sample in toluene was prepared. An NRL contact angle goniometer was used to measure their contact angles on a silicon wafer in a dip-and-touch mode. All polymer samples had contact angles ranging from 7.4 to 15.1 degrees, indicating excellent adhesion to the silicon wafer. Uniform thin films were readily spin cast onto Si wafers from 3 wt% toluene solutions of the polymers, with a thickness of 0.1 ~ 1 μm depending on spinning speeds. A FC-431 surfactant (3M) eliminated pinholes. No cracking was observed for all polymer samples, despite the high wt % of POSSMA content in some samples.

UV-radiated chemical amplification.

Tert-butyl (meth)acrylates play a key role in chemically amplified (CA) resists.[1,4] During the exposure, a catalytic amount of a strong acid is generated within the resist. During the subsequent post exposure bake (PEB) process, this acid attacks and induces decomposition of tert-butyl groups into carboxylic acid. The exposed area is then dissolved by a aqueous base developer, resulting in a positive-tone resist.[10-12] To test how the incorporation of POSSMA units will influence this chemical amplification process, we exposed polymer samples **3 ~ 7** to 365 nm UV radiation provided by a 100 Watt mercury lamp. Thin films were spin cast onto KBr disks from 3 wt% toluene solutions of these polymers (2 wt % triarylsulfonium hexafluoroantimonate with regard to the polymers was also added as a catalyst). After baking for 2 min at 125 °C, the films were exposed to UV radiation for 10 min, followed by post-exposure-bake (PEB) at 125 °C for 2 ~ 30 min. A Nicolet 560 FTIR spectrometer was used to track the formation of carboxylic acid. The result obtained for polymer **3** is shown in Figure 2. A broad peak at ~ 3300 cm⁻¹ that appeared after post-exposure-bake (PEB) indicated the expected formation of carboxylic acid from tert-butyl ester group in TBMA. Similar results were obtained for polymers **3 ~ 6.** However, to

our surprise polymer **7** was totally insensitive to the UV radiation at the wavelengths used. We believe that the relatively high POSSMA content might be the reason.
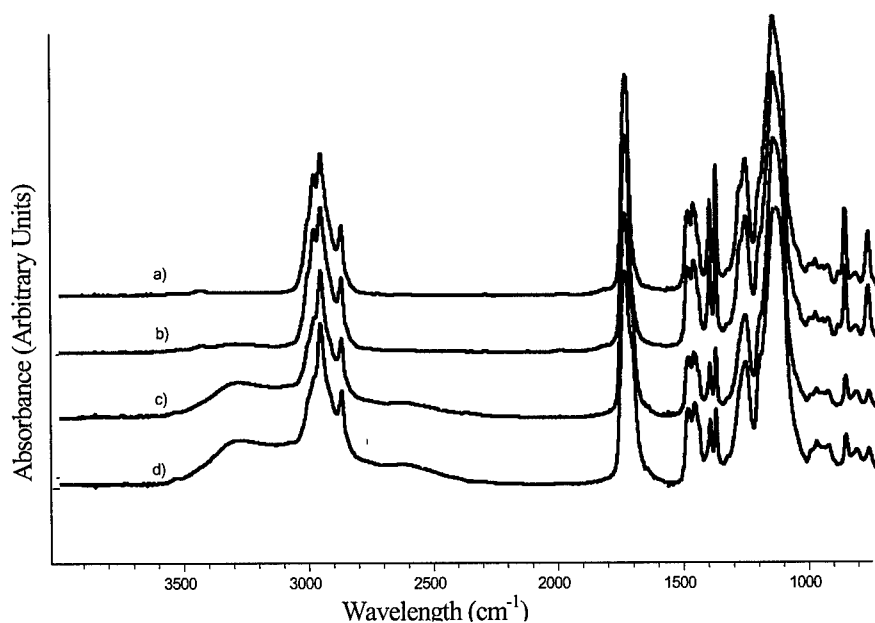
Figure 2. FTIR spectra of polymer **3**: a) exposed to UV radiation for 10 min. b) post-exposure-bake (PEB) at 125 °C for 2 min. c) PEB at 125 °C for 10 min. d) PEB 125 °C for 20 min.

Electron beam-radiated chemical amplification. When exposed to electron beam radiation, a positive-tone resist is subject to bond scissions, resulting in a solubility change in the exposed regions.[13] The trend in electron beam lithography has been to increase the electron voltage (up to 100 kV) to obtain high resolution. However, low voltage electron beam lithography has its own advantages.[14,15] First, electron energy deposition is more efficient at low voltage. Secondly, the low voltage can greatly reduce proximity effects and reduce substrate damage compared to higher energy exposure. Finally, the lower electron voltage can reduce resist charging possibly occurring at high voltage. We used 5 keV electron beam to initiate the chemical amplification process for polymer **6**. Thin films were spun cast onto silicon wafers from a 3 wt % toluene solution of polymer **6** (2 wt % triarylsulfonium hexafluoroantimonate with regard to the polymers was also added as a catalyst). After baking for 2 min at 125 °C, the films were exposed to 5 keV electron radiation for 5 min, followed by post-exposure-bake (PEB) at 125 °C for 10 min. The exposed films were then dissolved in chloroform for IR analysis. The result obtained for polymer **6** is shown in Figure 3. A broad peak at ~ 3300 cm^{-1} that appeared after post-exposure-bake (PEB) indicated the occurrence of chemical amplification. It is well known that this chemical amplification process can also be caused by thermal energy.[16] However, when we baked an unexposed polymer film at 125

^{0}C for as long as 20 hrs, no apparent OH group was formed as indicated by curve b) in Figure 4. This undoubtedly showed that the chemical amplification was mainly due to the 5 keV electron beam radiation.
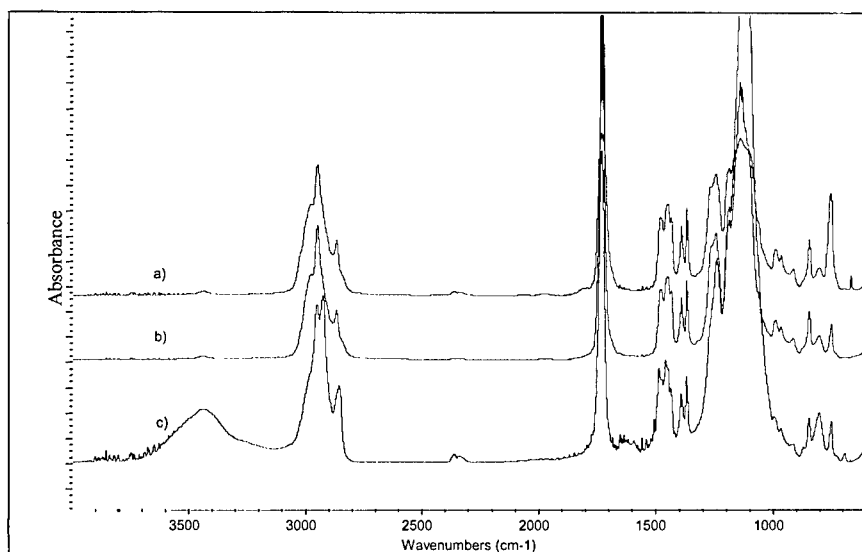
Figure 3 FTIR spectra of sample **6**: a) before exposure; b) unexposed sample but baked at 125 ^{0}C for 20 hrs; c) exposed to 5 keV e-beam. For details see the text.

X-ray exposure. Thin films (typically 90 ~ 150 nm thick) were spun cast onto silicon wafers from 1.5 wt% solutions in chloroform for samples **1**, **2**, **9**, and **10**. The films were then baked at 110 ^{0}C for about 1 hour each. The films were exposed to X-rays at doses ranging from 5000 mJ/cm^2 to 200 mJ/cm^2 using a synchrotron line, and finally underwent wet-development in a solution of 80% IPA and 20% MIBK. Although samples **9** and **10** did expose properly, as proven by the various exposed regions which appeared on the wafer even before wet development, the films on the wafers were stripped away when put in the developer solution. After irradiation, sample **2** was developed in a 80/20 mixture of IPA/MIBK for 90 seconds followed by rinsing with IPA for 30 seconds. The film developed well but the maximum dose of 5000 mJ/cm^2 was not enough to cause any significant change in film thickness upon development. On the contrary, under the same conditions sample **1** exhibited a significant variation in thickness allowing the drawing of normalized remaining thickness (NRT) curve vs X-ray dosage, shown in Figure 4. This sample exhibits a remarkably high contrast of 23.5 along with a sensitivity of 1350 mJ/cm^2 which is typically that of PMMA. Therefore, such a high contrast was obtained without sacrificing the sensitivity, which is quite unusual.
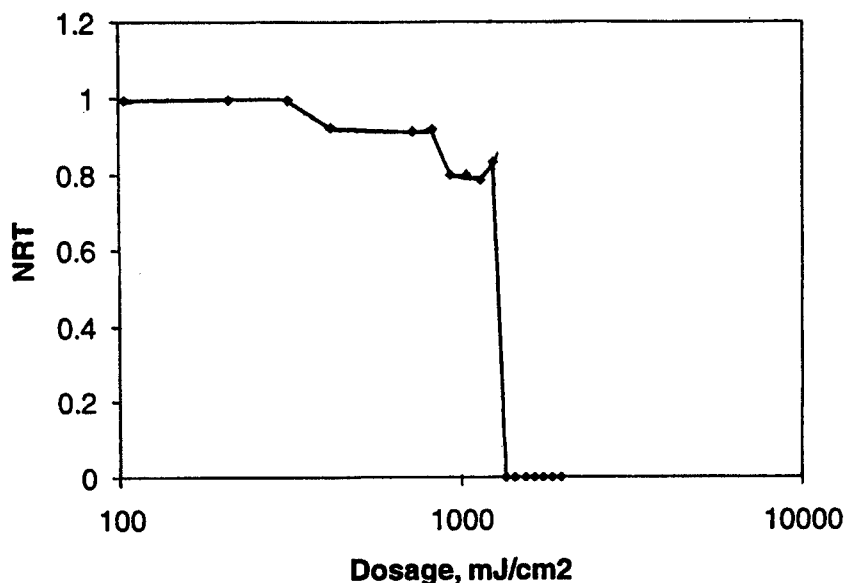
Figure 4 NRT curve for sample **1.** Initial film thickness: 0.12 ~ 0.15 μm. Sensitivity: 1350 mJ/cm^2. Contrast: 23.5

These preliminary results allow some initial interpretations about the radiolysis of the nanocomposite. POSSMA was anticipated to enhance the lithographic characteristics of the resist not only because it contains Si atoms but also because it is a cage structure. TBA-containing samples (**9** and **10**) showed a self-developing character under X-ray exposure most probably due to readily cleaved tert-butyl groups. For POSSMA/MMA copolymers (**1** and **2**), contrast enhancement was expected but at the expenses of sensitivity. The unexpected high contrast and sensitivity observed for sample **1** shows that the shape of the Si-containing cage structure plays a key role. Synergistic effects between MMA and POSSMA components during chain scissions by X-ray-generated photoelectrons are therefore most likely to explain the high contrast and sensitivity occurring for the same dose at the optimum MMA/POSS=85.8/14.2. The narrow range of molecular ratios where the above enhancement of lithographic characteristics occurs could even be thought of as "resonance-like phenomena" in the resist structure upon X-ray irradiation amplifying both contrast and sensitivity.

In summary, POSSMA-containing acrylate copolymers have been synthesized using common free radical polymerization methods. Their preliminary lithography-related characteristics have been investigated. By carefully manipulating components and compositions, this generic type of copolymers could be used as potential candidate resists for DUV, X-ray and e-beam exposure tools. The remarkably high contrast of 23.5 obtained without sacrificing the intrinsic sensitivity of the organic component shows not only that POSSMA-containing copolymers are promising systems for X-ray and eventually e-beam nanolithograpies, but also that the concept can be extended to other systems viz. 157 nm and EUV.

References

(1) Hutchinson, J. M.; Wallraff, G. M.; Hinsberg, W. D.; Opitz, J.; Oldham, W. G. *SPIE* **1995**, 2438, 486-495.

(2) Houlihan, F. M.; Wallow, T. I.; Nalamasu, O.; Reichmanis, Elsa *Macromolecules* **1997**, 30(21), 6517-6524.

(3) Rau, N.; Neureuther, A.; Ogawa, T.; Kubena, R.; Stratton, F.; Fields, C.; Willson, C. Grant *Proc. SPIE-Int. Soc. Opt. Eng.* **1998**, 3333, 1413-1419.

(4) Hashimoto, M.; Koreeda, T.; Koshida, N.; Komuro, M.; Atoda, N. *J. Vac. Sci. Technol. B* **1998**, 16, 2767.

(5) Hulteen, J. C.; Van Duyne, R. P. *J. Vac. Sci. Technol. A* **1995**, 13(3).

(6) Haddad, T. S.; Lichtenhan, J. D. *Macromolecules* **1996**, 29, 7302-7304.

(7) Gonsalves, K. E.; Wang, J.; Wu, H. *J. Vac. Sci. Technol. B*, Jan. 2000.

(8) Lichtenhan, J. D.; Otonari, Y. A.; Carr, M. J. *Macromolecules*, **1995**, 20, 8435-8437.

(9) Lichtenhan, J. D.; Noel, C. J.; Bolf, A. G.; Ruth, P. N. *Mat. Res. Soc. Symp. Proc.* **1996**, 435, 3-11.

(10) Reichmanis, Elsa; Nalamasu, O.; Houlihan, F. M. *Acc. Chem. Res.* **1999**.

(11) Kunz, R. R.; Allen, R. D.; Hinsberg, W. D.; Wallraff, G. M. *SPIE* **1993**, 1925, 167.

(12) Takahashi, M.; Takechi, S.; Nozaki, K.; Kaimoto, Y.; Hanyu, I.; Abe, N. *Proc. SPIE* **1995**, 2438, 422.

(13) Jones, R. G.; Cragg, R. H.; Davies, R. D. P.; Brambley, D. R. *J. Mater. Chem.* **1992**, 2(4), 371-377.

(14) Lercel, M. J.; Craighead, H. G.; Parikh, A. N.; Seshadri, K.; Allara, D. L. *Appl. Phys. Lett.* **1996**, 68(11), 11.

(15) Olkhovets, A.; Craighead, H. G. *J. Vac. Sci. Technol. B* **1999**, 17(4), 1336-1370.

(16) Carey, F. A.; Sundberg, R. J. *Advanced Organic Chemistry, Part B, 3rd ed.,* **1990**, Plenum Press, New York.

New High Resolution Liquid Crystal Electron Beam Resists

A.P.G. Robinson[*], R.E. Palmer[*], T. Tada[†], T. Kanayama[†], M.T. Allen[‡], J.A. Preece[‡] and K.D.M. Harris[‡]
[*]Nanoscale Physics Research Laboratory, School of Physics and Astronomy, The University of Birmingham, Birmingham, UK, a.p.g.robinson@bham.ac.uk.
[†]Joint Research Center for Atom Technology, NAIR, 1-1-4 Higashi, Tsukuba, Ibaraki 305-8562, Japan.
[‡]School of Chemistry, The University of Birmingham, Birmingham, UK.

Abstract

We report the development of a new family of electron beam resists based on liquid crystalline polysubstituted derivatives of triphenylene. These new resists show excellent performance in terms of both high resolution and high durability to plasma etching. Films of the derivatives have been produced in a controlled manner via room temperature spin coating on hydrogen terminated silicon substrates. The dissolution behaviour of the derivatives in various organic solvents was altered by exposure to a 20 keV electron beam. The solubility of the derivative hexapentyloxytriphenylene, in polar solvents, was substantially increased by electron doses greater than $\sim 3 \times 10^{-4}$ C/cm^2 (positive tone behaviour). Doses greater than $\sim 2.5 \times 10^{-3}$ C/cm^2 led to negative tone behaviour in both polar and non-polar solvents. Other derivatives also demonstrated a reduction in their dissolution rate for doses between $\sim 1 \times 10^{-3}$ and $\sim 7 \times 10^{-3}$ C/cm^2. The derivative sensitivity was found to be roughly proportional to the molecular mass. Negative tone patterns were found to have an etch durability ~ 70 % greater than that of a conventional novolac based negative tone resist (SAL601). The performance of these new resists has been demonstrated by the definition of line and space patterns with a resolution of ~ 14 nm, whilst structures with an aspect ratio of ~ 50 to 1 were etched into the silicon substrate.

Introduction

Current microelectronic devices require a lithographic resolution of ~ 0.18 μm, close to the limits of photolithography. However, further miniaturization is desirable not only to increase component packing density, but also for biodevices [1] and the exploitation of quantum effects in devices with features smaller than 100 nm [2-5]. The resolution limits of photolithography appear to lie at ~ 100 nm [6,7] and thus other methods will probably be required to extend miniaturization into the sub-100 nm regime.

Electron beam (e-beam) lithography [8] is a promising technique for the definition of such small features, since an e-beam can easily be focused to a spot size of 1 nm or less. The e-beam irradiates, and thus chemically modifies, a suitable resist coated on the substrate. The properties of the resist material used in the lithographic process can strongly influence the resolution. For instance, with commercial polymeric resists, e-beam irradiation causes either polymer cross-linking, giving larger less soluble molecules (negative tone), or polymer fragmentation into smaller, more soluble, molecules (positive tone). For negative tone polymer resists the smallest definable pattern is therefore limited by the size of the polymer molecule (~ 10 nm diameter [9,10]). Higher resolution is possible with positive tone resists, but the large molecular size of the resist polymer can lead to substantial linewidth fluctuations [10,11]. It is therefore desirable that the area of the resist molecules on the surface be as small as possible.

Several materials have been investigated to surmount this problem, including low molecular weight organic molecules [9,12,13], metal fluorides [14], fullerenes [15] and fullerene derivatives [16,17]. However, in order to reach high resolutions a variety of extra process steps, such as long bakes [12,13], unusual deposition techniques [15,18,19], high e-beam energies [12,20,21], secondary electron exposure [22], and complex developing methods [20,21], have often been necessary. Thus there is a demand for a resist that allows definition of high resolution patterns without introducing excessive process complexity.

We have previously reported [23] that the (liquid crystal) molecule 2,3,6,7,10,11-hexapentyloxytriphenylene [24] (C5/C5) allows relatively facile definition of ~ 14 nm patterns, at modest beam energy (30 keV), without the need for any complex pre- or post-irradiation processing of the resist. Furthermore, it was observed that the C5/C5 resist behaves in both a positive and a negative tone manner, dependent upon the electron dose. In this paper we summarize the results of a systematic study of 11 polysubstituted triphenylene derivatives, with the purpose of further exploring the properties of this new class of e-beam resist.

Experiments and Results

The derivatives studied are shown in fig. 1. The first nine derivatives shown in fig. 1 form a homologous series. In the case of C5/C5 the data obtained confirms our previous report [23]. The derivatives C6/C6 and C5/C5COOH, shown in fig. 1, were also studied. All of the derivatives bar C5/C0, C5/C1, C5/C2 and C5/C5COOH are liquid crystalline [25].

Films of the triphenylene derivatives were deposited from chloroform solution by spin coating at room temperature onto HF cleaned hydrogen terminated silicon. The film thickness, measured with a surface profiler (Dektak, Sloan), could be controlled in all cases by varying either the angular frequency of the spin coater or the concentration of the deposition solution. It was possible to produce films of thickness less than 10 nm to more than 300 nm for all of the derivatives, with the exception of C5/C5COOH, for which 10 – 60 nm thickness films were possible. (In the case of C5/C5, films as thick as 6 microns have been produced with concentrated deposition solutions). Smooth films were observed for all samples, with roughness of less than 5 nm (with the exception of the 6 micron film where the thickness variation was ~ 180 nm). However, the films of C5/C0, C5/C1, C5/C2, and C5/C5COOH crystallized slowly, rendering them unusable after approximately half a day. This is probably because these derivatives are not liquid crystals. Preliminary results from small angle x-ray scattering (SAXS) analysis of the films on H-Si suggests that the film smoothness may be due ordering of the molecules on the surface. Fig. 2 shows the SAXS spectrum of C5/C5 (100 nm film on H-Si). The sharp peak indicates a well ordered film. The d-spacing obtained is identical to the mesophase d-spacing [25] corresponding to the intercolumnar separation (d100), which implies that the molecules are ordered perpendicularly on the surface as shown in the inset to fig. 2.

To measure the response of the derivatives to e-beam irradiation films were exposed to a 20 keV beam using a
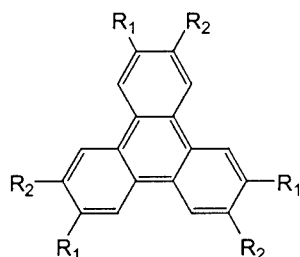
Code	Formula	Name
C5/C0	$R_1=OC_5H_{11}$ $R_2=OH$	2,7,10-tri-pentyloxy-3,6,11-tri-hydroxytriphenylene
C5/C1	$R_1= OC_5H_{11}$ $R_2= OC_1H_3$	2,7,10-tri-pentyloxy-3,6,11-tri-methyloxytriphenylene
C5/C2	$R_1= OC_5H_{11}$ $R_2= OC_2H_5$	2,6,10-tri-pentyloxy-3,7,11-tri-ethyloxytriphenylene
C5/C3	$R_1= OC_5H_{11}$ $R_2= OC_3H_7$	2,6,10-tri-pentyloxy-3,7,11-tri-propyloxytriphenylene
C5/C4	$R_1= OC_5H_{11}$ $R_2= OC_4H_9$	2,6,10-tri-pentyloxy-3,7,11-tri-butyloxytriphenylene
C5/C5	$R_1= OC_5H_{11}$ $R_2= OC_5H_{11}$	2,3,6,7,10,11-hexa-pentyloxytriphenylene
C5/C6	$R_1= OC_5H_{11}$ $R_2= OC_6H_{13}$	2,6,10-tri-pentyloxy-3,7,11-tri-hexyloxytriphenylene
C5/C7	$R_1= OC_5H_{11}$ $R_2= OC_7H_{15}$	2,6,10-tri-pentyloxy-3,7,11-tri-heptyloxytriphenylene
C5/C9	$R_1= OC_5H_{11}$ $R_2= OC_9H_{19}$	2,6,10-tri-pentyloxy-3,7,11-tri-nonyloxytriphenylene
C5/C5 COOH	$R_1= OC_5H_{11}$ $R_2=OC_5H_{10}COOH$	2,6,10-tri-pentyloxy-3,7,11-tri[5-(carboxy)pentyloxy]triphenylene
C6/C6	$R_1= OC_6H_{13}$ $R_2= OC_6H_{13}$	2,3,6,7,10,11-hexa-hexyloxytriphenylene

Fig. 1 Eleven polysubstituted triphenylenes were studied.
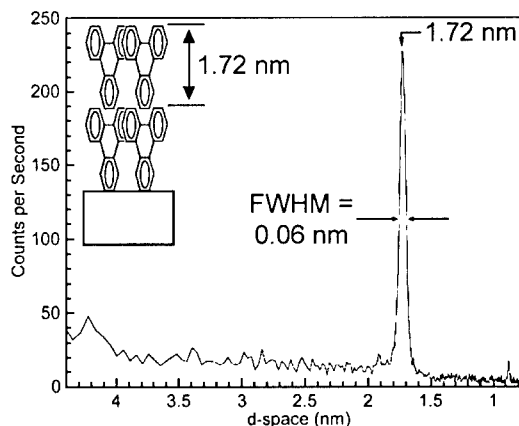
Fig. 2 Small angle x-ray scattering spectrum of 100 nm film of C5/C5 on H-Si. Inset, the proposed molecular ordering to explain the sharp peak. (C_5H_{11} chains omitted from molecules for clarity.)

Hitachi S4500 scanning electron microscope (SEM) equipped with a pattern generator (CPG1000, Crestec). This system is capable of defining features with a maximum resolution of ~ 20 nm in PMMA. Irradiation led to a decrease in the film thickness, prior to development, which was measured with the surface profiler. The reduction in thickness was found to have a power law dependence on the electron dose, as observed previously [23] for C5/C5, and is shown for three derivatives in the inset to fig. 3. The films were developed by immersion in monochlorobenzene (MCB) for 60 s. All of the derivatives showed a negative tone response after development in MCB. The response curves of three derivatives are shown in fig. 3. (In order to make comparison between the properties of the different resists easier the curves have been offset along the y-axis and normalized.) The sensitivity of a (negative tone) resist to electrons is defined as the dose at which the linear portion of the rising section of the response curve (fig. 3)

Fig. 3 The response of C5/C4, C5/C5 and C5/C6 to 20 keV electrons. Film thickness after development for 60 s in monochlorobenzene is plotted against the electron dose. Inset is the reduction in film thickness due to irradiation itself, prior to development.

reaches 50 % of the original film thickness [26]. Since there is a reduction of film thickness due to irradiation itself, the original film thickness for each derivative is taken as the average of the film thickness of areas receiving sufficient dose to be completely retained after development. This value has been used for subsequent normalization. The measured sensitivities for each of the derivatives are plotted in fig. 4 as a function of the derivative mass. The sensitivities range from $\sim 6.5 \times 10^{-3}$ C/cm^2 for C5/C0 to $\sim 1.5 \times 10^{-3}$ C/cm^2 for C5/C9, and are approximately linearly proportional to the derivative mass. For comparison, the sensitivity of negative tone PMMA under similar exposure conditions [27] is $\sim 5.0 \times 10^{-3}$ C/cm^2. The contrast of a resist is a measure of the speed of its transition from unexposed to exposed behaviour calculated from its response curve (e.g. fig. 3) [28]. The contrasts of the derivatives were measured to be between ~ 1.5 and ~ 4; no clear correlation to the sensitivity was observed.

C5/C5 also showed positive tone resist behaviour. Samples were prepared and irradiated as before, and developed using 2-hexanol, 2-pentanol or 3-pentanol. Fig. 5 shows the response curves of this resist with these developers. Immersion in any of these three developers for 2 s led to a complete removal of the film in areas receiving an electron dose of more than, respectively, ~ 2.0×10^{-4}, 3.0×10^{-4} or 4.0×10^{-4} C/cm^2. (Positive tone PMMA sensitivity under similar exposure conditions is 1×10^{-4}
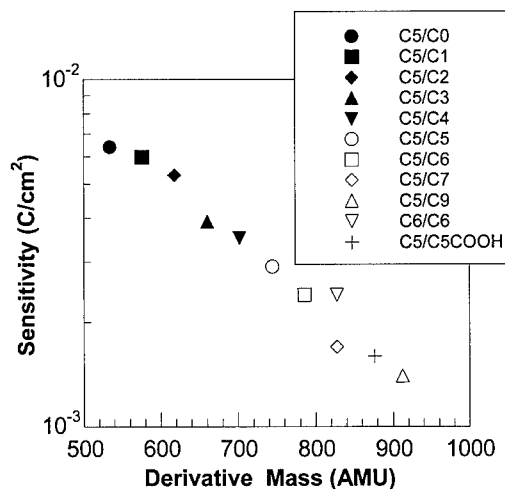
Fig. 4 The sensitivities of the derivatives shown in fig. 1 plotted as a function of the derivative mass.

C/cm² [27].) Less than 20 % of the unexposed area was removed by development (with the exception of the developer 2-hexanol, which has a very low positive tone contrast of 0.5). However, development for longer than ~ 4 s led to a substantial reduction in the film thickness. In all three cases negative tone behaviour is seen for electron doses higher than ~ 2.5 × 10⁻³ C/cm² (see fig. 5). Some evidence of positive tone behaviour was also obtained for the resists C5/C4 and C5/C6, though the developers used to date only partly remove the positively exposed areas.

For fabrication purposes it is necessary that a resist be sufficiently durable against the etching process used to transfer the defined pattern to the substrate. The etch resistance of the triphenylene compounds was evaluated using electron cyclotron resonance microwave plasma etching with

Fig. 5 The response of a film of C5/C5 to a low dose of 20 keV electrons. The depth of features produced after development with (●) 2-pentanol, (■) 3-pentanol and (◆) 2-hexanol for 2 s is shown.

SF_6. The SF_6 flow rate was 5 sccm at a pressure of 0.4 mtorr. The incident microwave power was 250 W, the rf power applied to the samples was 0.5 W/cm² and the etch was performed at 25°C. With the exception of the derivative C5/C5COOH, all of the resists have a very similar etch rate; the average value obtained is 1/5.2 (± σ_N ≈ 0.26) that of the silicon. The etch rate of C5/C5COOH is ~ 1/7.2 that of the silicon. For comparison, the etch rate of a commercial high durability resist, SAL 601 (Shipley), under the same conditions, is 1/3 of the rate of the silicon substrate. C5/C5 etched after development as a positive tone resist has an etch rate of 1/2.3 that of the silicon – more than double the durability of PMMA under the same ECR conditions.

To examine the viability of the resists for nanolithography, line and space patterns were defined in 20 nm thickness films of C5/C5 and C5/C5COOH using the SEM. The patterns were written with a 30 keV e-beam using a line dose of 6 × 10⁻⁶ C/m and the films developed for 60 s in MCB. The SEM was used to view the patterns. Fig. 6(a) shows 14 nm lines defined in the C5/C5 resist, and fig. 6(b) shows 20 nm

Fig. 6 (a) SEM micrograph of a series of 14 nm wide lines defined in a 20 nm thick film of C5/C5 after development with mono-chlorobenzene. (b) SEM micrograph of 20 nm wide lines defined in a 20 nm thick film of C5/C5COOH.

Fig. 7 (a) SEM micrograph of 30 –40 nm diameter dots defined in a 130 nm thick film of C5/C5. The sample tilt angle is 40°. (b) Low magnification micrograph of ~ 20 nm line defined in a 90 nm thick film of C5/C5.

lines defined in C5/C5COOH. In both cases the resolution is limited by the resolution of the lithographic tool; higher resolution was achieved in the former case due to advantageous environmental conditions (e.g. ambient noise, etc.). As can be seen there are no observable residues in the unexposed areas. Figs. 7(a) and (b) show patterns defined in films of C5/C5. Dots were defined in a 130 nm thick film of resist with a dose of 4×10^{-12} C/dot. Fig. 7(a) shows the 30 to 40 nm diameter dots with a tilt angle of 40°. The height of the dots is ~ 100 nm clearly indicating that the resist film is responsible for the negative action rather than contamination writing. Figure 7(b) shows a low magnification micrograph of ~ 20 nm lines defined in a 90 nm thick film of C5/C5. It can be seen from figure 7(b) that straight negative tone lines can be defined in this resist. By altering the film thickness and the etch conditions, it was also possible to fabricate structures with aspect ratios of ~ 50:1 using the C5/C5 resist. A film of 430 nm thickness was patterned with a line dose of 2.4×10^{-5} C/m at 30keV, developed and etched with the ECR microwave plasma etcher for 20 minutes with SF_6 (0.3 sccm, 0.25 mtorr) at -120°C. The incident microwave power was 250 W and the rf power was 0.5 W/cm^2. Fig. 8(a) shows a line of width ~ 50 nm and height 2500 nm, i.e. an aspect

Fig. 8 Pattern transferred from a patterned film of C5/C5 to the silicon substrate by ECR etching. (a) SEM micrograph of a 50 nm wide 2500 nm high wall. The sample tilt angle is 20°. (b) SEM micrograph of a section of the wall showing smooth sidewalls. The sample tilt angle is 20°. (The scan direction is perpendicular to fig 8(a)).

ratio of ~ 50:1. Fig. 8(b) shows a magnified section of the line and demonstrates that C5/C5 can be used to form high aspect ratio features with smooth sidewalls. Fine positive tone patterns have not yet been demonstrated in a triphenylene derivative resist as the current positive tone developers cause some roughening of the film surface. It will therefore be necessary to find an alternative developer in order to define fine positive tone patterns in these resists.

Conclusions

In conclusion, we have shown that several polysubstituted triphenylene derivatives can be deposited in a controlled fashion on the hydrogen terminated silicon surface. Liquid crystalline derivatives of triphenylene are particularly attractive since they form extremely smooth films. Preliminary SAXS measurements suggest this is due to an ordering of the molecules on the surface. These films are sensitive to electron beam irradiation, and demonstrate negative tone resist behaviour when using the developer monchlorobenzene, with sensitivities to electron dose in the range ~ 1.5 to ~ 6.5 $\times$ 10^{-3} C/cm^2. With the developers 2-pentanol, 3-pentanol and 2-hexanol, both positive and negative tone resist behaviour is found for the C5/C5 derivative (depending on the dose). There is some evidence that other polysubstituted triphenylenes are also capable of this dual action, but appropriate developers have not yet been identified. The negative tone sensitivity of the derivatives are similar to, or better than, the negative tone sensitivity of PMMA and the positive tone sensitivity of C5/C5 is slightly less than that of PMMA. The etch durability of these derivatives is almost double that of SAL601, and substantially greater than

that of PMMA. (The positive tone etch ratio of C5/C5 is more than double that of positive tone PMMA.) Line and space patterns have been defined with 14 nm resolution in films of C5/C5, while structures have been etched in silicon with aspect ratios of ~ 50:1 using the same derivative. Liquid crystal derivatives of triphenylene offer an attractive new route for the fabrication of high resolution high aspect ratio structures.

Acknowledgements

References

[1] E. Di Fabrizio, L. Grella, M. Baciocchi, M. Gentili, C. Ascoli, B. Cappella, C. Frediani and P. Morales, J. Vac. Sci. Technol. B, **15**, 2892 (1997).
[2] H.Shoji, Y. Nakata, K. Mukai, Y. Sugiyama, M. Sugawara, N. Yokoyama and H. Ishikawa, Appl. Phys. Lett., **71**, 193 (1997).
[3] Y. Tang, W.-X. Ni, C.M. Sotomayor Torres and G.V. Hansson, Electronics Letters, **31**, 1385 (1995).
[4] R.A. Smith and H. Ahmed, Appl. Phys. Lett., **71**, 3838 (1997).
[5] H. Ishikuro and T. Hiramoto, Appl. Phys. Lett, **71**, 3691 (1997).
[6] M.C. Peckerar, F.K. Perkins, E.A. Dobisz and O.J. Glembocki, *Handbook of Microlithography, Micromachining and Microfabrication Vol. I*, P. Rai-Choudhury, ed., (IEE, London, 1997), p. 686.
[7] J.A. Rogers, K.E. Paul, R.J. Jackman and G.M. Whitesides, Appl. Phys. Lett., **70**, 2658 (1997).
[8] M.A. McCord and M.J. Rooks, *Handbook of Microlithography, Micromachining and Microfabrication Vol. I*, P.Rai-Choudhury, ed., (IEE, London, 1997), Ch. 2 p. 139 – 249.
[9] H. Namastu, K. Kurihara, M. Nagase and T. Makino, Appl. Phys. Lett., **70**, 619 (1997).
[10] M. Yoshiiwa, H. Kageyama, Y. Shirota, F. Wakaya, K. Gamo and M. Takai, Appl. Phys. Lett., **69**, 2605 (1996).
[11] T. Yamaguchi, H. Namatsu, M. Nagase, K. Yamazaki and K. Kurihara, Appl. Phys. Lett., **71**, 2388 (1997).
[12] J. Fujita, Y. Ohnishi, Y. Ochiai and S. Matsui, Appl. Phys. Lett., **68**, 1297 (1996).
[13] S. Manako, J. Fujita, Y. Ochiai, E. Nomura, S. Matsui, Jpn. J. Appl. Phys., **36**, 7773 (1997).
[14] J. Fujita, H. Watanabe, Y. Ochiai, S. Manako, J.S. Tsai and S. Matsui, Appl. Phys. Lett., **66**, 3064 (1995).
[15] T. Tada and T. Kanayama, Jpn. J. Appl. Phys., **35**, L63 (1996).
[16] A.P.G. Robinson, R.E. Palmer, T. Tada, T. Kanayama and J.A. Preece, Appl. Phys. Lett., **72**, 1302 (1998).
[17] A.P.G. Robinson, R.E. Palmer, T. Tada, T. Kanayama, J.A. Preece, D. Philp, U. Jonas and F. Deiderich, Chem. Phys. Lett., **289**, 586 (1998).
[18] M.J. Lercel, H.G. Craighead, A.N. Parikh, K. Seshadri and D.L. Allara, Appl. Phys. Lett., **68**, 1504 (1996).
[19] C.S. Whelan, M.J. Lercel, H.G. Craighead, K. Seshadri and D.L. Allara, Appl. Phys. Lett., **69**, 4245 (1996).
[20] W. Chen and H. Ahmed, Appl. Phys. Lett., **62**, 1499 (1993).
[21] W. Chen and H. Ahmed, Appl. Phys. Lett., **63**, 1116 (1993).
[22] D.R.S. Cumming, S. Thoms, S.P. Beaumont and J.M.R. Weaver, Appl. Phys. Lett., **68**, 322 (1996).
[23] A.P.G. Robinson, R.E. Palmer, T. Tada, T. Kanayama,, M.T. Allen, J.A. Preece and K.D.M Harris, J. Phys. D., **32**, L75 (1999).
[24] N. Boden, R.C. Borner, R.J. Bushby, A.N. Cammidge and M.V. Jesudason, Liquid Crystals, **15**, 851 (1993).
[25] M. T. Allen, J.A. Preece and K.D.M Harris, Liquid Crystals, (In Press).
[26] S. Manako, J-I. Fujita, Y. Ochiai, E. Nomura and S. Matsui, Jpn. J. Appl. Phys., **36**, 7773 (1997).
[27] T.Tada and T. Kanayama, J. Vac. Sci. Technol. B, **13**, 2801 (1995).
[28] The contrast is equal to $(log_{10}(D_2/D_1))^{-1}$ where D_2 and D_1 are the doses at which the extrapolation of the linear section of the rising response curve intersects with the 100% and 0% levels for film retention, respectively.

Resist Materials Providing Small Line-Edge Roughness

Hideo Namatsu, Toru Yamaguchi and Kenji Kurihara
NTT Basic Research Laboratories
3-1 Morinosato Wakamiya, Atsugi, Kanagawa, 243-0198 JAPAN

ABSTRACT

Our research focuses on the line-edge roughness of resist patterns and how to reduce it in order to establish nanolithography as a practical tool. Commercially available e-beam resists exhibit a line-edge roughness of 3 nm (σ) or more. It is caused mainly by polymer aggregates in the resist. During development, they are extracted through dissolution of the surrounding polymer matrix. That is, the aggregates themselves dissolve more slowly than the surrounding matrix; and those that remain embedded in the resist produce line-edge roughness. To reduce the roughness, the effect of the aggregates must be suppressed. One way of doing this is to use a resist containing small aggregates. A good candidate is hydrogen silsesquioxane, which has a three-dimensional framework. Another way is to use a resist in which the aggregates are linked together, which makes them difficult to extract during development. A good example is an acrylate-type resist with a cross-linker mixed in.

INTRODUCTION

In order to make devices with dimensions of 100 nm or less, we need novel fabrication techniques and/or materials with increased resolution capabilities. In this regard, powerful exposure tools are now being developed that employ very short-wavelength optical lithography, or x-ray or e-beam lithography; and several resist materials optimized for these tools have been proposed. However, resolution is not the only important consideration; linewidth fluctuations can also have a direct impact on device characteristics at such small feature sizes. So, linewidth fluctuations in resist patterns are now attracting the attention of many lithographic researchers. The standard measure of such fluctuations is line-edge roughness (LER). And many reports on the degree of LER in various resists have appeared. But there are few reports on the cause of LER. One cause that is of particular interest is a property of resist materials themselves, namely, polymer aggregates [1-3]. These aggregates are made up solely of resist molecules and can reach a size of more than 30 nm in commercial e-beam resists. Size estimates are generally obtained from scanning-electron-microscope (SEM) and atomic-force-microscope (AFM) observations of the surface of resist patterns. These estimates have enabled the dependence of aggregate size on molecular weight [1] and molecular structure [2] to be determined. Furthermore, polymer aggregates have recently been observed even in a photoresist for ArF lithography [4]. So, the existence of polymer aggregates seems to be a problem common to all resist materials.

This article reports on the characteristics of aggregate formation in several resists. In addition, the process by which aggregate formation results in LER is discussed. Finally, guidelines for new resist materials that yield a smaller LER are proposed.

Polymer aggregates in resist films

Figure 1 shows the surface morphology of the commercially available positive resist ZEP-520 (Nippon Zeon Co.) as observed with an AFM in the dynamic-force mode. ZEP-520 has an average molecular weight (Mw) of 5.4×10^4. Figure 1(a) is an image of a pattern side wall obtained by direct observation of a sample set in a vertical position. The granular morphology is very clear. Figure 1(b), on the other hand, shows the surface of film after e-beam exposure at a low dose, followed by development. The morphology in this case is strikingly similar to that in Fig. 1(a).
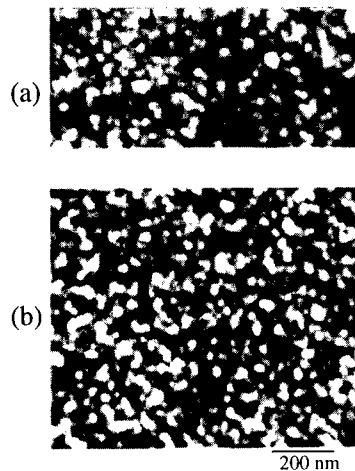
Fig. 1. AFM images of the surfaces of (a) resist pattern side wall and (b) lightly exposed resist film. The resist was ZEP-520. The pattern was formed at the optimum e-beam exposure and development conditions. The resist film was exposed to about half of the optimum dose and then developed.

This indicates that the surface morphology of lightly exposed film offers a good approximation to the morphology of a pattern side wall [7]. This is because a side wall is exposed to the tail of the beam profile, which has the same effect as exposing a film surface to a low dose. That means that observation of the surface of lightly exposed film can be used in place of estimating the degree of LER. The structures in the images are about 30 nm in diameter, which is larger than the diameter of
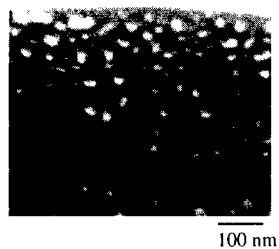
Fig. 2. Cross-sectional SEM image of ZEP-520 resist film that was neither baked nor exposed.

one molecule of polymer. They are polymer aggregates. The fact that such large aggregates exist suggests that they have a great influence on linewidth accuracy, and thus on LER.

Figure 2 shows a cross-sectional SEM image of ZEP-520 resist film that was neither baked nor exposed. Even in this case, many polymer aggregates appear in the film, which proves that aggregate formation is not due to either e-beam exposure or baking. The aggregates have already formed in the film coating. On the other hand, the aggregates could not have been produced by any residue in the solution, because the resist was dissolved in good solvent, such as o-dichlorobenzene. Therefore, aggregate formation must depend not on the resist process, but rather on the material properties of the resist itself.

Figure 3 shows an AFM image of a PMMA film formed by the Langmuir-Blodgett technique. Even though the film is very thin, granules with a flattened shape can be observed. The resist was dissolved in chloroform to a concentration of 0.1 mg/ml. Despite the diluteness of the solution, the original shape of the aggregates can still be seen. That means that the formation of aggregates is independent of the technique by which a film is made, the film thickness, and the initial concentration of resist.

100 nm
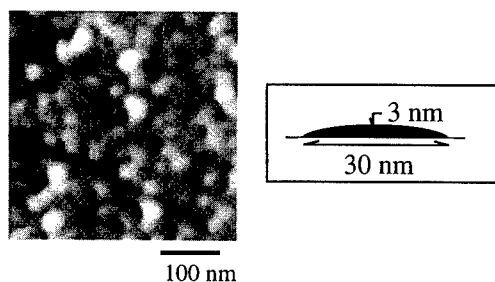
Fig. 3. AFM image of a thin film of PMMA formed by the Langmuir-Blodgett technique. Mono-dispersed PMMA with a molecular weight of 6×10^4 was spread onto purified water in a moving-wall trough, and then transferred three times to a Si wafer.

We speculate that polymer aggregates are formed by the entanglement of polymers in the resist solution [2]. The long linear polymer chains of conventional resists actually spread out in solution and easily become entangled with each other. Then, the shorter polymers with smaller molecular weights diffuse into the larger, spread-out chains and become entangled. This results in the formation of large aggregates. So, the formation of aggregates is probably due to the fact that polymer chains spread out to a certain extent in solution, and greater entanglement results from the increase in concentration during film formation. Greater entanglement probably produces larger aggregates.

Line-edge roughness caused by polymer aggregates

When polymer aggregates appear on the edge or side wall of a pattern, LER is generated. Figure 4 shows patterns in ZEP-520 and SAL-601 (Shipley Co.) resists. Both lines exhibit fluctuations in width of 3 nm (σ) or more due to polymer aggregates. Though this amount of roughness may seem

(a)   200 nm
             (b)
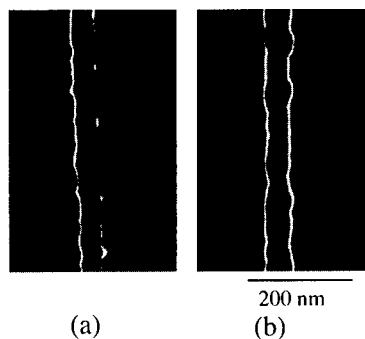
Fig. 4. SEM images of (a) ZEP-520 and (b) SAL-601 resist patterns showing line-edge roughness. SAL-601 was postexposure-baked at 95°C for 1 min. Development was carried out for 1 min. in hexyl acetate [6] for ZEP-520 and in an aqueous solution of 2.38% TMAH for SAL-601.

very small, it can definitely degrade the performance of devices when feature sizes reach 100 nm.

Figure 5 shows an SEM image of the Si pattern etched using SAL-601 resist as a mask. In the pattern sidewall, roughness with vertical stripe is formed. The stripe roughness agrees with the LER of the resist pattern. That is, the sidewall roughness of the etched pattern is caused by LER.

The process by which polymer aggregates produce LER is thought to be as follows. When a resist containing aggregates is developed, the rate of development is uneven because the dissolution process (i.e. solvation) proceeds more quickly in the surrounding polymer than in the aggregates. The difference in dissolution rate between aggregates and the surrounding polymer arises

200 nm
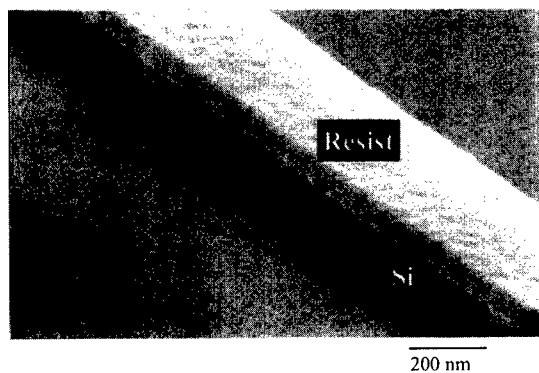
Fig. 5. SEM image of the Si pattern etched using SAL resist as a mask.

138

Polymer aggregate   Surrounding polymer

(a)   Resist film

(b)

(c)
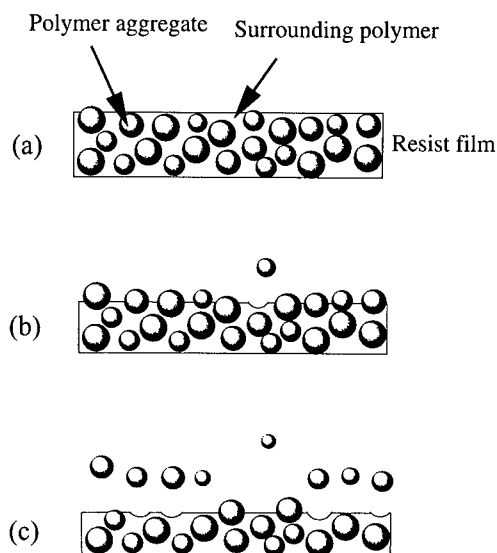
Fig. 6. Schematic diagrams showing the behavior of polymer aggregates during development. The initial resist film (a) changes to (b) and then (c) during development. This process is called aggregate extraction development.

from a difference in their densities [8]: the slightly greater density of aggregates makes their solvation rate much slower than that of the surrounding polymer. As a result, undissolved aggregates become separated from the surrounding polymer and are extracted into the developer, as shown in Fig. 6. We call this process "aggregate extraction development" [3]. Direct evidence of this process has already been obtained [8].

When resist films containing aggregates are developed, that is, when aggregate extraction development occurs in a patterned region, many aggregates remain embedded in the edges and side walls, which are only lightly exposed by the tail of the e-beam profile. This is because not all of the surrounding polymer is dissolved. So, parts of aggregates protrude from the edge or side wall and appear as roughness, as shown in Fig. 7. This phenomenon is common to both negative and positive resists; aggregate extraction development occurs in the exposed regions of positive resists and in the unexposed regions of negative resists. Consequently, the shapes of aggregates appear on the side walls of both types of patterns. And in both cases, when a region is only lightly exposed, aggregate extraction is more pronounced. As a result, the pattern profile reflects the roughness caused by the aggregates. This is the process by which aggregates produce LER, or linewidth fluctuations.

An important factor in the morphology of the edges and side walls of a pattern is the contrast of the developer [6], which determines how far large aggregates protrude out from the surrounding polymer [2]. As mentioned above, aggregates seem to appear readily in regions exposed to a light dose. In these regions, the thickness loss, as indicated by the shoulder of the sensitivity curve, is large when the contrast is low. A large thickness loss means that more of the polymer surrounding the aggregates dissolves, exposing not only a greater part of the aggregates on the surface but also

Positive | Negative
Scission | Cross-linking
EB exposure | EB exposure
Development | Development
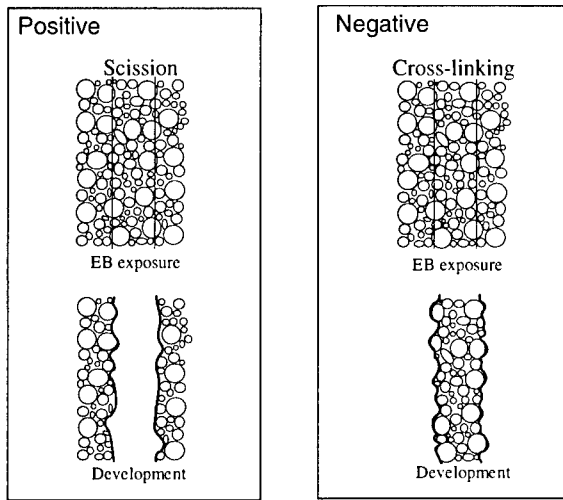
*Fig. 7. Schematic diagrams showing the process by which line-edge rough-
ness is generated in both positive and negative resists.*

those deeper in the resist. This makes patterns extremely rough. In fact, it has been reported that the standard deviation of the linewidth of ZEP resist was about 3 nm when the thickness loss was small, but over 4 nm when it was large [6]. Clearly, to suppress the appearance of aggregates, the thickness loss should be reduced, or in other words, the contrast should be enhanced. However, even with a high-contrast developer, the degree of LER is still not small enough for nanolithography. That means that resist materials themselves have to be improved.

Polymer aggregates may also affect resolution, in addition to LER [3]. In positive resists, large exposure doses are required to decompose aggregates in order to form well-defined patterns that are smaller than the size of aggregates. Larger doses mean more beam scattering and a consequent drop in critical resolution. For negative resists as well, patterning characteristics may depend on aggregates. That is, the critical dose for a negative pattern results in low mechanical strength in the resist, which makes very fine patterns collapse because there is probably only enough cross-linking in the resist to connect the aggregates. An overdose, which is needed for sufficient cross-linking, reduces the resolution. The possibility that resolution is influenced by aggregate extraction development deserves further attention.

Improved resist materials for small line-edge roughness

As mentioned above, the key to reducing LER is the suppression of the influence of aggregate extraction on pattern edges and side walls. There are two approaches to achieving that, as shown in Fig. 8. In one, the influence of aggregate extraction is reduced whenever it occurs by using a resist

140
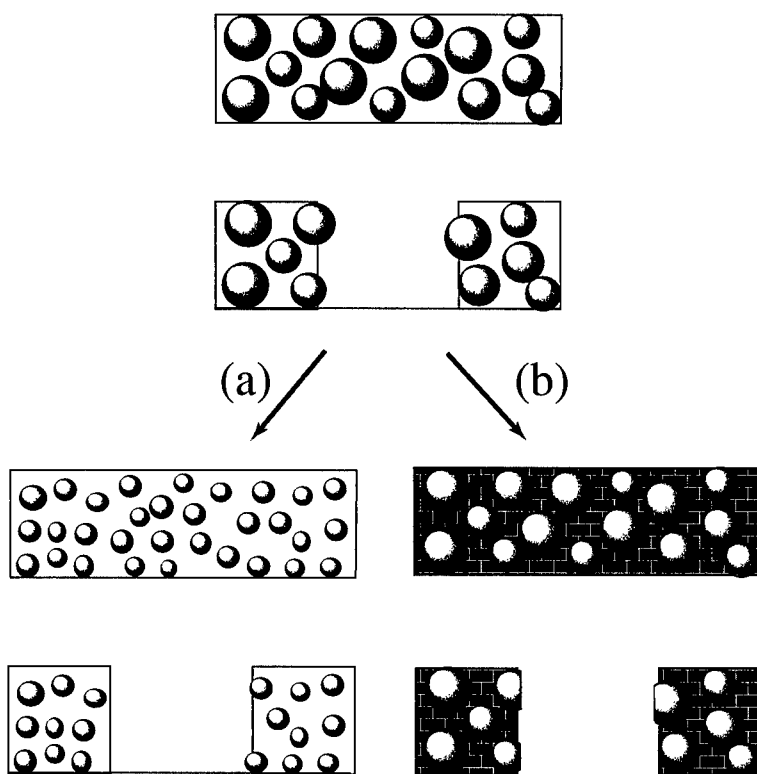
Fig. 8. Approaches to reducing line-edge roughness: (a) small aggregates and (b) the cross-linking of aggregates.

containing small aggregates. In the other, the extraction itself is suppressed, for instance, by cross-linking the aggregates. Needless to say, for either approach to work, the resist must have a high development contrast, as mentioned above.

1. Resist containing small aggregates

Two conditions for the formation of small aggregates are: chain structures that do not spread out in solution, and a small molecular weight. The influence of the chain structure is larger [2].

One candidate that satisfies these conditions is HSQ resist [2]. As mentioned above, polymer aggregates are mainly formed by the interaction of polymer chains in a concentrated solution, or more specifically, by the entanglement resulting from the interpenetration of several polymers. So, when it is difficult for the polymer to spread out and become entangled, the aggregates should be small. HSQ has a three-dimensional framework of $SiO_{3/2}$ units [9] that impedes the spreading-out of the molecules in solution. Evidence that this is true has been provided by size exclusion chromatography using a viscosity detector (SEC-viscometry) [2]. The aggregates in HSQ have been found to be as small as 10-15 nm in size. Calixarene, which has a cyclic structure, is another candidate [10]. However, its low sensitivity increases the roughness due to another factor, namely, noise in the e-beam machine.

Figure 9(a) is an SEM image of approximately 20-nm-wide HSQ patterns after development in tetramethylammonium hydroxide (TMAH). The patterns exhibit a rectangular cross section, because the developer had a high contrast of about 5. In addition, the small aggregates produce a small LER. Figure 9(b) shows patterns after Si etching with ECR chlorine plasma. The use of an HSQ mask enables the formation of fine Si patterns.

20 nm

(a) (b)
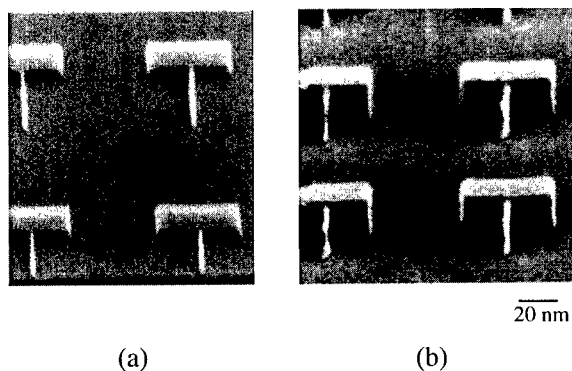
Fig. 9. SEM photographs of HSQ patterns (a) before and (b) after Si etching.

Figure 10 shows the surfaces of several resists that were exposed to a light dose and developed. The surface roughness is clearly much smaller for HSQ than for the others. This is due to the smaller aggregates. Figure 11 shows the LER of SAL, ZEP, and HSQ resist patterns, as determined from measurements of linewidth fluctuations [7]. The LER of HSQ was found to be much smaller than that of SAL or ZEP, as was the surface roughness of exposed resists. In fact, the linewidth fluctuations, which indicate the degree of LER, were less than 2 nm (σ) for HSQ patterns, but were 3 nm (σ) or more for ZEP and SAL [2]. So, a resist material that does not spread out much in
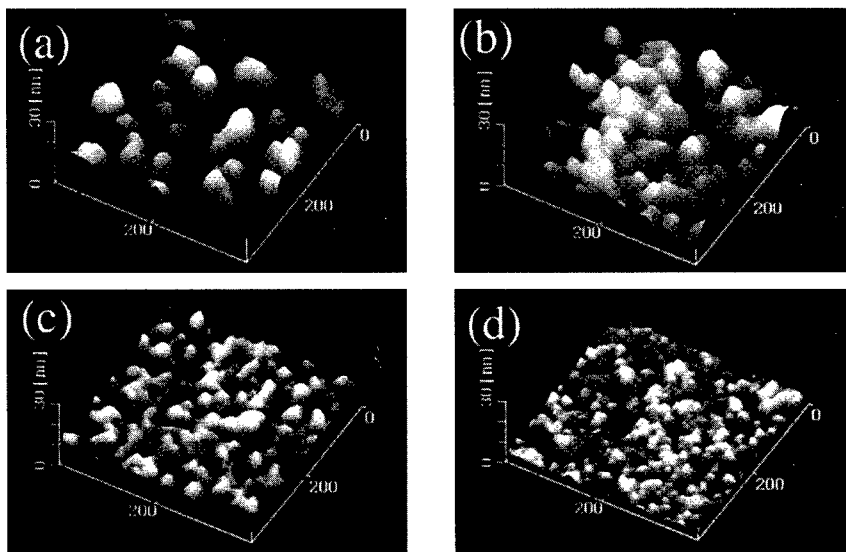
Fig. 10. AFM images of the surface of (a) PMMA film (Mw̄: 8.8 x 10⁵), (b) SAL-610 film (Mw̄: 2.1 x 10⁴), (c) ZEP-520 film (Mw̄: 5.4 x 10⁴) and (d) HSQ film (Mw̄: 1.1 x 10⁴) after exposure to a light dose and development. The remaining thickness of these samples was almost the same.

solution, such as HSQ, provides a small LER because of the small aggregates in the polymer.

2. Resist in which extraction is suppressed

To suppress aggregate extraction itself, it is necessary to reduce the difference in dissolution rate between aggregates and the surrounding polymers. A good way to do this is to induce the formation of giant molecules by cross-linking the aggregates. But care must be taken that the macromolecules are uniform and that the cross-linking does not degrade the resolution. These requirements are satisfied by a resist system with a cross-linker mixed in. This is different from a conventional copolymer-type resist, such as an acrylate-type resist containing glycidyl methacrylate, which employs intramolecular cross-linking.

In this study, ZEP-520 resist, which is an atactic copolymer of methyl α-chloroacrylate and α-methylstyrene, was selected as the base resist. The side chains of the base polymer (i.e. the aromatic rings of ZEP-520) are cross linked by mixing in a cross-linker. The components of the whole system are ZEP-520, cross-linker, and thermal acid generator in a ratio of 10:3:1. The cross-linker is 1,3,5-trimethyl-2,4,6,-(trimethoxymethyl)benzene, and the thermal acid generator is cyclohexylmethyl(2-oxocyclohexyl)sulfonium trifluoromethanesulfonate [5]. The solution was coated on a Si wafer, and cross-linking was induced by baking at 200°C for 2 min. These are the same conditions as those used to pre-bake conventional ZEP-520. In other words, the cross-linking
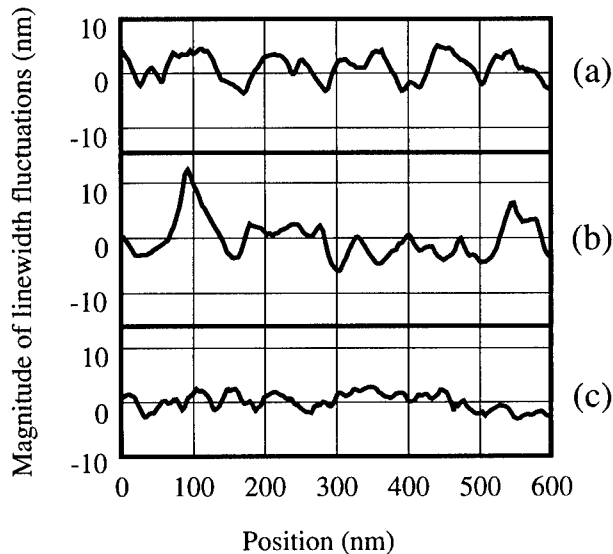
Fig. 11. Linewidth fluctuations of (a) SAL-601, (b) ZEP-520, and (c) HSQ resist patterns. The resist films were exposed to a 70-kV e-beam, and developed in hexyl acetate for ZEP-520 and in an aqueous solution of 2.38% TMAH for SAL-601 and HSQ. The linewidth fluctuations were measured with an AFM in the dynamic-force mode.

reaction is thermally induced in a coated film by a short period of baking before exposure. This is different from a conventional chemically amplified resist system.

Figure 12 shows the surface roughness of conventional and cross-linked resists. It can be seen that cross-linking dramatically reduces the roughness. This is because cross-linking makes aggregates difficult to extract during development. On the other hand, cross-linking also reduces the sensitivity. However, this can be improved by using a strong developer because unexposed areas are not entirely dissolved, even by a strong developer. Figure 13 shows a fine line in cross-linked ZEP. The cross-sectional profile is good and there is no residue. This demonstrates that cross-linking does not adversely affect patterning characteristics. In addition, the linewidth fluctuations are as small as about 2 nm. So, we can produce excellent patterns with a small LER not only by using a resist with small aggregates, but also by using a cross-linked resist.

CONCLUSION

In this study the cause of LER was investigated from the standpoint of resist structure. The major cause was found to be polymer aggregates in resist films. Some aggregates are extracted during development, and those remaining embedded in the pattern side wall cause roughness. There are two approaches to reducing LER. One is to use a resist containing small aggregates, since the
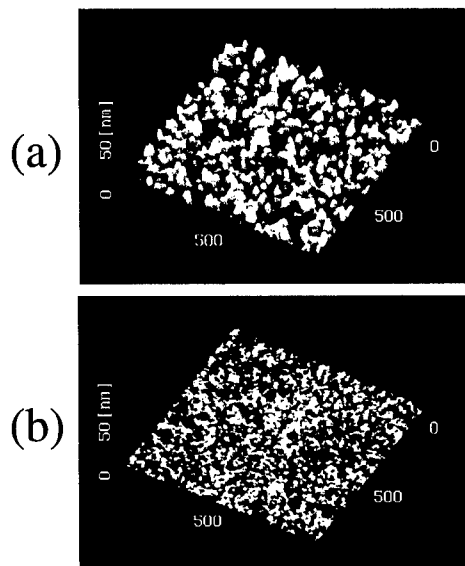
Fig. 12. AFM images of the surface of (a) ZEP-520, and (b) cross-linked ZEP-520 films after exposure to a light dose and development. The remaining thickness of these samples was almost the same.

Fig. 13. SEM image of a cross-linked ZEP-520 pattern. Development was carried out in hexyl acetate.

smaller they are, the less roughness they produce. One good candidate is HSQ resist. Its three-dimensional structure and small molecular weight do not easily allow large aggregates to form through the entanglement of polymer chains. This resist produces negative-tone patterns with a small LER. The other approach is to use a cross-linked resist in which thermally induced cross-linking prior to exposure suppresses aggregate extraction during development, thus reducing rough-

ness. This type of resist produces positive-tone patterns with a small LER.

ACKNOWLEDGMENTS

REFERENCES

1. T. Yamaguchi, H. Namatsu, M. Nagase, K. Yamazaki, and K. Kurihara, Appl. Phys. Let. **71**, 2388 (1997).
2. H. Namatsu, Y. Takahashi, K. Yamazaki, T. Yamaguchi, M. Nagase, and K. Kurihara, J. Vac. Sci. Technol. **B16**, 69 (1998).
3. H. Namatsu, M. Nagase, T. Yamaguchi, K. Yamazaki, and K. Kurihara, J. Vac. Sci. Technol. **B16**, 3315 (1998).
4. T. Yamaguchi, H. Namatsu, M. Nagase, K. Kurihara, and Y. Kawai, *Proceedings of SPIE 24th Annual International Symposium on Microlithography, SantaClara, California, 1999, p. 617.*
5. T. Yamaguchi, H. Namatsu, K. Yamazaki, M. Nagase, and K. Kurihara, Jpn. J. Appl. Phys., *to be published.*
6. H. Namatsu, M. Nagase, K. Kurihara, K. Iwadate, T. Furuta, and K. Murase, J. Vac. Sci. Technol. **B13**, 1473 (1995).
7. M. Nagase, H. Namatsu, K. Kurihara, K. Iwadate, K. Murase, and T. Makino, Microelectron. Eng. **30**, 419 (1996).
8. T. Yamaguchi, H. Namatsu, M. Nagase, K. Yamazaki, and K. Kurihara, *Proceedings of SPIE 23rd Annual International Symposium on Microlithography, Santa Clara, California, 1998, p.830.*
9. C. L. Frye and W. T. Collins, J. Am. Chem. Soc. **92**, 5586 (1970).
10. J. Fujita, Y. Ohnishi, Y. Ochiai, E. Nomura and S. Matsui, J. Vac. Sci,Technol. **B14**, 4272 (1996).

146

A New High Performance CA Resist for E-beam Lithography

Ranee Kwong, Wu-Song Huang, Wayne Moreau, Robert Lang, Christopher Robinson
David R. Medeiros*, Ari Aviram*, Richard C. Guarnieri*, Marie Angelopoulos*

IBM Microelectronics, Hopewell Junction, NY 12533
*IBM Thomas J. Watson Research Center, Yorktown Heights, NY 10598

ABSTRACT

Three major lithographic applications have emerged for electron beam exposure tools: optical mask fabrication, direct writing for device fabrication, and more recently projection e-beam printing. The traditional mask making process uses poly(butenesulfone) resist. A wet etch process was adopted to generate patterns on chrome. Recently, shrinking dimensions, optical proximity correction features, and the complexity of phase shift masks have forced the industry to a chrome dry etch process. ZEP, a poly(methyl α-chloroacrylate-co-α-methylstyrene) based resist, has been well accepted for most of the >180 nm device mask making. The acceptance of ZEP comes in spite of its low contrast, marginal etch resistance, organic solvent development, and concerns of resist heating associated with its high dose requirements. These issues have spawned interest in using chemically amplified resist (CAR) systems for direct write and mask making applications. We have developed a high contrast resist based on ketal protecting groups, KRS-XE, which is robust against airborne contamination and can be used for all forms of e-beam exposure in both chrome mask and silicon processing. This high contrast resist is processed with aqueous base developer and has a wide bake latitude. The development of KRS-XE has provided the capability of fabricating chrome masks for future generation (< 180 nm) devices and has potential for use with projection beam exposure systems.

INTRODUCTION

Although the mass production of silicon devices is based on optical lithography, electron beam lithography (EBL) has been the mainstay of chrome photomask fabrication [1] and is now being considered for next generation lithography (sub-100 nm devices) using projection exposure.[2] The three major applications of electron beam exposure tools in semiconductor lithography are direct writing (DW) of electron beam resists (EBR) on chrome for a 4X photomask manufacture; DW on silicon for custom circuits; and potentially projection electron beam using a 4X silicon membrane scatter mask.[2] To enable performance of all of the EBL strategies, adequate EBR's are needed that satisfy the different requirements associated with each specific product (device or mask) and exposure system. Table 1 outlines some of the desired performance requirements for EBR's.

The evolution of EBR's for Cr mask making has followed pathways that have focused on both the sensitivity and etch resistance. Among the first resists used was poly(butenesulfone), a chain scission (CS) positive-tone resist with a sensitivity of ~3 $\mu C/cm^2$ at 10 kV and was used with wet etching of chrome. For chrome mask fabrication for < 200 nm devices, a dry etch with chlorine/O_2 gas[3] is necessary , and a CS resist based on poly(methyl- α –chloroacrylate -co-α-methylstyrene), ZEP, is now being used at doses [1,4] of 8$\mu C/cm^2$ (10 kV). Despite the acceptance of ZEP, some enhancements are desirable such as higher contrast (> 2)[5], enhanced RIE resistance (< 2 to 1 resist/Cr etch ratio) , and lower dose (< 8 $\mu C/cm^2$ at 10 kV) for better

throughput and minimal heating effects. [6] The use of higher voltage beams to reduce forward scatter of electrons also requires the improvement of resist sensitivity by an order of magnitude relative to 10 kV exposure (< 6 μC/cm^2 at 100 kV).

Table 1 - Desirable Resist Requirements for Electron Beam Lithography (EBL)

EBR Requirement	DW on Silicon	DW on Cr Mask	EB projection on Si
Dose	5 μC/cm^2 at 50 kV	10 μC/cm^2 at 50 kV	5 μC/cm^2 at 100 kV
Resolution	< 100 nm contacts	150 nm L/S	< 100 nm L/S
Contrast	> 5	> 5	> 8
Aspect Ratio	> 5	> 3	> 5
PAB Latitude	> 1 °C	> 2 °C	> 1 °C
PEB Latitude	< 1 nm/°C	< 1 nm/°C	< 1 nm/°C
Adhesion	SiO$_2$, Si$_3$N$_4$, polySi	Cr	SiO$_2$, Si$_3$N$_4$, polySi
Developer	Aqueous Base	Aqueous Base	Aqueous Base
Shelf Life Dried Film	None	> 3 month	None
Reactive Ion Resist	Etch rate = SiO$_2$	Etch Rate = Cr	Etch Rate = SiO$_2$
Amine Tolerability	ppm level	ppm level	ppm level

Since reactive ion etching is key to finer resolution, more etch resistant resists would allow mask fabrication to proceed with thinner films and obviate the need for GHOST proximity corrections.[5] In GHOST, a positive resist is flood exposed (at 40 % dose) after the primary exposure. Considerable loss of the image can result with resists of contrast < 3.

Higher sensitivity resists could also reduce any beam-substrate heating effects, of particular concern when writing chrome on quartz substrates with vector scan EB tools.[6] For advanced electron beam projection tools a high sensitivity resist (5 μC/cm^2 at 100 kV) is necessary to sustain sufficient throughput. [7,8] In addition, for the photomask fabricator, a good shelf life of precoated resist plates are essential for both quality and cost factors. A resist that could work equally well on chrome or silicon would be desirable.

Traditionally, resists were based on the interaction of the comprising matter with radiation capable of directly breaking chemical bonds, as in the CS-resists outlined previously or in the conventional DNQ/Novolak systems. Since a typical optical resist of this type has a quantum efficiency of < 0.1, it was necessary to introduce a greater number of photons (10^{18}/cm^2) than the number of resist molecules present (10^{17}/cm^2). [9] Subsequently, chemically amplified resists (CAR's) based on catalytic deprotection, such as the acid catalyzed deprotection of poly(t-BOC-styrene) to base soluble poly(hydroxystyrene), resulted in a gain of this ratio by ~10^3. [10] Thus, inherent higher sensitivity can be obtained if sufficient acid is formed in the resist at a lower dose and the resist is then heated to provide the required activation energy of deprotection. In addition CAR's can provide higher resolution and higher sensitivity due to the increased dissolution rates of the exposed resist in aqueous base. However, several process factors have required specialized conditions to implement these resists into device or photomask manufacturing. These include:

- Environmental sensitivity to ppb levels of airborne base or to basic substrates that neutralize the acid generated during exposure.[11] Many commercial CAR's are still susceptible to ppb levels of amines.
- Poor storage life of precoated films on chrome mask plates (< 1 week).[12]

- Performance variation caused by inadequate temperature control in post-apply bake (PAB) and, moreover, in post-exposure bake (PEB). Control of < +/- 0.5 °C across the wafer or, in particular, the photomask plate. [13]   A PEB < 100 °C is also desirable for better heating control across the hotplate.
- Potential for outgassing of exposure-generated acid or deprotection products in a vacuum environment even at room temperature. [14]
- Pattern collapse of resist features with aspect ratios > 3 (thickness/line width) after development in aqueous system caused by high surface tension of rinse water. [15]

   With these considerations in mind, we are developing a CAR that will meet the demanding requirements of the various EBL strategies. Our primary focus is resist development for advanced mask making, however, the materials that we have developed show promise for projection exposure as well.

EXPERIMENTAL

   The matrix polymer in KRS-XE is based on the partial protection of poly(hydroxystyrene) with an acid sensitive ketal group of low volatility. Monodisperse poly(hydroxystyrene) was partially protected with a vinyl ether to form the ketal, as shown below.

A triphenylsulfonium salt (TPS$^+$A$^-$) was used as the acid generator and propyleneglycol methyl ether acetate (PMA) as the casting solvent. The developer used was 0.263N tetramethyl-ammonium hydroxide (TMAH). Films were PAB and PEB at 75-125 °C to study line width and
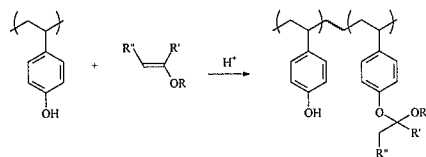
environmental sensitivity. Exposure was done using a vector scan, e-beam direct write tool on silicon wafers pretreated with HMDS or alternatively on chrome on glass mask blanks. Full field electron beam exposures were also done using a silicon membrane mask. A mixture of Cl$_2$ and O$_2$ was employed for the reactive ion etching of resist/chrome.

RESULTS and DISCUSSION

   The first phase for EBR design or evaluation was directed toward establishing the two primary targets of sensitivity and resolution. The initial evaluation of the contrast and dose to clear, shown in Figure 1, relative to ZEP mask making resist was performed to ascertain the suitability of the resist for "GHOST" flood proximity correction. If such a correction is applied to ZEP at 40 % of dose to clear about 35 % of the resist image would be removed. In contrast, KRS-XE resist could tolerate 40 % background dose without thinning. The sensitivity was also enhanced fourfold from 40 µC/cm^2 to 10 µC/cm^2 at 50 kV.
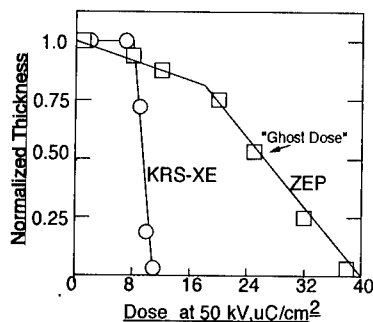
Figure 1- Contrast of KRS-XE and ZEP
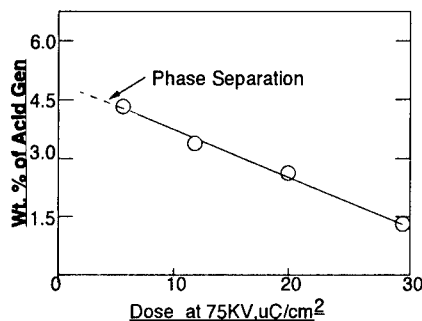
Figure 2- Effect of Acid Generator Loading on Dose

The inherent sensitivity of KRS-XE resist depends on the amount of energy absorbed by the protected phenolic polymer (POR) and/or the acid generator (AG). The acid could be formed indirectly as in steps (1) - (3) below or directly from excited AG as in step (4).

$$POR \rightarrow POR^* \qquad (1)$$
$$POR^* + AG \rightarrow AG^* \qquad (2)$$
$$AG^* \rightarrow Acid \qquad (3)$$
$$AG \rightarrow AG^* \rightarrow Acid \qquad (4)$$
$$Acid + POR \rightarrow POH + R + Acid \qquad (5)$$
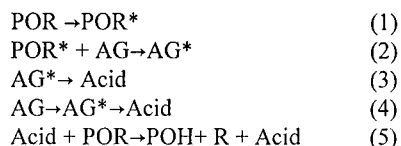
Once a given amount of acid is formed, i.e., the quantum yield of this photoprocess, the catalytic deprotection chain length of step 5 determines the final sensitivity.[16] The initial acid generator loading of 1 wt-% was increased to solubility limit of 5 wt-% and the corresponding dose was lowered to the 3-5 $\mu C/cm^2$ range, as in Figure 2. This indicates that a fast resist system is potentially available with a sensitivity of 1-5 $\mu C/cm^2$ over the 10-100 kV range. Current work is focusing on selection of the most efficient acid generators that are fully miscible with these polymers.

The high contrast (> 10) of KRS-XE implies high resolution. Figure 3 shows 100 nm L/S printed by scan exposure on a chrome mask. Figure 4 shows the resolution capabilities of this resist upon projection e-beam exposure on a silicon wafer.[7] The high surface tension of rinse water has the effect of "pushing on the walls" of the resist and can result in image collapse.[15] By adding a surfactant to the water, surface tension is decreased and images with an aspect ratio as high as 6 were achieved.
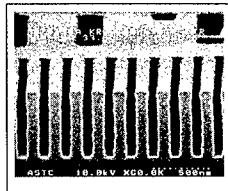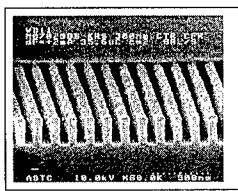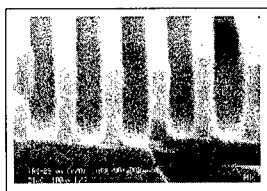
(a)   (b)

Figure 3: KRS-XE, 100 nm L/S on Cr   Figure 4: (a) 80 nm in 300 nm; (b) 100 nm in 600 nm KRS-XE.

Although a resist may be of high sensitivity and resolution, the robustness of the processing of the resist involves the practical considerations for users in various lithographic applications. For example, chrome mask fabrication has a lower resolution requirement at 4X circuit dimensions, but the thermal processing of PAB and PEB become more difficult due to the large mass of the quartz blank and poor hot plate uniformity.[4] To test the PAB latitude, the line width and dose to print were examined, as shown in Figure 5. Both were found to be very tolerant of heating effects. Line width varied by <1.0 nm/°C during PAB. Similarly, during the PEB process, the line width was also found to exhibit < 1.0 nm /°C variation over the same temperature range.

After exposure in the high vacuum of an e-beam exposure chamber and removal to an ambient environment, KRS-XE resist can absorb water and undergo a rapid deprotection reaction. The acidolysis reaction, shown below, is believed to be essentially over before the plate comes to thermal equilibrium. Likewise, during PEB the resist is tolerant of the absorption of amines (ppm level) from the atmosphere since conversion is over before any infusion of the acid
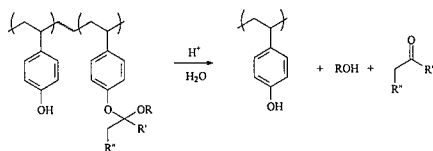
quencher can take place.

Examination of the relative RIE resistance of the film is of great importance since resist films thinner than currently used 350 nm of ZEP may possibly be used to minimize proximity effects. This is especially true for the etching of chrome in mask making. Table 2 shows a comparison of the relative etch rates of ZEP, KRS-XE, and a standard DNQ/Novolak resist for both Cr and SiO_2 type etching. The KRS-XE resist which has a higher aromatic content than the currently employed ZEP exhibits a 25 % reduction in etch resistance.

Table 2- Relative Etch Rate(ER) of Resist to Cr or SiO_2 Films		
Resist	Cl_2/O_2 ER rel. to Cr	CF_4 ER rel. to SiO_2
ZEP	2.2	1.5
KRS-XE	1.7	1.3
I Line Novolak	1.2	1.1

For mask making applications, a durable dried film that can be processed as precoated plates is desirable from a quality viewpoint. In normal resist processing a resist has to be stable for only a few minutes after PAB and PEB since wafers are continuously coated and used. The shelf life of the film of KRS-XE resist will depend on the stability of the acid generator and susceptibility of the weakest bond in the protecting group attached to the backbone phenolic polymer. The suspect agents that can deteriorate a stored plate include the absorption of water or acidic species, for example SO_2 or NO absorbed from air. These agents may participate in the final latent image acidolysis chemistry. To examine these phenomena, films of KRS-XE were stored under different relative humidity. As shown in Figure 6, dried films of this resist were found to be susceptible to hydrolytic attack. However, when stored in a sealed, dry system, the films were stable to at least 3 months. Additionally, it was found that films cast from hydrophilic ethyl lactate readily absorbed water, while PMA cast films were much less susceptible.[17] Work is continuing to examine the effects of hydrolytically stable acid generators and hydrophobic solvents to minimize or eliminate dark hydrolysis reactions.
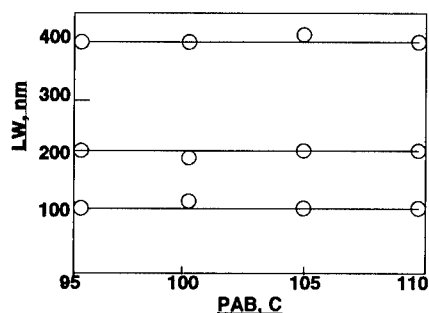
Figure 5- PAB vs. Linewidth for KRS-XE
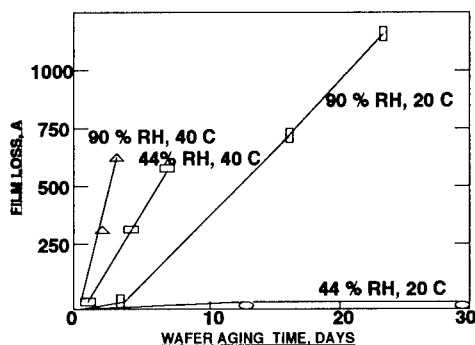
Figure 6- Effect of Humidity on Storage of KRS-XE

SUMMARY

As has been shown for optical lithography, chemically amplified resists based on acid catalysis offer major advantages over chain scission type resist on the basis of higher resolution, high sensitivity, high contrast, and good etch resistance for EBL as well. High resolution imaging with large process latitude have been demonstrated. Optimization of KRS-XE resist, with detailed attention paid to assuring wide PAB and PEB latitude, has afforded a resist system suitable for both mask or wafer lithography and is developable in aqueous base. Insensitivity of the resist during PEB to airborne contaminants allow processing in laboratory conditions. The long term storage of the cast films requires low humidity conditions.

The continued design of higher kV tools will require enhanced resist sensitivity for higher throughput and to minimize beam heating effects. Additionally, new developer schemes to overcome image collapse and improve the aspect ratio for nanometer images need to be considered.

REFERENCES

1. M. Lui, T. Coleman, C. Sauer, Proc. SPIE 3546, 98 (1998).

2. S. Stanton, J. Lidddle. W. Waskiewiscz, and A. Novembre, J. Vac. Sci. and Tech. B16, 3197 (1998).

3. K. Kwon, S. Kang, S. Park, H. Sung, D. Kim, and J. Moon, J. Materials Science, Letters 18, 1197 (1999).

4. T. Nishida, Jap. J. Appl. Phys. 31, 4508 (1992).

5. B. Cha, J. Kim, B. Kim, S. Choi, H. Yoon, and J. Soon, Proc. SPIE 3546, 55 (1998).

6. S. Babin, Proc. SPIE 3546, 389 (1998).

7. (a) W. Wasiewicz, L. Harriott, J. Liddle, S. Stanton, S. Berger, E. Munron, and X. Zhu, Microelectronic Engineering 41, 215 (1998). (b) M. Sato, K. Ohmori, K. Ishikawa, T. Nakayama, A. Novembre, and L. Ocola, Proc. SPIE 3676, 227 (1999).

8. H. Pfeiffer, et al., J. Vac. Sci. and Tech., to be published, (1999).

9. W. Moreau, *Semiconductor Lithography*, Plenum Press, 1989, pg. 34.

10. H. Ito and C. Willson, Polymer Eng and Sci. 23, 1012 (1983).

11. W. Hinsberg, S. McDonald, N. Clecak and C. Snyder, Proc. SPIE 1672, 24 (1992)

12. M. Arai, Proc. SPIE 2512, 74 (1995).

13. D. Seeger, Solid State Technology, June 1997, p.115.

14. O. Nalamasu, F. Houlihan, R. Cirelli, A.Timko, G. Watson, R. Hutton, J. Kometani, E. Reichmanis, A. Gabor, A. Medina, and S. Slater, J. Vac. Sci. and Tech. B16, 3716 (1998).

15. T.Tanaka, M. Morigami, and N. Atoda, Jap. J. Appl. Phys. 32, 12B, 6059 (1993).

16. T.Sakamizu,H. Yamaguchi, H. Shirashi, F. Murai, T. Ueno, J. Vac. Sci. and Tech. B11, 2812 (1993).

17. H. Ito and M. Sherwood, J. Photopolymer Sci.12, 625 (1999).

DIFFUSION AND DISTRIBUTION OF PHOTOACID GENERATORS IN THIN POLYMER FILMS

QINGHUANG LIN*, MARIE ANGELOPOULOS*, KATHERINA BABICH*, DAVID MEDEIROS*,
NARAYAN SUNDARARAJAN[+], GINA WEIBEL[+], CHRISTOPHER OBER[+]
* IBM T. J. Watson Research Center, P.O. Box 218, Yorktown Heights, NY 10598, qhlin@us.ibm.com
[+] Department of Materials Science and Engineering, Cornell University, 327 Bard Hall, Ithaca, NY 14853

ABSTRACT

Distribution and diffusion of two fluorinated ionic photoacid generators (PAGs) in thin polymer films have been investigated by depth profiling of the intrinsic label elements of both the PAGs and a silicon containing carrier polymer with Rutherford Backscattering Spectrometry (RBS) and dynamic Secondary Ion Mass Spectroscopy (SIMS). Distribution and diffusion of the PAGs in a bilayer film stack, which consists of a thin silicon containing polymer film on top of a thick thermally cross-linked Novolak film on a silicon substrate, have been studied as a function of the Novolak cross-linking temperature. Deposition of the PAG containing polymer films on top of the cross-linked Novolak films by spin coating results in an interphase with enriched PAG. Subsequent annealing of the film stack causes expansion of the interphase and diffusion of the PAG into the underlying Novolak film when Novolak is cross-linked at lower temperatures. On the other hand, there is a uniform PAG distribution and no detectable diffusion of the PAG into Novolak when it is cross-linked at high temperatures. The variations in the PAG distribution and diffusion are attributed to the changes in the chemical and physical properties of Novolak during cross-linking.

INTRODUCTION

Chemically amplified resist films generally contain certain amounts of small molecules, such as photoacid generators (PAGs), exposure-generated acids, dissolution inhibitors, base additives, and residual solvents in a polymer matrix. Distribution and diffusion of these small molecules in the resist films play important roles in the performance and stability of these resists as well as the quality of the resultant resist images [1]. Control of PAG distribution with block copolymers has been shown to improve resolution and image quality of a 193nm resist [2]. Diffusion of exposure-generated acids has been linked to resist sensitivity, resolution, image profile, as well as the stability of chemically amplified resists to basic contaminants [1,3-5]. Excessive acid diffusion is viewed to be a limiting factor to the ultimate resolution capability of chemically amplified resists [6,7].

Several techniques have been employed to probe acid diffusion in chemically amplified resists, including measurements of resist line width changes [8,9], ion conductivity measurements [10], quartz crystal microbalance measurements of acid absorption [11], fluorescence sensing technique[12], FTIR measurements of the deprotection of an acid sensitive detection polymer [6,13]. While valuable information has been extracted, these techniques are all indirect measurement methods. The acid diffusion in these measurements is convoluted with the photochemistry of the PAGs, resist reaction kinetics, and dissolution process. Moreover, the very useful concentration profiles are not readily attainable using these techniques.

The group at IBM has been developing a high performance chemically amplified bilayer resist for extension of 248nm optical lithography [14,15]. In this bilayer process, fine resist features are first delineated with a thin silicon containing top layer over a thick, planarizing organic underlayer. The images thus formed are then transferred into the underlayer through O_2-containing reactive ion etching (RIE). The IBM group has found that the underlayer material and its processing conditions greatly influenced the resolution and the image quality of the top layer resist. Clean, high resolution images were only attainable using certain underlayer materials and/or under certain processing conditions. The underlying mechanism was not clear.

The objectives of this work were to determine PAG distribution and diffusion in this bilayer system and to understand the mechanism of the varied lithographic performance on different underlayers. To this end, a bilayer system of a thin silicon containing polymer film over a thick thermally cross-linked Novolak film was chosen as a model system. The silicon containing polymer was a 80/20 copolymer of p-hydroxystyrene and tris(trimethylsilyl)silylethyl methacrylate. Direct measurements of the spatial distribution and diffusion of two fluorinated ionic PAGs were conducted by depth profiling of the intrinsic label elements of the PAGs with Rutherford Backscattering Spectrometry (RBS) and dynamic Secondary Ion Mass Spectroscopy (SIMS). Diffusion of the PAGs into the underlying thermally cross-linked Novolak films has been investigated as a function of the Novolak cross-linking temperature. The effects of changes in chemical and physical properties of Novolak during curing on the PAG distribution and diffusion are discussed.

EXPERIMENT

Materials

The silicon containing polymer for the top layer resist was an 80/20 copolymer of p-hydroxystyrene and tris(trimethylsilyl)silylethyl methacrylate (Si copolymer). It was synthesized by solution free radical polymerization [15]. Novolak was chosen for the underlayer. The photoacid generators used were di(t-butylphenyl) iodonium triflate (tBIT) and di(t-butylphenyl) iodonium perfluorooctane sulfonate (PFOS) (Scheme 1). The casting solvent was propylene glycol monomethyl ether acetate (PGMEA). Molecular weight (GPC) and bulk glass transition temperatures of the Si copolymer and Novolak are listed in Table 1.
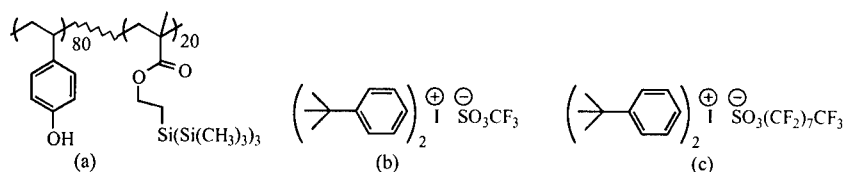
Scheme 1. The silicon containing polymer and PAGs used in this study. (a) Si copolymer; (b) tBIT; (c) PFOS

Table 1. Physical Properties of the Polymers Used in This Study

Polymer	M_n	M_w	M_w / M_n	T_g (°C)
Si copolymer	4400	7300	1.65	146
Novolak	1700	12100	7.03	98

Sample Preparation

Thin films of the top layer resist containing tBIT or PFOS were prepared by spin coating a 10wt% or 25wt% Si copolymer solution (with 5wt% or 20wt% PAG) on an appropriate substrate at 2000 rpm on a Headway spin coater. The substrates used for PAG distribution studies were silicon, carbon, or hard baked Novolak. The Novolak substrate was prepared by spin coating a 20wt% Novolak solution at 3000 rpm on a Si wafer followed by baking on a hot plate at various temperatures for 2min. For diffusion study, the bilayer film stack was annealed at 140°C for 5min. Unless otherwise specified, the nominal film thickness for the Si copolymer and Novolak was about 250nm and 700nm, respectively.

Characterizations

SIMS: Dynamic SIMS analysis was conducted on a Cameca IMS-5F ion microanalyzer with Cs+ as the primary ion and negative secondary ions of C, O, F, Si and I detected. To reduce charging effect, a thin layer of carbon was coated on the samples prior to measurements. Charge compensation was provided by an electron beam. Secondary ions were detected from the central part of the crater.

RBS: RBS measurements were performed at Cornell Ion Beam Analysis Lab. The heavy elements of I and Si were used as intrinsic labels for the PAG and the Si copolymer, respectively, during depth profiling. Detailed RBS experimental procedures are described elsewhere [16].

Others: FTIR spectra were collected on a Nicolet Magna 760 spectrometer equipped with a hot plate and an external noncontact reflectance attachment from Axiom Analytical Inc. Glass transition temperatures were determined with a TA 2920 Modulated DSC. The glass transition temperatures were taken from the reversible heat flow curves during the first heating runs. Film thickness was measured with an n & k analyzer from N & K Instrument.

RESULTS AND DISCUSSION

Distribution of PAGs in Polymer Thin Films

The spatial distribution of the two fluorinated ionic PAGs, di(t-butylphenyl) iodonium triflate (tBIT) and di(t-butylphenyl) iodonium perfluoro octane sulfonate (PFOS), in the Si copolymer film has been found to depend heavily on the nature of the substrate. A uniform distribution of tBIT and PFOS has been observed throughout the Si copolymer films on silicon or carbon substrates as well as Novolak films hard baked at elevated temperatures.

Figure 1 shows RBS spectra of a Si copolymer film containing 5wt% PFOS on a carbon substrate before and after exposure to a 248nm DUV light at a dose of 50mJ/cm^2. Here a thick Si copolymer film is used to achieve a better PAG concentration profile. In the spectra, the highest and the lowest channel numbers correspond to the polymer film/air interface and the polymer film/substrate interface, respectively, for a given element. As can be seen in Figure 1, the concentration of PFOS as indicated by the back scattered iodonium (I) ion yield is virtually constant throughout the polymer film. This iodonium ion yield also exhibits an almost constant value throughout the polymer film after exposure to a 248nm DUV light at a dose of 50mJ/cm^2. The absolute value of the I concentration decreases significantly after exposure presumably due to the evaporation of I containing photo products during exposure. Similar results were obtained in Si copolymer films containing the tBIT PAG on silicon and carbon substrates.
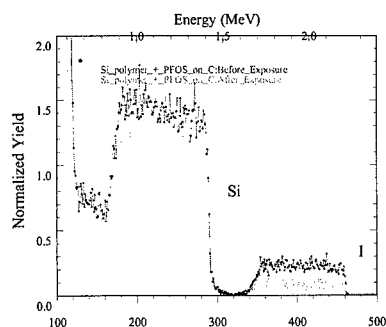
Figure 1. RBS spectra of a Si copolymer film containing 5wt% PFOS PAG on a carbon substrate before and after 248nm DUV exposure
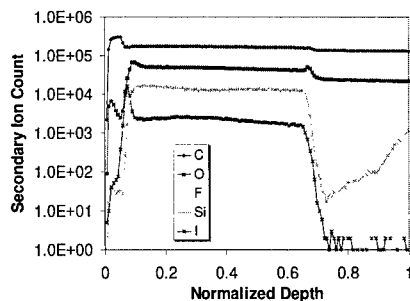
Figure 2. Dynamic SIMS spectra of Si copolymer film containing 5wt% tBIT on Novolak hard baked at 250°C for for 2 min.

The distribution of the fluorinated ionic PAGs in the Si copolymer film on a hard baked Novolak substrate shows an intricate dependence on Novolak baking temperature. At high baking temperatures, the PAG is distributed uniformly throughout the Si copolymer films. On the other hand, at low baking temperatures, the PAG shows a preferential segregation to the Si copolymer and Novolak interface, resulting in an intermediate layer with enriched PAG. Figure 2 depicts dynamic SIMS depth profiling of C, O, F, Si and I elements in the bilayer film stack (Si copolymer film containing 5wt% tBIT on top of a Novolak film hard baked at 250°C for 2min). Here F and I elements are used as labels for the tBIT PAG and Si is used as a label for the Si copolymer matrix. A bilayer structure can be easily observed in the SIMS spectra with a top layer rich in Si copolymer and the PAG. Within the top layer, the distribution of tBIT is essentially uniform. Moreover, the concentration profiles of Si, F and I are quite sharp at the Si copolymer and Novolak interface. This indicates that there is no major inter-mixing of the two polymers during spin coating. The noisy signals at the air and Si copolymer interface are due to the protective carbon coating.

The fluorinated ionic PAGs tend to aggregate to the Si copolymer and Novolak interface when Novolak is baked at lower temperatures (≤215°C). Figure 3 shows SIMS and RBS spectra of the Si copolymer film containing 5wt% tBIT on top of a Novolak film hard baked at 210°C for 2min. It is seen that spin coating Si copolymer film on top of the Novolak film results in a thin interphase between the Si copolymer and the Novolak film. This interphase contains a higher concentration of tBIT and a corresponding lower concentration of Si than those in the Si copolymer layer. These concentration profiles suggest that this interphase form through the migration of tBIT to the Si copolymer and Novolak interface during spin coating. The concentration profiles of Si, F and I elements are fairly sharp at the Novolak interface, again indicating no major intermixing of the Si copolymer and the hard baked Novolak.

The formation of the tBIT PAG enriched interphase was confirmed with RBS measurements (for Si copolymer containing 5wt% tBIT on Novolak baked at 210°C for 2min) (Figure 3b). The PAG enriched interphase can be clearly seen in the depth profiling of I element.
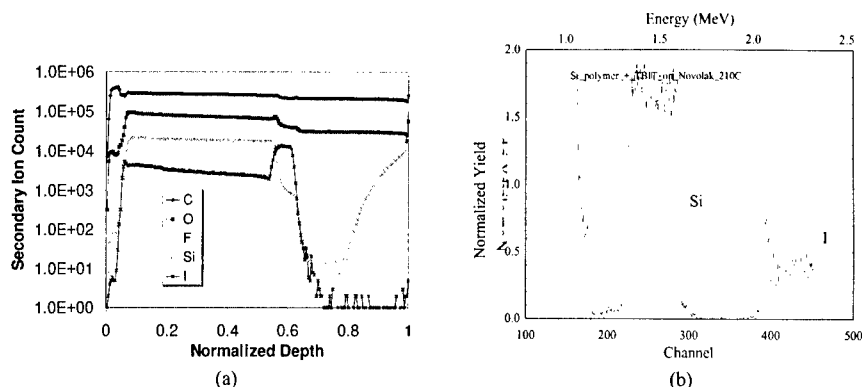
Figure 3. SIMS and RBS spectra of tBIT in a Si copolymer film over a Novolak film baked at 210°C for 2min, showing formation of a PAG enriched interphase.

In summary, both RBS and dynamic SIMS measurements showed that deposition of the Si copolymer films containing the tBIT PAG on top of the cross-linked Novolak film by spin coating results in an interphase with enriched tBIT when Novolak is hard baked at lower temperatures. On the other hand, a uniform spatial distribution of tBIT is found in the Si copolymer film when Novolak is baked at a higher temperature.

The distribution of PAGs in thin resist films is determined mainly by the interaction of PAG with the polymer matrix and interfacial energies at the two interfaces. A good polarity match of the PAG and polymer matrix, for example a polar PAG in a hydrophilic polymer matrix or a non-polar PAG in a hydrophobic polymer matrix, can lead to miscibility of the PAG and the polymer matrix. As a result, a uniform distribution of the PAG in the polymer matrix ensues. On the other hand, any mismatch of the polarities can cause microphase separation of the PAG and the polymer [2,3,17].

Another factor driving PAG distribution is the interfacial energy at the two interfaces of thin resist films. Consequently, the polarity of the substrates relative to those of the base polymer and the PAG becomes important. It is reasonable to expect that a hydrophilic substrate may attract a polar PAG from a relatively less hydrophilic polymer matrix to its interface. To evaluate the polarity change of Novolak substrate during curing, time resolved FTIR spectra were collected for Novolak hard baked at 230°C. The results shown in Figure 4 indicate a gradual decrease in the OH peak intensity and a corresponding increase in C=O peak intensity. These results suggest a change from a hydrophilic polymer to a less hydrophilic cross-linked network during hard baking, presumably due to the oxidation of the phenolic groups to less polar quinoidol groups. In the bilayer system, the virgin Novolak polymer bears a polar OH group and hence is more hydrophilic than the Si copolymer which has a bulky, highly hydrophobic tris(trimethylsilyl) silylethyl methacrylate comonomer. Therefore the uncured Novolak is expected to have a propensity to attract the polar ionic tBIT PAG from the hydrophobic Si copolymer matrix. The difference in the tBIT PAG distribution in the Si copolymer films on different Novolak substrates is then ascribed to the decrease in hydrophilicity of Novolak substrate during curing.
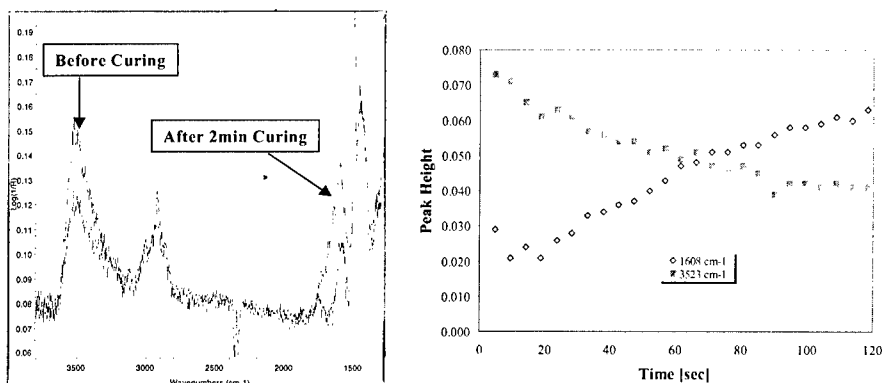
Figure 4. Time resolved FTIR results of Novolak cured at 230°C, showing a decrease in OH peak intensity and a corresponding increase in C=O peak intensity

158

Diffusion of PAGs in Polymer Thin Films

The cross-linking temperature of Novolak influences not only the spatial distribution of the fluorinated ionic PAG in Si copolymer films but also the diffusion of the PAG into the underlying Novolak film. When Novolak is baked at lower temperatures, annealing of the bilayer film stack at a temperature near the bulk glass transition temperature of the Si copolymer causes the expansion of the interphase at the expense of the Novolak film. Moreover, it also results in the diffusion of the PAG into the Novolak underlayer. When Novolak is baked at a higher temperature, there is not detectable change in the concentration profile of the PAG. Figure 5 depicts RBS depth profiling of I and Si elements in the bilayer film stack after annealing at 140°C for 5min. A significant difference in the concentration profiles of the I and Si elements is noted for a baking temperature of 220°C and the other two temperatures (210°C and 215°C). The tBIT PAG exhibits an essentially constant concentration profile in the Si copolymer film for the Novolak baked at 220°C. On the other hand, there exists a significant PAG enrichment at the bilayer interface for the Novolak baked at the lower temperatures. Furthermore, the PAG concentration profile broadens as Novolak baking temperature is decreased. The Si copolymer film also undergoes expansion during the annealing as indicated by the Si concentration profile. However, the extent of Si copolymer expansion is less than that of the PAG concentration profile. This implies that PAG diffuses into the Novolak film with the aid of Si copolymer film expansion.
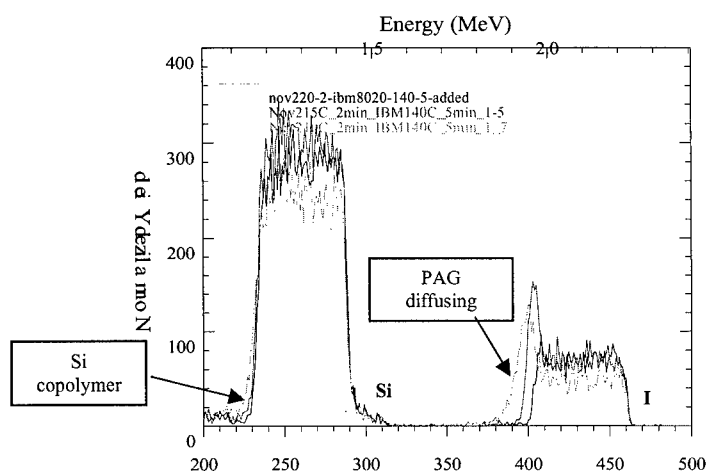
Figure 5. RBS depth profiling of I and Si elements in the bilayer film stack after annealing at 140°C for 5min. Novolak was baked at 210°C, 215°C, and 220°C for 2min.

This expansion of the Si copolymer film and diffusion of the PAG into Novolak has been confirmed with dynamic SIMS depth profiling of Si element for the Si copolymer and F and I elements for the tBIT PAG. Figures 6 and 7 show the effects of Novolak baking temperature on the F concentration profiles in the bilayer film stack before and after annealing at 140°C for 5min. The dramatic difference in the effects of Novolak baking temperature on tBIT diffusion is clearly seen. There is no significant concentration profile change for both the tBIT PAG and the Si copolymer matrix when Novolak is baked at a high temperature of 250°C for 2min. The slight decrease in Si copolymer film thickness is due to film densification during annealing. In sharp contrast, tBIT concentration profile shows an expanded interphase and diffusion into the Novolak film with a shallower concentration profile at the bilayer interface when Novolak is baked at a low temperature of 210°C for 2min. The expansion of the PAG concentration within the interphase is aided by the expansion of the Si copolymer film itself (Figure 7). There is no noticeable diffusion of the Si copolymer into Novolak. These results are consistent with the RBS observations.
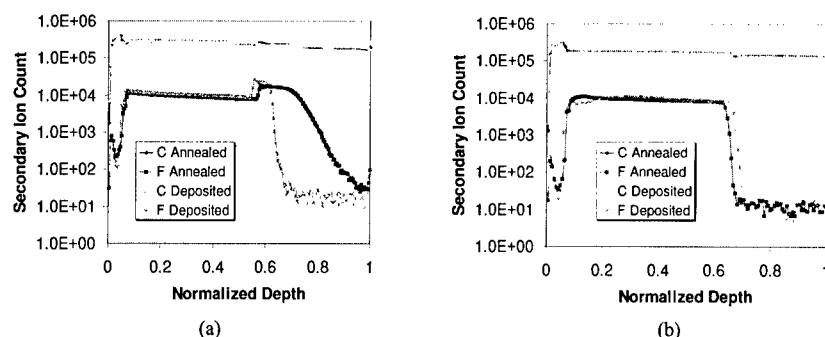
Figure 6. F concentration profile after annealing at 140°C for 5min in Si copolymer film containing tBIT on Novolak baked at 210°C (a) and 250°C (b) for 2min., showing the effect on Novolak baking on tBIT diffusion
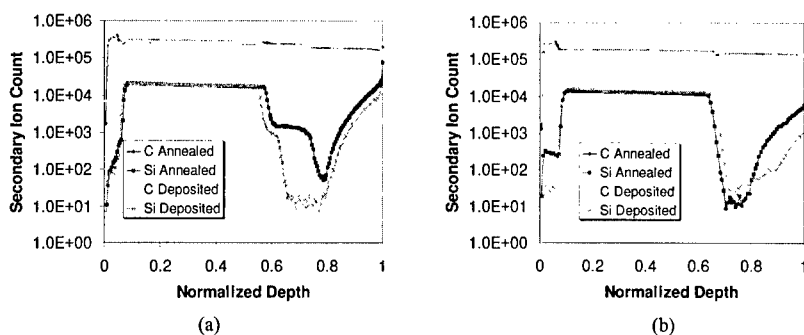
Figure 7. SIMS depth profiling of Si in Si copolymer film containing tBIT on Novolak baked at 210°C (a) and 250°C (b) for 2 min, showing expansion of the tBIT rich interphase for Novolak baked at 210°C

Tracer diffusion in a glassy polymer is determined in large part by the diffusion temperature relative to the glass transition temperature (T_g) of the polymer. At temperatures above T_g, diffusion of a small molecule is facilitated by the segmental motion of the glassy polymer in the rubbery state. Therefore, higher diffusion coefficients result. On the other hand, at temperatures below T_g, the small molecule diffuses by hopping from one void site (free volume) to another. Therefore, the amount of free volume in the glassy polymer becomes important to the diffusion in a glassy state. The diffusion coefficients of a small molecule in the glassy state are generally several orders of magnitude lower than those in the rubbery state for a given polymer [18].

To understand the microstructure evolution of Novolak during curing, the T_g of Novolak hard baked on silicon wafers at various temperatures was determined by modulated DSC. The T_g of the cross-linked Novolak was derived from the reversible heat flow during the first DSC heating runs. The results are tabulated in Table 2. As expected, hard baking Novolak leads to an increase in T_g due to thermally induced cross-linking. A higher baking temperature results in a higher T_g of the cured Novolak. The T_g of the Novolak cured at 250°C is at least 30°C higher than that cured at 210°C. The higher T_g of the Novolak cured at 250°C probably accounts for much of the less tBIT diffusion.

Table 2. Glass Transition Temperatures of Novolak Cured at Various Temperatures for 2 min.

Bake Temperature (°C)	None	170	190	210	230
T_g of Cured Novolak(°C)	98	129	138	170	>200

The glass transition temperatures of the Novolak cured at 210°C and 250°C are both higher than the annealing temperature. Any diffusion of the tBIT PAG into Novolak must have occurred in the glassy state of the cured Novolak. To estimate free volume change of Novolak during curing, we have determined the Novolak film thickness changes under various hard bake temperatures. The results are plotted in Figure 8. As expected, cross-

linking Novolak during hard baking gives rise to densification of the polymer film. Therefore, a high hard bake temperature of 250°C leads to a film with less free volume and hence less diffusion of the PAG into the film.
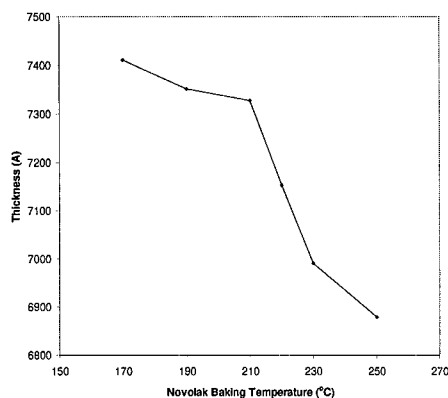
Figure 8. Novolak film thickness after curing at various temperatures for 2 min

SUMMARY

Distribution and diffusion of two fluorinated ionic photoacid generators (PAGs) in a silicon containing methacrylate copolymer have been found to be highly dependent on the nature and the processing conditions of the substrate by depth profiling of the intrinsic label elements of the PAG with Rutherford Backscattering Spectrometry (RBS) and dynamic Secondary Ion Mass Spectroscopy (SIMS). The polar PAGs are distributed uniformly throughout the Si copolymer film on hydrophobic carbon substrate or Novolak hard baked at higher temperatures. On the other hand, when Novolak is cross-linked at lower temperatures, deposition of the PAG containing polymer films on top of the cross-linked Novolak films by spin coating results in an interphase with enriched PAG. Subsequent annealing of the film stack causes expansion of the interphase and diffusion of the PAG into the underlying Novolak film. This diffusion is attributed to lower glass transition temperatures and less densification of the Novolak films at the lower curing temperatures.

ACKNOWLEDGEMENTS

REFERENCES

[1] G. M. Wallraff and W. Hinsberg, Chem. Rev. **99**, 1801-1821 (1999).

[2] N. Sundararajan, K. Ogino, S. Valiyaveettil *et al.*, Proc. SPIE **3678**, 78-85 (1999).

[3] D. R. McKean, R. D. Allen, P. H. Kasai *et al.*, Proc. SPIE **1672**, 94-103 (1992).

[4] H. Ito, G. Breyta, D. Hofer *et al.*, J. Photopolym. Sci. Technol. **7**, 433-448 (1994).

[5] T. Itani, H. Yoshino, M. Fujimoto *et al.*, J. Vac. Sci. Technolo. B **16** (6), 3026-3029 (1995).

[6] M. D. Stewart, S. V. Postnikov, H-V. Tran *et al.*, Polym. Mater. Sci. Eng. **81**, 58 (1999).

[7] S. V. Postnikov, M. D. Stewart, H. V. Tran *et al.*, J. Vac. Sci. Technol. B **to appear** (1999).

[8] L. Schlegel, T. Ueno, Hayashi *et al.*, J. Vac. Sci. Technol. **9**, 278 (1991).

[9] M. F. Cronin, M. Adams, T. Fedynyshyn *et al.*, Proc. SPIE **2195**, 214 (1994).

[10] T. Itani, H. Yoshino, S. Hashimoto *et al.*, J. Vac. Sci. Technol. B **14** (6), 4226-8 (1996).

[11] K. E. Mueller, W. J. Koros, C. A. Mack *et al.*, Proc. SPIE **4039**, 706-711 (1997).

[12]P. L. Zhang, A. A. Eckert, C. G. Willson *et al.*, Proc. SPIE **3049**, 898-909 (1997).

[13]G. M. Wallraff, W. D. Hinsberg, F. A. Houle *et al.*, Proc. SPIE **3678**, 138-148 (1999).

[14]Q. Lin, K.E. Petrillo, K. Babich *et al.*, Proc. SPIE **3678**, 241-250 (1999).

[15]R. Sooriyakumaran, G. M. Wallraff, J. Opitz *et al.*, Proc. SPIE **3333**, 219 (1998).

[16]N. Sundararajan, C. F. Keimel, N. Bhargava *et al.*, J. Photopolym. Sci. Technol. **12** (3), 457-468 (1999).

[17]K. E. Uhrich, E. Reichmanis, and F. A. Baiocchi, Chem. Mater. **6**, 295-301 (1994).

[18]D. Ehlich and H. Sillescu, Macromolecules **23**, 1600-1610 (1990).

PHOTO AND SCANNING PROBE LITHOGRAPHY USING
ALKYLSILANE SELF-ASSEMBLED MONOLAYERS

H. SUGIMURA[*], T. HANJI[*], O. TAKAI[*], K. FUKUDA[**] and H. MISAWA[**]
[*]Department of Materials Processing Engineering, Graduate School of Engineering, Nagoya University, Chikusa Nagoya 464-8603, JAPAN, sugimura@numse.nagoya-u.ac.jp
[**]Department of Ecosystem Engineering, Graduate School of Engineering, The University of Tokushima, 2-1 Minamijosanjima, Tokushima 770-8506, JAPAN

ABSTRACT

An organic film of a few nm in thickness was applied as a resist for photolithography and scanning probe lithography. This resist film was prepared on an oxide-covered Si substrate through chemisorption and spontaneous organization of organosilane molecules, e.g., n-octadecyltrimethoxy-silane. The film belongs to a class of materials referred to as self-assembled monolayer (SAM). A SAM/Si sample was irradiated through a photomask with vacuum ultraviolet (VUV) light at a wavelength of 172 nm. The photomask image was transferred to the SAM through the decomposition of the SAM. Furthermore, we demonstrate nano-scale patterning of the SAM using an atomic force microscope (AFM) with an electrically conductive probe. The SAM was electrochemically degraded in the region where the AFM probe had been scanned. Both the photo-printed and AFM-genereated patterns were successfully transferred into the Si substrates based on wet chemical etching or on dry plasma etching. At present, using these VUV and AFM-based lithographies, we have succeeded in fabricating minute features of 2 μm and 20 nm in width, respectively.

INTRODUCTION

Organosilane molecules form a thin layer on an oxide surface through chemisorption of the molecules to hydroxyl sites on the surface [1]. Due to hydrophobic and van der Waals interactions between the alkyl chains of the organosilane molecules, the molecules are spontaneously organized into a layer of monomolecular thickness in which the molecules are closely packed [2,3]. Such films are known as self-assembled monolayers (SAMs). The organosilane SAMs fulfill the requirements for high-resolution resist films including thickness, uniformity, patternability and compatibility to various pattern transfer processes and, therefore, have successfully served as resist films for lithography, e.g., photolithography, electron beam lithography and scanning probe lithography [4-7].

In this paper, we report recent progresses in our research on SAM-lithography. Photolithography based on vacuum ultra violet (VUV) and scanning probe lithography based on atomic force microscopy (AFM) are demonstrated using the SAM resists.

PREPARATION OF ORGANOSILANE SAM

An organosilane SAM was prepared on each of Si substrates by means of chemical vapor deposition (CVD) using octadecylsilyl-trimethoxysilane [$CH_3(CH_2)_{17}Si(OCH_3)_3$] as a precursor. Since the details of this CVD method have been published elsewhere [8,9], explanation here will be brief. Prior to CVD, the Si substrates were cleaned by a UV/ozone cleaning method in order to remove

organic contamination and to prepare a thin surface oxide layer, whose thickness was ca. 2 nm, on the substrates. This oxide surface was hydroxylated and, therefore, completely hydrophilic with a water contact angle of almost 0°. The cleaned Si substrates were then exposed to OTMS vapor at 150 °C for 3 h. Through the chemical reaction between the surface hydroxyl groups and the vapor-ized OTMS molecules, each of the OTMS molecules was fixed onto the substrate through a Si-O-Si bonding resulting in the formation of a SAM consisting of octadecylsilyl [$CH_3(CH_2)_{17}Si\equiv$, ODS] groups (ODS-SAM). The thickness of this monolayer was estimated by ellipsometry to be 1.9 ± 0.1 nm. The monolayer surface was hydrophobic showing a water contact angle of more than 100°.

VUV PHOTOPATTERNING
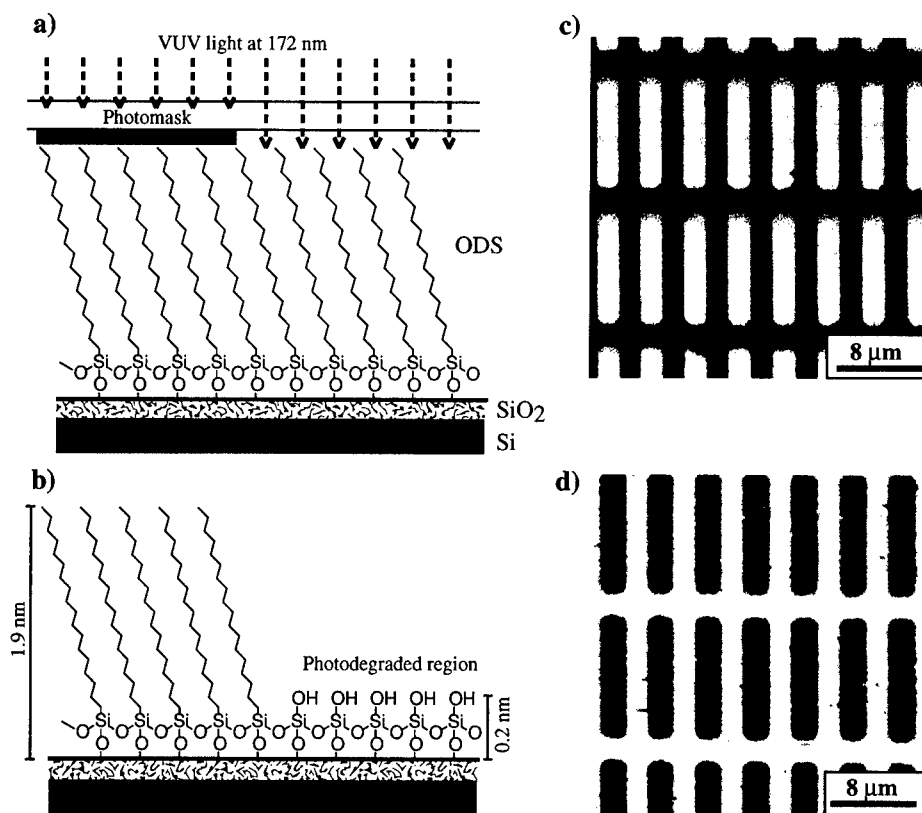
Fig. 1 VUV-patterning of ODS-SAM. a) VUV-irradiation through a photomask contacting to the SAM. b) Chemical strucutres of the photoittadiated and unirradiated regions. c) An LFM image of the photopatterned ODS-SAM. d) A topographic IC-AFM image of the photopatterned ODS-SAM.

A Si substrate coated with the ODS-SAM was photolithographically micropatterned as schematically illustrated in Figs. 1a and 1b. The SAM surface was irradiated for 600 s in vacuum (less than 10 Pa) with the VUV light through a photomask contacting the substrate surface. An Xe_2 excimer lamp at a radiation wavelength of 172 nm (Ushio Electric, UER20-172V, 10 mW/cm^2) was served as the light source. The photomask consisted of a 2-mm thick quartz glass plate with a 0.1 μm-thick chromium pattern. A weight, a quartz glass plate of 10 mm thick, was put on the photomask in order to attain a satisfactory contact between the mask and the SAM surface. The total light intensity at the SAM surface was 6.5 mW/cm^2. The photopatterned SAM surfaces were observed in the lateral force microscopy (LFM) mode using an AFM (Park Scientific Instruments, Autoprobe LS). Topographic images were also acquired in the intermittent-contact (IC) mode in which the AFM probe oscillates at a frequency near its resonance and periodically touches the sample surface once each vibration cycle.

Figure 1c shows an LFM image of the ODS-SAM surface irradiated through the photomask. The bright and dark regions in the image correspond to the photoirradiated and the masked areas, respectively. Microstructures composed of 2 μm × 10 μm rectangular features were photoprinted on the SAM surfaces and were clearly imaged through the difference in friction between the photoirradiated and the unirradiated areas. The photodegraded areas, which exhibited stronger lateral force than the hydrophobic, undegraded SAM surface, had to be hydrophilic as illustrated in Fig. 1b. Such hydrophilic surfaces of photodegraded SAMs chemically interact with an AFM-probe surface, which is also hydrophilic due to its surface oxide, resulting in a higher friction coefficient [10,11].

VUV light dissociatively excites chemical bonds, e.g., C-C, C-H, C-F and C-Si, and forms radicals which further react with oxygen and water molecules in the atmosphere. The ODS-SAM is supposed to be similarly degraded. A topography of the photopatterned SAM, as shown in Fig. 1d, shows that the photoirradiated regions are recessed from the surrounding unirradiated region. The recessed depths was 1.7 ± 0.3 nm. The SAM was concluded to be photodecomposed and removed in the photoirradiated regions. It is noteworthy that the both depths were smaller than the thicknesses of the SAM. As illustrated in Fig. 1b, a monolayer of SiO_2 remains on the substrate even when all organic parts are removed [12,13]. The thickness of this SiO_2 monolayer was ca. 0.2 nm as measured by ellipsometry.

PATTERN TRANSFER THROUGH A MICROPATTERNED SAM MASK

As shown in Fig. 2c, when the Si substrate covered with ODS-SAM was immersed in HF solution, its water contact angle gradually decrease from its initial value of 103° to ca. 85°, that is, the water contact angle of hydrogen-terminented Si (Si-H) surface which is formed when Si is treated in a dilute HF solution. It is most likely that the ODS-SAM was damaged and, consequently, removed due to chemical etching of the underlying SiO_2 layer. Finally, a Si-H surface is exposed. From these experi-
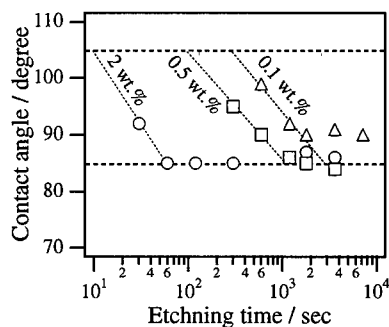
Fig. 2 Resistivity of ODS-SAM to HF.

mental results, it was estimated that the ODS-SAM was durable for 15, 100, and 3000 s in aqueous solutions of 2, 0.5 and 0.1 HF-wt.%, respectively. These durability times are longer than the periods necessary in order to etch photochemically grown 2nm-thick SiO_2 in the corresponding HF solutions. These periods were 5, 30 and 250 s, respectively. Therefore, in the region where the ODS-SAM has been removed, the SiO_2 layer can be etched completely without damaging the surrounding ODS-SAM, as illustrated in Fig. 3b.

Using patterned ODS-SAM and SiO_2 layer as an etching mask, microstructures can be fabricated on the Si substrate. Although several wet chemical etching processes are applicable [14, 15], plasma etching is more promising since microstructures with higher aspect ratios can be fabricated. Here, we demonstrate a preliminary result on plasma etching of Si using a micropatterned SAM mask. First, a VUV-patternd sample (Fig.3a) was etched in a 0.1 wt.% HF solution for 600 s in order to etch SiO_2 in the regions where the windows had been opened. Next, this sample was further etched in plasma of fluorine containing molecules for 30 s using an plasma etching apparatus (Sumitomo Precision Products, SPM-200). As can be seen in an AFM image and its cross section as shown in Figs. 3d and 3e, the substrate Si was selectively etched ca. 50 nm deep in the window regions, while the undecomposed ODS-SAM regions remained unetched. The capability of the ODS-SAM as plasma etching mask has been successfully shown although optimization of etching conditions are further needed in order to etch more deeply.
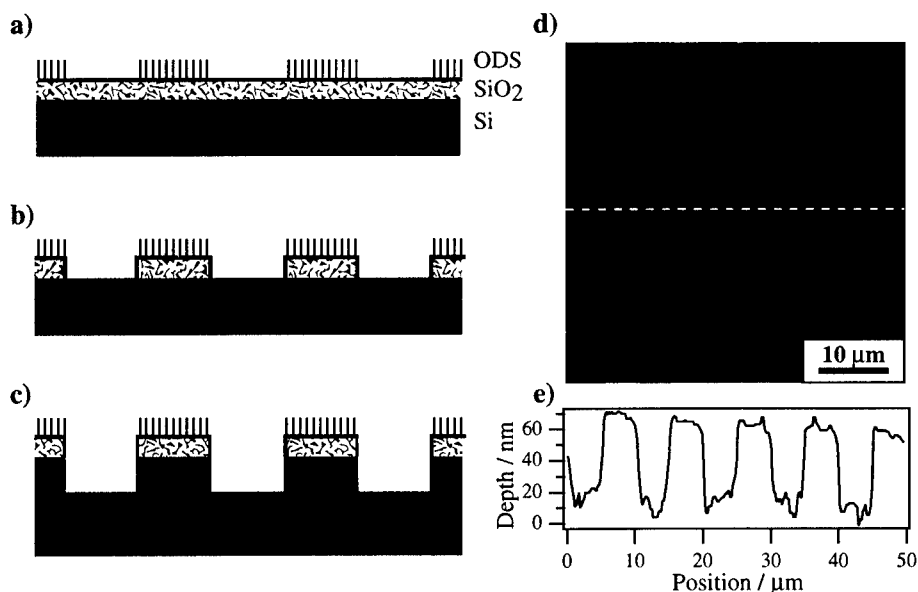
Fig. 3 Pattern transfer process. a) A photopatterned ODS-SAM/Si. b) SiO_2 etching in HF. c) Si etching. d) An AFM image of a plasma-etched Si microstructure. e) Cross section where indicated in the AFM image.

166

SCANNING PROBE LITHOGRAPHY

An amorphous Si (a-Si) film of 20 nm thick was deposited by ion-beam sputtering on a single crystal Si plate with a 20nm-thick thermally grown oxide. On this sample surface, ODS-SAM was formed as described before. This sample was patterned using an AFM with a conductive probe as shown in Fig. 4a. In order to inject current into the ODS-SAM, a bias voltage was applied between the AFM probe and the a-Si layer which was positively polarized. When an AFM is operated in the presence of atmospheric water vapor, the AFM probe-sample junction is connected through a water column created by capillarity of the adsorbed water and can serve as a minute electrochemical cell [16]. As a result of electrochemical reactions induced in this cell, the ODS-SAM was degraded in the region where the probe had been passed. In this current-injecting AFM-lithography, current flowing through the probe-sample junction is a key factor in order to control it. However, the controllability of the current was not satisfactory in using the constant bias mode. The relationship between the junction current and the bias voltage depended on several factors, such as the age and idiosyncrasies of the particular probe used. The current could not be precisely controlled by simply applying a defined bias voltage. Thus, a current feedback system, which enables to preform AFM-lithography in constant current mode, is crucial for reliable AFM-lithography [17]. In the present case, AFM patterning was conducted at a probe scan rate of 20 μm/s and a probe current of 1 nA.
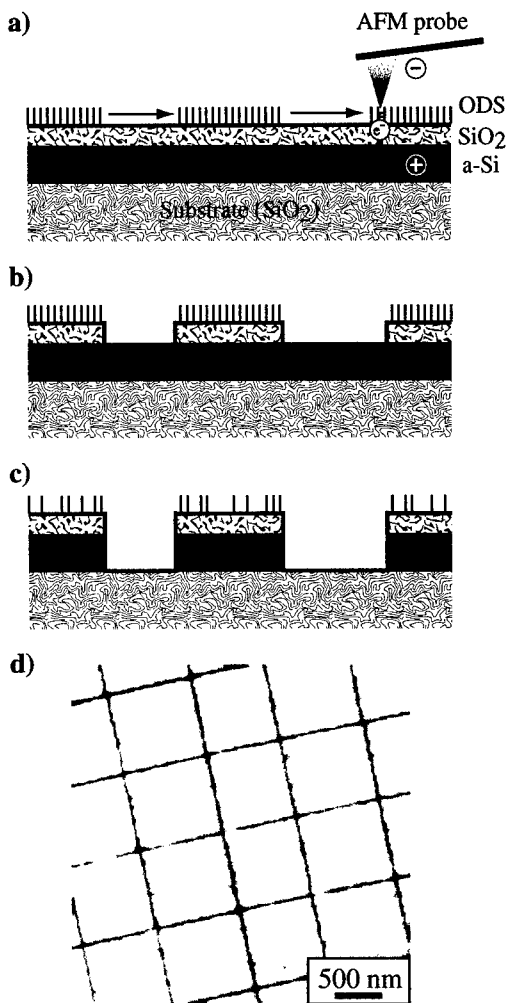
Fig. 4 Scanning probe lithography. a) AFM-based pattern drawing on ODS-SAM/a-Si. b) SiO_2 etching in HF. c) Si etching in TMAH. d) An AFM image of a etched a-Si.

A two-step chemical etching process was employed for pattern transfer from the ODS-SAM to the a-Si film. At the first step, the AFM-patterned sample was etched for 30 s in an aqueous solution of 0.5 wt.% HF (Fig. 4b). At the second step, the HF-etched sample was further treated for 180 s in an aqueous solution of 25 wt.% tetramethylammonium hydroxide (TMAH). In this solution, a-Si is effectively etched in the region where its surface oxide had been removed while the

surrounding region was masked form the etching by the SiO_2 layer. In addition, this a-Si etching actually stops when the whole a-Si layer is etched and the underlying substrate, i.e., thermal SiO_2, is exposed (Fig. 4c). The ODS-SAM might be damaged during the second step. As can be seen in an AFM image shown in Fig. 4d, the current-injected region became further etched with its depth of almost equal to the thickness of the a-Si film. Fine grooves near 50 nm in width were fabricated.

SUMMARY

An alkylsilane SAM less than 2 nm in thickness has been successfully applied to the resist for VUV-photolithography and scanning probe lithography. The image of a photomask was printed on the SAM through its photodecomposition. On the other hand, an AFM-probe scanning pattern was written on the SAM due to its electrochemical degradation locally induced beneath the AFM-probe tip. These micro or nano-scale pattern could be transferred into the Si substrates by wet chemical etching or dry plasma etching. At present, features of minimum widths of 2 μm and 20 nm were fabricated by the photolithography and the scanning probe lithography, respectively.

ACKNOWLEDGEMENT

REFERENCES

1. E. P. Plueddemann, *Silane Coupling Reagents* (Plenum Press: New York, 1991)
2. J. Sagiv, J. Am. Chem. Soc. **102**, 92 (1980).
3. S. R. Wasserman, Y.-T. Tao and G. M. Whitesides, Langmuir **5**, 1,074 (1989).
4. W. J. Dressick and J. M. Calvert, Jpn. J. Appl. Phys. **32**, 5829 (1993).
5. M. J. Lercel, R. C. Tiberio, P. F. Chapman, H. G. Craighead, C. W. Sheen, A. N. Parikh and D. L. Allara, J. Vac. Sci. Technol. B **11**, 2823 (1993).
6. C. R. K. Marrian, F. K. Perkins, S. L. Brandow, T. S. Koloski, E. A. Dobisz, and J. M. Calvert, Appl. Phys. Lett. **64**, 390 (1994).
7. H. Sugimura and N. Nakagiri, Langmuir **11**, 3623 (1995).
8. H. Sugimura and N. Nakagiri, J. Photopolym. Sci. Technol. **10**, 661 (1997).
9. A. Hozumi, K. Ushiyama, H. Sugimura and Osamu Takai, Langmuir **15**, 7600 (1999).
10. B. Lee and N. A. Clark, Langmuir **14,** 5498 (1998).
11. H. Sugimura and N. Nakagiri, Appl. Phys. A **66**, S427 (1998).
12. Y. Suzuki and M. Shin-Ogi, Jpn. J. Appl. Phys. **29**, L1517 (1990).
13. H. Brunner, T. Vallant, U. Mayer and H. Hoffmann, Langmuir **12**, 4614 (1996).
14. H. Sugimura O. Takai and N. Nakagiri, J. Vac. Sci. Technol. B **17**, p. 1605 (1999).
15. H. Sugimura K. Ushiyama, A. Hozumi and Osamu Takai, Langmuir, in press.
16. H. Sugimura T. Uchida, N. Kitamura and H. Masuhara, J. Phys. Chem. **98**, 4352 (1994).
17. H. Sugimura and N. Nakagiri, Nanotechnology **8**, A15 (1997).

Carbon Dioxide – Dilated Block Copolymer Templates for Nanostructured Materials

Garth D. Brown and James J. Watkins[*]

Department of Chemical Engineering, University of Massachusetts, Amherst, MA 01003

ABSTRACT

Periodic polymer/metal (Pt or Ag) and polymer/semiconductor (PbS) nanocomposites are prepared using block copolymers dilated with carbon dioxide (CO_2) as templates. Specifically, organometallic compounds (metal precursors) are dissolved into supercritical CO_2 and infused into polystyrene-block-poly(acrylic acid) or polystyrene-block-poly(vinylpyridine) copolymers. Upon infusion, the acid or pyridine block selectively binds the metal precursor. The excess is removed from the polystyrene phase by subsequent CO_2 extraction. Reduction of the bound organometallic with hydrogen or hydrogen sulfide yields the desired metal or semiconductor clusters, which are confined to the precursor-binding domain and remain positioned on the copolymer lattice. The composites are characterized by transmission electron microscopy, x-ray scattering and electron diffraction.

INTRODUCTION

The preparation of metal and semiconductor nanostructures is of considerable interest due to their size-dependent optical, catalytic and electrical properties. While the production of discrete clusters can be achieved using a number of techniques including ligand capping [1], micellar reactors [2] and aggregation with polymers in solution [3], the fabrication of practical devices for many applications requires the assembly of metal or semiconductor domains of precise size, shape and connectivity into periodic arrays with long-range order. One approach to such synthetic nanocomposites is to use self-assembled structures as molecular scaffolding (templates) to direct the microarchitecture of materials synthesized in their presence. Water-based surfactant systems are one class of candidate templates. For example, bicontinuous structures composed of lipid bilayers and water having the requisite dimensions can be formed, but their utilization depends on the difficult challenge of stabilizing and converting the fluid structures into solid state replicas without disrupting long-range order. Block copolymer melts offer a robust alternative. These materials can self-assemble into periodic mesostructures having domains on the order of 10 to 100 nm. Moreover, adjusting composition and block length can be used to tailor domain size, shape and spacing. To date, block copolymers have been used to template clusters either in solution [4-7], by preparation of block copolymers using an organometallic monomer for one of the blocks [8-10] or by *in situ* reaction within thin films laden with selectively bound organometallic compounds [11-14]. The latter approach preserves the morphology of the copolymer template, but mass-transfer limitations to reagent transport impede its use at bulk dimensions. Ideally, one would like to begin with a net-shape template and carry out selective metallization directly.

We recently demonstrated that solid polymers dilated with low weight fractions of supercritical carbon dioxide (SC-CO_2) are viable reaction media for the preparation of composites over bulk dimensions. For example, novel polymer blends can be prepared by the sequential infusion and polymerization of monomer / carbon dioxide solutions within bulk semi-crystalline polymer substrates [15]. Here we report this technique can be extended to the preparation of periodic polymer/metal nanocomposites by selective metallization within one phase of a block copolymer template. The composites are prepared by dissolving organometallic compounds in SC-CO_2, subsequent infusion of the solution into the copolymer template and

reduction of the precursor to yield the desired metal or semiconductor. The key to the process is sorption of low weight fractions of carbon dioxide, which significantly enhances reagent diffusivity [16-17] without destroying the copolymer morphology [18-19]. Phase-selectivity is conveyed by choosing one block that contains functional groups that selectively bind a suitable reactive precursor while selecting the other block to be inert: in this work, we choose either polystyrene-block-poly(acrylic acid) (PS-b-PAA) or polystyrene-block-poly(2-vinyl-pyridine) (PS-b-P2VP) copolymers. The acid or pyridine block selectively binds the metal precursor and the excess is removed from the (inert) polystyrene phase by CO_2 extraction. Reduction of the bound organometallic yields the desired clusters, which remain positioned on the copolymer lattice.

EXPERIMENTAL

PS-b-PAA was prepared via anionic polymerization of poly(styrene-b-*tert*-butyl acrylate) followed by hydrolysis. The architecture of the block copolymer was chosen such that poly(acrylic acid) is the minor phase (6.5 percent by volume), resulting in a spherical morphology. The molecular weights of the styrene and acrylic acid blocks are 100,000 and 7,000 respectively. PS-b-P2VP copolymer was purchased from Polymer Source. The molecular weights of the styrene and 2-vinyl pyridine blocks are 52,400 and 28,100 respectively, yielding a volume fraction of 0.336 PVP in a cylindrical morphology. (1,5-Cyclooctadiene) dimethylplatinum (II), [Pt(COD)Me$_2$], (Strem Chemical); Bis hexafluoroacetylacetonate lead, [Pb(hfac)$_2$], (Strem); (1,5-Cyclooctadiene) silver (hexafluoroacetylacetonate), [Ag(COD)(hfac)], (Aldrich); and dimethylformamide (DMF), (Aldrich) were used as received. Coleman grade carbon dioxide, ultra-high purity hydrogen, and hydrogen sulfide were purchased from Merriam Graves and used as received.

Transmission electron microscopy (TEM) and electron diffraction were conducted using a JEOL 100CX at 100kV. Sections for analysis (30 nm thick) were obtained via cryomicrotomy using a diamond knife or a freshly cut glass knife. Additional contrast enhancement for TEM was not needed for the samples containing either the bound metal precursor or the metal nanoclusters. X-ray diffraction was performed using a Siemens D-500 diffractometer with a copper anode.

The procedure for metallization of the template is depicted in Scheme 1. The copolymer templates were prepared by melt pressing or solvent casting. The substrates were then cut into small strips (about 5 mm x 10 mm x 0.5 mm thick) and placed into a high-pressure stainless steel reaction vessel containing a known quantity of the desired metal precursor. The vessel was sealed and placed into heating bath at the desired temperature. A known amount of CO_2 was then transferred into the vessel via a computer controlled syringe pump or a high-pressure manifold yielding ~0.5% weight percent solution of the precursor in CO_2. After an appropriate soaking time (2-6 hrs), the vessel was cooled to room temperature and vented slowly to suppress foaming of the substrate. Unbound precursor was then removed from the polystyrene phase by CO_2 extraction. The vessel was opened and part of the sample was sectioned away and retained for analysis. The remainder of the sample was returned to the vessel and treated with either neat hydrogen or hydrogen sulfide.
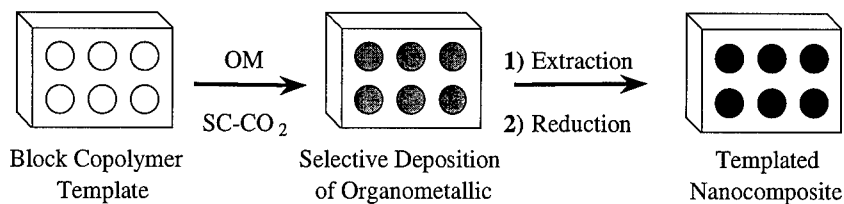
Scheme 1. Procedure for the preparation of templated nanocomposite. The organometallic (OM) is dissolved in CO_2, infused into the copolymer and selectively bound within the reactive phase of the copolymer. Excess precursor is removed from the inert phase by extraction. Reduction of the bound precursor yields the nanocomposite

RESULTS

The key to our approach is the selective confinement and reduction of precursor in one phase domain of the copolymer. Figure 1 shows a TEM micrograph of PS-b-P2VP copolymer metallized with platinum. This composite was prepared via Scheme 1 using a Pt(COD)Me₂/ CO_2 solution at 140 bar and 60 °C, a soaking period of 6 hours and subsequent reduction with hydrogen at 70 bar and 60 °C for 1 hour. The sample was not stained prior to analysis. Thus the contrast in the micrograph reveals that Pt deposition has been confined to cylindrical poly(2-vinyl pyridine) domains of the copolymer, which exhibit a spacing of about 50 nm. As we have made no attempt to orient the copolymer template, the metallized sample contains grains of random orientation. This is evident in the micrograph, which shows cylinders oriented parallel and perpendicular to the plane of the page. Selective metallization was apparent throughout the composite thickness (0.5 mm)
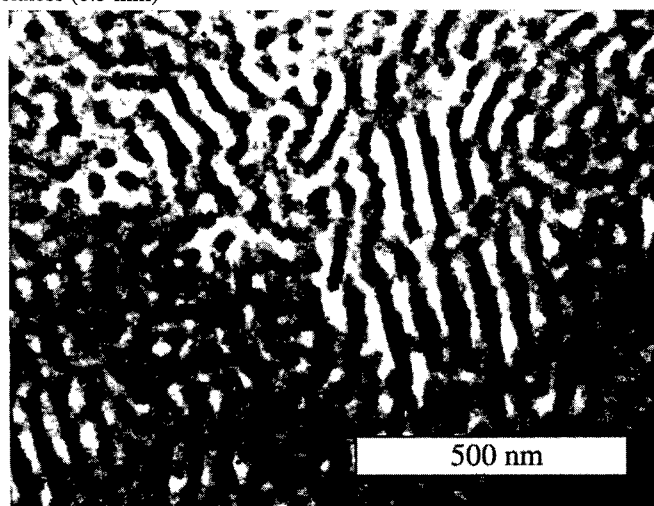
Figure 1. TEM micrograph of platinum metal deposited within cylindrical P2VP domains of a block copolymer.

Platinum metal clusters were prepared within the spherical PAA domains of PS-b-PAA. The template was cast from DMF solution and dried under vacuum for 24 hours. PS-b-PAA and the precursor [Pt(COD)Me₂] were loaded at 135 bar and 60 °C, After a 3 hour soak and two 2

extraction steps, the remaining bound precursor was reduced with hydrogen at 100 bar and 40 °C for 1 hour. Figure 2a, shows a TEM micrograph of the PS-b-PAA copolymer after infusion of Pt(COD)Me$_2$. The precursor is bound selectively within the PAA spheres, which are approximately 20 nm in diameter. Upon reduction with hydrogen, platinum metal nanoclusters are formed within the domains (Figure 2b). The micrograph suggests that using this precursor and template, multiple platinum metal clusters nucleate within each of the clusters. The presence of metallic Pt was confirmed by both by x-ray and electron diffraction (Figures 3a and 3b). Prior to reduction, only the diffraction pattern of the copolymers is observed.
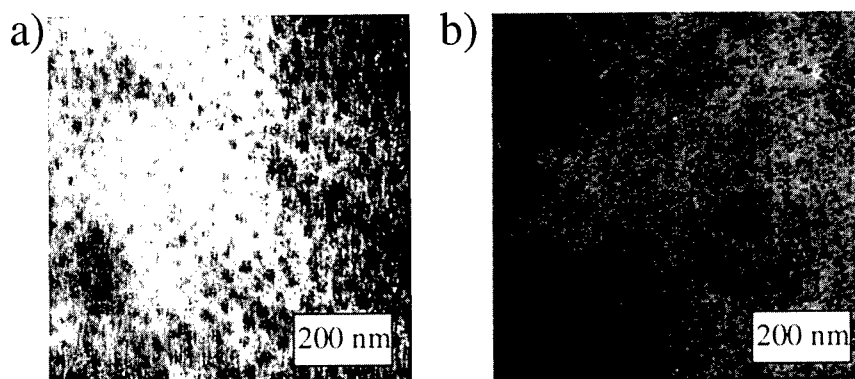
Figure 2. TEM micrographs of platinum deposited within PS-b-PAA. Figure 2a shows unreduced precursor [Pt(COD)Me$_2$] selectively bound within a spherical block of PAA. Subsequent reduction yields Pt clusters (Figure 2b).
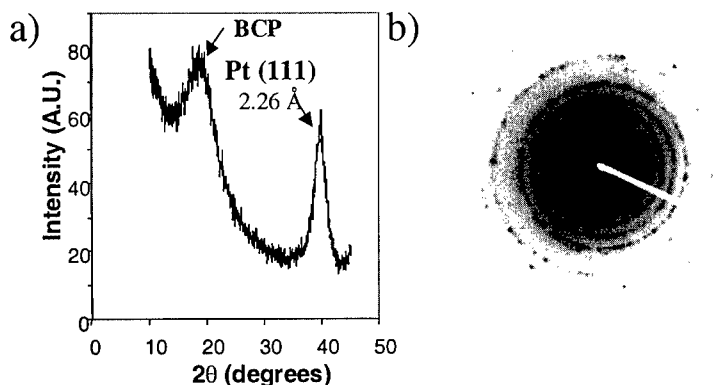
Figure 3. Wide-angle x-ray diffraction (Figure 3a) and electron diffraction (Figure 3b) confirm the presence of metallic Pt clusters. Prior to reduction, only scattering attributed to the block copolymer (BCP) was observed.

A similar procedure was used to prepare silver clusters within a PS-b-PAA template using Ag(COD)(hfac) as the silver precursor. Figure 4a shows unreduced Ag(COD)(hfac) bound within the PAA domains. Reduction with H_2 yields silver clusters confined within the PAA domains. (Figure 4b). Finally, the technique described here can readily be adapted for the preparation of semiconductors. Lead sulfide clusters were prepared within a PS-b-PAA template using [Pb(hfac)$_2$] as the precursor followed by reduction with hydrogen sulfide. The presence of PbS clusters was confirmed using x-ray diffraction (Figure 5).
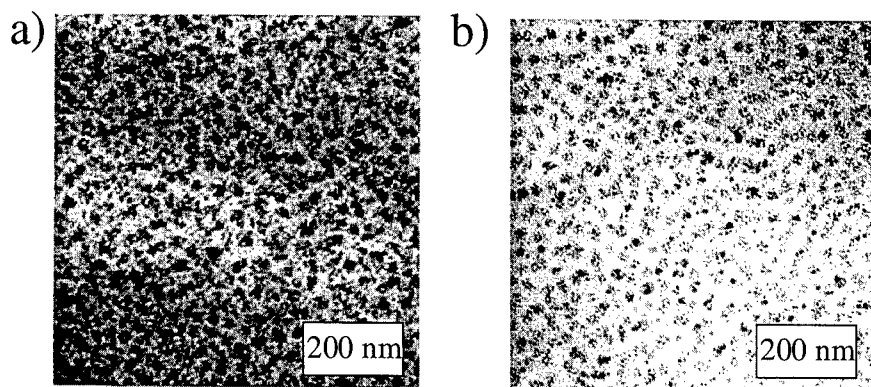
Figure 4. TEM micrographs of silver deposited within copolymer of PS-b-PAA. Figure 4a shows unreduced silver precursor selectively bound within a spherical block of PAA. Subsequent reduction yields silver clusters within the PAA domains (Figure 4b).
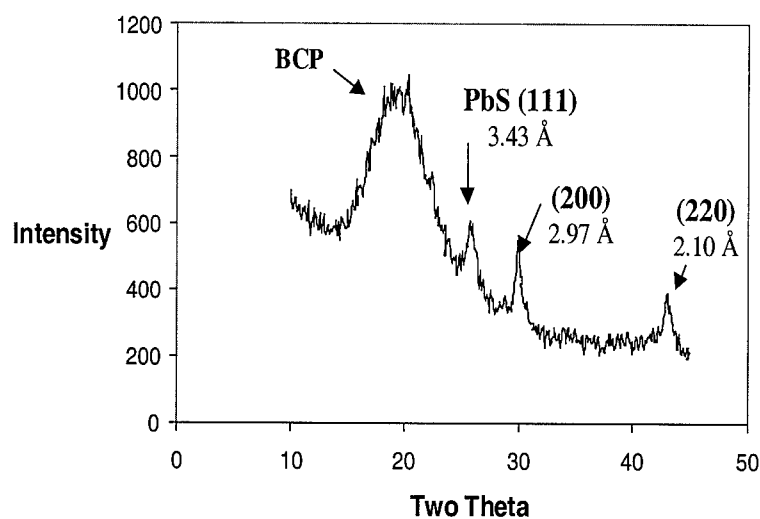
Figure 5. Wide-angle x-ray diffraction confirms the presence of PbS clusters in PS-b-PAA.

173

CONCLUSIONS

We have developed a novel technique for the preparation of polymer/metal and polymer/semiconductor nanocomposites. Metallization is confined exclusively to one domain of a block copolymer template, which provides a pathway to materials with long-range order. The use of supercritical CO_2 as a processing aid reduces mass transport limitations within the polymer substrates and can facilitate the preparation of bulk materials using a net shape template. Future work will focus on increasing metal loading within the metallized domains by employing multiple infusion and reduction cycles.

ACKNOWLEDGMENTS

REFERENCES

[1] Rettz, M. T.; Helbig, W.; Quaiser, S. A.; Stimming, U.; Breuer, N.; Vogel, R. *Science* **1995**, *267*, 367-369.

[2] Moffitt, M.; Eisenberg, A. *Chemistry of Materials* **1995**, *7*, 1178-1184.

[3] Forster, S. *Ber. Bunsenges. Phys. Chem.* **1997**, *101*, 1671-1678.

[4] Antonietti, M.; Thunemann, A.; Wenz, E. *Colloid Polymer Science* **1996**, *274*, 795-800.

[5] Antonietti, M.; Heinz, S.; Schmidt, M.; Rosenauer, C. *Macromolecules* **1994**, *27*, 3276-2381.

[6] Mayer, A. B. R.; Mark, J. E. *Colloid Polymer Science* **1997**, *275*.

[7] Moller, M.; Lenz, R. W. *Makromol Chemistry* **1989**, *190*, 1153-0068.

[8] Chan, Y. N. C.; Craig, G. S. W.; R.R.Schrock; Cohen, R. E. *Chemistry of Materials* **1992**, *4*, 885-894.

[9] Cummins, C. C.; Schrock, R. R.; Cohen, R. E. *Chemistry of Materials* **1992**, *4*, 27-30.

[10] Sankaran, V.; C.C.Cummins; Schrock, R. R.; Cohen, R. E.; Silbey, R. J. *Journal of the American Chemical Society* **1990**, *112*, 6858-6859.

[11] Yue, J.; Cohen, R. E. *Supramolecular Science* **1994**, *1*, 117-122.

[12] Yue, J.; Sankaran, V.; Cohen, R. E.; Schrock, R. R. *Journal of the American Chemical Society* **1993**, *115*, 4409-4410.

[13] Ciebien, J. F.; Clay, R. T.; Sohn, B. H.; Cohen, R. E. *New Journal of Chemistry* **1998**, 23, 685-691.

[14] Ciebien, J. F.; Cohen, R. E.; Duran, A. *Supramolecular Science* **1998**, *5*, 31-39.

[15] Watkins, J. J.; McCarthy, T. J. *Macromolecules* **1995**, *28*, 4067-4074.

[16] Berens, A. R.; Huvard, G. S.; Richard, W. K.; Kunig, F. W. *Journal of Applied Polymer Science* **1992**, *46*, 231-242.

[17] Chapman, B. R.; Gochanour, C. R.; Paulaitis, M. E. *Macromolecules* **1996**, *29*, 5635.

[18] Vogt, B. D.; Brown, G. D.; RamachandraRao, V. S.; Watkins, J. J. *Macromolecules* **1999**, *32*, 7907-7912.

[19] Watkins, J. J.; Brown, G. D.; RamachandraRao, V. S.; Pollard, M. A.; Russell, T. P. *Macromolecules* **1999**, *32*, 7737-7740.

Atomic Scale Characterization
and Measurement

A New Purged UV Spectroscopic Ellipsometer
to characterize 157nm nanolithographic materials

Pierre BOHER, Jean Philippe PIEL, Patrick EVRARD, and Jean Louis STEHLE
SOPRA S.A., 26 rue Pierre Joigneaux, 92270 BOIS COLOMBES, France.

ABSTRACT

Spectroscopic ellipsometry has long been recognized as the technique of choice to characterize thin films and multilayers. It is now intensively used in microelectronics and especially for the microlithographic applications. Instrumentation for the next generation of UV lithography at 157nm requires special optical setup since oxygen and water are extremely absorbing below 190nm. The ellipsometer discussed in this paper works into a purged glove box to reduce the oxygen and water contamination in the part per million ranges. The optical setup has been especially studied for microlithographic applications. It includes for example a premonochromator in the polariser arm to avoid resist photobleaching. Technical details of the system and some first measurement results on substrates and thin films are reported hereafter.

INTRODUCTION

Recently, there has been increasing interest in using 157nm laser sources in projection lithography as successors to 193nm based systems. This would follow the historical trends in the microelectronic industry where wavelength reduction is used to improve feature resolution. At 248 and 193nm, spectroscopic ellipsometry has shown to be a very efficient method to characterize photoresists and antireflective coatings [1]. Compared to more simple techniques like reflectance, ellipsometry has different advantages. First, the measurement is made on a ratio of two signals (Rp/Rs where Rp and Rs are the reflection coefficients of the two polarisations parallel and perpendicular to the incidence plane). So the measurement is independent of the source fluctuations and the accuracy of the measurement is generally better than a photometric one. There is also no need of reference sample since the measurement is self-calibrated. Finally, two independent parameters are measured simultaneously instead of one for reflectance or transmittance, which allows direct extraction of complex indices. The measurement can be also rapid now thanks to the development of multichannel detectors [2]. Photoresist behavior versus exposure dose has for example been determined by this method [3]. At 157nm, the layer thickness is generally smaller than for the old lithographic generations. So, due to enhanced correlation between thickness and indices, ellipsometry becomes one of best alternatives. On the other hand, primary lens material for projection systems will be metal fluorides such as CaF_2, MgF_2 or LiF which will require intensive characterization especially for their optical properties at 157nm. A metrologic tool capable to make photometric measurements will be also interesting.

Following this evolution, SOPRA has decided to develop a new spectroscopic ellipsometer capable to work down to 157nm. Additional possibilities such as variable incidence angle and photometric measurement have also been included to fulfill the characterization requirements of this new generation of photolithography. We describe here after the instrument with some first characterization results.

DESCRIPTION OF THE PURGED UV ELLIPSOMETER

Two main differences appear when we want to work at 157nm. First, because of the strong molecular absorption bands in O_2 and H_2O at 157nm, the entire beam path must be free of this kind of contamination. Second, the standard optical path used at SOPRA with a monochromator just before the detector and connected to the analyser arm of the ellipsometer by an optical fiber cannot be used. These two problems have been solved using the following solutions:
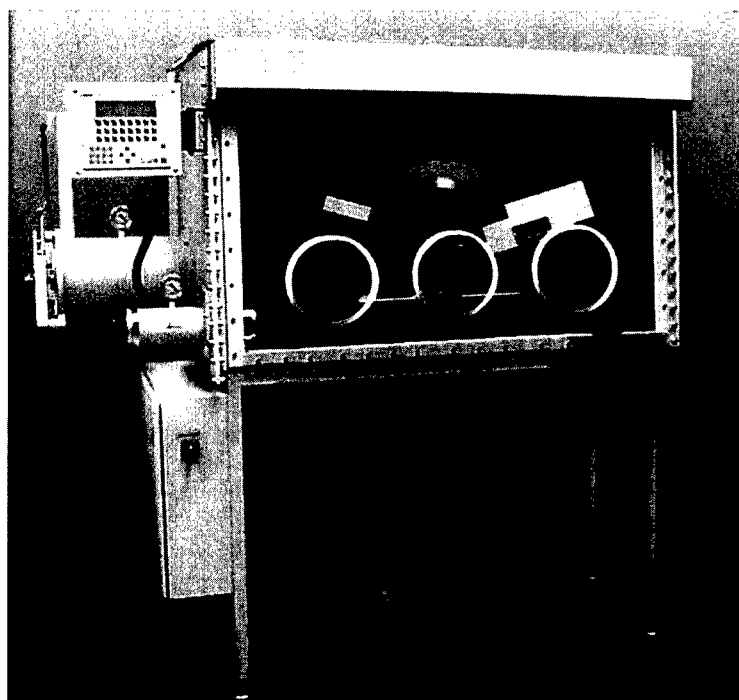
Figure 1: *General view of the SOPRA Purged UV Spectroscopic Ellipsometer.*

Spectroscopic ellipsometer setup

The double monochromator is included in the polariser arm just after the deuterium lamp. This mounting ensures an optimized straight light rejection with a minimized beam path. The light beam goes through a MgF_2 Rochon polarizer mounted on a stepper motor. The reflected beam passes through another Rochon analyser and is detected by a photomultiplier in photon counting mode. The two arms are mounted on a high precision goniometer. The angle of incidence can be changed automatically in the range 7-90°. The system works in rotating analyser mode to avoid parasitic polarisation due to the monochromator. Polarisation sensitivity of the detector is calibrated in straight line. The spectral range is 145-300nm but it can be extended in the visible range. In addition to ellipsometry, the system can make photometric measurements at fixed polarisation state (reflectance and transmittance). Scatterometric measurements are also possible.

Purged glove box

The entire system is installed inside a glove box with continuous H_2O and O_2 purification. Dry nitrogen is injected continuously in the box with automatic adjustment of the surpressure. The filters can be regenerated automatically every 3-months. One working face with three gloves allows adjustment of the different parts of the system, to mount the sample on the sample holder and to replace the deuterium lamp when needed. Samples up to 200mm diameter are introduced using a load lock. Residual H_2O and O_2 are measured continuously. They are in the part per million ranges during normal working conditions.
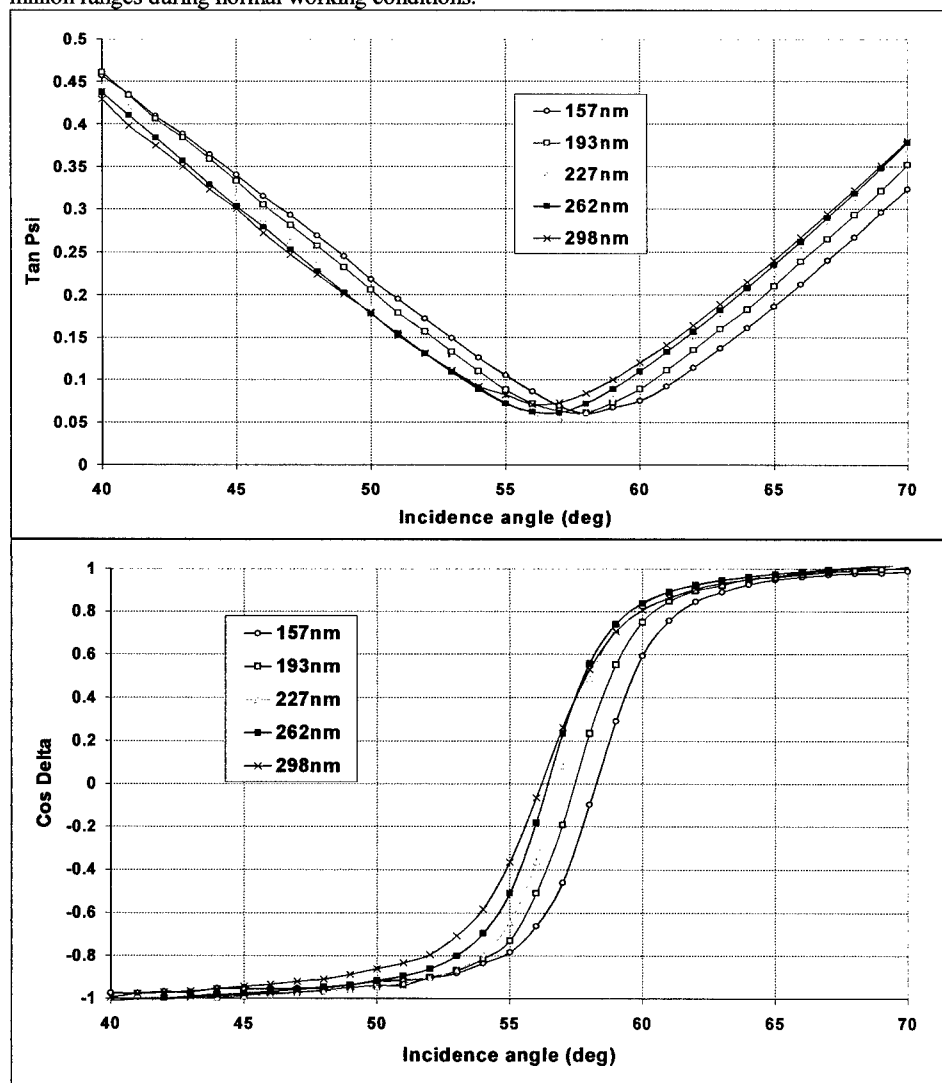
Figure 2: Experimental variable angle SE measurement made on a puropsil substrate.

EXPERIMENTAL RESULTS

Only variable angle spectroscopic ellipsometry measurements on substrates and thin film on substrate samples are presented here after. We have selected CaF_2 and puropsil (natural silica) substrates and more unusual LaF_3 layers on CaF_2 substrates.

Puropsil substrate

Variable angle SE measurements have been made at five different wavelengths (157.6, 193, 227, 262 and 298nm). The measurement is made from 40 to 70° of incidence at each wavelength. All the experimental spectra are reported in Figure 2. A well-defined Brewster angle is detected at each wavelength on the two ellipsometric parameters (minimum of TanΨ and zero crossing value for cosΔ). The shape of the cosΔ curve around the Brewster angle is due to the angular aperture of the measurement beam which is not negligible and must be taken into account during the analysis. Each curve is adjusted independently using a very simple model where only the refractive index of the substrate is adjusted. One example of such an adjustment is reported in Figure 3 for the 157nm wavelength. As can be seen on the figure, the adjustment is very good for all the angles. The refractive index is precisely determined at each wavelength (n = 1.629±0.003 at 157.6nm from Figure 3).
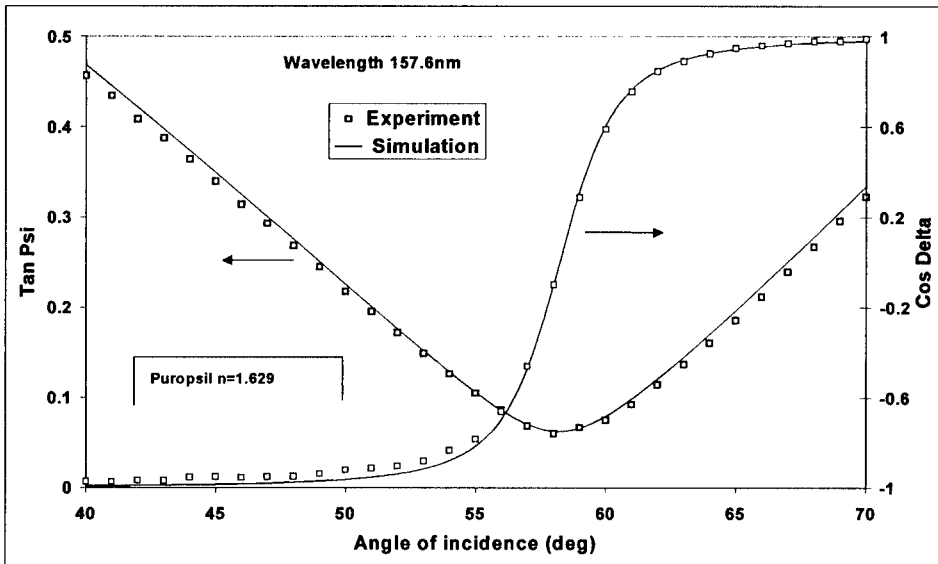
Figure 3: Analysis of the SE measurement at 157.6nm on the puropsil substrate.

Results obtained on the puropsil substrate are summarized in Figure 4 with some results of the literature concerning glass substrates [8-9]. We see that the measurements obtained here are slightly higher than the literature even if the diversity in the glass origins can produce this kind of differences. A limited surface contamination can also explain this type of difference as already see by others [12].
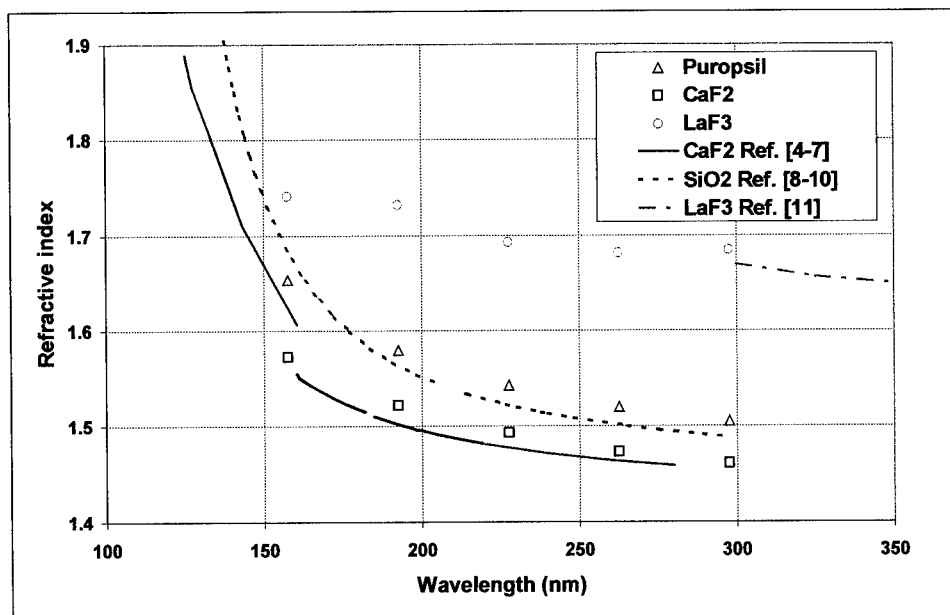
Figure 4: Summary of the measured refractive indices and some data of the literature.
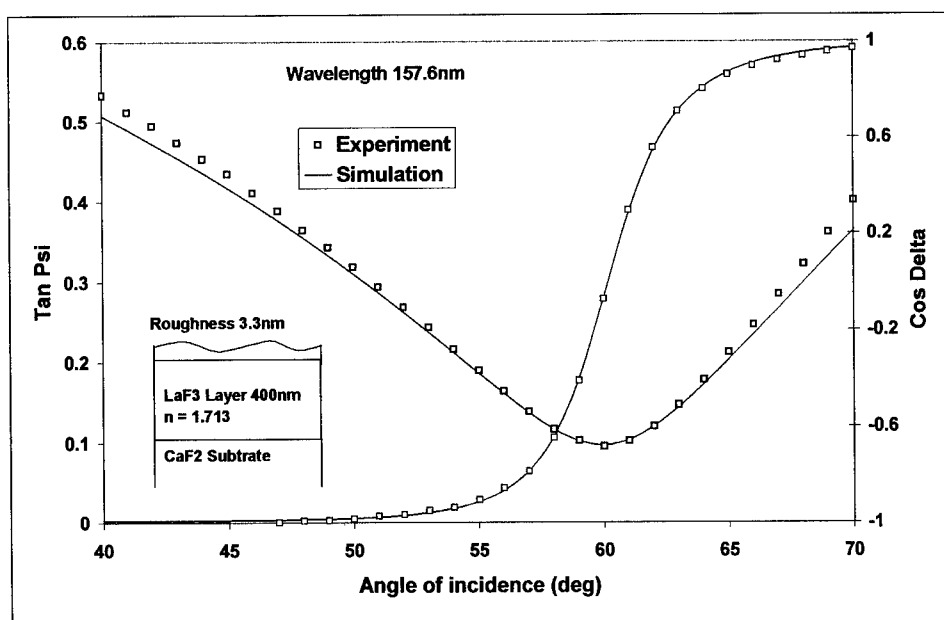
Figure 5: Analysis of the SE measurement at 157.6nm on the LaF₃/CaF₂ sample.

181

CaF$_2$ substrate

The same kind of measurement and analysis has been made for a CaF$_2$ substrate. Results at the same wavelength are also reported in Figure 4. Here also, our own results are slightly higher than expected. Surface contamination can be also a good explanation.

LaF$_3$ film on CaF$_2$ substrate

For the LaF$_3$ film deposited on CaF$_2$ substrate, we have assumed that the optical indices of the substrate are known (see above). We have this time made a regression on all the variable angle measurements at the same time adjusting the LaF$_3$ layer thickness and its refractive index using a dispersion law model (Cauchy law). This simple model does not work well, except if we had a limited roughness on top of the LaF$_3$ layer (mixed layer with 50% of void and 50% LaF$_3$). The thickness of this intermediate layer is adjusted at the same time. In this case, the adjustment is good as can be seen in the Figure 5 for the 157nm wavelength. The optical indices of the LaF$_3$ layer have been also reported in Figure 4 with the result of the literature at higher wavelength [11]. There are in good agreement with what can be expected in this wavelength range.

CONCLUSION

We have presented a new metrology system capable to measure optical properties of substrates and thin films in the range 145-300nm. This new system is a spectroscopic ellipsometer mounted inside a purged glove box to suppress strong absorption by O$_2$ and H$_2$O gases. In addition to spectroscopic ellipsometry, photometric (reflectance and transmittance) and scatterometric measurements are also possible. First experimental results have been presented. Next step will be to take care of the possible surface contamination of the samples before and during measurements. For this purpose, in situ cleaning procedure will be added using additional excimer laser.

REFERENCES

1. P.Boher, J.P.Piel, C.Defranoux, J.L. Stehle, L.Hennet, SPIE vol. 2729 (1996)
2. P. Boher, J.L Stehle, Materials. Science and Engineering, B37, 116 (1996)
3. P. Boher, C. Defranoux, J.P. Piel, J.L. Stehle, SPIE, vol. 3678, p. 126 (1999)
4. P. Boher, C. Defranoux, J.P. Piel, J.L. Stehle, SPIE symposium on microelectronic manufacturing technologies ,18-21 May 1999
5. R. Tousey. Phys. Rev. 50, 1057 (1936).
6. "Physikalisch-Chemische Tabellen," (W. A. Roth, K. Scheel, eds.), Edwards Brothers, Inc., Berlin, 911 (1923).
7. F. F. Martens. Ann. Physik 6, 603 (1901).
8. I. H. Malitson. Appl. Opt. 2, 1103 (1963).
9. Z. A. Weinberg, G. W. Rubloff, E. Bassous. Phys. Rev. B 19, 3107 (1979).
10. I. P. Kaminow, B. G. Bagley, C. G. Olson. Appl. Phys. Lett. 32, 98 (1978).
11. B. Brixner. J. Opt. Soc. Am. 57, 674 (1967).
12. P. Chinaudom, K. Vedam, Thin Solid Films, 234, 439 (1993).
13. T.M. Bloomstein, V. Liberman, M. Rothschild, SPIE vol. 3676, 342 (1999)

OPTICAL CHARACTERIZATION AND PROCESS CONTROL
OF TOP SURFACE IMAGING

YING-YING LUO, CRAIG STAUFFER*, CARLOS YGARTUA, DINH CHU and CLIVE
HAYZELDEN
KLA-Tencor Corporation, Film and Surface Technology Division, 160 Rio Robles,
San Jose, CA 95134, USA
*GENESIS, 3066 Scott Boulevard, Santa Clara, CA 95054, USA

ABSTRACT

The use of selectively silylated resists to facilitate top surface imaging offers the potential
for nanoscale lithography using both deep ultra violet (DUV) illumination and electron beam
techniques. In this process, an exposure-generated crosslinking prevents silicon incorporation
from silylating agents. In the non-crosslinked regions, a silylation agent reacts with OH groups in
the resist to form silicon-oxygen bonds. During subsequent dry development in an oxygen
plasma, the incorporated silicon attracts oxygen to form silicon dioxide, protecting the resist
underneath. The adjacent un-silylated resist erodes (develops) anisotropically 25-100 times faster
than the silylation-protected resist. The key to this process is the chemical formation of a
silylated region at the top of the resist. A challenge associated with the silylation process,
however, is lateral swelling of the silylated layer, which can lead to difficult dimensional control.
The amount of swelling depends on the amount of incorporated silicon. Therefore, the
uniformity and repeatability of the silylation process must be controlled. This paper will describe
how spectroscopic ellipsometry has been used to characterize and monitor the resist silylation
process in a non-destructive manner. The simultaneous characterization of the thicknesses and
optical properties of a series of silylated resists will be presented. Optical metrology of the
thickness of the silylated resists will be correlated with SEM cross-sectional analyses, and
process uniformity will be quantified using 49-site wafer maps.

INTRODUCTION

The scaling of integrated circuit design rules has resulted in the extensive application of
anti-reflective coatings (ARCs) in deep ultra violet (DUV) lithography, and great interest in
multi-layer resist systems for electron-beam (E-beam) direct writing techniques. With the help of
ARCs, 193 nm lithography can push optical lithography into the 1 GB (DRAM) range. E-beam
direct writing is increasing in importance because of its flexibility and high resolution, and could
be an alternative for printing critical layers at the 0.13 μm level and beyond. Top surface
imaging (TSI) processes employing the silylation of resist offer crucial advantages and push the
limits of DUV and e-beam lithography [1-3]. Figure 1 shows the process steps for a positive
resist process. After baking, the acid-catalyzed crosslinking prevents silicon incorporation in the
exposed regions, while the silylation agent reacts with OH groups in the unexposed resist to form
silicon-oxygen bonds. During dry development in an oxygen plasma, the incorporated silicon
further attracts the oxygen to form silicon oxide, protecting the resist underneath. A two-layer
resist structure is formed, with the silylated resist layer on top of un-silylated resist. A major
challenge for TSI processes is line edge roughness (LER) [4, 5]. While many factors contribute
to LER, the most problematic is poor silylation contrast, where the Si content incorporated into
resist is not uniform across the wafer. Poor contrast leads to non-uniform lateral swelling of the
silylated layer, which in turn leads to poor critical dimension (CD) control. The amount of
swelling depends on the amount of incorporated silicon. The uniformity of the silylation process

must be monitored as quickly as possible after the silylation process. A suitable measurement technique is non-destructive optical measurement. Optical differentiation of the un-silylated and silylated layers is possible due to the optical dispersion change with silicon incorporation.

This paper describes how the KLA-Tencor UV-1280SE spectroscopic ellipsometer (SE) was used to monitor a resist silylation process developed by GENESIS.
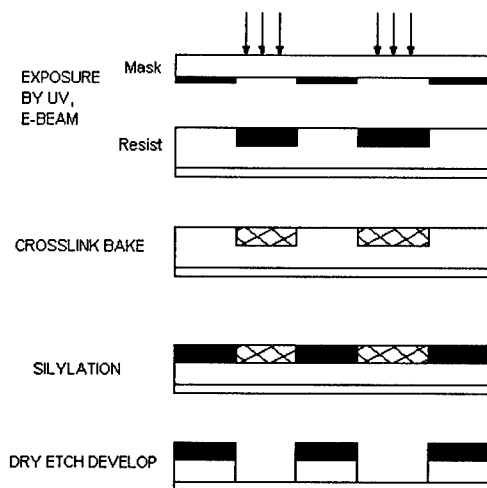
Figure 1. Silylation Process Steps

THEORY

Spectroscopic Ellipsometry

Spectroscopic ellipsometry relies on the detailed analysis of the wavelength dependence of polarized light reflected from the sample. The reflected polarized light is incident on the detector after passing through an analyzer. In the rotating polarizer implementation, the polarization state of the incident light is continuously varied and the integrated intensity of the reflected polarized light at each wavelength is measured at the detector. The integrated intensities corresponding to a complete rotation of the polarizer are used to mathematically compute the standard ellipsometry parameters, $Tan(\psi)$ and $Cos(\Delta)$ at each wavelength. These quantities are related to the two components R_P and R_S of the reflected polarized light, by the equation:

$$Tan(\psi)\exp(i\Delta) = R_p/R_s \qquad (1)$$

where R_P is the component of polarization parallel to the plane of the incident and reflected beams, R_S is the component perpendicular to that plane. A mathematical regression analysis is performed between the measured $Tan(\psi)$-$Cos(\Delta)$ spectra and theoretical computation.

The dielectric function is related to the optical constants by

$$\varepsilon = (n - ik)^2 \qquad (2)$$

where n is the refractive index, and k is the extinction coefficient.

RESULTS

Monitoring Thickness Using the UV-1280SE System

The system used to perform the silylation process was the GENESIS STAR—200. The resist used in this study, MXP-7, was provided by the Microlithography Chemical Corporation. In a spectroscopic ellipsometry measurement on the UV-1280SE system, the theoretical ellipsometry spectra Tan(ψ) and Cos(Δ), are calculated based on the film stack and the dispersion of the individual layer. Through the regression of the theoretical spectra to the measured spectra, thickness and dispersion information can be obtained. In this experiment, the harmonic oscillator model was used to define the optical dispersion properties of the resist films. Figure 2 shows typical dispersion curves for both the silylated and un-silylated resist films. It is easy to see that the most significant change of the dispersion occurs in the UV region. At a wavelength of 633nm, the index changes only slightly from 1.597 to 1.539.
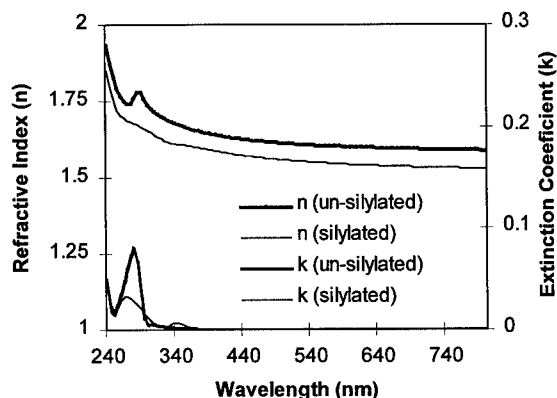
Figure 2 Dispersion of silylated and un-silylated resist.

An important role of the optical monitoring of the process is to predict thickness and material property changes with variations in processing conditions. In one experiment, several wafers were silylated for varying lengths of time, from 20 to 200 seconds. All other processing conditions except for the processing time were held constant. A single recipe was created and used to measure all of the wafers, including the thickness and refractive index of the top silylated layer, and the thickness of the bottom un-silylated layer. As expected, the increase of the silylated layer thickness slows down with the increase of silylation time due to the fact that the process of the silicon incorporation into resist
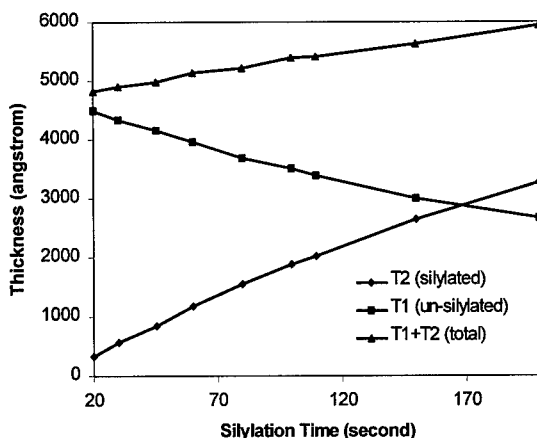
Figure 3 Thickness *versus* silylation time for a silylation process.

185

is diffusion controlled (Figure 3). Correspondingly, the decrease of the un-silylated layer thickness slows down with increasing silylation time. The total thickness, (T1+T2), increases with silylation time because of the swelling of the resist after silylation.

The uniformity of the silylation process over the whole wafer was monitored by a 49-site polar map measurement. As an example, Figures 4a and 4b show the thickness polar map of both the silylated layer and the un-silylated layer for one wafer processed with 80 seconds of silylation. The summary data are shown in Table 1.

Table 1. Summary of the 49-point polar map measurements for pre- and post-silylation wafers

Thickness	Post-Silylation				Pre-Silylation	
	Silylated		Un-silylated		Un-silylated	
	Mean	Std. Dev	Mean	Std. Dev	Mean	Std. Dev
	1561.5 Å	2.02%	3696.8 Å	0.66%	4762.6 Å	0.43%
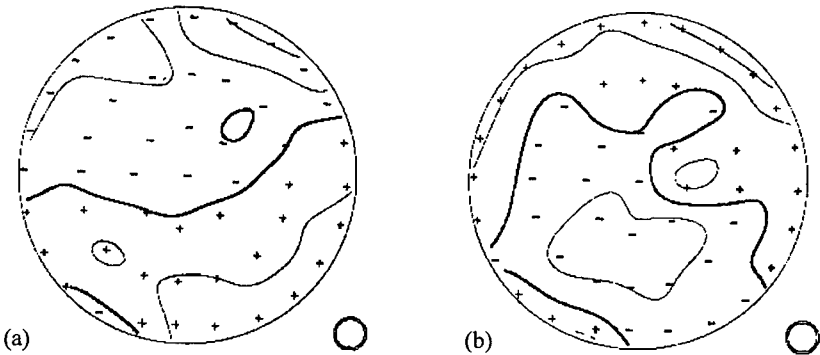
Figure 4 The 49-point polar maps of (a) the silylated layer (left) and (b) the un-silylated layer (right). The thick line stands for the mean of the thickness. The thin line stands for thickness of 1σ apart from the mean. Wafer orientation is shown with the wafer symbol at the lower right corner of the map.

Remaining Layer Measurement and Comparison to SEM

To investigate measurement accuracy, three wafers with almost identical resist thickness were silylated under the same conditions. On two of these wafers (Wafer 2 and Wafer 3), the silylated layer was immediately stripped off with xylene and the wafers were measured using the single-layer recipe. The other wafer (Wafer 1) was measured with the bi-layer recipe. Table 2 shows the measurement results for the three wafers. The pre-silylation thicknesses for all three wafers were in the range 4736 Å and 4756 Å. The remaining resist thicknesses for Wafers 2 and 3, 3478 Å and 3493 Å, respectively, match well to the 3514 Å remaining thickness on Wafer 1 in the bi-layer measurement.

Table 2. Comparison of bi-layer measurement to corresponding single layer measurement

Wafer		T2 (Silylated)	T1 (Remain)
1	Pre-	--	4746.2 Å
	Post-	1872.5 Å	3514.4 Å
2	Pre-	--	4755.9 Å
	Remain	--	3478.2 Å
3	Pre-	--	4736.0 Å
	Remain	--	3493.1 Å

In a separate experiment, two wafers silylated for either 80 seconds or 150 seconds were measured on the UV-1280SE system and immediately taken for a cross-section SEM. The micrographs from this experiment are shown in Figures 5 (a) and (b). The results are summarized in Table 3. Unfortunately, the normal SEM could not distinguish the boundary between the silylated and un-silylated layers, so that only the total thickness was measured. The good match in total thickness validates the bi-layer measurement.

Table 3. Comparison of results of UV1280 measurement to SEM

	Wafer 4 (150 sec)		Wafer 5 (80 sec)	
	UV-1280SE	SEM	UV-1280SE	SEM
T2 (silylated)	2575.4 Å	--	1501.2 Å	--
T1 (remain)	3040.7 Å	--	3747.1 Å	--
Total	5616.1 Å	5600 Å	5248.3 Å	5200 Å
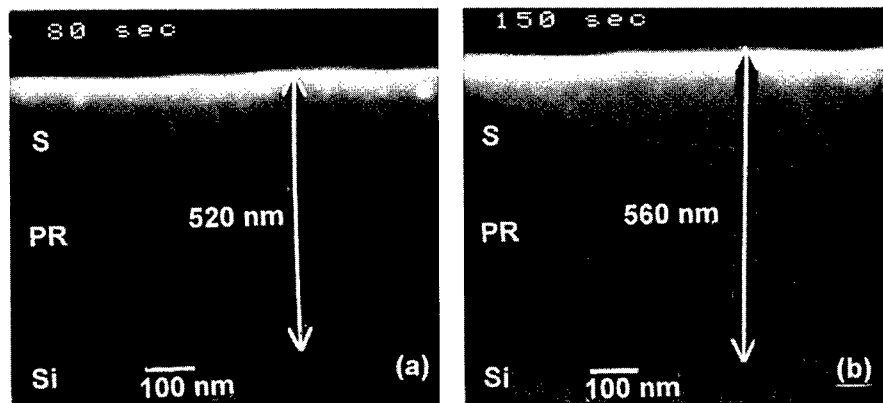
Figure 5 Cross-section Scanning Electron Micrographs of (a) a 80-second processed wafer and (b) a 150-second processed wafer.

Static Stability

A static stability test consisting of 30 measurements performed at the center of the wafer without moving the wafer between measurements was run on pre- and post-silylation wafers. In addition to evaluating measurement stability, this test checks if the exposure of the resist to ultraviolet light during measurement causes changes in the resist properties. As shown in Table 4, for pre-silylation resist, the 3-sigma standard deviation is as small as 2.3 Å out of the mean

value of 4725 Å, or 0.05%. For post-silylation resist bi-layer measurements, the 3-sigma standard deviation is 0.3% for the silylated layer and 0.1% for the un-silylated layer.

Table 4 Static stability measurement of pre- and post-silylated resist (30-site center)

	Pre-silylation	Post-silylation	
		T1: Un-silylated	T2: Silylated
Mean	4724.9 Å	3749.9 Å	1185.9 Å
Std.Dev (3σ)	2.3 Å	5.4 Å	4.0 Å
Range	3.01 Å	6.74 Å	4.97 Å

The trends of the 30-site measurement are shown in Figures 6 (a) and (b).
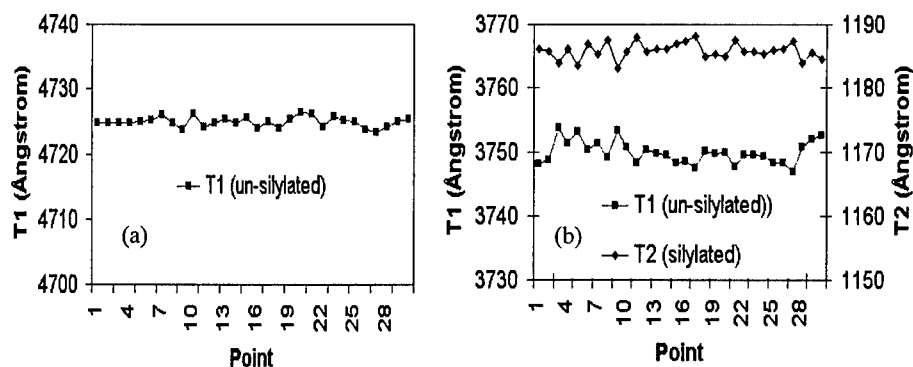
Figure 6 The 30-site static measurements for (a) a pre-silylation wafer and (b) a post-silylation wafer.

CONCLUSION

The results obtained with the UV-1280SE system showed excellent correlation with SEM. The 30-site static stability measurement showed stable performance of the UV-1280SE on photo-sensitive resist. Furthermore, a single measurement recipe was able to monitor the process variation across a wide process window. The test results prove that the spectroscopic ellipsometry of the UV-1280SE thin film measurement system is a powerful tool for monitoring the resist silylation process.

REFERENCE

1. C. Stauffer, W. Peterson, Genesis Technical Bulletin, #10, 1996.
2. C. Stauffer, W. Peterson, presented at 1996 Semicon Kansai, Japan.
3. M. Irmscher, B. Hofflinger, R. Springer, C. Stauffer, W. Peterson, J. Photopolymer Science and Technology, vol. 9, No. 3, 497 (1996).
4. D. E. Seeger, D. C. La Tulipe, Jr., R. R. Kunz, C. M. Garza, and M. A. Hanratty, IBM Journal of Research and Development, vol. 41, No. 1/2, 105 (1997)
5. S. C. Palmateers, S. G. Cann, J. E. Curtin, S. Deneault, A. R. Forte, R. R. Kunz, T. M. Lyszczarz, M. B. Stern, 4th Intl. Symp. On 193nm Litho. (Austria), Sept. (1998).

Improved Algorithm to Extract Force-distance Curves from Scanning Force Microscope Data

Steven J. Eppell,[*] Brian A. Todd,[*] Fredy R. Zypman[**]

[*] Biomedical Engineering Department, Case Western Reserve University, Cleveland, OH
[**] Department of Physics and Electronics, University of Puerto Rico, Humacao, PR

Abstract

Physically meaningful near-surface force fields are used to calculate simulated scanning force microscope cantilever deflection data. The simulated data is used to evaluate the ability of a few models to calculate forces from cantilever deflections. The conventional simple harmonic oscillator model is shown to be significantly inaccurate in converting deflections to forces. A bending beam model is developed which accurately converts deflections to forces. This model is shown to be necessary for accurate assignment of physical meaning to the calculated forces under high force gradient conditions.

Introduction

The interaction of surfaces with their surroundings can be described as arising from force fields generated by molecules at the surface of interest. This statement is equally true for magnetic interactions of computer storage media, electrostatic interactions of proteins on cell membranes, and steric interactions of macromolecules on polymer surfaces. To better understand these systems and ultimately to design superior materials, it is necessary to make direct measurements of these near-surface molecular scale force fields. Such measurements have been made for many years using the surface forces apparatus (SFA) with great impact on our understanding of the behavior of material surfaces.[1-5] One shortcoming of these measurements is their lack of molecular scale resolution in the plane of the surface of interest.

Scanning force microscopy (SFM) holds some promise in the endeavor to extend SFA type measurements to a full three dimensional submolecularly resolved space. Previous work in this area has shown that SFM allows for the measurement of the response of a single molecule to applied loads.[6-8] In addition, measurement of the interaction force between two molecules has been demonstrated.[9-11] While spectroscopic techniques have yielded the interaction energy between pairs of molecules, SFM provides a direct measure of the force itself. Investigators have measured the force of rupture of molecular bonds directly as well as the elastic response prior to bond failure.[12,13] SFM allows one to probe the near surface force fields on a scale relevant to what an individual molecule near that surface might sense.[14-21]

The success with which these experiments can be carried out depends largely on how well the information yielded by SFM (cantilever deflection and sample position) can be converted into the force sensed by the cantilever at a given tip-sample separation. A number of different algorithms have been proposed to accomplish this task that take as inputs either deflection of the loaded end of the cantilever or change in the resonant frequency of the cantilever.

Hooke's law ($F = kz$) is the standard algorithm. In this case, z (deflection of loaded end of cantilever) is given by the SFM and it is assumed that the cantilever is in static equilibrium. This assumption is justified for tip-sample separations outside of the snap-to-contact region and when the rate at which the tip-sample separation is varied is relatively small.

The Hooke's law assumption is too restrictive for ascertaining forces in the snap-to-contact region or for doing force-distance mapping at high speeds. The snap-to-contact region is generally of interest because it contains information about the bonding properties of the system. The region is of particular importance to the biological community since, at physiological pH

and ionic concentration, nearly all of the measurable force generated by a surface resident molecule is in the snap-to-contact region. The snap-to-contact region is also of interest for studying the van der Waals (vdW) force. This force is exceedingly small outside the snap-to-contact region. While vdW measurements can be made using high Q systems in vacuum, this is difficult in air and impossible in fluid. Thus, to test various models of the functional form of the vdW force, it is useful to obtain high quality data inside the snap-to-contact region. In general, when probing attractive near-surface forces prior to contact, F=kz is not a good model to use.

High speed force-distance measurements also present a problem when analyzed using Hooke's law. Typical force-volume measurements are made by cycling the tip-sample distance at ~10 Hz. This results in typical image collection times of ~100 minutes. In fact, all of the necessary information for making a force-volume measurement is contained in a typical intermittent/contact mode image which can be collected in 1-10 minutes. However, it can hardly be said that the cantilever is in equilibrium when it is snapping to contact and breaking free tens to hundreds of thousands of times a second.

A better model for converting SFM data into forces utilizes the simple harmonic oscillator (SHO) with mass, (F= kz + ma).[22] This model does a much better job than the massless Hookian spring at recovering the desired force distance curve since the inertial acceleration term allows for non-equilibrium analysis. The major shortcoming of this model is the assumption that the cantilever can move in only one mode. As long as the cantilever responds to a force-field containing small gradients (<k), this is certainly a good approximation. However, under large gradients which occur in the snap-to-contact region and during high speed force-distance mapping, this assumption is violated. We will show below that this shortcoming has negative consequences when trying to assign physical meaning to force-distance curves derived from SFM measurements.

A more accurate method for converting SFM data to force-distance curves involves modeling the cantilever as a bending beam.[23,24] This allows for non-equilibrium analysis and an infinite number of modes of the cantilever. Previously, we suggested analyzing frequency shifts in the bending beam model to obtain force gradients near a surface.[25] While this concept works to convert frequencies to force gradients, there are experimental limitations on the obtainable frequency resolution. In particular, in the snap-to-contact region, the curve exists for too short a time. This limits the frequency resolution so severely that force-distance curves cannot be determined. However, using the bending beam model to cast a solution in the time domain is a viable method for extracting force-distance curves from SFM data. In particular, assuming an initial shape for the cantilever and fitting it to agree with the measured z(t) data works.

Using the bending beam model, this paper shows how to take advantage of high speed cantilever displacement data to accurately calculate near-surface force fields. We briefly sketch out the theory used to accomplish this. Finally, we show an example of how our algorithm performs using a typical force field expected to exist at surfaces of interest.

Theory

A brief overview of the theory necessary for using the bending beam model to analyze SFM force-distance data is presented. The model presented here has been used to simulate SFM cantilevers interacting with surface forces.[24,25] In these simulations, equations for the force curve are specified along with the initial position and velocity of the cantilever and the time evolution of the cantilever's loaded end position, $z(L, t)$, was observed. To construct SFM force-distance data, one is presented with the inverse problem; $z(L, t)$ is known and the surface force has to be determined.

When simplifying the cantilever dynamics in the form of a quasistatic simple harmonic oscillator (Hooke's law) or the dynamic simple harmonic oscillator (SHO), the solutions to the inverse problem are,

$$F = kz(L,t) \qquad (1)$$

and

$$F = m\frac{\partial^2 z(L,t)}{\partial t^2} + kz(L,t) \qquad (2)$$

respectively, where $z(L,t)$ is the time dependent displacement of the cantilever's loaded end, k and m are the effective spring constant and mass of the model oscillator. Obtaining the force with these models involves using the $z(L,t)$ SFM measurement and the calibrated cantilever parameters (k and m) to compute the right-hand-sides of (1) and (2).

The more complete bending beam model utilizes a governing equation for the system that is,

$$\rho A \frac{\partial^2 z(x,t)}{\partial t^2} + EI \frac{\partial^4 z(x,t)}{\partial x^4} = 0 \qquad (3)$$

where $z(x,t)$ is the vertical displacement of the cantilever at position x and time t, with ρ, A, E, and I being geometric and material constants describing the cantilever. The boundary conditions follow from the rigid attachment at the cantilever base, $x = 0$

$$z(0,t) = 0, \qquad \frac{\partial z(0,t)}{\partial x} = 0 \qquad (4A,B)$$

and, at the loaded end, a balance between the surface force, F and the beam shear force,

$$\frac{\partial^2 z(L,t)}{\partial^2 x} = 0, \qquad -EI\frac{\partial^3 z(L,t)}{\partial^3 x} = F. \qquad (4C,D)$$

Finally, the initial position and velocity of the cantilever must be known,

$$z(x,0) = u(x) \qquad \frac{\partial z(x,t)}{\partial t} = v(x). \qquad (5)$$

While this model gives a more realistic representation of the cantilever, it also presents two difficulties for experimental use. First, the initial conditions require knowledge of the entire shape of the cantilever whereas most commercial SFMs measure deflections at only one location. We assume that the initial shape is the equilibrium shape. Second, the relationship between the measurable quantity, $z(L,t)$ and F is expressed using solutions to the boundary value problem that are not easily invertible. In other words, we cannot write a simple equation for F in terms of $z(L,t)$. However, if we have a set of experimental data giving the position of the cantilever's loaded end as a function of time, F can be obtained by a nonlinear least square regression of the deflection predicted by the model against the SFM deflection data.

We use this approach to reconstruct SFM force-distance curves and compare them to force curves reconstructed using Hooke's law and the simple harmonic oscillator. The SFM data was

generated using the simulation described by Turner et al.[24] F, The surface force used in the simulations was of the form

$$F = -\frac{A}{(D-D_0)^2} + \frac{B}{(D-D_0)^8} - \frac{M}{(D-D_0)^4}.$$ (6)

F includes a pair interaction of the form $-A/D^m + B/D^n$ (mn potential) appropriate for the vdW-hard-core interaction between a spherical SFM probe and an infinite plane (m=2, n=8) and a magnetic force term. The D_0 term accounts for unknown absolute separation between the SFM probe and the surface. The cantilever used in the simulation had an equilibrium spring constant of 0.6 N/m and a first mode resonant frequency of 40 kHz. The sample surface was cycled at a rate of 1 μm/s.

We reconstuct force curves from the simulated cantilever deflection data using the Hooke's law model, the SHO, and the bending beam model to demonstrate how each of the *cantilever* models works in the context of surface forces that are relevant to SFM force-distance experiments. The goal of such experiments is often to determine a physically appropriate form for the force equation and the value of its important parameters. To evaluate each of the cantilever models in this spirit, we reconstruct a force-distance curve, $F(D)$, using each of the cantilever models and then interpret it by finding the best fit to (6). The cantilever model used is shown to have a significant effect on the fitted parameters obtained and hence the physical interpretation of the force-distance data.

Results & Discussion

Cantilever deflection data was generated by simulating the SFM force-distance experiment. In the simulation the complete shape of the cantilever is known; However, for the force-distance curves reconstructed below, we retain only the deflection of the loaded end. This is the physical parameter recorded by most commercial SFM machines. Noise and viscous damping were neglected in this paper. It has been shown that viscous damping can be easily accounted for.[24] The lack of noise in our simulation yields results that are a best case scenario for testing the various models' ability to recover force-distance curves from SFM data. Finally, it was necessary to use simulated data since the actual force fields existing in nature are unknown at the length scales of interest. Thus, a meaningful comparison of the reconstructed force curves to the true force experienced by the SFM cantilever can only be rigorously performed using a mathematical simulation.
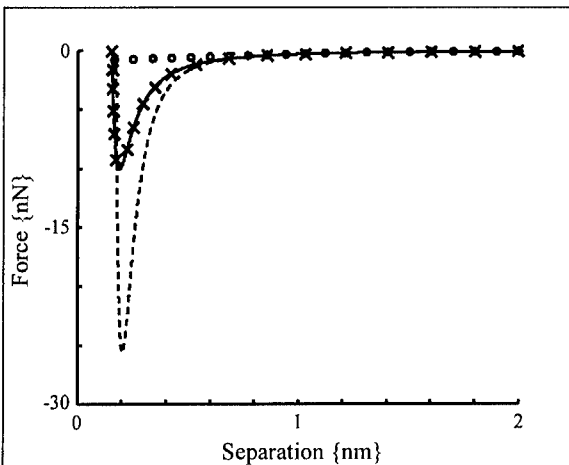

Figure 1. Reconstructed force separation curves from: Hooke's law (o), SHO (--), bending beam (x). The solid line is the force curve used in the simulation (true value).

192

Figure 1 shows the force-distance curves reconstructed using each of the cantilever models. The continuous line is the input force-distance curve (6) used to generate the simulated SFM data (true values). The circles are the result of using Hooke's law (1) to recover the force-distance curve. For tip-surface separations greater than ~1 nm, this model works well. However, this accounts for only 10 % of the attractive force range of the curve, a dramatic example of how little of the force is reflected by the position of the end of the tip at small tip-sample separations.

The dotted line in Figure 1 results from using the SHO model (2) to recover the force-distance curve. This model accurately recovers the input force curve for separations greater than about 0.6 nm. Again, this represents a small fraction of the total force range of the curve (~20 %). Qualitatively, this curve begins to reflect the nature of the input force-distance curve. By comparing the Hooke's law result (circles) with the SHO result (dotted line) it becomes apparent that much of the cantilever's response near the surface is reflected by the acceleration of the beam. However, the SHO model overestimates the force associated with the tip acceleration and overshoots the minimum of the input curve by more than a factor of two. The difference between the SHO model and the input curve is due to the SHO's inability to account for the dynamic shape of the cantilever when it is traversing high force gradient regions.

The X's in figure 1 result from using the bending beam model (3-5) to recover the force-distance curve. This model does an excellent job of recovering the input curve. It is worth mentioning that the bending beam model used here cannot be a simple inverse of the model used to generate the simulated data because the solutions are not easily invertible. This necessitated the use of nonlinear least squares curve fitting. We performed this fit by varying the coefficients in (6) until the best fit was obtained. It is also worth mentioning that since only the deflections at the loaded end of the cantilever are available the inverse problem for the multimodal beam is mathematically incomplete. We overcame this problem by assuming that the initial shape was given by the equilibrium deflection. The fact that the Hooke's law model is initially able to predict the correct loading force validates this assumption. The excellent reconstruction obtained with the bending beam model provides further validation.

The ultimate aim of the kind of force-distance analysis we have been discussing is to assign physically meaningful parameters to the SFM data. One way to accomplish this is to fit the SFM $F(D)$ data to an analytical expression containing physically meaningful terms. Equation 6 is such an expression. We fit the reconstructed curves from the three different cantilever models to this expression allowing A, B, M and D_o to vary. Table 1 shows the results of this fit. It is clear that both the Hooke's law and SHO model produce errors much greater than those normally tolerated as accurate SFM measurements. It should be kept in mind that we performed a very conservative curve fitting procedure assuming the correct form for $F(D)$ was known and asking the models to fit the coefficients in (6). We found that if the exponents are allowed to vary in the

Table 1				
Results of the best fit of the various cantilever models to Eq. 6. The terms in parentheses represent the percent error between the calculated value and the true value.				
Magnetic	A {N.nm^2}	B {N.nm^8}	M {N.nm^4}	Do {nm}
Hooke's	0.5167 (74%)	-1.1 X 10^{-3} (11,245%)	-0.1021 (10,310%)	-0.2564
SHO	0.0775 (74%)	4.6056 x 10^{-5} (367%)	0.0655 (555%)	0.0112
Beam	0.2961 (0%)	9.8696 x 10^{-6} (0%)	0.0100 (0%)	0.000
True	0.2961	9.8696 x 10^{-6}	0.0100	0.000

fit, the SHO model recovers the wrong values. This behavior would make it exceedingly difficult to use the SFM to accurately assign physical meaning to unknown forces in the near-surface region. In addition, we used the correct values for the various coefficients as the starting values in the fit. Still, the Hooke's law and SHO models diverged from the true values and proffered coefficients that were 100's to 1000's of percent off the true values. The Hooke's law model converted the repulsive portion of the mn force to an attractive term and converted the attractive magnetic force to a repulsive term. A particularly revealing aspect of the failure of the SHO model's fit was that it took power away from the vdW attractive term (B) and added to the attractive magnetic term (M). We found this false distribution of forces by the SHO model to be generally true. For example, when we added a screened Coulomb potential to the fitting function (data not shown), we found the SHO model used the Coulomb term to obtain the best fit. This occurred even though the simulated data was generated using no Coulomb term in the input force function. Figure 1 also shows that the errors introduced using Hooke's law and the SHO dramatically change the shape of the $F(D)$ curve; the errors are not simply different by a scaling factor. This would lead to an assumption of the incorrect form for a near surface force field because it better fit the distorted $F(D)$ curve reconstructed by Hooke's law or the SHO.

Conclusions

We have shown that when considering high gradient near surface force fields, it is necessary to use a more sophisticated model than a simple harmonic oscillator to convert SFM data into force-distance curves. Failure to do this results in significant quantitative errors in the calculated forces. In addition, significant errors result in the assignment of physical forces to the obtained data. Use of a bending beam model to convert SFM data to forces alleviates both of these problems allowing for quantitative physically meaningful analysis of near surface force fields.

1   J. N. Israelachvili, Surf Sci Rep 14, 109-159 (1992).
2   J. N. Israelachvili, Yl Chen, and H. Yoshizawa, J Adhes Sci Technol 8, 1231-1249 (1994).
3   Yl Chen, C. A. Helm, and J. N. Israelachvili, Langmuir 7, 2694-2699 (1991).
4   S. Yamada and J. Israelachvili, J Phys Chem B 102, 234-244 (1998).
5   J. L. Parker, Prog Surf Sci 47, 205-271 (1994).
6   M. Rief, F. Oesterhelt, B. Heymann, and H. E. Gaub, Science 275, 1295-1297 (1997).
7   T. Strunz, K. Oroszlan, R. Schafer, and H. J. Guntherodt, Proc Nat Acad Sci Usa 96, 11277-11282 (1999).
8   A. D. MacKerell and G. U. Lee, Eur Biophys J Biophys Lett 28, 415-426 (1999).
9   B. EssevazRoulet, U. Bockelmann, and F. Heslot, Proc Nat Acad Sci Usa 94, 11935-11940 (1997).
10   H. Grubmuller, B. Heymann, and P. Tavan, Science 271, 997-999 (1996).
11   Z. Yingge, Delu Z., B. Chunli, and W. Chen, Life Sci 65, PL253-PL260 (1999).
12   J. Fritz, D. Anselmetti, J. Jarchow, and X. Fernandez-Busquets, J Struct Biol 119, 165-171 (1997).
13   J. Fritz and D. Anselmetti, Eur J Cell Biol 74, 71-71 (1997).
14   W. Denk and D. W. Pohl, Appl. Phys. Lett 59, 2171-2173 (1993).
15   H. J. Butt, Biophys J 60, 1438 (1991).
16   H. J. Butt, M. Jaschke, and W. Ducker, Bioelectrochem Bioenerg 38, 191 (1995).
17   W. F. Heinz and J. H. Hoh, Biophys J 76, 528 (1999).
18   J. L. Hutter and J. Bechhoefer, J Vac Sci Technol B 12, 2251 (1994).
19   T. Ishino, H. Hieda, K. Tanaka, and N. Gemma, Jpn J Appl Phys Pt 1 33, 4718 (1994).
20   C. Rotsch and M. Radmacher, Langmuir 13, 2825 (1997).
21   S. H. Xu and M. F. Arnsdorf, Proc Nat Acad Sci Usa 92, 10384 (1995).
22   F. R. Zypman and Eppell S. J., J Vac Sci Technol B 15, 1853-1860 (1997).
23   S. Hirsekorn, U. Rabe, and W. Arnold, Nanotechnol 8, 57-66 (1997).
24   J. A. Turner, S. Hirsekorn, U. Rabe, and W. Arnold, J Appl Phys 82, 966-979 (1997).
25   F. R. Zypman and Eppell S. J., J Vac Sci Technol B 16, 2099-2101 (1998).

EXTENDING THE POSSIBILITIES OF NEAR-FIELD SCANNING OPTICAL MICROSCOPY FOR SIMULTANEOUS TOPOGRAPHICAL AND CHEMICAL FORCE IMAGING

N. NAGY, M. C. GOH
Department of Chemistry, University of Toronto, Toronto, ON M5S 3H6, CANADA

ABSTRACT

The Near-field Scanning Optical Microscope (NSOM) is an innovative new form of surface microscopy, which can be used to obtain local spectroscopic information about surfaces, enabling the characterization of nanometer-sized regions. The most important component of this instrument is the scanning probe tip. In this paper, we discuss the production of a novel fiber optic probe that can be used in local spectroscopy with an NSOM, but also for simultaneous imaging of topography and chemical forces. The probe consists of a bent, tapered silicon dioxide optical fiber. We have determined the rates of selective wet chemical etching of germanium dioxide doped pure silica optical fibers and used this information to optimize the probe etching process. A systematic approach for the development and testing of such probes is presented. The performance of the optical probes was characterized using surfaces prepared by the technique of microcontact printing. Phase and friction images of these surfaces were obtained using both standard atomic force microscopy tips and the optical fiber probe. The new optical probe was capable of distinguishing between different chemical regions on the patterned surface.

INTRODUCTION

The structure of a surface, both in terms of topography and chemical composition, determines its macroscopic properties. The characterization of such structures for real-life surfaces can be quite complex and difficult to describe. The evolution of probe microscopy techniques has facilitated this process, enabling one to obtain information about a surface and local material properties over a range of spatial resolution, and in ambient or fluid conditions. The basic principles of the scanning probe techniques such as the Atomic Force Microscope (AFM) are as follows: a sharp probe tip is brought into close proximity to a sample surface, and a feedback mechanism is used to keep either interaction or their separation fixed. As the tip and the sample are scanned relative to each other, the topographical structure of the surface can be obtained. This image neither distinguishes between chemically different features, nor does it provide the identity of the different structures.

Improvements in the AFM have given the ability to distinguish between different chemical domains, at least in some instances. For example, measurement of lateral forces during imaging is sometimes ascribed to frictional effects, and has been shown to generate excellent contrast between domains that have the same topography but differ in their chemistry [1]. Oscillating cantilever techniques, such as phase detection and force modulation imaging, show sensitivity to adhesive and elastic properties of materials [2]. For imaging purposes, contrast between different domains can be enhanced significantly in these new forms of the AFM. However, the detailed interpretation of the contrast mechanism, and hence their quantification, is still not completely understood.

Optical imaging- based probe microscopes, such as the NSOM [3], have attracted special interest because they can provide information about local material properties through spectroscopic means: fluorescent labels can be localized, absorbance of different domains can

195

be measured, and spectroscopic fingerprints can be obtained. The information obtained by the NSOM is mainly gathered from the topmost surface layer. However, depending on the instrumental configuration, this layer can be 100-200 nm, and information about the chemical functionalities exposed at the interface cannot be obtained directly. This issue is best addressed by chemical force microscopy, in which the probe tip is modified with different molecules so that the tip terminates with well-defined chemical functionalities [1]. The interaction between different surface functionalities can be tailored to give selectivity, thus providing the AFM with chemical sensitivity.

To date, no individual technique can provide all these types of information in a single measurement. Our goal is to build a novel hybrid instrument that can incorporate simultaneous topographic, spectroscopic and chemical force imaging of mesoscopic structures on surfaces. In this paper we will describe a systematic method for the preparation of probe tips that are useful in NSOM, but can also be derivatized to provide them with chemical sensitivity. We also report the initial tests in performing chemical force imaging with such probes.

EXPERIMENT

Microscope development

The microscope we are developing is based on an existing Digital Instruments Nanoscope III, Atomic Force Microscope (AFM), Santa Barbara, CA. The original configuration of the Nanoscope III AFM uses sharp probe tips mounted on microfabricated cantilevers. To allow optical data collection, we have substituted a bent optical fiber for the typical AFM probe tip. The distance sensing mechanism utilizes either the deflection of the cantilever when operating in contact mode, or the amplitude of the cantilever oscillation when using Tapping Mode™.

Optical probe preparation

The optical fibers were purchased from SpecTran Specialty Optics Company (Avon, CT). Chemical etching of fibers was done at room temperature without stirring of the etchant solution. All chemicals were purchased from Sigma-Aldrich Canada Ltd. (Oakville, ON). Images of the etched fibers were taken by a Field-emission Scanning Electron Microscope (SEM), Hitachi S-4500. The fibers were sputter coated with gold prior to SEM imaging. Fiber bending was carried out with a PFS-330 Optical Fiber Splicer (Power Technology Inc., Little Rock, Arkansas). The bent probe cantilever section was coated with 100 nm thermally evaporated aluminum.

Preparation of test surfaces

Test surfaces were prepared by a microcontact printing method [4]. Microscope cover slides, from Fisher Scientific (Unionville, ON), were used as substrates. The slides were coated with 10 nm of titanium and 300 nm of gold by thermal evaporation. Polydimethylsiloxane (Sylgard 184), obtained from Paisley Products Inc. (Scarborough, ON), elastomer stamps bearing a pattern of raised and recessed areas were prepared and inked with millimolar ethanol solution of hexadecane thiol. The stamp was dried with nitrogen and brought into contact with the gold surface. At the points of contact, the thiols transferred and the remaining regions of the substrate were subsequently filled with hexadecanoic acid by immersing the substrate in a hexadecanoic acid solution.

196

RESULTS

Both the topographical and optical resolution of an NSOM is a function of the tip's radius of curvature [5]. Besides its importance in image resolution, tip geometry also determines the tip-sample contact area and therefore the magnitude of forces acting between these surfaces. Because of these reasons, having a reproducible tip radius of curvature and known geometry becomes very important for quantitative measurements. We have explored two different techniques for tip formation: a wet chemical etching process and a tapering process.

The chemical etching process is based on the original structure and geometry of a commercial optical fiber. Step index fibers consist of two concentric cylinders with a common axis. The outer material, called the cladding, is pure fused silica, SiO_2; the inner material, called the core, is a mixture of fused silica and germanium dioxide (SiO_2 and GeO_2). When cleaved optical fibers were placed into a buffered hydrofluoric acid solution the etching occurs at different rates at the two regions. We observed that at the interface of the core and cladding, a distinct angle forms in the material which etches slower. The angle formed depends on the relative etch rates, and does not change in time (Figure 1.a-d.). As the etching continues, the original cylindrical geometry leads to the formation of a cone with a well-defined angle and a reproducible radius of curvature. As expected, the differential etching rates are directly related to the GeO_2 core concentration. Increasing the GeO_2 concentration further retards the etching of the core and increased the etching angle. The same conditions gave a 42° etching angle and a 30 nm tip radius of curvature for a fiber with 4mol% GeO_2 doped core. The etching angle and the radius of curvature was 59°, 15 nm for the 8mol% fiber (Figure 1 e-f).

Both the overall and the differential etch rates can be varied by changing the etchant composition. Figure 2 a-f shows that high ammonium concentrations resulted in the preferential etching of the cladding, forming a sharp tip, while low ammonium concentrations reversed the etching process: the core of the fibers was etched faster than the cladding. Figure 3. shows the etching angles as a function of etchant volume ratios. The "reversed" etching is represented by negative angles. We found that the most optimal condition for tip formation are at high ammonium concentrations. The pure fused silica etch rates were monitored by measuring the fiber outer diameter. We found the change to be linear in time (Figure 4).
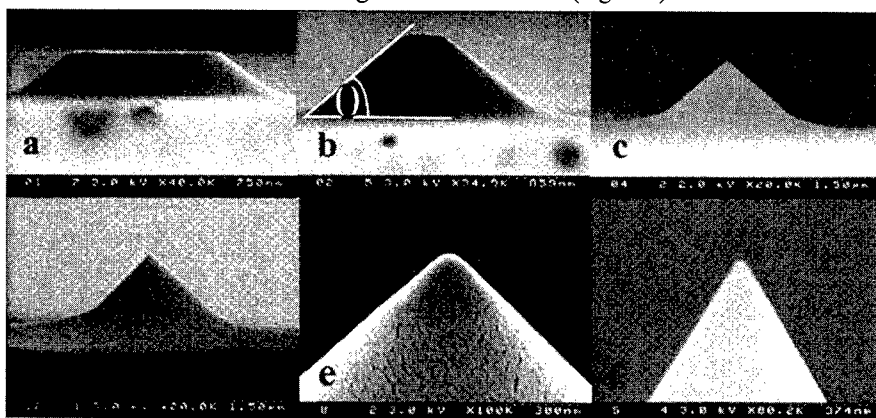
Figure 1. SEM images of etched fibers. Etching times: 15, 30, 60 min, 5 hours (a, b, c, d) and 2 hours (e, f) respectively. Etching angle (θ). Fiber core GeO_2 concentration: 4mol% (a-e), 8mol% (f). Etching solution concentration: (6:1:1) of (40w% NH_4F: cc HF : H_2O).

197
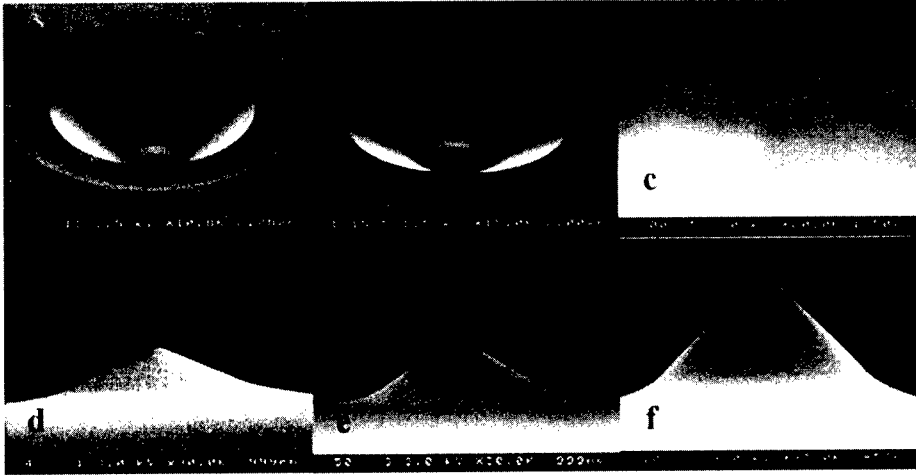
Figure 2. SEM images of etched fibers using different concentration solutions. Etchant composition: (X:1:1) of (40w% NH$_4$F: cc HF : H$_2$O). X= 0.5;1;1.5;2;2.5;11; a, b, c, d, e, f respectively. Fiber GeO$_2$ core concentration was 4mol%.

A different technique for preparing bent optical probes is a tapering process. In this approach, both fiber ends are held down in a fiber splicer and a stress is formed in the fiber along the vertical axis. When a spark is established between two electrodes, the material bends where stress was formed. After the bending, additional stress results in a tapering process and a sharp tip can be formed. Further selective etching can result in sharper tips as well.
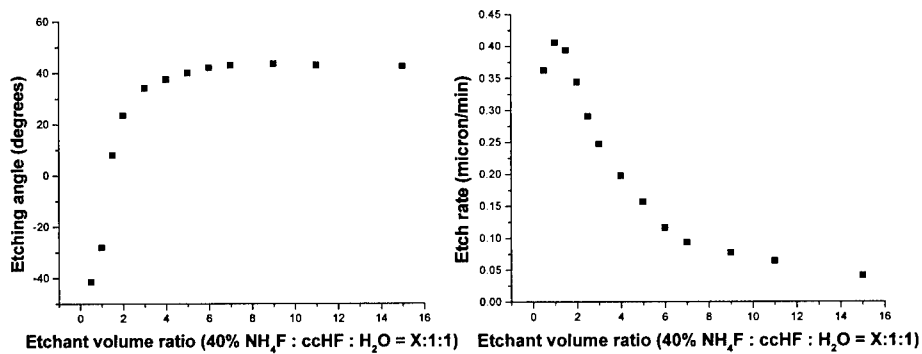
Figure 3. Etching angle as a function of etchant composition: (X:1:1) of (40w% NH$_4$F: ccHF : H$_2$O). Fiber GeO$_2$ core concentration was 4mol%.

Figure 4. Pure fused silica etching rates as a function of etchant composition: (X:1:1) of (40w% NH$_4$F: ccHF : H$_2$O

Our focus is to develop a technique that can provide direct chemical imaging of surface functional groups. To test whether our probes are sensitive enough to distinguish between different surface chemical groups, we prepared surfaces with known domains of methyl and carboxylic acid functionalities by the technique of microcontact printing. Such samples have no topographical features and are uniform in elastic properties, thus the image contrast is due to the magnitude of forces acting on the tip during scanning [6]. The difference in tip-sample interaction between the methyl (CH_3) and carboxylic acid (COOH) functionalized surface regions can be monitored by phase imaging or by friction imaging. Such images using single step bent and tapered optical probes were obtained (Figure 5 a-b). Both the phase and friction images clearly show the different surface domains. In air, we observed larger friction, corresponding to a brighter area, between the fused silica probe and the carboxylic acid functional groups, than between fused silica and methyl functional groups. Similarly, darker areas in the phase image show increased adhesion between the fused silica tip and the carboxylic acid terminated domains relative to the methyl terminated regions. The enhanced friction and adhesion, may be attributed to capillary forces between adsorbed water layers on both the hydrophilic silica tip and carboxylic acid terminated substrate domains.

Surface group functionalities will determine the type and magnitude of interaction between the surfaces in contact. To discriminate chemically different forces, our future work will focus on performing such experiments in a controlled atmospheric environment to minimize the effect of capillary forces. We hope that by modifying the probe tip surface by self-assembled organosilanes we can further tailor the interaction between tip and sample to be highly specific and we can obtain chemical recognition on the molecular scale.
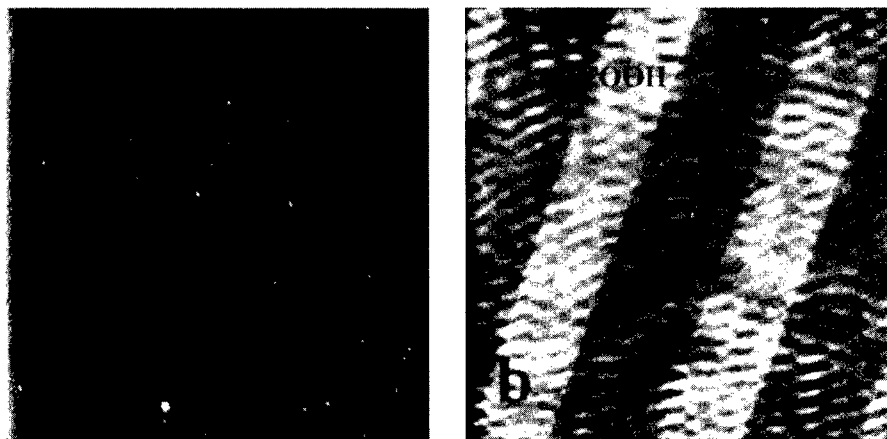
Figure 5. Phase, a, and friction, b, image of a surface patterned with methyl (CH_3) and carboxylic acid (COOH) functionalities obtained by a fiberoptic probe. Image size: 100x100 micron.

CONCLUSIONS

The frontier challenge in microscopy and surface analytical chemistry is the analysis of complex multi-component systems at the molecular level. Probe microscopy techniques can

give topographical information about a surface; however, the images generally lack chemical information. Near-field optical microscopy can collect optical data from the near-field of the sample surface and can permit the chemical identification of different features, but the technique still lacks the ability to show which functionalities are exposed at the interface. Chemical specification of a surface could be mapped by using different functionalized probes. Currently no technique can measure all these factors in a single, simultaneous measurement. We are developing a technique that can integrate the topographical, optical and chemical force imaging into a single step measurement. The most important aspect of such a technique are the probe tip geometry and the cantilever response. In this paper, we have showed that the probe tip radius of curvature as well as the outer diameter can be actively controlled by wet etching technique. Samples surfaces of known domains of surface functionalities were prepared and were used to show that the probes can distinguish between different chemical domains.

ACKNOWLEDGEMENTS

REFERENCES

1. C.D. Frisbie, L.F. Rozsnyai, A. Noy, M.S. Wrighton, and C.M Lieber, Science, **265**, p. 2071 (1994)

2. S.N. Magonov, V. Elings and M.-H. Whangbo, Surf. Sci. **375**, p. L385 (1997)

3. D.W. Pohl, W. Denk and M. Lanz, Appl. Phys. Lett., **44**, p. 651 (1984)

4. A. Kumar, H.A. Biebuyck, and G.M. Whitesides, Langmuir. **10**, p. 1498 (1994)

4. D.W. Pohl, Thin Solid Films, **264**, p. 250 (1995)

6. A. Noy, C.H. Sanders, D.V. Vezenov, S.S. Wong and C.M. Lieber, Langmuir, **14** p. 1508 (1998)

REAL-TIME OBSERVATION OF Pt-Si MICRO-DROPLET MIGRATION BY PHOTO-ELECTRON EMISSION MICROSCOPY

W. Yang, H. Ade, R.J. Nemanich
Department of Physics, North Carolina State University, Raleigh, NC 27695, USA

ABSTRACT

The formation and dynamics of Pt-Si liquid droplets on Si (001) substrates have been investigated by Photo-electron Emission Microscopy (PEEM). After ambient deposition of a 10nm Pt film, a uniform PtSi layer was transformed into an island structure at ~ 800°C. The PtSi islands of micrometer size began to melt and were transformed into molten Pt-Si alloy islands below the melting point of PtSi. At ~1100°C surface migration of the micro-droplets was observed. The moving droplets coalesced with nearby islands and grew in size. The motion was related to the temperature difference across the substrate, and droplet migration was observed from the cold to the hot regions of the surface. The migration velocity was measured as a function of temperature and droplet size. The driving force for migration is related to material diffusion, equilibrium at the solid-liquid interfaces, and surface energetics.

INTRODUCTION

The thermo-migration of metal-semiconductor droplets has been studied from both the fundamental and practical point of view. The migration of metal impurity pellets on a Si surface has been reported in early studies of Si growth processes [1]. Also, for the metals Au, and Al on Si, metal-Si alloy droplets were observed to form and droplet motion through the Si was observed. The results were explained on the basis of temperature gradient zone melting (TGZM) [2-4]. Recently, the migration of various metallic islands on Si surfaces has been described in terms of metal diffusion into the Si substrate [5]. However, without *in-situ*, real-time measurements of these complicated processes, the theoretical aspects could not be developed to consistently explain all of the experimental results.

In this study, the formation and dynamics of liquid micro-droplets of Pt-Si on Si (001) are studied using photo-electron emission microscopy (PEEM). PEEM is an emission microscopy technique in which images of a solid surface are formed by photo-excited electrons. The PEEM technique allows real-time observation and direct imaging during processing with exceptional surface sensitivity and high resolution. For this reason, PEEM is particularly suited for the measurement of dynamical processes on semiconductor surfaces. In PEEM, the image contrast mechanism for a metal deposited on a semiconductor is the energy difference between the work function (WF) of the metal and the photo-threshold of the semiconductor, which is the energy to excite an electron from the valence band to the vacuum level. Therefore, PtSi or Pt-Si alloy on a Si surface would be imaged by this contrast mechanism. The energy of the incident UV-light should be below the photo-threshold of the Si and above the WF of the PtSi, or Pt-Si alloy.

In this paper, it is shown that the molten Pt silicide islands nucleate below the melting point of PtSi. In particular, we monitor micro-droplet migration and droplet-droplet interactions while annealing at a temperature of 1100°C. We show detailed measurements of the velocity of the droplets as a function of droplet size and temperature. After droplet formation, the surfaces are analyzed *ex-situ* with AFM and SEM. The composition of Pt-Si

droplets is determined by micro-Raman spectroscopy. The dynamics of the droplets is described in terms of material diffusion and the surface energetics.

EXPERIMENT

The experiments were performed in a UHV- PEEM (Elmitech PEEM-III) system combined with the ultra-violet Free Electron Laser (UV-FEL) located at the Duke University Free Electron Laser Laboratory. The base pressure of the PEEM system is $< 2 \times 10^{-10}$ Torr. This system allows high-resolution imaging (~10nm) in addition to high temperature heating (>1200°C). The capabilities of the PEEM-FEL are described in more detail elsewhere [6]. The incident UV-light is obtained from either the tunable spontaneous emission of the UV-FEL with a photon energy range of 4.5 to 6.0eV or a 100W-Hg discharge lamp with a cut-off energy near 5.0eV.

Silicon (001) wafers (n-type, P-doped, resistivity 0.8-1.2 Ω-cm, 25mm diameter) were employed as the substrates in this study. The wafers were cleaned first by uv-ozone exposure and then by an HF based spin etch (HF:H_2O:ethanal=1:1:10). After *ex-situ* cleaning, the wafers were loaded into an UHV-MBE chamber (base pressure of 1×10^{-10} Torr). Before Pt deposition, the wafers were annealed to a temperature of 900°C for 10 minutes by filament radiation. Platinum was deposited from an e-gun Pt source onto the cleaned Si substrate at room temperature. The thickness of the Pt layer was 10 nm with a deposition rate of 0.05nm/sec. To observe droplet motion on a Si surface without Pt coverage, ~100μm dia. Pt dots (10 nm Pt) were deposited on the Si surface in a mesh pattern of dots separated by 500μm.

A section of the sample (9x9mm^2) was mounted to a sample holder and introduced into the PEEM chamber. To observe the reaction process of the Pt thin films, the samples were heated by filament radiation (< 800°C) and electron bombardment (>800°C) from the backside of the sample holder in the chamber. The annealing temperature range was 100°C to 1200°C in 100°C increments at intervals of 10 minutes. The temperature of the surface was measured with a finely focused (1mm diameter) optical pyrometer.

PEEM images are displayed on a phosphor screen with a microchannel plate, which is installed in the PEEM. The images were observed with a CCD camera and stored both digitally at the image processor and on videotape. For the data presented here, sixteen successive images were integrated with the image processor. The resulting images correspond to an integrated signal of 16/30th of a second. However, for velocity measurements of the moving droplets, single frame images (corresponding to 1/30 of a second) were obtained from the videotape recording. After the substrates were unloaded from the PEEM, *ex-situ* AFM, SEM and micro-Raman spectroscopy (beam size of ~ 2μm) were performed.

RESULTS

After deposition of a 10nm Pt film on a Si (001) substrate, we observed the formation and stability of Pt-Si droplets while the substrate was annealed to 1100°C. The PEEM of the as-deposited Pt film displayed a uniformly bright image. During annealing to 600°C, the uniformity of the emission did not change, however, the intensity of the emission decreased. This intensity decrease indicates that Si has diffused into the Pt overlayer and the PtSi phase has formed. At 800°C, the PtSi surface transformed from a uniform layer into a surface with unstructured islands of ~350nm in diameter. The PtSi islands were identified as bright regions in the images while the exposed underlying Si surface appeared as the darker regions. The image contrast originates from the photo-threshold difference between PtSi (4.85 eV) and Si

(>5.1 eV). As the temperature is increased, the islands grew larger through coalescence with smaller neighbor islands, and well-separated island structures formed. However, a significant transition of the shape and size of the islands was observed at 950°C. At this temperature the islands with an average size of ~450nm transformed into larger islands of ~1μm in size. The larger islands exhibited a more circular shape, and the circumference became smoother as shown in Fig. 1-a. This temperature is close to the eutectic temperature (~980°C) of the PtSi-Si system. This transition indicates that the PtSi islands may have started to melt at near the eutectic temperature.
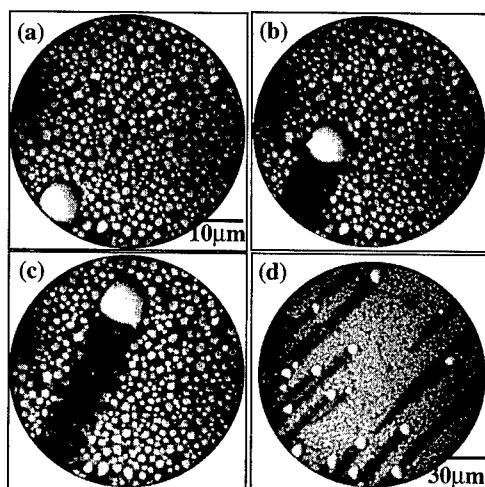
Fig. 1 A time sequence of PEEM images of Pt-Si liquid island migration on Si at 1100°C: (a) 0 sec (b) 20 sec (c) 50sec, respectively. Shown in (d) is a PEEM image with a field of view of 150μm showing the motion of many nearby islands. All Images were obtained at 1100°C. The incident light was from a Hg-discharge lamp.

Fig. 1 shows a time sequence of PEEM images of a 10nm thick Pt film held at 1100°C. It was observed that most of the islands stayed in place while some of the relatively larger islands migrated across the surface. As the annealing time progresses, an island of ~8 μm in diameter is observed to collect islands of ~ 1 μm during its traversing of the surface (Fig. 1-a to Fig. 1-c). At a 150μm field of view, several larger islands (> 2μm in diameter) can be seen to move uniformly in one direction (Fig. 1-d). Also, some of the larger moving islands were observed to coalesce with neighboring islands and form a larger circular island. This migration is characteristic of liquid droplets. Through *ex-situ* AFM images of different areas of the whole sample, it was found that the islands moved from the edge to the center of the substrate. During annealing of the sample, the temperature at the center of the substrate was ~ 50°C higher than at the edge. These results indicate that the droplets moved toward the hotter regions of the sample following the temperature gradient of the substrate.

Micro-Raman spectroscopy was used to examine the composition of a ~10μm diameter droplet and the trace left behind the droplet. The measurements were obtained after rapid cooling of the sample (Fig. 2). The Raman spectra of the droplet exhibited features at ~140 and 520cm^{-1} which are attributed to crystalline PtSi and Si, respectively [7]. In contrast, the
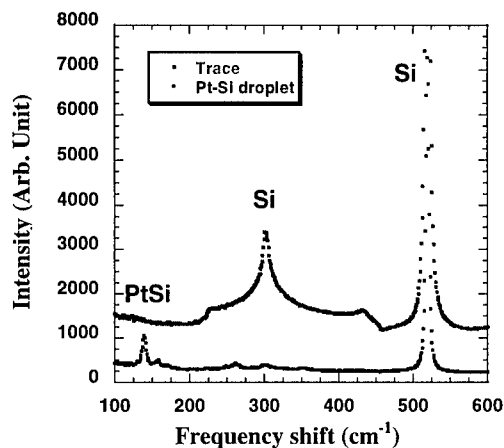
Fig. 2 Micro-Raman spectra of a 10μm droplet and
the trace left behind the droplet.

Fig. 3 A cross sectional SEM image
of a 2.5 μm diameter droplet.

spectra of the trace showed features at 300 and 520cm^{-1} without the feature at 140cm^{-1}. These
features are attributed to crystalline Si. These results indicate Si precipitates in the droplet
suggesting that the liquid droplet is a Si-rich Pt-Si alloy. In addition, the Si trace of the island is
recrystallized. Also, the interface between the droplet and the substrate was investigated by
cross sectional SEM (Fig. 3). The island extends below the Si surface. The contact angle with
the substrate seems to be symmetric between the advancing and the receding interface. This
indicates that the substrate surface and interface energies may be the same at both interfaces.

To avoid the coalescence of the droplets and to explore droplet migration on a Si
surface free of Pt, an array of 100μm dia. Pt dots was deposited on a Si surface. During
annealing of the film at 1100°C, various size droplets formed in the Pt dot region. These
droplets continued to move beyond the edge of the original dot and traveled on the Si surface
regions which were free of Pt. For a more detailed measurement of the droplet velocity, the
migration distance and the size of each droplet were analyzed using single frame images from
the real-time videotape recording. Fig. 4 shows the average migration velocity at various
annealing temperatures as a function of the droplet size. As the annealing temperature is
increased, the velocity of the droplet increases rapidly. The average velocities are 0.8, 2.2 and
3.6 μm/s for annealing temperatures of 1085, 1165 and 1210°C, respectively. Also, the
average velocity vs. droplet size (from 1.5μm to 7.0μm) was measured at each temperature.
The average velocity appears to be independent of the droplet size for a given temperature.

DISCUSSION

The formation of Pt-Si liquid droplets below the melting point of the PtSi (1229°C) can be
explained with reference to the Pt-Si binary phase diagram [8]. After the solid state reaction
leading to the formation of the stable PtSi islands on the Si surface, heating above the eutectic
temperature causes enhanced diffusion of Si into the PtSi island. The island would then melt
from this interface and continued Si diffusion would lead to a Pt-Si droplet composition at the
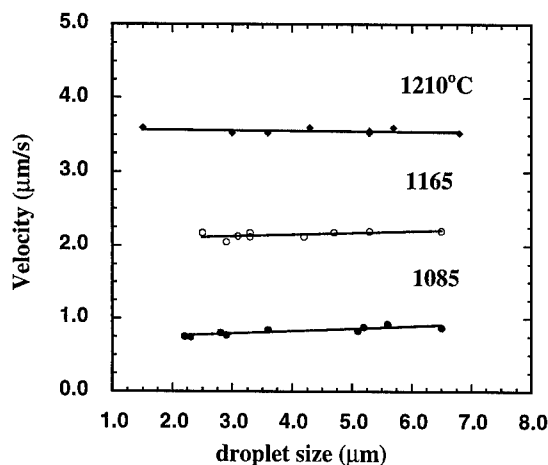
Fig. 4 The migration velocity of the droplets on a Si surface versus the droplet diameter at various annealing temperatures.

eutectic composition. At higher temperatures, the composition of the Pt-Si liquid droplets would follow the liquidus between the eutectic and Si up to the Si melting temperature of ~1414°C. As a result, the Pt-Si alloy liquid droplet is in equilibrium with the Si substrate. Rapid solidification of the island would be expected to yield PtSi and Si. This was verified in the features of the Raman spectra of the islands.

The results indicate that a temperature gradient causes the droplets to move toward the hotter regions of the sample. First, consider the variation in the surface tension of the droplet generated by the thermal gradient. As the amount of Si in the Pt-Si alloy liquid increases with increasing temperature, the surface tension of the liquid decreases [9]. Thus, the surface tension of the droplet will be lowest on the side of the droplet that is the hottest. We note that the tangential gradient of surface tension of a liquid droplet gives rise to Marangoni flow, which drives the droplet toward the region of high surface tension [10]. As a result, the Pt-Si droplet would be expected to migrate toward the colder region, i.e. toward higher surface tension. This is contrary to our observation. The variation of the substrate surface and interface energies induced by the temperature gradient can also drive the droplets toward the region of lower surface energies [10]. However, the measured contact angles of the solidified droplet were almost symmetric at both endpoints (Fig. 3). This indicates that the surface and interface energies do not vary, and their effects on the migration are not expected to be significant.

Second, consider the concentration variation of Si in the droplet induced by the thermal gradient of the substrate. As the temperature increases, Si is dissolved into the liquid Pt-Si droplet from the substrate. The Si concentration in the Pt-Si island will then be different at the hotter and colder interfaces. Consequently, a concentration gradient of Si is present in the liquid droplet. This concentration difference induces Si diffusion towards the cold interface in order to maintain concentration equilibrium in the liquid. As a result, the supersaturation at the cold interface results in the recrystallization of Si on the substrate and the undersaturation of Si at the hot interface induces continuous dissolution of Si from the substrate. These solution-

diffusion-deposition cycles of Si through the droplet causes the droplet migration on the Si surface.

The migration rate of the droplet can be limited by either Si diffusion through the liquid or the kinetics of Si dissolution and deposition at the interfaces. We can explore which mechanism controls the migration rate by measuring the velocity of the droplets as a function of droplet size. If the volume diffusion through the droplet is the limiting mechanism of the migration, then the migration rate should be independent of droplet size. In contrast, if the migration rate is limited by the interface reactions (such as dissolution and recrystallization), then the migration velocity will vary with droplet size [11]. In this experiment, the migration rate of the Pt-Si alloy droplet was independent of the droplet size for droplets in the range of 1.5-7.0 μm (Fig. 4). Consequently, the results presented here suggest that Si transfer through the droplet is the primary factor which determines the migration rate of the Pt-Si liquid droplets.

CONCLUSIONS

In this study, we have used PEEM to observe the transition of PtSi islands into Pt-Si liquid droplets and to observe the migration of the Pt-Si liquid droplets. The liquid Pt-Si droplets of micrometer size were formed below the melting temperature of PtSi. Characteristic of liquid droplets, the island grew through coalescence. The liquid micro-droplets were determined to be a Si-rich Pt-Si alloy. The droplets moved from cold to hot regions on the surface following the temperature gradient of the substrate. The migration rate of the droplet was independent of the droplet size. It is proposed that the Si concentration gradient in the droplet produced by the thermal gradient causes droplet migration, and the Si diffusion rate is the primary factor which determines the migration rate of the Pt-Si droplets.

ACKNOWLEDGEMENTS

REFERENCES

1. E. Biedermann, J. Electrochem. Soc.,Vol. 114, 207 (1967)
2. T.R. Anthony and H.E. Cline, J. Appl. Phys., vol. 43, 2473 (1972)
3. H.E. Cline and T.R. Anthony, J. Appl. Phys., vol. 47, 2325 (1976)
4. W.G. Pfann, Zone melting, Wiley, New York (1966)
5. T. Ichinokawa, H. Izumi, C. Haginoya, and H. Itoh, Phys. Rev. B, 47, 9654 (1993)
6. H. Ade, W. Yang, S. English, J. Hartman, R.F. Davis, R.J. Nemanich, V.N. Litvinenko, I.V. Pinayev, Y. Wu and J.M. Mady, Surface Review and Letters 5, (6) 1257 (1998)
7. R.J. Nemanich, M.J. Thompson, W. B. Jackson, C.C. Tsai, and B.L. Stafford, J. Vac. Sci. Technol. B1 (3), 519 (1983)
8. M. hansen, Constitution of binary alloys, McGraw-Hill, New York (1958)
9. J.L. Bocquet, G. Brebec, Y. Limoge, Physical metallurgy, edited by R.W. Chan (Elsevier, New York, 1983), chap. 8
10. F. Brochard, langmuir, 5, 432 (1989)
11. P. Shewmon, Trans. Met. Soc. AIME, vol. 230, 1134 (1964)

SECOND DERIVATIVE BALLISTIC ELECTRON EMISSION
SPECTROSCOPY IN Au/(AlGa)As

M. KOZHEVNIKOV *, V. NARAYANAMURTI *, D. L. SMITH **, YI-JEN CHIU ***
* Gordon McKay Laboratory, DEAS, Harvard University, Cambridge, MA 02138
** Los Alamos National Laboratory, Los Alamos, NM 87545
*** ECE Department, University of California, Santa Barbara, CA 93106

ABSTRACT

Our current study focuses on an analysis of the ballistic electron emission microscopy (BEEM) spectra of Au/(AlGa)As heterostructures to estimate quantitatively the effect of the carrier scattering in the metal, at the metal-semiconductor (m-s) interface and in the semiconductor on the multivalley carrier transport. The second derivative (SD)-BEEM spectra, representing the heterostructure transmission coefficient, show explicit partitioning of the contribution of different transport channels (Γ, L and X conduction valleys). Our analysis of SD-BEEM spectra by the developed theoretical model indicates that about 85-92% of the BEEM electrons are scattered at the nonepitaxial Au/GaAs interface. We also show that initial electron distribution among the conduction bands of the semiconductor, specified by the m-s interface scattering, is modified by the further hot-electron transport inside the semiconductor.

INTRODUCTION

Ballistic electron emission microscopy (BEEM), a three-terminal modification of scanning tunneling microscopy (STM), is a powerful low-energy tool for nondestructive local characterization of semiconductor heterostructures. Since the pioneering work of Kaiser and Bell,[1] applications of BEEM to various semiconductor surfaces and interfaces have already produced many interesting results. It was shown that the magnitude of the transmitted current into the substrate depends strongly on the local properties of the interface[2] as well as the scattering properties of the overlying metal film.[3,4] Although the BEEM technique was originally invented as a unique microscopic and spectroscopic method to probe the Schottky barriers on a local scale, the BEEM technique can be successfully used to study the electronic properties of buried heterostructures.[5-8]

To describe BEEM spectra, several theoretical models were developed. Two commonly used models, based on a planar tunneling formalism[9] and on the transverse momentum conservation at the metal-semiconductor (m-s) interface, are the Bell-Kaiser (BK) model[1] and the Ludeke-Prietsch (LP) model.[10] Both frequently fit the experimental data reasonably well.[6,11,12] Recently, extension of the BEEM theory to buried heterostructures was done by Smith and Kogan (SK).[13] In their work, the authors considered the quantum mechanical transmission at the heterojunction interface in addition to the m-s interface.

Transverse momentum conservation, assumed in the above models, is under question in nonepitaxial m-s interfaces, where the quality of the interface is far from the atomically abrupt. In this case, the carrier transport across the m-s interfaces may be diffuse rather than ballistic due to the carrier scattering at these interfaces. Indeed, a deviation from the ballistic picture was experimentally observed, e.g. for Au/Si,[14] Pd/Si[15] and Au/GaAs.[6,16] To analyze correctly the experimental data, the m-s interface-induced scattering (MSIS) model was proposed in Ref. 17. These authors showed that the experimental data for Au/Si and Au/GaAs systems can be fitted only by taking into account of the strong carrier scattering at the m-s interface.

207

To quantitatively estimate the electron scattering at the m-s interface, we analyze the second voltage derivative (SD) of the BEEM spectra of undoped GaAs/AlGaAs/GaAs single barrier (SB) structures. The analysis of the SD-BEEM within the MSIS model, which incorporates a strong scattering of the carriers at the m-s interface, indicates that about 85-92% of the BEEM electrons are scattered at the non-epitaxial Au/GaAs interface.

EXPERIMENTAL

The GaAs/AlGaAs/GaAs single barrier (SB) structures (with Al compositions of 0.0, 0.1, 0.2, 0.3 and 0.42) were grown on n$^+$ (001)-oriented GaAs substrates by molecular beam epitaxy. The structures consist of a 500 Å undoped GaAs buffer layer, a p-type (Be) δ-doped sheet, a 500 Å GaAs spacer layer, a 50 Å Al$_x$Ga$_{1-x}$As barrier, and a 50 Å or 300 Å GaAs cap layer. The Be sheet doping concentration of N_A=1.2×10^{12} cm^{-2} was designed to compensate for band bending leaving a flat band heterostructure in equilibrium. For each Al content value, two SB samples were grown with the same barrier thickness of 50 Å, and with different GaAs cap layer thicknesses of 50 Å and 300 Å. To make the Schottky contacts, Au layers (30-150 Å thick) were deposited by thermal evaporation through a shadow mask at a background pressure of 2×10^{-7} torr. The BEEM measurements were performed in a Surface/Interface AIVTB-4
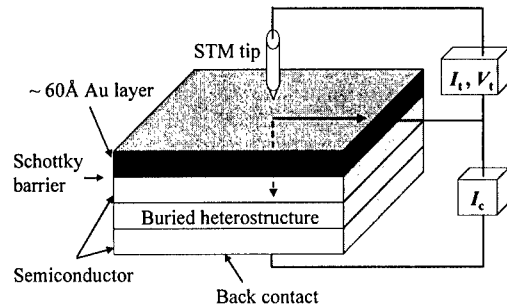
Fig. 1. A schematic of BEEM experimental set-up.

BEEM/STM using a Au tip (made using 0.5 mm gold wire). A schematic of the BEEM experimental set-up is shown in Fig. 1. The tip-to-base voltage (V_t) was varied between 0.7 and 2 V to acquire the BEEM current (I_c) while keeping a constant tunneling current (I_t) of 4 nA. Room temperature experiments were performed in air, while for lower temperature (77 K ≤ T ≤ 300 K) experiments, the STM head with a sample was immersed in cold He exchange gas in the nitrogen-cooled dewar.

RESULTS

Typical BEEM current data as a function of applied tip-to-base voltage is presented in Fig. 2(a) for reference GaAs layer (x=0.0). The first derivative (FD) and SD spectra were extracted from the measured data by numerical differentiation with a 10 meV window (Figs. 2(b) and 2(c), respectively). One can see clearly pronounced features in the SD-BEEM spectra. These peaks in the second voltage derivative are associated with the different transport channels (conduction valleys), specifically the Γ and L conduction bands.

To validate the identification of the observed peaks in the SD-BEEM spectra with electron transport through different conduction bands, we have studied the SD-BEEM spectra of several Au/GaAs/AlGaAs SB samples. The BEEM spectra in Fig. 3(a) show a uniform collector current magnitude over the samples (~20 pA at 0.5 V above the threshold), with a clear increase in the BEEM threshold with increasing Al content. However, since the observed BEEM spectra are a superposition of current contributions from several different transport channels, it is difficult to conclusively extract the different conduction band contributions directly from the BEEM spectra fitting. In the SD-BEEM spectra (Fig. 3(b)) however, we observe two energetically separated

Au/GaAs structure
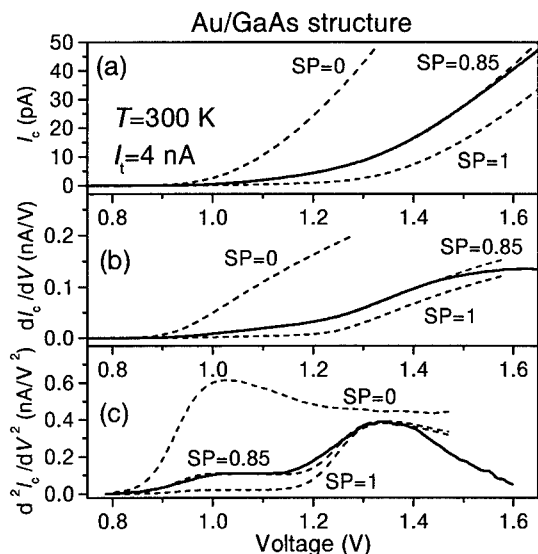
Fig. 2. The room-temperature BEEM (a), FD-BEEM (b) and SD-BEEM (c) spectra of the reference GaAs sample. The MSIS model calculations (dashed lines) are also presented for three values of SP, the electron scattering probability at the m-s interface.

features that are clearly resolved for $x = 0.0$, 0.1 and 0.2. As the Al concentration increases, these two observed peaks shift towards higher voltages and converge gradually into one peak for $x = 0.42$. The energy positions of the two peaks are in good agreement with the expected Γ and L minima positions from the AlGaAs band structure calculations.[18]

The observed vanishing X-channel contribution to the BEEM current is an initially unexpected result. One of the three X points projects on the Γ-point of the surface Brillouin zone and, thus, the contribution of the X-electrons to the BEEM current is expected to be large, independent of the scattering strength at the m-s interface. We explain this result by electron scattering inside the

SB structure (GaAs/Al$_x$Ga$_{1-x}$As/GaAs)
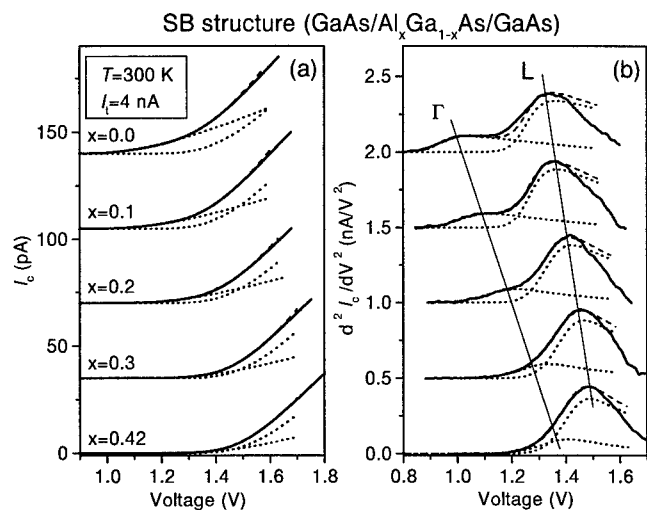
Fig. 3. BEEM (a) and corresponding SD-BEEM spectra (b) for five different Al compositions. For clarity, the SD-BEEM spectra are shifted along the vertical axis. Thin solid lines in Fig. 3(b) are eye-guides for the peaks position development. The model calculations show the separate Γ and L valley contributions (dotted lines) and their sum (dashed lines).

GaAs/AlGaAs heterostructure. The expected mean free path (mfp) lengths for the Γ, L and X electrons at T=300K in GaAs are ~1000 Å, ~100 Å and ~10 Å, respectively,[19] and the heterostructure thickness, the combined thickness of the GaAs cap layer and the SB layer, is 100 Å. Thus the X-electrons contribution to the BEEM spectrum is highly attenuated.

In order to show that scattering inside the semiconductor structure affects our measurements, we compare the BEEM spectra for several pairs of samples with the same Al composition but with cap layer thicknesses of 50 Å and 300 Å. Because of the mfp's for the three channels, changing the cap thickness in the range of 50-300 Å (corresponding to the total heterostructure thickness range of 100-350 Å) should affect mainly the L-electrons contribution to the BEEM current. The SD-BEEM spectra of the GaAs/Al$_{0.2}$Ga$_{0.8}$As/GaAs SB samples are shown in Fig. 4(a) at T = 85 K and 300 K. At T = 300 K, the L-electron contribution for the SB sample with a 300 Å-cap layer is reduced by factor of ~ 3 as compared with the 50 Å-cap layer SB sample, while the Γ-electron contribution is about the same for the two samples. As the temperature decreases from 300 K to 85 K, in addition to the spectrum shift expected from the temperature dependence of the energy gap, a strong increase in the signal is observed for the L-electrons in the SB sample with the 300 Å-cap layer. However, the SD-BEEM spectral shape remains essentially the same for the SB sample with the 50 Å-cap layer. These experimental results are in agreement with the expected increase in the mfp of the electrons with the decreasing temperature. As the temperature decreases from 300 K to 85 K, the calculated mfp near the energy threshold increases from ~1000 Å to ~1500 Å for Γ electrons, from ~100 Å to ~300 Å for the L electrons, and from ~10 Å to ~30 Å for X-electrons.[19] We conclude from our experimental findings, that the sample cooling does not change the Γ-electron transmission and removes some attenuation of the L-electrons observed at room temperature.

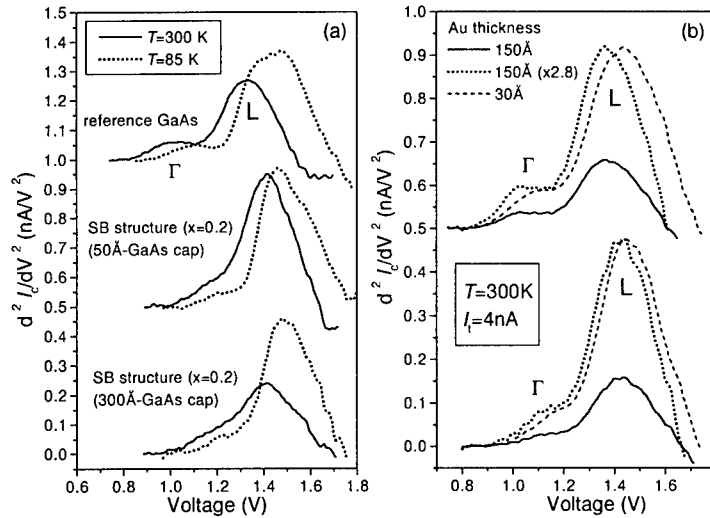Fig. 4. (a) SD-BEEM spectra for the reference GaAs sample and GaAs/Al$_{0.2}$Ga$_{0.8}$As/GaAs SB samples with 50 Å and 300 Å GaAs cap layers, taken at T = 300 K (solid curves) and T = 85 K (dotted curves). (b) The dependence of the SD-BEEM spectra on the Au layer thickness for reference GaAs sample and GaAs/Al$_{0.1}$Ga$_{0.9}$As SB structure. For clarity, the spectra are shifted along the vertical axis.

The L-electron collector current is found to be the strongest, whereas, if transverse momentum conservation is assumed, the contribution of the off-axis L minima gives only a very small BEEM current near the onset. The likely explanation for the large BEEM current observed due to the off-axis L valleys is that an additional transverse momentum is provided by scattering at the m-s interface. In the limit of strong m-s interface scattering, we can relax the requirements for transverse-momentum conservation, and the scattering of electrons into the L and X valleys occurs at the expense of the ballistic component provided mainly by Γ-electrons.

To estimate the electron scattering at the m-s interface, we analyze the SD spectra within the framework of the MSIS model.[17] In this model, the conduction process is described by carrier transport through the Γ, L and X conduction channels with corrections due to the scattering at the m-s interface interface, which depends on the m-s scattering probability SP. In the weak scattering limit (SP→0), the MSIS model is essentially equivalent to the SK model.

The theoretical fits to the SD-BEEM spectrum of the Au/GaAs sample are shown in Fig.2. The probability of electron scattering at the m-s interface was adjusted to fit the SD-BEEM spectra. The SD-BEEM spectra clearly separate the contributions from Γ and L electrons; thus, the weighting of the relative Γ and L channel contribution is a sensitive test of the model. The best fit to the SD-BEEM spectrum gives an 85% probability of the electron scattering at the m-s interface. For comparison, theoretical curves for 0% and 100% scattering are also shown. The MSIS model fits to the SD-BEEM spectra of the SB structures are shown in Fig. 3. The best fits are obtained with the scattering probability at the m-s interface varying between 85% and 92% for the different samples. This small variation in the scattering parameter indicates that our diode fabrication procedure is reproducible and results in approximately the same quality of the m-s interface from sample to sample.

Although the experimental results are in general agreement with the MSIS model fit, there is a discrepancy at the high-voltage side of the SD-BEEM spectra. The experimental SD-BEEM spectra decrease more steeply than it is predicted by the MSIS model. Electron scattering in the metal layer can not explain the high-voltage discrepancy between the experimental data and the MSIS model, since our attempt to change the scattering parameter in the metal in order to obtain a better fit at the high-energy side of the SD-BEEM spectra results in an unrealistically short mfp of electrons in the metal.

To study experimentally the effect of electron attenuation in the metal, we prepared several diodes of the same structure but with different Au base layer thicknesses. If the electron scattering in the metal triggers the drop of the high-voltage side of the SD-BEEM spectrum, not only the absolute BEEM current value but also the BEEM spectral shape should be very sensitive to the metal layer thickness. Fig. 4(b) shows the SD-BEEM spectra for two samples with Au layer thickness of 30 Å and 150 Å. One can see from this figure that the absolute SD-BEEM signal decreases by a factor of ~3 for both samples. This gives a mfp of ~150 Å in gold, in reasonable agreement with Ref. 20. However, there is essentially no change in the SD spectral shape at high voltages. (The small shift of the SD-BEEM spectra with the Au layer thickness is due to insufficient conductivity of the very thin metal layer). We conclude that another physical mechanism, rather than the electron scattering in the metal layer, is responsible for the SD signal drop at high voltages.

The likely explanation for the high voltage drop in the experimental SD-BEEM spectra is the effect of electron scattering in the semiconductor. Such an interaction may result in a back-scattering of the incoming electrons after they have reached the semiconductor. As a result of strong energy dependence of the electron-phonon scattering, the electron mfp in the GaAs/AlGaAs is reduced at higher energies, resulting in a lower BEEM current.

CONCLUSIONS

We systematically studied the SD-BEEM spectra of Au/GaAs/AlGaAs heterostructures for probing the effects of carrier scattering in the metal, at the m-s interface, and in the semiconductor on the multivalley hot carrier transport. Our analysis of BEEM and SD-BEEM spectra within the MSIS model shows that about 85-95% of the electrons are scattered at the nonepitaxial Au/GaAs interface. We also show that the distribution of BEEM current among the conduction channels is modified by hot-electron transport inside the semiconductor.

REFERENCES

1. L. D. Bell and W. J. Kaiser, Phys. Rev. Lett. **61,** 2368 (1988).
2. A. Fernandez, H. D. Hallen, T. Huang, R. A. Buhrman, and J. Silcox, Appl. Phys. Lett. **57,** 2826 (1990).
3. P. Niedermann, L. Quattropani, K. Solt, A. D. Kent, and O. Fischer, J. Vac. Sci. Technol. **B10,** 580 (1992).
4. A. Bauer, M. T. Cuberes, M. Prietsch, and G. Kaindl, Phys. Rev. Lett. **71,** 149 (1993).
5. H. Sirringhaus, E. Y. Lee, U. Kafader, and H. v. Kanel, J. Vac. Sci. Technol. **B13,** 1848 (1995).
6. J. J. O'Shea, E. G. Brasel, M. E. Rubin, S. Bhargava, M. A. Chin, and V. Narayanamurti, Phys. Rev. **B56,** 2026 (1997).
7. M. E. Rubin, G. Medeiros-Ribeiro, J. J. O'Shea, M. A. Chin, E. Y. Lee, P. M. Petroff, and V. Narayanamurti, Phys. Rev. Lett. **77,** 5268 (1996).
8. J. Smoliner, R. Heer, C. Eder, and G. Strasser, Phys. Rev **B58,** R7516 (1998).
9. J. G. Simmons, J. Appl. Phys. **34,** 1793 (1963).
10. R. Ludeke and M. Prietsch, J. Vac. Sci. Technol. **A9,** 885 (1991).
11. M. Prietsch, Phys. Rep. **253,** 163 (1995).
12. G. N. Henderson, P. N. First, T. K. Gaylord, and E. N. Glytsis, Phys. Rev. Lett. **71,** 2999 (1993).
13. D. L. Smith and S. M. Kogan, Phys. Rev. **B54,** 10354 (1996).
14. L. J. Schowalter and E. Y. Lee, Phys. Rev. **B43,** 9308 (1991).
15. R. Ludeke, Phys. Rev. Lett. **70,** 214 (1993).
16. M.-l. Ke, D. I. Westwood, C. C. Matthai, B. E. Richardson, and R. H. Williams, Phys. Rev. **B53,** 4845 (1996).
17. D. L. Smith, E. Y. Lee, and V. Narayanamurti, Phys. Rev. Lett. **80,** 2433 (1998).
18. S. Adachi, J. Appl. Phys. **58,** R1 (1985).
19. E. Y. Lee, S. Bhargava, M. A. Chin, and V. Narayanamurti, J. Vac. Sci. Technol. **A15,** 1351 (1997).
20. C. A. Ventrice, V. P. LaBella, G. Ramaswamy, H.-P. Yu, and L. J. Schowalter, Phys. Rev. **B53,** 3952 (1996).

Modeling and Atomistic Simulations

Modeling of Structural and Elastic Properties of $In_xGa_{1-x}N$ Alloys

Frank Grosse* and Jörg Neugebauer

Fritz-Haber-Institut der Max-Planck-Gesellschaft,

Faradayweg 4-6, D-14195 Berlin (Dahlem), Germany

November 26, 1999

Abstract

$In_xGa_{1-x}N$ alloys are investigated by combining density-functional theory (DFT) calculations and an extended valence force field model (VFF). Based on a large number of ordered $In_xGa_{1-x}N$ supercells we determined the accuracy of various valence force field models with respect to *ab initio* DFT calculations. To get the correct energy difference between the stable wurtzite and the metastable zincblende phase the inclusion of the ion-ion-interaction within the VFF model was necessary. As a direct consequence the inequivalent bonds of the wurtzite structure including the non-ideal c/a ratio and internal u parameter are described correctly. The wurtzite phase is found to be stable against the zincblende phase for all concentrations. The calculated elastic constants and their dependency on In alloy composition enables the determination of the local concentration by simultaneous measurement of the local lattice constants a and c.

1 Introduction

$In_xGa_{1-x}N$ alloys have attracted much attention due to their technological relevance as active region in blue light emitting lasers and diodes. In particular, the material quality in terms of homogeneity and its importance to device performance is still under investigation [1]. Further, strain effects in $In_xGa_{1-x}N$ layers are significant due to growth on lattice mismatched substrates (the most common substrate is sapphire with 14 % mismatch) and the large internal lattice mismatch between GaN and InN (11 %). The most widely used method to describe strain effects in group III-V alloys is the valence force field method (VFF) [2] in a form first proposed by Keating [3]. Its simplicity and proven validity for systems consisting of fourfold coordinated atoms (i.e. without defects or surfaces) and for

---
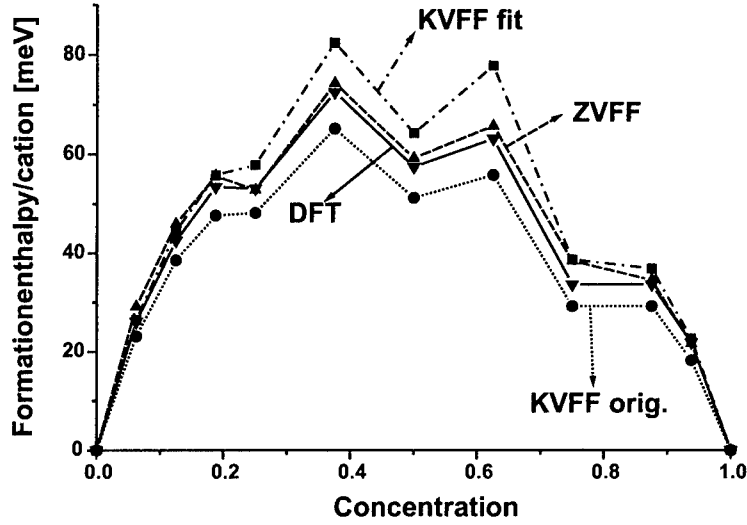
Figure 1: Formation enthalpies of ordered wurtzite $In_xGa_{1-x}N$ structures. Different valence force fields models are compared with density functional theory. Only ordered structures containing up to 32 atoms and with the lowest formation enthalpy for a given In-concentration x are shown.

a wide range of III-V compound semiconductors [3, 4, 5] made it attractive to study also the group-III nitrides [6, 7, 8, 9, 10, 11]. In the following we report calculations for a large number of ordered $In_xGa_{1-x}N$ structures employing density functional theory in the local density approximation. Based on these results we check the quality of different VFF models and extend these by including the long range ion-ion interaction (ZVFF). Using this model we are able to study large systems containing several thousand atoms. From these results we determine the elastic constants as function of In concentration and the stability of the zincblende versus the wurtzite phase.

2 Calculation methods

Reliable methods are needed to carry out predictive calculations with high accuracy. The method of choice for structural and electronic properties is the density functional theory (DFT) [12] which has been successfully applied to a large variety of systems. Its high computational demand however limits its applicability to smaller supercells. The extension to larger systems is possible by developing simplified models and using DFT-results as input.

Here a large number of small $In_xGa_{1-x}N$ supercells varying in concentration and arrangement of cations are investigated employing DFT within the local density approximation
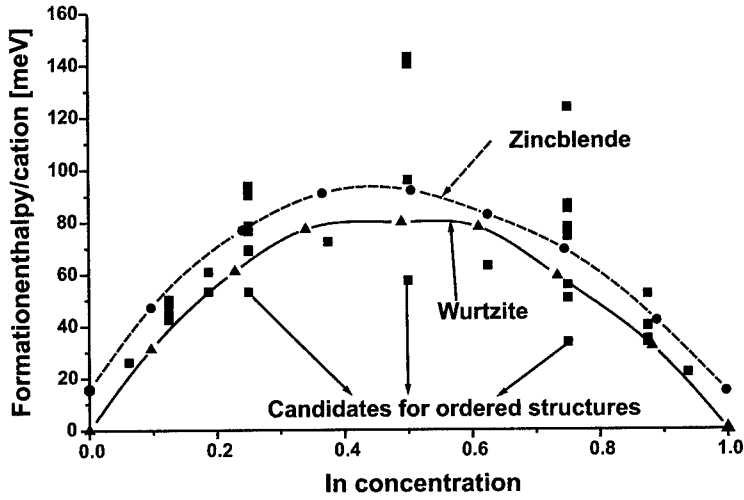
Figure 2: Formation enthalpies of random zincblende (circles and dashed line) and wurtzite alloys (triangles and solid lines). The calculation are carried out with the ZVFF model. Special ordered structures (squares) with low energies are candidates for long range ordering in $In_xGa_{1-x}N$ alloys.

(LDA) [13, 14]. We use *ab initio* norm conserving pseudopotentials [15] and the FHI98md program [16, 17]. Total energies of wurtzite $In_xGa_{1-x}N$ supercells with up to 32 atoms (equivalent to a 2x2x2 wurtzite unit cell) are calculated [18]. External lattice parameters and all internal degrees of freedom are fully relaxed. Convergence checks showed it to be essential to treat the Ga $3d$ and In $4d$ states as valence electrons [19, 20, 21]. Therefore, in order to describe the structural properties, alloy formation energies, and elastic constants correctly, a high plane wave energy cutoff of 80 Ry is used which make these calculations a demanding computational task.

The VFF model as proposed by Keating [3] contains two next neighbour harmonic contributions: a bond bending and a bond stretching term. These parameters can be easily determined from the zincblende elastic constants by well known analytic expressions [3]. A major drawback of the VFF model is its lack to distinguish between the wurtzite and zincblende crystal structure. First, the bond length of all bonds is exactly the same in contrast to experimental results and DFT calculations where both deviations in the internal u parameter and the external lattice parameters a, c are found. Second, the total energy for both crystal phases is identical within the VFF model. We have therefore extended the VFF model following the idea by Martin [4] and included the ion-ion interaction in a rigid point charge model (ZVFF). Based on this formalism we have derived a set of analytic relations be-

217
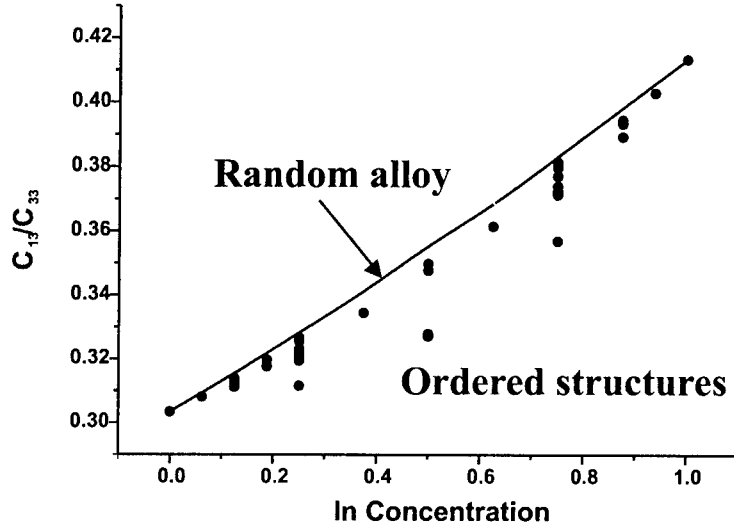
Figure 3: Calculated C_{13}^{wz}/C_{33}^{wz}-ratio dependent on In-concentration x. The resulting bowing is $b = 0.01$. The dots give the calculated ratio for ordered structures.

tween the force constants and the VFF parameters (see Ref. [22]). In order to treat a highly ionic system like group-III nitrides we found it crucial to take also the effect of the change in the equilibrium lattice constant due to the inclusion of the Coulomb interaction into account. The Coulomb interaction has been treated by a standard Ewald summation [23, 24].

The free parameters in the ZVFF model have been determined using as input the elastic constants of the *zincblende* binary compounds – GaN and InN – as calculated by DFT. Since we are focussing in this work solely on static properties we determined the effective charge of the ions from the total energy difference between the wurtzite and zincblende binary phase rather than fitting the LO-TO-phonon splitting.

3   Results

We have first tested the accuracy and applicability of the VFF and ZVFF model to describe $In_xGa_{1-x}N$ alloys in the wurtzite phase. The calculated formation enthalpies for a variety of different structures are compared with results from our DFT calculations. The supercells contain up to 32 atoms. Varying the local arrangement of In atoms for fixed In-concentration x we determined the structures with the lowest alloy formation enthalpy as shown in Fig. 1. Comparing *all* calculated structures we find an average error of the Keating VFF model (KVFF orig.) of 14.2 meV per cation with respect to the DFT calculations. The two parameters entering the VFF model have been determined by using the *zincblende* elastic
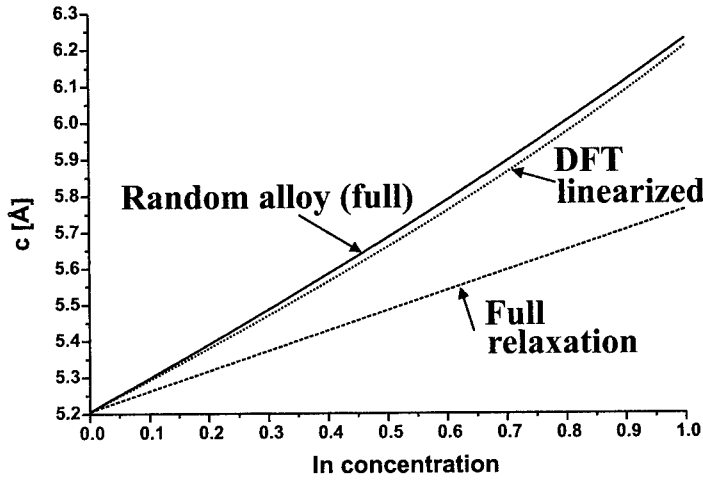
Figure 4: c-lattice constant as function of the In-concentration x for random $In_xGa_{1-x}N$ alloys pseudomorphically grown on GaN (solid line). Further included is the x-dependence for the case of fully relaxed $In_xGa_{1-x}N$ alloys (dashed line) and for pseudomorph alloys but assuming a *linear* dependence in the wz-Poisson ratio (dotted line; see text).

constants C_{11}^{zb} and C_{12}^{zb}. Since the VFF model consists of two parameters only, it is principally not possible to describe all three cubic elastic constants exactly. Indeed, the third cubic elastic constant C_{44}^{zb} is significantly underestimated (69 % for GaN, 60 % for InN). Therefore also all formation enthalpies of the ordered structures are underestimated in comparison with the DFT results. We have calculated a second set (KVFF fit) of force parameters by a least mean square fit to improve these first results. This approach reduces the error to 5.8 meV per cation. For the low energy structures shown in Fig. 1 we find an overestimation of the formation enthalpy with this second set. A further improvement could be achieved by explicitly treating the ion-ion Coulomb interaction within the ZVFF model: the error decreases further to finally 4.9 meV which is close to the expected accuracy of the DFT calculations. Based on this comparison we are confident that the ZVFF model gives an accurate description of the energetics of large supercells. We further find that the ZVFF model describes structural properties such as bond length and lattice parameters remarkably well with errors typically < 1 % (compared to DFT results). It correctly describes the two inequivalent bond lengths in the wurtzite crystal structure correctly. The ratio c/a of the external lattice constants is in agreement with DFT calculations below the ideal one. Only for [0001] superlattices (a sequence of Ga and In layers along (0001); see also below) the c/a ratio exceeds this value.

In a second step we applied the ZVFF model to describe random alloys. We therefore consider large supercells with up to 2500 atoms. The cations are randomly distributed with an average In concentration x. Both, wurtzite and zincblende lattices have been included. The resulting x-dependence of the formation enthalpy is shown in Fig. 2. Over the full x-range the wurtzite phase has a lower energy in clear contrast to a previous theoretical study [25]. We attribute the difference to the use of unit cells of only 32 atoms in Ref. [25]. A more detailed analysis showed that the energy difference is to a large amount given by the difference in the electrostatic energy (Madelung sum) between the zincblende and the wurtzite lattice. The smaller wurtzite Madelung constant ($\alpha_M^{WZ} = -1.641$) compared with the zincblende one ($\alpha_M^{WZ} = -1.638$) and the related lower Coulomb energy stabilizes the wurtzite crystal structure. Furthermore, our calculations show a small difference in the symmetry of the x-dependence of the formation enthalpies. Whereas the zincblende phase has the highest energy at concentrations slightly *below* 50 % In we find the wurtzite phase to be highest in energy for In-concentrations slightly *larger* than 50 %.

A remarkable feature shown in Fig. 2 is the existence of ordered structures with energies significantly lower than random alloys. These structures are candidates for the experimentally observed long range order in $In_xGa_{1-x}N$ alloys [26]. It is interesting to note that the ordering is not a sequence of pure In and Ga layers along (0001) as might be expected since this is the growth direction. Contrary, a closer inspection showed these structures to be very high in energy. A stabilization of these structures can be only by kinetics as has been recently proposed in Ref. [27]. Further investigations of the ordered structures revealed that they are mainly driven by a short range repulsion between the In atoms.

Finally, we have studied the elastic constants as function of the In concentration. We focus on pseudomorphic growth of $In_xGa_{1-x}N$ on GaN. In this case, the lateral lattice constant is fixed to that of GaN while the c-axis of the $In_xGa_{1-x}N$ alloy can be fully relaxed. The relaxation along the c-axis is given by the following relation

$$\frac{c - c_0(x)}{c_0(x)} = -2 \frac{C_{13}^{wz}(x)}{C_{33}^{wz}(x)} \frac{a - a_0(x)}{a_0(x)}. \tag{1}$$

where $a_0(x)$ and $c_0(x)$ are the a and c lattice constants for *fully* relaxed $In_xGa_{1-x}N$ alloys at composition x. a is the lateral lattice constant given by GaN ($a = a_{GaN}$) and $C_{13}^{wz}(x)$ and $C_{33}^{wz}(x)$ are the wurtzite elastic constants of $In_xGa_{1-x}N$. As can be seen in Eq. (1) the key quantity is the ratio $C_{13}^{wz}(x)/C_{33}^{wz}(x)$ plotted in Fig. 3 both for random alloys (solid line) and ordered structures (dots). The ratio $C_{13}(x)/C_{33}(x)$ has the same meaning here as the Poisson ratio $C_{12}^{zb}(x)/(C_{11}^{zb}(x) + C_{12}^{zb})$ in zincblende lattices. We call it therefore wz-Poisson ratio in the following. The wz-Poisson ratio for random alloys shows a small parabolic bowing with a bowing parameter $b = 0.01$. The elastic constants for ordered structures are generally close to those of the random alloys. Exceptions are for (0001) superlattices for which a significantly lower wz-Poisson ratio is found which is connected to their higher equilibrium c/a ratio.

Using Eq. (1) and the calculated elastic constants we have determined the c-lattice constant for pseudomorphically grown $In_xGa_{1-x}N$ alloys on GaN (solid line in Fig. 4). For comparison also included in Fig. 4 is the $c(x)$ dependence for *fully* relaxed $In_xGa_{1-x}N$ alloys

(dashed line): significant deviations from the pseudomorphic case are found. The knowledge of the c-lattice constant as function of In-concentration can be used to determine experimentally the local and average In concentration e.g. by measuring the local lattice constant. In fact, many experimental techniques such as x-ray or transmission electron microscopy (TEM) build on this relation. Since the x-dependence of the elastic constants of $In_xGa_{1-x}N$ had not been known so far it is common to use a linear approximation. In order to check the validity of this approach we have tested the relevance of the weak non-linearity in the elastic constants (see the bowing in Fig. 3). Applying Vegard's law to the lattice constants and assuming a linear x-dependence of the wz-Poisson ratio the dotted line in Fig. 4 is obtained. Since the deviation from the exact result is rather small we expect that in most cases the assumption of a linear x-dependence of the elastic constants is sufficient to determine the local In concentration.

4 Summary

An extension of the VFF model by including the long range electrostatic ion-ion interactions allows a realistic description of the structural and elastic properties of $In_xGa_{1-x}N$ alloys. In particular, within the same approach and using the same parameters both the stable wurtzite and metastable zincblende phase can be described: the differences in formation energies between both phases and the presence of inequivalent bonds in the wurtzite phase are reproduced correctly. Also, a good agreement with our first principles calculations is found both with respect to the energetics and structural properties. Based on these results we studied ordered and random $In_xGa_{1-x}N$ alloys. Our results show that the wurtzite phase is stable over the full In concentration range. Further, the x-dependence of the elastic constants is determined. This relation is a key quantity in the experimental analysis to determine local In concentrations.

5 Acknowledgements

References

[1] K. P. ODonnell, R. W. Martin, and P. G. Middleton, Phys. Rev. Lett. **82**, 237 (1999).

[2] M. J. P. Musgrave and J. A. Pople, Proc. Roy. Soc. **A 268**, 474 (1962).

[3] P. N. Keating, Phys. Rev. **145**, 637 (1966).

[4] R. M. Martin, Phys. Rev. B **1**, 4005 (1970).

[5] A. Silverman, A. Zunger, R. Kalish, and J. Adler, Phys. Rev. B **51**, 10795 (1995).

[6] K. Kim, W. R. L. Lambrecht, and B. Segall, Phys. Rev. B **53**, 16310 (1996).

[7] K. Kim, W. R. L. Lambrecht, and B. Segall, Phys. Rev. B **56**, 7018 (1997).

[8] L. Bellaiche, S.-H. Wei, and A. Zunger, Phys. Rev. B **56**, 13872 (1997).

[9] L. Bellaiche and A. Zunger, Phys. Rev. B **57**, 4425 (1998).

[10] T. Mattila and A. Zunger, J. Appl. Phys. **85**, 160 (1999).

[11] T. Saito and Y. Arakawa, Phys. Rev. B **60**, 1701 (1999).

[12] P. Hohenberg and W. Kohn, Phys. Rev. **136**, B864 (1964).

[13] D. M. Ceperley and B. J. Alder, Phys. Rev. Lett. **45**, 566 (1980).

[14] J. P. Perdew and A. Zunger, Phys. Rev. B **23**, 5048 (1981).

[15] N. Troullier and J. L. Martins, Phys. Rev. B **43**, 1993 (1991).

[16] M. Bockstedte, A. Kley, J. Neugebauer, and M. Scheffler, Comput. Phys. Comm. **107**, 187 (1997).

[17] M. Fuchs and M. Scheffler, Comput. Phys. Commun. **116**, 1 (1999).

[18] F. Große and J. Neugebauer, in *Proceedings of the 24th international conference on the physics of semiconductors*, edited by D. Gershoni (World Scientific, Singapore, 1999).

[19] A. F. Wright and J. S. Nelson, Phys. Rev. B **50**, 2159 (1994).

[20] A. F. Wright and J. S. Nelson, Phys. Rev. B **51**, 7866 (1995).

[21] C. Stampfl and C. G. Van de Walle, Phys. Rev. B **59**, 5521 (1999).

[22] F. Große and J. Neugebauer, in preparation.

[23] P. P. Ewald, Ann. d. Physik **64**, 253 (1921).

[24] E. R. Fuller and E. R. Naimon, Phys. Rev. B **6**, 3609 (1972).

[25] M. van Schilfgaarde, A. Sher, and A.-B. Chen, J. Crystal Growth **178**, 8 (1997).

[26] D. Doppalapudi, S. N. Basu, and T. D. Moustakas, Jour. Appl. Phys. **85**, 883 (1999).

[27] J. E. Northrup, L. T. Romano, and J. Neugebauer, Appl. Phys. Lett. **74**, 2319 (1999).

EFFECTS OF INTERFACE ROUGHNESS AND EMBEDDED NANOSTRUCTURES ON DEVICE PROPERTIES

D. Z.-Y. TING[†], T. C. MCGILL[*], N. Y. CHEN[††], J. N. WANG[**], R. G. LI[**], Y. Q. WANG[**], W. K. GE[**], J. N. SCHULMAN[†††]
[†] Jet Propulsion Laboratory, California Institute of Technology, Pasadena, CA 91109
[*] Dept. of Applied Physics,California Institute of Technology, Pasadena, CA 91125
[††]Dept. of Physics, National Tsing Hua University, Hsinchu, Taiwan 30043
[**]Dept. of Physics, Hong Kong University of Science and Technology, Clearwater Bay, Kowloon, Hong Kong
[†††] HRL Laboratories, LLC, Malibu, CA 90265

ABSTRACT

We give an overview of the open-boundary planar supercell stack method (OPSSM), as a means for treating 3D quantum transport in mesoscopic tunnel structures. The flexibility of the method allows us to examine a variety of physical phenomena relevant to quantum transport. In this work we focus on the effects of interface roughness and embedded nanostructures in tunnel devices. Four representative applications of OPSSM are discussed: (1) interface roughness in double barrier resonant tunneling structures, (2) self-organized InAs quantum dot insertions in GaAs/AlAs double barrier structures, (3) tunneling characteristics of ultra-thin oxides with interface roughness, and, (4) embedded quantum wire model of dielectric breakdown. These examples demonstrate scattering and localization effects under different biasing conditions.

1. INTRODUCTION

In modeling quantum transport in semiconductor heterostructures, one can often assume perfect periodicity in the lateral directions, thereby reducing the mathematical description to a 1D problem in which only potential variations along the growth direction are considered[1]. However, in treating realistic device structures we often need to consider the effects due to imperfections such as interface roughness, impurities, and alloy disorder. The presence of these inhomogeneities is incompatible with the assumption of translational invariance in the parallel directions. In this paper, we give an overview a theoretical method which we developed to treat quantum transport in devices containing structural inhomogeneities. The method is designed for flexibility so that it can also be used to treat transport in nanostructures with reduced dimensionality, such as quantum wires and quantum dots. The method has been successfully applied to a broad range of topics, including neutral impurities in tunneling structures[2], interface roughness effects in resonant tunneling structures [3, 4], fluctuations in the transmission properties of a quantum dot with interface roughness and impurities[5], resonant tunneling via self-organized quantum dot states[6], tunneling characteristics of non-uniform ultrathin oxides[7], and an embedded quantum wire model of dielectric breakdown[8].

In Section 2, we introduce the open-boundary planar supercell stack method (OPSSM), as a means for treating 3D quantum transport in mesoscopic tunnel structures. In Section 3, we also discuss four selected applications of OPSSM to illustrate the lessons we have learned by conduction numerical experiments using OPSSM. Section 4 summarizes the results.

2. METHOD

The device structure treated by the open-boundary planar supercell stack method (OPSSM)[9] consists of an active region sandwiched between two semi-infinite flat band electrode regions. We allow the active region to take on quasi-3D variations. Let the z axis be the direction perpendicular to the interfaces (i.e., the direction of current flow). Then the active region is composed of a stack of N_z layers perpendicular to the z-direction, with each layer containing a periodic array of rectangular planar supercells of $N_x \times N_y$ sites. Within each planar supercell, the potential assumes lateral variations as dictated by device geometry. A one-band nearest-neighbor tight-binding Hamiltonian is used to describe the potential and effective mass variations over this volume of interest. Our model is formally equivalent to the one-band effective mass equation[10]

$$-\frac{\hbar^2}{2}\nabla \cdot \frac{1}{m(\mathbf{x})}\nabla\psi + V(\mathbf{x})\psi = E\psi, \tag{1}$$

discretized over a Cartesian grid, and subject to periodic boundary conditions (with supercell periodicity) in the x- and y-directions, and open boundary conditions in the z-direction. Since the planar supercell model may be considered as a multiband model with $N_x \times N_y$ bands, transmission coefficients for structures described by the planar supercell stack can be determined by the direct application of the multiband quantum transmitting boundary method (MQTBM) described elsewhere[11]. Although conceptually similar to MQTBM, operationally, OPSSM is much more computationally intensive. In particular, OPSSM requires accurate and efficient solutions of large sparse linear systems, which is achieved using the quasi-minimal residual method [12].

Unlike 1D quantum transport methods where the in-plane crystal momentum ($\mathbf{k}_\parallel$) is conserved, the planar supercell stack method permits $\mathbf{k}_\parallel$ scattering. In general, a given $\mathbf{k}_\parallel$ can scatter into a continuous range of $\mathbf{k}'_\parallel$. However, in the planar supercell stack method, due to finite supercell size ($N_x \times N_y$ sites), $\mathbf{k}_\parallel$ can scatter only into a set of $N_x \times N_y$ parallel $\mathbf{k}$ vectors given by

$$\mathbf{k}'_\parallel = \mathbf{k}_\parallel + \mathbf{g}_{lm}, \tag{2}$$

$$\mathbf{g}_{lm} = (\frac{2\pi l}{N_x d_x}, \frac{2\pi m}{N_y d_y}, 0), \qquad l = 1, ..., N_x, \quad m = 1, ..., N_y, \tag{3}$$

where $\mathbf{g}_{lm}$'s are the $N_x \times N_y$ parallel reciprocal lattice vectors associated with the mini-Brillouin zone of the planar supercell, and d_x, d_y, and d_z are the discretization step sizes.

Since we are free to choose the values of $V(\mathbf{x})$ and $m^*(\mathbf{x})$ at each of the $N_x \times N_y \times N_z$ sites in our computational domain, we have tremendous flexibility in dictating the geometry of the device structure we simulate. OPSSM provides a prescription for solving the quantum mechanical scattering problem exactly for the 3D geometry described by the planar supercell stack, and allows us to compute transmission coefficients with a high degree of numerical accuracy and efficiency. Note that even though the supercell geometry imposes an artificial periodicity to make computations tractable, the use sufficiently large supercells can minimize supercell artifacts and yield excellent descriptions of the physical problem.

Incidentally, it is quite straight forward to incorporate the effects of transverse magnetic fields into the OPSSM formalism. In practice, this involves adding a field-dependent term to the on site energies, and multiplying the hopping matrix elements by a field-dependent phase factor. The modifications to OPSSM are minor, and has been successfully implemented [13].
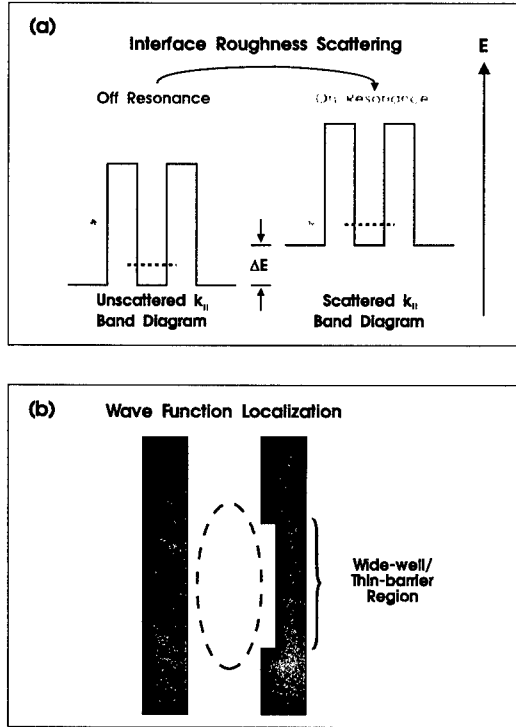
Figure 1: Schematic illustrations of two main effects of interface roughness on doubel barrier resonant tunneling diodes: (a) interface roughness assisted resonant tunneling, and, (b) wave function localization.

3. RESULTS

In this section we discussion four applications using OPSSM. The first two examples illustrate the effects of interface roughness and embedded nanostructures in low to moderate applied bias. The next two examples consider the high-bias (Fowler-Nordheim) regime as well.

3.1 Interface Roughness in Double Barrier Resonant Tunneling Structures

In one of the first applications, OPSSM was used to examine the effect of interface roughness on transmission properties of double barrier structures under flat-band conditions[3, 4]. The main conclusions from these simulations are: (1) Scattering of off-resonance states into on-resonance states provides the dominant contribution to interface roughness assisted tunneling. Analyses of scattering strength sensitivity to interface layer configurations reveals preferential scattering into $\Delta k_\parallel \approx 2\pi/\lambda$ states, where λ is the island size. (2) Roughness at interfaces adjacent to the quantum well can result in lateral localization of wave functions. This effect increases with island

GaAs/AlAs DBH L_B=3 L_W=11 L_I=1 (x4) λ=23-25 nm
E=0.150 eV a_x=a_y=2 nm a_z=0.2825 nm 32x32 s-cell

Figure 2: Transmission coefficients as functions of applied bias for a set of double barrier structures with different in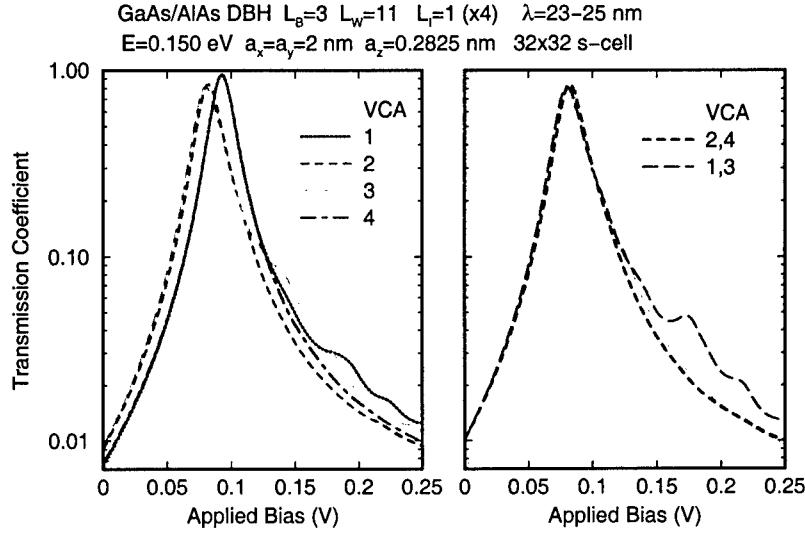terface roughness configurations. Each structures contain 3 monolayer(ML) AlAs barriers and 11 ML GaAs well. A single ML wide interfatial layer is inserted at each of the four interfaces.

size, and results in the broadening and shifting of transmission resonances, and the introduction of preferential transmission paths. Fig. 1(a)illustrates the interface roughness assisted resonant tunneling process. A nominally off-resonant incoming state can be elastically scattered by interface roughness into a different $k_\parallel$ state which it happens to be on-resonance, and experiences enhanced transmission through resonant tunneling. Fig. 1(b)schematically illustrates wave function localization. For island sizes larger than well width, the wave function associated with a resonance could become laterally localized to a region where, locally, the quantum well appears wider, and the barrier appears thinner. A wide well leads to a lower resonance level, and thinner barrier leads to larger resonance width. In addition, preferential tunneling paths are found over the thin barrier region.

Fig. 2 shows transmission coefficients as functions of applied bias for a set of double barrier structures with different interface roughness configurations. In all cases, the electron incident energy is fixed at 0.15 eV. All structures have $L_W = 11$ (monolayers) GaAs wells and $L_B = 3$ AlAs barriers. In addition, a monolayer wide interfacial layer is inserted at each GaAs-AlAs interface. Each interfacial layer can be either a random layer, consists of half GaAs sites and half AlAs sites, randomly forming islands with sizes range from 23 to 25 nm. Alternatively, it can also be a smooth VCA (virtual crystal approximation) layer of $Al_{0.5}Ga_{0.5}As$. In the left panel we illustrate the role of the individual interfaces. The interface layers are numbered 1 through 4, starting from the incident side. Four structures, each containing only one random interface layer are considered. In addition, a reference structure in which all interface layers are VCA layers is also included. Thus, the leading interface is rough in Configuration 1, etc. The results show that

large islands at interfaces 2 and 3 (which are adjacent to the quantum well) can induce lateral wave function localization, and lowers the resonance level. We also note that interface roughness scattering is the least important in Configuration 4, where the rough interfacial layer is located away from the incident side. This is because unless the incident electron is on resonance, and the transmission coefficient is reasonably large, the wave function is primarily located on the incident side, with extremely small probability of penetrating across the device structure to the transmitted side to sense the roughness at the far interface (4). Note also that interface roughness assisted resonant tunneling is weaker for interface 2 than 3.

In real structures, two of the four interfaces tend to be rougher. This is because the inverted interface, formed when GaAs is grown on top of AlAs, tends to be rougher than the normal interface, formed when AlAs is grown on top of GaAs. The left panel of Fig. 2 compare a structure with rough interfaces at 2 and 4 to one with rough interfaces at 1 and 3. In fact, the 1,3 structure is just the 2,4 structure turned around. Note that the 1,3 structure shows much stronger scattering above the main resonance peak. This indicates that the low temperature valley currents can be quite different in forward and reverse biases.

3.2 Self-organized InAs Quantum Dot Insertions in GaAs/AlAs double Barrier Structures

Interface roughness scattering tends to be the most effective when the rough interface is positioned where the amplitude of the wave function is large. One might imagine artificially introducing perturbations in the center of the well region of a double barrier resonant tunneling structure to achieve the maximum effect, since the wave functions associated with resonant tunneling states have the largest amplitude there.

It has been shown that the growth of a highly lattice mismatched semiconductor layer onto a substrate could lead to the spontaneous formation of semiconductor islands with sizes in the quantum range. This has been exploited for the InAs/GaAs system ($\sim$ 7% lattice mismatch) to produce self-organized InAs quantum dots in GaAs matrix by InAs sub-monolayer insertion. In a recent experiment, Wang and co-workers observed a series of sharp peaks in the I-V characteristics of a GaAs/AlAs double barrier structure with mid-well sub-monolayer InAs insertion[6]. The peaks are attributed to resonant tunneling through localized states associated with self-organized InAs quantum dots. OPSSM calculations reinforces this belief, and clarifies the nature of these quantum dot states. In our model we consider a set of GaAs/AlAs double barrier structures with well and barrier widths of 11 and 6 monolayers, respectively. All of the structures have InAs occupying 1/6 of mid-well layer, forming InAs quantum dots of varying sizes. We do this by first randomly populating the mid-well layer with InAs and GaAs at the proper stoichiometry. We then allow in-plane migration to take place using a simulated annealing algorithm[14]. With the appropriate choice of parameters, there would be a tendency for InAs (and GaAs, for that matter) to cluster. The average cluster size grows as the "annealing time" increases. Therefore, by taking snapshots of the annealing process at various stages, we can obtain a progression of InAs island sizes. Fig. 3 shows the transmission coefficient spectra for this set of structures. At small island sizes, the transmission spectrum is similar to that for the pure GaAs/AlAs structure, but with an added series of small shoulder peaks above the main resonance. As average island size increases, the peaks associated with quantum-dot states become more distinct and move to lower energies. By examining the lowest resonant transmitting state wave functions of the structures, we find that for small average island size ($\lambda = 2.8$ nm; compare with well width of 3.1 nm.) the wave function appears delocalized, as is more characteristic of a GaAs quantum well state. But as the average
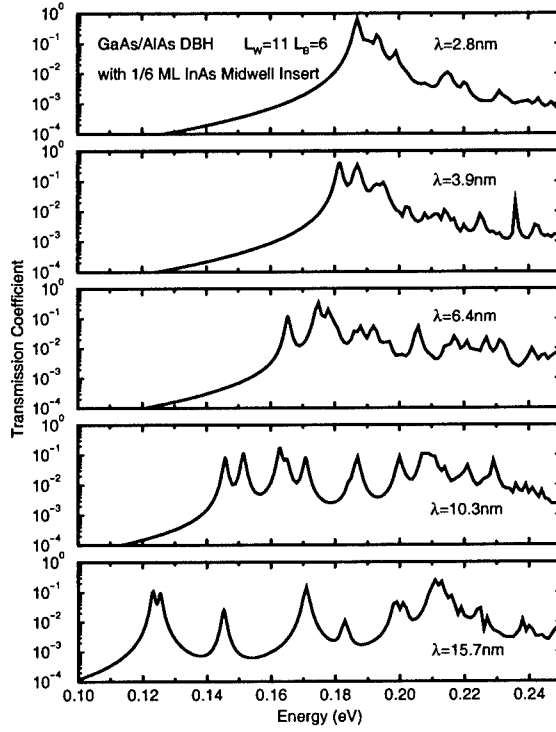
Figure 3: Transmission coefficient spectra for a set of GaAs/AlAs double barrier structures with 1/6 monolayer of InAs inserted at mid-well, forming islands of various sizes. The well and barrier widths are $L_W = 11$ ML and $L_B = 6$ ML, respectively. 64×64 supercells with $d_\perp = 0.2825$ nm and $d_\| = 1$ nm are used.

island size becomes larger, the wave function appears more localized. In each of $\lambda = 6.4$ nm and $\lambda = 10.3$ nm cases, the wave function of the lowest resonance appears to be strongly localized on the largest island in the supercell. Our model indicates that sub-monolayer InAs insertion in the middle of GaAs/AlAs double barrier structures can produce a series of resonances reminiscent of those seen in the experiments, provided that the lateral dimensions of the monolayer InAs dots are sufficiently large.

3.3 Tunneling Characteristics of Ultra-Thin Oxides with Interface Roughness

Tunneling through ultra-thin oxide barriers as a mechanism for leakage currents is of growing interest as the scaling of metal-oxide-semiconductor (MOS) device structures continues. Experimental evidence indicates that, in typical industrial oxides, roughness at the Si/SiO_2 interface increases with decreasing oxide layer thickness.[15] Thus interface roughness becomes even more important in ultra-thin oxides. We compute the current-voltage characteristics of heavily doped
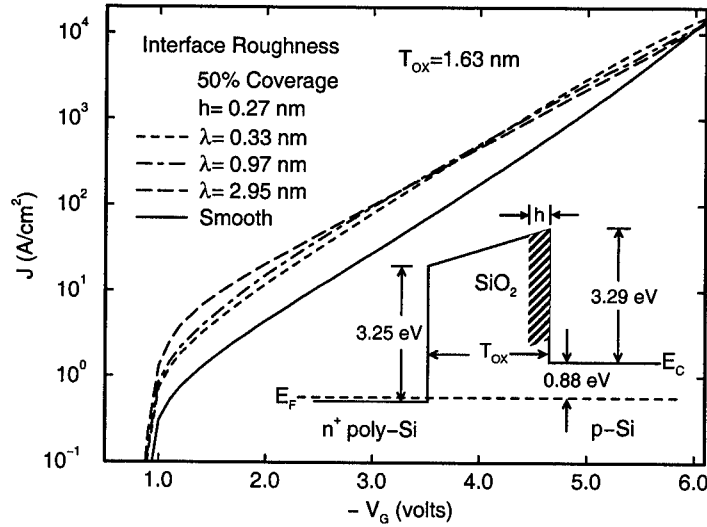
Figure 4: Supercell calculation of current density-voltage curves for a set of n^+ poly-Si/SiO$_2$/p-Si tunnel structures with varying degrees of interface roughness. The zero-bias band diagram is shown in the inset. Applied bias lowers the p-Si side with respect to the poly-Si side.

n-type polycrystalline silicon (n^+ poly-Si)/SiO$_2$/p-type silicon (p-Si) tunnel structures under negative gate biases. We use 32×32 planar supercells with discretization spacing of 0.136 nm. We consider an MOS tunnel structure with a 0.27 nm rough interfacial layer sandwiched in between a 1.36 nm pure oxide layer and the p-Si region. We assume that the rough interfacial layer consists of a 50%-50% mixture of oxide and Si in random configurations. The Si sites (and the oxide sites, for that matter) may aggregate and form patches, or islands, which are characterized by their lateral extent (island size λ) and the thickness of the interfacial layer (island height h).

Fig. 4 shows the calculated 300K J-V curves for three MOS tunnel structures with rough Si/SiO$_2$ interfaces characterized by island sizes of $\lambda = 0.33$, 0.97, and 2.95 nm. A zero-bias band diagram is depicted in the inset of Fig. 4. For comparison, we also include a reference structure with a smooth interface by replacing the rough interfacial layer with a pure oxide layer of the same thickness (resulting in a total oxide thickness of 1.63 nm). Under bias, the p-Si side is lowered with respect to the poly-Si side. We note that in the direct tunneling regime ($|V_G| < 4$V), current densities increase with island size. In the Fowler-Nordheim tunneling regime ($|V_G| > 4$V), however, current densities decrease with island size. These opposite trends are the result of the interplay between two physical mechanisms : localization and scattering.

The behavior in the direct tunneling regime is primarily due to lateral localization of tunneling electrons through regions of the barrier which are thinner. This is similar to the results seen in the case of double barrier structures discussed earlier. In this (low to moderate bias) regime, the wave function of a transmitting state becomes increasingly localized in the thinner portion of the rough interfacial layer. Preferential traversal through the thin-barrier regions leads to higher transmission probabilities and therefore higher current densities, as observed in Fig. 4.

The high-bias (Fowler-Nordheim) regime is quite different. Here the trailing edge of the barrier is biased below the energy level of the incident electron, and no longer acts as an energy barrier. Unlike in the direct tunneling regime, where an electron traverses the oxide portion of the rough interface with evanescent characteristics, in the Fowler-Nordheim tunneling regime, an electron transmits through both the oxide and silicon portions of the interfacial layer with propagating characteristics. Therefore the rough interface affects transport primarily through scattering, rather than lateral confinement. The larger islands produce more scattering, and thereby reduce the transmission amplitude in the forward direction. This account for reduction in Fowler-Nordheim current as island size in the rough interfacial layer increases. A more detailed analysis of this problem can be found in reference [7].

3.4 Embedded Quantum Wire Model of Dielectric Breakdown

OPSSM has also been used to study dielectric breakdown[8] in n^+ poly-Si/SiO$_2$/p-Si tunnel structures containing ultra-thin oxide layers. It is well known that high-field stressing of MOS structures in the Fowler-Nordheim tunneling regime can lead to oxide breakdown. Experiments by Sugino et al. [16] strongly suggests that breakdown spots are made of crystallized silicon extending across the oxide layer. We model the physical damage using an array of oxide-embedded cylindrical silicon quantum wires (nano-scale filaments) extending from the SiO$_2$/p-Si interface into the oxide layer with cylinder height h and diameter d, as illustrated in Fig. 5(a).

Fig. 5(b) shows calculated 300K and 77K current density-voltage (J-V) curves for structures with 4.5 nm thick oxides, embedded with quantum wires of $h = 0.8$, 1.5, 3.0 and 4.5 nm. A "fresh" ($h = 0$) structure is included for comparison. The wires have diameter of $d = 1.55$ nm, and account for 10% of the total cross-sectional area. We note that the low-bias current densities for structures with longer wires ($h = 3.0$ and 4.5 nm) show strong temperature dependence. This turns out to be due to resonant tunneling through high-lying quantum dot states localized in the tip of the cylinders.[8] In the intermediate regime, current densities increase exponentially with wire length h. This regime is characterized by highly localized conduction in the quantum wires, which act essentially as current funnels.[8] In the high-bias (Fowler-Nordheim)limit current densities for structures with shorter wires ($h = 0.8$ and 1.5 nm) converge with that for the fresh ($h = 0$) structure. This is again due to the fact that the trailing edge of the barrier, which the shorter wires are located, are now biased entirely below the energy of the incident electron, and therefore no longer act as barriers. Here tunneling property of the oxide is determined mainly by the leading edge of the barrier, therefore the short wires are rendered relatively inactive. A more detailed analysis on this topic can be found in reference [8].

4. CONCLUSIONS

Three-dimensional quantum transport in mesoscopic devices is examined with the exactly solvable, real-space, open-boundary planar supercell stack method (OPSSM)[9]. The flexibility of our method has enabled us to include elastic scattering effects due to impurities, interface roughness, and alloy disorder in our studies of 2D (double barrier heterostructures), 1D (quantum wires electron waveguides) , and 0D (quantum dots) mesoscopic device structures. Our studies reveal that structural imperfections can not only produce additional scattering processes in a perturbative sense, under the right circumstances, they can also substantially alter the quantized electronic states, leading to modified transport properties, as was demonstrated in the case of InAs quantum
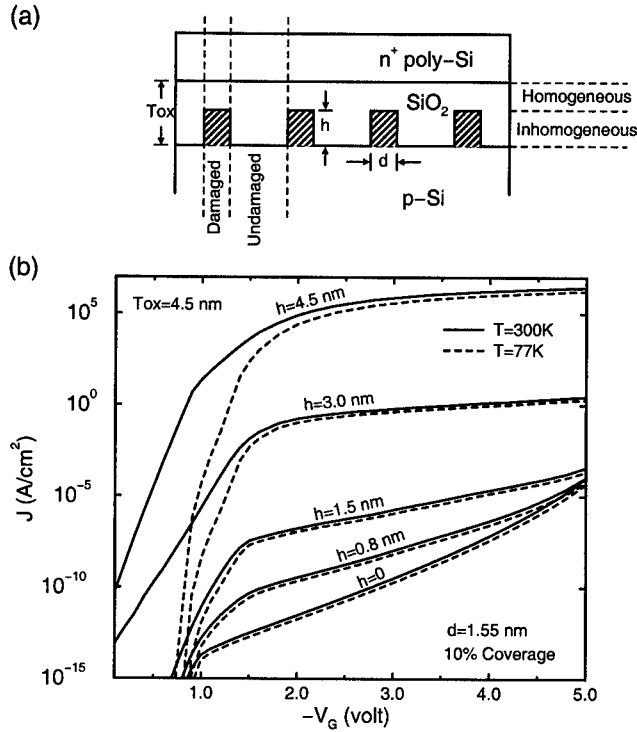
Figure 5: (a) Schematic illustration of an n^+ poly-Si/SiO$_2$/p-Si tunnel structure with oxide-embedded cylindrical quantum wires. (b) Calculated current density-voltage curves for such structures with various cylinder heights. Quantum wires cover approximately 10% of the cross-sectional area.

dot insertions in double barrier structures. Under low and moderate biasing conditions, interface roughness can induce wave function localization if the island sizes are sufficiently large compared to the electron deBroglie wavelengths. Localization effects can lead to the lowering of resonance positions, and introduce favorable current paths. In the high bias (Fowler-Nordheim) regime, localization effects may become less important, and scattering effects become more prominent.

ACKNOWLEDGMENTS

References

[1] R. Tsu and L. Esaki, *Appl. Phys. Lett.* **22**, 562 (1973).

[2] S. K. Kirby, D. Z.-Y. Ting, and T. C. McGill, *Phys. Rev. B*, **48**(20), 15237 (1993).

[3] D.Z.-Y. Ting, S.K. Kirby, and T.C. McGill, *Appl. Phys. Lett.*, **64**(15), 2004 (1994).

[4] D.Z.-Y. Ting and T.C. McGill, *J. Vac. Sci. Technol.* B**14**(4), 2790 (1996).

[5] S. K. Kirby, D. Z.-Y. Ting, and T. C. McGill, *Semicond. Sci. Tech.* **9**(5) Suppl. S , 918 (1994).

[6] J.N. Wang, R.G. Li, Y.Q. Wang, W.K. Ge, D.Z.-Y. Ting, *Microelectron Eng* **43-4** 1998, 341-347.

[7] D.Z.-Y. Ting, *Appl. Phys. Lett.* **73**(19), 2769 (1998).

[8] D.Z.-Y. Ting, *Appl. Phys. Lett.* **74**(4), 585 (1999).

[9] D. Z.-Y. Ting, S. K. Kirby, and T. C. McGill, *J. Vac. Sci. Technol. B* **11**(4), 1738 (1993)

[10] D. J. BenDaniel and C. B. Duke, *Phys. Rev.*, **152**, 683 (1966).

[11] D.Z.-Y. Ting, E.T. Yu, and T.C. McGill, *Phys. Rev. B*, **45**(7), 3583 (1992)

[12] R.W. Freund and N.M. Nachtigal, *Numer. Math.* , **60**(3), 315 (1991).

[13] N.Y. Chen, *Three-dimensional supercell simulations of quantum transport in a magnetic field*, Master degree thesis, National Tsing Hua University, Hsinchu, Taiwan, 1998.

[14] N. Metropolis, A. Rosenbluth, M.N. Rosenbluth, A. Teller, and E. Teller, *J. Chem. Phys.*, **21**, 1087 (1953).

[15] S. T. Cundiff et al., *Appl. Phys. Lett.* **70**, 1414(1997).

[16] R. Sugino, T. Nakanishi, K. Takasaki, and T. Ito, *J. Electrochem. Soc.* **143**, 2691 (1996).

CLUSTER MODEL STUDY OF THE INCORPORATION PROCESS OF EXCESS ARSENIC INTO INTERSTITIAL POSITIONS OF THE GaAs LATTICE

T. Marek, S. Kunsági-Máté*, H.P. Strunk,
Institute for Microcharacterisation, Friedrich-Alexander-University Erlangen-Nuremberg, 91058 Erlangen, Germany
* Institute for General and Physical Chemistry, Janus Pannonius University, 7601Pécs, Hungary

ABSTRACT

We study an As_2 molecule approaching a planar, non-reconstructed, As terminated GaAs(001) surface by using a suitable cluster and quantum mechanical ab-initio calculation methods. During our calculations the As_2 molecule is always oriented perpendicularly to the surface and its bonding length may vary. We find a metastable position below the growing surface which facilitates the incorporation of the leading As atom into an interstitial position of the crystal during growth. We give a first model for this incorporation process.

INTRODUCTION

GaAs layers are usually grown by molecular beam epitaxy (MBE). When the substrate temperature is about 600°C these layers are stoichiometric even under the generally used As rich conditions. If the temperature is choosen much lower, say less than about 300°C, the layers become non-stoichiometric e.g. [1]. A significant amount (up to 1.5%) of excess As is incorporated into the GaAs-lattice which results point defects, such as arsenic antisites, gallium vacancies and especially arsenic interstitials [1-3]. The incorporation of this excess As during the growth at the low substrate temperatures (LT-GaAs) plays the key role in understanding the unique electrical and optical properties of this material. LT-GaAs was brought into the focus of technological interest since it can be used as buffer layer in semiconductor devices or as an active layer for ultrafast optoelectronic devices [1-3].

In a recent theoretical paper [3] we study As_2 molecules approaching a planar, non-reconstructed GaAs(001) surface by using suitable clusters and quantum mechanical ab-initio calculation methods. The surface is either As or Ga terminated. During our calculations the As_2 molecule is always oriented perpendicularly to the (001) surface. It is only for the case of the As terminated surface that we obtained for the lower As atom of the As_2 molecule a metastable position below the growing surface.

This paper starts from this metastable position below the growing surface and develops a first theoretical model for the incorporation process of As atoms into interstitial positions during the growth process. We use again quantum mechanical ab-initio calculation methods to study the approach process of an As_2 molecule to the As-terminated GaAs(001) surfaces. In a second step we study then the incorporation process of the lower As atom (As_2 molecule) into an interstitial position.

CLUSTER MODEL AND CALCULATION PROCEDURE

We represent the GaAs crystal and its surface by a $Ga_2As_5H_8$ cluster, see Fig. 1. This cluster has the C_2 symmetry axis and represents a 1x1 unit-cell of the As terminated (001)-surface. The bonds on this surface are left dangling. The other bonds are saturated with hydrogen atoms (Fig. 1) in correspondence to the arguments in [4-8]. The interatomic distances between the Ga and As atoms are chosen according to the lattice constant of 5.654 Å, [9]. The Ga-H and As-H bond lengths are fixed to the values of 1.663 Å and 1.511 Å, respectively. These values are taken from the experimental observations on free GaH and AsH_3 molecules [10].
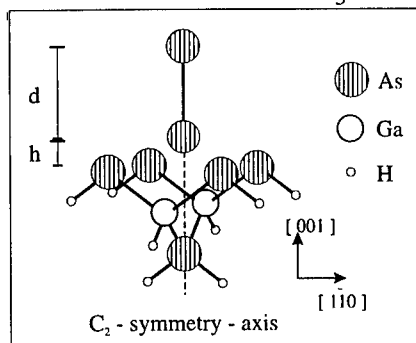

Fig. 1 $Ga_2As_5H_8$ cluster representing the As terminated surface and an As_2 molecule above the (001)-surface as treated by the ab-initio calculations. The parameters, As-As distance 'd' and the height 'h' above the cluster are introduced in the sketch.

For the calculation of the reaction paths towards the As-terminated (001) surface, we fix an As_2 molecule at different heights above the surface on the C_2 symmetry axis of the cluster. The As-As bond is oriented parallel to this symmetry axis (Fig. 1). We describe the reaction path of the As_2 molecule by the height 'h' of the *lower* As atom in the As_2 molecule above the As terminated surface and the distance 'd' between the As atoms in the molecule (Fig. 1). During the calculations we choose different heights 'h' and in these fixed positions we account for the possibility to change the distance 'd' between the As atoms (Fig. 1) until the value of the total energy of the system (cluster plus molecule) becomes minimal. We repeat these calculations for different heights 'h' between -0.5 Å and 2 Å. The value h = 0 Å denotes the in-plane position of the lower As atom in the (001) surface. The interaction energy 'E' between As_2 molecule and cluster is given by the difference between the total energy of the system (cluster and As_2 molecule) and the sum of the total energies of the separated cluster and As_2 molecule.

The total energies of the system are determined by ab-initio calculations. Hartree-Fock (HF) method, followed by the semi-direct second-order Møller-Plesset (MP2) correlation energy correction [11], is used. For the minimization of the total energy of the system (by variation the distance d between the As-atoms) the Berny geometry optimization is used [12]. These calculations (HF, MP2 and the geometry optimization) are performed with the GAUSSIAN 94 program package on a Fujitsu VP system. The Gaussian basis sets for all Ga and As atoms are the double zeta contracted Gaussian type orbitals [13-15].

RESULTS AND DISCUSSION

Fig. 2 shows the calculated interaction energy 'E' between the cluster and an As_2-molecule in dependence of the height 'h' of this molecule above and below the (001) surface (see insets). In connection with the incorporation process we focus now only on the local minimum at h = -0.2 Å. This configuration makes an incorporation of As atoms into interstitial positions during crystal growth very likely because this minimum lies 0.2 Å below the surfaces plane. We will now outline that this local minimum can be converted into a bonding state during growth.
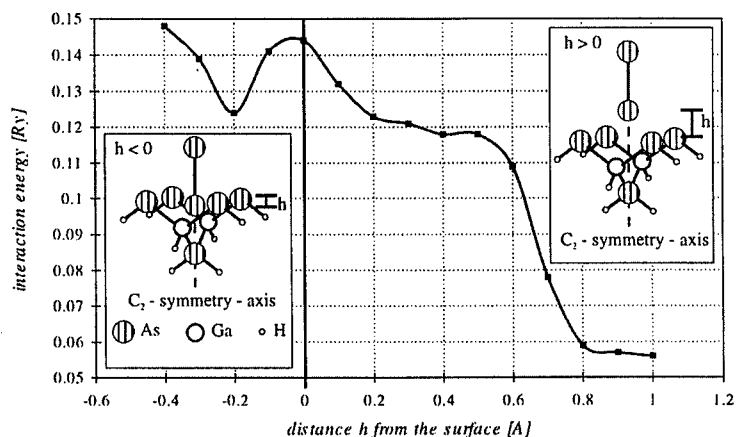

Fig. 2 The interaction energy 'E' between an As_2-molecule and the $Ga_2As_5H_8$ cluster as function of the height 'h' above the GaAs(001) surface. Ab-initio Hartree-Fock calculation, modified with second order Møller-Plesset perturbation.

One possible mechanism consists in a kind of 'stabilization' of the buried lower As atom of the As_2-molecule. Such stabilization can occur during the further growth. Two more Ga atoms bind regularly to the As terminated surface in such a way, that these form a cage for the As atom in the interstitial position (inset in Fig. 3). In this configuration the interaction energy 'E' is given by the difference between the total energy of the system (in this case: cluster, As_2 molecule and the two Ga atoms) and the sum of the total energies of the separated cluster, As_2 molecule and the two Ga atoms.

Fig.3 shows the corresponding interaction energy for h = -0.2 Å we have calculated for this configuration (see also inset). The value of the interaction energy of the system with the caged up As atom is much lower and lies in the negative region, i.e. -0.2 Ry, than without the additional two Ga atoms. This result, in fact, corresponds to a bond state for the interstitial As atom under the first surface layer during the growth process.
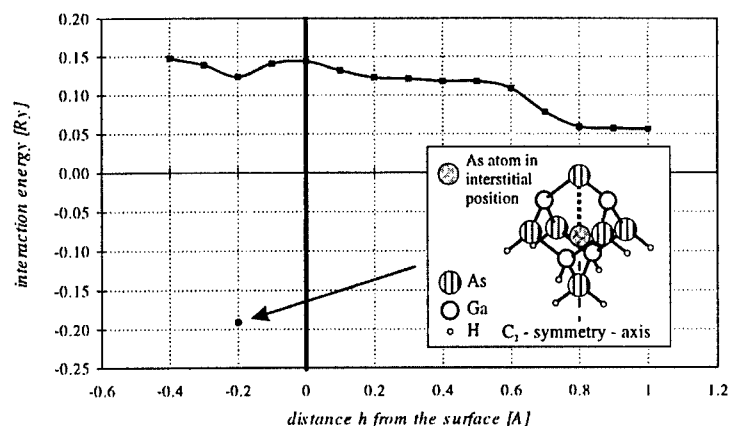
Fig. 3 The interaction energy at h = -0.2 Å between the Ga₂As₅H₈ cluster (plus two additionally attached Ga atoms) and the As₂ molecule (configuration see inset). For a comparison with the situation without the additional Ga atoms the curve from Fig. 2 is introduced.

We summarize now in Fig. 4 the model suggested for the incorporation process in three steps:

1. The As₂ molecule moves normally towards the surfaces (Fig. 4a).
2. The As₂ molecule touches the surface and reaches the metastable interstitial position under the first layer (Fig. 4b).
3. Two additional Ga atoms bind regularly to the As terminated surface during the growth process. These Ga atoms make bonds with the As atoms in the (001) surface of the cluster and with the upper As atom of the As₂ molecule and form a cage for the interstitial As atom.(Fig. 4c).
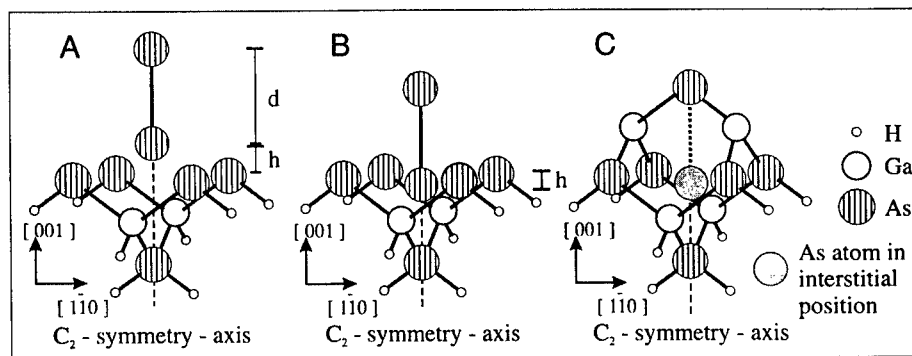

Fig. 4 Cluster model for the incorporation process of As into an interstitial position of the GaAs   lattice   during   the   growth   process.

236

CONCLUSION

Our theoretical work is focused on the study of the incorporation process of the excess As atoms into the growth surface during deposition. We presented a first study for a possible incorporation process of As atoms into stable interstitial positions during growth. We find a metastable position below the growing surface only for the As terminated GaAs(001) surface. This configuration makes an incorporation process of As atoms into interstitial positions during crystal growth possible. We suggested a mechanism, which consist in a 'stabilization' of the buried As atom. Two more Ga atoms bind regularly to the As terminated surface and thereby form a cage for the As atom in the interstitial position. The As atom is now in a stable interstitial position

These calculations based on a $Ga_2As_5H_8$ cluster are certainly far from understanding the corresponding process of a real growth experiment. Especially, the approaching As_2 -molecule is fixed to the C_2 symmetry axis and a more realistic calculation should give up this condition. However, such an ab-initio calculation appears out of range of presently possible calculations because of the required large computing time. On the other hand, our calculation bears physical significance.

ACKNOWLEDGMENT

REFERENCES

[1]   Low Temperature GaAs and Related Materials, ed.: G.L.Witt et al.,   MRS Symposia Proceedings Vol.241 (Material Research Society,Pittsburg, 1992)

[2]   Symposium on Non-Stoichiometric III-V Compounds, eds.: T. Marek, S.Malzer, P.Kiesel, Physik Mikrostrukturierter Halbleiter Vol. 6 (Friedrich-Alexander-Universität Erlangen-Nürnberg, Lehrstuhl Mikrocharakterisierung, Erlangen, 1998, ISBN: 3-932392-12-4)

[3]   T.Marek, S.Kunsagi-Mate, H.P.Strunk in 2nd Symposium on Non-Stoichiometric III-V Compounds, eds.: P.Kiesel, S.Malzer,T. Marek, Physik Mikrostrukturierter Halbleiter Vol. 10 (Friedrich-Alexander Universität Erlangen-Nürnberg, Lehrstuhl Mikrocharakterisierung, Erlangen, 1999, ISBN: 3-932392-19-1)

[4]   Y.Fukunishi, H.Nakatsuji, Surf. Sci. **291** (1993) 271.

[5]   S.Kunsági-Máté, N.Marek, T.Marek, H.P.Strunk, Surf.Sci. **365** (1996) 743.

[6]   L.C.Snyder and Z.Wasserman, Surf.Sci. **77** (1987) 52.

[7]   A.C.Kenton and M.W.Ribarsky, Phys.Rev.**B 23** (1981) 2897.

[8]   K.Hermann and P.S.Bagus, Phys Rev.**B. 20** (1979) 1603.

[9]   K.H.Hellwege, W.Pies and A.Weiss, Crystal Structure Data of Inorganic Compounds, Landolt Börnstein, New Series, Group III, **Vol.7** (Springer, Berlin, 1979)

[10] J.H.Callomon, E.Hirota, K.Kuchitsu, W.J.Lafferty, A.G.Maki and C.S.Pote, Structure Data of Free Polyatomic Molecules, Landolt Börnstein, New Series, Group II, **Vol.7** (Springer, Berlin,1976).

[11] M.J.Frisch, M.Head-Gordon and J.A,Pople, Chem.Phys.Lett., **166** (1990) 281.

[12] H.B.Schlegel, J.Comp.Chem., **3** (1982) 214.

[13] P.J.Hay and W.R.Wadt, J.Chem.Phys., **82** (1985) 270.

[14] W.R.Wadt and P.J.Hay, J.Chem.Phys., **82** (1985) 284.

[15] P.J.Hay and W.R.Wadt, J.Chem.Phys., **82** (1985) 299.

COMPUTER SIMULATION OF NUCLEATION ON PATTERNED SURFACES

A. Kuronen, L. Nurminen, and K. Kaski
Helsinki University of Technology, Laboratory of Computational Engineering
P.O.Box 9400, FIN-02015 HUT, FINLAND

ABSTRACT

We have studied qualitatively the effect of patterned substrate surface on adatom nucleation using Kinetic Monte Carlo simulations and solid-on-solid model. The inhomogeneity in the activation energies of adatom diffusion was incorporated into the simulations using two models: a) periodic variation of the adatom–substrate interaction energy as a function of the adatom lateral position and b) adding a direction dependent and periodically varying diffusion barrier energy to the adatom diffusion activation energy. The effect of the patterned surface was clearly manifested as a confinement of nucleated islands and, consequently, narrowing the island size distribution. The effect was strong in a narrow temperature range.

INTRODUCTION

Atomic or near-atomic scale structures are currently intensively studied because of their possible technological applications [1]. However, most applications require a large number of these structures with as little variation as possible in their shape and size.

One method to manufacture semiconductor quantum dots is the utilization of spontaneous self-organization of islands in heteroepitaxial thin film growth [1]. By growing several layers of these island ensembles on each other, the size distribution can be made narrower [2,3]. This vertical correlation of quantum dots can in some cases be explained by the effect of strain caused by the underlying islands on the further growth of islands, i.e. nucleation and growth on a patterned surface.

In some heteroepitaxial systems the strain due to lattice mismatch is relieved by formation of domains that are separated by a regular dislocation network [4]. One example is 2 monolayers (ML) of Ag on Pt (111) [5]. Further deposition of atoms on this structure produces preferred nucleation in the centers of the domains and a narrow size distribution of adatom islands. In this case the confinement effect on the adatoms is caused by the repulsive adatom-dislocation interaction.

The objective of this study is to investigate qualitatively the effect of the spatial variation of the adatom diffusion activation energies on their nucleation. The models presented are chosen so that the above-mentioned cases may be investigated in more detail in the future.

COMPUTATIONAL DETAILS

The evolution of the surface was described by using the Kinetic Monte Carlo (KMC) simulation method [6] and cubic solid-on-solid (SOS) model. Deposition of adatoms randomly on the surface was performed at a constant deposition rate F (ML/s). The diffusion of each adatom was described by the hopping probability P
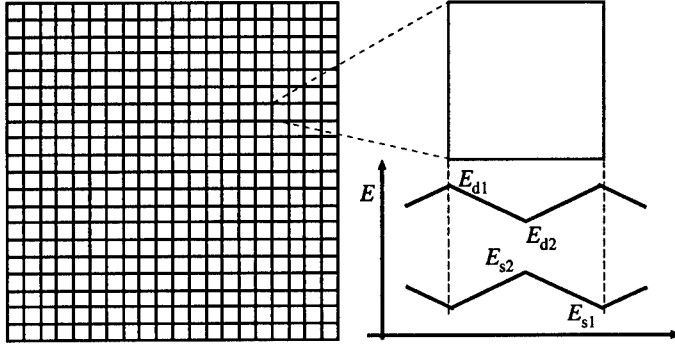
$$P = ke^{-E/k_B T},$$
(1)

Figure 1: Domain structure of the substrate in the simulation model. Also shown are the variations of E_s and E_d inside a single domain.

where k is the prefactor ($k = k_B T/h$) [7], E is the activation energy for diffusion, k_B is the Boltzmann constant and T is the temperature. The activation energy consists of the adatom-substrate interaction E_s and adatom-adatom interaction E_n:

$$E = E_s + nE_n, \qquad (2)$$

where n is the number of lateral nearest neighbor of the adatom. The evolution of the system was followed using the N-fold method algorithm [6].

In order to investigate the effect of the patterns on the substrate the lattice was divided into square-shaped domains as shown in Figure 1. The patterned surface was incorporated to the nucleation model in two ways (see Figure 1):

1. Letting the parameter E_s vary piecewise linearly as a function of the position on the surface.

2. Introducing an additional diffusion barrier E_d for adatom jumps towards the nearest domain boundaries. This barrier depends also on position of the adatom inside the domain.

These are designated as models A and B, respectively.

In all the simulations presented in this work the lattice size was chosen to be 352 × 352 sites and the domain size was selected to be 22 × 22 sites. Periodic boundary conditions were applied in both lateral dimensions. The model parameters $E_s = 0.75$ eV and $E_n = 0.18$ eV were taken from Ref. [8]. The order of magnitude of the diffusion barrier E_d and variation of adatom-substrate interaction E_s inside a domain were based on the studies of Brune et al. [5], i.e. values (see Figure 1) $E_{d1} = 0.02$ eV, $E_{d2} = 0$ eV, $E_{s1} = 0.65$ eV and $E_{s2} = 0.85$ eV were used. It should be noted that there is no intention in this work to study quantitatively any particular system but to investigate the qualitative behavior of the models presented. The deposition flux F was chosen to be 0.0033 ML/s. The studied temperature range was determined by the behavior of the system. For $T = 360 \ldots 420$ K the effect of the patterns on nucleation was most pronounced.
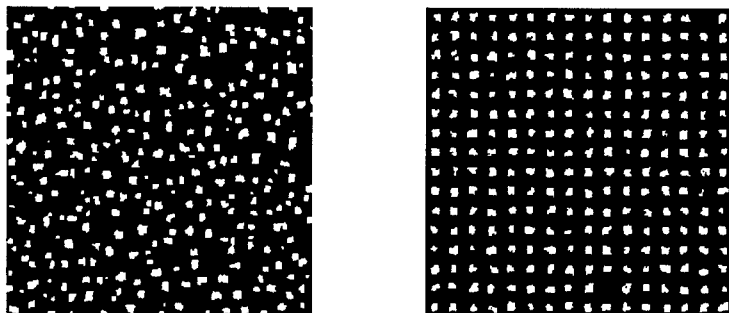
Figure 2: Examples of configurations generated by KMC simulations at the temperature of 390 K and at the adatoms coverage of 15 %. On the left is illustrated the results from simulations where the substrate was homogeneous. On the right is the lattice from simulations using model A for a patterned substrate. Dark areas designate the substrate and light areas the first layer of adatoms.

RESULTS AND DISCUSSION

All the results presented here are for systems simulated up to 15 % coverage of adatoms. At this coverage the islands are purely two dimensional. The results are averages of 50 simulation runs.

In Figure 2 are illustrated examples of surface structures for the homogeneous substrate and for the model A of a patterned substrate. Confinement of islands into the center areas of the domains is clearly seen for the patterned substrate. Some simulations were performed using a modification of the model B where the additional diffusion barrier due to dislocations was in effect only when the adatom was in the immediate vicinity of the dislocation. However, this model produced islands nucleation preferentially on the domain boundaries, not at the centers of the domains as has been observed experimentally for the Ag-Pt systems [5].

Island size distributions for all three cases at various temperatures are shown in Figure 3. The forms of the distributions can easily be understood [4]. At temperatures below 360 K all the distributions have similar forms. At these low temperatures the average diffusion length of adatoms is so short that the effect of inhomogeneity of the surface does not show up. At 360 K an additional maximum around $s = 70$ is observed. This is due to the fact that at these temperatures all the material deposited on a single domain is confined into a single island in this domain. For the coverage of 15 % and the domain of 22×22 lattice sites the size of this island is $s = 73$ particles. When the temperature is further increased the diffusion of adatoms across domain boundaries becomes possible resulting in coalescence of smaller islands into larger ones, thus leaving part of the domains empty.

The confining effect of the patterned surface can clearly be seen in Figure 4 where the average size of the islands $< s >$ and the standard deviation of the size distributions σ_s are plotted for the temperature range 320–440 K. There is a plateau in the curves of average island size around the temperature 390 K for both models A and B. The curves for the
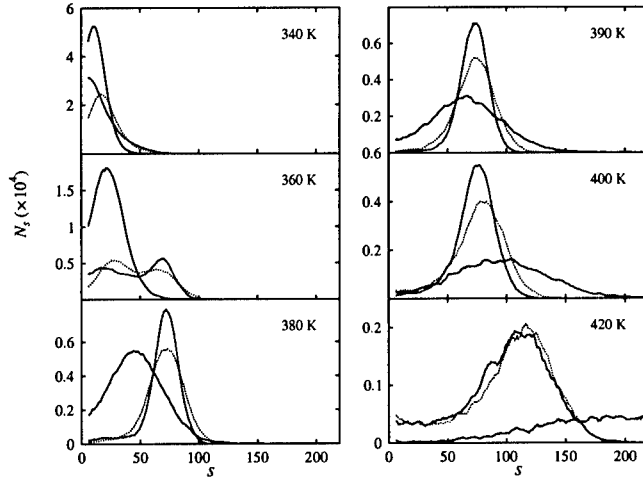
Figure 3: Island size distributions for 15 % coverage at different temperatures for the homogeneous substrate (solid line) and for the models A (dotted line) and B (dashed line). The horizontal axis is the number of particles in the island and the vertical axis is in units islands/lattice site.

standard deviation of the size distributions increase at low temperatures for all three cases. Around 360 K the curves for patterned surfaces decrease due to the confinement of islands inside domains. Although the average size curves for models A and B are similar for the temperature range 340–420 K the standard deviation curves differ for these two models. Moreover, the average island sizes of these models behave differently at low and high temperatures.

The effect of model parameters on results was studied by performing simulations using model A and varying the adatom-adatom interaction parameter E_n. The average island sizes and standard deviations of the island size distributions for these simulations are illustrated in Figure 5. A higher value of E_n results in a decrease in the confinement because the effect of the interaction between the adatom and substrate becomes smaller. The confinement also happens at higher temperatures when a larger value for parameter E_n is used. Also shown in Figure 5 are results of simulations using different strength of the patterns in the surface i.e. different values of adatom-substrate interaction energies E_{s1} and E_{s2}. Using a smaller E_{s1} and a larger E_{s2} makes the patterning of the surface stronger and increases the confinement. However, the curves for $< s >$ and σ_s remain unchanged at temperatures below 380 K. A similar effect of parameters E_{d1} and E_{d2} was found in the case of model B.

The parameters E_{s1}, E_{s2} and E_n have a different effect on the results. This suggests that it might be possible to extract these parameters from experimental data.

Figure 4: Average island size (on the left) and standard deviation of the island size distribution (on the right) for 15 % coverage at different temperatures for the homogeneous substrate (solid line) and for the models A (dotted line) and B (dashed line).
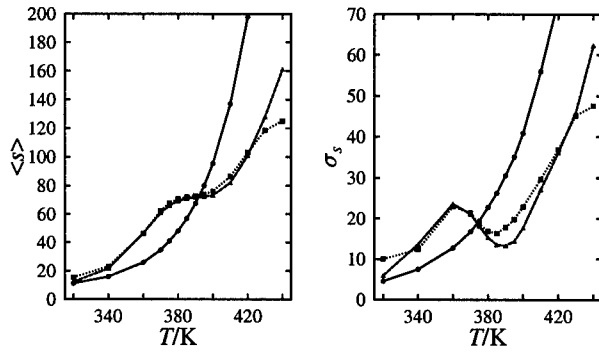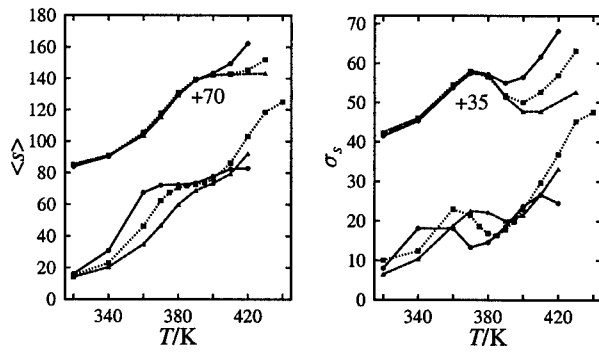

Figure 5: Average island size (on the left) and standard deviation of the island size distribution (on the right) for 15 % coverage at different temperatures for model A. The three lower curves correspond to simulations using parameter values $\{E_{s1}, E_{s2}, E_n\} = \{0.65, 0.85, 0.14\}$ eV (solid line), $\{0.65, 0.85, 0.18\}$ eV (dotted line) and $\{0.65, 0.85, 0.22\}$ eV (dashed line). The three upper curves are the results of simulations using parameter values $\{E_{s1}, E_{s2}, E_n\} = \{0.65, 0.85, 0.22\}$ eV (solid line), $\{0.60, 0.90, 0.22\}$ eV (dotted line) and $\{0.55, 0.95, 0.22\}$ eV (dashed line). Note that the upper curves are shifted vertically.

CONCLUSIONS

Periodic inhomogeneity in the activation energy of adatom diffusion can have a strong confining effect on adatom nucleation. The two models and parameter set studied in this work indicate that this confinement may happen in a narrow temperature range. The dependence of the results on model parameters suggests that information on their values could be extracted from experimental island size distributions; e.g. for the case of Ag-Pt system [5]. On the other hand, these parameter values could also be calculated by using realistic atomic level calculations.

ACKNOWLEDGMENTS

REFERENCES

1. D. Bimberg, M. Grundmann, and N. Ledentsov, *Quantum Dor Heterostructures* (John Wiley & Sons, Chichester, 1999).

2. I. Kegel, T. H. Metzger, and J. Peisl, Phys. Rev. B **60**, 2516 (1999).

3. J. Tersoff, C. Teichert, and M. G. Lagally, Phys. Rev. Lett. **76**, 1675 (1996).

4. H. Brune, Surface Science Reports **31**, 121 (1998).

5. H. Brune, M. Giovannini, K. Bromann, and K. Kern, Nature **394**, 451 (1998).

6. A. B. Bortz, M. H. Kalos, and J. L. Lebowitz, J. Comput. Phys. **17**, 10 (1975).

7. P. Šmilauer and D. Vvedensky, Phys. Rev. B **52**, 14263 (1995).

8. P. Šmilauer, M. Wilby, and D. Vvedensky, Phys. Rev. B **47**, 4119 (1993).

REALIZATION OF DETAILED KINETIC MODELS FOR THE GROWTH OF II-VI COMPOUNDS ADOPTING DFT CALCULATIONS AND EXPERIMENTAL EVIDENCES

Carlo Cavallotti, Valeria Bertani, Maurizio Masi, and Sergio Carrà
Dept. Chimica Fisica Applicata, Politecnico di Milano
Via Mancinelli, 7 20131 Milano Italy   carlo@chfi.polimi.it

ABSTRACT

The kinetics of deposition of CdTe, ZnS and ZnSe films was studied. An overall microkinetically reversible kinetic scheme consisting of elementary reactions, comprehensive of gas phase and surface processes was developed. Kinetic constants of gas phase reactions were either found in the literature or determined through quantum chemistry methods. Kinetic constants of surface reactions were first guessed combining kinetic theory with quantum chemical calculations and then their values were refined to reproduce experimental data. The kinetics schemes so developed were tested through the simulation of deposition reactors. Measured growth rates and gas phase compositions were thus compared with those calculated. The major finding of this studies is that the growth of CdTe, ZnS and ZnSe can be represented adopting a surface kinetic scheme constituted essentially by the same fundamental steps.

INTRODUCTION

The metal organic chemical vapor deposition (MOCVD) of II-VI semiconductors such as CdTe, ZnS, ZnSe and related compounds is a subject of research of great interest. The attention to this field is mainly due to the possibility of producing wide band gap semiconductors at growth rates significantly higher than those obtainable with molecular beam epitaxy (MBE). However still many technological problems forbid the industrial application of MOCVD deposited II-VI compounds. Among the major difficulties are the necessity to grow at low temperatures (<400°C), absence of pre-reactions between II and VI group alkyls, along with a reduced hydrogen incorporation and defect density in the film during the process [1]. A step toward the solution of these problems is the comprehension of the elementary gas phase and surface chemistry governing the film growth.

Following this way of thinking we adopted quantum chemistry calculations to study the reactivity of different gaseous and surface species of interest for the deposition of II-VI compounds. In particular we considered the deposition processes of CdTe, ZnS and ZnSe from $(CH_3)_2Cd$, $(CH_3)_2Te$, $(CH_3)_2Zn$, tBuSH, and $(tBu)_2Se$. The growth kinetics of three different II-VI compounds was considered since through the comparison of different processes at the same time a unified picture of the gas phase and surface chemical behavior of these compounds can be obtained. In particular the aim of the study was twofold. First we desired to increase our level of comprehension of the elementary chemical phenomena active during the growth of II-VI films. Then we wanted to produce a kinetic model that could be embedded in a fluid-dynamic simulation of a MOCVD reactor and adopted to optimize the growth process as a function of parameters such as substrate temperature, feed flow rate and chemical composition, reactor pressure.

QUANTUM CHEMISTRY CALCULATIONS

All calculations were performed using density functional theory methods, which have the advantage over other more precise quantum chemistry methods of scaling with the second-third power of the problem size, and the gaussian 98 suite of programs [2]. The Becke's three parameters exchange functional (B3) was adopted in all the calculations, while the Perdew Wang 91 (PW91) or the Lee Young Parr functional (LYP) of the correlation energy were adopted when considering Zn, S and Se or Cd and Te atoms, respectively. The choice of the best functional, as well as of the best basis set, to adopt to calculate the correlation energy was determined by systematic calculations performed with different DFT methods to simulate properties of compounds containing atoms belonging to the third or fourth row of the periodic table [3-5].

Different basis sets were adopted in the calculations, among which those giving best results were: the triple zeta basis set with added diffuse and polarization functions 6-311+G** for atoms belonging to the third row (i.e., Zn, and Se) and the split valence gaussian basis set 3-21G** for those belonging to the fourth row (i.e., Cd and Te). A composed basis set with an effective core potential (ECP2) for the core electrons and the double split basis set of Dunning and Huzinaga (D95) for the outer electrons (LANL2DZ) was adopted when only semi-quantitative information were required for ZnS compounds. No scaling factors were used for vibrational frequencies and, as a general rule, all frequency calculations were performed with the same basis set adopted to optimize the structures.

GAS PHASE KINETIC MODELS

The gas phase metal organic gas phase precursors considered in this study were $(CH_3)_2Cd$, $(CH_3)_2Te$, $(CH_3)_2Zn-N(C_2H_5)_3$, tBuSH, and $(tBu)_2Se$. All these species are supplied to the reactor diluted in a carrier gas which might be hydrogen or helium. The number and kind of active gas phase reactions is limited by the gas phase temperature (usually lower than 400 °C) that is too low to determine the homolitic cleavage of the bonds between the organic parts of the II-VI gas phase precursors and the metal atom. An exception to this general rule is the rupture of $(CH_3)_2Zn-N(C_2H_5)_3$ in $(CH_3)_2Zn$ and $N(C_2H_5)_3$. This reaction is pretty fast since it was experimentally found that $(CH_3)_2Zn-N(C_2H_5)_3$ is completely dissociated in the gas phase. We investigated through quantum chemistry the energy of the bond between $N(C_2H_5)_3$ and $(CH_3)_2Zn$ and found a value of about 5 kcal/mol which confirmed the fast dissociation pathway.
Another homolitic reaction that is likely to proceed fast in the gas phase is the beta elimination of C_4H_8 from $(tBu)_2Se$, which determines the formation of tBuSeH. The R-MeR bond energy for the compounds here considered is higher than 50 kcal/mol and therefore other homolitic reactions were not considered. Gas phase reactions can however be determined by reactions between radicals desorbing from the surface and gas phase molecules. The radicals that can be formed in the highest amount are H and CH_3 and therefore the reactions between these species and the metal organic precursors were estimated through quantum chemical methods and are reported in table 1. The kinetic constants of the gas phase reactions between CH_3Cd and $(CH_3)_2Te$, $(CH_3)_2Cd$ and $(CH_3)_2Te$, H_2S and $(CH_3)_2Zn$ are not active in the gas phase in the deposition systems here considered, but are of interest in order to understand the feasibility of some surface reactions and were therefore included in table 1. All kinetics constants reported in table 1 were calculated adopting transition state theory and localizing a transition state structure characterized by a single imaginary frequency. The kinetic constants of the reactions between H, tBu and CH_3 and hydrogen or other hydrocarbon species were found in the literature [6] and are reported in [5].

Table 1 Kinetic constants of gas phase reactions involving metal organic molecules calculated with quantum chemical methods ($k = A \cdot exp(-E_a/RT)$) units consistent with mol, cm^3, s)

	Reaction	$Log_{10}A$	E_a/R	Method
G1	$Cd(CH_3)_2 + H \rightarrow CdCH_3 + CH_4$	14.5	3150.	B3LYP/3-21G**
G2	$Te(CH_3)_2 + H \rightarrow TeCH_3 + CH_4$	13.8	3750.	B3LYP/3-21G**
G3	$Cd(CH_3)_2 + CH_3 \rightarrow Cd\ CH_3 + C_2H_6$	12.9	8450.	B3LYP/3-21G**
G4	$Te(CH_3)_2 + CH_3 \rightarrow TeCH_3 + C_2H_6$	11.1	7550.	B3LYP/3-21G**
G6	$Te(CH_3)_2 + Cd(CH_3)_2 \rightarrow CH_3TeCd\ CH_3 + C_2H_6$	10.1	28500.	B3LYP/3-21G**
G5	$Te(CH_3)_2 + Cd\ CH_3 \rightarrow CH_3TeCd + C_2H_6$	10.8	12550.	B3LYP/3-21G**
G7	$Zn(CH_3)_2 + H \rightarrow ZnCH_3 + CH_4$	13.0	18100.	B3LYP/6-311+G**
G8	$Zn(CH_3)_2 + CH_3 \rightarrow ZnCH_3 + C_2H_6$	12.8	14650.	B3LYP/6-311+G**
G9	$Zn(CH_3)_2 + H_2S \rightarrow CH_3ZnSH + CH_4$	9.5	8700.	B3LYP/6-311+G**
G10	$Zn(CH_3)_2-N(C_2H_5)_3 \rightarrow Zn(CH_3)_2 + N(C_2H_5)_3$	17.	2500.	B3LYP/6-311+G**

SURFACE KINETICS

The realization of a surface kinetic scheme for a chemical vapor deposition system can be pursued at different levels of complexity. The most simple approach considers the events occurring at the surface as lumped reactions of an overall process where gas phase and surface species react and determine the inclusion of one or more atoms of the impinging molecule in the growing film. In this case the reactions proposed are without physical meaning and their kinetic constants can be determined only by fitting growth rates on experimental data. Differently a physically and chemically detailed approach requires to consider all the reactive events occurring at the surface as elementary steps. A systematic method of realization of a kinetic scheme would therefore require to identify all the surface species that can be present during the growth and then to make them interact with gas phase species and among themselves. This approach requires a great amount of information on the composition and reactivity of the surface, which can be obtained either through surface science experiments or quantum chemistry calculations. The number of reaction pathways that may lead to the growth of the film is very large and physical intuition must be adopted in order to identify the key reaction steps that can determine the formation of the film and thus limit the dimension of the field of study. This is the approach we followed and the surface schemes we propose for the growth of ZnS and CdTe (reported in table 2 and 3) are the result of the consideration of many possible surface reactions. In table 2 and 3 we avoided reporting all the surface reactions we studied that were found to proceed too slowly (mainly because of too high activation energy barriers or too low frequency factors) to be active during the growth process.

Table 2. Proposed surface kinetic scheme for CdTe growth ($k = A \cdot T^\alpha \cdot exp(-E_a/RT)$ in mol, cm^2, s)

	Reaction	$Log_{10}A$	α	E_a/R	Notes
S1	$Cd(CH_3)_2 + \sigma \rightarrow [Cd(CH_3)_2]_{ads}$	9.6	0.5	0.	Coll. x 0.01
S2	$[Cd(CH_3)_2]_{ads} \rightarrow [CdCH_3]_{ads} + CH_3$	16.0	0.	16500.	est.
S3	$CH_3 + [CdCH_3]_{ads} \rightarrow [Cd(CH_3)_2]_{ads}$	9.1	0.5	0.	Coll.x0.001
S4	$[Cd(CH_3)_2]_{ads} \rightarrow Cd(CH_3)_2 + \sigma$	11.0	0.	5000.	est.
S5	$Te(CH_3)_2 + [CdCH_3]_{ads} \rightarrow [CdTeCH_3]_{ads} + C_2H_6$	18.0	0.	13500.	est.
S6	$[CdTeCH_3]_{ads} \rightarrow CdTe_{film} + CH_3 + \sigma$	12.0	0.	12500.	Fast
S7	$TeCH_3 + [CdCH_3]_{ads} \rightarrow CdTe_{film} +2\ CH_3 + \sigma$	18.0	0.	10000.	Fast
S8	$CdCH_3 + \sigma \rightarrow [CdCH_3]_{ads}$	11.6	0.5	0.	coll.

Table 3. Proposed surface kinetic scheme for ZnS growth ($k = A \cdot T^{\alpha} \cdot \exp(-E_a/RT)$ in mol, cm^2, s)

	Reaction	$Log_{10}A$	α	E_a/R	Notes
S9	$Zn(CH_3)_2 + \sigma \rightarrow [Zn(CH_3)_2]_{ads}$	11.5	0.5	0.	coll.
S10	$[Zn(CH_3)_2]_{ads} \rightarrow [ZnCH_3]_{ads} + CH_3$	13.0	0.	6000.	est.
S11	$[Zn(CH_3)_2]_{ads} \rightarrow Zn(CH_3)_2 + \sigma$	16.5	0.	14000.	est.
S12	$TbuSH + [ZnCH_3]_{ads} \rightarrow [ZnStBu]_{ads} + CH_4$	11.5	0.5	2500.	est.
S13	$[ZnStBu]_{ads} \rightarrow ZnS_{film} + tBu + \sigma$	17.3	0.	47000.	est.

A first result of this study is that the number of elementary reactions required to describe the film growth is very low. An intuitive representation of the reactive steps of table 2 is reported in fig. 1. The first step is assumed to be the adsorption of $Cd(CH_3)_2$ on two Te surface atoms. Successively the molecule might desorb or loose a methyl and give, in step 2, an adsorbed $CdCH_3$ molecule. In step 3 and 4 this surface species reacts with a $Te(CH_3)_2$ impinging molecule to yield $CdTeCH_3$ adsorbed over the surface and ethane. Finally adsorbed $CdTeCH_3$ reacts with a neighboring $CdTeCH_3$ species to desorb CH_3, give a CdTe species that enter the bulk of the film and give a Te surface site. The mechanism reported in table 3 for ZnS is very similar to that proposed for CdTe. In this case the molecule adsorbing on two S surface atoms is $Zn(CH_3)_2$, which successively loses a methyl, reacts with tBuSH to give CH_4 and adsorbed tBuSZn , which finally reacts with a similar surface species and gives a S surface atom. It is interesting to observe, and it can be considered as one of the main results of this study, that the growth kinetic of ZnS can be represented with a kinetic scheme that has the same fundamental steps of that proposed for CdTe.

The kinetic constants of the surface reactions were first determined adopting quantum chemical calculations of bond energies between adsorbed species (represented by an atomic cluster) and the surface and the kinetic theory. Successively they were finely tuned (*i.e.*, energies were changed by no more than 5 kcal/mol, which is assumed to be the calculation error) to reproduce experimental growth rate data .
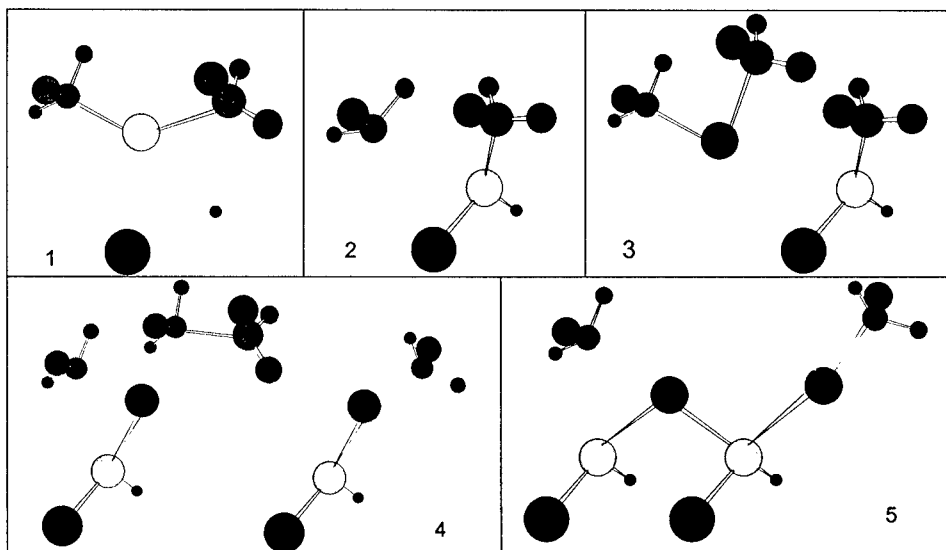

Fig. 1 Scheme of the elementary reactions that determine the growth of one layer of a CdTe film.

RESULTS AND DISCUSSION

The kinetic schemes developed above were adopted to simulate growth rates and gas phase compositions measured in experimental reactors. Indeed the development of kinetic schemes for surface process is strictly related with these simulations, since the capability to predict experimental data was adopted to test the feasibility of the surface kinetic schemes.

The reactors simulated were a tubular reactor adopted to grow CdTe films [7] and a horizontal Aixtron reactor for ZnS and ZnSe [8]. The fluid dynamic model adopted in the simulations is based on the boundary layer theory and is described in detail in [9]. Diffusion coefficients, viscosities and thermal conductivities were calculated from Lennard-Jones parameters, which were obtained from the normal boiling temperatures of the adopted precursors and from the Les Bas volume as explained in [10].

CdTe was deposited from $Cd(CH_3)_2$ and $Te(CH_3)_2$ diluted in a carrier gas, which could be either hydrogen or helium. A comparison between calculated and experimental growth rate for CdTe using hydrogen or helium as carrier gas is reported in fig. 2. The good agreement between the two sets of data can be ascribed to the fact that the deposition rate in a hydrogen carrier gas was adopted to fit the kinetic constant for reaction S5, assuming this as rate determining step of the deposition process. The value of the activation energy so determined (27 kcal/mol) is near that of the corresponding gas phase reaction (25 kcal/mol), while the pre-exponential factor is much higher than that calculated from collisional theory. This can be explained only assuming that the reaction proceed through a precursor state where $Te(CH_3)_2$ forms with $[CdCH_3]_{ads}$ an intermediate species which successively reacts to give the desorbing ethane molecule. Since $CdCH_3$ is a radical species, this seems to be a reasonable hypothesis. When helium replaces hydrogen as carrier gas it is observed that the growth rates decreases by a factor of three. This is fairly predicted by the model and is due to the decreased concentration of hydrogen atoms in the gas phase. Atomic hydrogen is produced in the reaction between methyl radicals coming from the surface and hydrogen molecules. H quickly reacts with $Cd(CH_3)_2$ and $Te(CH_3)_2$ according to reactions G1 and G2 to give the very reactive gas phase species $CdCH_3$ and $TeCH_3$, which adsorb on the surface according to reaction S7 and S8 and thus increase the film growth rate. The model is also able to predict the concentrations of methane and ethane measured in the gas phase at the exit of the reactor, as reported in fig. 3a.

Zns films were grown adopting $(CH_3)_2Zn-N(C_2H_5)_3$ and tBuSH as gas phase precursors, while $(tBu)_2Se$ was adopted to grow ZnSe films.
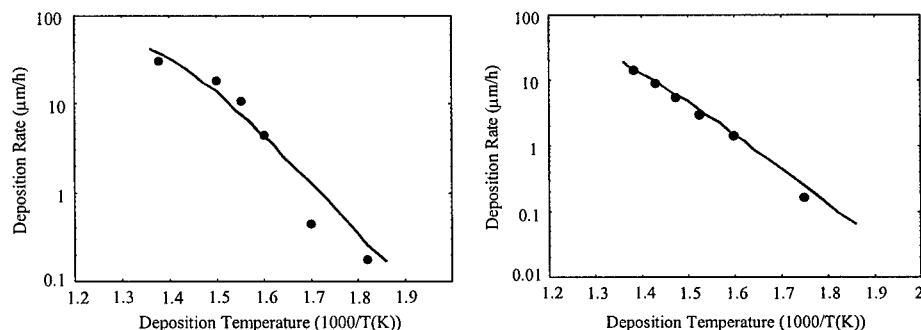

Fig. 2 Growth rate of CdTe reported in function of deposition temperature for H_2 (left) and He (right) carrier gas. Experimental (points) and calculated (lines) data.
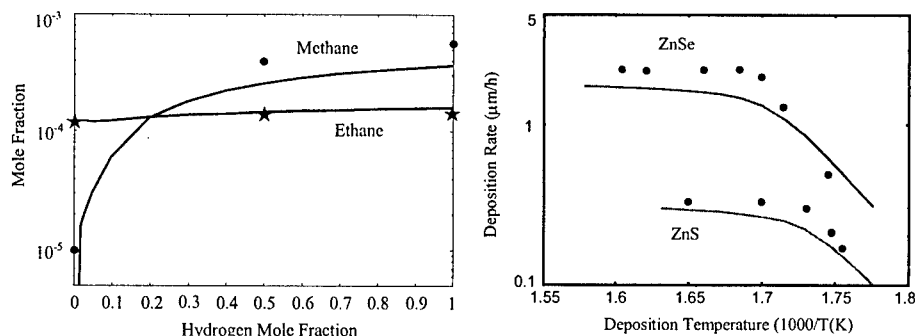
Fig. 3 Gas phase composition at the exit of a CdTe deposition reactor (left) and ZnS growth rate in function of the deposition temperature(right).

The comparison between experimental and calculated growth rates is reported in fig. 3. The measured activation energy of the growth process is very high (47 kcal/mol) and it is therefore likely that the growth rate is limited by a surface desorption reaction. Here we identified this reaction in the cleavage of the bond between tBu and S of reaction S13. The activation energy for this reaction could not be calculated directly through quantum chemistry because of the size of the surface cluster that should have been considered. It is however near the value that can be calculated subtracting from the energy required to break the tBu-S bond the energy of the Zn-S bond that get formed and adding the energy of the bond between Zn and the surface, which is broken when the ZnS bond is formed. A value of about 35 kcal/mol is thus obtained which is not too far from the measured 47 kcal/mol. The pre-exponential factor for the tBu desorption reaction fitted over experimental data is about 10^{18}, which value is consistent with the dissociation of a bond between a hydrocarbon radical of this size (with large rotational partition functions, even if rotation will be partially hindered) and the surface.

In conclusion we tried to give a unified picture of the growth kinetics for II-VI compounds. The kinetic models we propose constitute a way to link phenomena taking place at the atomic scale (elementary reactions) with those observable at the reactor scale (growth rates, gas phase composition)

REFERENCES

1. A.C. Jones and P. O'Brien , *CVD of compound semiconductors: precursors synthesis, development and application*, VCH, Weinheim, 1997.
2. Gaussian 98, M.J. Frisch et al. Gaussian, Inc., Pittsburgh PA, 1998.
3. L.A. Curtiss, K. Raghavachari, G.W. Trucks, and J. A. Pople, J.Chem.Phys. **94**, 7221 (1991).
4. C. Cavallotti, M. Masi, N. Lovergine, P. Prete, A.M. Mancini and S. Carrà, J. de Physique IV, **Pr8**, 33 (1999).
5. C. Cavallotti, V. Bertani, M. Masi and S. Carrà, J. Electrochem. Soc. **146**, 3277 (1999).
6. W.Tsang and R.F. Hampson, J. Phys. Chem. Ref. Data, **15**, 887 (1987).
7. A.H. McDaniel, B. Liu, and R.F. Hicks, J. Crystal Growth, **124**, 676 (1992).
8. N. Lovergine, P. Prete, G. Leo, L. Calcagnile, R. Cingolani, A.M. Mancini, F. Romanato and A.V. Drigo, Crys. Res. Technol. **33**, 183 (1998).
9. M. Masi, C. Cavallotti, G. Radelli and S. Carrà, Crys. Res. Technol. **32**, 1125 (1997).
10. C.Reid, J.M. Prausnitz, and B. E. Poling, *The Properties of Gases and Liquids*, McGraw-Hill, New York (1987).

Effect of Hydrogen Coverage on Silicon Thin Film Growth: Molecular Dynamics Investigation

SHINYA MURAMATSU , MASATOSHI SHIMADA and MASAHIKO HIRAO
Department of Chemical System Engineering, The University of Tokyo, Tokyo 113-8656, Japan

ABSTRACT

Silicon thin films grown by CVD processes take various structures depending on the reaction conditions. In the case of low-temperature CVD, hydrogen coverage on the silicon substrate affects the growth as well. In order to analyze the effect of hydrogen coverage on elementary surface reactions, we performed molecular dynamics simulations in which gas-phase radicals, H and SiH_3, fell onto a hydrogen-terminated silicon surface. We prepared monohydride and dihydride Si(100) surfaces and modified their hydrogen coverage in a certain area in the range from 0.5 to 2.0 monolayers so as to describe the growing surface. As a result of our simulation, H radicals mainly caused H adsorption and H abstraction reactions and altered the hydrogen coverage of the surface. While reactions of SiH_3 radicals with monohydride or dihydride surfaces rarely occurred, these radicals reacted more frequently with the modified surfaces. These results indicate that the change in the local hydrogen coverage caused by H radicals may induce subsequent surface reactions.

INTRODUCTION

When silicon thin films are grown by chemical vapor deposition (CVD) processes, many reaction conditions influence the growth. Among those conditions, the hydrogen coverage on the silicon substrate has a great influence. In general, surface hydrogen is considered to inhibit silicon crystal growth [1]; thus, the creation of dangling bonds through H abstraction is said to be the rate-limiting step in film growth [2]. On the other hand, it is also reported that sufficient hydrogen coverage of a silicon surface helps the surface diffusion of silicon hydride species and results in microcrystal growth [3].

Furthermore, other reaction conditions such as substrate temperature and source gas composition have an effect on hydrogen coverage. For example, when a hydrogen-terminated silicon substrate is heated, hydrogen molecules desorb from the surface and several kinds of periodic surface structures are constructed according to the temperature. The coverage is also changed by various surface reactions. It has been predicted that SiH_3 radicals play the role of H abstraction, and recently, the energetics and dynamics of the abstraction were analyzed by molecular dynamics (MD) simulations [4]. Hydrogen radicals induce both H abstraction [5] and H adsorption reactions [6]. Nevertheless, it is said that equilibrium hydrogen coverage increases when a silicon substrate is sufficiently exposed to atomic hydrogen. As described in these examples, hydrogen coverage is closely related to various conditions, thus it is difficult to understand its direct effect.

In this paper, we report on the results of MD simulations in which gas-phase radicals fell onto a hydrogen-terminated Si(100) surface, and discuss the effect of hydrogen coverage on elementary surface reactions.
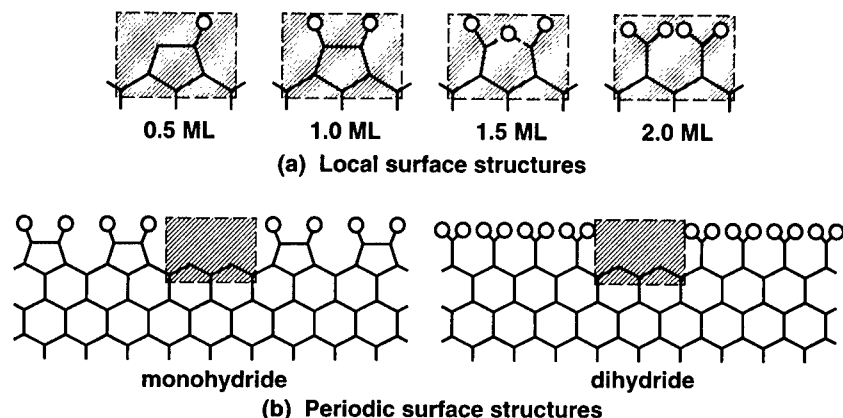
Figure 1: Local and periodic structures of a hydrogen-covered Si(100) surface. Local structures correspond to 0.5–2.0 ML hydrogen coverage.

CALCULATION METHOD

We performed a MD simulation in which one gas-phase radical fell onto a hydrogen-terminated Si(100) surface. By repeating such a simulation against several substrates which differ in their hydrogen coverage, the effect of hydrogen coverage was investigated. It is considered that hydrogen coverage of a silicon surface changes continuously during silicon thin film growth owing to surface reactions with radicals. In order to model such a growing surface, the hydrogen coverage of a local structure was separated from that of a periodic structure, as shown in Fig.1. Namely, the substrate used in this simulation has a periodic surface structure, while it has a different local surface structure only where radicals fall. The four local structures shown in Fig.1(a) were selected. Those structures are stable and representative ones for 0.5–2.0 monolayers (ML) of hydrogen coverage. As the uniformly hydrogenated silicon surface, the monohydride and dihydride surfaces shown in Fig.1(b) were prepared. An initial structure was constructed by combining these local and periodic structures. The unit cell consisted of 20 layers of 100 Si atoms and additional surface H atoms to satisfy its hydrogen coverage. Two-dimensional periodic boundary conditions were applied so as to model a surface.

As gas-phase radicals, H and SiH_3 were selected since many H radicals are produced when the source gas is diluted with hydrogen, and SiH_3 is the main species when plasma-enhanced CVD is used for silicon thin film growth [2]. Those radicals were first placed above the local surface structure and then fell onto the substrate with kinetic energies according to the velocity distribution at 300 K.

Simulations were performed applying the condition of constant energy so that the transfer of heat produced by surface reactions is correctly simulated. Twelve simulations were performed using the substrate with the same hydrogen coverage at the same temperature. To deal with a system of Si and H atoms, an extended form of the Tersoff potential [7] was used.
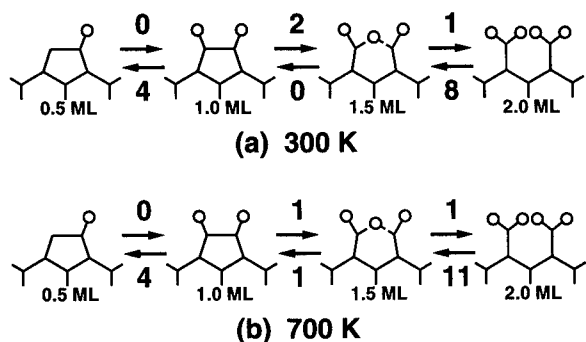
Figure 2: Transition of hydrogen coverage caused by H radicals. The right-directed arrows and left-directed arrows designate H adsorption and H abstraction reactions, respectively. The numbers beside the arrows indicate the frequency of that reaction over twelve simulations.

Density functional (DFT) calculations were carried out in order to verify the results of MD simulations. In the calculation, the local surface structures which had been used in MD simulations were optimized. By comparing the resulting minimum energies, energy changes accompanying surface reactions were investigated. We used a slab model which consisted of eight layers of two Si atoms. The top layer of Si atoms was hydrogen-terminated so as to satisfy the 0.5–2.0 ML hydrogen coverage, and all the dangling bonds at the bottom were terminated with H atoms. During the optimization, the four bottom layers of Si atoms and the bottom H atoms were fixed in space. Wave functions were expanded in a numerical orbital basis of atom-localized functions: double-numerical basis functions for Si and H atoms, and additional polarization functions for Si atoms. The Perdew Wang form of the local exchange-correlation potential [8] was used.

RESULTS AND DISCUSSION

As a result of MD simulation, H radicals mainly caused H adsorption and H abstraction reactions, and altered hydrogen coverage. Figure 2 shows the transition of hydrogen coverage caused by H radicals. The right arrows and left arrows designate adsorption and abstraction reactions, respectively. The numbers beside the arrows indicate the frequency of that reaction over twelve simulations. Although there were cases which resulted in the formation of other surface structures, such cases are not counted here. Focusing on the direction of reactions, reactions which generate the 0.5 ML or 1.5 ML structures occurred more frequently than their opposite reactions. Thus it is expected that H radicals have the effect to increase the number of 0.5 ML and 1.5 ML structures.

On the other hand, SiH$_3$ radicals caused many kinds of reactions such as adsorption, H abstraction and self-decomposition. Among them, adsorption reactions occurred most frequently; therefore, the results were summarized in terms of how the adsorption probability varied according to hydrogen coverage and substrate temperature. Table I shows

Table I: The effect of hydrogen coverage and substrate temperature on SiH$_3$ adsorption probability. The numbers indicate the frequency of adsorption reaction over twelve simulations.

substrate temperature	monohydride			dihydride			
	0.5 ML	1.0 ML	1.5 ML	0.5 ML	1.0 ML	1.5 ML	2.0 ML
300K	5	0	3	5	1	5	0
700K	4	2	2	6	0	6	0

Table II: Energy changes accompanying reactions with H radicals, obtained by DFT calculation. The energy unit is kJ/mol.

Reaction	Hydrogen coverage of substrate			
	0.5 ML	1.0 ML	1.5 ML	2.0 ML
H adsorption	+252.4	+151.4	+315.0	
H abstraction	+213.5	+314.5	+150.9	

the effect of hydrogen coverage and substrate temperature on SiH$_3$ adsorption probability. This table indicates the frequency of the adsorption reaction over twelve simulations. Judging from the results in Table I, no direct effect of temperature was observed since the results were similar whether the temperature was 300 K or 700 K. Instead, the effect of local hydrogen coverage was clearly observed; while SiH$_3$ radicals rarely reacted with the 1.0 ML or 2.0 ML local surface structure, they reacted more frequently with the 0.5 ML or 1.5 ML local surface structure. Since it is considered that those 0.5 ML and 1.5 ML structures are mainly generated by reactions with H radicals, we can say that easier adsorption of SiH$_3$ is realized if H radicals have altered the local hydrogen coverage.

Table II shows the energy changes accompanying reactions with H radicals obtained by DFT calculation. The values are the energy differences before and after the reaction. For example, the values on the extreme right row are calculated as follows:

$$E_{\text{adsorption}} = (V_{1.5\text{ML}} + V_{\text{H}}) - V_{2.0\text{ML}}$$

$$E_{\text{abstraction}} = (V_{2.0\text{ML}} + V_{\text{H}}) - (V_{1.5\text{ML}} + V_{\text{H}_2}).$$

These values indicate that all the reactions are exothermic and the system is stabilized by these reactions. Moreover, it is indicated that such reactions occur more frequently than their reverse reactions. Thus if the 1.5 ML structure is generated by H radicals, it will not spontaneously revert to the original structure without the help of other radicals or its surroundings. However, the heat of reaction accompanying the production of the 1.5 ML structure is higher than others; thus, it seems that the 1.5 ML structure is a metastable structure.

In this simulation, a local surface structure corresponding to 1.5 ML hydrogen coverage was introduced, which was frequently observed after surface reactions. Although a few periodic structures are known to be stable structures of a hydrogenated silicon surface, they correspond to hydrogen coverages of 1.0 ML, 1.33 ML and 2.0 ML; the existence of the 1.5 ML structure has not been reported. Then the question arises as to whether a stable 1.5 ML structure exists. When we discuss this question, we should not overlook the following two points. First, the 1.5 ML structure is not a periodic structure but a local structure. As described above, the 1.5 ML structure is a metastable structure; two neighboring 1.5 ML structures are less stable than two neighboring 1.0 ML and 2.0 ML structures, according to our quantum mechanical calculation. Second, it must be noted that the 1.5 ML structure is not a static structure but a dynamic one. Although only one kind of 1.5 ML structure is shown in Fig.1, there are other 1.5 ML structures as stable as that shown in Fig.1. and transition between those structures occurred continuously during the MD simulation. For these reasons, we believe that an isolated 1.5 ML structure can exist, and that it is an instantaneous structure which continuously changes its shape.

As mentioned above, the 1.5 ML structure may play an important role in the growth. We think that the 1.5 ML structure will be produced more efficiently by H abstraction caused by gas-phase radicals than by thermal desorption of surface H atoms. Microscopically, thermal desorption requires two neighboring surface H atoms. In other words, even if the 1.5 ML structure is produced by thermal desorption, it will be accompanied by the production of another 1.5 ML structure in its neighborhood. Thus it is difficult to consider that the 1.5 ML structure produced by thermal desorption can exist for a long time because two neighboring 1.5 ML structures are not stable. On the other hand, gas-phase radicals such as H and SiH_3 abstract one surface H atom and produce an isolated 1.5 ML structure. This isolated 1.5 ML structure will not be broken until another 1.5 ML structure appears via surface diffusion of H atoms or a surface reaction.

Based on the result of the simulation, hydrogen coverage seems to decrease rather than increase upon reactions with H radicals. This is somewhat different from other experimental results in which equilibrium hydrogen coverage increases when the silicon substrate is exposed to H radicals. This difference is due to the limitation of the scope of our simulation to the initial stage of film growth. Although model substrates whose local hydrogen coverage was modified were introduced, they do not sufficiently represent the growing surface because they have completely flat surfaces. Therefore, we cannot conclude equilibrium hydrogen coverage from these results. However, whichever direction hydrogen coverage may go toward an equilibrium state, it is considered that both adsorption and abstraction reactions are induced by H radicals, microscopically.

It is said that when a silicon substrate surface is sufficiently covered with hydrogen, silicon hydride species diffuse on the surface until they reach an active site. In our simulation, however, many SiH_3 radicals were repelled at the surface and return to gas phase, and surface diffusion of those radicals was rarely observed. This tendency was considerable, particularly in the case of high hydrogen coverage. One explanation for this result may be that the cutoff radius of the potential function used in our simulations is too short. Certainly, the Tersoff potential, the original form of this potential, has been applied to the system of a silicon crystal and a silicon surface, and has successfully reproduced their properties. Also, the potential used in this simulation was made with the expectation of such an ability. However, if the potential is applied to such a hydrogen-terminated surface, silicon hydride species will easily move outside the cutoff radius and fly away when

only small repulsive force acts on it from surface H atoms. For this reason, it might be reasonable to expect that some of the radicals repelled in the simulation should diffuse on the surface originally. Further investigation should be done, however, to judge whether or not the cutoff radius is sufficient for simulating such surface phenomena.

CONCLUSIONS

In summary, the effect of hydrogen coverage on elementary surface reactions has been examined by MD simulations in which gas-phase radicals fell onto a hydrogen-terminated Si(100) surface. It has been shown that H radicals alter the hydrogen coverage of the silicon surface and generate local surface structures which correspond to 0.5 ML or 1.5 ML hydrogen coverage. While the adsorption probability of SiH$_3$ radicals changes according to hydrogen coverage, the probability is high for the 0.5 ML or 1.5 ML structures. The results of DFT calculation also suggested the generation of those local surface structures. These results indicate that the change in the local hydrogen coverage caused by H radicals may induce subsequent surface reactions.

ACKNOWLEDGMENTS

REFERENCES

1. M. Copel and M. Tromp, Phys. Rev. Lett. **72**, 1236 (1994).

2. J. R. Abelson, Appl. Phys. **A 56**, 493 (1993).

3. A. Matsuda and T. Goto, Mater. Res. Soc. Symp. Proc. **164**, 3 (1989).

4. S. Ramalingam, D. Maroudas, E. S. Aydil, and S. P. Walch, Surf. Sci. **418**, L8 (1998).

5. E. Srinivasan, H. Yang, and G. N. Parsons, J. Chem. Phys. **105**, 5467 (1998).

6. J. J. Boland, Surf. Sci. **261**, 17 (1992).

7. M. V. R. Murty and H. A. Atwater, Phys. Rev. **B 51**, 4889 (1995).

8. J. P. Perdew and Y. Wang, Phys. Rev. **B 45**, 13244 (1992).

A KINETIC MONTE CARLO MODEL OF SILICON CVD GROWTH FROM A MIXED H$_2$/SiH$_4$ GAS SOURCE

M. FEARN, M. SAYED, J.H. JEFFERSON AND D.J. ROBBINS
Electronics Sector, DERA, St. Andrews Road, Great Malvern, Worcs. WR14 3PS. UK.

ABSTRACT

We report the development of an atomistic scale Kinetic Monte Carlo model of silicon CVD growth. By employing a variable time step algorithm, simulations have been performed over a range of time scales, enabling direct comparison with experimental data. The validity of using the kinetic theory of gases for evaluating steady state incoming particle fluxes within the model is demonstrated by comparison with computational fluid dynamics simulations. The model is applied to study hydrogen desorption rates from Si(001) and the dependence of silicon growth rate on substrate temperature, with results found to be in good agreement with experimental data. An experimentally observed decrease of growth rate with increasing H$_2$ partial pressure is also reproduced by the model and shown to be caused by a decrease in silane adsorption on a hydrogen-rich surface.

INTRODUCTION

Chemical vapour deposition (CVD) is a widely used technique for producing thin film layers for device applications. In ultra-high vacuum and low pressure CVD reactors the growth process is dominated by a complex heterogeneous gas/surface chemistry involving adsorption, decomposition and surface diffusion of molecular species. In this paper we discuss the development of an atomistic scale Kinetic Monte Carlo (KMC) simulation model which is suitable for modelling CVD growth of (001) silicon from a mixed H$_2$/SiH$_4$ precursor gas source and which may be used to gain insight into the complex CVD process. By employing an efficient variable time step algorithm, the model can simulate growth over macroscopic time scales enabling direct comparison with experimental data.

We begin by describing the algorithm employed by the model, paying particular attention to the handling of incident fluxes and adsorption events. In the results section the model is initially applied to study hydrogen desorption rates in both the low and high hydrogen coverage regimes. These calculations are used to derive a simplified description of surface diffusion which is then employed in applications of the model to the growth of silicon. The dependence of silicon growth rate on both substrate temperature and hydrogen partial pressure is investigated. In each application of the model, comparisons to existing experimental data are made.

METHOD

The KMC model is based on the work of Battaile *et al* [1, 2] who developed the method and applied it with considerable success to the CVD growth of diamond films. The model is lattice based and fully 3-dimensional. At each Monte Carlo step a reaction table is set up based on the configuration of the surface at that time. The table stores the rate and surface location of each possible reaction. The reactions considered are shown in Table 1 which, for silane, follows the scheme proposed by Gates [3] except for the de-hydrogenation of SiH$_2$, which is modelled in a single step. The rate of each reaction is calculated using an Arrhenius form, $R = k \times exp(-E/k_B T)$ where E is an activation energy. We also take account of dimerisation and the switching of dimer orientation between layers when setting up the table.

The total rate of adsorption per unit area for each precursor species, corresponding to the first two reactions in Table 1, is given by $R_{ads} = S_i F_i$ where S_i is a surface

Reaction	k (s^{-1})	E_a(eV)
$SiH_4(g) + 2\_ \rightarrow \underline{SiH_3} + \underline{H}$	-	-
$H_2(g) + 2\_ \rightarrow 2\underline{H}$	-	-
$\underline{SiH_3} + \_ \rightarrow \underline{SiH_2} + \underline{H}$	1.0×10^{13}	1.00
$2\underline{SiH_2} \rightarrow 2\underline{Si} + 2H_2(g)$	1.0×10^{13}	1.40
$2\underline{H} \rightarrow H_2(g)$	5.5×10^{15}	2.51

Table 1: Reactions and their rate coefficients for silicon (001) growth[5][6], _ represents a silicon dangling bond site and (g) a gas species. The evaluation of the adsorption reaction rates is discussed in the text.

configuration dependent sticking coefficient for species i and F_i is the incident particle flux. The sticking coefficient depends on the density of clean silicon dimers, N_{db}, through,

$$S_{R,i} = N_{db} \ k_i \ exp(-\frac{E_i}{k_B T_w});$$ (1)

where T_w is the substrate (wafer) temperature. The activation energies for H_2 and SiH_4 adsorption are taken to be 17.3 and 3 kcal/mole respectively [4, 7]. The pre-exponential factor k_i is fitted to yield sticking coefficients on a clean surface at 673K of 2×10^{-6} for molecular hydrogen and 2.5×10^{-4} for silane [4].

Incident fluxes to the surface for each gas species, F_i, are evaluated using the kinetic theory of gases expression [8],

$$F_i = \frac{P_i}{\sqrt{2\pi m_i k_B T_w}}$$ (2)

where P_i and m_i are the partial pressure and molecular mass of species i respectively. The validity of this expression is demonstrated in Table 2 where the kinetic theory fluxes are compared to those derived from computational fluid dynamics simulations of a custom low pressure reactor. Details of the CFD calculations, which are particularly valuable for studying transient effects during complex growth procedures, will be reported in a later publication [9].

Wafer Temp. (K)	SiH_4 Flux	H_2 Flux
723.0	0.375 (0.381)	1.073 (1.070)
823.0	0.345 (0.350)	0.988 (0.983)
1123.0	0.311 (0.316)	0.905 (0.903)

Table 2: Comparison of incident silane and hydrogen fluxes (in units of 10^{19} molecules/cm^2/s) evaluated using the kinetic theory of gases (Equation 2) and from computational fluid dynamics (CFD) calculations. The CFD results are given in brackets. In both calculations the flow rates into the reactor were 376 sccm H_2 and 52.5 sccm SiH_4.

A single reaction is chosen randomly at each time step from the constructed table but weighted according to the rate of each reaction. The time clock of the simulation is then incremented, following the N-fold Way Monte Carlo approach [10], by an amount $\delta t = ln(r)/W$ where r is a random number between 0 and 1 chosen from a uniform distribution and W is the sum of reaction rates stored in the reaction table at that step. Thus, the time step in the model is variable, increasing when only slow reactions are

occuring and decreasing when fast processes are possible. Having chosen a reaction to occur, the system is updated accordingly, a new reaction table is constructed, and the process repeated.

RESULTS

The model was initially used to study the kinetics of hydrogen desorption from Si(001). To enable this, hydrogen surface diffusion along the dimer rows was added to the reaction database. Two regimes of high and low initial hydrogen coverages were modelled at a range of substrate temperatures. It was found necessary, particularly in the intermediate to low coverage regime, to promote hydrogen pairing on the surface in order to get good agreement with experimental data [5, 11]. This supports the interpretation provided in [11] of the preference towards pairwise hydrogen occupation of silicon dimers. The resulting time dependence of the hydrogen coverage is shown in Figure 1.
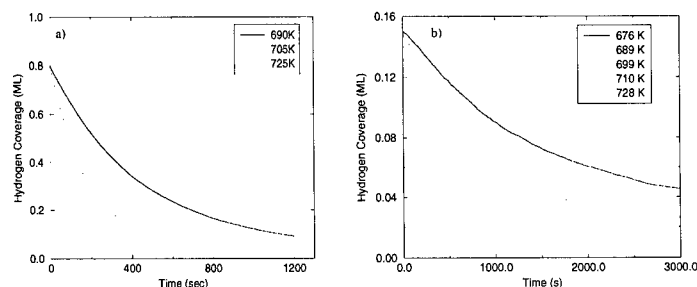
Figure 1: Modelled time dependence of hydrogen coverage for various substrate temperatures in the high (panel a) and low (panel b) initial coverage regimes.

During the growth of silicon (001), adatom surface diffusion occurs at a considerably faster rate than adsorption, desorption and decomposition type reactions [4]. This unfortunately leads to a high computational workload within a rigorous KMC model with surface diffusion included explicitly since a large proportion of the CPU effort is spent performing surface diffusion events and not growing the film. To overcome this problem we have employed a simplified description of surface diffusion in applications of the model to film growth. From the hydrogen desorption calculations described above we evaluated the fraction of hydrogen in a paired state as a function of hydrogen coverage. This was found to be relatively insensitive to temperature. The simplified KMC model employs a polynomial fit to this data and, for a given hydrogen coverage, mimics the diffusion process by randomly rearranging the correct fraction of paired hydrogens on the surface.

Using this approximate surface diffusion model, we have performed simulations of silicon growth for a range of substrate temperatures. Flow rates of 376 sccm H_2 and 52.5 sccm SiH_4 were considered. The calculated growth rates and associated hydrogen coverage are shown in Figure 2. Good overall agreement with measured data [4] is found.

Finally, the model has been applied to investigate the dependence of growth rate on H_2 partial pressure. Experimental data [12] displays a decrease in growth rate with increasing H_2 pressure. The KMC model, as shown in Figure 3, reproduces this trend well. Snapshots from the simulation corresponding to the extremes of hydrogen pressure considered are also shown and demonstrate an increased hydrogen coverage at the high hydrogen pressure. The decrease in observed growth rate follows from the reduced silane sticking coefficient on this hydrogen-rich surface, due to the reduced density of clean

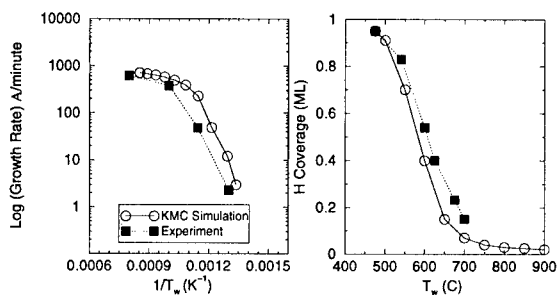silicon dimers, N_{db} (Eq.1). This process may be described as "hydrogen blocking".

Figure 2: Calculated (open circles) growth rate and associated hydrogen coverage as a function of substrate temperature. Flow rates of 376 sccm H_2 and 52.5 sccm SiH_4 were considered. The experimental data was taken from Figures 1 and 2 of Ref. 4.
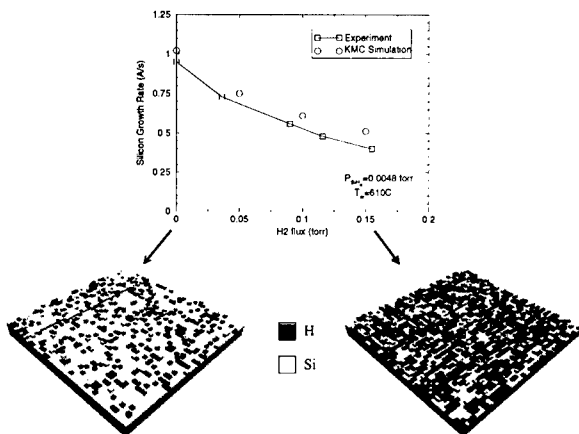

Figure 3: Calculated and experimental data of growth rate dependence on H_2 partial pressure. The silane partial pressure was held fixed at 0.0048 torr. Snapshots from the simulations corresponding to the extremes of H_2 partial pressures considered are also shown.

CONCLUSIONS

We have described the development of an atomistic scale Kinetic Monte Carlo model of silicon CVD growth from a mixed H_2/SiH_4 gas source. The kinetic theory of gases was shown to be a good approximation in deriving incident steady-state particle fluxes for the model. The model has been applied to study the kinetics of hydrogen desorption and the variation of silicon growth rate with wafer temperature and hydrogen partial pressure. Good agreement with experimental data was found in each case. Following this success the model is presently being extended to include the germane precursor gas species to enable the simulation of CVD growth of the SiGe alloy. Further refinements could include a more accurate representation of the surface after diffusion by incorporating, in the statistical model, correlations between the positions of hydrogen dimers and other species on the surface.

ACKNOWLEDGMENTS

REFERENCES

1. C.C. Battaile, D.J. Srolovitz and J.E. Butler, J. Appl. Phys. **82**, 6293 (1997).

2. C.C. Battaile, D.J. Srolovitz and J.E. Butler, Diamond and Related Materials **6**, 1198 (1997).

3. S.M. Gates, C.M. Greenlief and D.B. Beach, J. Chem. Phys. **93**, 7493 (1990).

4. S.M. Gates and S.K. Kulkami, Appl. Phys. Lett. **58**, 2963 (1991).

5. M.L. Wise, B.G. Koechler, P. Gupta, P.A. Coon and S.M. George, Surface Science **258**, 166 (1991).

6. D.R. Bowler, "A theroetical investigation of gas source growth of the Si(001) surface", Ph.D. thesis, Oxford University, 1997.

7. P. Bratu, W. Brenig, A. Grob, M. Hartmann, U. Höfer, P. Kratzer and R. Russ, Phys. Rev. B **54**, 5978 (1996).

8. P.M. Garone, J.C. Sturm, P.V. Schwartz, S.A. Schwarz and B.J. Wilkens, Appl. Phys. Lett. **56**, 1275 (1990).

9. M. Sayed, M. Fearn, S. Taylor and D.J. Robbins (in preparation).

10. A.B. Bortz, M.H. Kalos and J.L. Ledowitz, J. Phys. Chem. **17**, 10 (1975).

11. U. Höfer, Leping Li and T.F. Heinz, Phys. Rev. B **45**, 9485 (1992).

12. D.J. Robbins, (unpublished data).

MOLECULAR DYNAMICS SIMULATIONS OF SOLID PHASE EPITAXY OF SI: GROWTH MECHANISM AND DEFECT FORMATION

T. MOTOOKA[*], S. MUNETOH[**], K. NISIHIRA[*], K. MORIGUCHI[**], A. SHINTANI[**]
[*]Department of Materials Science and Engineering, Kyushu University, Hakozaki,
Fukuoka 812, Japan, motooka@zaiko.kyushu-u.ac.jp
[**]Electronics Engineering Laboratories, Sumitomo Metal Industries, Ltd., Hyougo 660,
Japan

ABSTRACT

We have investigated crystal growth and defect formation processes during solid phase epitaxy (SPE) of Si in the [001] direction based on molecular dynamics (MD) simulations using the Tersoff potential. From the Arrhenius plot of the growth rates obtained by MD simulations, we have found that the activation energy of SPE at lower temperatures is in good agreement with the experimental value, approximately 2.7 eV, while it becomes lower at higher temperatures. This can be attributed to the difference in the amorphous/crystalline (a/c) interface structure. In the low temperature region, the a/c interface is essentially (001) and the rate-limiting step is two-dimensional nucleation on the (001) a/c interface. On the other hand, the a/c interface becomes rough due to {111} facets formation in the high temperature region and the rate-limiting step is presumably a diffusion process of Si to be trapped at the kink sites associated with these facets. Defect formation is found to be initiated by 5-membered rings created at the a/c interface. These mismatched configurations at the interface give rise to {111} stacking faults during further SPE growth.

INTRODUCTION

Solid phase epitaxy (SPE) of Si is one of the basic processes in Si microelectronics fabrication technologies. Various experimental works were carried out to determine the growth rate of thermal SPE by using furnace and laser annealing, and the activation energy was found to be ≈2.7 eV.[1] Recently, extensive investigations have been performed on ion-beam-induced epitaxial crystallization (IBIEC) where ion-beam-induced defects play an important role for crystallization, and the activation energy is found to be varied from 0.18 to 0.40 eV depending on ion mass and temperature.[2] Based on these results, it is generally believed that crystallization occurs at amorphous/crystal (a/c) Si interfaces in both thermal SPE and IBIEC processes. However, the atomistic mechanism of crystallization at the a/c interface is not well understood.

In this paper, we have investigated crystal growth and defect formation processes in SPE based on molecular dynamics (MD) simulations by employing the Tersoff interatomic potential of Si.[3] Although the Tersoff potential gives rise to high melting temperature 2547 K,[4] it can well reproduce the structural properties of a-Si[5] and liquid Si[6], and thus it is considered to be useful to describe crystallization as well as defect formation processes during SPE of Si.

METHOD

MD simulations have been performed using a MD cell including an a/c interface. The typical MD cell size is 21.7x21.7x43.4Å^3 (tetragonal prism) and the number of Si atoms, 1024 was determined by using the crystalline Si density, 2.33 g/cm^3. Atomic movements were determined by solving Langevin equations

$$m\ddot{r}_i(t) = F_i(t) - m\gamma\dot{r}_i(t) + R_i(t), \qquad (1)$$

where m is the atomic mass, $r_i(t)$ the position vector of the i-th atom at time t, $F_i(t)$ the interatomic force calculated by the Tersoff potential, and γ and $R_i(t)$ are the friction constant and random force to control temperature, respectively. We employed the scheme developed by Gusteren and Berendsen for numerical integrations of the Langevin equation.[7] The time step for the integration was set at 0.001 ps and the friction constant γ was chosen to be 5 (ps)$^{-1}$.

The initial a/c interface was prepared by attaching 8 c-Si(001) layers to a block of bulk a-Si obtained by rapid quenching of liquid Si.[5] The MD cell was pre-annealed at 1000K for 20ps and then heated at various temperatures between 1450 and 2000K for crystallization at the a/c interface. In order to examine atomic motions during SPE growth, atomic coordinates contained in the central region including the diagonal (110) plane of the tetragonal cell with a thickness of 10Å were projected on the (110) plane. In order to investigate defect formation processes during SPE, we have utilized a larger MD cell with a size of 65.1x65.1x43.4Å^3 made by combining the nine small MD cells described above.

RESULTS AND DISCUSSIONS

Growth Mechanism

Figures 1(a) shows an example of the typical SPE processes obtained by MD simulations at 2000K. These simulations indicated that the a/c interface was rough for the temperatures larger than 1600K, while it was rather flat for the temperatures less than 1550K. Figure 1(b) shows a magnified view of the part enclosed by the squares in Fig. 1(a). From Fig. 1(b), it is suggested that a stable {111} facet is formed at the a/c interface as
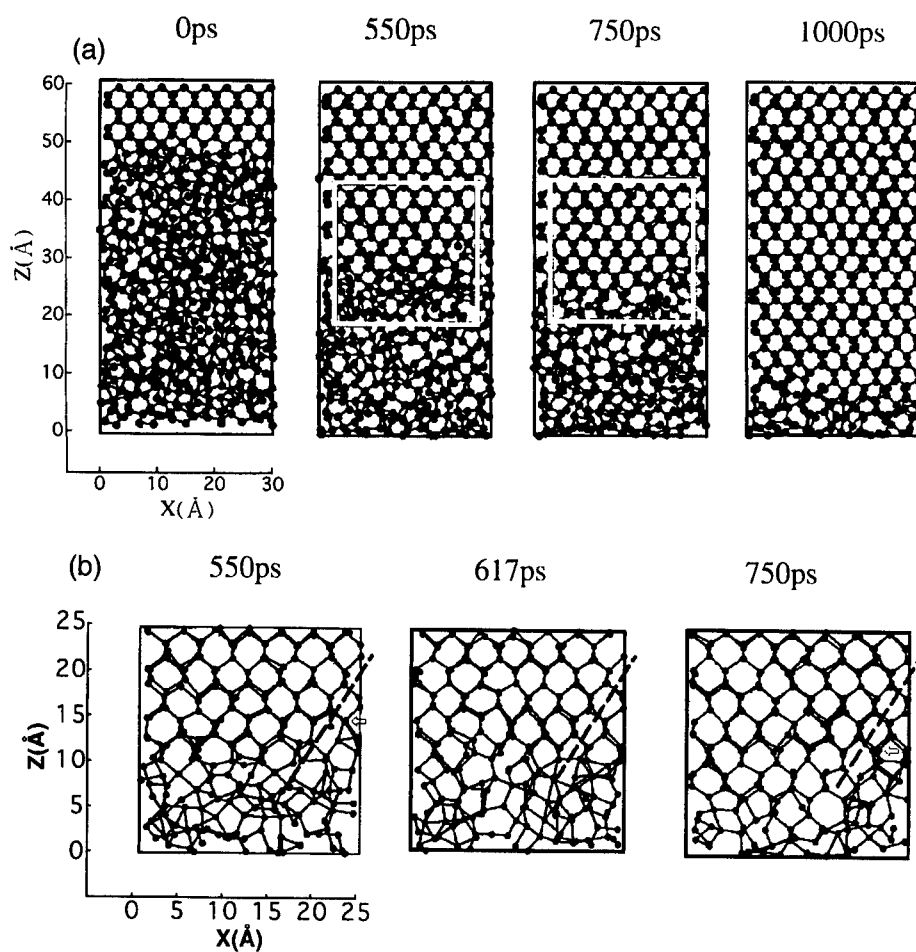
Fig. 1 Typical MD simulation results of SPE growth at 2000K for 1000 ps (a) and a magnified view of the part enclosed by the squares (b).
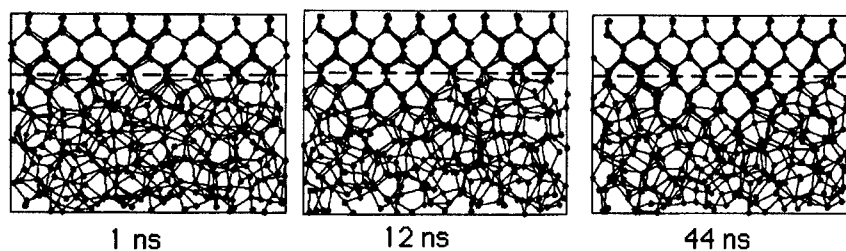

Fig. 2 Typical snapshots of atomic movements during SPE growth at 1450K.

shown by the dashed lines and the crystal growth along the {111} facet is the rate-limiting step of SPE in the [001] direction. That is, the kink site indicated by the arrow at 550 ps is recrytallized at 617 ps and the next kink site is almost recrytallized at 750 ps as shown by the arrow. Figure 2 shows typical snapshots of the SPE process annealed at 1450 K suggesting clearly that layer-by-layer crystallization occurs along the (001) plane. The a/c interface position was obtained as a function of the annealing temperature and the SPE
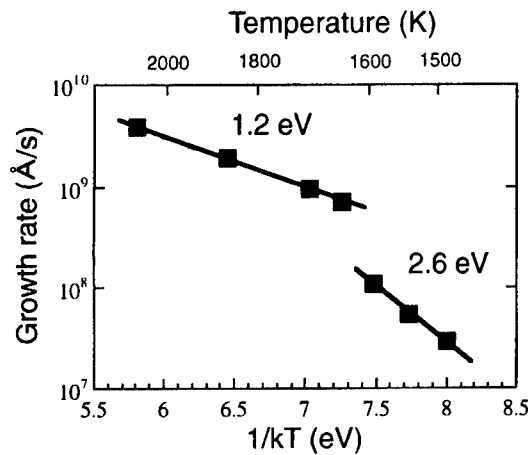
Fig. 3 Arrhenius plot of the [001] SPE growth rates.

growth rate was determined for each temperature. Figure 3 shows the Arrehnius plot of these SPE growth rates. There exist two activation energies: 2.6eV determined in the lower temperature region and 1.2eV in the higher temperature region. The former is in good agreement with the experimental value, $\approx$2.7eV obtained in thermal SPE, while no experimental value corresponds to the latter.

From these MD simulation results, we can envisage the SPE growth mechanisms in the lower and higher temperature regions as follows. In the lower temperature region, the a/c interface is essentially (001), and the rate-limiting step of crystallization can be considered to be 2-dimensional nucleation on the (001) a/c interface which gives rise to the activation energy, 2.6eV. On the other hand, in the higher temperature region, the a/c interface is predominantly composed of {111} facets and the rate-limiting step is a trapping process of Si at the kink sites associated with these facets. Thus, the activation energy 1.2 eV may correspond to the surface diffusion barrier on the (111) surface. Abrink et al.[8] estimated, based on molecular beam epitaxy (MBE) experiments, this barrier height to be about 0.2 eV for <112> diffusion on a step-free {111} plateau, while Joyce et al.[9] gave a value of ~2eV from their nucleation experiments by gas-source MBE.

It should be noted that the Tersoff potential gives rise to high melting temperature(2547K), while it can well reproduce thermodynamic properties such as the Gibbs free energy and thermal expansion coefficient in the temperature region less than $\approx$1500 K.[10] Therefore, we must conclude that it is not appropriate to use the Tersoff potential for correct estimation of the activation energy in the higher temperature region larger than 1500K. Nevertheless, we believe, there is a general trend that the structure of the a/c interface changes from a flat (001)-like surface to a rough surface composed of

800 ps

1600 ps

2600 ps

4000 ps

[110] view   [$\bar{1}$10] view
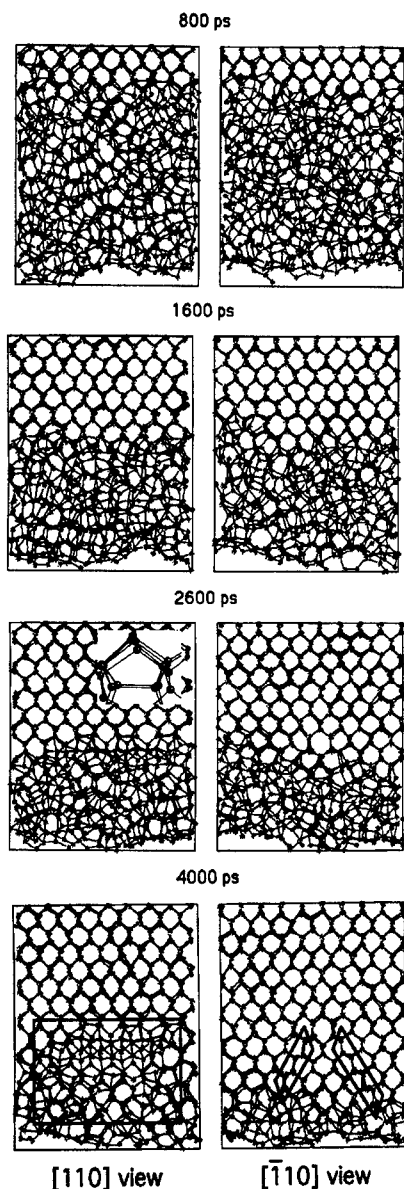
{111} facets during SPE growth of Si in the [001] direction as annealing temperature increases. In fact, similar rough surfaces can be observed in the solid/liquid interface of Si obtained by local laser-heating of polycrystalline Si thin films on quartz substrates capped by deposited SiO_2 films.[11] These results also suggest that the low activation energy ~0.3 eV observed in IBIEC may well be due to not only ion-beam-induced defects as generally considered but also structural change at the a/c interface during ion-beam irradiation.

Defect Formation

Figure 4 shows an example of the defect formation processes during SPE at 2000 K for 4000ps obtained by using the large MD cell including approximately 10000 atoms. The atomic motions were examined not only in the [110] direction but also in the [-110] direction. No defects can be seen in the SPE growth up to 2600ps. However, 5-membered rings formed at the a/c interface observed in the [110] view at 2600 and 4000ps are stable like the 2x1 reconstructed structure of the Si(001) surface. These 5-membered rings initiate the creation of hexagonal configurations which give rise to {111} stacking faults during the further SPE growth as can be seen at 4000ps in the regions enclosed by the solid lines.

Fig. 4 An example of defect formation during SPE of Si obtained by MD simulations at 2000K for 4000ps. Stable 5-membered rings observed in the [110] view at 2600ps (an enlargement is shown in the inset) initiate the creation of {111} stacking faults at 4000ps in the regions enclosed by the solid lines.

CONCLUSION

We have investigated the atomistic mechanisms of crystallization and defect formation during SPE of Si by using MD simulations. The growth mechanism was found to be different in the lower and higher temperature regions. In lower temperatures, the rate-limiting step is 2-dimensional nucleation on the amorphous/crystal Si(001) interface and the activation energy is found to be 2.6 eV which is in good agreement with the experimental value observed in thermal SPE. On the other hand, in higher temperatures, {111} facets are formed at the a/c interface and the rate-limiting step is considered to be a diffusion process of Si on the (111) plane which may result in a lower activation energy. It was also found that 5-membered rings created at the a/c interface initiated the formation of {111} stacking faults.

ACKNOWLEDGMENTS

REFERENCES

1. G. L. Olson and J. A. Roth, Mat. Sci. Rep. **3** , 1(1988).
2. A. Kinomura, J. S. Williams, and K. Fujii, Phys. Rev. B**59**, 15214(1999).
3. J. Tersoff, Phys. Rev. B**37**, 6991(1988).
4. S. J. Cook and P. Clancy, Phys. Rev. B**53**, 7176(1996).
5. M. Ishimaru, S. Munetoh, and T. Motooka, Phys. Rev. B**56**, 15133(1997).
6. M. Ishimaru, K. Yoshida, T. Kumamoto, and T. Motooka, Phys. Rev. B**54**, 4638(1996).
7. W. F. van Gunsteren and H. J. C. Berendsen, Molec. Phys. **45**, 637(1982).
8. H. C. Abrink, R. M. Broudy, and G. P. McCarthy, J. Appl. Phys. **39**, 4673(1968).
9. R. A. Joyce, R. R. Bradley, and G. R. Booker, Phil. Mag. **15**, 1167(1967).
10. L. Porter, S. Yip, M. Yamaguchi, H. Kaburaki, and M. Tang, J. Appl. Phys. **81**, 96(1997).
11. U. Landman, W. D. Luedtke, R. N. Barnett, C. L. Cleveland, M. W. Ribarsky, E. Arnold, S. Ramesh, H. Baumgart, A. Martinez, and B. Khan, Phys. Rev. Lett. **56**, 155(1986).

MULTIMILLION-ATOM SIMULATIONS OF ATOMIC-LEVEL SURFACE STRESSES AND PRESSURE DISTRIBUTION ON InAs/GaAs MESAS

XIAOTAO SU*, RAJIV K. KALIA*, ANUPAM MADHUKAR**, AIICHIRO NAKANO*, and PRIYA VASHISHTA*
*Concurrent Computing Laboratory for Materials Simulations, Dept. of Physics & Astronomy, Dept. of Computer Science, Louisiana State University, Baton Rouge, LA 70803, xsu@lsu.edu
**Photonic Materials and Devices Laboratory, Dept. of Materials Science, University of Southern California, Los Angeles, CA 90089

ABSTRACT

Large-scale molecular dynamics simulations are performed to investigate the atomic-level stresses on InAs/GaAs mesas. The simulations are based on an interatomic-potential scheme for InAs/GaAs systems which depends on the local chemical composition. Multiresolution techniques are used to speed up the simulations. InAs/GaAs square mesas with {101}-type sidewalls are studied. The atomic-level pressure distribution and surface atomic stresses on the sidewalls with 12, 10, 8 and 6 monolayers of InAs overlayers have been calculated.

INTRODUCTION

The large (~ 7%) lattice mismatch and associated strain at InAs/GaAs (001) interfaces has recently been utilized to fabricate a number of nanostructures.[1-4] On infinite planar substrates, the strain relief leads to the formation of three-dimensional island structures above a critical amount, ~ 1.6 monolayers (ML), of InAs deposition.[1] When InAs is deposited on <100> oriented GaAs square mesas of size ≤ 75 nm, however, no island formation is observed and films of flat morphology form with a self-limiting thickness of ~ 11 ML.[3] At the early stage of InAs deposition, In atoms migrate from the sidewalls to the mesa top. Once the InAs thickness on the mesa top reaches ~ 11 ML, however, In atoms migrate away from the mesa top. A possible origin of the migration-direction reversal is the build-up of strain energy in the InAs film and the associated change in the surface stress gradient direction.

We have used molecular dynamics (MD) simulations to investigate the atomic-level surface stresses, and the mechanical stresses on InAs/GaAs nanomesas. Reliable interatomic potentials are essential ingredients of MD simulations. Our interatomic potentials consist of two-body and three-body terms,[5]

$$V = \sum_{i<j} u_{ij}\left(\left|\vec{r}_{ij}\right|\right) + \sum_{i,j<k} v_{jik}\left(\vec{r}_{ij}, \vec{r}_{ik}\right). \tag{1}$$

The two-body terms represent steric repulsion, Coulomb interaction due to charge transfer, charge-dipole interaction due to large polarizability of negative ions, and van der Waals interactions,

$$u_{ij}(r) = \frac{H_{ij}}{r^{\eta_{ij}}} + \frac{Z_i Z_j}{r}\exp\left(-\frac{r}{a}\right) - \frac{D_{ij}}{r^4}\exp\left(-\frac{r}{b}\right) - \frac{W_{ij}}{r^6}. \tag{2}$$

The three-body terms include the effects of covalent bond-bending and bond-stretching,

$$v_{jik}(\vec{r},\vec{r}') = B_{jik}\exp\left(\frac{\gamma}{r-r_0} + \frac{\gamma}{r'-r_0}\right)\frac{1}{C + \left(\frac{|\vec{r}||\vec{r}'|}{\vec{r}\bullet\vec{r}'}\right)^2}\Theta(r_0-r)\Theta(r_0-r'), \tag{3}$$

where $\Theta(x)$ is a step function.

The adjustable parameters in these terms have been determined so that a set of experimental data and first-principle calculations of electronic structures can be reproduced. Our potentials reproduce well the experimental crystalline lattice constant, cohesive energies, elastic constants, surface energies, high-pressure structural transitions, phonon density-of-states, and neutron-scattering data for liquid and amorphous structure.

In order to study InAs/GaAs mesas, we need to develop an interatomic-potential scheme to represent the mixed environment experienced by the atoms at the interface of even a chemically ideal InAs/GaAs interface. Recently, we have developed a scheme to combine interatomic potentials of binary materials in such a way that the resulting potential depends on the local chemical composition. For systems involving Ga, In, and As, we use a linear interpolation scheme to combine the interatomic potentials for GaAs and InAs. This scheme is adaptive in which As atoms are classified into different types according to the number of Ga and In neighbor atoms.[5]

SIMULATION PROCEDURE

Figure 1 shows a schematic view of an InAs/GaAs mesa with <100> oriented square base and {101} sidewalls on a GaAs (001) substrate. Periodic boundary conditions are applied to the GaAs substrate of size L = 474.9 Å in both x and y directions. The GaAs mesa top size is 124.4 Å X 124.4 Å and the system consists of 2.2 million atoms.

The initial configuration of the InAs/GaAs mesa is constructed by setting the lattice constant of InAs the same as that of GaAs. The system is then quenched by scaling the atomic velocities. After the system reaches a locally stable state, the atomic level stresses are calculated.[6]
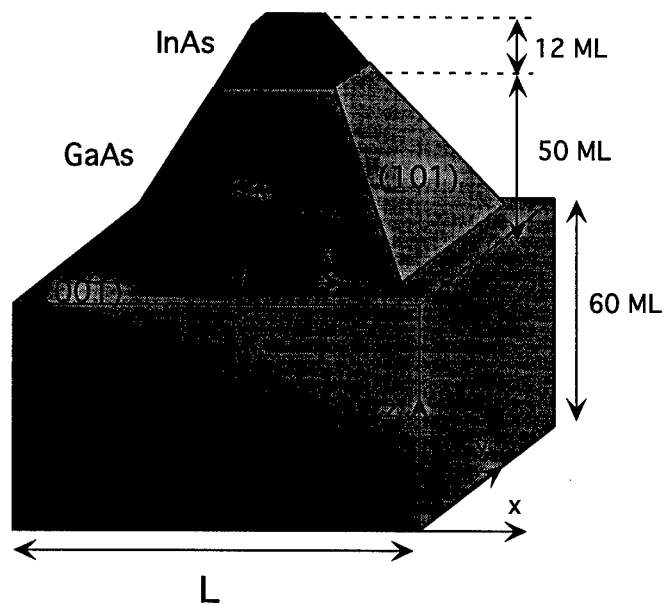
Fig. 1. Schematic view of an InAs/GaAs mesa with <100> oriented square base and {101} sidewalls on a GaAs (001) substrate.

RESULTS

Figure 2 shows the atomic-level pressure distribution of an InAs/GaAs mesa with 12 ML InAs overlayer. Due to the lattice mismatch, a tensile stress well is formed in GaAs immediately below the InAs/GaAs interface.

Due to the presence of the free mesa surfaces, the strain relief of the highly lattice mismatched system is achieved in part by the relaxation of InAs overlayers. Figure 3 shows an enlarged view at the center of the mesa. One can clearly see the gradual relaxation of InAs overlayer. On the top of 12 ML InAs overlayer, the lattice spacing is 6.8% larger than that of the GaAs substrate in the bottom.

Next, we discuss the surface atomic stress on the sidewalls. Surface stress gradients are expected to play a major role in determining the migration direction of adatoms.[2] Figure 4 shows the atomic stresses of surface As atoms on a {101} sidewall of an InAs/GaAs mesa with 12 ML InAs overlayer. The figure plots the stress component σ_{YY} along the Y-axis (see Figure 1) on the sidewall, relevant to the adatom migration. It is found that

271

σ_{YY} reaches the maximum value at the GaAs/InAs interface and surface stress gradient along the Y-axis points from the interface toward the InAs overlayer.

We have also calculated atomic-level stresses for InAs/GaAs mesas with 10, 8, and 6 ML InAs overlayers, with the sizes of GaAs substrate and GaAs mesa top fixed. Similar behaviors have been observed on both the atomic-level pressure distribution and the surface atomic stress along the Y-axis. However, lattice relaxation of InAs overlayers is different. On the top of 10, 8, and 6 ML InAs overlayers, the lattice relaxation with respect to GaAs substrate in the bottom is 6.7%, 6.2%, and 5.0% respectively.
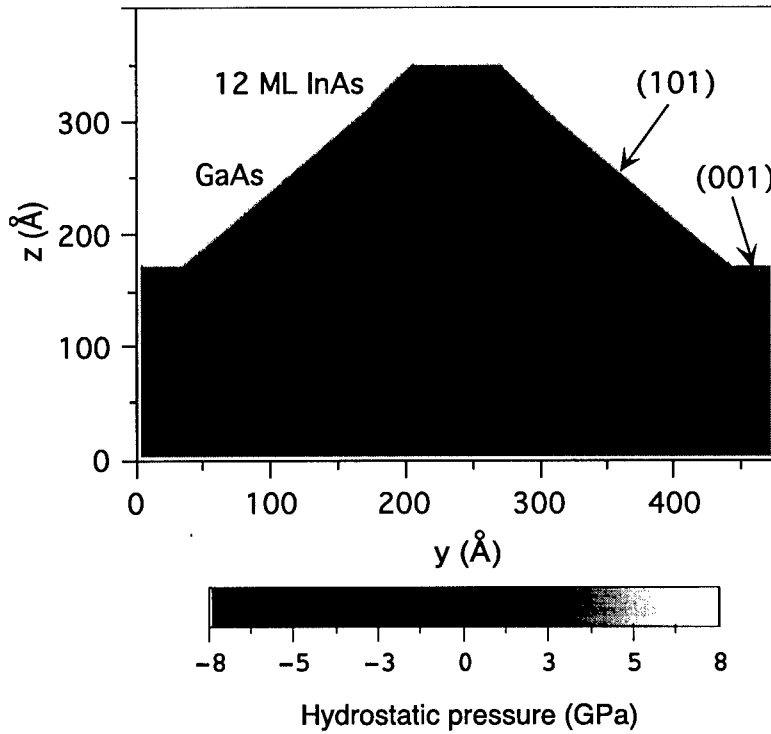
Fig. 2. Atomic-level pressure distribution in an InAs/GaAs square mesa with 12 ML InAs overlayer. Negative pressure means tensile and positive pressure means compressive. The figure shows a slice at the center of the mesa.
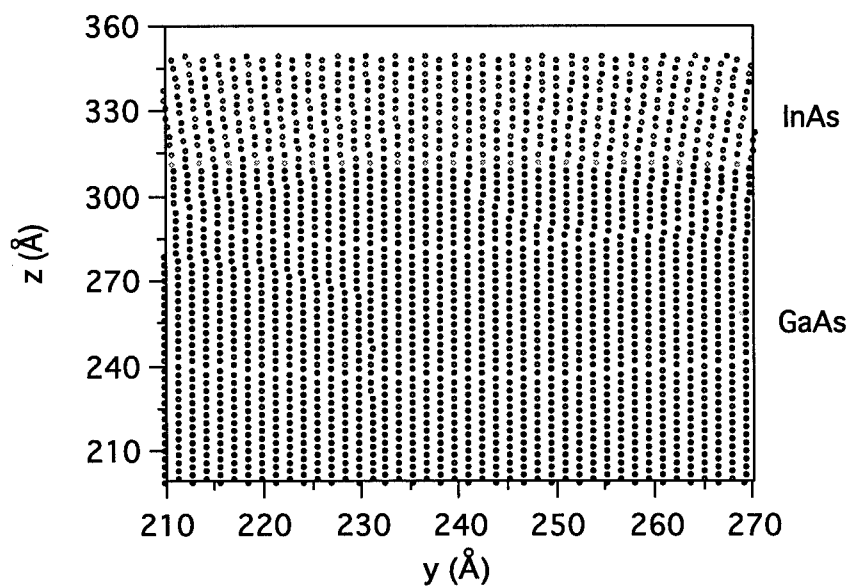
Fig. 3. Enlarged view of an InAs/GaAs square mesa with 12 ML InAs overlayer. The figure shows a slice at the center of the mesa.
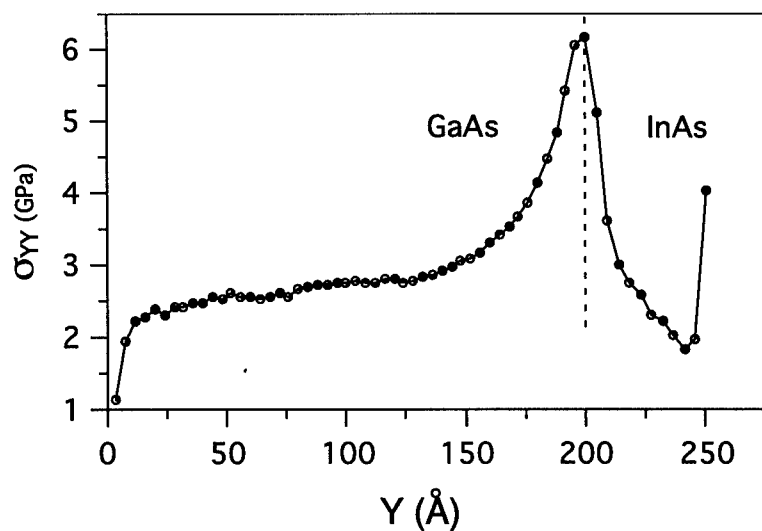
Fig. 4. Atomic stresses of surface As atoms on a {101} sidewall of an InAs/GaAs mesa with 12 ML InAs overlayer.

CONCLUSIONS

We have performed large-scale molecular dynamics simulations to investigate the atomic-level stresses on InAs/GaAs mesas. For InAs/GaAs mesas with <100> oriented square base and {101} sidewalls on GaAs (001) substrate, we have studied systems with 12, 10, 8 and 6 ML InAs overlayers. Tensile stress well is formed in GaAs immediately below the InAs/GaAs interface. It is found that the surface stress component σ_{YY} reaches the maximum value at the GaAs/InAs interface and surface stress gradient along the Y-axis points from the interface toward the InAs overlayer.

ACKNOWLEDGMENTS

REFERENCES

1. Q. Xie, A. Madhukar, P. Chen, and N. P. Kobayashi, Phys. Rev. Lett. **75**, 2542 (1995); S. Guha, A. Madhukar, and K. C. Rajkumar, Appl. Phys. Lett. **57**, 2110 (1990).
2. A. Konkar, K. C. Rajkumar, Q. Xie, P. Chen, A. Madhukar, H. T. Lin, and D. H. Rich, J. Cryst. Growth **150**, 311 (1995).
3. A. Konkar, A. Madhukar, and P. Chen, Mat. Res. Soc. Symp. Proc. **380**, 17 (1995).
4. A. Konkar, A. Madhukar, and P. Chen, Appl. Phys. Lett. **72**, 220 (1998).
5. A detailed discussion of the interatomic potential and the parameters will be published elsewhere, P. Vashishta, I. Ebbsjö, R. K. Kalia, and A. Nakano, J. Rino, F. Shimojo, to be published.
6. W. Yu and A. Madhukar, Phys. Rev. Lett. **79**, 905 (1997).

EFFECTS OF THE ELECTRONIC STRUCTURE ON THE STABILITY OF METALLIC SUPERLATTICES. SEMI-EMIPIRICAL CALCULATIONS OF THE TOTAL ENERGY

A.M.MAZZONE

C.N.R. LAMEL-via Gobetti 101 - Bologna-40129-Italy-mazzone@lamel.bo.cnr.it

ABSTRACT

In this work the total energy of metallic superlattices is evaluated at semi-empirical level. The superlattice has an heterogenous composition and it has two shapes, i.e.(*i*) two facing A/B wires and (*ii*) a hut-shaped island of the element A deposited on a rigid B substrate. The elements A and B are Ag, Cu, Pd, Pt and Fe. The calculations show the existence of competing bonding contributions. In fact, a strong bond arises from charge exchanges at the A/B interface and from the bulk-like bonds of interior atoms. On the contrary, surface atoms are undercoordinated and reduce the strength of bonding. These contributions act on opposite sense on the large structures and the geometry dependence of the binding energy suggests a self-limited growth, rather than Ostwald ripening.
Keywords : semi-empirical calculations, metallic superlattices.

INTRODUCTION

To date, epitaxial architecture has been almost exclusively one dimensional and a film thickness in the range 1000 Å represents the current standard. However many experimental researches are currently aimed at the development of structures which take full advantage of a limited size. Therefore the design of two and three dimensional superlattices, with linear dimensions in the range 100 Å or below, needs to be considered. The conventional way to fabricate such structures by litography, etching and overgrowth of heterostructures is at the limits of feasibility. One alternative is to use the spontaneous formation of islands which is observed during epitaxial growth of semiconductors and metals. This has fueled the interest for the mechanisms of islanding and 'superlattice' and 'island ' are often regarded as synonym.

At the present state of the art, structural studies on superlattices center on semiconductors. However, even for these widely investigated systems, there is no unifying view as to which is the most effective mechanism leading to the formation of islands. In fact, it is hotly contended if the island structure has to be interpreted as a structure in equilibrium or as the result of the dynamical processes taking place during deposition. Depending on the one or the other of these views, island formation has been explained as an inherent instability of strained epitaxial layers or as a coverage-dependent effect [1,2,3].

In the field of metallic structures the focus of structural studies is on thin films, rather than on superlattices. This leaves the structural genesis of metallic superlattices ill-defined. This study attempts to contribute to this problem by clarifying some general
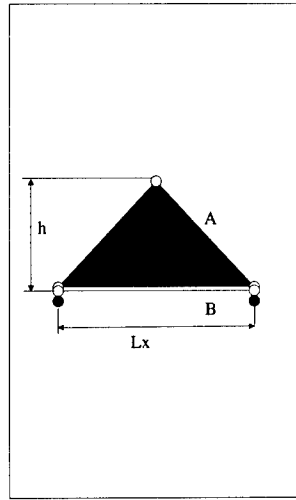
Fig.1 -
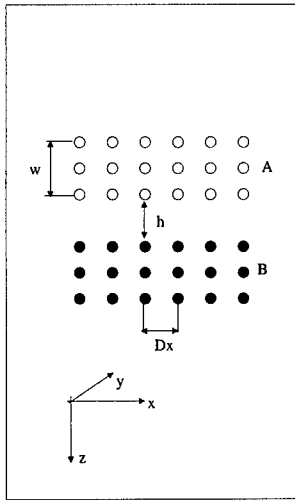
Figure 1: The superlattices structures.

properties valid under equilibrium conditions. The total energy of two representative structures, that is an isolated, hut-shaped island deposited on a rigid substrate and two coupled wires, is evaluated at semi-empirical level. The purpose of the calculations is to map the configurational phase space defined by the geometrical parameters of these structures to find energy minima. These structures, which are energetically preferred, should appear also under dynamical conditions.

THE SUPERLATTICES STRUCTURE.THE EVALUATION OF THE TOTAL ENERGY

Theories and experiments indicate that a superlattice structure is the combined result of the growth conditions and of island-substrate and inter-islands interactions. The structures used in the following calculations are chosen to elicit the physical nature of these interactions. The structures, shown in Fig.1, are : (i) two AB wires, with a rectangular section, running parallel. This structure, taken from [1], illustrates the case of stacked structures of high density. (ii) a hut-shaped structure formed by an element A deposited on an infinitely rigid B substrate. This structure, taken from [2], represents the dilute limit and shows the effects of the island geometry on its coupling with the substrate.

The elements forming the system are A,B=Ag,Cu,Pd,Pt and Fe. For both the coupled wires and the island the lattice structure is crystalline with a fcc geometry. A bcc lattice has been used only for systems containing Fe. The phase space mapped by the calculations
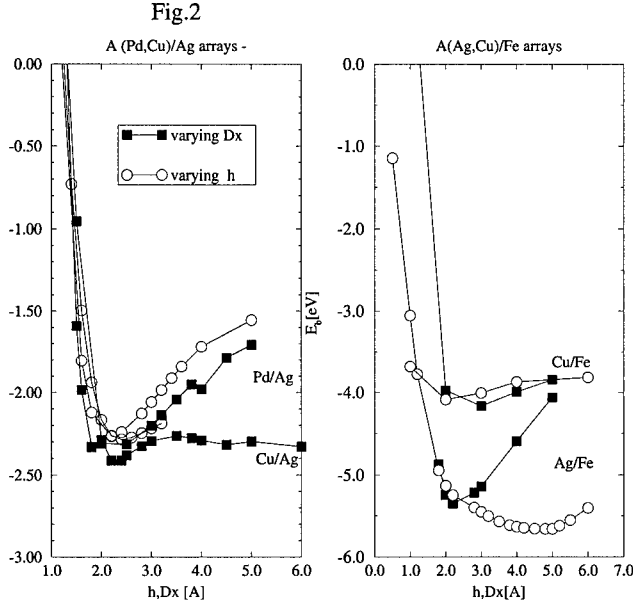
Fig.2

Figure 2: The binding energy of the wirelike structures with $w=0$.

is defined by the geometrical parameters of the superlattice. For the coupled wires these parameters are the lattice spacing Dx, the distance h of the two elements A/B, the lengths L_x, L_y along x and y and the thickness w of each wire. The ones of the hut-shaped structures are the height h and the linear dimensions of the basis L_x, L_y (in these calculations Dx is equal to the lattice parameter of the element A). The choice of these parameters mediates between the values typical of monolayer epitaxis and the ones of thin film growth. For both superlattice structures the maximum size of L_x is ~ 400 Å. L_y has been kept fixed to 50Å and a larger size ~ 100Å has been used only in a few test calculations. The height h of the hut-shaped island may reach 30 Å.

The total energy of the structure is evaluated at semi-empirical level using the Hartree-Fock theory within the Extended Debye Hueckel Approximation (EHA) using QCPE software. The accuracy of the method has been tested by comparing EHA with higher order calculations and experiments on Ag and Cu dimers and on small Fe clusters (these results are reported in [4]). The parameter used to describe the electronic configuration of the superlattices is the binding energy per atom E_b, that is the energy difference of the total energy in the structure with respect to the one of an ensemble of free atoms with the same size and composition.

RESULTS.BONDING IN SUPERLATTICES

Owing to the similarity of the lattice parameter, good epitaxis is expected for all the
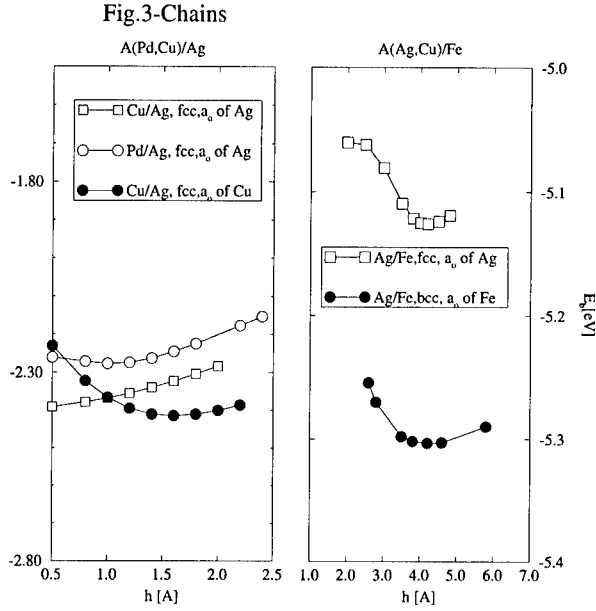
Fig.3-Chains

A(Pd,Cu)/Ag

A(Ag,Cu)/Fe

□——□ Cu/Ag, fcc,a_o of Ag

○——○ Pd/Ag, fcc,a_o of Ag

●——● Cu/Ag, fcc,a_o of Cu

□——□ Ag/Fe,fcc, a_o of Ag

●——● Ag/Fe,bcc, a_o of Fe

E_g[eV]

h [A]

h [A]

Figure 3: The binding energy of the wirelike structures with finite thickness. a_o indicates the lattice parameter of the solid.

elements used in the simulations and is experimentally observed for thin film structures. However this scenario may remarkably change when submonolayer growth is considered. In fact, the valence charge Z (equal to 12,12,10,10,8 for Ag,Cu,Pd,Pt and Fe, respectively) significantly changes from element to element. From the imbalance of the charge on A and B effects dictated by a charge equalization condition[5] are to be expected especially in systems, like A/Fe, with noticeably different Z.

These mechanisms are best illustrated by the coupled wires and this case is shown first in Figs.2 and 3. Figure 2 represents the limit case of zero thickness. This structure is formed by two equispaced arrays of single atoms and its geometry is defined by h, Dx and L_x. Negative binding energies, and therefore stable structures, are observed for all geometries and composition, provided that h and Dx are above a minimum size dominated by intranuclear repulsion. Furthermore deeper lying E_b values are observed in systems, such as Ag/Fe, where the atomic charges of the two components have a remarkable different size. Mulliken population analysis shows that in these structures an effective charge exchange between the two facing chains take place. This charge acts as a ligand and reduces E_b. This result is in no way dependent on the length of the array. In fact extensive calculations using L_x=50, 100,200,400Å did not show significant changes with respect to the data reported in Fig.2.
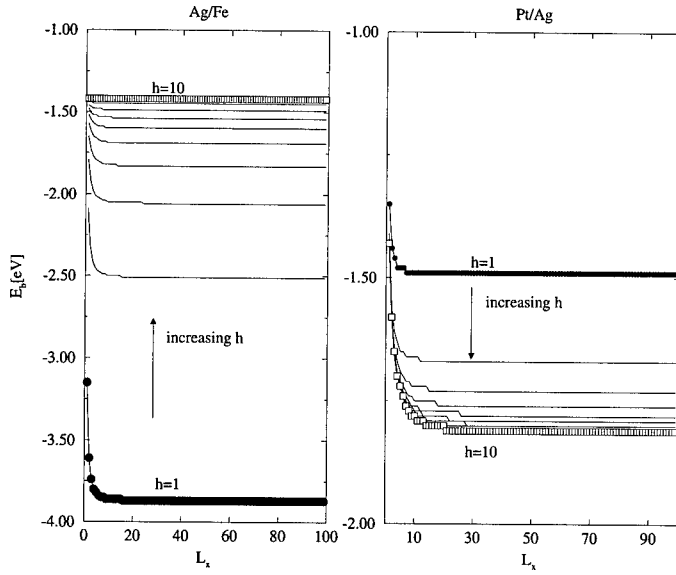
Fig.4 Hut-shaped structures

Figure 4: The binding energy of the hut-shaped structures. h and L_x are normalized to the lattice parameter of the element A.

The increase of the wires thickness does not increase their stability. As shown by Fig.3, E_b of wires with w from 4 to 10 Å is larger than the one in the limit of zero thickness and,as shown by Pd/Cu, the structure tend to be destabilized. In fact, the increase of w increases both the number of atoms in the wire interior and on its surface. The binding energy of the interior atoms is close to the cohesive energy E_c of the bulk. On the contrary, the surfacial atoms are under-coordinated. The calculations show that their energy is in the range of the binding energy E_{AA} of the AA dimer which is of factor two smaller than E_c. Owing to the low value of E_{AA}, the contribution of the interior atoms is offset by the weak bonding at the surface. Therefore, even in the case of a finite w, the wire stability is essentially maintained by the strong bond at the A/B interface. As for Fig.2, no perceptible effect of L_x was observed. Similarly to our conclusions, in [3] it is shown that in heterogeneous systems a stabilizing contribution to the island energy arises from the mixing energy due to A/B interactions.

The binding in hut-shaped structures represents the suitable transcription of the one of the wires. In systems where E_c is remarkably large (such as Pt on Ag in Fig.4) large structures are energetically preferred owing to the formation of strong bulk-like bonds in the island interior. On the contrary, in systems where E_c is low (such as Ag on Fe in Fig.4) small islands are stabilized by the strong bond across the interface. As the island size

increases, the adverse effect of the surface increases and leads to the destabilization of the structure. This result is worth being underlined as it is in agreement with a well-known experimental result, that is the fragmentation of large Ag islands deposited on Pt [6].

Furthermore in Fig.3 it is observed that for both Ag and Pt the E_b values of islands with large h and L are very close. It is therefore plausible than thermal fluctuations generates a process alternating growth and decrease, rather than the continuous growth prescribed by the Ostwald ripening.

CONCLUSIONS

The main finding of the calculations is the strong component of bonding arising from charge exchange and hybridization at the A/B boundary. Noticeable elements at variance with the Stranski-Krastanow growth mode are also observed. In fact, in the cases of coupled wires 'arrays' are favored, rather than thicker 3D structures. For the hut-shaped structures a tendency to a self-limited growth can be envisaged from the geometry-dependence of E_b. These results can be, admittedly, vitiated by the simple Hamiltonian used in the calculations. It is, however, plausible that more refined effects of electron-electron correlation play a secondary role in the large structures analyzed in this study.

References.

[1]C.Ratsch and A.Zangwill, Surf.Science,293,123,1993.

[2]J.Tersoff, Phys.Rev.Lett.,81,3183,1998.

[3]H.T.Dobbs, D.Vvedensky, A.Zangwill, J.Johansson, N.Carlsson and W.Seifert, Phys.Rev.Lett.,79,897,1997.

[4] A.M.Mazzone, Modelling and Simulation in Materials Science and Engineering, in press.

[5] P.P.Singh and A.Gonis,Phys.Rev.B.,49,5,1642,1994.

[6]A.F.Becker, G.Rosenfeld, B.Poelsema and G.Comsa,Phys.Rev.Lett.,70,477,1993.

**Nanodevices and
Nanostructures**

GATE TECHNOLOGY ISSUES FOR SILICON MOS NANOTRANSISTORS

D.M Tennant[1], G.L. Timp[2], L.E. Ocola[2], M. Green[2], T. Sorsch[2], A. Kornblit[2], F. Klemens[2], R. Kleiman[2], D.A. Muller[2], Y. Kim[2], and W. Timp[3]

[1]*Bell Laboratories, Lucent Technologies, Holmdel, N.J. 07733,*
[2]*Bell Laboratories, Lucent Technologies, Murray Hill, N.J. 07974 ,*
[3]*University of Illinois, Champaign-Urbana, Illinois 61820*

ABSTRACT

This article reviews technology issues in scaling conventional planar transistors to a physical gate length of 30nm that are expected to produce an effective channel length of 10 nm. Gate fabrication features direct write e-beam lithography to form a ring structure capable of exploring the practical limits of gate processing while requiring only a single level of lithography. Other processing elements include ultra-thin gate dielectric formation ($\sim$ 0.6nm); highly selective transformer coupled plasma (TCP) etching; and low energy ion implantation. DC electrical results obtained for high performance n-MOS and p-MOS type nanotransistors made using this process are discussed as are simulations of sub-threshold currents for n-MOS transistors with physical gate lengths down to 26nm

INTRODUCTION

Continued advancement of planar high performance sub-60 nm transistors requires ultra-thin gate dielectrics (<2nm) and ultra-shallow junctions (< 50nm), both to achieve a high saturation current with a low power supply voltage and to control short channel effects [1]. We review here the recent progress toward a scaled 30 nm gate technology [2,3]. We discuss lithographic and pattern transfer related results from this scaled silicon transistor initiative and include results from both n- and p- channel transistors. While the most stringent requirements for high performance CMOS technology are dictated by the pMOS transistor, due to boron diffusion through the gate dielectric and transient enhanced diffusion in the contacts, both nMOS and pMOS share the difficulties of gate level lithography and etch selectivity. To more rapidly optimize the overall process, we employ a transistor test structure requiring only one level of lithography, performed by direct write e-beam lithography. After completion these devices are directly probed electrically. Electrical performance is correlated with the fabrication process via ananlysis of cross-sectioned structures by scanning capacitance microscopy (SCM) and transmission electron microscopy (TEM). These have provided data on physical and electrical channel dimensions, while electron energy loss spectroscopy (EELS) has provided insight into the limits of conventional gate dielectrics.

We have targeted 30nm physical gate devices since they represent the minimum gate length required to produce non-shorted channels. We report on materials and processes used in fabrication, the electrical characterization of n- and p- type transistors, and simulation results based on these measurements which help predict the limitations of both the process and the practicality of large scale integration of such transistors.

FABRICATION

The gate stack for this work consists of 80nm of TEOS hard mask over 80nm of WSi$_x$ on 50nm of poly-crystalline silicon on gate oxides ranging in thickness from 0.55-2.0nm thick on epitaxial (100) silicon substrates. Prior to gate oxide growth, the substrates used for the pMOS transistors were implanted with As and P while the nMOS substrates received B implants. The gate oxide was grown by rapid thermal oxidation (RTO) in pure oxygen. The 40-50 nm layer of silicon in the gate stack is deposited by chemical vapor deposition and is in-situ doped with phosphorus. The as-deposited film is amorphous but is annealed to form polycrystalline material. The 80 nm WSi$_x$ (x~2.7) is dc magnetron sputter deposited. The final layer of the gate stack is the 80 nm hard-mask, which is a conformal, low temperature LPCVD oxide deposited using a TEOS decomposition process. Following the poly and WSi$_x$ deposition, the gate stack was implanted with boron at 8keV for pMOS and 40 keV As at for the nMOS.

The wafers are subsequently patterned using a single level of electron beam lithography to define the gate, source, and drain contacts simultaneously. The gate electrode (325 μm x 325 μm) entirely surrounds both the source and drain contacts (both 25 μm x25 μm) in a ring geometry as shown in Fig. 1. Sufficient isolation of the gate conductance for this design is provided by the long channel and high threshold associated with the parasitic portions of the transistor.
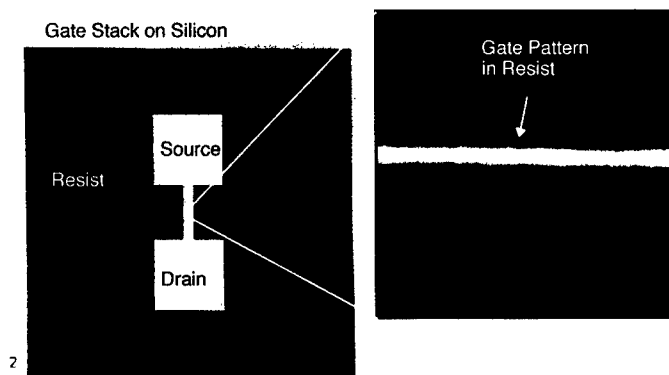
Figure 1. Scanning electron micrograph of the e-beam patterned ring structure at (left) low magnification and (right) high magnification used to study and optimize the gate process.

In order to achieve our goal of producing 30 nm physical gates we investigated options for enhancing the performance of the NEB series of negative chemically amplified resists (CAR) over prior work with 60 nm gate length transistors [4]. We investigated use of thinner NEB 22 resist films and the utility of a less sensitive, higher resolution resist formulation, NEB-31. All resist exposures were performed with a JEOL JBX6000FS thermal field emission direct write system at a 50 kV acceleration voltage

using a spot of 10 to 20 nm. The PAB and PEB conditions were varied to provide best resist profiles. The developer used was MF-321 from Shipley, a TMAH 0.21N aqueous developer. All samples were rinsed in de-ionized water, and dried with dry nitrogen. The findings from these studies are detailed elsewhere [5] but are summarized in Fig. 2. Samples prepared with NEB-22 resist thicknesses ranging from 1.1 μm down to 0.110 μm are plotted showing the highest resolution achieved and the maximum aspect ratio obtained. We observe not only that finer linewidths require thinner resists, but that the maximum achievable aspect ratio decreases with decreasing film thickness. As the gate lithography is reduced down to the 30 nm regime, the highest achievable aspect ratio with NEB 22 decreases to 3. Also plotted is a single linewidth datum for the NEB 31formulation which produced the minimum linewidth. The corresponding SEM image is shown at the right of Fig. 2 and represents the narrowest line to date for the NEB series. This 29 nm resist structure obtained in NEB-31 in a layer thickness of 110 nm, yields an aspect ratio of about 3.8. Clearly this is an improvement over the NEB 22 result, but is very near the useful limit. Slightly narrower 25 nm structures, which were otherwised resolved, collapsed , indicating that aspect ratios above 4 were not practical.
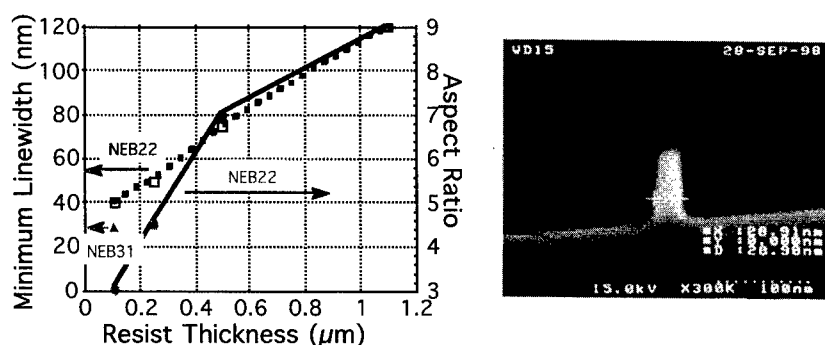
Figure 2. Plot of minmum linewidth and maximum aspect ratio dependence on resist thickness for NEB 22 resist. (left figure). SEM cross section of 29 nm wide resist feature patterned in 110 nm thick negative tone resist, Sumitomo NEB 31, patterned by electron beam lithography (right figure). The single corresponding datum appears in the plot in the left figure.

After lithography the gate pattern is subsequently transferred into the gate stack using a RIE sequence. The TEOS hard mask is etched in CHF_3 / SF_6 (65:3) and overetched in CHF_3 / CF_4 /Ar (30:4:60). The etch into the hard mask is performed in a magnetically enhanced RIE system. Following the hard mask etch, the resist is removed. The remaining gate stack RIE is performed in the TCP etcher. The tungsten silicide is etched using Cl_2 in a 20% He/ O_2 background. The gate structure is completed by transferring the pattern into poly-crystalline silicon using HBr / He /O_2 mixture in order to stop on the ultra-thin gate oxide with very high selectivity. Optical emission end point detection is used to determine a consistent stopping point.

After RIE defines the gate of the MOSFET, ultra-shallow self-aligned source-drain extensions are implanted using 4keV As for the NMOS and 0.50 keV B for PMOS to form ultra-shallow junctions with high conductivity, necessary to diminish short channel effects without compromising device performance. [6]

Following the deposition of an undoped TEOS sidewall and a sidewall etch, a high dose (3×10^{15} cm^{-2}) of B was implanted at 1keV for PMOS (for NMOS, As at 60keV) to form the contacts. The implants were activated using RTA at 1000C for 5 seconds. We form either Ti or Co silicide in the contacts to reduce the sheet resistance to 4-8 Ω/square prior to probing.

The etch sequence described above to transfer the gate pattern in the gate stack typically narrows the lithographic features by 10 to 20 nm. As a result, gate level lithography requires a minimum resist CD of 40 to 50 nm, which has been met using the NEB 22. As etch fidelity improves, however, 30nm CD in gate lithography may be required. The resolution improvement obtained using Sumitomo NEB 31 described above makes it a good replacement candidate.

A representative etched nMOSFET gate structure is shown in Fig. 3. A nominal physical gate length of 35 nm is obtained after the etch of the gate stack. We observe that the structure is close to vertical, and the etch has sufficient selectivity to stop on a gate oxide here of only 1.0 nm thick. Using split lots of wafers, we have systematically explored gate stacks with gate dielectric layers of 0.55 to 2.0 nm. A high magnification TEM image of the region under the polysilicon with a 1.0 nm gate oxide is shown at the right of Fig. 3. The micrograph demonstrates the uniformity of the dielectric growth even in these extremely thin layers.
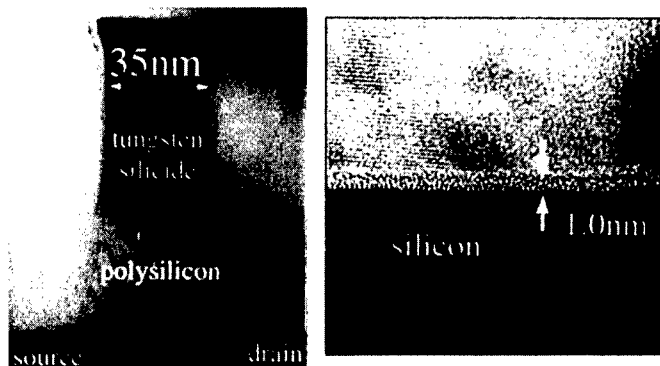
Figure 3. TEM cross sections of a 35 nm nMOS device with a thin gate stack. The right figure shows a magnified view of a gate oxide region with a 1.0 nm ultra-thin gate oxide.

286

SCM and EELS ANALYSES

In SCM, an atomic force microscope is used with an electrically conductive probe, which acts as a resonant capacitance sensor to map the changes in capacitance, interpreted as changes in the carrier concentration –revealing both the magnitude and sign of the carrier concentration. SCM used in conjunction with ultra-sharp silicon tips, have been used to investigate junction profiles in MOSFETs [7,8]. Figure 4 shows a 2-D SCM scan obtained in this manner. Identifying the dC/dV=0 signal as the junction position, the 2-D dopant profile directly determines the effective channel length. The 2D profile of the ultra-shallow junctions in the pMOSFET of Fig. 4 is observed to be about 55 nm deep with a corresponding lateral extension of 35 nm. Discrepancies between simulations and SCM measurements suggest an enhanced diffusion of boron which results in an effective channel length of only 20 nm instead of the expected 40 nm in the (L_g = 80 nm) pMOSFET shown. SCM measurement of L_{eff}, the effective channel length, for a wide range of physical gate length PMOSFET devices has allowed improved shallow junction formation and more accurate simulation.
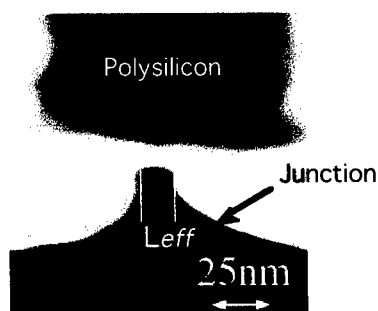
Figure 4. A 2-D scanning capacitance microscopy image of the cross section of a pMOS transistor. The junction is defined to be where dC/dV=0, allowing the effective channel length to be measured.

Initially an offset of approximately 50 nm was observed between L_g and L_{eff}. Using information from SCM measurements to calibrate simulation programs, we designed the "30 nm process" described above and estimate that these offsets can be reduced to 30 nm and 20 nm for pMOS and nMOS, respectively with optimization. The same simulations predict that physical gate lengths of 20 to 30 nm are shorted between source and drain, leaving gate lengths near 30 nm as a practical limit for gate definition. Progress toward this optimization is reflected in the transistor results presented below.
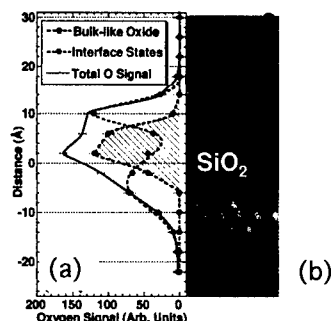
Figure 5. Electron energy loss spectroscopy measurements for thin RTO gate oxides used in the MOS transistor process. The data (a) obtained from EELS spectra show that there is an interfacial oxide layer at both the upper and lower surfaces surrounding the bulk-like SiO_2. (b) A STEM annular dark field image showing the physical layers. The circles denote the locations of the EELS spectra used in (a). This data suggests an explanation for the observed lack of improvement in device performance for gate oxide thicknesses below 1.2nm.

In similar fashion, a scanning transmission electron microscope (STEM) can provide information on the practical limits for gate oxide thicknesses [9] as illustrated in Fig 5 for a nominal (determined by ellipsometry) 1nm thick gate oxide. Figure 5b. is an annular dark field STEM image of the gate oxide region showing the bulk silicon, gate oxide, and polysilicon gate regions. The circles denote the locations of EELS measurements (not shown) used to determine the oxide properties plotted in Fig 5a. The changes observed in the oxygen- K signature in the EELS spectra are used to distinguish the SiO_2 bulk-like properties from the interfacial oxide region. Fig 5a summarizes the oxide property findings in the region of the gate oxide. The bulk-like region is significantly narrower than the total oxide thickness. The interfacial oxide (about 0.35 nm per side) therefore sets a fundamental limit on the layer thickness needed to prevent shorting of the gate. These data suggest that the minimum gate oxide thickness is 0.7 nm. The practical limit must allow for sufficient bulk-like dielectric to prevent tunnelling (0.4 to 0.6 nm) yielding minimum of about 1.1 to 1.3 nm, consistent with the measured electrical properties. Other non- ideal properties such as surface roughness (estimated at ~0.2 nm per side) contributes to the transistor drive performance but also may add an additional thickness to reach the needed dielectric reliability required for large scale integration. A detailed discussion of the measurements of the oxide chemical properties is given by Muller, et. al. in reference [9] and a theoretical treatment is given by Neaton, et. al. in reference [10].

TRANSISTOR MEASUREMENTS

Figure 6 shows some recently obtained measured dc results for our scaled gate stack process. They represent some improvement over earlier devices [11,12]. The figure

depicts high dc performance nMOSFETs and pMOSFETs with physical gate lengths of 40 nm and gate oxides of 1.3 nm and 1.5 nm, respectively and nominal channel doping of $1 \times 10^{18}/$ cm $^{-3}$. At a supply voltage, V_{DD}, of 1.5 V, the nMOSFET drive current, $I_{on} = 2.1$ mA/μm which drops to 1.3 mA/μm at a supply voltage of 1.0 V. The threshold voltage, $V_t = 0.2$ V and the subthreshold leakage current, I_{off}, is 2 μA/μm. The pMOSFET exhibited a drive current, $I_{on} = -0.61$ mA/μm at a supply voltage of 1.5V which is reduced to 0.37 mA/μm at −1.0 V. The pMOS threshold voltage, $V_t = -0.22$ V and $I_{off} = 1.6$ μA/μm. While the drive currents are very promising, the leakage currents exceed the values assigned by the SIA *International Technology Roadmap for Semiconductors* for the predicted needs of logic circuits. Process modifications did lower I_{off} to within the desirable range but the corresponding drive currents, I_{on} were reduced by about 40%.

While simulations of ideal devices allow for still further improvement, the measured devices do not yet fully satisfy the SIA *International Technology Roadmap for Semiconductors* requirements which call for a power supply voltage below 1 V. Projections for the 35 nm and 50 nm node are for a 0.75 mA/μm drive current for NMOS and 0.35 mA/μm drive current for the PMOS at a 0.5 to 0.6V power supply voltage and a subthreshold leakage < 10nA/μm for memory and < 80 to 160 nA/μm for logic. The nMOS the values presented nearly meet those required for microprocessor circuits at those nodes.
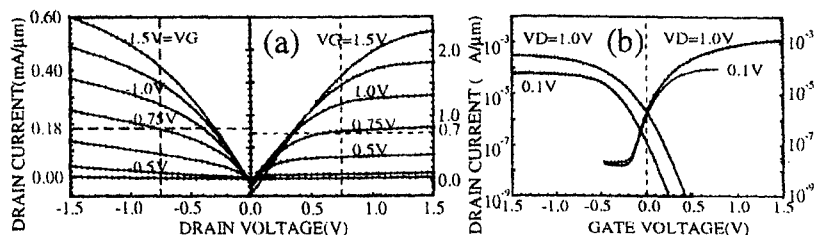
Figure 6. DC electrical performance data for an NMOS (positive voltages) and PMOS (negative voltages) transistor pair. For both, L_g=40 nm, $V_{tn} = -V_{tp} \sim 0.2$V, and t_{ox}=1.3nm for the nMOS and 1.5nm for the pMOS.

SIMULATION AND DISCUSSION

We have used our simulation program, PADRE, to predict the effect of linewidth variations on sub-threshold current for nMOS transistors with gate lengths below 40 nm. The model assumes a gate oxide of 1.3nm and the same process parameters incorporated in our scaled process described above. Figure 7 illustrates the dramatic increase that occurs in I_{off} at room temperature as the gate length is decreased down to 26 nm. We have plotted a large number of devices with gate lengths varying from 40 nm down to 26 nm in steps of 1 or 2 nm. A complete set is plotted for three different supply voltages 0.5 (left), 1.0 (middle), and 1.5 V (right), the probable useful range for circuits. We see that

at 1.5 V, where the I_{on} is most readily achievable, even the 40 nm transistors are nearly two orders of magnitude too "leaky" to meet the projected standard. Nearly a factor of ten improvement in I_{off} is obtained by decreasing the supply voltage to 0.5V. However, the accompanying slope increase associated with this decrease in supply voltage makes tolerances for variation in linewidth even tighter. We note that none of these devices meet the SIA technology roadmap for subthreshold leakage current (10 nA/μm) for memory but that the lower transistor count required for microprocessor type applications lowers the requirements on I_{off} to 160 nA/μm (50 nm node) and 80 nA/μm (35 nm node). These values of I_{on} and I_{off} can probably be met for nMOS with this process. Comparing the values found for the measured transistors described in Fig. 6 we see that there is still some room for improvement in the process. The pMOS performance still exhibits a performance gap, however.
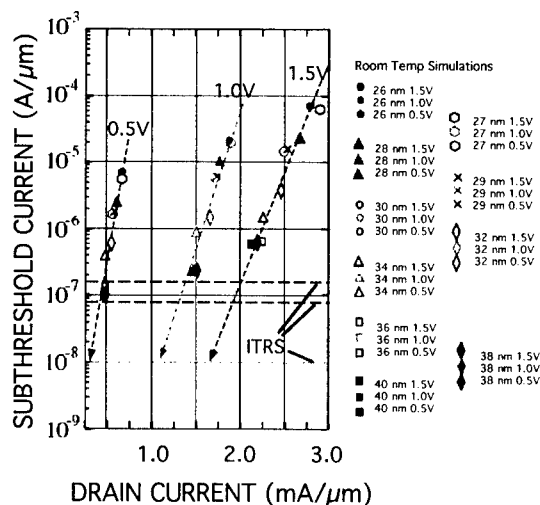
Figure 7. Simulation of subthreshold current variation with drain current for nMOS transistor with gate lengths from 40 nm down to 26 nm for three different power supply voltages, 0.5 V (leftmost), 1.0 V (middle), and 1.5 V (rightmost). The indicated lines are the estimated requirements from the SIA Technology Roadmap for microprocessor chips at the 50 nm and 35 nm nodes.

The plots in Fig. 7 also illustrate the critical role that linewidth variations may play in the practicality of transistor designs. The logarithmic vertical scale causes small variations in gate length to result in large departures from acceptable leakage currents. Ultimately this affects the density of transistors which can packed into a given chip. As an example, at a 1 V power supply voltage, if one specifies a maximum leakage current variation of a factor of 2, that implies a limit in gate length variation of 2 nm. This represents a control of about 5% on gate length. This same principle also applies to

290

variations within a single gate, therefore making edge roughness during lithography and pattern transfer especially stringent, especially if low power supply voltages (e.g., 0.5 V) are adopted. It may be that high performance transistor below 40nm can only be inserted sparingly in VLSI designs or that they will be limited to logic applications with fewer transistor counts.

SUMMARY and CONCLUSIONS

We have demonstrated an improved MOS transistor process capable of producing high performance devices down to $L_g = 40$ nm with an estimated $L_{eff} = 20$ nm. Direct SCM measurements of L_{eff} for our n and p channel MOSFETs determine that a best effort may allow $L_g = 30$ nm to produce working transistors. To this end we have explored the various gate technologies needed to fully exploit this capability. Using direct write e-beam lithography we have used the NEB series of resists from Sumitomo as a high throughput, high resolution candidate, to produce suitable resist profiles down to 29 nm. The gate stack for the " 30 nm gate process" comprises several thinner layers to accomodate a less aggressive RIE sequence thereby permitting formation of nearly vertical profiles while stopping on gate oxides ~1 nm thick. The etch has successfully demonstrated gate formation down to 35 nm. We have presented device results which show high performance nMOS and pMOS transistors with gate lengths of 40 nm. Further work will be needed to simultaneously meet the high drive current and low leakage current requirements dictated by the ITRS projections, however. Simulations of leakage current in NMOS transistors scaled even further to gate lengths in the range 26 to 40 nm and with power supply voltages from 0.5 to 1.5 V predict greater difficulty to satisfy the SIA required leakage current specification. The simulations clearly indicate that small variations in gate length will result in large departures from acceptable leakage currents, making a significant process control challenge for gate definition technology.

REFERENCES

1. G. Timp, A. Argarwal, F.H. Baumann, T. Boone, M. Buonanno, V. Donnelly, M. Green, H. Gossmann, D. Jacobson, R. Kleiman, A. Kornblit, F. Klemens, J. T-C. Lee, W. Mansfield, S. Moccio, M.L. O'Malley, J. Rosamilia, J. Sapjeta, P. Silverman, T. Sorsch, W.W. Tai, D. Tennant, B. Weir, IEDM Technical Digest 930 (1997).
2. D. Tennant, F. Klemens, T. Sorsch, F. Baumann, G. Timp, N. Layadi, A. Kornblit, B.J. Sapjeta, J. Rosamilia, T. Boone, B. Weir, and P. Silverman, J. Vac. Sci. Technol. B 15 (6), (1997).
3. D. Tennant, G.L. Timp, L.E. Ocola, M. Green, T. Sorsch, A. Kornblit, F. Klemens R. Kleiman, Y.O. Kim, W. Timp, (to be published) J. Vac. Sci. Technol. B (1999).
4. L.E. Ocola, C.J. Biddick, D.M. Tennant, W. K. Waskiewicz, and A.E. Novembre, J. Vac. Sci. Technol. B 16, 3705 (1998).
5. L.E. Ocola, D. Tennant, G. Timp and A. Novembre, (to be published) J. Vac. Sci. Technol. B (1999).
6. S. Thompson et al., Technical Digest of IEEE VLSI Tech Symp., 132(1998).
7. R.N. Kleiman, M.L. O'Malley, F.H. Baumann. J.P. Garno, W.G. Timp, Technical Digest of IEEE VLSI Tech Symp.,138(1998).
8. W.G. Timp, M.L. O'Malley, R.N. Kleiman, J.P. Garno, Technical Digest IEEE Intl. Electron Devices Meet.,555(1998).

9. D. Muller, T. Sorsch, S. Moccio, F. Baumann, K. Evans-Lutterodt, and G.L. Timp, Nature (to be published) (1999).
10. J.B. Neaton, D.A. Muller, and N.W. Ashcroft, Phys. Rev. Lett., (in press) (1999).
11. G. Timp, K.K. Bourdelle, J.E. Bower, F.H. Baumann, T. Boone, R. Cirelli, K. Evans-Lutterodt, J. Garno, A. Ghetti, H. Gossmann, M. Green, D. Jacobson, Y. Kim, R. Kleiman, F. Klemens, A. Kornblit, C. Lochstampfor, W. Mansfield, S. Moccio, D.A. Muller, L.E. Ocola, M.L. O'Malley, J. Rosamilia, J. Sapjeta, P. Silverman, T. Sorsch, D. Tennant, W. Timp, B.E. Weir Technical Digest IEEE Intl. Electron Devices Meeting, 615 (1998).
12. G. Timp, A. Argarwal, K.K. Bourdelle, J.E. Bower, T. Boone, A. Ghetti, M. Green, J. Garno, H. Gossmann, , D. Jacobson, R. Kleiman, A. Kornblit , F. Klemens, S. Moccio, M.L. O'Malley, L.E. Ocola , J. Rosamilia, J. Sapjeta, P. Silverman, T. Sorsch, W. Timp, D. Tennant, Technical Digest IEEE Intl. Electron Devices Meeting, 1041(1998).

NANOSTRUCTURE FABRICATION USING ELECTRON BEAM

SHINJI MATSUI
Laboratory of Advanced Science and Technology for Industry, Himeji Institute of Technology
3-1-2 Koto, Kamigori, Ako, Hyogo 678-1205, JAPAN, matsui@lasti.himeji-tech.ac.jp

ABSTRACT

Nanofabrication strategies developed by using electron beam (EB) are described. Ten-nm structures of organic positive and negative resist patterns have been achieved by using a commercially available EB lithography system. As one of the applications of EB nanolithography to nanodevices, an electrically variable shallow junction MOSFET (EJ-MOS) is described. As a novel approach, material-wave nanotechnology using de Broglie wave has been developed. Line and dot patterns with 100-nm periodicity were exposed on a PMMA resist by EB holography with a thermal field-emitter gun and an electron biprism. This technique allows us to produce nanoscale periodic patterns. Furthermore, the possibility of nanostructure fabrication by atomic-beam holography has been demonstrated by using a laser-trap technique and a computer-generated hologram made by EB lithography.

INTRODUCTION

Electron beam (EB) lithography is the most widely used and versatile lithography tool for fabricating nanostructure devices. Because of the availability of high-quality electron sources and optics, EB can be focused to diameters of less than 10 nm.

Figure 1 shows the resolution of various resists, which were confirmed by experiments with electrons and ions. Minimum sizes of 8 nm for PMMA [1,2], 10 nm for ZEP (Nippon Zeopn Co.) positive resists [3], 20 nm for SAL601 (Shipley Co.) [4], and 10 nm for CALIXARENE negative resists [5, 6] have been demonstrated using EB lithography. Nano-scale patterns have also been written in inorganic resists such as AlF_3, NaCl, and SiO_2 using STEM [7, 8] and SEM [9]. Furthermore, carbon contamination patterns of 8 nm have been fabricated with SEM [10], and 8-nm PMMA patterns have been demonstrated by using Ga^+ FIB [11].

In this paper, nanofabrication using EB and its application to devices are described.

ELECTRON BEAM NANOLITHOGRAPHY

10-NM LITHOGRAPHY USING ORGANIC RESIST

Nanodevice fabrication requires not only high resolution but also high overlay accuracy. High-speed exposure very effectively meets the requirements because overlay accuracy is improved due to less beam drift on the nanometer scale. Moreover, it enables the use of a highly sensitive resist such as ZEP520 [12], which has sufficient resolution and high dry etching durability for nanolithography. A 10-nm-scale resist pattern was obtained using ZEP520 positive resist. The ZEP520 resist was spin-cast onto a Si wafer (layer thickness of 50 nm), and prebaked at 200 ℃. After EB exposure, the ZEP520 was developed with hexyl acetate for 2 min and rinsed with 2-propanol. Figure 2 shows a ZEP520 resist pattern, in which the lines are 10 nm wide and have a pitch of 50 nm [3].

CALIXARENE has a cyclic structure, as shown in Fig. 3, and works as an ultrahigh-

resolution negative EB resist [5, 6]. Such characteristics seem to be convenient for a nanodevice fabrication process. It is roughly a ring-shaped molecule with a diameter of about 1-nm. The basic component of CALIXARENE is a phenol derivative which seems to have high durability and stability, originating from the strong chemical coupling of the benzene ring. The threshold of sensitivity is about 800 μ C/cm^2, which is almost 20 times higher than that of PMMA. CALIXARENE negative resist exposure was carried out. A thirty nm-thick resist was coated on a bare Si wafer. After prebaking at 170 ℃ for 30 min, EB exposure was carried out and then the resist was developed in xylene for 20 s and was rinsed in IPA for 1 min.

The etching durability of CALIXARENE was tested using a DEM-451 (ANELVA Corp.) plasma dry-etching system with CF$_4$ gas. The etching rate of CALIXARENE is almost comparable to that of Si, and the durability is about four times higher than that of PMMA. This durability seems to be sufficient to make a semiconductor or a metal nanostructure.

Nanodot arrays are useful not only for quantum devices but also for studying exposure properties. In this experiment, the EB current was fixed to 100 pA at 50 kV accelerating voltage, for which the spot size is estimated to be about 5 nm. All the dot arrays were fabricated on Si substrates. The typical exposure dose (spot dose) was about 1x10^5 electrons/dot. Figure 4 shows typical dot array patterns having 15-nm diameter with 35-nm pitch.

Germanium pattern transfer is shown in Fig. 5. The 20-nm-thick Ge layer requires at least a 5-nm-thick CALIXARENE layer to be etched down, and the resist thickness was 30 nm. Figure 5(a) shows the line patterns of the resist on Ge film exposed at a line dose of 20 nC/cm. Delineation was done using the S-5000 (Hitachi Corp.) SEM with a beam current of 100 pA at a 30-kV acceleration voltage. A 10-nm-line width and a smooth line edge were clearly observed. This smoothness is the key point in fabricating quantum nanowires by etching processes. Figure 5(b) shows the transferred pattern treated by 1 min of overetching, followed by oxygen-plasma treatment to remove the resist residues. A Ge line of 7-nm width was clearly observed without short cutting. Narrowing by overetching is a standard technique to obtain a fine line, however, side-wall roughness limits the line width [13]. The smoothness of the CALIXARENE side wall enables the line width to be narrowed below the 10-nm region by overetching. CALIXARENE is a single molecule and thus is monodispersed with a molecular weight of 972. In contrast, other phenol-based resists have dispersive weights from 1000 to 100 000, which set a resolution limit. The molecular uniformity of CALIXARENE and its small molecular size is the origin of such surface smoothness and the resulting ultrahigh resolution.
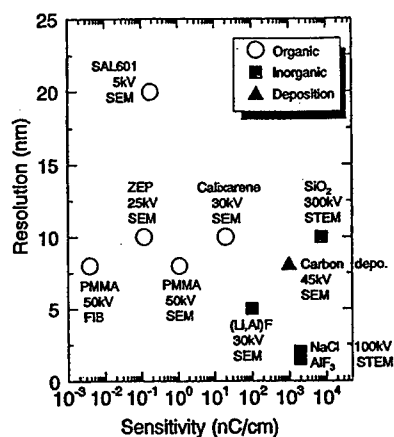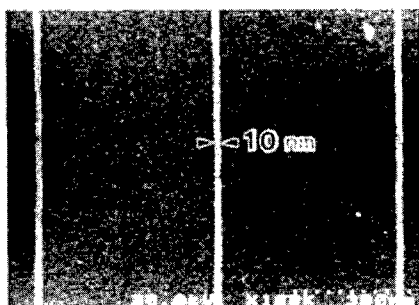
Fig. 1   Resolution of various resists
for electrons and ions.

Fig. 2   10-nm linewidth ZEP patterns.
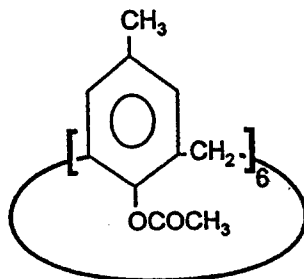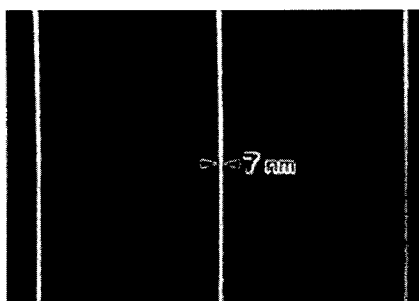

(a) 10 nm linewidth CALIXARENE pattern

Fig. 3   Structure of CALIXARENE.

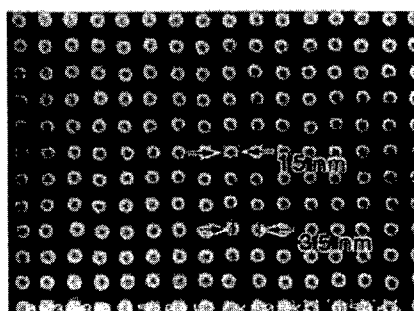(b) transferred 7-nm linewidth Ge pattern.

Fig. 4   CALIXARENE dot array patterns
with 15-nm diameter and 35-nm pitch.

Fig. 5   Pattern transfer to Ge.

14-NANOMETER-GATE-LENGTH MOSFETs

An electrically variable shallow junction MOSFET (EJ-MOS) with an ultra-shallow source/drain junction has been fabricated to investigate transistor characteristics and physical phenomena in ultrafine gate MOSFETs [14].

Figure 6 shows a schematic cross section of the EJ-MOSFET. The lower gate, which corresponds to the "gate" in conventional MOSFETs, controls the drain current. A positive upper-gate bias induces source/drain regions at the silicon surface. Because the source/drain regions are electrically formed, they are extremely shallow, typically 5 nm deep. The EJ-MOSFET was fabricated in a similar way as conventional Si-MOSFETs. To suppress short-channel effects (SCEs) caused by the lateral expansion of the depletion layers, a relatively high boron concentration of 2×10^{18} cm^{-3} was used within the substrate. The boron concentration was controlled by means of the boron ion implantation and the thermal drive-in. The n^+ regions were formed by arsenic ion implantation. A gate oxide (tox = 5 nm) was formed by thermal oxidation and a 40-nm-thick poly-Si layer was grown by chemical vapor deposition (CVD). Phosphorus was doped into the poly-Si film in a $POCl_3$ atmosphere. The ultrahigh-resolution EB resist CALIXARENE [5, 6] was spin-coated onto the poly-Si film and EB direct writing with a 5-nm diameter and a 50-kV acceleration energy was performed. After the developing procedure, the resist pattern was transferred to the poly-Si film by reactive ion etching (RIE) with CF_4 gas.

Figure 7 shows a TEM cross-sectional view of a 14-nm long poly-Si lower gate. The lower gate was well defined. The 20-nm-thick intergate oxide layer was grown by CVD, which was followed by N_2 annealing and H_2 annealing. Finally, the upper gate and source/drain electrodes were formed by Au/Al evaporation.

The electrical characteristics of the fabricated devices with gate length (L_{Lg}) ranged from 14 to 98nm at 300 K. To form source/drain regions, an upper-gate voltage (V_{UG}) of 7 V was applied. Figure 8 shows the I-V characteristics of a 14-nm -gate-length device. Although the device does not exhibit clear saturation characteristics at a high drain bias, a transistor operation in the 14-nm gate length was confirmed by this experiment.
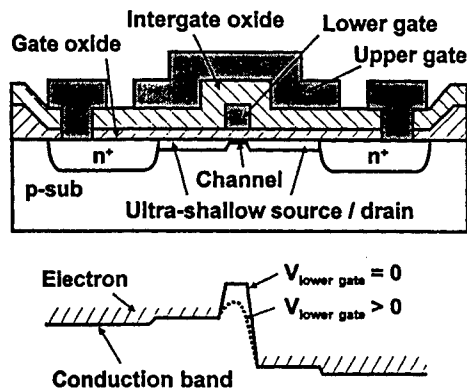
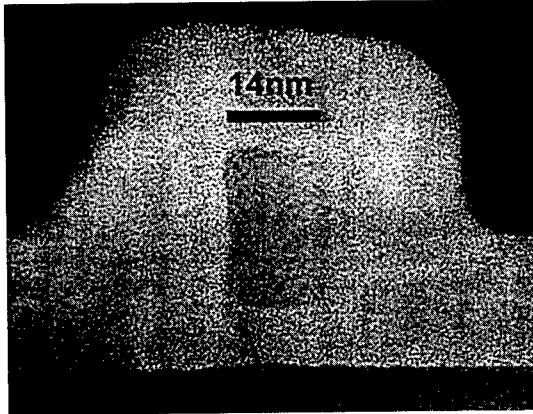Fig. 6 Schematic cross section of an EJ-MOSFET.

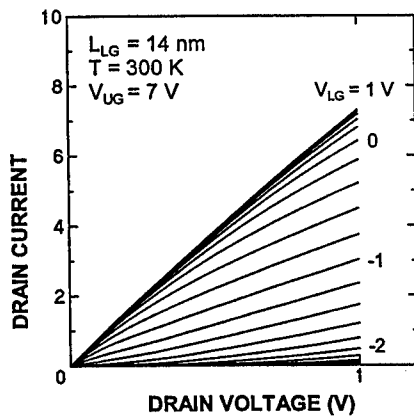Fig. 7 TEM cross-section view of a 14-nm-gate-length poly-Si lower gate.

Fig. 8 I-V characteristics of a 14-nm-gate-length EJ-MOSFET at 300 K.

NANOTECHNOLOGY USING A DE BROGLIE WAVE

ELECTRON BEAM HOLOGRAPHY

Holographic lithography has an advantage that it can produce a number of periodic patterns simultaneously. Electron holographic lithography was applied to nanofabrication. Electron interference fringes were recorded on a PMMA resist by using of a W(100) TFE gun and an electron biprism, and the fabricated patterns were observed with a conventional TEM and AFM [15, 16].

The electron optics of TEM with a W(100) TFE gun for electron holographic lithography is schematically illustrated in Fig. 9. An electron beam of 40 kV is focused above an electron biprism with two condenser lenses. The Möllenstedt-type electron biprism is constructed of two grounded plane electrodes and a fine-wire electrode, called a filament, between them. When a positive voltage, V_B, is supplied to the filament, electron waves traveling on both

297

sides of the filament are deflected and superimposed to form interference fringes on an observation plane. A Pt wire of $0.6\,\mu$m in diameter was used as the filament. As is well known, two coherent waves overlapping at an angle of θ produce interference fringes with spacing, s, represented by

$$s=(\lambda/2)/(\sin(\theta/2)) \qquad (1)$$

where λ denotes the de Broglie wavelength of 6.0×10^{-3} nm in this case.

Figure 10 shows four-wave interference fringes through an X-biprism. Setting an X-biprism below two condenser lenses instead of the Möllenstedt-type biprism, which has two filaments placed normal to each other and both are supplied with V_B, four coherent waves produce fringes like a checkerboard below the intersection of filaments, with the same spacing, s, as given by Eq. (1). Thus, electron holographic lithography would be, in principle, capable of generating lines and dot patterns whose minimum spacing is $\lambda/2$, which is comparable to the crystal lattice spacing.

A 30-nm-thick PMMA film, spin-cast on a 50-nm-thick self-supporting SiNx membrane and prebaked at 170 ℃ for 20 min, was set on the observation plane 70 mm below the biprism. The self-supporting nitride (SiN) membrane was about 60 μm square and used to place the PMMA below interference fringes appropriately. Electron exposure to produce line patterns was carried out for 18 s with a dose of 25 μC/cm^2 which was measured at the fringe part. Then, the PMMA was developed in MIBK: IPA = 1:3 for 1.0 min and rinsed in IPA for 30 s. Similarly, PMMA dot patterns were exposed, at half the dose as that for the line patterns, in order to maintain whole dots. The electron exposure to produce dot patterns was carried out for 9.0 s with a dose of 13 μC/cm^2. The PMMA was developed in MIBK : IPA for 3.0 min and rinsed in IPA for 1.0 min.

Figure 11(a) shows interference fringes of the Möllenstedt-type electron biprism which was magnified 530 times by the lenses below the observation plane and recorded on a photoplate with 1.0 s exposure. Figure 11(b) shows the AFM image of the same interference fringes as those in Fig. 11(a), which was recorded on PMMA. The thickness of PMMA is represented by a photo-contrast in Fig. 11(b), and the thicker PMMA corresponds to the brighter part of the image. The supplied voltage to the filament of the electron biprism, V_B, was 5.3 V and the spacing of fringes, s, was 108 nm in Figs. 11(a) and 11(b). Figure 12(a) shows interference fringes of the X-biprism magnified and recorded on a photoplate, and Fig. 12(b) shows the AFM image of interference fringes recorded on PMMA. The supplied voltage to the filament, V_B, was 5.0 V and the spacing of fringes, s, was 125 nm in Figs. 12(a) and 12(b). In Fig. 12(a), dot patterns are found at the intersection where four-wave interference occurred and line patterns around the dot patterns where two-wave interference occurred. In Fig. 12(b), about 10x10 dots clearly appear, but lines are not observed, owing to the reduction of dose. Consequently, Figs. 11(b) and 12(b) show that line and dot patterns were fabricated successfully, and the dose needed for lines is about twice as that for dots. More precise fabrication would be possible by optimizing the dose.

In order to produce patterns finer than 100-nm in period, a larger overlapping angle θ, i.e. a larger voltage supplied to the filament V_B, should be selected. A simple assessment suggests that the spacing, s, becomes 1 nm when V_B is 2.4-kV with the same electron optics. Carbon contamination line patterns with a period of 20-nm was fabricated with a 30-kV SEM [17].
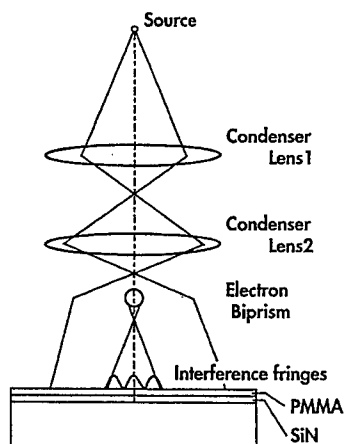
Fig. 9   Scheme of electron optics of
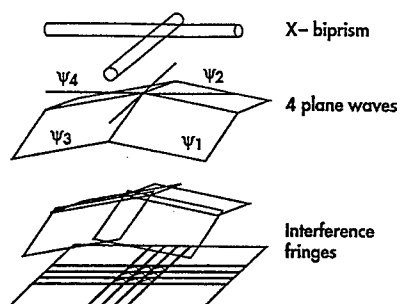TEM for electron holographic lithography.

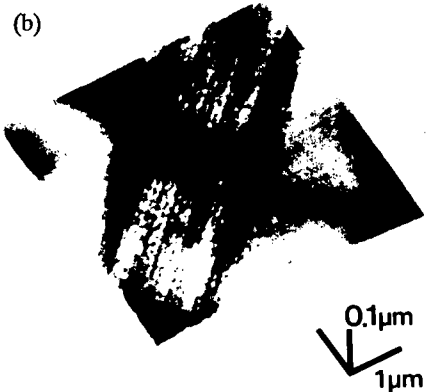Fig. 10   Four-wave interference fringes
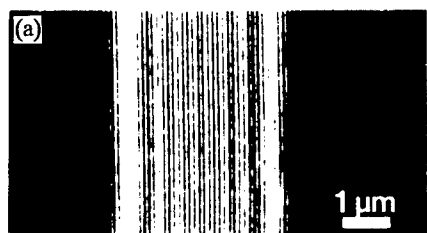through an X biprism.

Fig. 11 V_B: 5.3 V and s: 108 nm
  (a) Two-wave interference fringes
magnified and recorded on a photoplate.
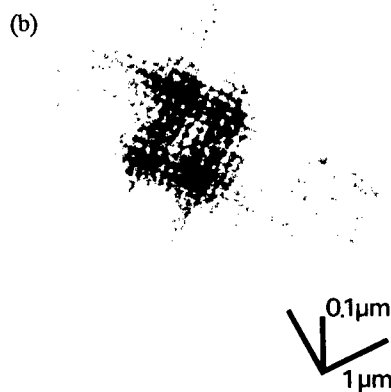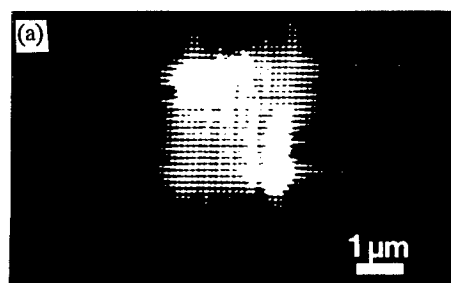 (b) Interference fringes corresponding
    to (a) recorded on PMMA.

Fig. 12 V_B: 5.0V and s: 125 nm
  (a) Two- and four-wave interference
fringes magnified and recorded on a photoplate.
  (b) Interference fringes corresponding
    to (a) recorded on PMMA.

ATOMIC-BEAM HOLOGRAPHY

Atomic manipulation based on a holographic principle has been demonstrated by using a laser trap technique and a computer generated hologram (CGH) made by EB lithography [18]. One approximation of a CGH is the binary hologram, in which the hologram takes a binary value, either 100% transparent or 100% opaque. The 100% transmission area of the binary hologram is formed by cutting out the pattern on a film. A monochromatic atomic wave reconstructs an atomic pattern by passing the hologram.

The hologram used in this experiment was a Fourier hologram, which produced the Fourier-transformed wavefront of the object. When the hologram is illustrated with a plane wave, the far-field pattern of the diffracted wave produces an image of the object. The object used in this experiment was a transparent F-shaped pattern, in which the transparent portion had a constant amplitude and random phase distribution. The object was represented by the complex transmission amplitude at points on a 128x128 matrix covering the F-shape pattern. The two-dimensional array of numbers was Fourier-transformed using a fast Fourier tranform (FFT) algorithm, and resulted in a 128x128 complex areas (cells) of the Fourier hologram. The transmission function of each cell of the hologram was expressed by a matrix of 4x4 subcells.

A 100-nm-thick SiN membrane was used for the hologram. The binary pattern was transferred to a ZEP resist on the SiN membrane by an EB writing system. Subsequent CF_4 plasma etching created through-holes in the membrane. A scanning electron micrograph of the hologram is shown in Fig. 13. The size of the subcell was 0.3x0.3 μ m square, so the size of the entire hologram was 153.6x153.6 μ m. To increase the intensity of the deflected beam, the same pattern was repeated 10 times along the x and y directions, making the overall size of the hologram 1.5x1.5 mm.

A schematic diagram of this experiment is shown in Fig. 14. The ultra-cold Ne atomic beam was generated by the method reported in [19]. The cloud of Ne atoms in the trap was $\sim$ 0.3 mm in diameter, and the one-directional average velocity of the atoms was 20 cm s^{-1}. The hologram was placed 40 cm below the trap and was mounted on the top of a 0.2-mm-diameter diaphragm. The size of the diaphragm limited the resolution of the image of the Fraunhofer hologram. The position of the hologram was not adjusted because any small portion of the hologram could produce the same image. The average atomic velocity at the hologram was 2.8 ms^{-1}, corresponding to a de Broglie wavelength λ of 7.1 nm. The acceleration due to gravity reduced the relative velocity spread to $\sim$0.28%. To detect the Fraunhofer diffracted pattern from the hologram, MCP (multi-channel plate) detector was placed 45 cm below the hologram. Figure 15(a) shows the reconstructed F-pattern. The data was accumulated for 10 h, and the total atom number of spots on the figure was 6x10^4. Figure 15(b) shows another example of reconstructed patterns which represents characters of "atom, Ne, and ψ".

In this experiment, a focusing lense for imaging was not used, but it is possible to combine the function of a focusing lens into the hologram [20]. In such a hologram, the resolution is determined by the same rule as applies to an optical lens. The binary hologram does not control the phase and amplitude of the wave inside a hole. Atomic beam holography has the potential to make not only a binary pattern but also an analog (gray scale) pattern. The minimum feature size expected is theoretically the same as the wavelength, i.e., several nanometers [21, 22].

Fig. 13   Binary CGH hologram on SiN membrane made by EB lithography.
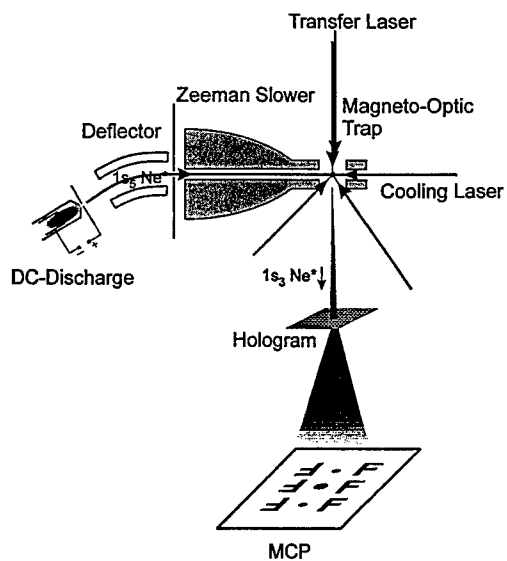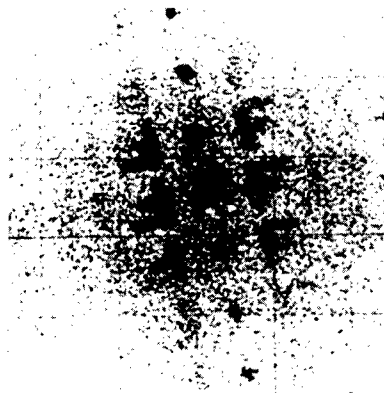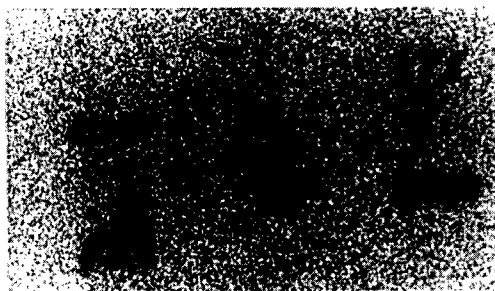

Fig. 14   Experimental apparatus of atomic beam holography.

(a) " F " pattern.

(b) " atom, Ne, and Ψ " pattern.

Fig. 15   Reconstructed image .

SUMMARY

Nanofabrication and its application to nanodevices using EB have been demonstrated. Electron beam lithography with a commercially available machine using an organic resist has already achieved 10 nm features, which is the same size as a virus. As a new approach, material-wave nanotechnology using electron-and atomic-beam holography has been developed. This technique allows nano- and atomic- scale structures to be produced simultaneously. As one of the applications to nanodevices of EB lithography, a 14-nm-gate Si MOSFET device has been demonstrated by EB nanolithography using an organic resist.

ACKNOWLEDGEMENTS

302

REFERENCES

1. F. Emoto, K. Gamo, S. Namba, N. Samoto, and R. Shimizu, Jpn. J. Appl. Phys., **24**, p. L809 (1989).
2. W. Chen and H. Ahmed, Appl. Phys. Lett., **63**, p. 1116 (1993).
3. K. Kurihara, K. Iwadate, H. Namatsu, M. Nagase, H. Takenaka, and K. Murase, Jpn. J. Appl. Phys., **34**, p. 6940 (1995).
4. T. Yoshimura, Y. Nakayama, and S. Okazaki, J. Vac. Sci. Technol., **B10**, p. 2615 (1992).
5. J. Fujita, Y. Ohnishi, Y. Ochiai, and S. Matsui, Appl. Phys. Lett., **68**, p. 1297 (1996).
6. J. Fujita, Y. Ohnishi, Y. Ochiai, E. Nomura, and S. Matsui, J. Vac. Technol., **B14**, p. 4272 (1996).
7. M. Isaacson and A. Murray, J. Vac. Sci. Technol., **19**, p. 1117 (1981).
8. D. R. Allee and A. N. Broers, Appl. Phys. Lett., **57**, p. 2271 (1990).
9. J. Fujita, H. Watanabe, Y. Ochiai, S. Manako, J. S. Tsai, and S. Matsui, Appl. Phys. Lett., **66**, p. 3065 (1995).
10. A. N. Broers and W. W. Molzen, J. J. Cuomo, and N. D. Wittles, Appl. Phys. Lett., **29**, p. 596 (1976).
11. R. L. Kubena, J. W. Ward, F. P. Stratton, R. J. Joyce, and G. M. Atkinson, J. Vac. Sci. Technol., **B9**, p. 3079 (1991).
12. T. Nishida, M. Notomi, R. Iga, and T. Tamamura, Jpn. J. Appl. Phys., **31**, p. 4508 (1992).
13. T. Yoshimura, H. Shiraishi, J. Yamamoto, and S. Okazaki, Appl. Phys. Lett., **63**, p. 764 (1993).
14. H. Kawaura, T. Sakamoto, Y. Ochiai, J. Fujita, and T. Baba, "Extended Abstract of the 1997 International Conference on Solid State Devices and Materials," Hamamatsu, Japan, 1997, pp. 572-573.
15. K. Ogai, S. Matsui, Y. Kimura, and R. Shimizu, Jpn. J. Appl. Phys., **32**, p. 5988 (1993).
16. K. Ogai, Y. Kimura, and R. Shimizu, J. Fujita, and S. Matsui, Appl. Phys. Lett., **66**, p. 1560 (1995).
17. S. Fujita, S. Maruno, H. Watanabe, Y. Kusumi, and M. Ichikawa, Microelectronic Engineering, **30**, p. 435 (1996).
18. J. Fujita, M. Morinaga, T. Kishimoto, M. Yasuda, S. Matsui, and F. Shimizu, Nature, **380**, p. 691, (1996).
19. F. Shimizu, K. Shimizu, and H. Takuma, Opt. Lett., **16**, p. 339 (1991).
20. M. Morinaga, M. Yasuda, T. Kishimoto, F. Shimizu, J. Fijita, and S. Matsui, Phys. Rev. Lett., **77**, p. 802 (1966).
21. J. Fujita, K. Kishimoto, M. Morinaga, S. Matsui, F. Shimizu, J. Vac. Sci. Technol., **16**, p. 3855 (1998).
22. T. Kishimoto, J. Fujita, S. Mitake, and F. Shimizu, Jpn. J. Appl. Phys., **38**, p. L683 (1999).

NANOSCALE ELECTRON-BEAM PROCESSES AND
ITS APPLICATION TO NANODEVICES

Masanori KOMURO
Electrotechnical Laboratory, Tsukuba, Ibaraki, 305-8568, Japan, komuro@etl.go.jp

ABSTRACT

In this paper, electron beam (EB) lithography and direct processes are summarized for application to nanometer-scale electron devices such as single electron transistor. As decreasing line width in lithography, the delineated patterns has fluctuation of line width, which is so-called line-edge-roughness. It is kwon that such a roughness is caused by aggregates of resist molecules. Therefore to avoid the rougphness to make smooth line edge, we have to use rather low molecular weight resist materials. As one of such candidates, EB exposure characteristics of thermally oxidized SiO_2 film are described. Although the sensitivity of the resist is about a few C/cm^2 which is lower than conventional resists, it is possible to delineate fine line and space pattern with 15 nm pitch and 5 nm width. This technique is extended to make miniature metal/insulator/metal junctions using SiO_2/Si bilayer resist system and the following metal liftoff process. Metal layer is directly deposited on SiO_2 substrates in WF_6 gas ambient simultaneously with EB irradiation. The resistivity of the deposited film is about $6x10^{-4}$ Ωcm depending on hydrocarbon contamination of the substrate itself. We can make the deposited lines with line-width of about 10 nm using 3 nm diameter of the incident EB. From current-voltage characteristics for single tunnel junctions with various tunnel resistances, the barrier height is estimated to be about 0.2 eV. This result indicates clearly the junction properties can be controlled at least with the accuracy of minimum deflection increment of the EB system used here. It is successfully observed that single-electron-transistor produced by EB-induced deposition exhibits Coulomb oscillation at temperature of 230 K.

1.INTRDUCTION

Shrinkage of electron devices dimension has been proceeding in industrial and also in advanced research and development. The gate length of MOS transistor for recent LSI is pursuing to be less than 130 nm dimension and 10-nm gate length MOS transistor has been also successfully produced by electron beam lithographic procedures. On the other hand nanometer scale devices such as single-electron transport is expected to be future integrated circuits such as memory and logic, probably, which will be combined with CMOS systems. Thus the lithography technology required for development of advanced LSI and also nano-devices is strongly needed. There have been a lot of reports to produce miniature structures with nanometer dimension such as self-assembled material growth technique and scanning probing methods. However electron beam (EB) lithography is most powerful tool and technique because of its finely focused performance, its flexibility for pattern delineation and rather high writing speed. Resist materials exposed to EB is important to get sharp and smooth line edge and also to transfer patterns with fidelity such as etching and deposition. When the fine line patterns are written on the conventional polymer resist, the edge of the line becomes rough with a standard deviation of about 2-4 nm partly due to instrumentation error which is called nano-edge roughness. Several research groups have investigated the origin of this roughness. The NTT group has revealed that the cause of nano-edge roughness is structure of granular and/or aggregates of resist molecules with about 20-30-nm diameter [1-3]. They have also showed that the size of aggregates is increased with the increase of molecular weight, so that a resist film with lower molecular weight may indicate smaller roughness. Thus the requirement for nanometer scale lithography is development of high-

resolution resist system in addition to development of fine EB exposure system.

In this review article, EB exposure properties of thermally grown SiO2 film and its application of metal liftoff process for producing metal/insulator/metal (MIM) tunnel junctions are described [4-9]. In addition, EB induced direct deposition technique for MIM structures are summarized [10-14], which has advantages of process simplicity, without etching or metal liftoff and of the independent controllability of junction parameters such as capacitance and resistance. In EB-induced deposition, Matsui et al. [15,16] reported that metallic films and 15 nm diameter W rods were produced using electron-stimulated dissociation of adsorbed precursor molecules such as WF_6 and SiH_2Cl_2, although these reports did not measure electrical properties. Koops et al. [17,18] measured the resistivity of 10^{-2} Ωcm and 1 Ωcm deposition using Me_2Au (tfac) and $CpPtMe_3$ gases as precursor molecules and degradation was assumed due to the crystallite structure of the deposit and inclusion of C and O from the legand of the precursor molecule and from residual ambient.

2. EXPERIMENT

The EB exposure system used here has a sample chamber evacuated down to 4×10^{-9} Torr, and a beam diameter of about 3 nm measured at full width at half maximum at a typical beam current of 100 pA [19]. A line exposure to make a single-wire was conducted with a minimum increment of 2.5 nm in deflection. SiO_2 with a thickness of 0.32 μm was prepared by heating Si(100) in dry oxygen at 1100 ℃ for 4 h. The samples were uniformly irradiated with a 20 keV EB with doses ranging from 0.1 to 2 C/cm^2, where about 30 μm squares were irradiated with an EB by raster scanning. The thickness of SiO_2 is much smaller than the range of about 2.6 μm of a 20 keV electron in SiO_2. After EB irradiation, samples were processed in a barrel-type oxygen plasma asher for 3 min to remove the contamination layer grown by the EB irradiation. The oxygen pressure was 0.9 Torr and the RF power was 100 W. Then, the samples were dipped in various HF based solutions (listed in Table I): NH_4F (40%), HNO_3 (70%), or aqueous saturated KOH (at 70 ℃). The etching processes, except for in KOH, were carried out at room temperature. Further studies on the composition dependence were performed for buffered HF (BHF) solutions of which the compositions were 1 mol/l HF with 0.125 to 8 mol/l NH_4F. The etched steps developed in the solutions were measured by a surface profilometer.

The nozzle was also installed in the sample chamber of the EB system, which enabled us to introduce reactive gas such as WF_6 gas up to about 2×10^{-6} Torr. The nozzle exit was located about 1 mm away from the substrate surface so that the ambient gas pressure

Table I   Composition of solutions and calculated concentration for SiO2 etching.

| | | Quantity per liter | | | Calculated concentrations | | Each rate of unirradiated |
		50% HF (cm^3)	70% HNO_3 (cm^3)	40% NH_4F (cm^3)	[HF] (mol/l)	[HF_2^-] (mol/l)	SiO_2 (nm/min)
A)	Buffered HF 1	25		30	4.3×10^{-1}	2.9×10^{-1}	12.8
B)	P-etch	46	31		1.3	4.9×10^{-2}	12.0
C)	Modified P-etch	42	125		1.2	1.1×10^{-2}	10.5
D)	Diluted HF	10			2.3×10^{-1}	2.2×10^{-2}	2.4
E)	HF+HNO_3	10	990		2.9×10^{-1}	9.5×10^{-5}	9.5
F)	Buffered HF 2	100		900	3.8×10^{-2}	2.9	78.0

determined basically molecular flux on the surface. We used Au/Cr electrodes with a spacing of 0.8 μm on 0.2 μm-thick SiO_2 on a Si wafer in order to measure the current-voltage (I-V) characteristics of the deposited film. After depositing W films, we studied the shape of deposits mainly using Atomic Force Microscopy (AFM) with contact mode operation, and measured the I-V characteristics at 300 and 230 K in a vacuum of 10^{-6} Torr.

3.INORAGANIC RESIST PROCESS

3.1 Exposure Characteristic of SiO_2 resists

The dependence of the selectivity on the EB dose for various solutions is shown in Fig. 1, where the selectivity means the ratio of etch rate at EB irradiated area to that of non-exposed area. The selectivities are saturated at 1.6 to 3.3 at a dose of about 2 C/cm^2 for HF-based solutions while it is almost unity for aqueous KOH. The sensitivity for

Fig. 1   Selectivity of SiO2 film as a function of EB dose.

various solutions used here does not change at all. Since neither irradiated nor unirradiated areas are etched for NH_4F and HNO_3, it is found that the main species, which attack irradiated SiO_2, are [HF] and/or [HF_2^-] similarly for unirradiated SiO_2 [20,21]. Table I lists the concentrations of [HF] and [HF_2^-] calculated by using the equilibrium state of HF solution. Solution A, which shows the highest saturated selectivity in our experiment, is composed of [HF] and [HF_2^-] in nearly equal quantities, while solutions B-E, mainly composed of [HF], show intermediate selectivity, and solution F, mainly composed of [HF_2^-], shows the lowest selectivity. We can see that the selectivity is improved with appropriate compositions of [HF] and [HF_2^-]. The dependencies of the selectivity and the etch rate on composition for BHF solutions containing 1 mol/l HF are investigated. The etch rate of unirradiated SiO_2 is well described by the linear combination of [HF] and [HF_2^-] [20]. At a high concentration of NH_4F the etch rate of irradiated SiO_2 decreases while that of unirradiated SiO_2 saturates. As a result, selectivity decreases. Thus we find that the selectivity is the maximum for the mixture of [HF] and [HF_2^-] in nearly equal quantities. In order to predict the cross section of grooves fabricated by line exposure, we compared the results of experiment with the theoretical time-evolution curves of the cross section. The beam used here has a diameter of 0.1 μm, which is so large that the etched profile is observed, well. Figure 2 shows the comparison between the results of the experiments and calculations, where the left micrographs show the cross-sectional views of grooves developed in P-etch for 12 min and the right curves show the calculated profiles for an etching interval of 2 min. The calculation was carried out using a string model, where etching progresses normal to the surface under the relationship between selectivity and electron dose shown in Fig. 1. Here, we assume that the current density distribution is Gaussian, electrons are not scattered and energy deposition is constant regardless of the depth of the target. Using this simple model, the calculated profile agrees well with the experimental results for this range of linedoses.
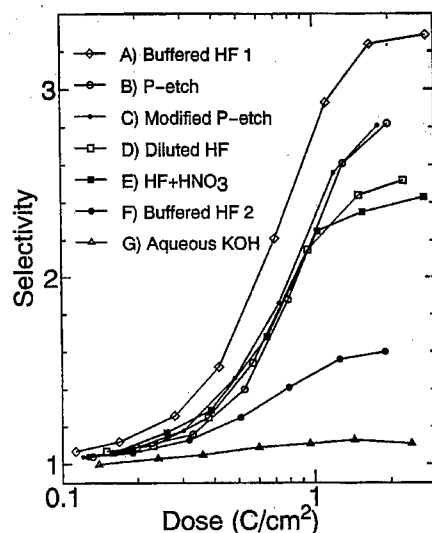
307
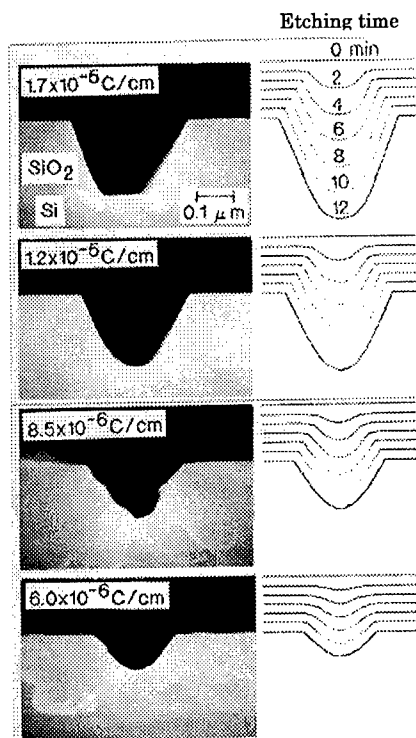
Fig.2 Comparison of cross-sectional view between experimental and calculated ones.

40 nm pitch lines
linedose = 0.61 nC/cm

15 nm pitch lines
linedose = 2.0 µC/cm

Fig.3 SEM pictures of 40 nm pitch lines on PMMA and 15 nm pitch lines on SiO_2.

1.EB Exposure

60 nm SiO
80 nm poly-Si
100 nm SiO
Si Substrate

2.Development & Selective Etching of poly-Si

3.Al Deposition & Oxidation

1) Al   2)Oxygen 3) Al
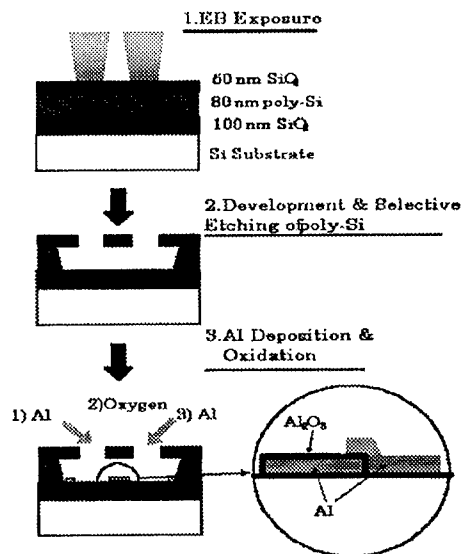
Fig.4 Process flow for producing MIM tunnel junction by metal liftoff and oxidation.

Figure 3 shows Scanning electron microscopy (SEM) pictures of line and space patterns written on PMMA resist and on SiO_2 film. In the PMMA picture, we can observe a large amount of edge roughness and also lines peeling from the substrate because of insufficient adhesion. On the other hand, the 5-nm wide pattern with 15-nm pitch can be clearly resolved in the SiO_2 film. Thus the SiO_2 resist is very powerful for nano-fabrication, although the sensitivity is not enough.

3.2 MIM junction

Using SiO_2 resist, we are attempting to produce MIM tunnel junction and single electron transistor. Process flow is illustrated in Fig. 4, where silicon-on-insulator substrate whose top surface is thermally oxidized is used. After EB irradiation and sequential etching of top SiO_2 film, the underlying Si layer (c-Si) is partially removed by using solution of NMD-3 (Tokyo Ohka Co. Ltd.) which is mainly composed of tetra-methyl-ammonium-hydroxide. This NMD-3 solution dissolves Si layer about 1000 times faster than SiO_2, so that we can

produce suspended mask structures for additional metal liftoff process. Vacuum evaporation of metals such as Al and Ti were carried out onto the mask, so that we can produce structures of metal dots and/or MIM through the oxidation in oxygen ambient. Plan-view of the suspended mask with 12 nm open window is shown in Fig. 5, where surrounding bright contrast region shows remained underlying c-SI. In Fig. 6, metal dots structure with about 20-nm diameter is indicated which shows Coulomb staircase at 140 K.
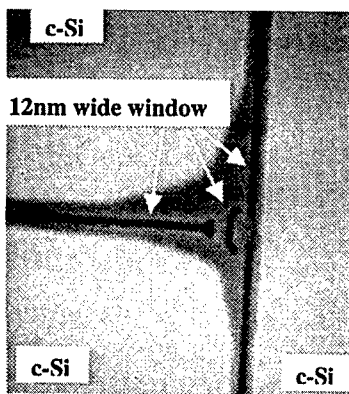
Fig.5 Plan-view of SiO2 mask in bilayer inorganic resist system.
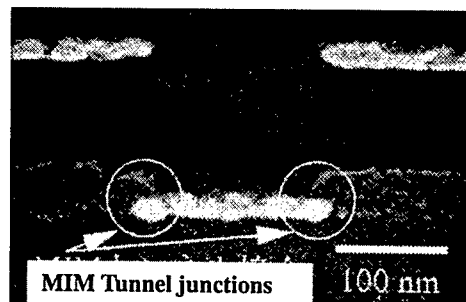
Fig.6 SEM picture of Ti/TiOx/Ti tunnel junction afer metal liftoff.

4. EB induced deposition
4.1 Single-wire conductance

Figure 7 shows dependence of single-wire conductance on the EB dose measured at 300 K and 230 K, where the width of wires were about 15 nm. Both curves rapidly increases in dose range between 8 and 15 pC/shot. On the other hand, peak wire thickness increases proportionally with the EB dose. The conductance at the two temperatures is not so different in doses exceeding 15 pC/shot. However, it decreases slightly at low doses less than 15 pC/shot when the temperature is lowered. Deposited film with doses exceeding 15 pC/shot has a constant resistivity estimated at $6 \times 10^{-4} \Omega$ cm from the cross section of the wire evaluated by AFM. Since wires produced by doses less than 15 pC/shot appear to be continuous wires as observed by AFM, the rapid decreases in conductance in Fig. 7 is caused by a
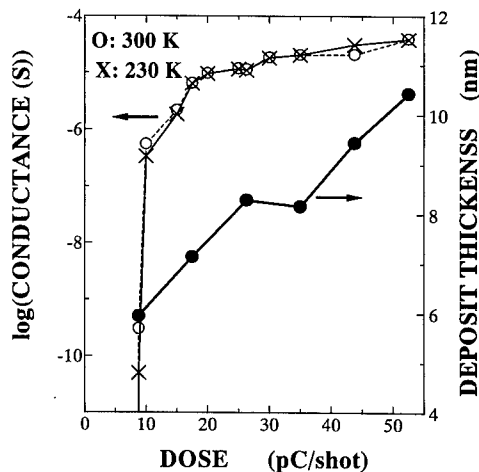
Fig. 7 Conductance and thickness of deposited wires by EB induced technique.

change in film property itself. Matsui et al. [16] reported Auger analysis of deposited film using WF_6 gas and a SiO_2 substrate, surmising that the depth profile of the deposited film composition consisted of W, F, and O probably from the substrate. Thus, a transition region less than 15 pC/shot is probably due to initial film growth, which mainly includes the O and F that causes low conductance. The decreased conductance at lower temperature in this dose region may also be due to the annihilation of carriers by trap states in the deposited film. Note that wire conductance does not change with the temperature decrease at higher doses, which lets us measure single-electron transport phenomena in this temperature region.
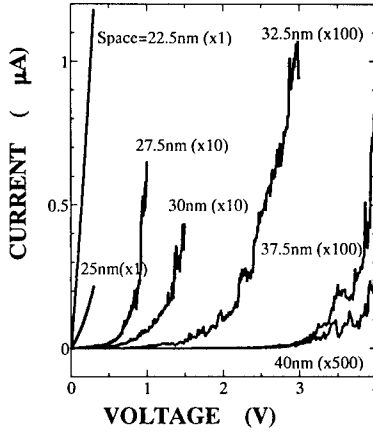
Fig. 8 I-V characteristics of single tunnel junctions produced by EB-deposition.

4.2 Single-tunnel junction properties

To confirm controllability in producing tunnel junctions, we attempted to fabricate wire with spacing where we expected the formation of junction composed of deposited metallic wire and SiO_2 layer underlying the space. The designed space, which we call nominal space, was increased to a 2.5 nm step, the minimum deflection increment. Figure 8 shows I-V characteristics for a junction produced with 50 pC/shot at 300 K. At spacing less than 25 nm, the curve is nearly linear, but curves exhibit nonlinear relationship for the larger space junctions. From Fowler-Nordheim (FN) plots, linear relationships are clearly obtained. From the gradient of FN plot, we estimate the barrier height of 0.17- 0.22 eV, which is smaller than that for W/SiO_2 system of about 2 eV. The transition region in Fig. 7 where conductance is greatly changed from metallic to insulator may be the major reason for the result of smaller barrier height. Namely, the metallic property in the deposited film is located just under the primary EB exposed area similar in area to the beam diameter of 3 nm. Although film deposition occurs between the adjacent irradiated positions, the film property here becomes insulating because of a dose less than the transition dose. Thus, such an insulating deposited film acts as a tunneling barrier resulting in the lower barrier height compared with the pure W/SiO_2 junction.

Figure 9 shows a AFM image of transistor structure, where a 3-dot array with 20 nm spacing was produced at the nominal space with a gate electrode 300 nm away from the dot array area. The gate voltage dependence of the drain current is
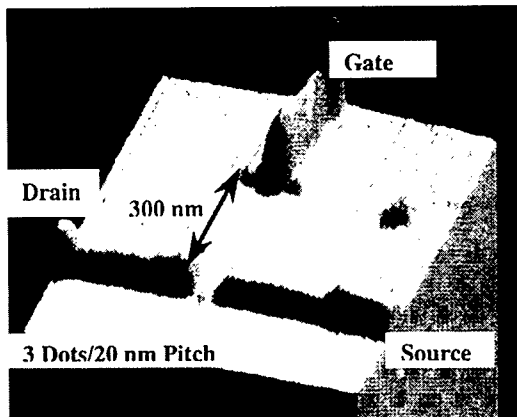
Fig. 9 AFM image of single electron transistor produced by EB deposition, where 3 dots were made in the space between source and drain.

310

shown in Fig. 10 at 230 K. Oscillation with a voltage period of 0.33 V is clear. The sizes of dots may be similar to the incident beam diameter of 3 nm and hence the capacitance of these junctions is approximately set to the self-capacitance of the island. Assuming these dots are spherical shapes, the junction capacitance is 1.7×10^{-19} F. Using this value, we carried out computer calculation of the gate voltage dependence of the drain current, basically similar to that reported by Mullen et al. [22] which is a kind of Monte-Carlo method using temperature-dependent tunneling probability. We can obtain a similar current swing to the experimental. Thus, we conclude that the oscillation obtained here is due to single-electron transport in a series of 4-tunnel junctions controlled by the gate electrode.
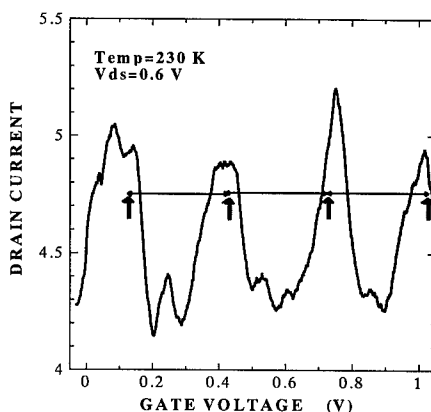
Fig. 10 Coulomb oscillation observed at 230 K.

5. SUMMARY

We demonstrated that thermally oxidized SiO_2 film is useful for the nanometer scale pattern in order to avoid the nano-edge roughness which appears in using convention polymer resist due to aggregates of resist molecule. The minimum line-width of 5 nm was possible in the SiO_2 film. By using bilayer inorganic resist system (SiO_2/c-Si), the process for MIM tunnel junctions was investigated and we indicated the feasibility to produce metal pattern with dimension of 10-20 nm.

EB-induced deposition using WF_6 gas was applied to fabricating wires less than 20 nm wide, single-tunnel junctions and a dot array for single-electron devices. Single-wire conductance was measured at 300 K and 230 K, depending upon the EB exposure dose. At both temperatures, conductance indicates a tremendous change of five orders of magnitude in the low-dose region, and in higher doses the wire has a constant resistivity of 6×10^{-4} Ωcm, probably due to the high content of O and F atoms at the initial stage of film growth. I-V characteristics for a lateral tunnel junction produced with a barrier thickness of 2.5 nm increment were fitted to a FN plot in an applied voltage exceeding 3 V. Barrier height is estimated to be 0.17-0.22 eV. A single-electron transistor composed of 3 dots connected to wires with a gate electrode exhibited clear Coulomb oscillation at 230 K, which agreed with the result of computer simulation by the Monte-Carlo method using temperature-dependent tunneling probability.

REFERENCES

1.M. Nagase, H. Namatsu, K. Kurihara, K. Iwadate, K. Murase, T. Makino, Microelc. Eng., **30**,

p.419 (1996).

2.T. Yamaguchi, H. Namatsu, M. Nagase, K. Yamazaki, K. Kurihara, Appl. Phys. Lett., **71**, p.2,388 (1997).

3.H. Namatsu, T. Yamaguchi, M. Nagase, K. Yamazaki, K. Kurihara, Microelc. Eng., **41/42**, p.331 (1998).

4.D. R. Allee, A. N. Broers, Appl. Phys. Lett., **57**, p.2,271 (1990).

5.H. Hiroshima, M. Komuro, Jpn. J. Appl. Phys., **32**, p.6,153 (1993).

6.T. Wada, M. Hirayama, S. Haraichi, K. Ishii, H. Hiroshima, M. Komuro, Jpn. J. Appl. Phys., **34**, p.6,961 (1995).

7. S. M. Gorwadkar, T. Wada, S. Haraichi, H. Hiroshima, K. Ishii, M. Komuro, Jpn. J. Appl. Phys., **35**, p.6,673 (1996).

8. T. Wada, S. Haraichi, K. Ishii, H. Hiroshima, M. Komuro, M. Hirayama, J. Vac. Sci. Technol., **A14**, p.1,850 (1996).

9. T. Wada, S. Haraichi, K. Ishii, H. Hiroshima, M. Komuro, S. M. Gorwadkar, J. Vac. Sci. Technol., **A16**, p.1,430 (1998).

10.M. Komuro, H. Hiroshima, Microelec. Eng., **35**, p.273 (1997).

11. M. Komuro, H. Hiroshima, J. Vac. Sci. Technol., **B15**, p.2,809 (1997).

12. M. Komuro, H. Hiroshima, Jpn. J. Appl. Phys., **36**, p7,686 (1997).

13.H. Hiroshima, M. Komuro, Nanotechnol. **9**, p.108 (1998).

14.M. Komuro, H. Hiroshima, A. Takechi, Nanotechnol. **9**, p.104 (1998).

15. T.Ichihashi , S. Matsui, J. Vac. Sci. Technol., **B6**, p.1,869 (1988).

16. S. Matsui, T. Ichihashi, M. Mito, J. Vac. Sci. Technol., **B7**, p.1,182(1989).

17. W.P.Koops, J.Kretz, M.Rudolph, M.Weber, G.Dahm, K.L.Lee, Jpn. J. Appl. Phys., **33**, p.7,099(1994).

18. H.W.P.Koops, A.Kaya and M.Weber, J. Vac. Sci. Technol., **B13**, p.2,400(1995).

19. H. Hrisoshima, S.Okayama, M.Ogura, M.Komuro, H.Nakazawa, Y.Nakagawa, K.Ohi, K.Tanaka, J. Vac. Sci. Technol., **B13**, p.2,514(1995).

20. J. S. Judge, J. Electrochem. Soc. 118, p.1,772(1971).

21.H. Nielsen, D. Hackleman, J. Electrochem. Soc. **130**, p.708(1983).

22.K.Mullen, E.Ben-Jacob, Phys. Rev B, **32**, p.98(1988).

THE NOVEL TECHNIQUE OF NANOMETER-SIZE FABRICATION BY USING CONVENTIONAL PHOTOLITHOGRAPHY

Shingi Hashioka and Hideki Matsumura,
JAIST(Japan Advanced Institute of Science and Technology),
Tatsunokuchi, Ishikawa-ken 923-1292, JAPAN, shingi@jaist.ac.jp

ABSTRACT

A novel method to prepare nanometer-size patterns by using currently available mass-production technology is proposed. In this study, a contact pattern-mask with nanometer-size slit is fabricated by combination of photolithography and anodic oxidation of metal. The slit width of the pattern-mask can be controlled in the order of nano-meters by anodic voltage during oxidation of side-wall of the metal. 10nm width trench is formed in Si substrate by using such nanometer slit-mask. It is suggested that the technique can be utilized as fabrication process of the nano-scale devices.

INTRODUCTION

The development of ultra large scale integrated circuits(ULSIs) strongly depends on improvement of lithographic technique. However, the minimum feature size of the most advanced ULSIs is decreasing farther than the wavelength of the exposure light. It is believed that as the feature size is reduces below 100nm, the photolithographic technique will be limited because the applicable wavelength of exposure light cannot be obtained. Thus, a new nano-technology is required to solve this problem.

Recently, a new method to fabricate nanometer patterns has been reported, in which a nanometer region of metals is oxidized using a tip of a scanning tunneling microscope (STM)[1]. When an STM tip is scanned on the surface of the metals, the precise area of the scanned region is oxidized with a width of about 10nm. This technology is used for fabrication of single electron transistor (SET)[2]. However, this does not appear as an industrially acceptable technique. If a conventional lithographic technique such as photolithography can be applied to fabricate such nanometer-size structures, it would be highly useful.

In this study a new nano-technology utilizing conventional photolithography is proposed and then a contact pattern-mask with nanometer-size slits is fabricated by combination of conventional photo-lithography and anodic oxidation of side-wall of metal [3]. The mask of a 10nm slit width is fabricated by this technique, and a nanometer-size trench is fabricated in the Si substrate by using such a slit-mask. The technique might be useful for fabrication of the nano-scale devices such as SET and metal/insulator tunnel transistor(MITT) [4] at mass-production level.
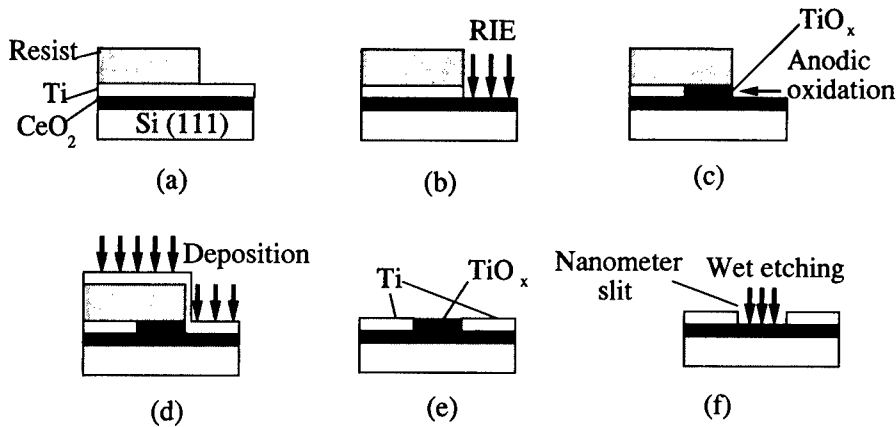
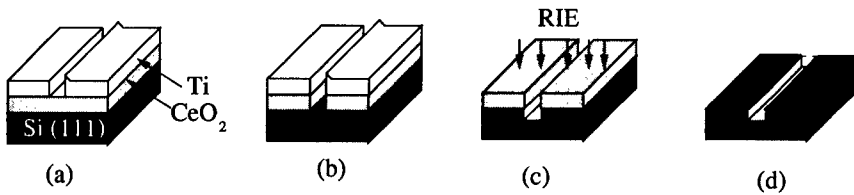Fig.1: Fabrication processes of the nanometer pattern-mask

Fig.2: Fabrication processes of the nanometer-size trench

Fabrication of the nanometer pattern-mask

Figure 1 shows the fabrication processes of the nanometer pattern-mask. Firstly, the Cerium oxide(CeO_2;ceria) layer is deposited on a Si(111) substrate by RF(Radio Frequency) sputtering method. It is expected that CeO_2 can adhere on Si(111) substrate strongly. CeO_2 is used as an interlayer to protect the substrate from the following fabrication processes. Additionally, the CeO_2 can be etched selectively for Ti of the pattern-mask when the substrate is fabricated. The Ti layer is deposited by vacuum evaporation on the CeO_2 layer. Then, photoresist is coated on it and a part of it is removed by photolithographic process, and the Ti is exposed (Fig.1(a)). The exposed Ti layer is etched vertically by reactive ion etching(RIE) using a mixture of chlorine(Cl_2) and boron trichloride(BCl_3) (Fig.1(b)). The steep side-edge of the Ti layer under the resist is oxidized laterally to convert to titanium oxide(TiO_x) in ethylene glycol dissolved ammonium tetraborate (20.2 wt.%,24 ℃)(Fig.1(c)). The thickness of titanium oxide TiO_x obtained by anodic oxidation can be controlled in the ranges of several-tens of nanometer by changing the anodic

voltage. Actually, it is found that the thickness of TiO_x is expressed by the relation of 2nm/V[3]. The Ti layer is deposited again over the whole surface(Fig.1(d)). And the metal/insulator/metal(MIM)structure is obtained after the Ti layer over the resist is removed by a lift-off technology(Fig.1(e)). Then, the TiO_x is etched by H_2SO_4/H_2O_2 solution, and thus a pattern-mask with nanometer-size slit is obtained(Fig.1(f)).

Fabrication of the nanometer-size trench

Figure 2 shows the fabrication processes of the nanometer-size trench. Firstly, the nanometer pattern-mask is fabricated on the Si substrate(Fig.2(a)) by the above processes. Then, the CeO_2 layer is etched through the slit of the nanometer pattern-mask by HNO_3/H_2O_2 solution(Fig.2(b)). After the processing layer is exposed, it is etched by RIE(Fig.2(c)) to make the nanometer-size trench because CeO_2 is resistive against RIE. Finally, to make observation simple, the CeO_2 layer is etched by HF solution(Fig.2(d)).

RESULTS AND DISCUSSIONS

Observation of the nanometer pattern-mask
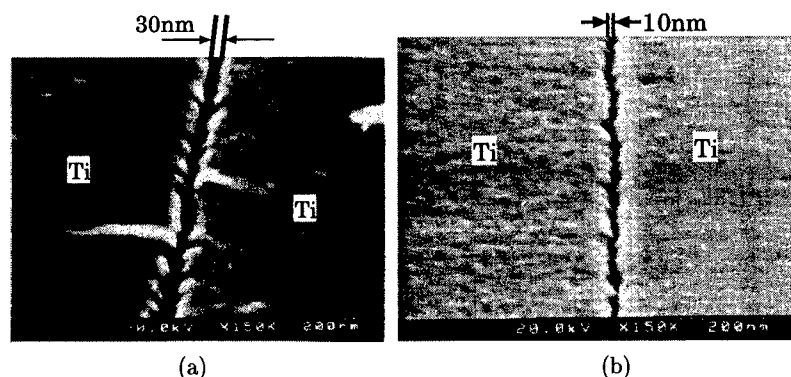
Fig.3: SEM photographs of the nanometer pattern-mask.

To fabricate the nanometer pattern-mask, only TiO_x should be selectively etched in MIM structure by H_2SO_4/H_2O_2 solution. After the etching of TiO_x, the mask with a nanometer-size slit is fabricated as mentioned in Fig.1(f). Figure 3(a) and (b) show SEM photographs of the pattern-mask with a slit. In Fig.3(a) it is confirmed that the slit is fabricated between two Ti layers and the width at the bottom of the slit(slit width) is about 30nm. Fig.3(b) shows the minimum size obtained in the previous experiment. The result indicates that fabrication of metal-slit whose minimum size is about 10nm can be formed by using conventional photolithography.

Observation of the nanometer-size trench

(a)   (b)
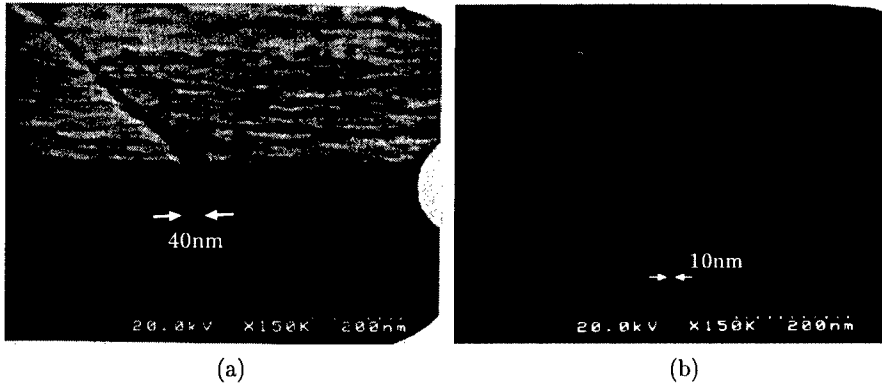
Fig.4: SEM photographs of the nanometer-size trench.

Figure4(a) and (b) show the SEM photographs of the nanometer-size trench. In Fig.4(a) it is confirmed that V-shaped trench is fabricated on the Si substrate and the width at the top of the trench(trench width) is about 40nm. Fig.4(b) shows the minimum size of 10nm obtained. The result indicates that the nanometer-size trench fabrication appears feasible by using the nanometer pattern-mask.

Controllability of this fabrication technique

(a)   (b)
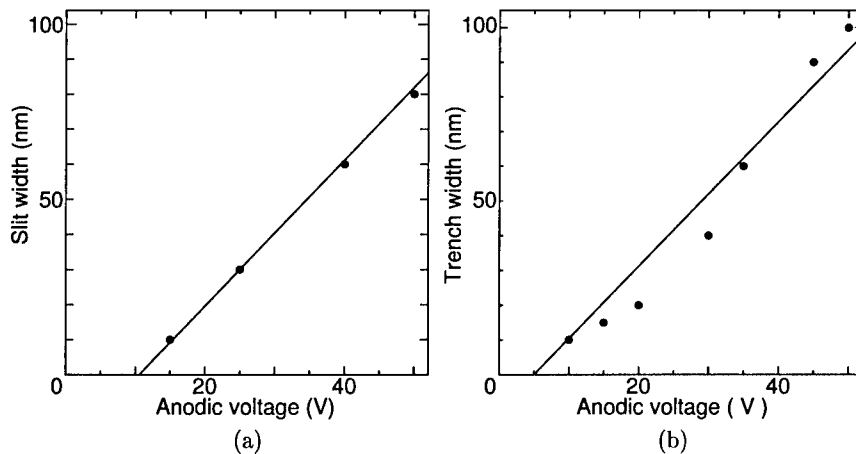
Fig.5: Relationship between anodic voltage and (a) the slit width and (b) the trench width.

Since the width of TiO_x line can be controlled by anodic voltage, the slit width and also the trench width can be controlled in a similar way. Figure 5 show the relationship between anodic voltage and (a) the slit width and (b)the trench width. The plots are derived from observation by the SEM. Fig.5(a) shows that the slit width increases in proportion to anodic voltage. Thus, it is confirmed that the slit width can be controlled simply at nanometer order by anodic voltage. Fig.5(b) shows that the trench width can be controlled similarly. Both slopes of the line in figure follow the relation of 2nm/V which is same to the relation of TiO_x growth on the Ti side-wall. The lines do not cross at the point of 0. This may be probably due to the existence of the layer which cannot be etched by H_2SO_4/H_2O_2 solution in the TiO_x layer.

CONCLUSIONS

From above studies, the following results were obtained;

1. The nanometer pattern-mask with metal slit was fabricated by the conventional photolithography.

2. The nanometer-size trench was fabricated in the Si substrate by etching through the metal slit of nanometer size.

3. It was shown that both the slit width and the trench width can be controlled simply at nanometer order by anodic voltage. The minimum size experimentally obtained is about 10nm.

By this study it is indicated that this novel technique for nanometer-size fabrication by using the conventional photolithography can be utilized as fabrication process of the nano-scale devices.

ACKNOWLEDGMENTS

REFERENCES

1. H. Sugimura, T. Uchida, N. Kitamura and H. Masuhara: J. Phys. Chem. **98**, 4352 (1994).

2. K. Nakazato and J. D. White: IEDM Tech. Dig., 487 (1992).

3. K. Fujimaru, T. Ono, R. Nagai and H.Matsumura: Jpn. J. Appl. Phys. **36**, 7786 (1997).

4. K. Fujimaru, R. Sasajima and H. Matsumura: J. Appl. Phys. **85**, 6912 (1999).

SPM BASED LITHOGRAPHY FOR NANOMETER SCALE ELECTRODES FABRICATION

A. NOTARGIACOMO[*], E. GIOVINE[§], E. CIANCI[o], V. FOGLIETTI[*], F. EVANGELISTI[*,§]

[*]Istituto di Elettronica dello Stato Solido (IESS), CNR, Roma, Italy

[§]Unità INFM, Dip. di Fisica "E. Amaldi", Università di Roma TRE, Roma, Italy

[o]Osservatorio Astronomico di Roma, Monteporzio Catone, Italy

E-mail: notargiacomo@iess.rm.cnr.it

ABSTRACT

Scanning probe assisted nanolithography is a very attractive technique in terms of low-cost, patterning resolution and positioning accuracy. Our approach makes use of a commercial atomic force microscope and silicon probes to build simple nanostructures, such as metal electrode pairs, for application in novel quantum devices.

Sub-100 nm patterning was successfully performed using three different techniques: direct material removal, scanning probe assisted mask patterning and local oxidation.

INTRODUCTION

In recent years there has been an increasing interest in both standard and unconventional nanofabrication techniques for the development of nanodevices to be used in fundamental physics as well as in applied research. Novel devices will require a circuit patterning resolution and a positioning accuracy ranging beyond the limits of the present fabrication processes. A possible solution is the integration of conventional lithography with scanning probe microscopy (SPM) based techniques allowing the definition of circuit patterning down to a nanometer scale. Applying different principles, several attempts were made using SPM to induce modification of insulators, semiconductors and metals on the nanometer scale: low-energy exposure of resists [1], thermo-mechanical writing [2], local oxidation [3,4], mechanical modification [5].

We report here a study on the nanolithographic capabilities of the atomic force microscope (AFM), which takes advantage of the imaging facility and the ability of moving a probe over the sample surface in a controllable way. Our goal is to achieve sub-100 nm patterning definition for the fabrication of metallic nanoelectrode pairs.

EXPERIMENTS AND RESULTS

A Digital Instruments D3100 AFM operating in ambient air was used for both processing and imaging. The nanolithographic steps were made with both commercial and home-made silicon probes. In the following we describe the techniques used to fabricate metallic nanoelectrode pairs.

Direct Material Removal

Our first approach to nanolithography was the direct modification induced by scratching a sample. Indeed it is possible to remove material from a metal stripe by applying an amount of force of several μN [6]. The samples we used were aluminum stripes patterned on an oxidized silicon wafer by standard electron-beam lithography (fig. 1(a)).

319

In order to directly remove the material we had to use high spring constant cantilevers. Commercial silicon probes are available with spring constant values between 20 and 100 N m^{-1} and a tip radius ~ 10 nm. This type of cantilevers is not suitable for imaging in contact-mode. However, an accurate control of the scanning parameters allowed us a proper alignment to the scratching site before processing, without a significant wear of the sample.

The scratches were made at a rate of 0.1 μm s^{-1}, having found that different rate values resulted in a bad cut-profile and material removal. An exact evaluation of the force applied is not possible because the cantilever spring constant is not well known. However, a rough estimate using the typical value of 40 N m^{-1} for that type of cantilever led to a value of about 25 μN as the force necessary to scratch an aluminum stripe.

The regions of the stripes where engraving was performed were about 10 nm thick and 80 nm wide. A good material removal required passing several times over the same scratching site resulting in a widening of the gap size. Sub-100 nm gaps, down to 60 nm, were obtained with series of 6 writing passes. In fig. 1 it is shown a three-dimensional view of a metal stripe before (a) and after (b) scratching, and a longitudinal section profile of the processed sample (c).
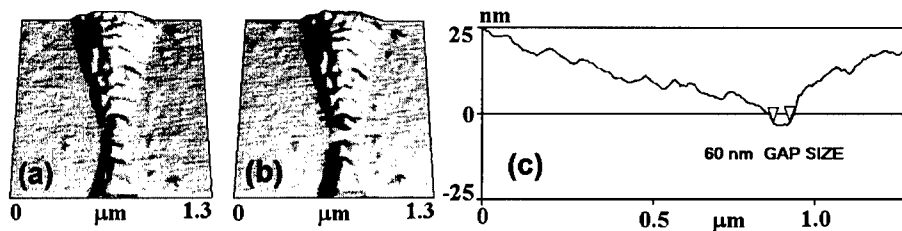
Fig. 1. Three-dimensional view of an aluminum stripe before (a) and after (b) scratching the metal. The section profile (c) shows a 60 nm wide gap obtained after material removal.

A contribution that increases the gap dimension is that of the wear of the tip during each scratching pass. Therefore narrower gaps are difficult to obtain. Such damaging of the probe results in a poor accuracy in further operations performed with the same tip and a new probe is required for an accurate quantitative analysis of the results even after just one complete series of scratching passes.

Stripes thicker and wider than those discussed were also considered but required many scratching passes resulting in wider gaps, and the material removal was often unsatisfactory.

AFM Assisted Mask Patterning

In order to obtain nanometer size gaps an alternative technique was tried which avoided the direct interaction between the tip and the metal to be patterned. In this case two sacrificial layers covered the samples [7,8] according to the multilayer structure depicted in fig. 2. An advantage of this procedure is the reduced wear of the tip, which remains available for further processes.

The samples to be processed were 30 nm thick titanium stripes deposited on 2" oxidized silicon wafers. As a first step the samples were covered by a 60 nm thick polymeric film. The polymer deposition was carried out using CHF$_3$ gas in a plasma system, consisting of a conventional parallel-plate reactor where the plasma is sustained by a 13.5 MHz source. We found plasma conditions which induced polymerization at a controllable rate, resulting in films of good quality, in terms of small roughness, good adhesion to the substrate and thickness

uniformity. By using a pressure of 500 mTorr and a power density of 0.25 W cm^{-2}, a constant deposition rate of 10 nm min^{-1} was obtained. A further advantage of this type of deposition is that the polymer covered conformally the sample so that the underlying structures were readily located with the AFM, resulting in a precise alignment and positioning of the cut on the metal stripes.

Subsequently, the polymer layer was thermally treated at 180°C for 30 min. in air and exposed to UV broadband light. We found that this post-deposition treatment strengthens the polymer and is very effective for improving its mechanical properties, its resistance to wet chemical etchers and the adhesion of the sacrificial metal layer deposited on top.

Finally, a 5 nm thin aluminum sacrificial layer (see fig. 2) was deposited by sputtering technique, obtaining a smooth metal surface which completely wetted the polymer.
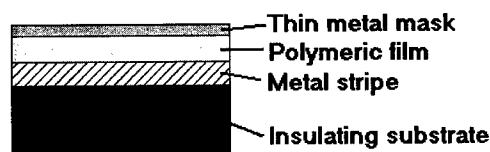
Fig. 2. Layout of the sample multilayer structure

We found that an applied force of about 1 μN is required to pattern the aluminum mask. For this purpose we used commercial silicon cantilevers with 2-3 N m^{-1} spring constant which provide both small forces for imaging during the alignment steps and high enough forces to pattern the aluminum mask. Home-made cantilevers were also considered with various geometry (V-shaped and straight cantilevers with different lengths) to find which probe features mainly affect the lithographic step.

In fig. 3 is reported a typical result of the lithographic patterning i.e. the engraving of the top aluminum sacrificial layer. The AFM three-dimensional view (fig. 3(a)) shows a series of lines patterned on the aluminum mask with a different amount of force applied. In the profiles in fig. 3(b) increasing depth and material pile up are apparent upon increasing the applied force. This series is a typical calibration procedure made in order to establish the best lithography parameters. The need of a correct calibration has already been reported in the literature [8] and it is fundamental for a good yield. The low tip wear allows many calibration series before cutting the desired scratch without appreciable tip degradation.
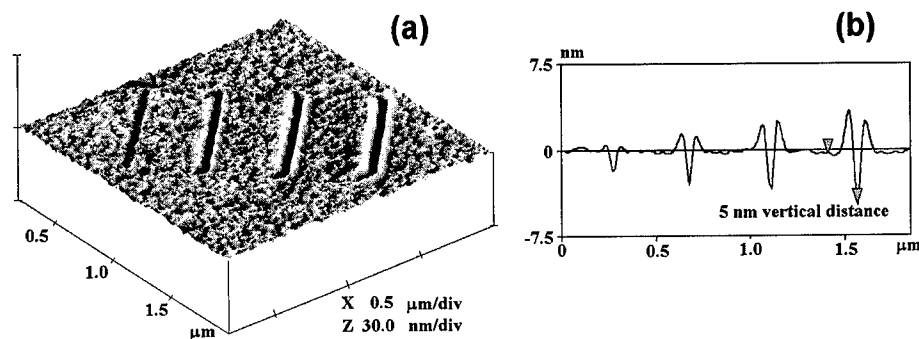
Fig. 3. AFM three-dimensional view (a) of a series of scratches obtained with increasing amount of force applied. The section profile (b) shows the groves average depth.

We found that a single line can be patterned in a readily controllable way whereas a continuous pattern that extends in two dimensions results in an inhomogeneous line depth and width, and require an *ad hoc* adjustment of the parameters during the lithography process.

The mask patterning technique discussed above was applied to open a narrow gap in a titanium stripe according to the procedure schematically depicted in fig. 4.
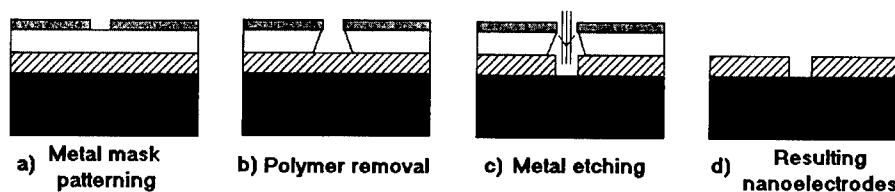

a) **Metal mask patterning**   b) **Polymer removal**   c) **Metal etching**   d) **Resulting nanoelectrodes**

Fig. 4. Schematic of the process steps: thin metal mask patterning (a), polymer ashing (b), metal stripe etching (c) and sacrificial layers removal (d).

The result of patterning the upper sacrificial layer is shown as a thin furrow in fig. 5(a). After the AFM lithography, the gap opened in the top aluminum layer was transferred to the polymer layer underneath by means of an ashing process using oxygen plasma. The aluminum/polymer bilayer acted as a mask for the subsequent titanium etching by a second dry etching process using a SF_6-CHF_3-O_2 mixture. This three-gas mixture can produce very anisotropic profiles even at very low power density [9]. We used an extremely low power density of 0.15 Wcm^{-2} which led to a low self-voltage bias of ~ 40 V. In these conditions the very thin top metallic layer was able to sustain the whole etching process without being appreciably backsputtered. Finally, the aluminum film and the residual polymer film were removed respectively by wet etching and oxygen plasma.

We have obtained gaps as narrow as 40 nm (see fig. 5(b)). In the section profile, reported in fig. 5(c), the gap width is taken at the base of the stripe that is located at a depth of 30 nm, while the exceeding depth is due to an over-etching performed in order to ensure the gap opening.
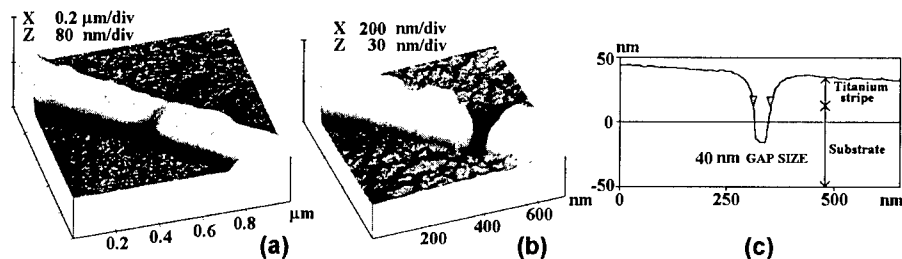
Fig. 5. Scratch onto the sacrificial polymer/aluminum layers (a). A thin furrow, a few nanometers deep, crosses the titanium stripe. Three-dimensional view (b) and section profile (c) of a 40 nm wide gap obtained on a titanium stripe by dry etching technique.

Local Oxidation

SPM assisted local oxidation (LO) was observed when a conducting negative biased tip is moved in the near proximity of semiconductor or metal samples in air ambient, where water

from the ambient humidity plays the role of the electrolyte. LO is a very attractive technique due to the controllable thickness and line width of the oxidized pattern as a function of the applied voltage. An example of the application of the LO is shown in fig. 6 for a silicon substrate where 1.2 μm lines were patterned at a 1μm s^{-1} rate with increasing applied voltage.
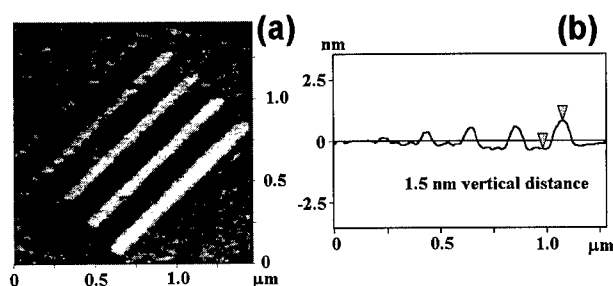

Fig. 6. Topography (a) and section profile (b) of oxide lines patterned on silicon substrate with increasing sample to tip voltage.

Using this technique it is possible to reduce [10] or even interrupt the electrical conduction in a metal stripe with the formation of an oxide barrier. Our approach was to apply LO process to obtain metal nanoelectrodes starting from 9 nm thick aluminum stripes that are deposited by sputtering technique and patterned by standard lithographic processes. For the LO step it is possible the use of common n$^+$ doped silicon probes without a metallic coating. However the silicon tip oxidizes itself and the oxidation efficiency is rapidly reduced. An increased probe lifetime, obtained by a 15 nm chromium/gold bilayer deposition, was preferred despite the increase in the tip radius. Commercial cantilevers as well as home made probes were metallized to perform LO with good results. Contact-mode AFM configuration with no humidity control was used for both the preliminary alignment and the LO lithographic step.

The aluminum oxide removal was performed by a selective wet etching using a CrO$_3$-H$_3$PO$_4$-H$_2$O mixture [11] at 40°C. The samples were initially dipped in the etching solution to remove the native oxide layer in order to increase the oxidation efficiency. After oxide lines were patterned across the metal stripes, the samples were immediately processed to remove the aluminum oxide. Gaps of about 40 nm were obtained, as shown in fig. 7
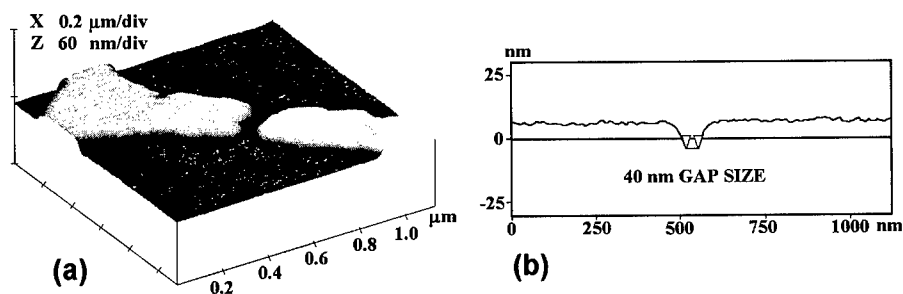
Fig. 7. Three-dimensional view (a) and section profile (b) of a 40 nm wide gap obtained onto an aluminum stripe by local oxidation and wet etching technique.

The process described above requires few steps and exhibits a good reproducibility. It was found that a single pass was enough to oxidize the whole thickness of 9 nm with a low voltage

applied, unlike the case of silicon and other metals. This is probably due to the material structure which is very sensitive to the deposition technique. At the moment we are optimizing the LO technique in order to reduce the line width.

CONCLUSIONS

AFM lithography is a suitable method for patterning circuit elements with good reproducibility and positioning accuracy. Its use led to nanometer size gaps as small as 60 nm by direct scratching of metal stripes. Better results, in terms of increased probe lifetime and smaller gap sizes (down to 40 nm) required a more complex set-up such as the use of sacrificial layers and dry etching processes. Nevertheless the most promising techniques was found to be the SPM assisted local oxidation due to a high versatility: it applies to both semiconductors and metals and requires a minimal sample preparation. Gap sizes down to 40 nm were produced with a highly reliable technique.

These preliminary results are very encouraging but further optimization of these techniques is required in order to use these structures for electronic device fabrication.

ACKNOWLEDGEMENT

REFERENCES

1. K. Wilder and C. F. Quate , Appl. Phys. Lett. **73**, 2527 (1998).

2. H. J. Mamin, Appl. Phys. Lett. **69**, 433 (1996).

3. P. M. Campbell, E. S. Snow and P. J. McMarr, J. Appl. Phys. **84**, 1776 (1995).

4. P. A. Fontaine, E. Dubois and D. Stievenard, Appl. Phys. Lett. **73**, 2527 (1998).

5. R. Magno and B. R. Bennett, Appl. Phys. Lett. **70**, 1855 (1997).

6. H. Bruckl, R. Rank, H. Vinzelberg, I. Monch, L. Kretz and G. Reiss, Surf. and Interface Anal. **25**, 611 (1997).

7. S. Hu, S. Altmeyer, A. Hamidi, B. Spangenberg and H. Kurz, J. Vac. Sci. Technol. B **16**, 1983 (1998).

8. S. Hu S, A. Hamidi, S. Altmeyer, T. Koster, B. Spangenberg and H. Kurz, Vac. Sci. Technol. B **16**, 2822 (1998).

9. I. W. Rangelow and H. Löschner, J. Vac. Sci. Technol. B **13**, 2394 (1995).

10. E. S. Snow, D. Park and P. M. Campbell, Appl. Phys. Lett. **69**, 169 (1996).

11. G. C. Schwartz and V. Platter, J. Electrochem. Soc. **122**, 1508 (1975).

FABRICATION OF ISOLATED NANOPARTICLE CIRCUITRY VIA LENSLESS OPTICAL TWEEZING ("L. O. T. s")

M. T. Dearing, G. C. Spalding
Laboratory for Mesoscopics and Quantum Microscopies and Department of Physics,
Illinois Wesleyan University, Bloomington, Illinois 61702-2900, gspalding@titan.iwu.edu

ABSTRACT

We propose a novel method for trapping a nanometer-scale particle into a stable structure useful for a variety of interesting electrical measurements. The particle to be trapped can be dielectric or metallic, magnetic or non-magnetic. Our methodology was developed, in part, to ensure the absence of extraneous nanoparticles in the region of the device under test; it also allows a possible feedback mechanism to indicate when a nanoparticle has been successfully trapped. In particular, we irradiate a substrate containing a tiny etch-pit hole. On the transmission side of the substrate, the diffracted or evanescent optical fields should contain large enough gradients to localize a nanoparticle to the region of the hole.

INTRODUCTION

Our recent work has centered on various schemes for initiating self-assembly or directed assembly of a large number of small particles. Such techniques can be useful for building physically interesting nanocomposite structures as well as, perhaps, fabricating functional devices from particle arrays. However, as the size of the particle involved is reduced, new approaches are often required. In particular, this paper is meant to address incorporation of nanoparticles into an electrical circuit. Unlike much of our previous work, the goal here is specifically to ensure that only one such particle will be incorporated and that no stray particles remain in the vicinity.

Many groups are interested in single-electron device fabrication [1] and in performing tunneling spectroscopy measurements on single nanoparticles. Several groups have deposited particles onto a substrate containing closely spaced electrodes to successfully confine a single particle between two electrodes [2]. However, such devices are littered with stray particles surrounding the junctions of interest. Stray charge and capacitive coupling or, in some experiments, the magnetic moments of these extra particles can interfere with the desired measurements or the function of the single particle device. It is critical for single particle devices that the particle be well isolated.

EXPERIMENT/THEORY

Conventional optical trapping (using lenses) has been developing for over two decades [3]. Tightly focusing a laser with an objective lens can produce an intensity gradient capable of trapping a dielectric particle. In fact, any type of particle can be trapped, including metallic, non-metallic, magnetic, *etc*. The only additional requirement for trapping metallic particles is that they be smaller than their skin depth, so they will act as a dielectric. A more general condition for forming a stable trap is that the gradient force must be larger than the scattering force, which is

325

due to momentum transfer and tends to push the particle along the beam axis and out of the trap. We propose a novel *lensless* optical tweezing technique, suitable for confining a completely *isolated*, small particle. Our technique utilizes near-field radiation emanating from sub-wavelength holes in order to trap nanoparticles into those holes. Surface forces ensure that such a trap is permanent, allowing for subsequent measurements.

Typically optical tweezers can easily trap particles on the order of a micron; still, there have been attempts at optically trapping *smaller* particles [3]. Svoboda, *et al.* were able to trap metallic nanoparticles, however, their trap tended to be metastable; a particle would be trapped for only a few seconds [4]. A non-conventional approach to trapping smaller particles has been theoretically proposed by Novotny, *et. al.* [5]; an appropriately illuminated STM tip can produce evanescent fields that have large gradients over a region of several nanometers. Novotny's calculation indicates that these gradients can trap a five-nanometer particle at the tip. An important advantage of using purely evanescent fields is that there are no scattering forces since there is no net forward momentum carried in the decaying wave. Our method was inspired by the work of Novotny, however, our geometries differ significantly from theirs and allow for the construction of robust devices, which remain permanent after the trapping radiation is removed.

By illuminating a sub-wavelength aperture, we produce an evanescent field with a large enough gradients to trap a small (nanometer scale) particle into that aperture. For this paper, we illuminated an array of holes in a silicon nitride substrate and deposited a *small* number of particles onto the other side. As our calculations show, a particle entering this evanescent wave, will be drawn into the substrate hole, where surface forces can keep the particle permanently trapped (assuming the hole is slightly smaller than the particle to be trapped).

Researchers at NEC recently demonstrated that the transmission through a sub-wavelength hole can be greatly enhanced if the transmission side of the substrate is metalized and patterned (say, with an array of holes or dimples) [6]. This enhanced transmission is due to the coupling of the diffracted light to surface plasmons on the metal. The plasmon excitations re-radiate waves that add to the overall transmission. Depending upon the geometry of the patterned substrate, certain wavelengths can be transmitted with an efficiency greater than unity.

We have begun to explore such schemes in order to extend our basic trapping process, via a careful tailoring of the evanescent wave. By *tuning* the coupling of the diffracted radiation to a metalization on the transmission side of the substrate, we hope to gain two distinct advantages. First, by allowing a measurable emission of light we hope to detect the moment that a particle becomes trapped, as it alters the transmission pattern. Additionally, the added intensity provides a deeper potential well, allowing us to trap particles directly from colloidal suspensions. Since nanoparticles are often prepared in solution, working with colloid is more direct – and in any case is an extremely simple and efficient way to deposit nanoparticles onto the substrate surface. Additional advantages can be present in working with biological and organic nanoparticles.

We are beginning numerical simulations for a variety of particular metalization geometries. However, at this stage, we present only preliminary calculations which indicate that the basic approach should work, and that it should improve as we work with smaller and smaller particles. For this purpose, we begin with Bethe's model of diffraction by small holes [7]. While other workers have produced a variety of corrections to Bethe's model, it suffices to elucidate basic dependences. This model yields, for the radiation emitted from a hole of diameter b, the Poynting vector:

$$|S| = \frac{1}{r^2} \frac{c}{36\pi^3} k^4 b^6 \left[4H_0^2 \cos^2\theta \cos^2\alpha + \left(E_{0,x}\sin\theta - 2H_0\sin\alpha\right)^2 \right] \tag{1}$$

Our own calculations extend Bethe's through an examination of the basic trapping condition describe above ($F_\nabla \gg F_{scatt}$). In the Rayleigh limit, where the particle size, $a \ll \lambda$, expressions for these two forces can be found in terms of the Poynting vector [8]. Incorporating Equation 1 into these expressions yields an approximate result:

$$\frac{F_\nabla}{F_{scatt}} = \frac{3\lambda^4(\varepsilon + 2\varepsilon_0)}{32\pi^4 a^3(\varepsilon - \varepsilon_0)} \frac{1}{r} \tag{2}$$

Figure 1 plots this ratio as a function of distance from the aperture for a 100 nm particle. Our calculations indicate that, for our geometries, the gradient force should exceed the scattering force even when the particle is a significant distance from the aperture (about 1 micron for $a = 100$ nm). That is, the particle should feel a significant gradient force if they travel along any trajectory near the hole; this indicates that we could also have success trapping particles from colloid or aerosols.

More importantly, Figure 2 shows that the ability to trap significantly increases as we move to smaller and smaller particle sizes. This is largely due to the fact that the scattering force has less of an effect on smaller particles. At the same time, we note that when this technique is applied to trapping a particle from solution, the potential well formed by the optical tweezer must also be larger than the thermal energy. Smaller particles in solution are subject to significant Brownian motion, so the intensity required to trap a 50 nm particle, say, is greater under this sort of circumstance. Thus, appropriate tuning of the coupling to surface plasmons becomes important. We are currently exploring numerical models of this coupling in the hope of identifying optimum conditions (substrate material, particle material, hole size, metalization geometry, etc.). Still, we can say that at this point proof of principle of lensless optical tweezing has been established.
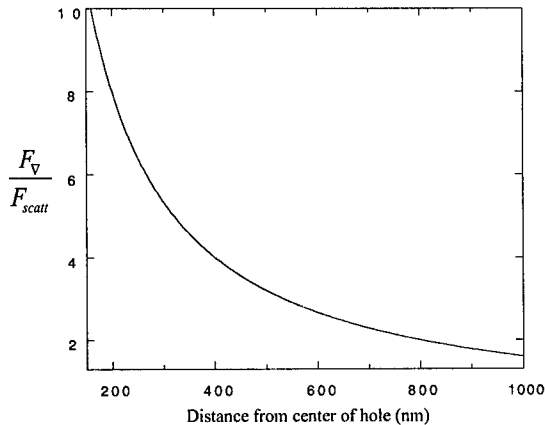
Figure 1. The ratio of the trapping force to the scattering force is plotted for a 100 nm particle.
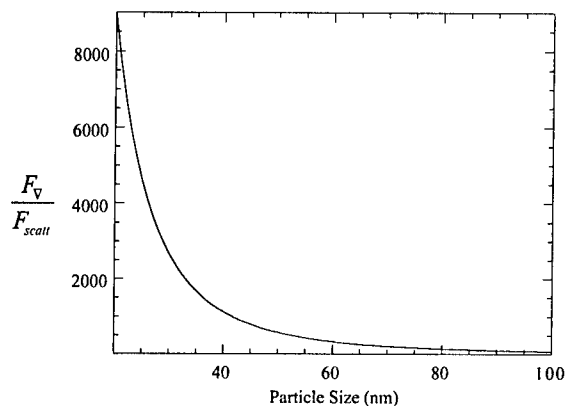
Figure 2. The ration of the trapping force to the scattering force is plotted versus particle size.

RESULTS

Our first experiments used a 500 nm hole array (only slightly sub-wavelength, given HeNe laser illumination) and 500 nm silica particles deposited from a very dilute aqueous solution. Again, our calculations indicate that trapping should be *easier* for smaller particles. In Figure 3 we can see that particles have been successfully placed into holes. Because we deposited a low density of particles there are no stray particles in the immediate vicinity of a trapped particle, *i.e.*, each is well isolated. As we increase the concentration of particles the occurrence of trapping also increased. However, a key feature of our process is that we can work with a very low density of particles and yet still reasonably expect to trap a particle into the desired location.

CONCLUSION

In conclusion, we have introduced, and explained, a new technique for isolating small particles. While our early tests used 500 nm particles, we have shown that the method could
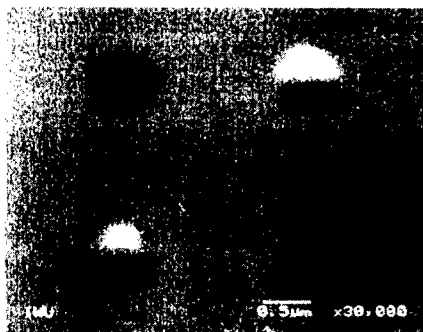
Figure 3. Here 500 nm silica particles are trapped into holes of similar size.

328

work well for much smaller particles. Our geometries are compatible with electrical measurements: subsequent metalization of each side of the substrate yields a stable junction containing a well-isolated nanoparticle [9]. Unlike STM junctions, this method allows direct measurement of tunneling spectroscopy, as a function of temperature, without concern over differential thermal contraction between tip and nanoparticle. By utilizing near-field optics to create large gradients for trapping nanometer scale particles, we have introduced, and demonstrated the feasibility of, lensless optical tweezing (LOTs). For some applications of this new technique, it is critical to tune the balance between the gradients required for trapping and the enhanced transmission needed for trapping detection or trapping in solution. We plan to use numerical simulations to optimize the design for such applications, and to provide the most efficient LOT for a given particle.

REFERENCES

1. *e.g.*, D. L. Klein, R. Roth, A. K. L. Lim, A. P. Alivisatos, and P. L. McEuen, Nature **389**, 699 (1997).

2. *e.g.*, A. Bezryadin, C. Dekker, and G. Schmid, Appl. Phys. Lett. **71**, 1273 (1997).

3. A. Ashkin, J. M. Dziedzic, J. E. Bjorkholm, S. Chu, Opt. Lett. **11**, 288 (1986).

4. K. Svoboda and S. M. Block, Opt. Lett. **19**, 930 (1994).

5. L. Novotny, R. X. Bian, X. S. Xie, Phys. Rev. Lett. **79**, 645 (1997).

6. H. F. Ghaemi, T. Thio, D. E. Grupp, T. W. Ebbesen, and H. J. Lezec, Phys. Rev. B **58**, 6779 (1998).

7. H. A. Bethe, Phys. Rev. **66**, 163 (1944).

8. Y. Harada, T. Asakura, Opt. Commun. **124**, 529 (1996).

9. S. Gueron, Mandar M. Deshmukh, E. B. Myers, D. C. Ralph, Phys. Rev. Lett. **83**, 4148 (1999).

LOCALIZED CHARGE STORAGE IN CeO_2/Si(111) BY ELECTROSTATIC FORCE MICROSCOPY

J. T. Jones, P. M. Bridger, O. J. Marsh, and T. C. McGill
Watson Laboratories of Applied Physics 128-95
California Institute Of Technology, Pasadena, California 91125

ABSTRACT

In this report, the local patterning of charge into CeO_2/Si structures by scanning probe microscopy is examined. An electrostatic force microscope (EFM) has been used to write and image localized dots of charge on to double barrier CeO_2/Si/CeO_2/Si(111) structures. By applying a large tip bias $V_{tip} = 6 - 10$ V and reducing the tip to sample separation to $z = 3 - 5$ nm for write times of $t = 30 - 60$ s, arrays of charge dots 60 - 250 nm FWHM have been written. The dependence of dot size and total stored charge on various writing parameters such as tip writing bias, tip to sample separation, and write time is examined. The total stored charge is found to be $Q = 5 - 200$ e per charge dot. These dots of charge are shown to be stable over periods of time greater than 24 hrs, with an initial charge decay time constant of $\tau \sim 9.5$ hrs followed by a period of much slower decay with $\tau > 24$ hrs. Charge decay time constants are found to be dependent on the thickness of the lower CeO_2 tunneling barrier.

INTRODUCTION

Cerium oxide (CeO_2) is an insulating material with a lattice mismatch of only 0.35 % to silicon (Si) and an energy bandgap of ~ 5.5 eV. This attractive set of properties has the potential to lead to a fully functional silicon heterojunction technology. A significant amount of work has been done examining the growth and characterization of CeO_2 crystals on Si [1, 2, 3, 4, 5], and the growth of single crystal Si on to CeO_2/Si heterostuctures [6] has been recently reported. Based on these promising results, a silicon resonant tunneling diode, an improved silicon-on-insulator (SOI) technology, and stacked silicon electronics have all been proposed. A valuable and interesting addition to this array of technologies would be the capacity for electrostatic patterning and charge storage.

EXPERIMENTAL DETAILS

The sample preparation has been previously reported [7], and is included here for completeness. Samples were produced from commercially available 3" Si(111) wafers, n-type with 3.0-4.3 Ω-cm resistivity. After being subjected to a standard acetone, isopropyl alcohol, de-ionized water degrease in ultrasound, the wafer was etched in 50:1 HF solution until hydrophobic, rinsed in de-ionized water, and immediately introduced into vacuum. Electron beam evaporation was used to deposit material from an undoped Si charge and a 99.99 % CeO_2 charge to grow the structures. Initially, a 200 Å Si buffer layer was grown and examined by RHEED to assure the characteristic (7×7) reconstruction was apparent, indicative of a clean Si surface ready for further growth. Cerium oxide thin films were grown at a wafer temperature of 550 °C, with chamber pressures ranging from $1 \times 10^{-7} - 2 \times 10^{-6}$ Torr due primarily to outgassing from the CeO_2 charge. Silicon thin films were also grown at a wafer temperature of 550 °C, with chamber pressures of $5 \times 10^{-8} - 2 \times 10^{-7}$ Torr. A double barrier structure, CeO_2/Si/CeO_2/Si(111), was produced with symmetric 35 Å CeO_2 barriers and an intermediate 25 Å Si film. In situ RHEED was again used to monitor film growth
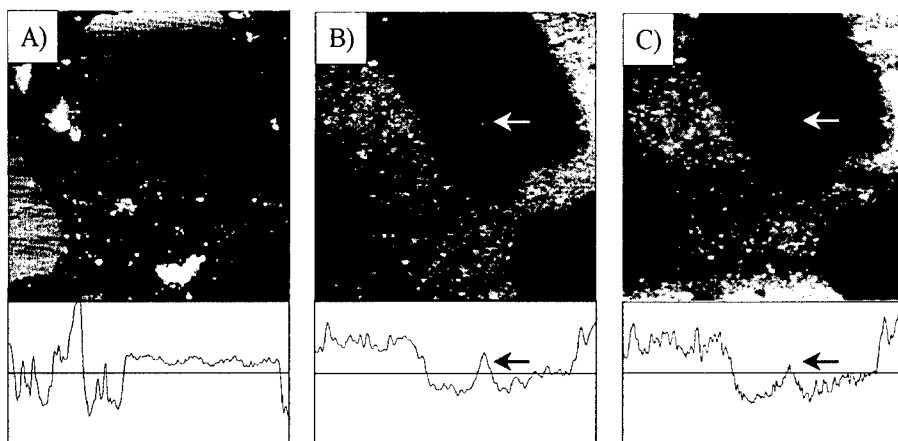
Figure 1: A 5 μm × 5 μm AFM image (A) and EFM image (B) of a $CeO_2/Si/CeO_2$ mesa immediately after applying 10 V to the tip for 60 s at a separation of 3 nm to the sample. Corresponding linescans exhibit the mesas to be topographically flat (A) but with a distinct electrostatic feature (B) corresponding to the written charge dot. A similar EFM image (C) taken 90 minutes later exhibits a slight lateral spreading and decrease in total charge of the charge dot.

and showed the CeO_2 barriers and intermediate Si film to be polycrystalline. Standard photolithography was used to define square mesas 2 μm on a side, and a 3 min 10:1 buffered HF etch was used to etch through the $CeO_2/Si/CeO_2$ structure to the Si buffer layer.

The EFM data were collected using a Digital Instruments Nanoscope IIIa controller and a Bioscope scanning probe microscope operating in tapping mode. To detect the electrostatic forces, a voltage is applied to commercially available cobalt coated tapping mode atomic force microscopy (AFM) tips which are scanned across the surface at a constant tip to sample separation. Phase differences induced by electrostatic forces on the oscillating tip during scanning are detected and provide a measurement of the local charge density. In all cases, topographical AFM images were taken in tapping mode and electrostatic EFM images were recorded simultaneously in interleaved lift mode.

DATA AND ANALYSIS

By reducing the tip to sample separation and applying a charging bias to the EFM tip, charge dots can be written in to the $CeO_2/Si/CeO_2$ structures as shown in Fig. 1. Writing was performed by restricting the EFM tip to a 1 nm^2 area, bringing it to within 3 nm of the sample, and applying a charging bias of 10 V for 60 s. Subsequent imaging of the resultant charge dots was performed over a 5 μm × 5 μm area by increasing the tip to sample distance to 30 nm and imaging at a tip bias of 1 V. No change in the topographical AFM image was detected, Fig. 1A, but a positive dot of charge 250 nm FWHM is clearly visible in the EFM image and corresponding linescan, Fig. 1B. Attempts to write charge to the bare Si in the areas between mesas were unsuccessful, indicating that charge storage is occuring within the CeO_2 or at the CeO_2/Si interfaces. Application of a positive charging bias to the tip has been found to result in positive charge features in the subsequent EFM imaging at $V_{tip} = 1$ V at a lift mode tip separation of $z = 30$ nm. It was further shown that by repeating the write sequence at the same location with a charging voltage of opposite polarity, a charge
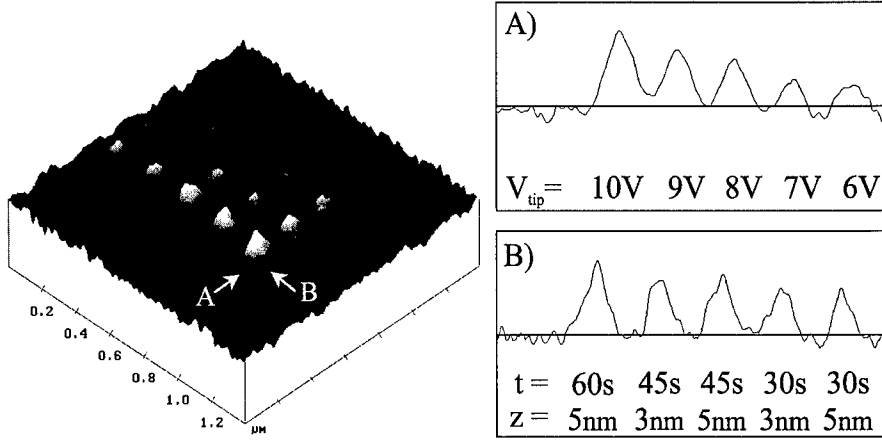
Figure 2: An EFM image (arbitrary units) of an array of charge dots written at different tip voltages, tip to sample separations, and writing times. In a linescan (A) taken at fixed write time t=60 s and tip to sample separation z=5 nm, the strong increase in charge dot intensity and size with increasing tip voltages is apparent. In a linescan (B) taken at fixed tip voltage V_{tip}=10 V, the weaker effects of write time and tip to sample separation become evident. In this case, increasing the write time increases the total stored charge modestly, while decreasing the tip to sample separation increases the total stored charge and charge dot area.

dot could be effectively rewritten with one of an opposite charge.

To examine the effects of writing parameters on charge dot size and local charge densities, an array of positive charge dots was written at various EFM tip biases, tip to sample distances, and write times as shown in Fig. 2. Line scans were then taken across the low pass filtered image to extract charge dot sizes and local charge densities, q. The effect of tip voltage, V_{tip}, is found to be the most dramatic as shown in Fig. 2A. It was found that no detectable charge could be written for $V_{tip} < 6$ V, with a roughly linear increase in size and q with increasing tip voltages up to our maximum $V_{tip} = 10$ V. The effect of both write time, t, and tip to sample separation, z, are examined in Fig. 2B. As expected, q is found to increase slightly with increased write times, while the area of the charge dots increases slightly with decreased tip to sample separation.

To compute the total stored charge, Q, we use an electrostatic analysis as previously presented in Ref. [7] and in similar fashion to Ref. [8] to compute the localized stored charge, q, from a frequency shift, Δf. When the detected phase difference, $\Delta\phi$, is very small, the relationship between $\Delta\phi$ and Δf is nearly linear and is found to be $\Delta f \sim 3.5\Delta\phi$ Hz/deg for our tip. The frequency shift, Δf, is related to the gradient of the force by the expression $\Delta f = -f_0 f'(z_0)/(2k)$, where $z_0 = 30$ nm is the tip to sample separation during imaging, $f_0 = 59.8$ kHz is the resonant frequency of the tip, and $k = 3$ N/m is the estimated spring constant of the tip. The force the tip feels under an applied DC bias will be due to charge-charge interactions and is given by

$$F(z) = \frac{1}{(z + (2d_{CeO_2}/\epsilon_{CeO_2}) + (d_{Si}/\epsilon_{Si}))^2} \times \left(-\frac{d^2_{CeO_2}q^2}{\epsilon^2_{CeO_2}\epsilon_0 a} + \frac{2d_{CeO_2}qV_{EFM}}{\epsilon_{CeO_2}} + \frac{\epsilon_0 aV^2_{EFM}}{2} \right)$$

where z is again the tip to sample separation, d and ϵ are the thickness and dielectric constant of the CeO_2 and Si films, as indexed, V_{EFM} is the bias applied to the tip, and a is the area of the charged region. Simple modeling predicts the EFM image of a localized charge to be 56 nm FWHM, with an area $a = 2450$ nm^2. The first term in the bracket in Eq. 1 is found to be negligibly small [8], and the last term provides a constant background independent of the charge. Using only the middle term and the values given above, an approximation to the localized stored charge is then given by $q = 43\Delta\phi$ e/deg. Computing the total stored charge in our EFM images of area A, we find $Q = q(A/a)$ e. For our array of dots in Fig. 2, we compute the total stored charge on the largest dot ($\Delta\phi = 0.57°$, $a = 9000$ nm^2) to be $Q = 90$ e, and the total stored charge on our smallest dots ($\Delta\phi = 0.11°$, $a = 2640$ nm^2) to be $Q = 5$ e.

To examine the time evolution of the total stored charge, Q, a total of three structures were studied with varied lower CeO_2 barrier thickness: a 35 Å CeO_2/25 Å Si/35 Å CeO_2 sample, a reduced barrier 35 Å CeO_2/25 Å Si/15 Å CeO_2 sample, and a 35 Å CeO_2 control with no lower barrier. In each case, charge dots were written to the structures and monitored until they were no longer detectable by our EFM. After writing at $V_{tip} = 10$ V, $z = 3$ nm, and $t = 60$ s, the resultant charge dots were continuously imaged at $V_{tip} = 1$ V and $z = 30$ nm at a read speed of 21 reads/hr for the first 4 hrs, after which imaging was performed intermittently for the remainder of the experiment. Charge decay time constants, τ, were then extracted by an exponential fit to the data. In all cases, the general trend was for a leakage of charge accompanied by a slow spreading of the charge dots, as seen in Fig. 1 (B,C). In the cases of the control and the reduced barrier samples, charge decay was relatively quick with lifetimes of $\tau \sim 0.2$ hrs and $\tau \sim 0.3$ hrs, respectively. However, in the case of the full 35 Å CeO_2 lower barrier sample, the charge remained detectable for $t > 40$ hrs, with an initial decay time constant $\tau \sim 9.5$ hrs for the first 10 hrs, followed by a period of much slower decay with $\tau > 24$ hrs. Additionally, as the charge lifetime is found to be invariant to whether the tip was continuously or intermittently engaged, charge leakage back to the EFM tip is ruled out, and the primary decay mechanism is determined to be tunneling through the lower barrier into the Si substrate. Furthermore, the ability to store charge in the control sample indicates that charge is being stored at crystalline defects within the upper CeO_2 barrier or at the upper CeO_2/Si interface, ruling out the polycrystalline Si well as a potential storage site.

CONCLUSION

In conclusion, an EFM was used to write and image localized dots of charge to double barrier CeO_2/Si structures. By applying tip voltages of $V_{tip} = 6 - 10$ V and reducing the tip to sample separation to $z = 3 - 5$ nm for write times of $t = 30 - 60$ s, charge dots $60 - 250$ nm FWHM have been written. An array of charge dots of different size and local charge densities was written, and the dependence of charge dot size and total stored charge on various writing parameters such as tip bias, tip to sample separation, and write time has been examined. The total stored charge may be varied from $Q = 5 - 200$ e per charge dot by appropriate selection of write conditions. These charge dots are shown to be stable over periods of time greater than a day, with a maximum charge decay time constant of $\tau \sim 9.5$ hrs exhibited in a sample with a 35 Å CeO_2 lower barrier.

ACKNOWLEDGEMENTS

References

[1] T. Inoue, Y. Yamamoto, S. Koyama, S. Suzuki, Y. Ueda, Appl. Phys. Lett. **56**, 1332 (1990).

[2] L. Luo, X. Wu, R. Dye, R. Muenchausen, S. Foltyn, Y. Coulter, C. Maggiore, T. Inoue, Appl. Phys. Lett. **59**, 2043 (1991).

[3] T. Inoue, Y. Yamamoto, M. Satoh, A. Ide, S. Katsumata, Thin Solid Films **281-282**, 24 (1996).

[4] T. Chikyow, S. Bedair, L. Tye, N. El-Masry, Appl. Phys. Lett. **65**, 1030 (1994).

[5] S. Yaegashi, T. Kurihara, H. Hoshi, H. Segawa, Jpn. J. Appl. Phys. **33**, 270 (1994).

[6] J. Jones, E. Croke, C. Garland, O. Marsh, T. McGill, J. Vac. Sci. Technol. B **16**, 2686 (1998).

[7] J. Jones, P. Bridger, O. Marsh, T. McHill, Appl. Phys. Lett. **75**, 1326 (1999).

[8] D. Schaadt, E. Yu, S. Sankar, A. Berkowitz, Appl. Phys. Lett. **74**, 472 (1999).

[9] Dror Sarid, Scanning Force Microscopy, Oxford University Press, New York, 1991.

[10] W. Nabhan, B. Equer, A. Broniatowski, G. DeRosny, Rev. Sci. Inst. **68**, 3108 (1997).

[11] M. Nonnenmacher, M.P. O'Boyle, H.K. Wickramasinghe, Appl. Phys. Lett. **58**, 2921 (1991).

AUTHOR INDEX

338

SUBJECT INDEX

ab initio calculation, 33
AlGaAs heterostructures, 207
anodic oxidation, 313
arsenic interstitial, 33
atomic(-)
    beam, 293
    force microscopy, 195, 319
    level stresses, 269

ballistic electron emission spectroscopy, 207
beam-induced deposition, 305
block copolymers, 169

cantilever, 189
carbon dioxide, 169
CdTe, 245
cerium oxide, 331
chrome mask, 147
cluster model, 233
CVD, 169, 257
cyclo-olefin polymers, 23

defect formation, 263
density functional theory, 215, 245
desorption, 257
diffusion, 155
distribution, 155
domain boundaries, 59
droplet migration, 201

elastic properties, 215
electron
    beam, 33, 85, 147, 293, 305
    proximity effect, 97
electrostatic force microscopy, 331
epitaxial growth, 71
etching, 163, 195
excess arsenic, 233

force-distance, 189
fullerene, 103, 115

gate technology, 283
germanium, 77
growth, 251
    mechanism, 71, 263

heterostructure, 331
holography, 293
hot-electron transport, 207
hydrogen, 257
    coverage, 251

imaging, 33
InAs/GaAs mesa, 269
InGaN, 215
interface roughness, 223
ion beam analysis, 155
iron oxide nanorods, 97

ketal, 147
kinetic model, 251, 257

line-edge roughness, 135
liquid crystal, 129
lithography, 11, 23, 33, 183, 325
    electron
        beam, 103, 129, 135, 283
        projection, 97
    ion projection, 3
    photo, 313
local oxidation, 319

magnetic storage media, 3
material diffusion, 201
metal
    electrode, 319
    on oxide, 71
metallic superlattices, 275
methanofullerene, 115
migration process, 269
molecular
    dynamics, 251, 263, 269
    electronics, 45
    wires, 45
Monte Carlo simulations, 239, 257

nanocomposite, 103, 169
nanodevices, 305
nanofabrication, 33, 313
nanolithography, 11, 45, 85, 103, 115, 121,
    129, 147, 305, 319
nanometer pattern-mask, 313
nanoparticle, 325
nano-patterning, 3, 313
nanostructures, 223, 239, 293
nanotransistors, 283
near-field optical microscopy, 195
non-epitaxial Au/GaAs interface, 207
non-stoichiometry, 233
nucleation, 239

optical
    characterization, 183
    fiber, 195
    tweezers, 325

organosilane, 163
oxide breakdown, 223

PEEM, 201
photoacid generators, 155
polyhedral oligosilsesquioxane
    methacrylate, 121
polymer aggregate, 135
poly(methylmethacrylate), 97
Pt-Si droplet, 201
purged UV ellipsometer, 177

quantum transport, 223

reconstruction, 59
resist, 23, 85, 103, 135, 147
    electron beam, 115, 129
    high contrast, 121
    inorganic, 305
    organic/inorganic, 97
resistless surface modification, 3

scanning
    force microscope, 189
    probe microscopy, 163
self-assembled monolayers, 85, 163
self-organization, 59
semi-empirical calculations, 275

silicon, 59, 77, 257, 263
    thin film, 251
silylation, 183
solid phase epitaxy, 263
spectroscopic ellipsometry, 177, 183
step, 59, 77
stress, 77
structure, 215
supercritical fluids, 251
surface growth, 239
synthesis, 45

temperature difference, 201
thin polymer films, 155
top surface imaging, 183
triphenylene, 129

ultra-thin oxide, 223

vacuum ultraviolet light, 163
valence force field, 215
vicinal surface, 77

x-ray, 11

ZnS, 245
zone plates, 11